



---

# Re-Examining Minimum Reinforcement Requirements for Shear Design: Final Report

Technical Report 0-7114-R1

---

Cooperative Research Program

TEXAS A&M TRANSPORTATION INSTITUTE  
COLLEGE STATION, TEXAS

sponsored by the  
Federal Highway Administration and the  
Texas Department of Transportation  
<https://tti.tamu.edu/documents/0-7114-R1.pdf>





1. Report No. <b>FHWA/TX-24/0-7114-R1</b>		2. Government Accession No.		3. Recipient's Catalog No.	
4. Title and Subtitle <b>RE-EXAMINING MINIMUM REINFORCEMENT REQUIREMENTS FOR SHEAR DESIGN: FINAL REPORT</b>				5. Report Date <b>Published: November 2024</b>	
				6. Performing Organization Code	
7. Author(s) <b>Petros Sideris, Anna Birely, Mary Beth Hueste, Stefan Hurlebaus, Maria Koliou, Stephanie Paal, Suhaib Alfaris, Nikhil Potnuru, and Wonsuh Sung</b>				8. Performing Organization Report No. <b>Report 0-7114-R1</b>	
9. Performing Organization Name and Address <b>Texas A&amp;M Transportation Institute The Texas A&amp;M University System College Station, Texas 77843-3135</b>				10. Work Unit No. (TRAIS)	
				11. Contract or Grant No. <b>Project 0-7114</b>	
12. Sponsoring Agency Name and Address <b>Texas Department of Transportation Research and Technology Implementation Office 125 E. 11<sup>th</sup> Street Austin, Texas 78701-2483</b>				13. Type of Report and Period Covered <b>Technical Report: August 2021–August 2024</b>	
				14. Sponsoring Agency Code	
15. Supplementary Notes <b>Project sponsored by the Texas Department of Transportation and the Federal Highway Administration. Project Title: Re-Examining Minimum Reinforcement Requirements for Shear Design URL: <a href="https://tti.tamu.edu/documents/0-7114-R1.pdf">https://tti.tamu.edu/documents/0-7114-R1.pdf</a></b>					
16. Abstract <b>Minimum shear reinforcement requirements in the Association of State Highway Transportation Officials Load and Resistance Factor Design (LRFD) Bridge Design Specifications are based on tests conducted on reinforced concrete panels and beams. The extension of these requirements to prestressed concrete beams has not been comprehensive and may have introduced significant conservatism in the current LRFD provisions for shear design. More accurate provisions could reduce conservatism and help maintain acceptable safety. The objective of this project was to investigate the validity of the minimum shear reinforcement requirements and develop new/revised design guidelines that can be used to inform the design process and specifications. To achieve this goal, researchers performed an extensive literature review on shear design methods and standards, synthesized a comprehensive dataset of load tests on prestressed concrete beams, complemented this dataset with full-scale tests on 22 prestressed concrete Texas Department of Transportation beam designs on 11 girder specimens as well as finite element analyses, produced data-driven analytical models of cracking and ultimate shear strength (and their ratio, termed reserved shear strength index) based on the synthesized comprehensive dataset, and developed design guidelines for minimum reinforcement requirements based on the produced models. This report describes all steps of this research study and all major findings.</b>					
17. Key Words <b>Minimum Shear Reinforcement, Prestressed Beam, Shear Tests, High-Strength Concrete, High-Strength Reinforcement</b>			18. Distribution Statement <b>No restrictions. This document is available to the public through NTIS: National Technical Information Service Alexandria, Virginia <a href="http://www.ntis.gov">http://www.ntis.gov</a></b>		
19. Security Classif. (of this report) <b>Unclassified</b>		20. Security Classif. (of this page) <b>Unclassified</b>		21. No. of Pages <b>538</b>	
				22. Price	



# **RE-EXAMINING MINIMUM REINFORCEMENT REQUIREMENTS FOR SHEAR DESIGN: FINAL REPORT**

by

Petros Sideris, Ph.D.

Associate Professor, Zachry Department of Civil and Environmental Engineering  
Assistant Research Scientist, Texas A&M Transportation Institute

Anna Birely, Ph.D.

Associate Professor, Zachry Department of Civil and Environmental Engineering  
Associate Research Scientist, Texas A&M Transportation Institute

Mary Beth Hueste, Ph.D., P.E., F.ACI

Professor, Zachry Department of Civil and Environmental Engineering  
Research Engineer, Texas A&M Transportation Institute

Stefan Hurlebaus, Ph.D., P.E.

Professor, Zachry Department of Civil and Environmental Engineering  
Research Engineer, Texas A&M Transportation Institute

Maria Koliou, Ph.D.

Associate Professor, Zachry Department of Civil and Environmental Engineering  
Assistant Research Scientist, Texas A&M Transportation Institute

Stephanie Paal, Ph.D.

Associate Professor, Zachry Department of Civil and Environmental Engineering  
Assistant Research Scientist, Texas A&M Transportation Institute

and

Suhaib Alfariis, Nikhil Potnuru, and Wonsuh Sung

Graduate Assistant Researchers, Texas A&M Transportation Institute

Report 0-7114-R1

Project 0-7114

Project Title: Re-Examining Minimum Reinforcement Requirements for Shear Design

Sponsored by the  
Texas Department of Transportation  
and the  
Federal Highway Administration

Published: November 2024

TEXAS A&M TRANSPORTATION INSTITUTE  
College Station, Texas 77843-3135



## **DISCLAIMER**

This research was sponsored by the Texas Department of Transportation (TxDOT) and the Federal Highway Administration (FHWA). The contents of this report reflect the views of the authors, who are responsible for the facts and the accuracy of the data presented herein. The contents do not necessarily reflect the official view or policies of FHWA or TxDOT. This report does not constitute a standard, specification, or regulation.

## **ACKNOWLEDGMENTS**

This project was sponsored by TxDOT and FHWA. The authors thank the project manager, Jade Adediwura, and the Project Monitoring Committee members, Zoran Umicevic, Steven Austin, Courtney Holle, Olaniyi Arowojulo, Lianxiang Du, Yi Qiu, Ahmed Al-Basha, Joe Roche, and Phillip Hempel.

The project was conducted at Texas A&M University through the Texas A&M Transportation Institute. The authors would like to acknowledge the support of Rema Taha, Madalyn Salcido, and Mary Levien. The authors would also like to acknowledge lab personnel Charlie Droddy and Kirk Martin for their support in experimental testing at the Center for Infrastructure Renewal.

# TABLE OF CONTENTS

	Page
<b>LIST OF FIGURES .....</b>	<b>xiv</b>
<b>LIST OF TABLES .....</b>	<b>xxx</b>
<b>CHAPTER 1: INTRODUCTION.....</b>	<b>1</b>
1.1    Background and Significance .....	3
1.2    Objective and Scope .....	7
1.3    Report Outline.....	8
<b>CHAPTER 2: LITERATURE REVIEW .....</b>	<b>11</b>
2.1    Failure Modes of Concrete Beams.....	11
2.1.1    Flexural Failure .....	12
2.1.2    Shear Failure .....	13
2.2    Mechanisms of Shear Transfer .....	16
2.2.1    Uncracked Compression Zone .....	17
2.2.2    Aggregate Interlock.....	18
2.2.3    Residual Tensile Stress.....	18
2.2.4    Dowel Action .....	19
2.2.5    Arch Action .....	20
2.3    Shear Strength Models.....	20
2.3.1    Truss Model.....	21
2.3.2    Compression Field Theory .....	22
2.3.3    Modified Compression Field Theory .....	25
2.4    Parameters Influencing Shear Capacity .....	28
2.4.1    Beam Depth.....	28
2.4.2    Shear Span-to-Depth Ratio.....	29
2.4.3    Longitudinal Reinforcement Content.....	30
2.4.4    Bond of the Longitudinal Reinforcement.....	31
2.4.5    Tensile Strength of Concrete.....	31
2.4.6    Level of Prestressing .....	32

2.4.7	Shear Reinforcement .....	33
2.4.8	Coarse Aggregate Size .....	34
2.4.9	Lightweight Concrete .....	35
2.5	Minimum Shear Reinforcement.....	35
2.5.1	Factors Affecting Minimum Shear Reinforcement .....	37
2.5.2	Determining the Minimum Shear Reinforcement—Key Research Studies .....	44
2.5.3	Minimum Shear Reinforcement Provisions in ACI and AASHTO Codes .....	50
2.5.4	Experimental Studies on Development of Eurocode 2 .....	54
2.5.5	Experimental Studies on Development of <i>fib</i> Model Code.....	56
2.6	Shear Design Provisions in Codes of Practice.....	58
2.6.1	AASHTO LRFD Design Specifications, 9th Edition.....	58
2.6.2	AASHTO LRFD Design Specifications, 6th Edition.....	62
2.6.3	ACI 318-19 Building Code Requirements for Structural Concrete .....	66
2.6.4	<i>fib</i> Model Code 2010.....	70
2.6.5	Eurocode 2.....	71
2.6.6	TxDOT Shear Design Specifications .....	74
2.6.7	Minimum Shear Standards for State DOTs.....	75
2.7	Summary .....	83
<b>CHAPTER 3: DATASET ANALYSIS.....</b>		<b>85</b>
3.1	Introduction.....	85
3.2	Experimental Dataset Development .....	85
3.2.1	Dataset Overview .....	85
3.2.2	Dataset Composition .....	88
3.3	Exploratory Data Analysis.....	91
3.3.1	Overview .....	91
3.3.2	Statistical Distribution of Design Variables.....	92
3.3.3	Determining Experimental Specimens from Dataset Analysis .....	96
3.3.4	Trends between Response Parameters and Design Variables .....	99
3.4	Nonlinear Regression.....	106
3.4.1	Overview .....	106
3.4.2	Optimization Problem .....	106



3.4.3	Shear Force at Onset of Diagonal Crack, $V_{cr}$ .....	107
3.4.4	Shear Force at Shear Failure, $V_{fail}$ .....	111
3.5	Genetic Programming .....	114
3.5.1	Overview .....	114
3.5.2	Genetic Programming .....	115
3.5.3	Parameters for Genetic Programming .....	117
3.5.4	Shear Force at the Onset of Diagonal Crack, $V_{cr}$ .....	118
3.5.5	Shear Force at Shear Failure, $V_{fail}$ .....	122
3.6	Summary .....	126
<b>CHAPTER 4: FULL-SCALE TESTING: DESIGN OF EXPERIMENTAL</b>		
	<b>PROGRAM .....</b>	<b>127</b>
4.1	Prototype Design.....	128
4.2	Parametric Study for Prototype Girder .....	129
4.2.1	Size of the Girder .....	130
4.2.2	Length of the Girder .....	133
4.2.3	Remarks.....	134
4.3	Test Specimens and Loading System .....	135
4.4	Test Matrix.....	136
4.4.1	Shear Reinforcement Spacing in Test Specimens.....	137
4.4.2	Effect of Deck .....	138
4.4.3	Experimental Specimens .....	139
4.4.4	Effect of Major Design Parameters via Experimental Comparisons .....	143
4.5	Summary .....	144
<b>CHAPTER 5: FULL-SCALE TESTING: CONSTRUCTION OF SPECIMENS.....</b>		<b>145</b>
5.1	Embedded Gauges on R-Bars .....	145
5.2	Casting of Girders .....	147
5.3	Concrete Material Properties .....	150
5.4	Casting of the Deck for Girder G1*.....	154
5.5	Summary .....	160
<b>CHAPTER 6: FULL-SCALE TESTING: EXPERIMENTAL TESTING OF</b>		
	<b>GIRDERS .....</b>	<b>161</b>

6.1	Test Setup .....	161
6.2	Loading Protocol.....	164
6.3	Instrumentation and Data Acquisition .....	165
6.3.1	Embedded Rebar Strain Gauges.....	166
6.3.2	Concrete Surface Strain Gauges.....	168
6.3.3	Linear Variable Differential Transformers .....	170
6.3.4	String Potentiometers .....	171
6.3.5	Data Acquisition for Sensor Arrays .....	174
6.3.6	Digital Image Correlation.....	174
6.3.7	Optotrak Motion Capture System .....	178
6.4	Testing Procedure .....	180
6.5	Summary .....	182
<b>CHAPTER 7: FULL-SCALE TESTING: OBSERVATIONS AND RESULTS .....</b>		<b>183</b>
7.1	Girder Testing and Observations .....	183
7.1.1	G1* Test .....	183
7.1.2	G1 Test .....	187
7.1.3	G2 Test .....	191
7.1.4	G3 Test .....	195
7.1.5	G4 Test .....	199
7.1.6	G5 Test .....	202
7.1.7	G6 Test .....	206
7.1.8	G7 Test .....	209
7.1.9	G8 Test .....	212
7.1.10	G9 Test .....	215
7.1.11	G10 Test .....	218
7.1.12	Full-Scale Testing Observations .....	221
7.2	Effective Comparisons.....	226
7.2.1	Effect of Deck .....	226
7.2.2	Effect of Shear Reinforcement Spacing .....	234
7.2.3	Effect of Yield Strength of R-Bars.....	244
7.2.4	Effect of Harped Strands .....	247

7.2.5	Effect of Prestressing Ratio .....	252
7.2.6	Effect of Concrete Strength .....	256
7.2.7	Effect of Shear Span-to-Depth Ratio .....	262
7.2.8	Effect of Cross-Section Depth.....	267
7.3	Summary .....	271
<b>CHAPTER 8: FINITE ELEMENT ANALYSIS PARAMETRIC STUDY.....</b>		<b>273</b>
8.1	Introduction.....	273
8.2	Model Description .....	274
8.2.1	Geometry and Meshing .....	274
8.2.2	Material Modeling.....	277
8.2.3	Defining Loading Steps.....	285
8.2.4	Constraints and Contact between Elements .....	286
8.2.5	Boundary Conditions and Loading .....	286
8.2.6	Simulation with Element Deletion .....	287
8.3	Model Comparison with the Experimental Data .....	288
8.3.1	G1* Test .....	288
8.3.2	G1 Test .....	296
8.4	Extracting Data from Finite Element Analysis.....	304
8.4.1	Cracking Shear Force .....	305
8.4.2	Maximum Shear Force .....	305
8.4.3	Inclination Angle Measurement .....	306
8.5	Parametric Study .....	307
8.5.1	Effect of Shear Reinforcement Spacing .....	308
8.5.2	Effect of Deck Slab Width .....	322
8.5.3	Effect of Presence or Not of Deck Slab .....	327
8.5.4	Effect of Grade of Shear Reinforcement.....	337
8.5.5	Effect of Shear Reinforcement Size .....	343
8.5.6	Effect of Shear Span-to-Depth Ratio .....	352
8.5.7	Effect of Concrete Strength.....	359
8.5.8	Effect of Prestressing Force .....	368
8.5.9	Effect of Tendon Path .....	377

8.6	Summary .....	383
<b>CHAPTER 9: EVALUATION OF PARAMETERS AFFECTING MINIMUM</b>		
	<b>SHEAR REINFORCEMENT .....</b>	<b>385</b>
9.1	Effect of Deck Slab Presence.....	385
9.2	Effect of Shear Reinforcement Spacing.....	386
9.3	Effect of Grade of Shear Reinforcement .....	387
9.4	Effect of Size of Shear Reinforcement .....	388
9.5	Effect of Harped Strands.....	389
9.6	Effect of Prestressing .....	390
9.7	Effect of Concrete Strength .....	391
9.8	Effect of Shear Span-to-Depth Ratio .....	392
9.9	Effect of Cross-Section Depth .....	393
9.10	Summary .....	394
<b>CHAPTER 10: REFINEMENTS TO DATA-DRIVEN MODELING AND</b>		
	<b>ESTIMATION OF THE RESERVE SHEAR STRENGTH INDEX.....</b>	<b>395</b>
10.1	Refined Nonlinear Regression .....	395
10.1.1	Refinements to Nonlinear Regression Process.....	395
10.1.2	Final Nonlinear Optimization Process .....	398
10.1.3	Comprehensive Regression Model.....	402
10.1.4	Simplified Regression Model.....	406
10.2	Estimation of Reserve Shear Strength Index .....	411
10.2.1	Reliability Analysis .....	412
10.2.2	Proposed Reliability Analysis .....	413
10.2.3	Implementation of Proposed Reliability Analysis Method .....	417
10.3	Summary .....	423
<b>CHAPTER 11: DESIGN GUIDELINES FOR MINIMUM SHEAR</b>		
	<b>REINFORCEMENT.....</b>	<b>425</b>
11.1	Prototype Girders .....	425
11.2	Evaluation of Existing Provisions.....	427
11.3	Proposed Design Guidelines .....	428
11.3.1	Recommendation on Minimum Shear Reinforcement Ratio .....	428

11.3.2 Recommendation on Maximum Stirrup Spacing .....	430
11.3.3 Comparison of Proposed Guidelines with Existing Provisions.....	431
11.4 Summary .....	432
<b>CHAPTER 12: SUMMARY AND CONCLUSIONS .....</b>	<b>435</b>
12.1 Evaluation of Minimum Shear Reinforcement via Literature Review .....	436
12.2 Database Development .....	437
12.3 Full-Scale Testing .....	439
12.4 Parametric Finite Element Analysis Study .....	441
12.5 Mechanics-Informed Data-Driven Model Development .....	443
12.6 Design Guidelines for Minimum Shear Reinforcement .....	444
<b>REFERENCES.....</b>	<b>447</b>
<b>APPENDIX A: DETAILED DRAWINGS FOR THE PRESTRESSED CONCRETE</b>	
<b>GIRDER SPECIMENS .....</b>	<b>455</b>
<b>APPENDIX B: REINFORCEMENT DETAILING FOR THE DECK.....</b>	<b>497</b>
<b>APPENDIX C: DETAILED INSTRUMENTATION PLAN AND DRAWING.....</b>	<b>499</b>

## LIST OF FIGURES

	<b>Page</b>
Figure 1.1. Prestressed concrete bridge construction (Hewson 2003).....	1
Figure 1.2. Bridge condition over the last 2 decades in Texas (TxDOT 2020).....	2
Figure 1.3. Region controlled by minimum shear reinforcement based on design. ....	3
Figure 1.4. Inclined cracks and shear reinforcement (Wight 2015). ....	4
Figure 1.5. Ultimate shear failure in prestressed concrete girders (Hillebrand and Hegger 2020). ....	4
Figure 1.6. TxDOT I-girder cross-section dimensions (TxDOT 2022).....	5
Figure 2.1. Image detailing different types of failure cracks forming under loading (ACI318-19).....	12
Figure 2.2. Flexural failure in a beam (Kotsovos 1987).....	12
Figure 2.3. Diagonal tension shear failure in a beam (Robertson 1985). ....	14
Figure 2.4. Flexure-shear failure in a beam (Nguyen et al. 2019).....	14
Figure 2.5. Web shear failure in a beam (Frosch and Wolf 2003).....	15
Figure 2.6. Strand slip failure in a beam (Avendaño and Bayrak 2008). ....	16
Figure 2.7. Internal forces in a cracked beam with stirrups (MacGregor 1999).....	16
Figure 2.8. Principal stresses in the uncracked compression zone (Wight 2015).....	17
Figure 2.9. Transmitting shear stresses across crack by aggregate interlock (Walraven and Reinhardt 1981). ....	18
Figure 2.10. The Dowel effect, bent steel reinforcement bar in a crack (Bennett and Banerjee 1976).....	19
Figure 2.11. Arch action in a beam for (a) point load and (b) uniformly distributed load (Ismail 2016).....	20
Figure 2.12. Shear test on a beam showing the shear span (Bentz et al. 2006).....	21
Figure 2.13. Truss analogy model for concrete beams (Vecchio and Collins 1988).....	22
Figure 2.14. Strains in a cracked concrete element in a reinforced concrete beam (Vecchio and Collins 1982).....	23
Figure 2.15. Basics of CFT (Mitchell and Collins 1974). ....	24

Figure 2.16. Average and principal stresses in a concrete element (Vecchio and Collins 1986). .....	26
Figure 2.17. Basics of MCFT (Vecchio and Collins 1986). .....	27
Figure 2.18. Effect of beam height and coarse aggregate size on shear stress (Shioya 1989). ....	28
Figure 2.19. Response of beams under different $a/d$ (Hu and Wu 2018). .....	29
Figure 2.20. Reserve strength variation for beams with varying longitudinal reinforcement content (Lee and Kim 2008). .....	30
Figure 2.21. Effect of concrete compressive strength on the shear strength of (a) RC beams without shear reinforcement and (b) with shear reinforcement (Angelakos et al. (2001)). .....	32
Figure 2.22. Effect of concrete strength on shear force capacity of reinforced concrete beams without shear reinforcement (Ismail 2016). .....	32
Figure 2.23. Load-versus-midspan deflection curves: (a) effect of concrete strength; (b) effect of prestressing force; and (c) effect of shear reinforcement ratio (Teoh et al. 2002). .....	33
Figure 2.24. Effect of shear reinforcement ration on the shear strength of RC beams (Rahal and Al-Shaleh 2004). .....	34
Figure 2.25. Effect of aggregate size on the shear strength of (a) RC beams without shear reinforcement and (b) with shear reinforcement (Taylor 1970). .....	34
Figure 2.26. Inclined cracks and shear reinforcement (Wight 2015). .....	36
Figure 2.27. Distribution of internal shears in a beam (modified from ASCE 426 [ACI-ASCE426 1973]). .....	36
Figure 2.28. Load versus deflection comparison for effect of concrete strength (Teoh et al. 2002). .....	38
Figure 2.29. Shear force versus deflection for varying stirrup yield strength (Munikrishna et al. 2011) .....	40
Figure 2.30. Shear force versus deflection for varying span-to-depth ratio (Hu and Wu 2018). .....	41
Figure 2.31. Comparison of crack widths for the effect of harped tendons (Hawkins and Kuchma 2007b). .....	42

Figure 2.32. Load versus deflection curves for effect of prestressing in cases with and without shear reinforcement (Kim et al. 2018). .....	43
Figure 2.33. Influence of beam depth on shear stress at failure (Shioya 1989). .....	44
Figure 2.34. Test specimens with their cross sections used by Hawkins and Kuchma (2007b). .....	48
Figure 2.35. Calculation procedure for determining $\epsilon_s$ (AASHTO 2020). .....	60
Figure 3.1. Overview of prestressed concrete shear test dataset. ....	92
Figure 3.2. Distribution of cross-section height. ....	93
Figure 3.3. Distribution of shear span over effective depth for total dataset. ....	93
Figure 3.4. Distribution of compressive strength of concrete for total dataset. ....	94
Figure 3.5. Distribution of effective prestress in concrete for total dataset. ....	94
Figure 3.6. Distribution of transverse reinforcement spacing for stirrup dataset. ....	95
Figure 3.7. Distribution of transverse reinforcement spacing over effective depth for stirrup dataset. ....	95
Figure 3.8. Distribution of stirrup ratio for stirrup dataset. ....	96
Figure 3.9. Yield strength of shear reinforcement versus (a) cross-section height and (b) concrete compressive strength. ....	97
Figure 3.10. Stirrup spacing ratio versus cross-section height. ....	98
Figure 3.11. Shear span-to-depth ratio versus cross-section height. ....	98
Figure 3.12. Effective prestressing force ratio versus cross-section height. ....	99
Figure 3.13. Normalized shear stress at diagonal crack versus effective depth. ....	100
Figure 3.14. Normalized shear stress at shear failure versus effective depth. ....	100
Figure 3.15. Normalized shear stress at diagonal crack versus shear-span-to-effective-depth ratio. ....	101
Figure 3.16. Normalized shear stress at shear failure versus shear-span-to-effective-depth ratio. ....	101
Figure 3.17. Normalized shear stress at diagonal crack versus effective shear stress in concrete. ....	102
Figure 3.18. Normalized shear stress at shear failure versus effective shear stress in concrete. ....	102
Figure 3.19. Normalized shear stress at diagonal crack versus stirrup spacing. ....	103



Figure 3.20. Normalized shear stress at shear failure versus stirrup spacing. ....	103
Figure 3.21. Normalized shear stress at diagonal crack versus stirrup spacing over effective depth ratio. ....	104
Figure 3.22. Normalized shear stress at shear failure versus stirrup spacing over effective depth ratio. ....	105
Figure 3.23. Normalized shear stress at diagonal crack versus shear reinforcement ratio. ....	105
Figure 3.24. Normalized shear stress at shear failure versus shear reinforcement ratio. ....	106
Figure 3.25. Train, test data split result for normalized shear force at the diagonal crack. ....	109
Figure 3.26. Train dataset: (a) predicted versus actual normalized shear stress at onset of diagonal cracking, (b) predicted versus actual shear force at onset of diagonal cracking, and (c) zoom-in plot of (b) plot up to 50 kips. ....	110
Figure 3.27. Test dataset: (a) predicted versus actual normalized shear stress at onset of diagonal cracking, (b) predicted versus actual shear force at onset of diagonal cracking, and (c) zoom-in plot of (b) plot up to 50 kips. ....	111
Figure 3.28. Train, test data split result for shear force at shear failure. ....	112
Figure 3.29. (a) Predicted versus actual shear stress at shear failure of train dataset, and (b) zoom-in plot of (a) plot up to 200 kips. ....	113
Figure 3.30. (a) Predicted versus actual shear stress at shear failure of the test dataset, and (b) zoom-in plot of (a) plot up to 200 kips. ....	114
Figure 3.31. Typical crossover operation in GP (Gandomi et al. 2010). ....	116
Figure 3.32. Typical mutation operation in GP (Gandomi et al. 2010). ....	116
Figure 3.33. Flowchart for GP (Koza 1994). ....	117
Figure 3.34. Fitness value change as generation increases ( $V_{cr}$ ). ....	120
Figure 3.35. GP results for the train dataset: (a) predicted versus actual shear stress at the onset of diagonal cracking, and (b) zoom-in plot of (a) plot up to 50 kips. ....	121
Figure 3.36. GP results for the test dataset: (a) predicted versus actual shear stress at the onset of diagonal cracking, and (b) zoom-in plot of (a) plot up to 50 kips. ....	121
Figure 3.37. Distribution of ratio of predicted over actual shear stress at the onset of diagonal crack of total dataset. ....	122
Figure 3.38. Fitness value change as generation increases ( $V_{fail}$ ). ....	124

Figure 3.39. GP results for (a) predicted versus actual shear stress at shear failure for the train dataset, and (b) zoom-in plot of (a) plot up to 100 kips. ....	124
Figure 3.40. GP results for (a) predicted versus actual shear stress at shear failure for test dataset, and (b) zoom-in plot of (a) plot up to 100 kips. ....	125
Figure 3.41. Distribution of ratio of predicted over actual shear stress at shear failure of total dataset. ....	126
Figure 4.1. Bridge cross section (TxDOT 2022). ....	128
Figure 4.2. R-bars and S-bars used for shear reinforcement. ....	130
Figure 4.3. Spacing plots for economical span lengths for different girder sizes. ....	132
Figure 4.4. Spacing plots for different lengths of Tx54 girder. ....	134
Figure 4.5. Example of test specimen extraction from prototype girder. ....	136
Figure 4.6. Experimental setup of a typical girder specimen. ....	136
Figure 4.7. Parameters for $s_{v,max} = h_w / (2 \tan \theta)$ ....	138
Figure 4.8. Equivalent design between 8-ft slab and 3-ft slab. ....	139
Figure 5.1. Strain gauging of R-bars. ....	146
Figure 5.2. Protection for the strain gauge wires. ....	146
Figure 5.3. R-bar installation and verification. ....	147
Figure 5.4. Concrete pouring into the girder formwork. ....	148
Figure 5.5. Preparation and storage of concrete samples. ....	149
Figure 5.6. Slump flow test for the SCC with more than 20 in. ....	151
Figure 5.7. Sample compressive strength test on a cylinder. ....	151
Figure 5.8. Sample tests for (a) MOE, (b) STS, and (c) MOR. ....	154
Figure 5.9. Cross section of Girder G1* with the deck. ....	155
Figure 5.10. Elevation view of Girder G1* showing extent of deck. ....	156
Figure 5.11. Cross-section view of deck formwork. ....	156
Figure 5.12. Plan and elevation views for deck formwork. ....	157
Figure 5.13. Reinforcement detailing in the deck depicting layers. ....	157
Figure 5.14. Reinforcement detailing plan in the deck. ....	157
Figure 5.15. Constructed formwork and reinforcement cage for the deck. ....	158
Figure 5.16. Casting of the deck. ....	159
Figure 6.1. Test setup of a typical girder specimen. ....	161

Figure 6.2. End elevation of actuator position with respect to a girder specimen. ....	162
Figure 6.3. Drawings of standard bearing pad used at each support pedestal. ....	163
Figure 6.4. Girder test setup in the lab. ....	163
Figure 6.5. Shear force and bending moment diagrams for 4-point bending system (from Katz (2016)). ....	164
Figure 6.6. Strain gauges attached to R-bars. ....	167
Figure 6.7. Embedded strain gauge layout for half of a girder specimen. ....	167
Figure 6.8. Concrete surface strain gauge layout for half of a girder specimen. ....	169
Figure 6.9. LVDT layout for half of a girder specimen. ....	170
Figure 6.10. Plan for string potentiometers for one of the girders. ....	172
Figure 6.11. DAQ system for sensor arrays. ....	174
Figure 6.12. Parametric study for DIC speckle pattern. ....	176
Figure 6.13. Pixels versus speckle diameter for DIC. ....	176
Figure 6.14. Camera distance versus span covered for DIC. ....	176
Figure 6.15. Speckle pattern painted on the web surface. ....	177
Figure 6.16. Plan for the DIC and Optotrak systems. ....	178
Figure 6.17. Sample Optra target layout. ....	179
Figure 6.18. Final DIC setup for one side of the girder. ....	179
Figure 6.19. Final Optotrak setup for one side of girder. ....	180
Figure 6.20. Instrumented girder with sensor arrays. ....	181
Figure 6.21. Final setup of the girder before testing. ....	181
Figure 7.1. West side of G1* at cracking load. ....	184
Figure 7.2. East side of G1* at cracking load. ....	184
Figure 7.3. West side of G1* after ultimate failure. ....	185
Figure 7.4. East side of G1* after ultimate failure (after unloading). ....	186
Figure 7.5. Shear force versus displacement plots for G1* girder (west and east sides). ....	187
Figure 7.6. West side of G1 girder at cracking load. ....	188
Figure 7.7. East side of G1 girder at cracking load. ....	189
Figure 7.8. West side of G1 girder at ultimate failure. ....	189
Figure 7.9. East side of G1 girder at ultimate failure. ....	190
Figure 7.10. Shear force versus displacement plots for G1 girder (west and east). ....	190

Figure 7.11. West side of G2 girder at cracking load. ....	192
Figure 7.12. East side of G2 girder at cracking load. ....	192
Figure 7.13. West side of G2 girder at ultimate failure. ....	193
Figure 7.14. East side of G2 girder at ultimate failure.....	193
Figure 7.15. Detailed damage at ultimate failure in G2 west. ....	194
Figure 7.16. Shear force versus displacement plots for G2 girder (west and east).....	195
Figure 7.17. West side of G3 girder at cracking load. ....	196
Figure 7.18. East side of G3 girder at cracking load. ....	197
Figure 7.19. West side of G3 girder at ultimate failure. ....	198
Figure 7.20. East side of G3 girder at ultimate failure.....	198
Figure 7.21. Shear force versus displacement plots for G3 girder (west and east).....	199
Figure 7.22. West side of G4 girder at cracking load. ....	200
Figure 7.23. East side of G4 girder at cracking load. ....	200
Figure 7.24. West side of G4 girder at ultimate failure. ....	201
Figure 7.25. East side of G4 girder at ultimate failure.....	201
Figure 7.26. Shear force versus displacement plots for G4 girder (west and east).....	202
Figure 7.27. West side of G5 girder at cracking load. ....	203
Figure 7.28. East side of G5 girder at cracking load. ....	204
Figure 7.29. West side of G5 girder at ultimate failure. ....	204
Figure 7.30. East side of G5 girder at ultimate failure.....	205
Figure 7.31. Shear force versus displacement plots for G5 girder (west and east).....	205
Figure 7.32. West side of G6 girder at cracking load. ....	207
Figure 7.33. East side of G6 girder at cracking load. ....	207
Figure 7.34. West side of G6 girder at ultimate failure. ....	208
Figure 7.35. East side of G6 girder at ultimate failure.....	208
Figure 7.36. Shear force versus displacement plots for G6 girder (west and east).....	209
Figure 7.37. West side of G7 girder at cracking load. ....	210
Figure 7.38. East side of G7 girder at cracking load. ....	210
Figure 7.39. West side of G7 girder at ultimate failure. ....	211
Figure 7.40. East side of G7 girder at ultimate failure.....	211
Figure 7.41. Shear force versus displacement plots for G7 girder (west and east).....	212

Figure 7.42. West side of G8 girder at cracking load. ....	213
Figure 7.43. East side of G8 girder at cracking load. ....	213
Figure 7.44. West side of G8 girder at ultimate failure. ....	214
Figure 7.45. East side of G8 girder at ultimate failure.....	214
Figure 7.46. Shear force versus displacement plots for G8 girder (west and east).....	215
Figure 7.47. West side of G9 girder at cracking load. ....	216
Figure 7.48. East side of G9 girder at cracking load. ....	216
Figure 7.49. West side of G9 girder at ultimate failure. ....	217
Figure 7.50. East side of G9 girder at ultimate failure.....	217
Figure 7.51. Shear force versus displacement plots for G9 girder (west and east).....	218
Figure 7.52. West side of G10 girder at cracking load. ....	219
Figure 7.53. East side of G10 girder at cracking load. ....	219
Figure 7.54. West side of G10 girder at ultimate failure. ....	220
Figure 7.55. East side of G10 girder at ultimate failure.....	220
Figure 7.56. Shear force versus displacement plots for G10 girder (west and east).....	221
Figure 7.57. Cracking shear strength ratio comparison between experimental tests, ACI, and AASHTO.....	224
Figure 7.58. Ultimate shear strength ratio comparison between experimental tests, ACI, AASHTO, and finite element method (FEM).....	225
Figure 7.59. Shear force versus displacement comparison of G1*-W versus G1-W. ....	228
Figure 7.60. Shear force versus displacement comparison of G1*-E versus G1-E. ....	228
Figure 7.61. Interface slip of deck in G1* girder.....	231
Figure 7.62. Comparison of girder profile at cracking and ultimate: G1* versus G1. ....	233
Figure 7.63. Shear force versus displacement comparison: G1-W versus G2-W versus G2-E. ....	235
Figure 7.64. Shear force versus displacement comparison: G3-W versus G3-E.....	235
Figure 7.65. Shear force versus displacement comparison: G7-W versus G7-E.....	237
Figure 7.66. Shear force versus displacement comparison: G8-W versus G8-E.....	237
Figure 7.67. Shear force versus displacement comparison: G10-W versus G10-E.....	238
Figure 7.68. Shear force versus displacement comparison: G1*-W versus G1*-E.....	245
Figure 7.69. Shear force versus displacement comparison: G1-W versus G1-E.....	245

Figure 7.70. Shear force versus displacement comparison: G1-W versus G3-E.....	249
Figure 7.71. Shear force versus displacement comparison: G2-E versus G3-W.....	249
Figure 7.72. Shear force versus displacement comparison: G5-E versus G2-W versus G6-W.....	253
Figure 7.73. Shear force versus displacement comparison: G5-W versus G2-E versus G6-E.....	253
Figure 7.74. Shear force versus displacement comparison: G1-W versus G7-E versus G8-E.....	258
Figure 7.75. Shear force versus displacement comparison: G2-E versus G7-W versus G8-W.....	258
Figure 7.76. Shear force versus displacement comparison: G4-E versus G1-W versus G9-E.....	263
Figure 7.77. Shear force versus displacement comparison: G4-W versus G2-W versus G9-W.....	263
Figure 7.78. Shear force versus displacement comparison: G10-E versus G1-W.....	268
Figure 7.79. Shear force versus displacement comparison: G10-W versus G2-W. ....	268
Figure 8.1. Three-dimensional view of the girder with strands and reinforcement.....	274
Figure 8.2. Relationship between FE size and error. ....	275
Figure 8.3. 3-D view of model mesh. ....	276
Figure 8.4. Meshing of steel reinforcement: (a) R-bars and (b) S-bars. ....	276
Figure 8.5. Compressive stress–strain relationship (Behnam et al. 2018).....	278
Figure 8.6. Compressive behavior for concrete. ....	280
Figure 8.7. Uniaxial tensile-stress–strain relationship for concrete.....	280
Figure 8.8. Transition points along the three-point bending beam load-displacement curve (Mirgal et al. 2023). ....	281
Figure 8.9. Modified post-peak tensile stress versus cracking displacement (fib Model Code 2010).....	282
Figure 8.10. Tensile behavior of concrete. ....	282
Figure 8.11. ABAQUS model geometry for splitting tensile test.....	283
Figure 8.12. Stress versus strain curve for mild steel Grade 60. ....	284
Figure 8.13. Stress versus strain curve for mild steel Grade 80. ....	284

Figure 8.14. Stress versus strain curve for low relaxation strands Grade 270.....	284
Figure 8.15. Boundary conditions and applied loads on FE models. ....	287
Figure 8.16. Shear force versus displacement comparison between tests and FE models for G1* girder: (a) west side, (b) east side.....	290
Figure 8.17. Results of FE model at peak load of G1* east. ....	291
Figure 8.18. Results of FE model at peak load of G1* west. ....	292
Figure 8.19. Shear force versus displacement comparison between tests and FE models for G1* girder: (a) west side, (b) east side.....	294
Figure 8.20. Results of FE model at peak load of G1* west side. ....	295
Figure 8.21. Results of FE model at peak load of G1* east side. ....	296
Figure 8.22. Shear force versus displacement comparison between tests and FE models for G1 girder: (a) west side, (b) east side.....	298
Figure 8.23. Results of FE model at peak load of G1 west side. ....	299
Figure 8.24. Results of FE model at peak load of G1 east side. ....	300
Figure 8.25. Shear force versus displacement comparison between tests and FE models for G1 girder: (a) west side, (b) east side.....	302
Figure 8.26. Results of FE model at peak load of G1 west side. ....	303
Figure 8.27. Results of FE model at peak load of G1 east side. ....	304
Figure 8.28. Tension damage at various stages of loading. ....	305
Figure 8.29. Plastic strain at various stages of loading.....	306
Figure 8.30. Axial stress in R-bars at various stages of loading.....	306
Figure 8.31. Inclination angle measurement using an online protractor.....	307
Figure 8.32. Shear force versus displacement plots for Tx54.....	310
Figure 8.33. Shear force versus displacement plots for Tx70.....	310
Figure 8.34. Tension damage in FE model at peak load for Tx54: (a) 18 in., (b) 26 in., (c) 38 in., (d) 48 in., and (e) without shear reinforcement. ....	313
Figure 8.35. Plastic strain in FE model at peak load for Tx54: (a) 18 in., (b) 26 in., (c) 38 in., (d) 48 in., and (e) without shear reinforcement. ....	314
Figure 8.36. Axial stress in R-bars in FEM at peak load for Tx54: (a) 18 in., (b) 26 in., (c) 38 in., and (d) 48 in. ....	315

Figure 8.37. Tension damage in FE model at peak load for Tx70: (a) 18 in., (b) 26 in., (c) 38 in., (d) 48 in., and (e) without shear reinforcement. ....	316
Figure 8.38. Plastic strain in FE model at peak load for Tx70: (a) 18 in., (b) 26 in., (c) 38 in., (d) 48 in., and (e) without shear reinforcement. ....	317
Figure 8.39. Axial stress in R-bars in FEM at peak load for Tx70: (a) 18 in., (b) 26 in., (c) 38 in., and (d) 48 in. ....	318
Figure 8.40. Shear force versus displacement plots for Tx54 with element deletion. ....	319
Figure 8.41. Shear force versus displacement plots for Tx70 with element deletion. ....	320
Figure 8.42. Tension damage in FE with element deletion model at peak load for Tx54: (a) 18 in., (b) 26 in., (c) 38 in., (d) 48 in., and (e) without shear reinforcement. ....	321
Figure 8.43. Tension damage in FE with element deletion model at peak load for Tx70: (a) 18 in., (b) 26 in., (c) 38 in., (d) 48 in., and (e) without shear reinforcement. ....	322
Figure 8.44. Shear force versus displacement plots for Tx54. ....	323
Figure 8.45. Shear force versus displacement plots for Tx70. ....	324
Figure 8.46. Tension damage in FE model at peak load for Tx54: (a) 3-ft deck slab, and (b) 8-ft deck slab. ....	325
Figure 8.47. Plastic strain in FE model at peak load for Tx54: (a) 3-ft deck slab, and (b) 8-ft deck slab. ....	325
Figure 8.48. Axial stress in R-bars in FE model at peak load for Tx54: (a) 3-ft deck slab, and (b) 8-ft deck slab. ....	326
Figure 8.49. Tension damage in FE model at peak load for Tx70: (a) 3-ft deck slab, and (b) 8-ft deck slab. ....	326
Figure 8.50. Plastic strain in FE model at peak load for Tx54: (a) 3-ft deck slab, and (b) 8-ft deck slab. ....	327
Figure 8.51. Axial stress in R-bars in FE model at peak load for Tx70: (a) 3-ft deck slab and (b) 8-ft deck slab. ....	327
Figure 8.52. Shear force versus displacement plots for Tx46. ....	328
Figure 8.53. Shear force versus displacement plots for Tx54. ....	329
Figure 8.54. Shear force versus displacement plots for Tx62. ....	329
Figure 8.55. Shear force versus displacement plots for Tx70. ....	330



Figure 8.56. Tension damage in FE model at peak load for Tx46: (a) with deck slab, and (b) without deck slab.....	332
Figure 8.57. Plastic strain in FE model at peak load for Tx46: (a) with deck slab, and (b) without deck slab.....	332
Figure 8.58. Axial stress in R-bars in FE model at peak load for Tx46: (a) with deck slab, and (b) without deck slab.....	333
Figure 8.59. Tension damage in FE model at peak load for Tx54: (a) with deck slab, and (b) without deck slab.....	333
Figure 8.60. Plastic strain in FE model at peak load for Tx54: (a) with deck slab, and (b) without deck slab.....	334
Figure 8.61. Axial stress in R-bars in FE model at peak load for Tx54: (a) with deck slab, and (b) without deck slab.....	334
Figure 8.62. Tension damage in FE model at peak load for Tx62: (a) with deck slab, and (b) without deck slab.....	335
Figure 8.63. Plastic strain in FE model at peak load for Tx62: (a) with deck slab, and (b) without deck slab.....	335
Figure 8.64. Axial stress in R-bars in FE model at peak load for Tx62: (a) with deck slab, and (b) without deck slab.....	336
Figure 8.65. Tension damage in FE model at peak load for Tx70: (a) with deck slab, and (b) without deck slab.....	336
Figure 8.66. Plastic strain in FE model at peak load for Tx70: (a) with deck slab, and (b) without deck slab.....	337
Figure 8.67. Axial stress in R-bars in FE model at peak load for Tx70: (a) with deck slab and (b) without deck slab.....	337
Figure 8.68. Shear force versus displacement plots for Tx54.....	338
Figure 8.69. Shear force versus displacement plots for Tx70.....	339
Figure 8.70. Tension damage in FE model at peak load for Tx54: (a) Grade 60 ksi, and (b) Grade 100 ksi. ....	341
Figure 8.71. Plastic strain in FE model at peak load for Tx54: (a) Grade 60 ksi, and (b) Grade 100 ksi. ....	341

Figure 8.72. Axial stress in R-bars in FEM at peak load for Tx54: (a) Grade 60 ksi, and (b) Grade 100 ksi. ....	342
Figure 8.73. Tension damage in FE model at peak load for Tx70: (a) Grade 60 ksi, and (b) Grade 100 ksi. ....	342
Figure 8.74. Plastic strain in FE model at peak load for Tx70: (a) Grade 60 ksi, and (b) Grade 100 ksi. ....	343
Figure 8.75. Axial stress in R-bars in FEM at peak load for Tx70: (a) Grade 60 ksi and (b) Grade 100 ksi. ....	343
Figure 8.76. Shear force versus displacement plots for Tx54.....	344
Figure 8.77. Shear force versus displacement plots for Tx70.....	345
Figure 8.78. Tension damage in FE model at peak load for Tx54: (a) No. 3, (b) No. 4, and (c) No. 5. ....	347
Figure 8.79. Plastic strain in FE model at peak load for Tx54: (a) No. 3, (b) No. 4, and (c) No. 5. ....	348
Figure 8.80. Axial stress in R-bars in FEM at peak load for Tx54: (a) No. 3, (b) No. 4, and (c) No. 5. ....	349
Figure 8.81. Tension damage in FE model at peak load for Tx70: (a) No. 3, (b) No. 4, and (c) No. 5. ....	350
Figure 8.82. Plastic strain in FE model at peak load for Tx70: (a) No. 3, (b) No. 4, and (c) No. 5. ....	351
Figure 8.83. Axial stress in R-bars in FEM at peak load for Tx70: (a) No. 3, (b) No. 4, and (c) No. 5. ....	352
Figure 8.84. Shear force versus displacement plots for Tx54.....	353
Figure 8.85. Shear force versus displacement plots for Tx70.....	354
Figure 8.86. Tension damage in FE model at peak load for Tx54: (a) 2.5, (b) 3, and (c) 4. ....	356
Figure 8.87. Plastic strain in FE model at peak load for Tx54: (a) 2.5, (b) 3, and (c) 4. ....	356
Figure 8.88. Axial stress in R-bars in FE model at peak load for Tx54: (a) 2.5, (b) 3, and (c) 4. ....	357
Figure 8.89. Tension damage in FE model at peak load for Tx70: (a) 2.5, (b) 3, and (c) 4. ....	357
Figure 8.90. Plastic strain in FE model at peak load for Tx70: (a) 2.5, (b) 3, and (c) 4. ....	358

Figure 8.91. Axial stress in R-bars in FE model at peak load for Tx70: (a) 2.5, (b) 3, and (c) 4. ....	358
Figure 8.92. Shear force versus displacement plots for Tx54.....	360
Figure 8.93. Shear force versus displacement plots for Tx70.....	361
Figure 8.94. Tension damage in FE model at peak load for Tx54: (a) 5 ksi, (b) 8.5 ksi, and (c) 14 ksi. ....	363
Figure 8.95. Plastic strain in FE model at peak load for Tx54: (a) 5 ksi, (b) 8.5 ksi, and (c) 14 ksi. ....	364
Figure 8.96. Axial stress in R-bars in FE model at peak load for Tx54: (a) 5 ksi, (b) 8.5 ksi, and (c) 14 ksi.....	365
Figure 8.97. Tension damage in FE model at peak load for Tx70: (a) 5 ksi, (b) 8.5 ksi, and (c) 14 ksi. ....	366
Figure 8.98. Plastic strain in FE model at peak load for Tx70: (a) 5 ksi, (b) 8.5 ksi, and (c) 14 ksi. ....	367
Figure 8.99. Axial stress in R-bars in FE model at peak load for Tx70: (a) 5 ksi, (b) 8.5 ksi, and (c) 14 ksi.....	368
Figure 8.100. Shear force versus displacement plots for Tx54.....	369
Figure 8.101. Shear force versus displacement plots for Tx70.....	370
Figure 8.102. Tension damage in FE model at peak load for Tx54: (a) 13.2 percent, (b) 16.6 percent, and (c) 23.7 percent. ....	372
Figure 8.103. Plastic strain in FE model at peak load for Tx54: (a) 13.2 percent, (b) 16.6 percent, and (c) 23.7 percent. ....	373
Figure 8.104. Axial stress in R-bars in FE model at peak load for Tx54: (a) 13.2 percent, (b) 16.6 percent, and (c) 23.7 percent. ....	374
Figure 8.105. Tension damage in FE model at peak load for Tx70: (a) 13.2 percent, (b) 16.6 percent, and (c) 23.7 percent. ....	375
Figure 8.106. Plastic strain in FE model at peak load for Tx70: (a) 13.2 percent, (b) 16.6 percent, and (c) 23.7 percent. ....	376
Figure 8.107. Axial stress in R-bars in FE model at peak load for Tx70: (a) 13.2 percent, (b) 16.6 percent, and (c) 23.7 percent. ....	377

Figure 8.108. ABAQUS model geometry and reinforcement location for (a) Tx54 specimen and (b) Tx70 specimen. ....	378
Figure 8.109. Shear force versus displacement plots for Tx54.....	379
Figure 8.110. Shear force versus displacement plots for Tx70.....	379
Figure 8.111. Tension damage in FE model at peak load for Tx54: (a) straight path, and (b) harped path. ....	381
Figure 8.112. Plastic strain in FE model at peak load for Tx54: (a) straight path, and (b) harped path. ....	381
Figure 8.113. Axial stress in R-bars in FE model at peak load for Tx54: (a) straight path, and (b) harped path. ....	382
Figure 8.114. Tension damage in FE model at peak load for Tx70: (a) straight path, and (b) harped path. ....	382
Figure 8.115. Plastic strain in FE model at peak load for Tx54: (a) straight path, and (b) harped path. ....	383
Figure 8.116. Axial stress in R-bars in FE model at peak load for Tx70: (a) straight path and (b) harped path. ....	383
Figure 10.1. Predicting $V_{cr}$ higher than $V_{fail}$ problem (see dashed circle).....	397
Figure 10.2. Predicting $V_{cr}$ and $V_{fail}$ for experimental value problem.....	397
Figure 10.3. Data distribution, (a) including transverse reinforcement, (b) including transverse reinforcement after filtering, (c) not including transverse reinforcement, and (d) not including transverse reinforcement after filtering. ....	399
Figure 10.4. Predicted versus actual shear force at the onset of diagonal cracking: (a) train dataset, and (b) test dataset. ....	403
Figure 10.5. Predicted versus actual shear force at the shear failure: (a) train dataset, and (b) test dataset. ....	403
Figure 10.6. Predicted versus actual RSS index: (a) train dataset and (b) test dataset. ....	404
Figure 10.7. Predicted versus actual experimental value: (a) shear force at the onset of diagonal cracking, (b) shear force at shear, and (c) RSS index. ....	406
Figure 10.8. Predicted versus actual shear force at the onset of diagonal cracking: (a) train dataset, and (b) test dataset. ....	408

Figure 10.9. Predicted versus actual shear force at the shear failure: (a) train dataset, and (b) test dataset. ....	408
Figure 10.10. Predicted versus actual RSS index: (a) train dataset and (b) test dataset. ....	409
Figure 10.11. Predicted versus actual experimental value: (a) shear force at the onset of diagonal cracking, (b) shear force at shear, and (c) RSS index. ....	411
Figure 10.12. Model uncertainty evaluation flowchart.....	415
Figure 10.13. Reliability analysis flowchart. ....	417
Figure 10.14. Simplified explicit model: (a) histogram of C, (b) Gaussian KDE of C. ....	418
Figure 10.15. AASHTO LRFD model: (a) histogram of C, (b) Gaussian KDE of C. ....	418
Figure 10.16. Curves of $P_g < 0$ versus $A_v$ s for all girder designs, using the (a) simplified regression model, and (b) simplified AASHTO LRFD model. ....	420
Figure 10.17. $P_g < 0$ vs Mean RSS index.....	421
Figure 10.18. Stirrup spacing ( $A_v = 0.4 \text{ in}^2$ ) when $P_g < 0 = 0.25$ . ....	423
Figure 10.19. Stirrup spacing ( $A_v = 0.4 \text{ in}^2$ ) when $P_g < 0 = 0.05$ . ....	423

## LIST OF TABLES

	Page
Table 1.1. Minimum shear reinforcement ratios for TxDOT girders with other provisions. ....	6
Table 2.1. Values of $\beta$ and $\theta$ for sections with transverse reinforcement (AASHTO 2012).....	63
Table 2.2. Values of $\beta$ and $\theta$ for sections with less than minimum transverse reinforcement (AASHTO 2012).....	64
Table 2.3. Minimum shear reinforcement ratios of TxDOT I-girders with different provisions.....	75
Table 2.4. Summary of state DOT minimum shear provisions. ....	76
Table 3.1. List of past studies included in the database.....	85
Table 3.2. Content list in dataset.....	89
Table 3.3. Performance evaluations for train, test, and total dataset for the predicted $V_{cr}$ .....	111
Table 3.4. Performance evaluations for the train, test, and total datasets for predicted $V_{fail}$ . ...	114
Table 3.5. Modifiable parameters on GP Learn package (Stephens 2015). ....	118
Table 3.6. Dimensionless variables used for model for shear force at onset of diagonal crack.....	119
Table 3.7. Parameter settings of the best result ( $V_{crack}$ ). ....	119
Table 3.8. GP performance evaluations for train, test, and total dataset for predicted $V_{cr}$ . ....	122
Table 3.9. Parameters settings of the best result ( $V_{fail}$ ). ....	123
Table 3.10. GP performance evaluations of the train, test, and total datasets for computing the predicted $V_{fail}$ . ....	125
Table 4.1. Test matrix for girder specimens. ....	142
Table 5.1. Summary of concrete samples for girders. ....	150
Table 5.2. 28-day concrete compressive strength of casted girders. ....	152
Table 5.3. 28-day MOE, STS, and MOR results of casted girders.....	153
Table 5.4. 28-day concrete material testing results for deck. ....	160
Table 6.1. Sample loading protocol developed for the girder test. ....	165
Table 6.2. Summary of embedded strain gauges. ....	168
Table 6.3. Summary of concrete surface strain gauges. ....	169

Table 6.4. Summary of LVDTs. ....	171
Table 6.5. Summary of string potentiometers.....	173
Table 7.1. Design parameters for G1* girder. ....	183
Table 7.2. Design parameters for G1 girder. ....	187
Table 7.3. Design parameters for G2 girder. ....	191
Table 7.4. Design parameters for G3 girder. ....	196
Table 7.5. Design parameters for G4 girder. ....	199
Table 7.6. Design parameters for G5 girder. ....	202
Table 7.7. Design parameters for G6 girder. ....	206
Table 7.8. Design parameters for G7 girder. ....	209
Table 7.9. Design parameters for G8 girder. ....	212
Table 7.10. Design parameters for G9 girder. ....	215
Table 7.11. Design parameters for G10 girder. ....	218
Table 7.12. Summary of shear force results for all the girders.....	223
Table 7.13. Comparison of design parameters between G1* and G1.....	226
Table 7.14. Visual comparison of G1*-W versus G1-W.....	229
Table 7.15. Visual comparison of G1*-E versus G1-E. ....	230
Table 7.16. Comparison of crack measurement for G1* versus G1.....	231
Table 7.17. Comparison of design parameters for G1-W versus G2-W versus G2-E.....	234
Table 7.18. Comparison of design parameters for G3-W versus G3-E.....	234
Table 7.19. Comparison of design parameters for G7-W versus G7-E.....	236
Table 7.20. Comparison of design parameters for G8-W versus G8-E.....	236
Table 7.21. Comparison of design parameters for G10-W versus G10-E.....	236
Table 7.22. Visual comparison of G1-W versus G2-E versus G2-W.....	239
Table 7.23. Visual comparison of G3-W versus G3-E.....	240
Table 7.24. Visual comparison of G7-W versus G7-E.....	241
Table 7.25. Visual comparison of G8-W versus G8-E.....	242
Table 7.26. Visual comparison of G10-W versus G10-E.....	243
Table 7.27. Comparison of design parameters for G1*-W versus G1*-E.....	244
Table 7.28. Comparison of design parameters for G1-W versus G1-E.....	244
Table 7.29. Visual comparison of G1*-W versus G1*-E.....	246

Table 7.30. Visual comparison of G1-W versus G1-E. ....	246
Table 7.31. Comparison of design parameters for G1-W versus G3-E. ....	248
Table 7.32. Comparison of design parameters for G2-E versus G3-W. ....	248
Table 7.33. Visual comparison of G3-W versus G2-E. ....	250
Table 7.34. Visual comparison of G3-E versus G1-W. ....	251
Table 7.35. Comparison of design parameters for G5-E versus G2-W versus G6-W. ....	252
Table 7.36. Comparison of design parameters for G5-W versus G2-E versus G6-E. ....	252
Table 7.37. Visual comparison of G5-E versus G2-W versus G6-W. ....	254
Table 7.38. Visual comparison of G5-W versus G2-E versus G6-E. ....	255
Table 7.39. Comparison of design parameters for G1-W versus G7-E versus G8-E. ....	257
Table 7.40. Comparison of design parameters for G2-E versus G7-W versus G8-W. ....	257
Table 7.41. Visual comparison of G1-W versus G7-E versus G8-E. ....	259
Table 7.42. Visual comparison of G2-E versus G7-W versus G8-W. ....	261
Table 7.43. Comparison of design parameters for G4-E versus G1-W versus G9-E. ....	262
Table 7.44. Comparison of design parameters for G4-W versus G2-W versus G9-W. ....	262
Table 7.45. Visual comparison of G1-W versus G4-E versus G9-E. ....	265
Table 7.46. Visual comparison of G2-W versus G4-W versus G9-W. ....	266
Table 7.47. Comparison of design parameters for G10-E versus G1-W. ....	267
Table 7.48. Comparison of design parameters for G10-W versus G2-W. ....	267
Table 7.49. Visual comparison of G10-E versus G1-W. ....	269
Table 7.50. Visual comparison of G10-W versus G2-W. ....	270
Table 8.1. Plastic damage parameters. ....	277
Table 8.2. R-bars spacing comparison of Tx54 and Tx70 results with different code results....	312
Table 8.3. Slab width comparison of Tx54 and Tx70 results with different code results. ....	324
Table 8.4. Presence of slab comparison of Tx46, Tx54, Tx62, and Tx70 results with different code results. ....	331
Table 8.5. Grade of R-bars comparison of Tx54 and Tx70 results with different code results. ....	340
Table 8.6. Size of R-bar comparison of Tx54 and Tx70 results with different code results. ....	346
Table 8.7. Shear-span-to-depth comparison of Tx54 and Tx70 results with different code results. ....	355



Table 8.8. Material properties for concrete.....	359
Table 8.9. Compressive strength comparison of Tx54 and Tx70 results with different code results. ....	362
Table 8.10. Prestressing force comparison of Tx54 and Tx70 results with different code results. ....	371
Table 8.11. Tendon path comparison of Tx54 and Tx70 results with different code results. ....	380
Table 10.1. Performance evaluation for comprehensive complex model.....	405
Table 10.2. Performance evaluation for simplified explicit model. ....	409
Table 10.3. Statistical parameters of random variables. ....	415
Table 10.4. Design values based on TxDOT girders.....	419
Table 10.5. Statistical parameter for RSS based on target $P_g < 0$ .....	421
Table 10.6. Statistical parameter for RSS when $P_g < 0 = 0.25$ .....	422
Table 10.7. Statistical parameter for RSS when $P_g < 0 = 0.05$ .....	422
Table 11.1. Economic span lengths of TxDOT I-girders.....	426
Table 11.2. Design parameters of economical span TxDOT I-girders. ....	426
Table 11.3. Comparison of minimum shear spacing from different provisions. ....	427
Table 11.4. Comparison of minimum shear spacing from proposed guidelines. ....	432



## **CHAPTER 1:**

### **INTRODUCTION**

Prestressed concrete bridges represent a significant advancement in civil engineering, offering superior structural performance and durability compared to traditional reinforced concrete bridges. The introduction of prestressing techniques allows for the construction of longer spans, thinner sections, and more efficient use of materials. This process results in bridges that are not only stronger and more resilient to dynamic loads, such as traffic and environmental forces, but that also exhibit reduced deflections and cracking. Consequently, prestressed concrete bridges provide enhanced load-bearing capacity and longevity, reduce maintenance costs, and ensure safer, more reliable infrastructure. Their ability to withstand heavy and continuous loads makes prestressed concrete bridges ideal for modern transportation networks—which require accelerated construction techniques—due to their advantages in time and cost (Figure 1.1).

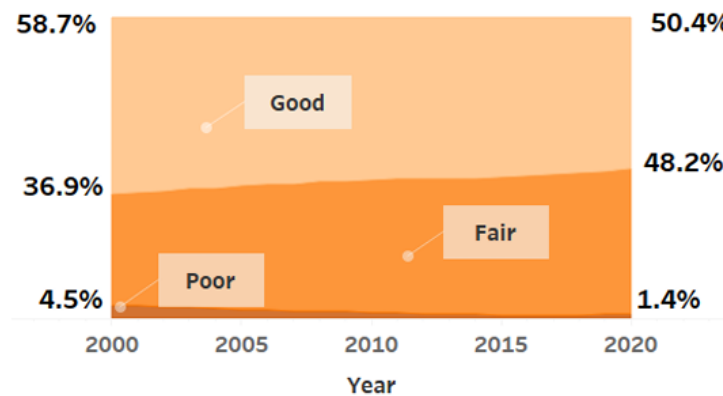


**Figure 1.1. Prestressed concrete bridge construction (Hewson 2003).**

According to the American Road and Transportation Builders Association (ARTBA) 2022 Bridge Report, there are 619,588 bridges in the United States, of which more than 108,000 are prestressed concrete structures. The data are based on the Federal Highway Administration (FHWA) National Bridge Inventory updated in 2022. The report also discussed the structural integrity of the bridges and detailed the need to replace 78,800 bridges of the total number. Further, it also reported nearly 48 percent of the total number of bridges are in fair condition, meaning they are close to their service life and show evidence of minor deterioration or cracks. These fair-condition bridges are described as being at an inflection point and might exhibit

accelerated deterioration over the next several years. The noticeable increase in this problem brings out the need for new construction that needs to be time and cost-beneficial and points in a direction toward more usage of prestressed concrete bridges.

In the *Report on Texas Bridges* by the Texas Department of Transportation (TxDOT 2020) detailing bridge statistics and inspection data, it was reported that 48.2 percent of the total number of bridges are in fair condition. The percentage of bridges in fair condition has been increasing over the past 2 decades, as shown in Figure 1.2, resulting in more bridges nearing their service lifespan. According to their report, in 2022 the number of bridges in fair condition remained almost the same, at 48.1 percent. In addition, they added that 350 bridges on average are added to Texas' inventory per year.



**Figure 1.2. Bridge condition over the last 2 decades in Texas (TxDOT 2020).**

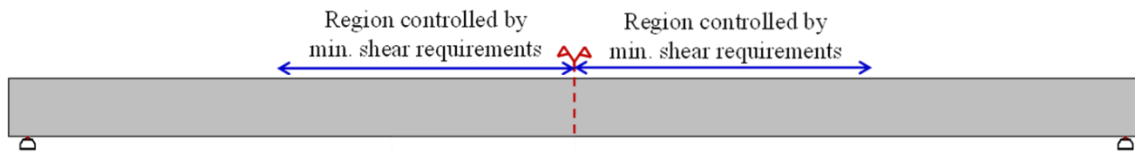
Based on the Texas' bridge bid summary for each fiscal year, prestressed concrete bridges are the main type constructed, with different types of girders like I-beams, box beams, slab beams, etc. Due to the increase in the construction of bridges and the need for repair or replacement of the bridges nearing the lifespan, the bridge design provisions need to be evaluated and revised to ensure structural integrity and safety.

The shear capacity of prestressed concrete girders depends significantly on various parameters, such as the quality of materials, the prestressing technique, the geometry of the girder, and the environmental conditions under which they operate. As infrastructure demands grow in unison with increased traffic and environmental loads, understanding the need for shear reinforcement becomes crucial. It prevents sudden and catastrophic shear failure by providing additional

strength to resist shear forces. Shear reinforcement contributes to the ductility of beams, allowing them to undergo significant deformation before failure. This reinforcement helps control crack formation and propagation, thereby maintaining structural integrity.

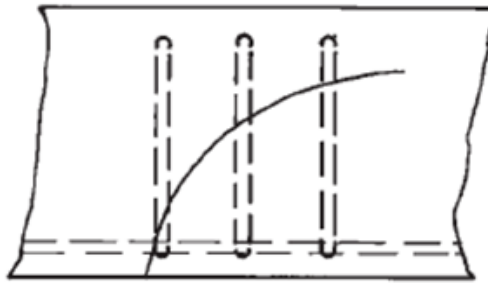
## 1.1 BACKGROUND AND SIGNIFICANCE

In the design practice, large portions of prestressed concrete girders are subjected to very low loading demands for which very low or no reinforcement can be used. Contrary to no shear reinforcement, these zones, as shown in Figure 1.3, are provided with minimum shear reinforcement, as determined by various design codes and standards.



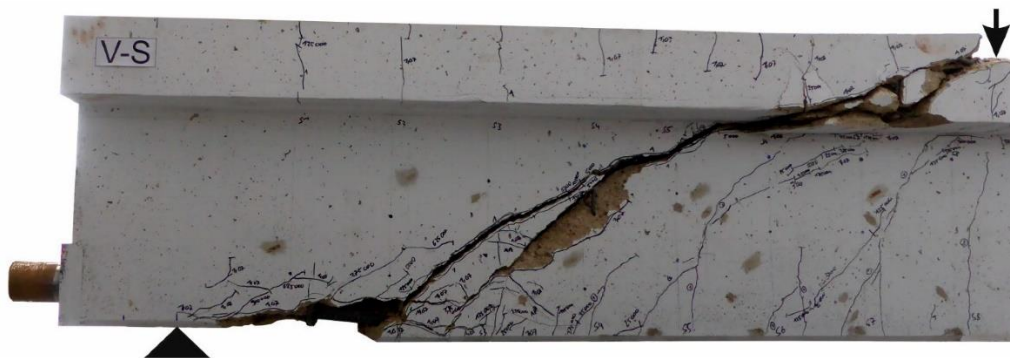
**Figure 1.3. Region controlled by minimum shear reinforcement based on design.**

The primary role of the minimum shear reinforcement (Hawkins and Kuchma 2007a; Kuchma et al. 2008) is to ensure adequate force transfer across inclined cracking (following the onset of the cracking) and restrain the growth of inclined cracking so that (a) ductility is improved and brittle shear failures that would occur upon the formation of the first diagonal cracks are avoided; (b) the concrete contribution to shear resistance,  $V_c$ , is maintained at least until yielding of the shear reinforcement; and (c) crack widths at service loads are controlled. However, this is difficult to achieve due to the low deformations that activate only low stirrup reactions. To ensure that cracks will be sufficiently arrested and crack widths may better be controlled at service loads, not only must a minimum amount of shear reinforcement (steel reinforcement ratio) be provided, the maximum stirrup spacing ( $s/d$ ) must also be limited to ensure that shear reinforcement crosses any potential diagonal crack (Hawkins and Kuchma 2007a; Kuchma et al. 2008), as shown in Figure 1.4.



**Figure 1.4. Inclined cracks and shear reinforcement (Wight 2015).**

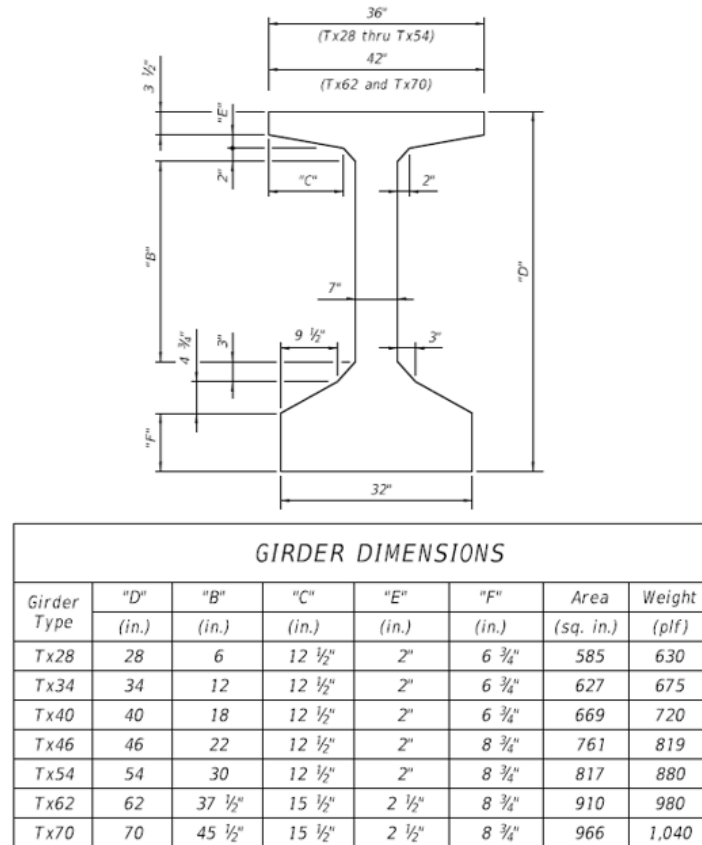
For prestressed concrete members, the minimum required amount of shear reinforcement is particularly important because large portions of their length may only contain that minimum required amount. The ACI-ASCE Committee 425 indicates that the minimum shear reinforcement does not prevent cracks from forming (Ozcebe et al. 1999) because concrete can withstand only a very small strain; however, the shear reinforcement's role comes only after the cracks have formed. After inclined cracking is formed, the stirrups start to participate in resisting the applied shear. Once the stirrups cross the crack yield, the shear contribution provided by the stirrups remains constant (or mildly increases due to strength hardening) for higher applied shear loading. Eventually, the inclined crack opens more rapidly until either the stirrups fracture, or a splitting failure occurs, or the web crushes, or the concrete compression diagonal crushes and causes significant damage to the girder (Figure 1.5).



**Figure 1.5. Ultimate shear failure in prestressed concrete girders (Hillebrand and Hegger 2020).**

TxDOT's standard usage of prestressed concrete girders includes different types of girders, such as I-beams, box beams, slab beams, U-beams, etc. The I-girders that are in practice now (Figure 1.6) were mostly introduced between 2007 to 2010, with a complete switch to the new

design by 2013. These new I-girders result in lower construction costs associated with improvements in span-to-depth ratio, wider beam spacings, and material innovations. Over the last 10 years, the TxDOT I-girders have contributed to 61 percent of total bridge construction on average, with the percentage increasing every year. This fact further emphasizes the need to evaluate the design of minimum shear reinforcement requirements due to the rapid usage of prestressed concrete girders.



**Figure 1.6. TxDOT I-girder cross-section dimensions (TxDOT 2022).**

A review of provisions in standards for the prestressed concrete bridge design and the codes of practice across the United States shows the difference in usage by each state. Considering the minimum shear reinforcement provisions from the American Association of State Highway and Transportation Officials (AASHTO; 2020) and ACI 318-19 (2019), along with the code of practice from TxDOT and other states, provides an understanding of the minimum shear reinforcement provided in the girders designed. The calculated value of minimum shear reinforcement ratio from TxDOT standards  $\rho_{v,min,TxDOT}$  for sections Tx28 and Tx34 is 0.476

percent. In contrast, the calculated value of the minimum shear reinforcement ratio based on different provisions are smaller, as shown in Table 1.1. Specifically, for Tx28 and Tx34 based on the AASHTO Load and Resistance Factor Design (LRFD), 9th edition,  $\rho_{v,min,AASHTO}$  ranges from 0.117 percent to 0.143 percent depending on the concrete compressive strength. Also,  $\rho_{v,min,ACI}$  ranges from 0.088 percent to 0.107 percent. Moreover, for deeper TxDOT I-girders,  $\rho_{v,min,TxDOT}$  is 0.317 percent, while  $\rho_{v,min,AASHTO}$  ranges from 0.117 percent to 0.148 percent, and  $\rho_{v,min,ACI}$  ranges from 0.088 percent to 0.111 percent. In addition, the usage of minimum shear reinforcement requirements is based on the AASHTO LRFD 9th edition for most of the other states, with maximum spacing limits defined differently by respective states. The difference between design recommendations and provisions in codes of practice further increases the need for this study.

**Table 1.1. Minimum shear reinforcement ratios for TxDOT girders with other provisions.**

<b>Girder</b>	<b>Provided <math>\rho_{v,min,TxDOT}</math></b>	<b><math>\rho_{v,min,AASHTO}</math></b>	<b><math>\rho_{v,min,ACI}</math></b>
Tx28	0.476	0.117-0.143	0.088-0.107
Tx34	0.476	0.117-0.137	0.088-0.103
Tx40	0.317	0.131-0.148	0.098-0.111
Tx46	0.317	0.117-0.138	0.083-0.103
Tx54	0.317	0.117-0.141	0.088-0.106
Tx62	0.317	0.117-0.147	0.088-0.110
Tx70	0.317	0.117-0.151	0.088-0.114

The motivation for this research resulted from concerns of major transportation agencies about potential over-design or insufficient design of large portions of prestressed concrete girders for which only the minimum shear reinforcement is required. This element becomes an even more challenging issue for existing bridges because decisions need to be made about their structural integrity, and often such decisions rely on the sufficiency of the minimum shear reinforcement that has already been provided.



## 1.2 OBJECTIVE AND SCOPE

Despite the critical role of shear reinforcement in maintaining the structural integrity of prestressed concrete girders, current design standards and codes of practice often rely on historical data and traditional methodologies to determine minimum shear reinforcement requirements. Consequently, these approaches may not fully encapsulate the effects of new materials, such as high-strength concrete and steel, and new design methods. Furthermore, the significant differences for minimum shear reinforcement requirements due to different standards and codes of practice adds to this uncertainty and intensifies the need for a comprehensive evaluation of the foundational assumptions and methods used to determine minimum shear reinforcement requirements.

The goal of this project was to investigate minimum shear reinforcement requirements for TxDOT bridge girders and develop new/revised guideline specifications. The research objectives toward achieving this goal were:

- Perform a literature review to synthesize a unique database of load tests for prestressed concrete beams and subsequently analyze this database to identify major design parameters and missing information that will inform an experimental program. This literature review also included an evaluation of existing codes in terms of their minimum shear reinforcement requirements.
- Conduct full-scale tests on 22 prestressed concrete TxDOT beam designs on 11 girder specimens based on a prototype study combining a range of identified design parameters to comprehensively re-examine the minimum reinforcement requirements of AASHTO LRFD Bridge Design Specifications and to account for reserve strength and ductility as well as performance under service conditions.
- Complement the findings of the experimental program by analytical/computational modeling to expand its impact.
- Develop design guidelines for the minimum reinforcement requirements based on the synthesized comprehensive dataset complemented by the full-scale tests and analytical modeling. The produced guidelines should allow for potential integration within the AASHTO LRFD Bridge Design Specifications.

### **1.3 REPORT OUTLINE**

The research report consists of 12 chapters that detail the information from the literature review, experimental program, dataset development, database analysis, finite element (FE) analysis, data-driven model development, and design guidelines.

Chapter 1 describes the background, significance, objective, and research goals of the study and briefly discussed the outline for the report.

Chapter 2 presents a comprehensive literature review of the theoretical foundations of shear failure in beams that emphasizes the necessity of minimum shear reinforcement. It examines various failure modes, mechanisms of shear transfer, and shear strength models developed for predicting shear resistance to provide a comprehensive understanding of shear reinforcement theory. The review also discusses factors influencing shear capacity and the rationale behind minimum shear reinforcement requirements, drawing insights from diverse experimental studies. Furthermore, it investigates current state-of-the-art practices in shear design and summarizes existing databases that compile experimental shear test data.

Chapter 3 discusses the development of an experimental test database on prestressed concrete beams subjected to shear failures and presents an analysis of the database to identify potential gaps in the literature and quantify the significance of various design parameters.

Chapter 4 discusses the design of the experimental program on full-scale TxDOT girders. This chapter summarizes the experimental setup, prototype design, and selection of the prototype girder for development of test specimens. Further, the development of the test matrix is discussed, and the resulting effective comparisons are noted. Chapter 5 discusses the construction of test specimens, which includes casting of girders and concrete samples for material properties. Chapter 6 presents the design of the experimental testing program on the 11 TxDOT girders, including loading protocol, instrumentation, data acquisition, and testing procedure. Chapter 7 discusses the experimental observations from the tests and presents comparisons of key parameters that are significant in shear strength and minimum shear reinforcement.

Chapter 8 describes computational modeling using FE analysis and a parametric study on major design parameters. The chapter details major steps of the FE model development, including validation with experimental data. Furthermore, significant data are extracted for the parametric study of key factors affecting minimum shear reinforcement. Chapter 9 presents overarching findings from the experimental study and FE analyses.

Chapter 10 presents the development of minimum shear reinforcement equations based on data-driven models that are further supported by reliability analysis. The minimum shear reinforcement equation is developed by using different data-driven models for the shear strength at the onset of cracking and failure, which incorporate the effects of key design parameters. The reliability analysis offers a path to introduce acceptable safety into the developed requirements.

Chapter 11 further delves into the key objective of this study, which is the development of design guidelines for minimum shear reinforcement requirements. This chapter details a comparison among various spacing provisions for design examples of TxDOT girders to identify the key differences and further details the proposed guidelines based on the experimental study and data-driven models. Chapter 12 provides the overall summary of the research report and major findings from the various tasks of this project.

The appendices of this report contain detailed drawings for the casting of experimental specimens and the deck slab casted as a part of experimental testing, and detailed instrumentation plans and drawings for a sample girder.



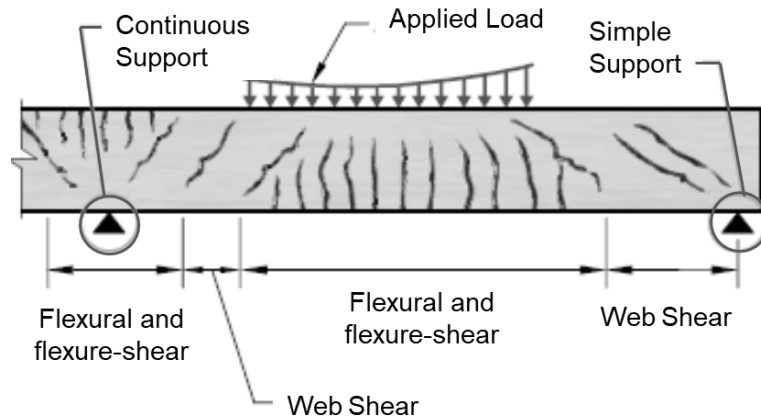
## **CHAPTER 2:**

### **LITERATURE REVIEW**

The primary aim of this project was to re-evaluate the minimum shear reinforcement requirements for the prestressed concrete beams. However, the study required a critical review of the shear behavior of concrete girders and the need for minimum shear reinforcement, along with knowledge about current state-of-the-art practices. This literature review focuses on the failure modes, the mechanisms of shear transfer and shear strength, and the corresponding models developed to predict the shear strength. It then shifts toward the parameters influencing shear capacity and the need for minimum shear reinforcement. Various experimental studies are reviewed and summarized to identify potential research findings. Furthermore, state-of-the-art practices in shear design are summarized, along with existing databases containing experimental shear test data. The first section begins with a comprehensive understanding of the failure modes in concrete beams.

#### **2.1 FAILURE MODES OF CONCRETE BEAMS**

The mode of failure in concrete beams subjected to in-plane mechanical load is determined by observing crack formation and propagation. These crack patterns align with principal compressive stresses and are normal to principal tensile stresses. In this section, major failure modes of reinforced concrete beams (Frosch and Wolf 2003) such as flexural failure, flexure-shear failure, web shear failure, and anchorage failure are discussed. Crack patterns for flexural failure, flexure-shear failure, and web shear failure mechanisms are graphically shown in Figure 2.1.



**Figure 2.1. Image detailing different types of failure cracks forming under loading (ACI318-19).**

### **2.1.1 Flexural Failure**

Flexural failures occur when the moment due to applied load exceeds the flexural capacity of a beam section. Flexural cracks initiate from the tension fiber (bottom part) of the beam in the vicinity of the section where the moment is greatest and practically propagate straight and normal to the beam axis—that is, vertically in Figure 2.2. Flexural cracks begin to appear at about 50 percent of the flexural capacity of the beam (Nawy 1996). These cracks mainly develop due to horizontal principal stresses, and as the external loading increases, further cracks start to develop, and the existing ones start to propagate to the neutral axis and eventually higher. The beam also displays a clear deflection when it is showing a flexural failure mode.



**Figure 2.2. Flexural failure in a beam (Kotsovos 1987).**

Flexural failure is classified into three types (Zwoyer 1953): first, flexural tension failure, which occurs when the beam is under-reinforced, in which case the reinforcement exceeds the yield strain and fails before the concrete fails in compression. The second type of failure is flexural compression failure, which occurs in over-reinforced concrete beams. In that case, concrete compression failure occurs in the compression zone of the beam section prior to the yield of the reinforcement. The third type of failure is when the beam is under-reinforced, whereby the reinforcement yields prior, but the final failure is due to concrete compression, and it occurs because the concrete reaches its ultimate failure strain before the steel reaches its failure strain.

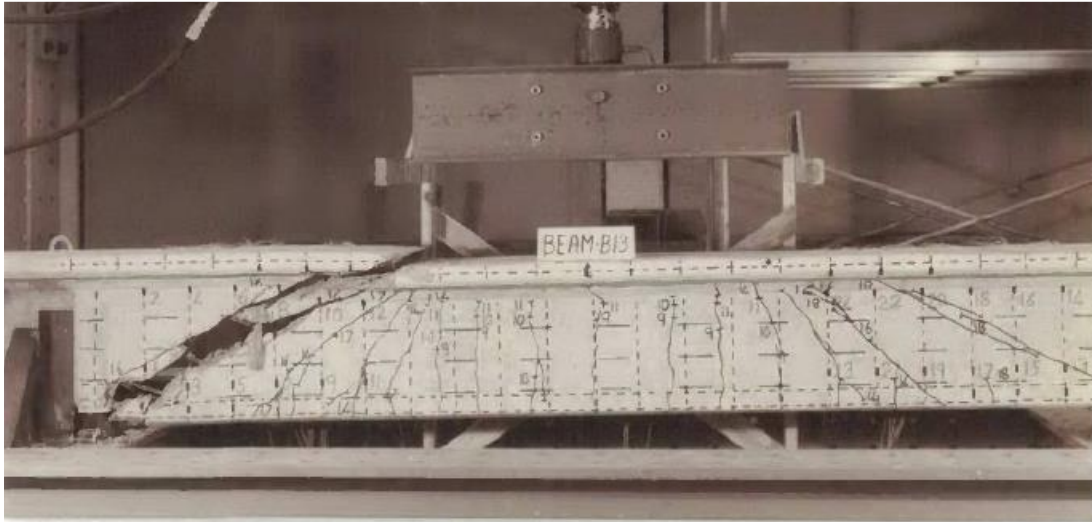
### **2.1.2 Shear Failure**

Shear failures can be dominated by different response mechanisms, such as diagonal tension and web diagonal compression crushing. Occurrence of these mechanisms depend on various parameters (see also Section 2.4), with the shear-span-to-depth ratio probably being the most influential.

#### *2.1.2.1 Diagonal Tension Shear Failure*

Diagonal tension shear failure in nonprestressed and prestressed concrete girders is dominated by inclined cracking that follows the path of the compressive principal strains. Thus, the orientation of these cracks depends on the relative magnitude of the moment over the magnitude of the shear force, which is expressed by the shear-span-to-depth ratio. Absent of shear reinforcement, diagonal tension failure is a brittle response mechanism that occurs almost instantaneously. The shear strength primarily depends on the tensile strength of the concrete material, yet other factors may play a role as well (see also Section 2.4). Shear reinforcement can be used to prevent a crack opening or to “stitch” the crack when it opens, thus increasing the shear capacity of the beam. In this case, the failure mechanisms are controlled by yielding of the stirrups. In the unlikely case the stirrups are not sufficiently anchored in the compression zone, failure may initiate from anchorage failure of the stirrups. The most commonly used theory to explain the shear response of reinforced concrete beams is the truss analogy model, which was introduced in 1899 and 1902 by the Swiss engineer Ritter and the German engineer Mörsch, respectively, in independently published papers (Hofer and McCabe 1998). Since then, various models have been developed (see Section 2.3). Diagonal tension shear failure is the most commonly observed shear failure

mechanism (Zwoyer 1953b; Yang 2014). A special case of the diagonal tension failure is the so-called **flexure-shear failure**, which essentially includes yielding of the longitudinal reinforcement that is followed by diagonal tension (shear) failure before the flexural strength of the member is reached (see Figure 2.3 and Figure 2.4).



**Figure 2.3. Diagonal tension shear failure in a beam (Robertson 1985).**

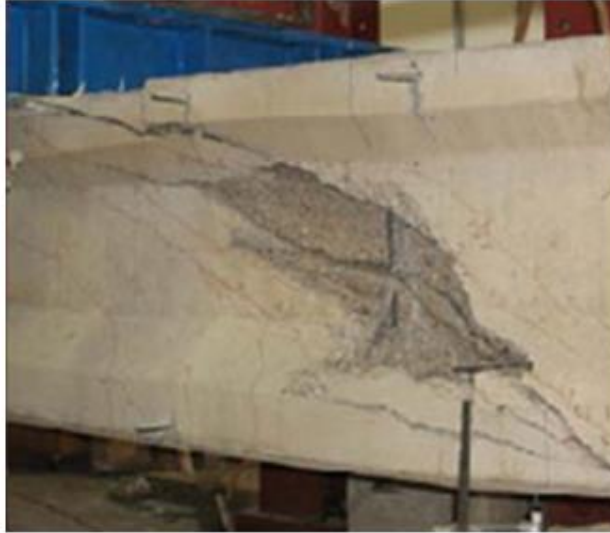


**Figure 2.4. Flexure-shear failure in a beam (Nguyen et al. 2019).**

#### *2.1.2.2 Web Compression Crushing Shear Failure*

As indicated by the truss analogy model, the compression diagonals in the web are subjected to compression as a result of equilibrium conditions. If the applied stresses exceed the compression strength of concrete, a crushing failure occurs, which is often brittle. Crushing of the compression diagonals usually occurs when large amounts of shear reinforcement are provided, which results in crushing of the concrete before the yielding of the stirrups (De Wilder 2014). Pretensioned beams are more prone to web compression crushing due to the applied axial compressive loads from the tendons (Magnusson et al. 2014). An example of a web compression crushing failure is shown in Figure 2.5.

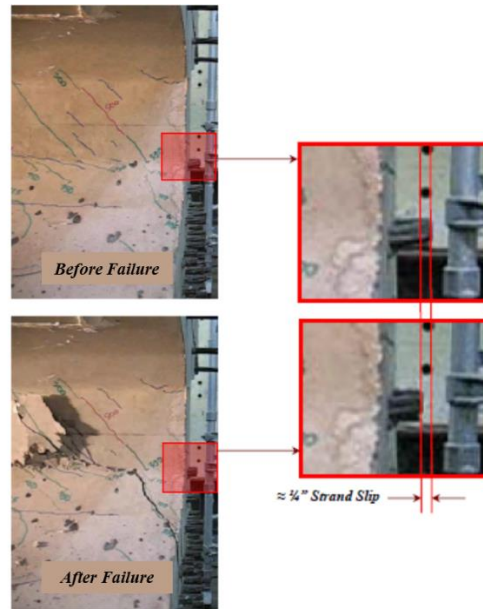




**Figure 2.5. Web shear failure in a beam (Frosch and Wolf 2003).**

#### *2.1.2.3 Tension Chord Shear Failure*

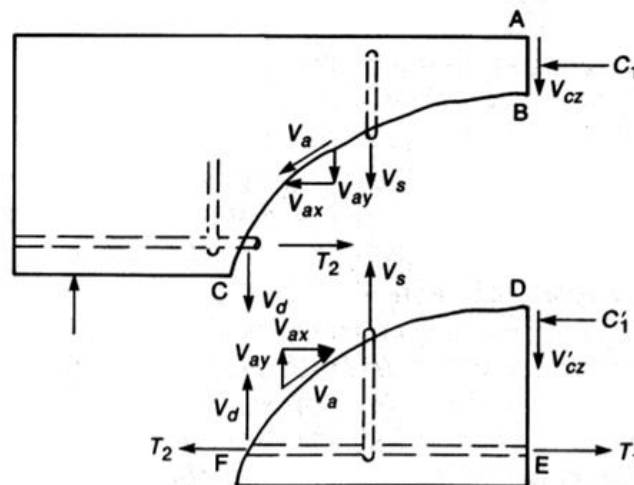
The tension (flexural) reinforcement is essential to generating the truss action of the shear response mechanisms. At the supports, tension is applied to the flexural reinforcement due to the applied shear load even when the moment demand is zero. If insufficient development length has been provided to the tension reinforcement at the supports, failure will initiate in the form of bond failure or splitting failure or dowel failure along the tension reinforcement, as shown in Figure 2.6. This form of failure is more common in deep beams, which have very low shear span-to-depth ratios ( $a/d$ ).



**Figure 2.6. Strand slip failure in a beam (Avendaño and Bayrak 2008).**

## 2.2 MECHANISMS OF SHEAR TRANSFER

The shear capacity of concrete elements results from the contribution of various shear transfer mechanisms. MacGregor (1999) summarized the contribution of various component actions in a reinforced concrete member, which can be seen in the free body diagram shown in Figure 2.7. In the diagram, shear is transferred across line A–B–C by the shear in the compression zone,  $V_{cz}$ , and across the crack by interlock of the aggregate particles,  $V_a$ , the dowel action of the longitudinal reinforcement,  $V_d$ , and by the transverse reinforcement,  $V_s$ .



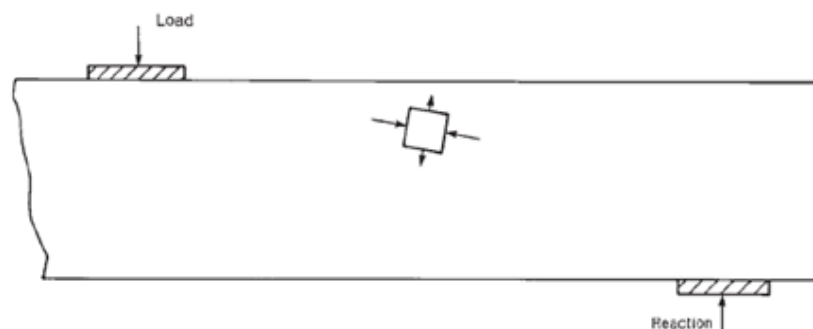
**Figure 2.7. Internal forces in a cracked beam with stirrups (MacGregor 1999).**

For concrete members with longitudinal reinforcement, there are six major mechanisms of shear transfer. These mechanisms, described in the following sections, are:

- Shear stresses in the uncracked concrete.
- The dowel effect of the longitudinal reinforcement.
- Aggregate interlock.
- The shear transferred in the stirrups.
- Residual tensile stresses transmitted directly across cracks.
- Arch action.

### 2.2.1 Uncracked Compression Zone

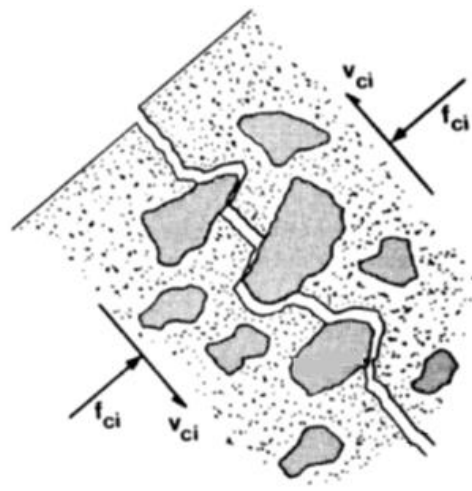
Shear forces can be transferred through the uncracked compression zone by inclined principal tensile and compressive stresses, as shown in Figure 2.8. The shear resistance of the uncracked portion of the section is determined by integrating the shear stress distribution over the uncracked compression zone. The uncracked zone, that is, the compressive zone, carries a magnitude of shear force after the emergence of the initial flexural fractures. The shear stress distribution in the compressive zone can be approximated (Yang 2014) using the elasticity theory after the boundary conditions in the compressive zone are applied. Both compressive and shearing forces are applied to the uncracked part of a cracked concrete beam. As a result, this section of the concrete beam aids in shear resistance. The depth of the uncracked concrete determines the degree of resistance.



**Figure 2.8. Principal stresses in the uncracked compression zone (Wight 2015).**

### 2.2.2 Aggregate Interlock

The effect of aggregate interlock was first presented by Fenwick and Paulay (1968), who studied the shear force capacity of concrete beams with different crack sizes and differing roughnesses of the crack surfaces. Because of the size of the aggregates, when concrete cracks, the cracking surfaces are rough and uneven. Aggregates in the cracks protrude and prevent slippage between the crack surfaces, which is known as the aggregate interlock phenomenon (Figure 2.9). The shear resistance of the concrete elements is enhanced by the contact between the fracture surfaces. The amount of shear force transferred via aggregate interlock has been found to be significantly dependent on the crack width, which is proportional to the product of crack spacing times horizontal strain (Malm 2006). As a result, any factor that influences crack spacing and horizontal strain will have an impact on the shear strength of concrete elements. Other factors affecting the shear forces transferred due to aggregate interlock are the concrete compressive strength, fracture energy, aggregate size, and the type of aggregate (Martín-Pérez and Pantazopoulou 2001; Huber et al. 2019).



**Figure 2.9. Transmitting shear stresses across crack by aggregate interlock (Walraven and Reinhardt 1981).**

### 2.2.3 Residual Tensile Stress

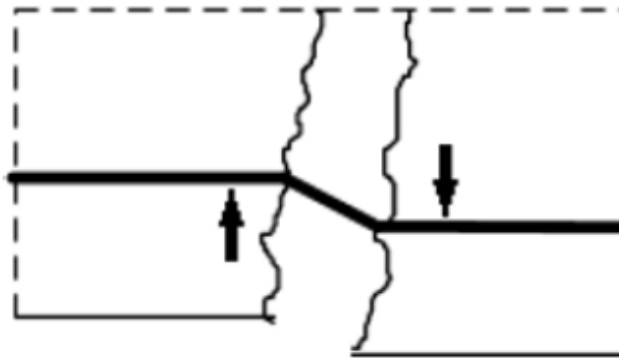
Concrete has a much smaller tensile strength than compressive strength; therefore, it is common to ignore the tensile concrete strength when considering the strength of concrete elements.

However, this is not always feasible. For example, the shear capacity of concrete beams without

shear reinforcement is primarily dependent of the concrete's tensile strength, which controls the strength of the diagonal crack; therefore, the shear strength is contributed by the concrete alone. In a study done by Evans and Marathe (1968), it was shown that concrete cracks around 0.1 mm wide have a capacity to carry a small amount of tensile stress. However, even after the development of an inclined shear crack, shear can still be transferred, and this feature depends on the aggregate interlock capacity. Once a crack in a beam has formed, all of the concrete in the crack's plane retains its ability to withstand tension. The concrete can bridge small cracks and still provide additional tensile strength across the crack width. ACI-ASCE Committee 445 indicated that these forces can exist until cracks exceed widths of 0.002–0.006 in. (0.05–0.15 mm).

#### **2.2.4 Dowel Action**

The dowel action was first investigated by Krefeld and Thurston (1966). Dowel action is generated by the longitudinal reinforcement when a shear crack intersects it. The dowel action generates vertical bearing reactions in the surrounding concrete that prevent the concrete pieces from slipping (Figure 2.10), thus increasing the shear capacity of the beam.



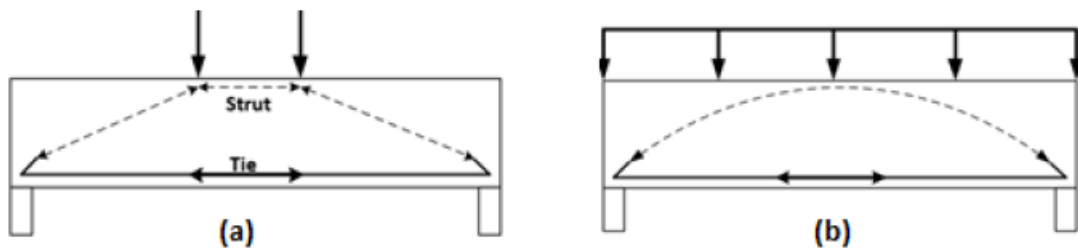
**Figure 2.10. The Dowel effect, bent steel reinforcement bar in a crack (Bennett and Banerjee 1976).**

Dowel action is limited by the tensile strength of the concrete cover that houses the reinforcement. Bennett and Banerjee (1976) showed that the diameter of the reinforcement had low impact on the dowel effect, but the amount of reinforcement had a significant impact. The amount of longitudinal reinforcement and the efficacy of transverse reinforcement in preventing splitting cracks affects the contribution of dowel action to shear resistance. Concrete cover,

concrete material properties, steel reinforcement material properties, and axial stress in the dowels all affect the dowel action (Cavagnis et al. 2018).

### 2.2.5 Arch Action

When the geometry of the beam and placement of the load allows, the force from the load may transmit directly from the point of application to the supports of the beam (Figure 2.9). This direct compression strut together with the longitudinal reinforcement creates tied arch action that helps resist shear (Kim and Jeong 2011). Arch action is primarily prevalent in beams with  $a/d$ s less than 2.5. When arch action does not contribute to shear resistance, shear is considered to be transferred by beam action. Beams with a small  $a/d$  develop a so-called arch effect in which the tensile forces are carried by the flexural reinforcement and the shear load is transported by compression to the supports. The shear load of beams with an  $a/d$  between 1 and 1.5 are fully supported by the arch effect. The arch action also differs between point load and evenly distributed load (Figure 2.11).

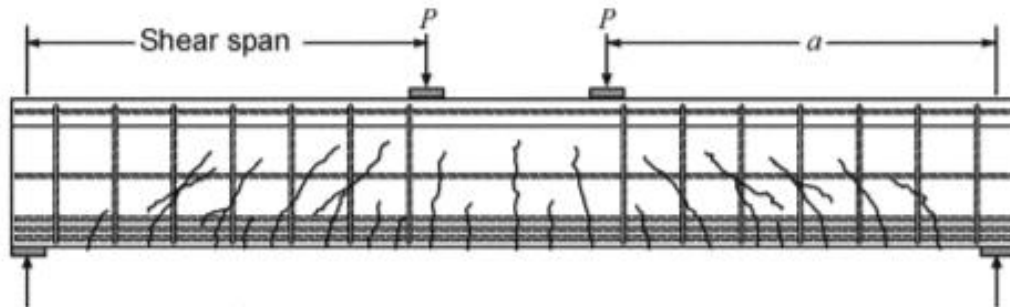


**Figure 2.11. Arch action in a beam for (a) point load and (b) uniformly distributed load (Ismail 2016).**

## 2.3 SHEAR STRENGTH MODELS

The shear behavior of Reinforced Concrete (RC) beams has been extensively examined, yet accurate predictions of the shear strength of reinforced concrete and prestressed concrete beams remain a challenge. As a result, different design code provisions in use provide different predictions of shear strength that often differ by a factor of 2 or more. The flexural strength anticipated by these identical codes, on the other hand, are unlikely to vary by more than 10 percent. However, there is no universally accepted theory for the shear behavior and predictions of shear failure in RC beams (Vecchio and Collins 1986). The next sections briefly discuss the three most popular models that have been used over the years for predictions of shear strength

and failure, namely, the truss model, the compression field theory, and the modified compression field theory (MCFT). A typical shear test is shown in Figure 2.12, which also indicates the shear span of the beam.

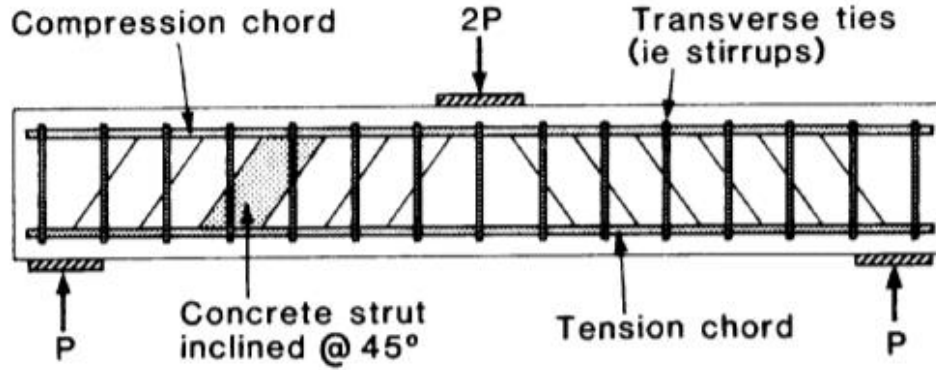


**Figure 2.12. Shear test on a beam showing the shear span (Bentz et al. 2006).**

### **2.3.1 Truss Model**

The truss model, as discussed in Runzell et al. (2007), is a theoretical model used for the estimation of shear strength in concrete beams. The truss model was introduced in 1899 and 1902 by the Swiss engineer Ritter and the German engineer Mörsch, respectively, in independently published papers (Wight 2015). When a truss is under load, the moment resistance in the truss is taken by a couple formed between compression and tensile forces in the upper and lower chords, respectively. These forces include the member forces and also the horizontal component of the diagonal members. The ability of the truss to resist the forces can be computed by finding the moment couple.

The theory considers the concrete beam is to be treated as a truss, as shown in Figure 2.13. The uncracked block forms the compression members or compression diagonals of the truss, and the longitudinal reinforcement is taken as the tensile member. The vertical members of the truss are the stirrups. The diagonal compression elements of the truss are considered to be formed in the concrete. Through these forces, and similar to the calculation of the moment couple in a truss, the moment resistance of the concrete beam section can be calculated. The vertical component of the diagonal cracks formed is treated as the shear force or the tension in the stirrups (if present). By choosing relevant parameters and applying equilibrium equations, the shear strength can be computed.



**Figure 2.13. Truss analogy model for concrete beams (Vecchio and Collins 1988).**

The truss model assumes that the compressive diagonal stresses resist the shear load in the web of the cracked concrete beam section. The flanges in the beam are pushed apart due to these diagonal stresses that are resisted by the stirrups developing the tension. The beam is estimated to carry a shear stress of  $\rho_z f_y$  after the yielding of stirrups, where  $\rho_z$  is the ratio of the shear reinforcement to area of the web, and  $f_y$  is the yield stress of the shear reinforcement.

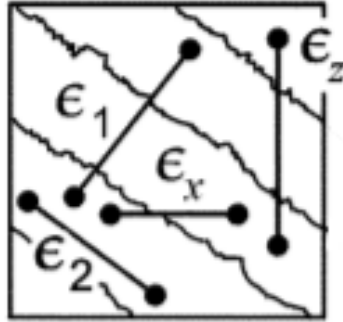
### 2.3.2 Compression Field Theory

The main shortcoming of the truss model was that the 45-degree angle model ignores the concrete tensile strength that can take the diagonal tension, thereby giving a conservative estimate for beams having a low percentage of shear reinforcement. During the 1970s and 1980s, Vecchio and Collins (1982) developed a theoretical model in which the angle  $\theta$  of the compression diagonals is variable; thus, it can be different than 45 degrees. Utilizing the truss model, the shear strength of the web could be estimated as  $\rho_z f_y \cot \theta$ . The difficulty lies in determining an appropriate value for  $\theta$ .

The compression field theory (CFT) was an important step toward the development of an acceptable theory for the prediction of shear strength. Unlike previous models, determination of  $\theta$  involves adoption of strain conditions in the web. The authors tested 30 RC beams subjected to biaxial stresses to identify the relation between diagonal compressive stresses  $f_2$  and strains  $\epsilon_2$ . The findings identified that the stress  $f_2$  also depends on the principal tensile strain  $\epsilon_1$ , as shown in Figure 2.14. They also discovered that tension existed in the cracked surface of concrete even



after extensive diagonal cracking. This tension combined with the shear stresses carried by the cracked surfaces increased the shear resistance capacity of cracked concrete (see Figure 2.15).



**Figure 2.14. Strains in a cracked concrete element in a reinforced concrete beam (Vecchio and Collins 1982).**

They proposed angle  $\theta$  be determined in this manner:

$$\tan^2 \theta = \frac{\epsilon_x + \epsilon_2}{\epsilon_z + \epsilon_2} \quad (2.1)$$

where:

$\epsilon_x$  = Longitudinal strain in the web.

$\epsilon_z$  = Transverse tensile strain in the web.

$\epsilon_2$  = Diagonal compressive strain

The strains are shown graphically for a part of the beam in Figure 2.15. Because  $\epsilon_x$  is usually much smaller than  $\epsilon_z$ , the angle  $\theta$  might be significantly smaller than 45 degrees, ultimately increasing the estimated web shear strength. Also, when the beam is under prestressing forces or axial compression, the longitudinal strain  $\epsilon_x$  significantly decreases, which reduces the angle  $\theta$  and increases the shear strength.

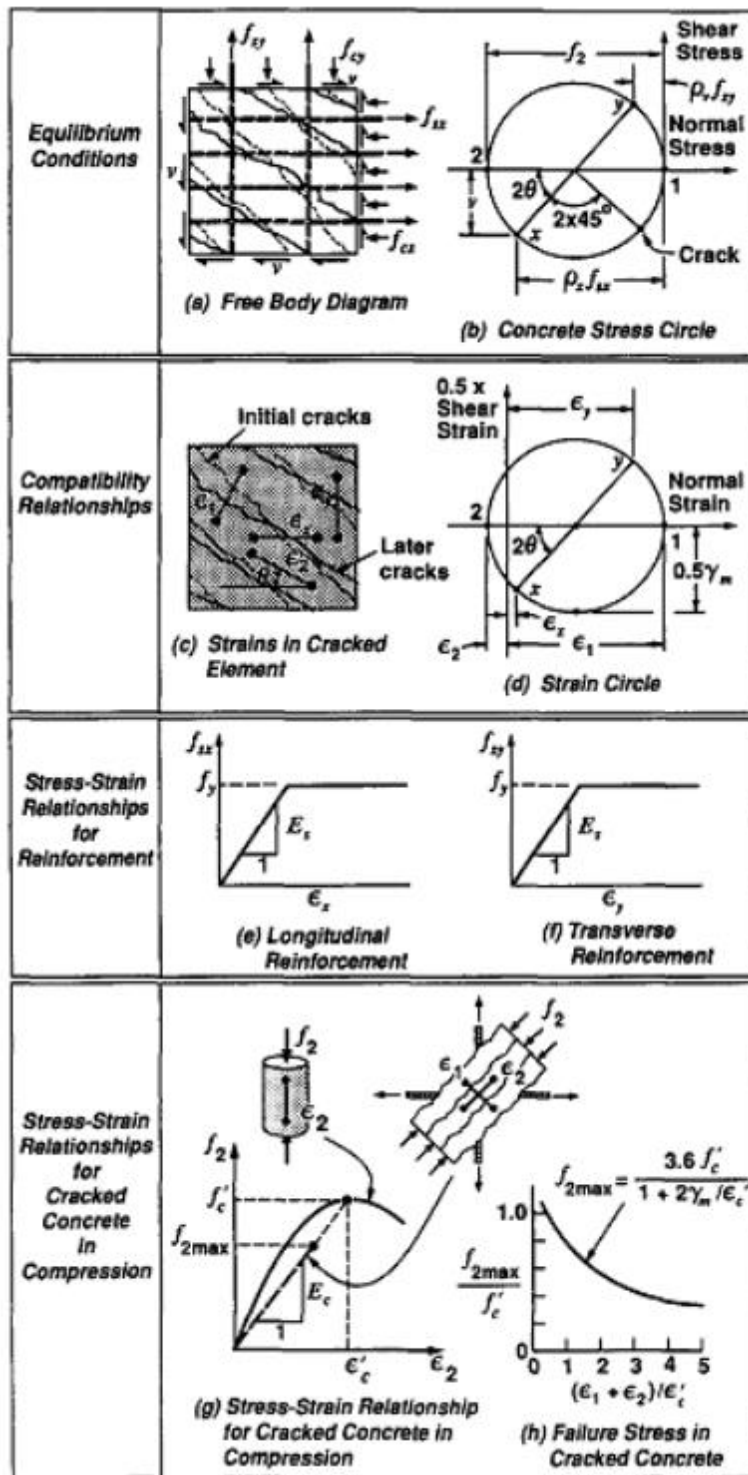


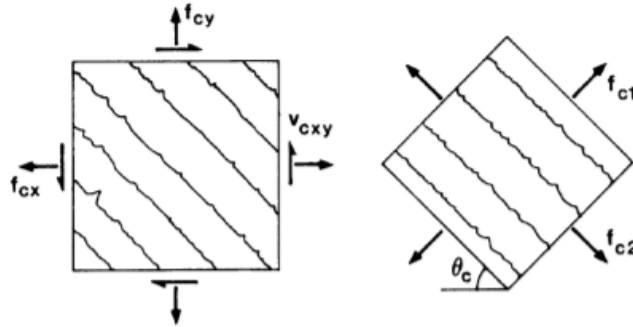
Figure 2.15. Basics of CFT (Mitchell and Collins 1974).

### 2.3.3 Modified Compression Field Theory

In 1986, Vecchio and Collins proposed the MCFT on the basis of further experimentation on RC elements subjected to pure shear. Although such experiments were more difficult to carry out, the results provided new insights on the shear behavior of reinforced concrete. The MCFT particularly focuses on building the relationship between axial and shear stresses on a concrete beam and the resulting axial and shear strains.

The key idea behind MCFT is to determine the onset of failure and the angle of the compression diagonals. Using these parameters, the role of concrete in the total shear strength can be estimated. The geometric, constitutive, and equilibrium relations of the MCFT were modified from CFT by accounting for the effect of average principal tensile stresses in the cracked concrete. Using these principles, the MCFT model accounts not only for  $V_s$  (shear strength carried by steel), but also for the combined effect of complex shear resistance mechanisms that contribute to  $V_c$  (shear strength carried by concrete) without having to consider each mechanism individually.

The MCFT states that there are two states of tensile stress that govern the constitutive relationship at the surface of a crack, which is the average state and the local state, as shown in Figure 2.16. Based on static equilibrium, the vertical component of the average principal tensile stresses must be equivalent to the vertical component of stresses on the surface of the crack. According to MCFT, the vertical component of the average tensile stress is carried by tensile tension in the shear reinforcement until the stirrups yield since the local tensile stress in the concrete at a crack face is zero. After the stirrups yield, any increase in the vertical component of the average tensile stresses must be carried by the vertical component of the shear stresses on the crack interface, otherwise known as an aggregate interlock. Therefore, the principal tensile stress  $f_1$  is dependent upon the width of the concrete cracks. The MCFT also defines a relationship wherein the width along the crack is related to the magnitude of the principal tensile strain  $\epsilon_1$  because larger  $\epsilon_1$  results in a wider crack. The tests performed by Vecchio and Collins (1986) conveyed this ratio as the average  $\epsilon_1$  to average  $f_1$ .



**Figure 2.16. Average and principal stresses in a concrete element (Vecchio and Collins 1986).**

The MCFT also includes the effect of prestressing on the average tensile strain and a method to check the tensile stresses in the longitudinal steel and the compression diagonals. Both the CFT and MCFT can predict the shear behavior of beams with shear reinforcement for all types of loading combinations. However, the CFT predicts that for members without shear reinforcement there will be no shear strength because it fails to include the contribution of the tensile strength in the cracked concrete (Hawkins 2005). This variation is due to additional consideration of the aggregate interlock mechanism in cracked concrete in the MCFT. The AASHTO LRFD 2004 provisions for shear reinforcement are based on the MCFT and have been used to date.

Several research studies have looked at the comparison between the usage of the MCFT in the shear design (AASHTO) and the method used in ACI 318. In a study by Kuchma et al. (2008b) that looked into simplified shear provisions of the AASHTO LRFD Bridge Design Specifications, a database of experimental data with 1359 beams was assembled to calculate the test versus calculated shear strength ratio. Of the many key findings, the one relevant to the minimum shear reinforcement was the shear strength ratio (test/code) was often less than 1.0 for members with a minimum amount shear reinforcement according to ACI 318-02. This finding shows the necessity of higher minimum shear reinforcement provided by AASHTO, which used the MCFT method.

In another study, Agarwal et al. (2021) looked at the reliability of reinforced concrete beams designed for shear according to the MCFT. The research looked at computing the model error when the comparison was done on an experimental database developed to include experiments with and without stirrups (168 and 368 specimens, respectively). The statistics were also developed for beams with minimum stirrups. The results showed higher reliability than the

targeted values for the case of minimum stirrups when the MCFT general method was used. Figure 2.17 shows the basics of MCFT as detailed in Vecchio and Collins (1986).

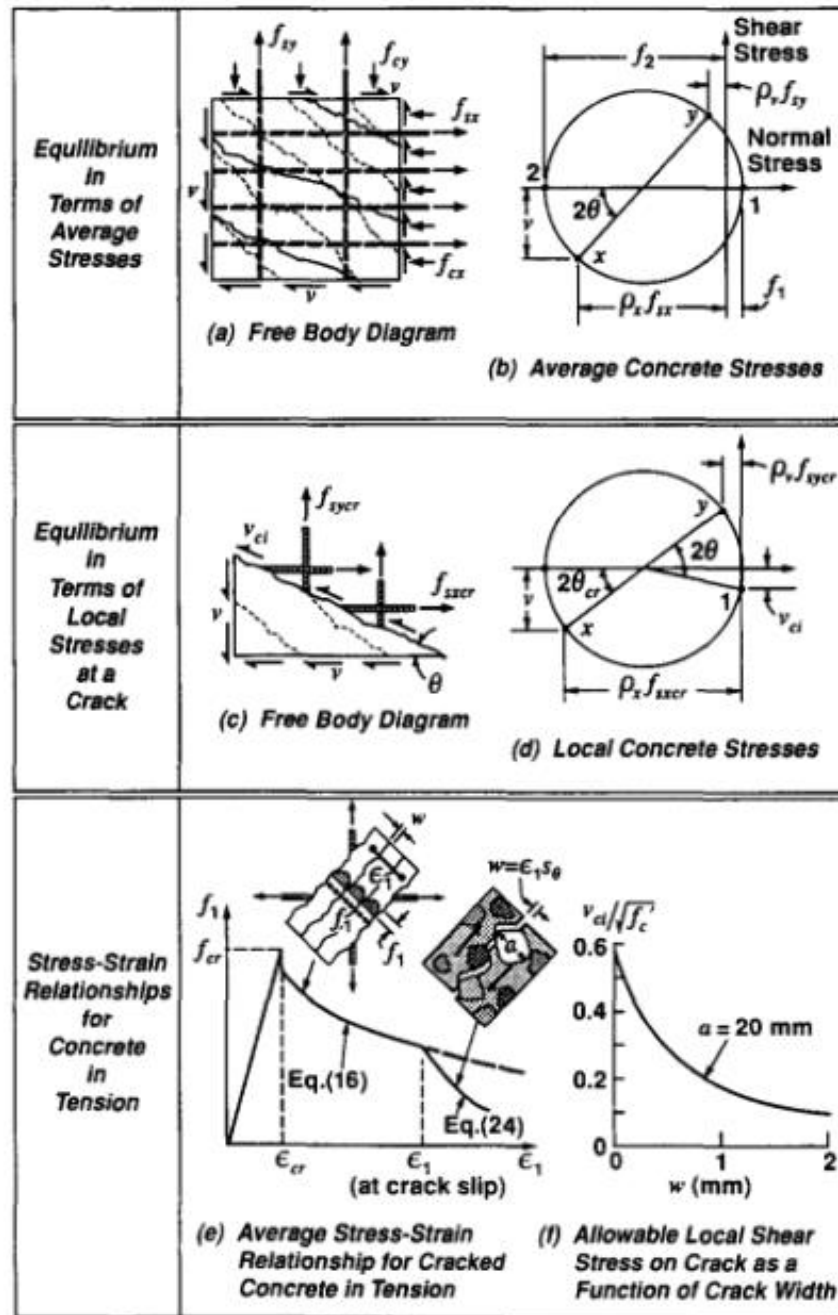


Figure 2.17. Basics of MCFT (Vecchio and Collins 1986).

## 2.4 PARAMETERS INFLUENCING SHEAR CAPACITY

Several parameters affect the shear strength in Reinforced Concrete (RC) and Prestressed Concrete (PC) beams. The most significant of those parameters are discussed below.

### 2.4.1 Beam Depth

The shear strength of concrete appears to be larger for smaller beam cross-sectional heights. It is well-known that the strength of cohesive granular material increases for smaller size samples. This phenomenon is called the *size effect* and has been observed in various material tests, such as compression testing of concrete cylindrical samples of various absolute sizes (and same aspect ratios). This phenomenon has also been observed in both reinforced and prestressed concrete beams. Kani (1967) reported the first shear tests that demonstrated size effects in slender beams. The tests done by Shioya (1989b) examined beams with various depths ranging from 4 to 120 in. to quantify size effects in shear strength. The results (see Figure 2.18) showed that the shear stress at the failure of the largest beam was only about one-third that of the smallest beam, and the ultimate shear stress of the largest beam was less than half of the value calculated using ACI 318-02.

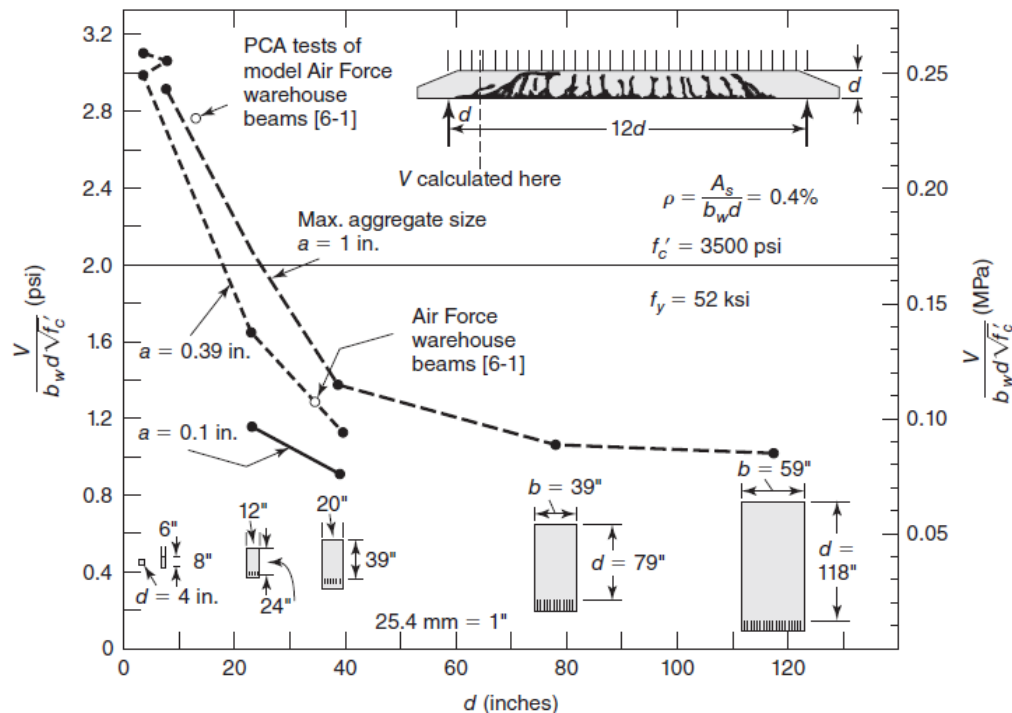
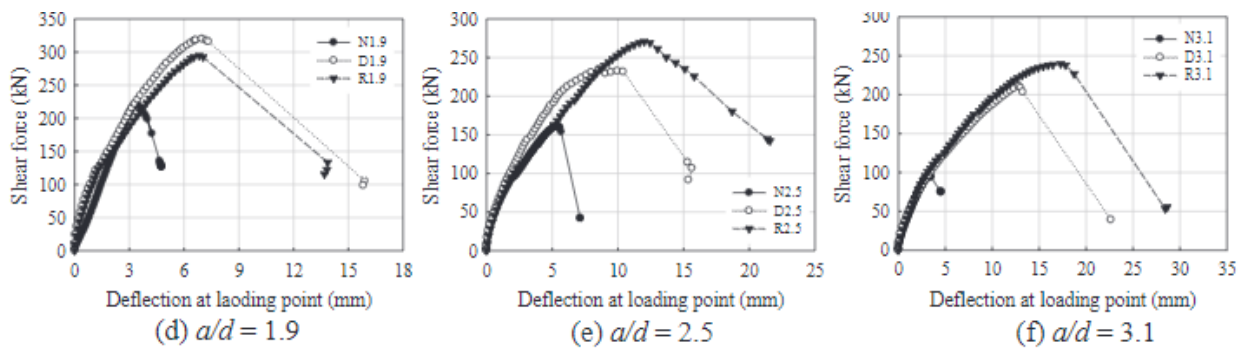


Figure 2.18. Effect of beam height and coarse aggregate size on shear stress (Shioya 1989).

Collins and Kuchma (1999) aimed to evaluate the parameters that affect the influence of size effect in shear strength. The research involved experimentation on 22 large, lightly reinforced concrete beams, out of which nine were made of high-strength concrete. The results from the testing showed that high-strength concrete beams are more prone to size effects than normal concrete beams. Chen et al. (2019) identified one potential reason for size effects in beams is the deterioration of the shear transfer strength by aggregate interlock of the critical shear crack due to the increase of the beam depth. The results are further supported by FE models. Chen et al. also observed that as shear reinforcement increases in RC beams, size effects decrease or are nearly eliminated. For this reason, ACI 318-19 accounts for the contribution of size effects only for cases with reinforcement that is below the minimum.

## 2.4.2 Shear Span-to-Depth Ratio

Shear span-to-depth ratio is defined as  $a/d$ , where  $a$  is the distance from the support of the location at which the shear force diagram crosses the zero value, and  $d$  is the effective depth of the concrete beam. In a simple beam with a single point load or with two symmetrical point loads,  $a$  is the distance from the load point to the nearest support. Equivalently, the  $a/d$  can be expressed as the ratio of the peak moment over peak shear times effective cross-section depth,  $M/(Vd)$ . The  $a/d$  affects (or more accurately correlates with) the orientation of principal stress fields and the resulting inclined cracking, which in turn controls the observed shear failure mechanism. Beams with  $a/d$  exceeding 5 or 7 are mostly flexure-critical, whereas beams with  $a/d$  less than 3 are more likely to fail in shear (e.g. Magnusson et al. [2014] and Hu and Wu [2018]). Furthermore, it has been observed that smaller  $a/d$  ratios result in larger shear capacities (see Figure 2.19).

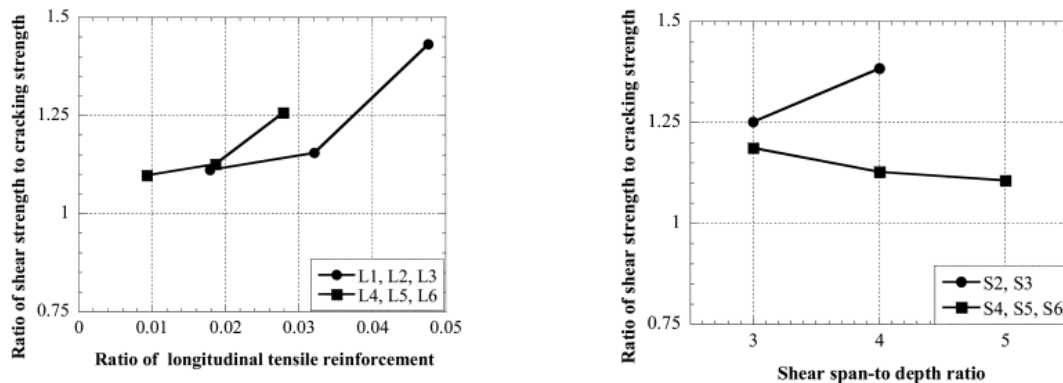


**Figure 2.19. Response of beams under different  $a/d$  (Hu and Wu 2018).**

In the National Cooperative Highway Research Program (NCHRP) project report by Hawkins (2005), the effect of  $a/d$  on shear strength of prestressed concrete girders was investigated based on the database of experiments they assembled. It was observed that as  $a/d$  decreases, the shear strength increases. The increase in the strength is significant for members with  $a/d$ s less than 2.5–3.0 because a significant amount of shear may be transmitted directly to the support by an inclined strut. This mechanism is frequently referred to as arch action, and the magnitude of the direct load transfer increases with decreasing  $a/d$ .

### 2.4.3 Longitudinal Reinforcement Content

The amount of longitudinal reinforcement affects the shear strength through various mechanisms. First, the depth of the compression zone increases, which enables the compression zone to withstand a greater amount of shear force. As the longitudinal reinforcement increases, it becomes increasingly difficult for the cracks to expand, resulting in increased friction between cracked surfaces. And finally, the dowel force increases, which is the resistance to transverse displacement in the reinforcement (see also Section 2.2.4). The effect of longitudinal reinforcement has been analyzed experimentally in various research studies by Lee and Kim (2008), Słowik (2013), and Jensen and Lapko (2009), which ultimately showed the effect of this ratio on reserve shear strength (RSS) and deflection as shown in Figure 2.20.



**Figure 2.20. Reserve strength variation for beams with varying longitudinal reinforcement content (Lee and Kim 2008).**

Similar results were found by Collins and Kuchma (1999), who experimented on 22 regular and 13 continuous RC beams with different properties; longitudinal reinforcement content was also investigated. The experimental results showed that the decreasing trend of failure shear stress



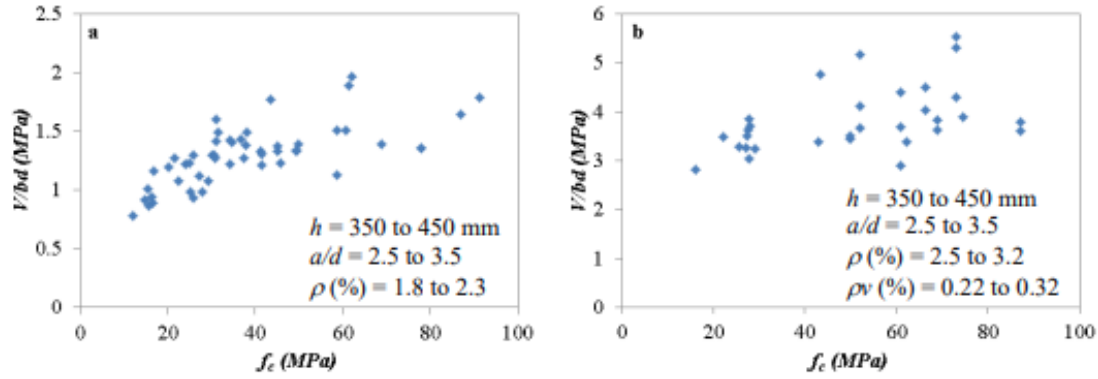
was affected more significantly by the spacing between longitudinal tensile reinforcement than by the beam depth. Thus, the beams having longitudinal bars distributed over their height reported smaller crack spacings and ultimately improved the shear strength significantly.

#### **2.4.4 Bond of the Longitudinal Reinforcement**

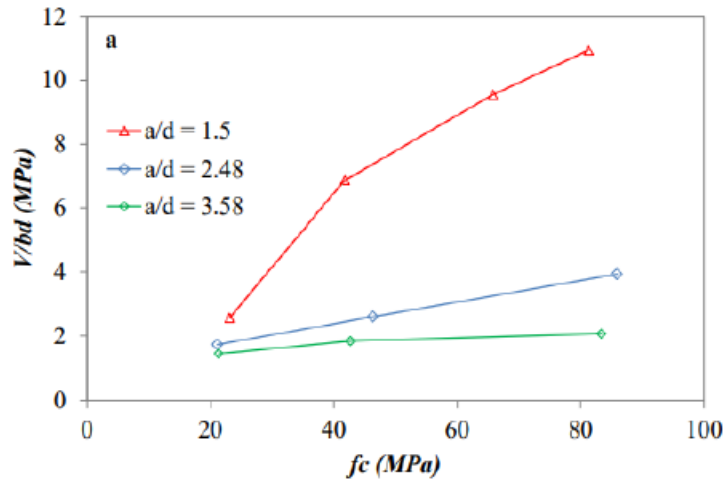
The force in the concrete element between two cracks gives an inner bending moment, which in turn can cause the cracks to grow (Azad 2021). A study by Carmona and Ruiz (2014) investigated the influence of size effects and bond strength on the shear strength of RC beams without stirrups. The authors discovered that stronger interfaces lead to narrower openings and shorter cracks for the same applied load because a stronger bond leads the steel bars to yield before the crack reaches the critical depth that ultimately causes shear failure. In beams with smooth bars and thus poor bond, large bending cracks grow in the middle of the beam, and the moment is large, but the shear forces are low. Therefore, a strong bond between the reinforcement and surrounding concrete has a negative impact on the risk of flexure-shear failure.

#### **2.4.5 Tensile Strength of Concrete**

In RC and PC beams, interaction between the flexural and shear stresses causes diagonal tension. The shear cracks develop when these tensile stresses exceed the tensile strength of concrete. Therefore, the shear strength of the section can be increased by a corresponding increase in the tensile strength of the concrete. The tensile strength of the concrete is commonly related to the square root of the compressive strength,  $\sqrt{f'_c}$ . The shear capacity of the concrete beams increases with the concrete strength. This effect is studied in various experimental studies (Angelakos et al. 2001; Ismail 2016), as shown in Figure 2.21 and Figure 2.22.



**Figure 2.21. Effect of concrete compressive strength on the shear strength of (a) RC beams without shear reinforcement and (b) with shear reinforcement (Angelakos et al. (2001).**



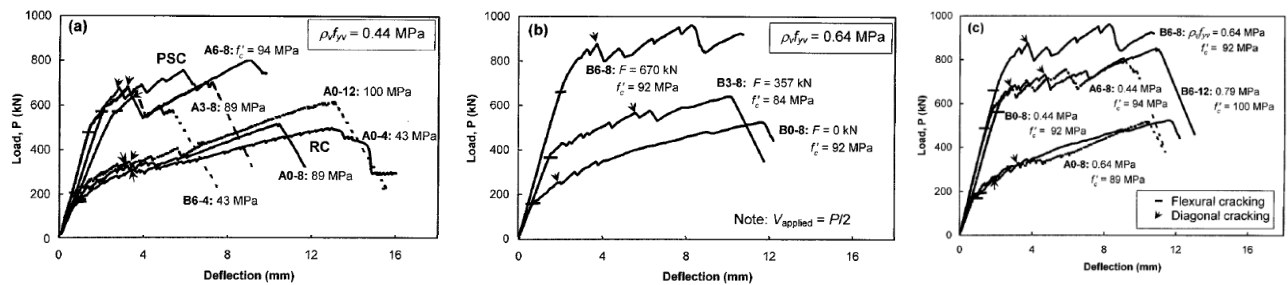
**Figure 2.22. Effect of concrete strength on shear force capacity of reinforced concrete beams without shear reinforcement (Ismail 2016).**

#### 2.4.6 Level of Prestressing

In prestressed concrete beams, the axial load introduced in the section from the tendons delays diagonal cracking, thus increasing the cracking shear capacity of otherwise reinforced concrete elements. As Hawkins (2005) described, the axial compression increases the depth of the uncracked compressive zone and decreases the width of shear cracks, resulting in a better shear transfer at the interface. This action also results in a decrease of the crack angle so that the angle of diagonal compression is flattened, thereby ultimately increasing the effectiveness of shear reinforcement, which leads to an increase in shear capacity with an increase in axial compression.

Collins (1978) looked into the effect of prestressing on the shear capacity of the beams. The effect of prestressing, along with a few other parameters, was studied with experimental tests. The experimental behavior showed that the prestressing significantly affects the response of beams in shear by increasing the shear stiffness of diagonally cracked beams and also increasing the shear at which the shear reinforcement yields. This finding is also supported by the analysis of Nakamura (2011) on the University of Texas' Prestressed Concrete Shear Database (UTPCSDB)-2011 experimental database, which showed the shear strength of prestressed concrete members increases with the prestressing force.

The effect of prestressing has also been observed by the Public Works Research Institute (1995) in an experiment on 25 pretensioned beams. It was concluded that the shear strength at the formation of the flexural shear crack highly increased due to prestress force. Moreover, the shear strength increase caused by prestress force was more significant than the increase caused by the usage of high-strength concrete. Figure 2.23 shows the load versus deflection curves detailing the effect of prestressing (b), as presented by Teoh et al. (2002a).

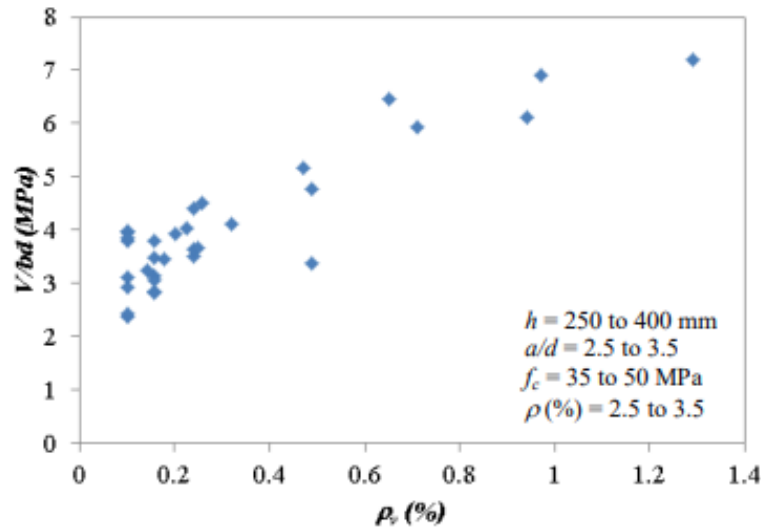


**Figure 2.23. Load-versus-midspan deflection curves: (a) effect of concrete strength; (b) effect of prestressing force; and (c) effect of shear reinforcement ratio (Teoh et al. 2002).**

## 2.4.7 Shear Reinforcement

In members with shear reinforcement, a major portion of shear force is carried by shear reinforcement after the diagonal cracking occurs, and preferably shear failure occurs with the yielding of these stirrups. The shear reinforcement also provides resistance to the growth of inclined cracks, resulting in ductile behavior. It also provides the dowelling resistance to the shear displacements occurring along the shear crack. The diagonal cracks that occur due to shear forces are considerably wider than the flexural cracks (Al-Nasra and Asha 2013). An

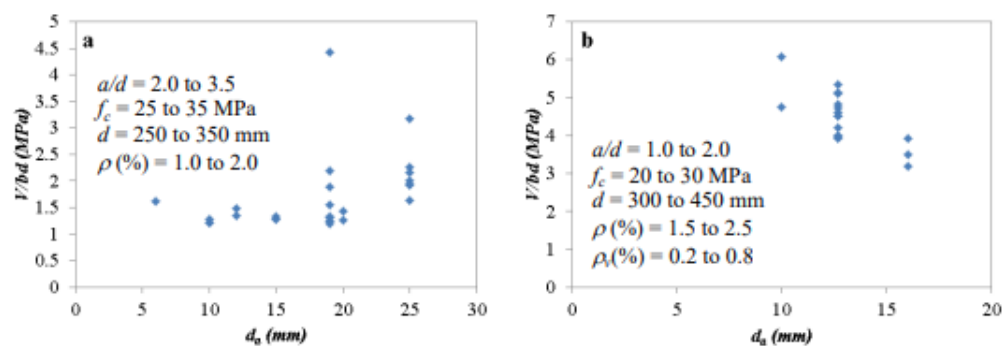
experimental study by Rahal and Al-Shaleh (2004) showed that increasing shear reinforcement ratio increases the shear capacity of the beam (Figure 2.24).



**Figure 2.24. Effect of shear reinforcement ratio on the shear strength of RC beams (Rahal and Al-Shaleh 2004).**

#### 2.4.8 Coarse Aggregate Size

The roughness, and by extension the friction, between crack surfaces increases with the size of the coarse aggregate, which facilitates higher transfer of shear stresses across the cracks. An experimental study by Taylor (1970) found that the relative magnitude of shear force transferred by aggregate interlock to between 33 percent and 50 percent. This mechanism is controlled by the roughness of the crack surfaces. The effect of the coarse aggregate size on the shear strength can be seen in Figure 2.25.



**Figure 2.25. Effect of aggregate size on the shear strength of (a) RC beams without shear reinforcement and (b) with shear reinforcement (Taylor 1970).**

Shioya (1989b), Shioya (1989) as shown in Figure 2.18, studied the influence of the aggregate size using analytical models. The results showed that when the maximum aggregate size was considered in proportion to the depth, the effect of depth on the shear strength diminishes at beam depths exceeding 60 cm. In some concrete beams that used lightweight or high-strength concrete, smoother crack surfaces were observed that were formed by the cracks going through individual aggregates. This response decreased the shear stresses that could be transferred along the cracks by aggregate interlock, thus reducing  $V_c$  (Collins and Kuchma 1999).

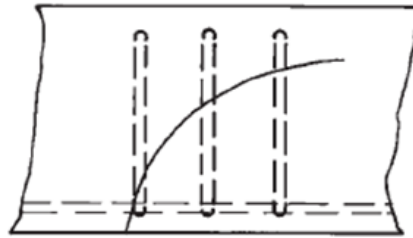
#### **2.4.9 Lightweight Concrete**

Lightweight concrete is a mixture made with lightweight coarse aggregates. The effect of the tensile strength of concrete on the shear strength—that shear strength increases by an increase in tensile strength of the concrete—was noted earlier. This effect was clearly seen in concrete beams without shear reinforcement. The tensile strength of the concrete is directly related to the square root of the compressive strength, which results in lightweight concrete having a lower tensile strength than normal concrete. Thus, the shear strength equations had to be modified for members with lightweight concrete (Wight 2015). The ACI Code implemented this change through a factor  $\lambda$ , the values of which are available in ACI 318.

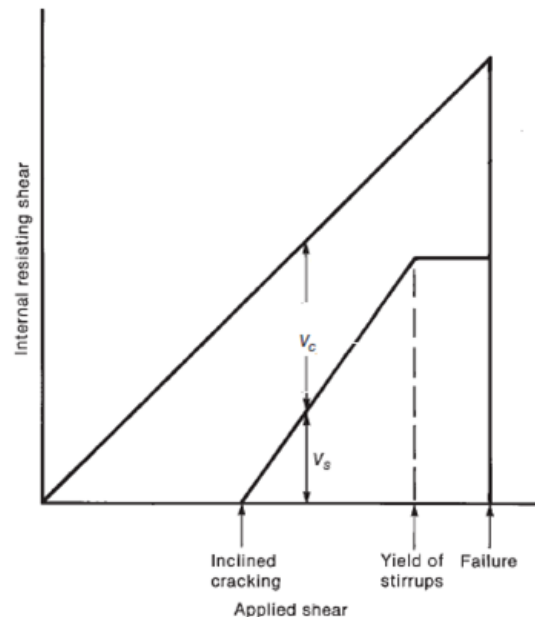
### **2.5 MINIMUM SHEAR REINFORCEMENT**

The primary role of minimum shear reinforcement (Hawkins and Kuchma 2007a; Kuchma et al. 2008) is to ensure adequate force transfer across inclined cracking following the onset of the cracking and to restrain the growth of inclined cracking so that (a) ductility is improved and brittle shear failures that would occur upon the formation of the first diagonal crack are avoided, (b) the concrete contribution to shear resistance,  $V_c$ , is maintained at least until yielding of the shear reinforcement, and (c) crack widths at service loads are controlled (Figure 2.26). However, controlling cracks are difficult to achieve due to the low deformations that activate only low stirrup reactions in service conditions. To ensure that cracks will be sufficiently arrested and crack widths may better be controlled at service loads, not only must a minimum amount of shear reinforcement (steel reinforcement ratio) be provided, but also the maximum  $s/d$  must be limited to ensure that shear reinforcement crosses any potential diagonal crack (Hawkins and Kuchma 2007a; Kuchma et al. 2008).

For prestressed concrete members, the required amount of minimum shear reinforcement is particularly important because large portions of their length may only contain that minimum required amount. ACI-ASCE Committee 425 indicated that the minimum shear reinforcement does not prevent cracks from forming because concrete can withstand only a very small strain; however, the shear reinforcement's role comes only after the cracks have formed. After inclined cracking is formed, the stirrups start to participate in resisting the applied shear. Once the stirrups that cross the crack yield, the shear contribution provided by the stirrups remains constant for higher applied shear loading. Eventually, the inclined crack opens more rapidly, until either a splitting failure occurs, or the web crushes, or the compression diagonal crushes (Figure 2.27).



**Figure 2.26. Inclined cracks and shear reinforcement (Wight 2015).**



**Figure 2.27. Distribution of internal shears in a beam (modified from ASCE 426 [ACI-ASCE426 1973]).**

For beams without shear reinforcement, after the formation of the critical flexural cracks, shear failure occurs as a result of the loss in aggregate interlock or crushing of concrete in the compression zone. However, Ozcebe et al. (1999) have shown that the use of minimum shear reinforcement significantly increases the ductility and shear strength of the beam. Therefore, the minimum shear reinforcement is essential to providing a ductile response and avoiding brittle shear failure mechanisms. The design practice that has been mostly adopted in the codes for minimum shear reinforcement is that it should be provided when the design demand exceeds half of the design capacity provided by the concrete itself together with the component of the prestressing force in the direction of the shear (see Section 2.6).

### **2.5.1 Factors Affecting Minimum Shear Reinforcement**

The study of minimum shear reinforcement begins with a theoretical understanding of various factors influencing the effect on shear capacity. As shown in the available literature, some of the major factors affecting the minimum required shear reinforcement are shown below.

#### *2.5.1.1 Reinforcement Detailing*

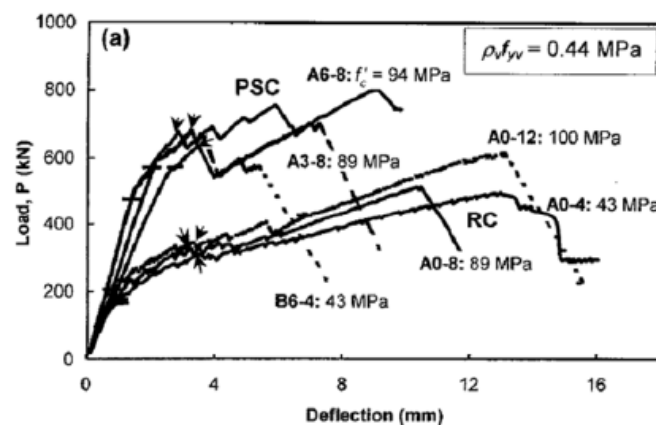
Research has shown that the reserve strength of prestressed beams increases with the number of stirrups intercepting an inclined crack, thus underscoring the critical need to limit the maximum spacing of shear reinforcement. According to studies by Teoh et al. (2002a) and Kim and Jeong (2011), the strength of prestressed beams is approximately proportional to the number of transverse reinforcements intersecting the crack. This factor highlights the necessity for design provisions that ensure at least one stirrup crosses each diagonal crack, which can be achieved by limiting  $s/d$  to a fraction of the beam's total depth.

The role of shear reinforcement extends beyond simply preventing crack propagation; it also contributes to the ductility and structural integrity of the beam. Once diagonal cracking occurs, the shear reinforcement bears a significant portion of the shear forces, ideally leading to stirrup yielding rather than brittle failure. This reinforcement arrangement not only arrests the development of inclined cracks but also provides resistance to shear displacements through dowelling. According to Al-Nasra and Asha (2013), a reduction in the transverse reinforcement ratio can lead to decreased stiffness and wider cracks, further emphasizing the importance of

optimal shear reinforcement detailing in enhancing the structural performance of prestressed concrete beams.

### 2.5.1.2 Concrete Tensile Strength

Several investigations, including Ozcebe et al.'s (1999), have established that the required minimum shear reinforcement in concrete structures should be adjusted upwards with an increase in concrete tensile strength. This adjustment is necessary due to the greater forces that need to be redistributed when diagonal cracking initiates or progresses in structures made from stronger concrete. This correlation between higher concrete tensile strength and the need for increased shear reinforcement has been further supported by other research, such as a study conducted by Teoh et al. (2002a), which specifically examined beams fabricated using high-strength concrete. These studies conclusively demonstrated that beams made with high-strength concrete require a greater amount of shear reinforcement to maintain structural integrity (see Figure 2.28).



**Figure 2.28. Load versus deflection comparison for effect of concrete strength (Teoh et al. 2002).**

Expanding on this finding, Elzanaty and Nilson (1986a) also highlighted similar findings through experimental testing on prestressed concrete beams using high-strength concrete, including a comparison of the experimentally measured shear strengths with the values predicted by ACI 318-19 (2019) standards. Moreover, additional literature underscores the significance of considering other related variables such as the beam depth, the quality of the aggregate, and the loading conditions, all of which can influence the minimum shear reinforcement requirements. For instance, deeper beams and those under variable or cyclic loading conditions exhibit

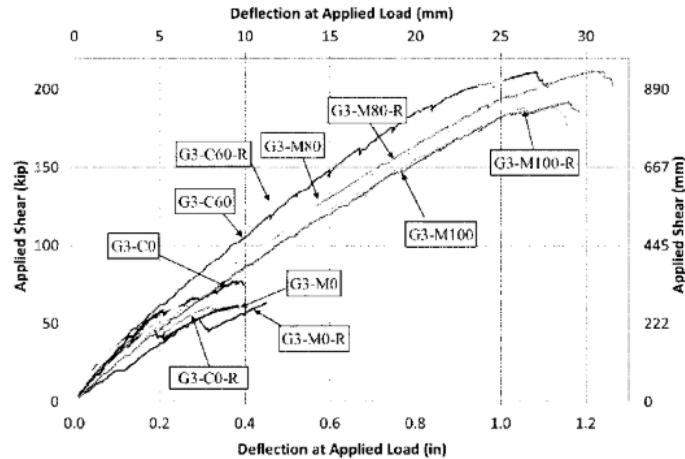


different stress distributions, necessitating tailored reinforcement strategies. These findings advocate for a nuanced approach to designing shear reinforcement in prestressed concrete girders, suggesting that current guidelines and codes may need updates to incorporate these complex interactions and ensure structural safety effectively.

#### *2.5.1.3 Yield Strength of Stirrups*

The exploration into the use of high-strength stirrups (such as Grades 75, 80, and 100) in concrete beams has been limited, but it is hypothesized that these reinforcements can influence the minimum required shear reinforcement in two primary ways. First, high-strength stirrups can allow for maximum allowable spacing, which affects the girder's performance due to the reduced number of stirrups intercepting diagonal cracks, thereby impacting the RSS. Studies like those by Teoh et al. (2002a) have shown that an increase in the number of stirrups across a crack correlates with higher RSS. Second, the lower deformation capacity of high-strength steel compared to normal-strength steel might reduce the overall ductility and increase the risk of early stirrup fracture under load.

Research by Lee et al. (2011) on simply supported RC beams with high-strength stirrups revealed that beams with a yield strength of up to 101,500 psi experienced shear failure at their yield strains regardless of concrete compressive strength, while those with higher yield strengths showed varying failure modes dependent on the concrete strength. Similarly, Munikrishna et al. (2011) conducted tests on large-sized beams reinforced with high-strength steel stirrups and found comparable shear strengths with lower reinforcement ratios than those reinforced with standard Grade 60 stirrups, even while the beams maintained adequate crack width and deflection levels as shown in Figure 2.29.



**Figure 2.29. Shear force versus deflection for varying stirrup yield strength (Munikrishna et al. 2011)**

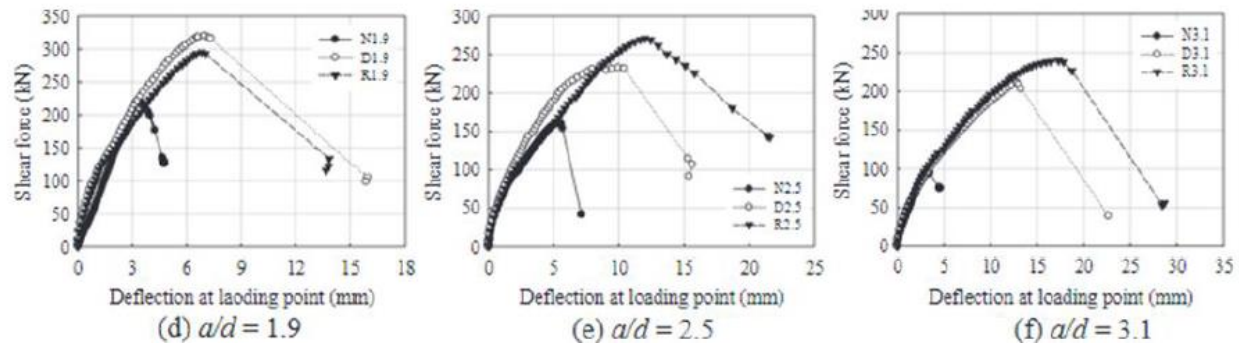
These studies indicate that while high-strength stirrups can be beneficial in terms of reducing the quantity of reinforcement needed and controlling crack widths, they also necessitate careful consideration of ductility and the potential for premature failure, thereby underscoring the need for specific guidelines in design codes to manage these factors effectively.

#### *2.5.1.4 Shear Span-to-Depth Ratio*

The  $a/d$  is a critical factor in determining the shear strength of prestressed concrete beams, especially in the absence of shear reinforcement. Studies by Hawkins (2005) and others have demonstrated that while this ratio significantly influences shear strength, its effect is reduced when shear reinforcement is incorporated. This ratio indicates the distance from the nearest support to the point where the shear force diagram crosses zero, relative to the beam's effective height, and it plays a pivotal role in dictating the orientation of principal stress fields and the development of inclined cracks.

Research, including that by Hu and Wu (2018), has shown that beams with higher  $a/d$  ratios typically exhibit a greater dependence on transverse reinforcement for shear strength due to better confinement and aggregate interlock, thus enhancing the reinforcement's effectiveness. Conversely, lower  $a/d$  ratios increase the concrete's contribution to shear strength due to more effective confinement within the compression zone. In their study, beam specimens with varying  $a/d$  ratios displayed differing contributions to shear strength from both concrete and transverse

reinforcement, depending on the ratio and type of stirrups used as shown in Figure 2.30. This outcome underlines the importance of optimizing the minimum shear reinforcement in beams to ensure a uniform response across different  $a/d$  ratios, thereby enhancing overall structural integrity and resistance to shear failure.



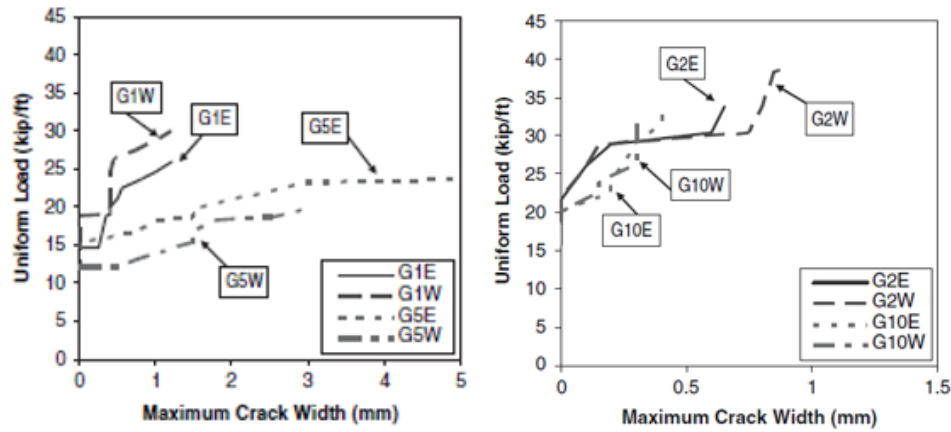
**Figure 2.30. Shear force versus deflection for varying span-to-depth ratio (Hu and Wu 2018).**

#### 2.5.1.5 Presence of Harped Tendons

The prestressed concrete beam design also includes an addition of harped tendons to provide a vertical component of compression that counteracts tensile stresses induced by shear near beam supports, where shear forces are typically heightened. Harped tendons in prestressed concrete girders significantly influence shear reinforcement requirements by modifying stress distribution and crack behavior. This adjustment in stress trajectory not only delays crack initiation, enhancing ductility and potentially reducing immediate shear reinforcement needs but also helps control crack location and width. Overall, the strategic use of harped tendons can improve the diagonal tension capacity of concrete, effectively enhancing the structural integrity and performance of prestressed concrete members.

The research by Hawkins and Kuchma (2007a) also looked into the effect of harped tendons in the shear behavior of prestressed concrete. Their results clearly showed an increase in the shear capacity owing to the vertical component of the harped tendons. However, further study needs to look into the effect on minimum shear reinforcement. In addition, Laskar et al. (2010) investigated the effect of various factors, including the presence of harped tendons affecting the shear capacity of prestressed concrete beams, using experimental tests. The study showed that

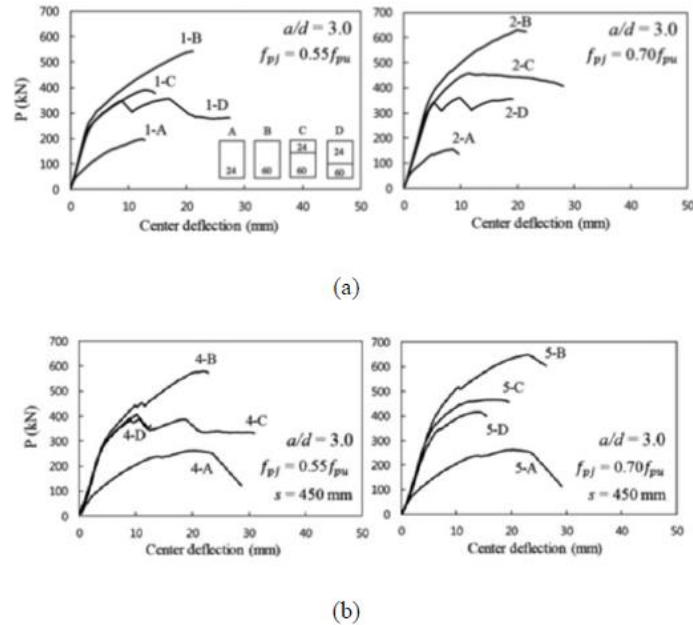
the shear capacity of prestressed concrete beams is enhanced due to the harping of the prestressing strands in both cases of web shear and flexural shear (see Figure 2.31).



**Figure 2.31. Comparison of crack widths for the effect of harped tendons (Hawkins and Kuchma 2007b).**

#### 2.5.1.6 Level of Prestressing

Prestressing in concrete beams plays a crucial role in enhancing their shear capacity by delaying diagonal cracking. This process effectively raises the cracking shear capacity beyond that of conventionally reinforced concrete. The degree of prestressing has been shown to significantly impact the shear strength because higher levels of prestressing force lead to an increase in shear strength. This principle was demonstrated in studies such as the one by Kim and Jeong (2011), which analyzed the shear strength of simply supported prestressed concrete composite beams. These beams, subjected to four-point bending tests, varied in prestress levels and  $a/d$  ratios, with different configurations of shear reinforcement. The results underscored that greater prestressing forces improve the beam's shear strength (see Figure 2.32).

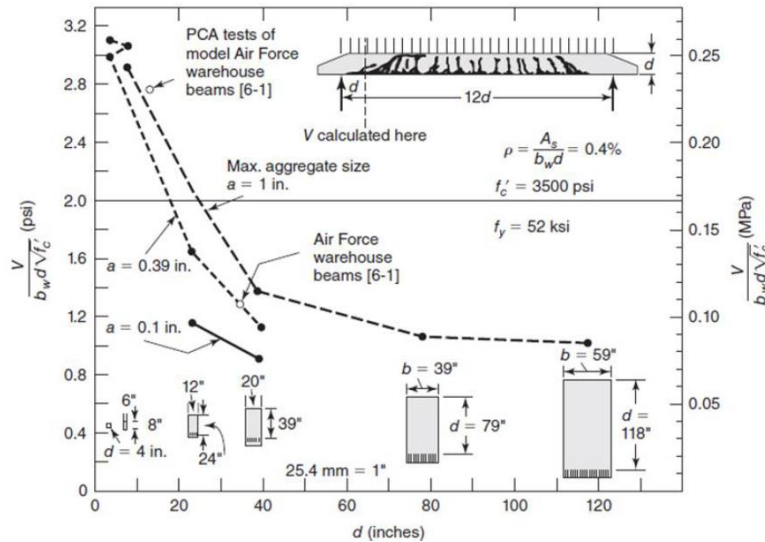


**Figure 2.32. Load versus deflection curves for effect of prestressing in cases with and without shear reinforcement (Kim et al. 2018).**

As further support for this finding, Collins and Kuchma (1999) explored how prestressing affects beam shear capacity by testing four box beams and noted an increase in section stiffness and consequently enhanced shear behavior, especially in beams with lower amounts of longitudinal steel. Similarly, Nakamura (2011) reviewed the UTPCSDB-2011 experimental database and confirmed that an increase in prestressing force correlates with heightened shear strength in prestressed concrete members. These findings collectively highlight the pivotal role of prestressing in optimizing the structural integrity and performance of concrete beams.

#### 2.5.1.7 Depth of the Beam

The concept of the size effect in concrete beams, particularly regarding shear strength, has been extensively documented and shows that smaller beam cross-sectional heights exhibit greater shear strength. This phenomenon, notable across both reinforced and prestressed concrete beams, suggests that the strength of cohesive granular materials like concrete increases as the sample size decreases. Historical tests by Kani (1967) first demonstrated this effect in slender beams, and subsequent studies by Shioya (1989b) reinforced these findings by showing that larger beams had significantly lower shear stress at failure compared to smaller beams as shown in Figure 2.33.



**Figure 2.33. Influence of beam depth on shear stress at failure (Shioya 1989).**

Further research by Collins and Kuchma (1999), and Chen et al. (2019) has explored the parameters influencing this size effect. They found that high-strength concrete beams are particularly sensitive to size effects due to the deterioration of shear transfer strength through the aggregate interlock at the critical shear crack, which worsens with increasing beam depth. This deterioration impacts the overall shear strength, an observation supported by FE models. Moreover, studies have shown that increasing the shear reinforcement in reinforced concrete beams can mitigate or even eliminate these size effects. Most recently, Fan et al. (2023) conducted tests under monotonic loading on high-strength concrete beams of various depths and confirmed that deeper beams, irrespective of the web reinforcement ratio, demonstrated reduced ultimate shear strength and exhibited larger stiffness and more extensive crack development. These findings have led to design considerations in codes such as ACI 318-19 (2019), which now include provisions to address size effects, particularly when reinforcement is below minimum levels.

## 2.5.2 Determining the Minimum Shear Reinforcement—Key Research Studies

Minimum shear reinforcement has been primarily calculated in several studies (Ozcebe et al. 1999; Teoh et al. 2002; Avendaño and Bayrak 2011) based on the RSS index proposed by Johnson and Ramirez (1989). The RSS is defined as the ratio of the shear strength at failure,  $V_{fail}$ , over the shear strength against the first crack,  $V_{cr}$ . Johnson and Ramirez tested eight

rectangular beams that were designed to fail in shear and had concrete compressive strengths ranging from 5,000 to 10,500 psi and a shear reinforcement index ranging from 0 to 100 psi. The ultimate shear behavior of those elements was predicted using truss models. *The overall RSS after diagonal tension cracking decreased with the increase of the concrete compressive strength of beams with the minimum amount of shear reinforcement.* These researchers also mentioned that for beams with larger shear-span-to-depth ratios and less longitudinal steel, this issue would be more problematic. Johnson and Ramirez concluded that as  $f'_c$  increases, one solution to the loss of RSS is to increase the amount of the minimum shear reinforcement. In addition to the RSS, which is mostly used as an indirect measure of the ductility capacity, crack control requirements under service loads have also been considered when determining the minimum required shear reinforcement (Ozcebe et al. 1999; Teoh et al. 2002; Avendaño and Bayrak 2011). It was determined that a uniform reserve strength and reserve deflection should be maintained in order to reduce the brittle failures. The reserve deflection is defined as the ratio between the deflection corresponding to the ultimate load of beams with shear reinforcement and the deflection of beams without shear reinforcement.

Using the RSS, analytical expressions for the minimum required shear steel reinforcement ratio can be derived by setting  $V_{cr}$  equal to the concrete contribution to the shear strength,  $V_c$ , and setting  $V_{fail}$  equal to the total shear strength due to the contributions of both the shear reinforcement and concrete  $V_c + V_s$ , which results in the expression:

$$V_s = (RSS - 1)V_c \quad (2.2)$$

This approach was initially used by the Ozcebe et al. (1999) to derive an expression for the minimum required shear reinforcement. Ozcebe et al. tested 13 nonprestressed RC beams with the minimum shear reinforcement determined on the basis of ACI 318-83, the Turkish code, and with the equation derived using  $RSS = 1.3$ . Concrete strength varied between 8.7 and 11.6 ksi, and three  $a/d$  values were used: 1.9, 3, and 5. Based on their findings, the ACI 318-83 minimum shear reinforcement had less RSS at higher concrete strengths, and the crack width identified at the stage of shear cracking was crossing the permissible serviceability limits. Conversely, beams with shear reinforcement based on the proposed equation had at least 40 percent reserve capacity, and their crack widths remained permissible.

The amount of minimum shear reinforcement predicted by Equation (2.2) can be increased by a small percentage, between 0 percent and 15 percent, to account for uncertainties (i.e., the dispersion in the experimental data). An experimental study conducted by Teoh et al. (2002a) used  $RSS = 1.3$  and increased the resulting amount by 15 percent based on dispersion (uncertainty) observed in the data from their tests and another six experimental programs. That study investigated the adequacy of the minimum shear reinforcement provided by various codes, including ACI 318-99, the 1994 version of the Canadian code, the 1997 version of the British code, and the 1994 version of the Australian code. The resulting relationship was:

$$\rho_{v,min} f_{yt} = 0.35 \frac{V_{c,ACI}}{b_w d} \quad (2.3)$$

in which  $V_{c,ACI} = \min (V_{ci}, V_{cw})$ ;  $V_{ci}$  = the nominal shear strength provided by concrete when diagonal cracking results from combined shear and moment; and  $V_{cw}$  = the nominal shear strength provided by the high principal tensile stress in the web. This expression accounts for both nonprestressed and prestressed concrete beams. The test results of Teoh et al. (2002a) for RC beams indicated that, after the formation of diagonal cracking, the arch action provides sufficient RSS if the longitudinal reinforcement is provided adequately. In contrast, the reserve strength of prestressed beams was found to be dependent on the number of individual stirrups crossing the crack due to a higher cracking load. The authors proposed Equation (2.3) using the RSS index as a measure for the factor of safety that was *not* addressed appropriately by guaranteeing a satisfactory margin in both the American and Canadian provisions of the time. Assuming a minimum concrete shear strength of  $2\sqrt{f'_c}b_w d$ , the above equation can be rearranged as:

$$\rho_{v,min} f_{yt} = 0.70 \sqrt{f'_c} \quad (2.4)$$

This expression is very similar to the current minimum shear reinforcement requirements of ACI 318-19, as shown below:

$$\rho_{v,min} f_{yt} = 0.75 \sqrt{f'_c} \quad (2.5)$$

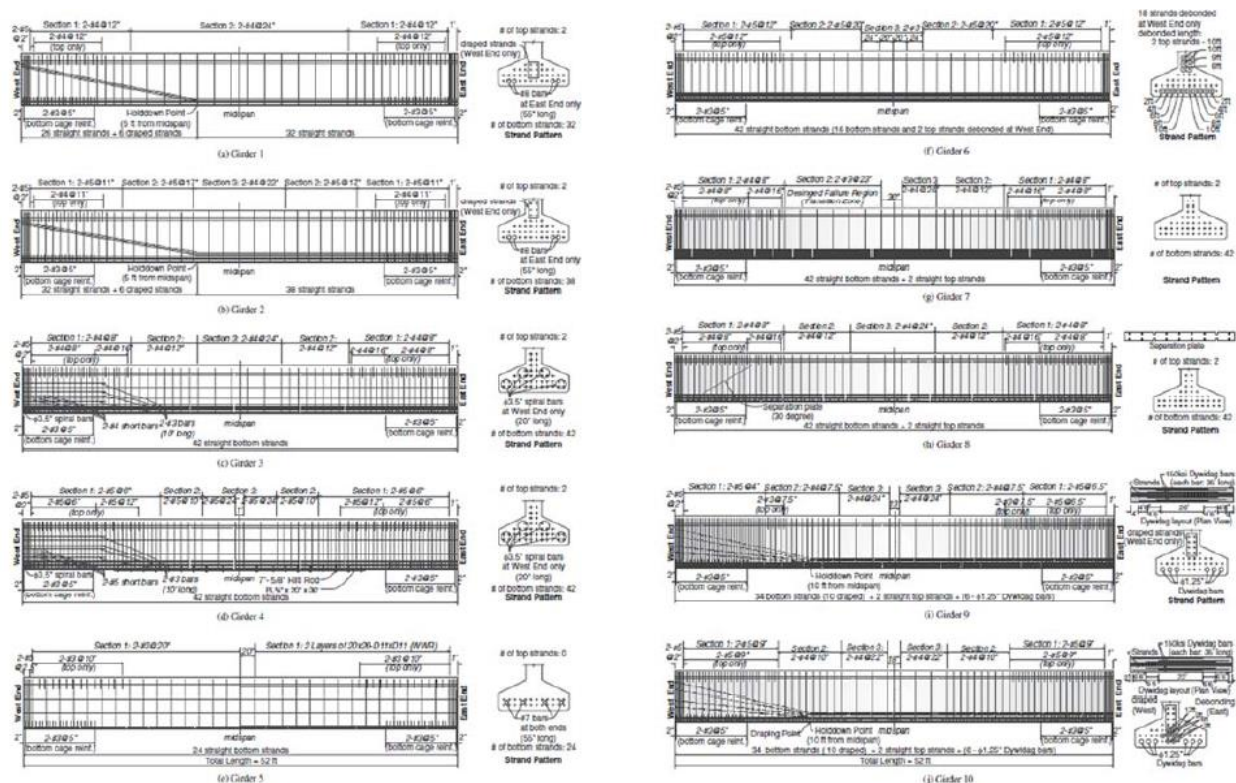


The RSS of the beam also helped in identifying the potential effect of longitudinal tensile reinforcement and  $a/d$  on minimum shear reinforcement in RC beams, as shown in research done by Lee and Kim (2008). The research involved testing 26 RC beams having the minimum shear reinforcement based on ACI 318-05. The research stated that the minimum shear reinforcement provisions in various design codes during 2005 did not include the effect of percentage of longitudinal reinforcement and the  $a/d$ . The test results showed a decreasing trend in the reserve strength and deflection as the percentage of longitudinal reinforcement decreased. The test results also showed that, to maintain a uniform RSS as  $a/d$  increases or decreases, the provided minimum shear reinforcement should also be increased or decreased. The authors also concluded that reserve strength above diagonal cracking strength declined as concrete strength increased in experimental tests on beams using higher-strength concrete of more than 70 MPa (10.15 ksi). To examine this influence of high-strength concrete on the minimum shear reinforcement, the authors said that further experimentation on RC beams with higher-strength concrete was necessary.

Hawkins (2005), as a part of an NCHRP research project (NCHRP Project 12-61, Report 549), developed a shear design procedure that can be used for both reinforced and prestressed concrete beams. It involves the integration of a simpler method within the AASHTO LRFD procedures that uses the MCFT method. The study also looked at developing a database of shear tests on both reinforced and prestressed concrete beams and measured the accuracy of shear strength predictions made by ACI 318-02, AASHTO LRFD 2002, and a few other international codes. The total number of tests that were looked at was 1,359 test results. The authors concluded that the AASHTO LRFD was the best method based on the lowest coefficient of variation (COV) and consistent conservative estimates. After that, they also showed that for prestressed members only, both with shear reinforcement and no shear reinforcement, ACI 318 expressions were the best, observing a mean value of the test result to a calculated value ratio of 1.32 (smallest of all) and a COV of 0.248 (smallest of all).

A subsequent research study by Hawkins and Kuchma (2007b) intended to provide experimental evidence that would enable AASHTO LRFD Bridge Design Specifications to raise the limit of compressive strength of concrete from 10 ksi to higher strengths without compromising safety. The study analyzed how the shear strength ratio,  $V_{\text{test}}/V_{\text{LRFD}}$ , varied with respect to several

factors such as concrete strength, ultimate shear stress, compliance with minimum shear reinforcement requirements, overall member height, and percentage of longitudinal reinforcement (Figure 2.34). Their experimental findings (together with test data from other studies) showed that the compressive strength limit could be raised to 18 ksi. Out of the 10 girders tested (with two tests per girder, one for each half), one was cast with only the minimum required amount of shear reinforcement. Its shear performance was found to be excellent, with stirrup strains at ultimate resistance being reached in excess of several times the yield strain, and stirrups in some locations being ruptured before the final girder failure occurred at a load in excess of the LRFD-calculated shear strength. These test results, together with test data from other studies, showed that the LRFD specifications were typically conservative for members cast with very light amounts of shear reinforcement, including amounts that were somewhat less than the minimum required amount of shear reinforcement by the LRFD specifications. Overall, the LRFD minimum required amount of shear reinforcement was found to be somewhat conservative for strength, but not conservative when serviceability requirements were considered.



**Figure 2.34. Test specimens with their cross sections used by Hawkins and Kuchma (2007b).**

In another research study by Avendaño and Bayrak (2011), the current specifications for minimum shear reinforcement and maximum nominal shear strength for prestressed concrete members were evaluated. This study used the UTPCSDB for various comparisons. The study used a similar approach to Teoh et al. (2002a) but adopted a different RSS value of 1.25. The resulting expression obtained was:

$$\rho_{v,min}f_{yt} = 0.25 \frac{V_{c,ACI}}{b_w d} \quad (2.6)$$

Upon comparison with the existing test results in the literature, they observed that the proposed minimum shear reinforcement requirements would result in more shear reinforcement than required up to a factor of 4. However, in comparison with the ACI 318 expression, which is the only specification accounting for prestressed concrete, and for cases wherein the prestressing term controls, the proposed expression demanded less shear reinforcement in 59 percent of the specimens considered in the database. Moreover, the authors did not explicitly show that the RSS would maintain its desired lower bound of 1.25 as considered. From the database results, the authors also concluded that for the prestressed concrete beams, none of the current minimum shear reinforcement requirements presented a clear distinction between desirable and undesirable RSS. They did not, however, precisely quantify the ductility capacity achieved by various minimum shear reinforcement levels, which could have led to an obvious trend.

Based on all the experimental and research studies, the contribution of prestressing is considered in ACI 318-19 for determining the minimum shear reinforcement. However, this is not the case for the most recent (9th) edition of AASHTO LRFD Bridge Design Specifications, which used the following expression:

$$\rho_{v,min}f_{yt} = \lambda \sqrt{f'_c} \quad (2.7)$$

where  $\lambda$  = the concrete density modification factor that accounts for use of lightweight concrete. This process might be due to the fact that the research studies that exclusively investigated the minimum shear reinforcement requirements showed that the equations used were adequate in performance. As mentioned earlier, the study by Hawkins and Kuchma (2007b) included a prestressed beam with only minimum shear reinforcement; they found that the beam behaved as

intended, with failure by yielding followed by rupture of the shear reinforcement along the diagonal cracks.

### 2.5.3 Minimum Shear Reinforcement Provisions in ACI and AASHTO Codes

The 1963 version of ACI318-63 (1963) included an expression for minimum shear reinforcement for prestressed concrete elements that was proposed by Olesen et al. (1965). The expression is given as:

$$A_{v,min} = \frac{A_{ps}f_{pu}s}{80 f_{yt}d} \sqrt{\frac{d}{b_w}} \quad (2.8)$$

where  $f_{pu}$  = the specified ultimate tensile strength of the prestressing steel (psi);  $A_{ps}$  = the area of prestressing steel in flexural tension zone (in.<sup>2</sup>);  $d$  = the distance from the extreme compression fiber to the centroid of longitudinal tension reinforcement (in.);  $s$  = transverse reinforcement spacing (in.);  $f_{yt}$  = the specified yield strength of transverse reinforcement (psi); and  $b_w$  = the web width (in.). Olesen et al. (1965) tested 129 simply supported prestressed concrete beams with minimum web reinforcement and investigated the effect of minimum shear reinforcement on the strength and failure mechanism. Equation (2.8) has practically remained in the ACI 318 code since its introduction and currently complements the minimum shear reinforcement requirement of ACI-318-19 (together with two more limiting values). The minimum required shear reinforcement in ACI 318-19 for prestressed beams (with  $A_{ps}f_{se} \geq A_{ps}f_{pu} + A_s f_y$ ) is:

$$\rho_{v,min} f_{yt} = \min \left\{ \frac{A_{ps}f_{pu}}{80db_w} \sqrt{\frac{d}{b_w}}, \max\{0.75\sqrt{f'_c}, 50\text{psi}\} \right\} \quad (2.9)$$

where  $\rho_{v,min} = A_{v,min}/(b_w s)$ ; and  $f_{se}$  = the effective prestressing stress (psi). Also, maximum  $s/d$ ,  $s_{max}$ , is either the minimum of 0.75h and 24 in. or the minimum of 0.375h and 12 in., depending on the shear stress demand.

The AASHTO Standard 1979 Interim Specifications required the minimum shear reinforcement to provide shear stress of at least 100 psi:

$$\rho_{v,min}f_{yt} = 100 \text{ psi} \quad (2.10)$$

It also included a maximum  $s/d$ ,  $s_{max}$ , of  $0.75h$ , where  $h$  is the member height.

The shear design provisions in the 1983–2002 AASHTO Standard Specifications were based on a research study by MacGregor (1960) at the University of Illinois. In these specifications, the concrete shear strength was calculated as the smaller of the shear force associated with flexural shear cracking and the shear force that causes web shear cracking. The minimum required shear reinforcement for prestressed beams in these specifications, however, was half that required in the 1979 Interim Specifications and corresponded to a minimum shear stress of 50 psi, or, in other words,  $\rho_{v,min}f_{yt} = 50 \text{ psi}$ . Also, the maximum  $s/d$ ,  $s_{max}$ , was either the minimum of  $0.75h$  and 24 in. or the minimum of  $0.375h$  and 12 in., depending on the shear stress demand.

This minimum shear stress requirement corresponding to 50 psi, was also adopted in ACI 318 in versions prior to 2002. However, multiple research findings indicated that this limit should be reconsidered based on several other factors that affect the shear transfer mechanism. In research done by Krauthammer (1993), the study focused on minimum shear reinforcement provisions in RC beams estimated based on transfer of shear strength across cracked surfaces. The researchers also looked at recent experimental findings and data to identify the value of normal concrete stress that can be used in their proposed method and modifications in the shear reinforcement provisions. This research ultimately concluded that the limit should be changed to 65 psi until further information is obtained for reasonable usage.

A research study by Nakamura et al. (2013), looked into characteristics of the shear tests that are covered in the UTPCSDB. The experimental dataset on prestressed concrete members included specimens after 1986 with overall members' heights greater than 12 in. This trend is supposed to eliminate size effects in study of the behavior of shear in PC beams since most of the PC beams in use are taller than 12 in. A similar trend also appears in the strength of concrete for the test specimens. The average value of compressive strength of concrete increased after 1980, thus implying the usage of higher-strength concrete.

The study done by Frosch (2000) looked into the behavior of large-scale RC beams that have minimum shear reinforcement. This research investigated the influence of the size effect, which

means that as the beam depth decreases, there will be an increase in the shear strength of the section. ACI Committee 445 stated that the size effect is caused due to larger diagonal cracks in bigger beams. The research involved two large-scale beams with minimum shear reinforcement subjected to constant shear. The test results showed a lower shear strength developed in the specimens compared to the equations in the ACI Code. The author summarized that the ability of the shear reinforcement in resisting the shear was not affected by the beam size based on the test results and concluded that it might be due to a lower percentage of longitudinal reinforcement because test results showed that minimum shear reinforcement provided was effective in terms of yielding after the formation of shear cracks. The author suggested further experimentation is needed to identify the effect of beam size along with the longitudinal reinforcement on beams with minimum shear reinforcement. The research also made a comparison of the tested beam results with reduced size specimens experimented on in Johnson and Ramirez (1989) and stated that the post-cracking behavior or the shear strength by transverse reinforcement was not affected.

The research toward an update to minimum shear reinforcement was also driven by progressively increased usage of higher concrete strengths. Many research studies focused on examining the shear capacity and reinforcement limits for high-strength concrete beams. Roller and Russel (1990) conducted an experimental study of the shear strength in high-strength concrete beams with stirrups designed based on the ACI 318-83. The beam specimens were made of concrete, with compressive strengths of 10, 17, and 18 ksi. The percentage of shear reinforcement provided in the beams varied between the minimum provisions stated in ACI 318-83 to the maximum shear reinforcement allowed. The experimental result of the shear strength was compared to the expected shear strength utilizing ACI 318-83 regulations. The authors concluded that to compensate for the missing role of higher-strength concrete in the contribution of concrete to shear strength  $V_c$ , the minimum shear reinforcement provisions in the ACI 318-83 code ( $A_{v,min} = 50 \frac{b_w s}{f_y}$ ) must be raised as the concrete compressive strength increases.

Another experimental study carried out by Ozcebe et al. (1999) evaluated the minimum shear reinforcement provisions from the ACI, Canadian, and Turkish codes. When high-strength concrete beams were tested, the ACI 318-83 provisions did not meet the intended performance. The crack width identified after the onset of shear cracking exceeded the allowable serviceability

limits and had lesser RSS than others. The authors verified that the most essential factor in establishing the minimum shear reinforcement is reserve strength. The authors further concluded that it is reasonable to develop an equation by magnifying the observed cracking strength to the final shear strength, which gives a factor of safety in the final equation.

Based on this research, ACI 318-02 added a new minimum shear stress requirement that was proportional to the tensile strength of the concrete, which was proportional to the square root of the compressive strength of the concrete. The adopted minimum shear stress was:

$$\rho_{v,min}f_{yt} = K\sqrt{f'_c} \quad (2.11)$$

where  $f'_c$  = the specified concrete compressive strength (psi). The factor K was selected to be 0.75 and has remained unchanged to date.

The shear design provisions in the AASHTO LRFD Bridge Design Specifications are based on the MCFT developed at the University of Toronto by Vecchio and Collins (1986), marking a significant transition from more traditional shear design methods used in the AASHTO Standard Specifications (and ACI 318). This shear design method relies on the use of equilibrium, strain compatibility, and material constitutive relations to determine the concrete and steel reinforcement contributions to the shear strength. For the minimum required shear reinforcement, these specifications adopted Equation (2.11), with  $K = 1$ , which has remained unchanged since its adoption. It is noted that this is a more conservative requirement than that of the AASHTO Standard Specifications. The maximum  $s/d$ ,  $s_{max}$ , of the AASHTO LRFD Bridge Design Specifications has been either the minimum of  $0.75d_v$  and 24 in. or the minimum of  $0.375d_v$  and 12 in., depending on the shear stress demand. The effective depth  $d_v$  is defined as the distance between the tensile and compressive resultant forces due to flexure and should not be less than  $0.72h$  or  $0.9d_e$  ( $d_e$ : effective depth).

It is noted that while some contribution from the prestressing is considered in the ACI 318-19 for determining the minimum required shear reinforcement, that is not the case for the most recent (9th) Edition of AASHTO LRFD Bridge Design Specifications. This change is because research studies, despite not thoroughly or exclusively investigating minimum shear reinforcement requirements, showed that Equation (2.11) resulted in adequate performance. For example, the

studies by Hawkins and Kuchma (2007a) and Kuchma et al. (2008a) included a prestressed beam with only minimum shear reinforcement and found that the beam behaved as intended; in other words, it failed after general yielding and subsequent rupture of the transverse reinforcement along the length of the critical diagonal crack.

#### **2.5.4 Experimental Studies on Development of Eurocode 2**

Eurocodes play a significant role in the structural concrete design industry in design provisions followed by different nations around the world. Eurocodes are Europe's common design rules for load-bearing structures of buildings and infrastructures. The main idea is that all the European Union countries follow similar rules and regulations to have a safer construction industry (Azad 2021). These standards are administered by the European Committee for Standardization (*Comité Européen de Normalisation* [CEN]), which is an association that brings together the national standardization bodies of 34 European countries. Between 1992 and 1998, most of the Eurocodes were published as pre-standards due to nonagreements on certain factors between the countries, but they were later finished and published with definitive values in the early 2000s (Athanasopoulou et al. 2019). The first generation of the Eurocodes as full CEN standards were published between 2002 and 2007.

The Eurocodes allow individual national adaptation through nationally determined parameters (NDPs). In addition to the Eurocodes, each country has published a national annex (NA) stating the NDP values that apply in the country (Hicks 2020). However, there has not been an update in these standards since their first version. This led toward the development of the second generation of Eurocodes, which involved many experts across Europe, along with input from UK industries (BSI Committee B/525, 2014). The CEN aims at the reduction of NDPs for greater harmonization and ease of usage. Currently, the research has progressed heavily toward the development of the new Eurocodes. The current shear design provisions in Eurocode 2 (2004) are discussed in Section 2.6.5, but this section covers the various research studies that assisted in the development of the revised Eurocode 2 (CEN, working draft D7 prEN 1992-1-1, 2020).

Jensen and Lapko (2009) investigated the design of shear reinforcement for concrete beams based on the theory of plasticity. The authors addressed some research studies, such as Collins et al. (2008) and Lee and Kim (2008), that investigated the shear capacity of RC beams with an



emphasis on mechanisms and especially on modeling of shear failures. The study investigated the estimates of the inclined strut model for the design of shear reinforcement used in various codes, including Eurocode 2. The authors analyzed the problem of the inclination of the compression strut in the truss model depending on the percentage of shear reinforcement and compressive strength of concrete. To address these problems, the authors used the theory of plasticity of reinforced concrete in shear and showed that the failure of reinforced concrete beams needs significant yielding in the shear reinforcement and inclined crack widths, especially at lower amounts of shear reinforcement. The authors pointed out that the translation capacity of the beams should be considered similarly to consideration of rotational capacity of frames.

Several studies also focused on the effects of the longitudinal tensile reinforcement ratio and the  $a/d$  on the minimum shear reinforcement ratio. Lee and Kim (2008) conducted experiments on 26 RC beams having minimum shear reinforcement based on ACI 318-05 to identify this effect, which was also not addressed in Eurocode 2. The experimental studies by Słowik (2013, 2014) investigated the effects of longitudinal reinforcement and concrete strength on the basis of the author's own experimental results and test results from published literature for shear capacity in RC beams without shear reinforcement. The results from the study by Lee and Kim (2008) showed that 12 RC beams having minimum shear reinforcement showed a decrease in RSS as the longitudinal reinforcement ratio decreases. In addition, 10 RC beams showed that the minimum shear reinforcement should be increased as  $a/d$  increases to maintain a uniform RSS. Thus, these two factors should be accounted for in the calculation of minimum shear reinforcement. Similar results have been identified in studies done by Słowik (2013, 2014) when experimenting on the basis of Eurocode provisions.

Bogdándy (2021) investigated differences between predictions from a proposed expression for shear resistance of members without shear reinforcement and empirical expressions used in Eurocode 2. The study involved experimental tests on reinforced concrete beams without stirrups to develop a comparison for the predicted values by the empirical expressions. From the experimental results and the comparison, the author found that if the stress in the extreme compression fiber is less than  $0.60f_{cm}$  when the shear failure occurs, the shear strength according to Eurocode 2 is overestimated. The conclusion was also supported by comparison to experimental results reported by Collins and Kuchma (1999), which also stated that the shear

strength estimates of Eurocode 2 are highly conservative. Thus, Bogdándy (2021) recommended a change in the minimum value of shear resistance in Eurocode 2 by a factor of  $0.7/\gamma_c$ , where  $\gamma_c$  is the partial (safety) factor for concrete.

### **2.5.5 Experimental Studies on Development of *fib* Model Code**

Another set of major design provisions is the *fib* (Fédération Internationale du Béton) Model Code for concrete structures. The shear design provisions for beams have been through extensive debates and research studies since there is not an international consensus on the variables, governing mechanisms, and how to standardize the current understanding. In the development of *fib* Model Code for Concrete Structures 2010, the key goals were that the provisions should be based on mechanical models that are easily understandable, including influential factors observed from experimental tests, and should be open for further development (Sigrist et al. 2013).

The development of shear provisions have been through significant changes for the *fib* Model Code, as summarized in Nakamura (2011). In terms of shear design equations for prestressed girders, the CEB-FIP (*Comité Euro-International du Béton* [CEB] and the *Fédération Internationale de la Précontrainte* [FIP]) Model Code (CEB 1978) adopted the decompression moment to account for the prestress force effect. The next update of Model Code 1990 (CEB 1990) introduced two different methods: (1) the strut-and-tie model, and (2) an equation incorporating axial stresses developed due to the prestressing. The most recent version, Model Code 2010, adapted the MCFT for development of shear design equations. These equations are functionally equivalent to the AASHTO LRFD 2010. The Model Code 2010 incorporated three procedures that were referred to as levels of approximation (LoA) based on their complexity and accuracy. For higher LoA, a greater design effort would be needed. The highest level, Level III, adopted equations equivalent to those in AASHTO LRFD 2010 and the other two levels are simple equations developed by adding several assumptions to the Level III procedure. The minimum shear reinforcement provided in Model Code 2010 (see Section 2.6.4) is greater than those minimum reinforcements found in ACI 318 and AASHTO LRFD 2010.

The development of *fib* Model Code 2020 has been through many international workshops and the *fib* Model Code 2020 Core Group meeting in Madrid (December 2015). Matthews et al.

(2018) discussed the key aspects inserted into the development of the new *fib* Model Code. The fundamental idea was to integrate the provisions for design of new concrete structures with matters relating to existing structures, such as in-service assessment and repairs needed. This process was aided by several research studies that investigated several factors influencing the shear design provisions. Major studies are discussed below.

Sykora et al. (2018) investigated the uncertainties of shear design models based on various LoA presented in the *fib* Model Code 2010. The study involved developing model uncertainties by comparing model predictions with experimental measurements via large databases for reinforced concrete beams with and without shear reinforcement. The sensitivity was analyzed for basic variables involved. The authors concluded that for beams with stirrups, Level III analysis was recommended to avoid overestimation considering practical applications. The uncertainties for this level were shown to be independent of the amount of shear reinforcement and have reasonable bias and distribution when compared with experimental data. The Level II analysis was found to overestimate shear strength for lightly reinforced beams, and a distinction is needed between moderate to highly reinforced beams. The Level I analysis was found to always provide excessively conservative estimates, and it is not at all recommended for practical applications. The authors suggested a revision of the approximation levels considering the model uncertainties when it accounts for practical usage.

Another study by Olalusi and Viljoen (2019) looked into assessment of simplified and advanced models of shear strength for reinforcement concrete beams with stirrups. This research involved the assessment of mean and design value predictions of several shear design models in the latest design provisions and technical literature. The mean and design values are compared to one another and also to experimental results based on several parameters for various codes that also involved *fib* Model Code 2010 (Level III Model) and MCFT-based analysis program Response 2000. The key findings involved the effect of percentage of longitudinal reinforcement, which upon reduction showed that the shear capacity prediction by *fib* decreases. This influence on shear resistance was not included in Eurocode 2 and the simplified method of ACI 318. The authors ultimately conceded the difficulty of making accurate and precise predictions of shear resistance from different methods. The extent of scatter of various parametric curves showed the uncertainty involved in shear design and reinforcement provisions.

## 2.6 SHEAR DESIGN PROVISIONS IN CODES OF PRACTICE

The shear design provisions for prestressed concrete girders adopt different technical principles and procedures. These provisions are reviewed in the following five design specifications:

- *AASHTO LRFD Design Specification*, 9th Edition.
- *AASHTO LRFD Design Specification*, 6th Edition.
- ACI 318-19 Building Code Requirements for Structural Concrete.
- *fib* Model Code 2010.
- Eurocode 2 2004.

### 2.6.1 AASHTO LRFD Design Specifications, 9th Edition

The AASHTO LRFD Bridge Design Specifications, 9<sup>th</sup> Edition (AASHTO 2020) provided the nominal shear strength,  $V_n$ , as the lesser of two values calculated by:

$$V_n = V_c + V_s + V_p \quad (2.12)$$

$$V_n = 0.25f'_c b_v d_v + V_p \quad (2.13)$$

where  $V_n$  = nominal shear resistance of the section considered (kip);  $V_c$  = nominal shear resistance provided by tensile stresses in the concrete (kip);  $V_s$  = shear resistance provided by shear reinforcement (kip);  $V_p$  = component in the direction of the applied shear of the effective prestressing force; positive if resisting the applied shear (kip).

The AASHTO LRFD Bridge Design Specifications adopted a set of conservative simplifying assumptions for the MCFT-based shear design procedure. The concrete shear,  $V_c$ , in the AASHTO LRFD 2020 specifications is given by:

$$V_c = 0.0316\beta\lambda\sqrt{f'_c}b_v d_v \quad (2.14)$$

where  $\beta$  = factor relating to the effect of longitudinal strain on the shear capacity of concrete in prestressed sections, which represents the ability of diagonally cracked concrete to transmit tension, and shall be determined as:

$$\beta = \frac{4.8}{(1 + 750\varepsilon_s)}, \text{ if } A_v \geq A_{v,\min} \quad (2.15)$$

$$\beta = \frac{4.8}{(1 + 750\varepsilon_s)} \frac{51}{(39 + s_{xe})}, \text{ if } A_v < A_{v,\min} \quad (2.16)$$

where  $\varepsilon_s$  = average tensile strain in cracked concrete in the direction of tension tie. The strain  $\varepsilon_s$  is calculated from a relationship of axial force, shear force, flexural moment, prestress force, and stiffness of flexural reinforcement, as shown in Figure 2.35, and shall be determined as:

$$\varepsilon_s = \frac{(\frac{|M_u|}{d_v} + 0.5N_u + |V_u - V_p| - A_{ps}f_{po})}{E_sA_s + E_pA_{ps}} \quad (2.17)$$

If the calculated value of  $\varepsilon_s$  is negative, it should be taken as zero, or the value should be recalculated with the denominator replaced by  $(E_sA_s + E_pA_{ps} + E_cA_{ct})$ , where:

$$-0.4 \times 10^{-3} \leq \varepsilon_s \leq 6 \times 10^{-3} \quad (2.18)$$

The crack spacing parameter,  $s_{xe}$ , shall be determined as (in.):

$$s_{xe} = s_x \frac{1.38}{\alpha_g + 0.63} \quad (2.19)$$

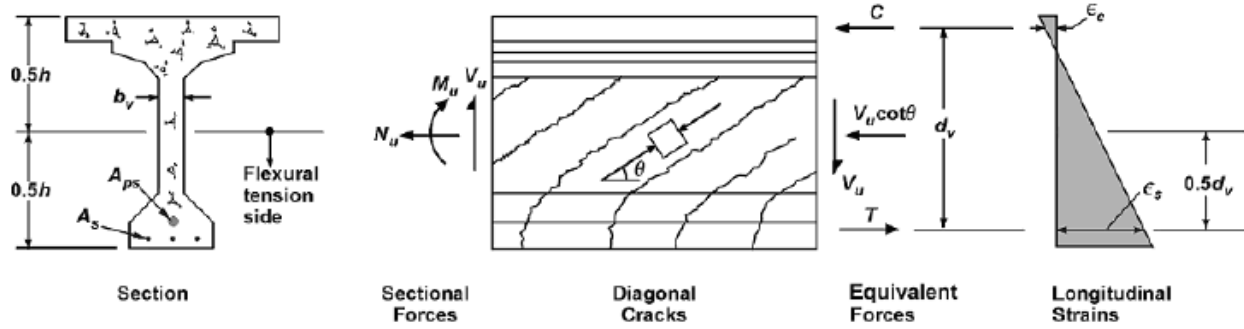
where  $12.0 \text{ in.} \leq s_{xe} \leq 80.0 \text{ in.}$ ;  $M_u$  = factored moment at the section factored moment, not to be taken less than  $|V_u - V_p| d_v$  (kip-in.);  $N_u$  = applied factored axial force, taken as positive if tensile (kip);  $V_u$  = factored shear force at section (kip);  $f_{po}$  = a parameter taken as modulus of elasticity (MOE) of prestressing tendons multiplied by the locked-in difference in strain between the prestressing tendons and the surrounding concrete. For the usual levels of prestressing, a value of  $f_{po} = 0.7f_{pu}$  will be appropriate for both pretensioned and post-tensioned members (ksi);  $f_{ps}$  = average stress in prestressing steel at the time for which the nominal resistance of member is required (ksi);  $s_x$  = crack spacing parameter taken as the lesser of either  $d_v$  or the maximum distance between layers of longitudinal crack control reinforcement, where the area of the reinforcement in each layer is not less than  $0.003b_v s_x$  (in.);  $\alpha_g$  = maximum aggregate size (in.)  $d_v$  = effective shear depth taken as the distance, measured perpendicular to the neutral axis,

between the resultants of the tensile and compressive forces due to flexure. It need not be taken to be less than the greater of  $0.9d_e$  or  $0.72h$ , or shall be determined as:

$$d_v = \frac{M_n}{A_s f_y + A_{ps} f_{ps}} \quad (2.20)$$

where  $M_n$  = nominal flexural resistance (kip-in.); and  $d_e$  = effective depth from extreme compression fiber to the centroid of the tensile force in the tensile reinforcement, which shall be determined as:

$$d_e = \frac{A_{ps} f_{ps} d_p + A_s f_y d_s}{A_{ps} f_{ps} + A_s f_y} \quad (2.21)$$



**Figure 2.35. Calculation procedure for determining  $\epsilon_s$  (AASHTO 2020).**

The web reinforcement shear,  $V_s$ , is determined as:

$$V_s = \frac{A_v f_y d_v (\cot \theta + \cot \alpha) \sin \alpha}{s} \lambda_{duct} \quad (2.22)$$

where  $\alpha$  = angle of inclination of transverse reinforcement to the longitudinal axis (degrees), and  $\theta$  is the angle of inclination of diagonal compressive stresses (degrees), and is determined as:

$$\theta = 29 + 3500 \epsilon_s \quad (2.23)$$

Furthermore,  $\lambda_{duct}$  is the shear strength reduction factor accounting for the reduction in the shear resistance provided by the transverse reinforcement due to the presence of a grouted post-tensioning duct. It shall be determined as:

$$\lambda_{\text{duct}} = 1 - \delta \left( \frac{\phi_{\text{duct}}}{b_w} \right)^2 \quad (2.24)$$

where  $\delta$  = duct diameter correction factor, taken as 2.0 for grouted duct;  $\phi_{\text{duct}}$  = diameter of post-tensioning duct present in the girder web within depth  $d_v$  (in.); and  $b_w$  = gross width of web, not reduced for the presence of post-tensioning duct (in.). For girders with ungrouted ducts,  $\lambda_{\text{duct}}$  should be taken as 1.0, and  $b_v$  must be reduced to account for the duct diameter.

#### 2.6.1.1 Minimum Shear Reinforcement

A minimum amount of shear reinforcement is required to prevent the growth of diagonal cracks and to ensure a smooth load redistribution from the uncracked to the cracked state. In AASHTO LRFD 2020, the expression of the minimum amount of shear reinforcement is:

$$A_{V,\min} \geq 0.0316 \lambda \sqrt{f'_c} \frac{b_v s}{f_y} \quad (2.25)$$

where  $f_y$  = yield strength of transverse reinforcement (ksi), and  $f_y$  is not permitted to exceed 100 ksi. This reinforcement is required when the design demand is larger than half of the concrete strength, in other words, when  $V_u > \phi(V_c + V_p)$ .

#### 2.6.1.2 Maximum Spacing of Transverse Reinforcement

The spacing of transverse reinforcement as defined in AASHTO LRFD 2020 shall not exceed the maximum allowed spacing,  $S_{\max}$ , verified by Shahrooz et al. (2011) for prestressed and nonprestressed members and shall be determined as:

If  $v_u < 0.125f'_c$ , then:

$$S_{\max} = 0.8d_v \leq 24.0 \text{ in.} \quad (2.26)$$

If  $v_u \geq 0.125f'_c$ , then:

$$S_{\max} = 0.4d_v \leq 12.0 \text{ in.} \quad (2.27)$$

where  $v_u$  = shear stress (ksi) on the concrete and shall be determined as:

$$v_u = \frac{|V_u - \phi V_p|}{\phi b_v d_v} \quad (2.28)$$

## 2.6.2 AASHTO LRFD Design Specifications, 6th Edition

The AASHTO LRFD Bridge Design Specifications 2012 (AASHTO 2012) provided two techniques to determine the terms  $V_c$  and  $V_s$  for prestress concrete beams: (1) the general procedure; and (2) the simplified procedure. The simplified procedure for prestressed and nonprestressed has not been included in the AASHTO LRFD 8th and 9th editions.

### 2.6.2.1 General Procedure

The general procedure is based on a set of conservative simplifying assumptions of the MCFT-based shear design procedure. Prior to the 2008 interim revisions, the general procedure was iterative and required the use of tables for the evaluation of  $\beta$  and  $\theta$ , as shown in Table 2.1 and Table 2.2. With the 2008 revisions, this design procedure was modified to be non-iterative, and algebraic equations were introduced for the evaluation of  $\beta$  and  $\theta$ . The concrete shear,  $V_c$ , and web reinforcement shear,  $V_s$ , in the AASHTO LRFD 2017 specifications are given in:

$$V_c = 0.0316\beta\sqrt{f'_c}b_v d_v \quad (2.29)$$

$$V_s = \frac{A_v f_y d_v (\cot\theta + \cot\alpha) \sin\alpha}{s} \quad (2.30)$$



**Table 2.1. Values of  $\beta$  and  $\theta$  for sections with transverse reinforcement (AASHTO 2012).**

$\frac{v_u}{f'_c}$	$\epsilon_x \times 1,000$								
	$\leq -0.20$	$\leq -0.10$	$\leq -0.05$	$\leq 0$	$\leq 0.125$	$\leq 0.25$	$\leq 0.50$	$\leq 0.75$	$\leq 1.00$
$\leq 0.075$	22.3 6.32	20.4 4.75	21.0 4.10	21.8 3.75	24.3 3.24	26.6 2.94	30.5 2.59	33.7 2.38	36.4 2.23
$\leq 0.100$	18.1 3.79	20.4 3.38	21.4 3.24	22.5 3.14	24.9 2.91	27.1 2.75	30.8 2.50	34.0 2.32	36.7 2.18
$\leq 0.125$	19.9 3.18	21.9 2.99	22.8 2.94	23.7 2.87	25.9 2.74	27.9 2.62	31.4 2.42	34.4 2.26	37.0 2.13
$\leq 0.150$	21.6 2.88	23.3 2.79	24.2 2.78	25.0 2.72	26.9 2.60	28.8 2.52	32.1 2.36	34.9 2.21	37.3 2.08
$\leq 0.175$	23.2 2.73	24.7 2.66	25.5 2.65	26.2 2.60	28.0 2.52	29.7 2.44	32.7 2.28	35.2 2.14	36.8 1.96
$\leq 0.200$	24.7 2.63	26.1 2.59	26.7 2.52	27.4 2.51	29.0 2.43	30.6 2.37	32.8 2.14	34.5 1.94	36.1 1.79
$\leq 0.225$	26.1 2.53	27.3 2.45	27.9 2.42	28.5 2.40	30.0 2.34	30.8 2.14	32.3 1.86	34.0 1.73	35.7 1.64
$\leq 0.250$	27.5 2.39	28.6 2.39	29.1 2.33	29.7 2.33	30.6 2.12	31.3 1.93	32.8 1.70	34.3 1.58	35.8 1.50

**Table 2.2. Values of  $\beta$  and  $\theta$  for sections with less than minimum transverse reinforcement (AASHTO 2012).**

$s_{xe}$ , in.	$\epsilon_x \times 1,000$										
	$\leq -0.20$	$\leq -0.10$	$\leq -0.05$	$\leq 0$	$\leq 0.125$	$\leq 0.25$	$\leq 0.50$	$\leq 0.75$	$\leq 1.00$	$\leq 1.50$	$\leq 2.00$
$\leq 5$	25.4	25.5	25.9	26.4	27.7	28.9	30.9	32.4	33.7	35.6	37.2
	6.36	6.06	5.56	5.15	4.41	3.91	3.26	2.86	2.58	2.21	1.96
$\leq 10$	27.6	27.6	28.3	29.3	31.6	33.5	36.3	38.4	40.1	42.7	44.7
	5.78	5.78	5.38	4.89	4.05	3.52	2.88	2.50	2.23	1.88	1.65
$\leq 15$	29.5	29.5	29.7	31.1	34.1	36.5	39.9	42.4	44.4	47.4	49.7
	5.34	5.34	5.27	4.73	3.82	3.28	2.64	2.26	2.01	1.68	1.46
$\leq 20$	31.2	31.2	31.2	32.3	36.0	38.8	42.7	45.5	47.6	50.9	53.4
	4.99	4.99	4.99	4.61	3.65	3.09	2.46	2.09	1.85	1.52	1.31
$\leq 30$	34.1	34.1	34.1	34.2	38.9	42.3	46.9	50.1	52.6	56.3	59.0
	4.46	4.46	4.46	4.43	3.39	2.82	2.19	1.84	1.60	1.30	1.10
$\leq 40$	36.6	36.6	36.6	36.6	41.2	45.0	50.2	53.7	56.3	60.2	63.0
	4.06	4.06	4.06	4.06	3.20	2.62	2.00	1.66	1.43	1.14	0.95
$\leq 60$	40.8	40.8	40.8	40.8	44.5	49.2	55.1	58.9	61.8	65.8	68.6
	3.50	3.50	3.50	3.50	2.92	2.32	1.72	1.40	1.18	0.92	0.75
$\leq 80$	44.3	44.3	44.3	44.3	47.1	52.3	58.7	62.8	65.7	69.7	72.4
	3.10	3.10	3.10	3.10	2.71	2.11	1.52	1.21	1.01	0.76	0.62

### 2.6.2.2 Simplified Procedure

The basis of the simplified procedure is compatible with the ACI 318-19 detailed method, in which the term  $V_c$  is taken as the lesser of the nominal shear resistance,  $V_{ci}$ , provided by concrete when inclined cracking results from combined shear and moment, and the nominal shear resistance,  $V_{cw}$ , provided by concrete when inclined cracking results from excessive principal tensions in the web shear resistances  $V_{ci}$  and  $V_{cw}$ , shall be determined as:

$$V_{ci} = 0.02\sqrt{f'_c}b_vd_v + V_d + \frac{V_iM_{cre}}{M_{max}} \geq 0.06\sqrt{f'_c}b_vd_v \quad (2.31)$$

$$V_{cw} = (0.06\sqrt{f'_c} + 0.3f_{pc})b_v d_v + V_p \quad (2.32)$$

where  $V_d$  = shear force at section due to unfactored dead load and includes both DC and DW (kip);  $V_i$  = factored shear force at section due to externally applied loads occurring simultaneously with  $M_{max}$  (kip);  $M_{max}$  = maximum factored moment at section due to externally applied loads (kip-in); and  $M_{cre}$  = moment (kip-in) causing flexural cracking at section due to externally applied loads. Moment  $M_{cre}$  shall be determined as:

$$M_{cre} = S_c(f_r + f_{cpe} - \frac{M_{dnc}}{S_{nc}}) \quad (2.33)$$

where  $S_c$  = section modulus for the extreme fiber of the composite section where tensile stress is caused by externally applied loads (in.<sup>3</sup>);  $f_r$  = modulus of rupture (MOR) of concrete (ksi);  $f_{cpe}$  = compressive stress in concrete due to effective prestress forces only (after allowance for all prestress losses) at the extreme fiber of section where tensile stress is caused by externally applied loads (ksi);  $M_{dnc}$  = total unfactored dead load moment acting on the monolithic or noncomposite section (kip-in.); and  $S_{nc}$  = section modulus for the extreme fiber of the monolithic or noncomposite section where tensile stress is caused by externally applied loads (in.<sup>3</sup>)

The shear resistance provided by shear reinforcement shall be determined by the equation adopted by the general procedure but with a different angle of inclination of diagonal compressive stresses' equations, as follows:

$$V_s = \frac{A_v f_y d_v (\cot\theta + \cot\alpha) \sin\alpha}{s} \quad (2.34)$$

where  $\theta$  = angle of inclination of diagonal compressive stresses (degrees), and  $\cot\theta$  shall be determined as:

$$\cot\theta = \begin{cases} 1.0, & \text{when } V_{ci} < V_{cw} \\ 1.0 + 3 \left( \frac{f_{pc}}{\sqrt{f'_c}} \right) \leq 1.8, & \text{when } V_{ci} \geq V_{cw} \end{cases} \quad (2.35)$$

### 2.6.3 ACI 318-19 Building Code Requirements for Structural Concrete

The ACI 318-19 specifications (ACI318-19 2019) provide the shear capacity of a prestressed concrete member based on the modified truss analogy. The primary difference between the truss analogy and the modified truss analogy is that the latter accounts for the contribution of the concrete compression zone in resisting shear load (Bruce 1969). The nominal shear strength,  $V_n$ , is typically calculated as a sum of two shear contributions, namely that of concrete  $V_c$  and that of the shear reinforcement  $V_s$ :

$$V_n = V_c + V_s \quad (2.36)$$

The ACI 318-19 provisions usually assume that the diagonal members in the truss are inclined at 45 degrees and that shear reinforcement needs to be provided to resist only the shear exceeding that which causes inclined cracking, that is,  $V_c$ . Also,  $V_s$  shall be determined as:

$$V_s = \frac{A_v f_{yt} d}{s} \quad (2.37)$$

and  $V_s$  should not exceed  $8\sqrt{f'_c}b_w d$ , which represents the strength due to failure of the compression diagonal.

The ACI 318-19 code provides two procedures to calculate  $V_c$  for prestressed concrete girders, often called (a) the approximate method, and (b) the detailed method, both of which are discussed below.

#### 2.6.3.1 Approximate Method

This procedure adopts a simple method of calculating  $V_c$  for prestressed concrete beams derived by MacGregor and Hanson (1969). This provision is applicable to beams having prestressed reinforcement only or to members reinforced with a combination of prestressed and nonprestressed reinforcement, with effective prestress greater than 40 percent of the tensile strength of flexural reinforcement ( $A_{ps}f_{se} \geq 0.4(A_{ps}f_{pu} + A_s f_y)$ ). According to this method,  $V_c$  is calculated as the least of:

$$V_c = \left( 0.6\lambda\sqrt{f'_c} + 700 \frac{V_u d_p}{M_u} \right) b_w d \quad (2.38)$$

$$V_c = (0.6\lambda\sqrt{f'_c} + 700) b_w d \quad (2.39)$$

$$V_c = 5\lambda\sqrt{f'_c} b_w d \quad (2.40)$$

However,  $V_c$  need not be less than  $2\lambda\sqrt{f'_c} b_w d$ .

### 2.6.3.2 Detailed Method

This procedure accounts for two different types of inclined cracks that are commonly observed in concrete members: (1) web shear cracking; and (2) flexure-shear cracking. Web shear cracking initiates from an interior point in a beam when the principal tensile stresses exceed the tensile strength of the concrete, while flexure-shear cracking initiates from flexural cracking at the tension fiber and propagates on the web, following a progressively inclining path determined by the principal compressive stress field.

According to the detailed method, the nominal shear strength provided by the concrete,  $V_c$ , is assumed equal to the lesser of flexural shear strength,  $V_{ci}$ , and web shear strength,  $V_{cw}$ . The flexural shear strength is calculated by the least of:

$$V_{ci} = 0.6\lambda\sqrt{f'_c} b_w d_p + V_d + \frac{V_i M_{cre}}{M_{max}} \quad (2.41)$$

$$V_{ci} = 2\lambda\sqrt{f'_c} b_w d \text{ , if } A_{ps} f_{se} \geq 0.4(A_{ps} f_{pu} + A_s f_y) \quad (2.42)$$

$$V_{ci} = 1.7\lambda\sqrt{f'_c} b_w d \text{ , if } A_{ps} f_{se} < 0.4(A_{ps} f_{pu} + A_s f_y) \quad (2.43)$$

where  $V_d$  = shear force at the section due to an unfactored dead load (lb);  $V_i$  = factored shear force at section due to externally applied loads occurring simultaneously with  $M_{max}$  (lb); and  $M_{cre}$  = moment (lb-in.) causing flexural cracking at section due to externally applied loads. Moment  $M_{cre}$  is calculated by:

$$M_{cre} = \left(\frac{I}{y_t}\right)(6\lambda\sqrt{f'_c} + f_{pe} - f_d) \quad (2.44)$$

where  $I$  = moment of inertia of section about the centroidal axis (in.<sup>4</sup>);  $y_t$  = distance from the centroidal axis of the gross section (in.);  $f_{pe}$  = compressive stress in concrete due to effective prestress force only at the extreme fiber of section where tensile stress is caused by externally applied loads (psi);  $f_d$  = stress due to unfactored dead load at the extreme fiber of section where tensile stress is caused by externally applied loads (psi); and  $M_{max}$  = maximum factored moment at section due to externally applied loads reinforcement, to tension face (lb-in.).

The web shear strength,  $V_{cw}$ , was derived from an analysis using Mohr's circle and based on the assumption that web shear cracking initiates at a shear level, thus causing principal tensile stress of approximately  $4\lambda\sqrt{f'_c}$  at the centroidal axis of the cross section. The web shear strength is calculated by:

$$V_{cw} = (3.5\lambda\sqrt{f'_c} + 0.3f_{pc})b_wd_p + V_p \quad (2.45)$$

where  $f_{pc}$  = compressive stress in concrete at the centroid of cross section resisting externally applied loads or at the junction of web and flange when the centroid lies within the flange (psi); and  $V_p$  = vertical component of effective prestress force at the section without load factors (lb).

### 2.6.3.3 Minimum Shear Reinforcement

The ACI 318-19 Code states that a minimum amount of shear reinforcement should be provided when  $V_u > \phi\lambda\sqrt{f'_c}b_wd$  for nonprestressed beams and  $V_u > 0.5\phi V_c$  for prestressed beams. The ACI 318-19 employs two expressions for the minimum amount of shear reinforcement for reinforced and prestressed concrete beams. The first expression is applicable to both nonprestressed concrete beams and prestressed concrete beams with effective prestress in prestressing steel less than 40 percent of its tensile strength ( $A_{ps}f_{se} < 0.4(A_{ps}f_{pu} + A_s f_y)$ ):

$$A_{v,min} \geq 0.75\sqrt{f'_c} \frac{b_w S}{f_{yt}} \quad (2.46)$$

but not less than:

$$A_{v,min} \geq 50 \frac{b_w S}{f_{yt}} \quad (2.47)$$

where  $f_{se}$  = effective stress in prestressed reinforcement after allowance for all prestress losses (psi).

The second expression is applicable only for prestressed concrete members with effective prestress in prestressing steel that is at least 40 percent of its tensile strength ( $A_{ps}f_{se} \geq 0.4(A_{ps}f_{pu} + A_s f_y)$ ) and shall be determined as the lesser of two values calculated by:

$$A_{v,min} \geq \frac{A_{ps}f_{pu}}{80f_{yt}d} \sqrt{\frac{d}{b_w}} \quad (2.48)$$

$$A_{v,min} \geq 0.75\sqrt{f'_c} \frac{b_w S}{f_{yt}} \geq 50 \frac{b_w S}{f_{yt}} \quad (2.49)$$

#### 2.6.3.4 Maximum Spacing of Transverse Reinforcement

The maximum spacing of transverse reinforcement along length as defined in ACI 318-19 for nonprestressed and prestressed concrete beams shall be determined as:

If  $V_s \leq 4\sqrt{f'_c}b_w d$ , then:

$$s_{max} = d/2 \leq 24.0 \text{ in., for nonprestressed concrete beams;}$$

$$s_{max} = 3h/4 \leq 24.0 \text{ in., for prestressed concrete beams.}$$

(2.50)

If  $V_s > 4\sqrt{f'_c}b_w d$ , then:

$$s_{max} = d/4 \leq 12.0 \text{ in., for nonprestressed concrete beams;}$$

$$s_{max} = 3h/8 \leq 12.0 \text{ in., for prestressed concrete beams.}$$

### 2.6.4 *fib* Model Code 2010

The shear resistance design of the *fib* Model Code 2010 is also based on the MCFT. For this reason, it has a lot of parts that are the same as the AASHTO LRFD, which also employs the MCFT for shear design. The *fib* Model Code 2010 has three LoA for calculating the shear resistance. The complexity of the method and the accuracy of the results differ based on the LoA. As the level goes up, it is appropriate to be used for a member in a more complex loading state or a more elaborate assessment of a structure. The design shear resistance is calculated by adding the  $V_{Rd,c}$  and  $V_{Rd,s}$  which are shear resistances provided by each concrete and stirrups, and they are calculated as:

$$V_{Rd,s} = \frac{A_{sw}}{s_w} z f_{ywd} (\cot \theta + \cot \alpha) \sin \alpha \quad (2.51)$$

$$V_{Rd,c} = k_v \frac{\sqrt{f_{ck}}}{\gamma_c} z b_w \quad (2.52)$$

where  $A_{sw}$  = area of shear reinforcement;  $s_w$  = spacing of shear reinforcement;  $z$  = internal lever arm;  $f_{ywd}$  = design of tension yield stress of nonprestressing reinforcement;  $\theta$  = the selected inclination of the compression stresses, taken as  $36^\circ$  for Level 1,  $20^\circ + 10000\varepsilon_x \leq \theta \leq 45^\circ$  for Level 2, and  $29^\circ + 7000\varepsilon_x$  for Level 3; and  $\varepsilon_x$  = the longitudinal strain at the mid-depth of the member. The strain  $\varepsilon_x$  is calculated as:

$$\varepsilon_x = \frac{\frac{M_{Ed}}{z} + V_{Ed} + 0.5N_{Ed} - A_p f_{po}}{2(E_s A_s + E_p A_p)} \quad (2.53)$$

where  $\alpha$  = inclination of the stirrups relative to the beam axis; and  $k_v$  depends on the level of approximation. For Level 1:

$$k_v = \begin{cases} \frac{200}{(1000 + 1.3z)} \leq 0.15, & \text{if } \rho_w = 0 \\ 0.15, & \text{if } \rho_w \geq \frac{0.08\sqrt{f_{ck}}}{f_{yk}} \end{cases} \quad (2.54)$$



For Level 2,  $k_v = 0$ , and for Level 3:

$$k_v = \begin{cases} \frac{0.4}{(1 + 1500\varepsilon_x)} \cdot \frac{1300}{(1000 + 0.7k_{dg}z)} \leq 0.15, & \text{if } \rho_w = 0 \\ 0.15, & \text{if } \rho_w \geq 0.08\sqrt{f_{ck}}/f_{yk} \end{cases} \quad (2.55)$$

where  $k_{dg} = \frac{48}{16+d_g} \geq 1.15$  (for concrete strength exceeding 70MPa,  $d_g$  should be taken as 0);

$d_g$  = aggregate diameter;  $f_{ck}$  = characteristic value of cylinder compressive strength of concrete,  $f'_c$ , derived from strength test by the criterion that 5 percent of measurements for the specified concrete is assumed to be below the value  $f_{ck}$ ;  $\gamma_c$  = partial safety factor for concrete material properties, shall be taken as 1.2 or 1.5; and  $b_w$  = width of web.

For designing the shear reinforcement, the *fib* Model Code 2010 provides the minimum shear reinforcement requirement as follows:

$$A_{sw,min} = 0.12\sqrt{f_{ck}} \frac{b_w s_w}{f_{yk}} \text{ (MPa, mm)} \quad (2.56)$$

where  $f_{yk}$  = characteristic value of yield strength of shear reinforcement.

Also, the *fib* Model Code 2010 derives maximum shear strength  $V_{Rd,max}$  from the following:

$$V_{Rd,max} = k_c \frac{f_{ck}}{\gamma_c} b_w z \frac{\cot \theta + \cot \alpha}{1 + \cot^2 \theta} \text{ (MPa, mm, N)} \quad (2.57)$$

where  $k_c = 0.5 \left( \frac{30}{f_{ck}} \right)^{1/3} \leq 0.5$  ( $f_{ck}$  in MPa) for Level 1, and  $0.55 \left( \frac{30}{f_{ck}} \right)^{1/3} \leq 0.55$  ( $f_{ck}$  in MPa) for Levels 2 and 3.

### 2.6.5 Eurocode 2

The *Standardization* (2004) introduces two processes to calculate the shear resistance. The two processes are separated based on the presence (or not) of the shear reinforcement. Also,  $V_{Ed}$  is the design shear force in the section considered resulting from external loading and prestressing, which determines whether the member requires shear reinforcement.

### 2.6.5.1 Members Not Requiring Design Shear Reinforcement

For members that do not require shear reinforcement, the shear resistance is contributed only by  $V_{Rd,c}$  which is given as:

$$V_{Rd,c} = [C_{Rd,c} k (100 \rho_l f_{ck})^{1/3} + k_1 \sigma_{cp}] b_w d \text{ (MPa, mm, N)} \quad (2.58)$$

with the minimum value of  $V_{Rd,c}$  being provided as:

$$V_{Rd,c} = (v_{\min} + k_1 \sigma_{cp}) b_w d \text{ (MPa, mm, N)} \quad (2.59)$$

where  $C_{Rd,c}$  = can be found in National Annexes, and its recommended value is  $\frac{0.18}{\gamma_c}$ ;  $\gamma_c$  = partial factor for concrete and shall be taken as 1.5 for general situations or 1.2 for accidental expect fire situations;  $k = 1 + \sqrt{\frac{200}{d}} \leq 2.0$ , where  $d$  is in mm;  $d$  = effective depth of a cross section (mm);  $\rho_l = \frac{A_{sl}}{b_w d} \leq 0.02$ ;  $A_{sl}$  = area of the tensile reinforcement, which extends  $\geq (l_{bd} + d)$  beyond the section considered ( $\text{mm}^2$ );  $b_w$  = the smallest width of the cross section in the tensile area (mm);  $f_{ck}$  = characteristic compressive cylinder strength of concrete at 28 days (MPa);  $k_1$  = can be found in National Annexes, and its recommended value is 0.15;  $\sigma_{cp} = \frac{N_{ed}}{A_c} < 0.2 f_{cd}$  (MPa);  $N_{ed}$  = axial force in cross section due to loading or prestress force (N);  $A_c$  = area of concrete cross section ( $\text{mm}^2$ );  $f_{cd}$  = design value of concrete compressive strength; and  $v_{\min}$  = can be found in National Annexes, and its recommended value is  $0.035 k^{3/2} f_{ck}^{1/2}$ .

In prestressed single-span members without shear reinforcement, the shear resistance of the regions that remain uncracked in bending is calculated as:

$$V_{Rd,c} = \frac{I b_w}{S} \sqrt{(f_{ctd})^2 + \alpha_l \sigma_{cp} f_{ctd}} \quad (2.60)$$

where  $I$  = second moment of area ( $\text{mm}^4$ );  $b_w$  = width of the cross section at the centroidal axis (mm);  $S$  = first moment of the area above and about the centroidal axis ( $\text{mm}^3$ );  $f_{ctd}$  = design tensile strength of concrete (MPa);  $\alpha_l = l_x / l_{pt2} \leq 1.0$  for pretensioned tendons and 1.0 for other types of prestressing;  $l_x$  = the distance of section considered from the starting point of the

transmission length (mm);  $l_{pt2}$  = the upper bound value of the transmission length of the prestressing element (mm); and  $\sigma_{cp}$  = concrete compressive stress at the centroidal axis due to axial loading and/or prestressing (MPa).

#### 2.6.5.2 Members Requiring Design Shear Reinforcement

For members that require shear reinforcement, the shear resistance is contributed only from  $V_{Rd,s}$ . The angle  $\theta$  between the concrete compression strut and the beam axis perpendicular to shear force should be limited based on the values found in the National Annexes, and the recommended limits are  $1 \leq \cot \theta \leq 2.5$ . The shear resistance  $V_{Rd,s}$  can be calculated as:

$$V_{Rd,s} = \frac{A_{sw}}{s} z f_{ywd} \cot \theta \quad (\text{MPa, mm, N}) \quad (2.61)$$

and shall not exceed:

$$V_{Rd,max} = \frac{\alpha_{cw} b_w z v_1 f_{cd}}{\cot \theta + \tan \theta} \quad (\text{MPa, mm, N}) \quad (2.62)$$

where  $A_{sw}$  = cross-sectional area of the shear reinforcement ( $\text{mm}^2$ );  $s$  = spacing of the stirrups (mm);  $z$  = inner lever arm for a member with a constant depth, corresponding to bending moment in the element under consideration,  $0.9d$  for shear analysis of reinforced concrete without axial force (mm);  $f_{ywd}$  = design yield strength of the shear reinforcement (MPa);  $\theta$  = angle between concrete compression strut and the beam axis perpendicular to shear force;  $\alpha_{cw}$  = coefficient accounting for the state of the stress in the compression chord and taken as 1 when the members are not prestressed. For prestressed members, the coefficient shall be determined as:

$$\alpha_{cw} = \begin{cases} 1 + \frac{\sigma_{cp}}{f_{cd}}, & \text{if } 0 < \sigma_{cp} \leq 0.25f_{cd} \\ 1.25, & \text{if } 0.25f_{cd} < \sigma_{cp} \leq 0.5f_{cd} \\ 2.5 \left( 1 - \frac{\sigma_{cp}}{f_{cd}} \right), & \text{if } 0.5f_{cd} < \sigma_{cp} \leq f_{cd} \end{cases} \quad (2.63)$$

where  $\sigma_{cp}$  = compression stress in concrete from axial force or prestress force (MPa);  $f_{cd}$  = design value of concrete compressive strength (MPa);  $b_w$  = minimum width between tension and compression chords (mm);  $v_1$  = strength reduction factor for concrete cracked in shear, taken as 0.6 when design stress of shear reinforcement is below 80 percent of characteristic yield strength and  $f_{ck} \leq 60$  MPa, and  $0.6 \left(1 - \frac{f_{ck}}{250}\right)$  when design stress of shear reinforcement is below 80 percent of characteristic yield strength and  $f_{ck} \geq 60$  MPa. Also,  $f_{ck}$  = characteristic compressive cylinder strength of concrete at 28 days (MPa).

## 2.6.6 TxDOT Shear Design Specifications

The design for shear reinforcement by TxDOT is made in order to adopt the 9th edition of the AASHTO LRFD Bridge Design Specifications. The TxDOT Design Manual (TxDOT 2023) specifies the use of the AASHTO LRFD General Procedure for the design of shear reinforcement in reinforced concrete beams. However, TxDOT does not recommend provisions of Appendix B5 of the AASHTO LRFD Bridge Design Specifications (general procedure for shear design with tables to calculate the value of  $\theta$  and  $\beta$ ).

TxDOT Bridge Standards (TxDOT 2022) of prestress concrete girders use No. 4 stirrups Grade 60 for shear reinforcement. TxDOT's standards show the spacing ranges between 3 in. and 18 in. along the entire length of prestressed concrete I-girders, and the maximum spacing for shear reinforcement is 12 in. for Tx28 and Tx34 and 18 in. for deeper girders (Tx40, Tx46, Tx54, Tx62, Tx70). The 3 in. spacing used at girder ends is intended to help minimize the number and size of cracks that may appear there. Also, TxDOT's standards show the maximum spacing limit is 12 in. for box beams and 18 in. for U-beams. However, the TxDOT Bridge Design Manual uses size No. 5 but not larger than No. 6 stirrups as transverse reinforcement for reinforced and post-tensioned concrete bent caps and limits the spacing of shear reinforcement within transfer lengths to a minimum of 4 in. and a maximum of 12 in.

The calculated value of minimum shear reinforcement ratio from TxDOT standards,  $\rho_{v,min,TxDOT}$ , for Tx28 and Tx34 girders is 0.476 percent. In contrast, the calculated value of minimum shear reinforcement ratio based on different provisions are smaller, as shown in Table 2.3. Specifically, for Tx28 and Tx34, based on the AASHTO LRFD 9th

edition,  $\rho_{v,min,AASHTO}$  ranges from 0.117 percent to 0.143 percent depending on the concrete compressive strength. Also,  $\rho_{v,min,ACI}$  ranges from 0.088 percent to 0.107 percent, while  $\rho_{v,min,fib}$  and  $\rho_{v,min,EC2}$  range from 0.166 percent to 0.204 percent. Moreover, for deeper TxDOT I-girders,  $\rho_{v,min,TxDOT}$  is 0.317 percent, while  $\rho_{v,min,AASHTO}$  ranges from 0.117 percent to 0.148 percent,  $\rho_{v,min,ACI}$  ranges from 0.088 percent to 0.111 percent, and  $\rho_{v,min,fib}$  and  $\rho_{v,min,EC2}$  range from 0.166 percent to 0.211 percent.

**Table 2.3. Minimum shear reinforcement ratios of TxDOT I-girders with different provisions.**

Structure	$\rho_{v,min,AASHTO}$ (%)	$\rho_{v,min,ACI}$ (%)	$\rho_{v,min,fib}$ (%)	$\rho_{v,min,EC2}$ (%)
Tx28	0.117-0.143	0.088-0.107	0.166-0.204	0.166-0.204
Tx34	0.117-0.137	0.088-0.103	0.166-0.195	0.166-0.195
Tx40	0.131-0.148	0.098-0.111	0.186-0.211	0.186-0.211
Tx46	0.117-0.138	0.083-0.103	0.166-0.196	0.166-0.196
Tx54	0.117-0.141	0.088-0.106	0.166-0.201	0.166-0.201
Tx62	0.117-0.147	0.088-0.110	0.166-0.209	0.166-0.209

## 2.6.7 Minimum Shear Standards for State DOTs

Although different states adopt different design guidelines and provisions, the majority of these provisions are aligned with different editions of the AASHTO LRFD Bridge Design Specifications. However, many of the states adopt AASHTO LRFD minimum shear reinforcement ratio equations having different maximum spacing provisions based on the state's practice. In addition, there is also a key difference in the size of the stirrups being used—varying between No. 4, No. 5, and No. 6 bars. The minimum shear reinforcement provisions adopted by all states identified from DOT bridge design manuals are summarized in Table 2.4.

**Table 2.4. Summary of state DOT minimum shear provisions.**

State	Adopt the Use of the AASHTO LRFD for the Structural Design of Highway Bridges	Edition of AASHTO LRFD Bridge Design Specifications	$\frac{A_{v,min}}{s}$	$S_{max}$	Stirrups Size
Alabama	yes	9 <sup>th</sup> (2020)	$\geq 0.0316\sqrt{f'_c} \frac{b_v}{f_y}$	12 in.	#5
Alaska	yes	6 <sup>th</sup> (2012)	$\geq 0.0316\sqrt{f'_c} \frac{b_v}{f_y}$	18 in.	NA
Arizona	yes	AASHTO 1979	$\geq \frac{100b'}{f_{sy}}$	$S_{max} \leq \frac{3}{4}h$	NA
Arkansas	yes	7 <sup>th</sup> (2014)	$\geq 0.0316\sqrt{f'_c} \frac{b_v}{f_y}$	$S_{max} = 0.8d_v \leq 24.0 \text{ in.}$ If $V_u < 0.125f'_c$ ,  $S_{max} = 0.4d_v \leq 12.0 \text{ in.}$ If $V_u \geq 0.125f'_c$ ,	NA
California	yes	8 <sup>th</sup> (2017)	$\geq 0.0316\sqrt{f'_c} \frac{b_v}{f_y}$	$S_{max} = 0.8d_v \leq 18.0 \text{ in.}$ If $V_u < 0.125f'_c$ ,  $S_{max} = 0.4d_v \leq 12.0 \text{ in.}$ If $V_u \geq 0.125f'_c$ ,	#5

State	Adopt the Use of the AASHTO LRFD for the Structural Design of Highway Bridges	Edition of AASHTO LRFD Bridge Design Specifications	$\frac{A_{v,min}}{s}$	$S_{max}$	Stirrups Size
Colorado	yes	9 <sup>th</sup> (2020)	$\geq 0.0316\sqrt{f'_c} \frac{b_v}{f_y}$	18 in.	#4
Connecticut	yes	NA	NA	NA	NA
Delaware	yes	8 <sup>th</sup> (2017)	$\geq 0.0316\sqrt{f'_c} \frac{b_v}{f_y}$	24 in.	#4
Florida	yes	8 <sup>th</sup> (2017)	$\geq 0.0316\sqrt{f'_c} \frac{b_v}{f_y}$	18 in.	#5
Georgia	yes	9 <sup>th</sup> (2020)	$\geq 0.0316\sqrt{f'_c} \frac{b_v}{f_y}$	$S_{max} = 0.8d_v$ $\leq 24.0$ in. If $V_u < 0.125f'_c$ ,  $S_{max} = 0.4d_v$ $\leq 12.0$ in. If $V_u \geq 0.125f'_c$ ,	$\leq \#6$
Hawaii	NA	NA	NA	NA	NA
Idaho	NA	NA	NA	NA	NA
Illinois	yes	9 <sup>th</sup> (2020)	$\geq 0.0316\sqrt{f'_c} \frac{b_v}{f_y}$	18 in.	#4
Indiana	yes	9 <sup>th</sup> (2020)	$\geq 0.0316\sqrt{f'_c} \frac{b_v}{f_y}$	$S_{max} = 0.8d_v$ $\leq 24.0$ in. If $V_u < 0.125f'_c$ ,	#4

State	Adopt the Use of the AASHTO LRFD for the Structural Design of Highway Bridges	Edition of AASHTO LRFD Bridge Design Specifications	$\frac{A_{v,min}}{s}$	$S_{max}$	Stirrups Size
				$S_{max} = 0.4d_v$ $\leq 12.0$ in.  If $V_u \geq 0.125f'_c$ ,	
Iowa	yes	8 <sup>th</sup> (2017)	$\geq 0.0316\sqrt{f'_c} \frac{b_v}{f_y}$	19 in.	#4
Kansas	yes	AASHTO 1979	$\geq \frac{50b'}{f_{sy}}$	24 in. or $0.75d_v$	#4
Kentucky	yes	NA	NA	NA	#4
Louisiana	yes	AASHTO 2012	$\geq 0.0316\sqrt{f'_c} \frac{b_v}{f_y}$	12 in.	NA
Maine	yes	2 <sup>nd</sup> (1998)	$\geq 0.083\sqrt{f'_c} \frac{b_v}{f_y}$	12 in.	$\geq$ #4
Maryland	yes	NA	NA	NA	#4 or #5
Massachusetts	yes	8 <sup>th</sup> (2017)	$\geq 0.0316\sqrt{f'_c} \frac{b_v}{f_y}$	20 in.	#4 or #5
Michigan	yes	NA	NA	NA	NA
Minnesota	yes	7 <sup>th</sup> (2014)	$\geq 0.0316\sqrt{f'_c} \frac{b_v}{f_y}$	$S_{max} = 0.8d_v$ $\leq 24.0$ in.  If $V_u < 0.125f'_c$ ,  $S_{max} = 0.4d_v$ $\leq 12.0$ in.	#4 or #5



State	Adopt the Use of the AASHTO LRFD for the Structural Design of Highway Bridges	Edition of AASHTO LRFD Bridge Design Specifications	$\frac{A_{v,min}}{s}$	$S_{max}$	Stirrups Size
				If $V_u \geq 0.125f'_c$ ,	
Missouri	NA	NA	NA	NA	NA
Mississippi	yes	NA	NA	18 in.	NA
Montana	yes	NA	NA	NA	NA
Nebraska	NA	NA	NA	NA	NA
Nevada	yes	6 <sup>th</sup> (2007)	$\geq 0.0316\sqrt{f'_c} \frac{b_v}{f_y}$	$S_{max} = 0.8d_v \leq 24.0 \text{ in.}$ If $V_u < 0.125f'_c$ ,  $S_{max} = 0.4d_v \leq 12.0 \text{ in.}$ If $V_u \geq 0.125f'_c$ ,	NA
New Hampshire	yes	NA	NA	NA	NA
New Jersey	yes	NA	NA	NA	NA
New Mexico	NA	NA	NA	NA	NA
New York	yes	9 <sup>th</sup> (2020)	$\geq 0.0316\sqrt{f'_c} \frac{b_v}{f_y}$	24 in.	#4
North Carolina	yes	NA	NA	NA	#4 or #5
North Dakota	yes	NA	NA	NA	NA

State	Adopt the Use of the AASHTO LRFD for the Structural Design of Highway Bridges	Edition of AASHTO LRFD Bridge Design Specifications	$\frac{A_{v,min}}{s}$	$S_{max}$	Stirrups Size
Ohio	yes	NA	NA	NA	NA
Oklahoma	yes	6 <sup>th</sup> (2007)	$\geq 0.0316\sqrt{f'_c} \frac{b_v}{f_y}$	12 in.	#5
Oregon	yes	9 <sup>th</sup> (2020)	$\geq 0.0316\sqrt{f'_c} \frac{b_v}{f_y}$	18 in.	#4
Pennsylvania	yes	8 <sup>th</sup> (2017)	$\geq 0.0316\sqrt{f'_c} \frac{b_v}{f_y}$	21 in.	#4 or #5 if the spacing required for #4 bars is less than 3 in.
Rhode Island	yes	6 <sup>th</sup> (2007)	$\geq 0.0316\sqrt{f'_c} \frac{b_v}{f_y}$	$S_{max} = 0.8d_v \leq 24.0 \text{ in.}$ If $V_u < 0.125f'_c$ ,  $S_{max} = 0.4d_v \leq 12.0 \text{ in.}$ If $V_u \geq 0.125f'_c$ ,	NA
South Carolina	yes	3 <sup>rd</sup> (2004)	$\geq 0.0316\sqrt{f'_c} \frac{b_v}{f_y}$	$S_{max} = 0.8d_v \leq 24.0 \text{ in.}$ If $V_u < 0.125f'_c$ ,	NA

State	Adopt the Use of the AASHTO LRFD for the Structural Design of Highway Bridges	Edition of AASHTO LRFD Bridge Design Specifications	$\frac{A_{v,min}}{s}$	$S_{max}$	Stirrups Size
				$S_{max} = 0.4d_v$ $\leq 12.0$ in.  If $V_u \geq 0.125f'_c$ ,	
South Dakota	yes	9 <sup>th</sup> (2020)	$\geq 0.0316\sqrt{f'_c} \frac{b_v}{f_y}$	18 in.	NA
Tennessee	yes	9 <sup>th</sup> (2020)	$\geq 0.0316\sqrt{f'_c} \frac{b_v}{f_y}$	$S_{max} = 0.8d_v$ $\leq 24.0$ in.  If $V_u < 0.125f'_c$ ,  $S_{max} = 0.4d_v$ $\leq 12.0$ in.  If $V_u \geq 0.125f'_c$ ,	NA
Texas	yes	9 <sup>th</sup> (2020)	$\geq 0.0316\sqrt{f'_c} \frac{b_v}{f_y}$	18 in. for Tx-70, Tx-62, Tx-54, Tx-46 and Tx-40 girders  12 in. for Tx-34 and Tx-28 girders	#4
Utah	yes	7 <sup>th</sup> (2014)	$\geq 0.0316\sqrt{f'_c} \frac{b_v}{f_y}$	18 in.	$\geq \#4$ and $\leq \#6$
Vermont	yes	6 <sup>th</sup> (2007)	$\geq 0.0316\sqrt{f'_c} \frac{b_v}{f_y}$	$S_{max} = 0.8d_v$ $\leq 24.0$ in.	NA

State	Adopt the Use of the AASHTO LRFD for the Structural Design of Highway Bridges	Edition of AASHTO LRFD Bridge Design Specifications	$\frac{A_{v,min}}{s}$	$S_{max}$	Stirrups Size
				<p>If <math>V_u &lt; 0.125f'_c</math>,</p> <p><math>S_{max} = 0.4d_v \leq 12.0</math> in.</p> <p>If <math>V_u \geq 0.125f'_c</math>,</p>	
Virginia	yes	8 <sup>th</sup> (2017)	$\geq 0.0316\sqrt{f'_c} \frac{b_v}{f_y}$	<p><math>S_{max} = 0.8d_v \leq 24.0</math> in.</p> <p>If <math>V_u &lt; 0.125f'_c</math>,</p> <p><math>S_{max} = 0.4d_v \leq 12.0</math> in.</p> <p>If <math>V_u \geq 0.125f'_c</math>,</p>	#4
Washington	yes	9 <sup>th</sup> (2020)	$\geq 0.0316\sqrt{f'_c} \frac{b_v}{f_y}$	18 in.	$\leq \#5$
West Virginia	yes	7 <sup>th</sup> (2014)	$\geq 0.0316\sqrt{f'_c} \frac{b_v}{f_y}$	<p><math>S_{max} = 0.8d_v \leq 24.0</math> in.</p> <p>If <math>V_u &lt; 0.125f'_c</math>,</p> <p><math>S_{max} = 0.4d_v \leq 12.0</math> in.</p> <p>If <math>V_u \geq 0.125f'_c</math>,</p>	NA

State	Adopt the Use of the AASHTO LRFD for the Structural Design of Highway Bridges	Edition of AASHTO LRFD Bridge Design Specifications	$\frac{A_{v,min}}{s}$	$S_{max}$	Stirrups Size
Wisconsin	yes	9 <sup>th</sup> (2020)	$\geq \frac{(V_n - V_c)}{f_y d_v \cot \theta}$ or $\geq 0.0316 \sqrt{f'_c} \frac{b_v}{f_y}$	18 in.	$\geq \#4$
Wyoming	yes	9 <sup>th</sup> (2020)	$\geq 0.0316 \sqrt{f'_c} \frac{b_v}{f_y}$	$S_{max} = 0.8d_v \leq 24.0 \text{ in.}$ If $V_u < 0.125f'_c$ ,  $S_{max} = 0.4d_v \leq 12.0 \text{ in.}$ If $V_u \geq 0.125f'_c$ ,	NA

Note: NA = data not available.

## 2.7 SUMMARY

The literature review delves into the theoretical foundations of shear failure modes and mechanisms of shear transfer, emphasizing the significance of key factors affecting girder shear capacity and the critical role of minimum shear reinforcement. It thoroughly evaluates the minimum shear reinforcement provisions in various codes of practice, such as ACI 318-19 and AASHTO 2020, and identifies pivotal research studies that contributed to the development of these provisions. Key findings from these studies highlight the impact of material, geometric, and prestressing design properties on minimum shear reinforcement. The review also identifies the RSS as a crucial parameter that quantifies the reserve strength in beams after diagonal shear cracking.

Additionally, the review reveals that AASHTO's minimum shear reinforcement equation does not consider the effects of prestressing, unlike ACI 318-19, and that the maximum spacing provision often governs due to the underestimated minimum shear reinforcement requirement in AASHTO. The review further notes that TxDOT's standard practice specifies a minimum shear reinforcement spacing of 12 in. for Tx28 and Tx34 girders and 18 in. for other I-girders. The review also points out that many state DOTs follow AASHTO provisions, indicating a broader implication for potential changes. The findings underscore the necessity of revising the current provisions to incorporate influential design parameters and address the associated uncertainties to improve girder performance and reliability.

## **CHAPTER 3:**

### **DATASET ANALYSIS**

#### **3.1 INTRODUCTION**

The goal of this project was to investigate minimum shear reinforcement requirements for TxDOT bridge girders and develop new/revised guideline specifications. In achieving this goal, data-driven analyses quantifying shear strengths and exploring minimum shear reinforcement requirements were performed. To perform such analyses, a holistic dataset of shear tests on prestressed concrete girders was synthesized. Using this dataset, an exploratory data analysis was conducted to inform the experimental program so that the selected girder designs would be complementary to those in the dataset. Additionally, use of data-driven methods, such as nonlinear regression and genetic programming (GP), were investigated as a means of deriving analytical expressions for the shear strength at the onset of cracking and at shear failure.

#### **3.2 EXPERIMENTAL DATASET DEVELOPMENT**

##### **3.2.1 Dataset Overview**

The dataset contains 882 specimens reported in 87 past experimental studies conducted between 1954 and 2020. Those 87 references included peer-reviewed journal publications, project reports, and theses. In Table 3.1, a complete list of all references gathered for the dataset collection is provided. Among the 882 specimens, 497 specimens had transverse reinforcement, and the other 385 specimens did not have transverse reinforcement included in their design. When data were derived from two or more references, the first published reference was listed.

**Table 3.1. List of past studies included in the database.**

<b>No.</b>	<b>Authors (Year)</b>	<b>Number of Tests</b>	
		<b>With</b>	<b>Without</b>
1	Zwoyer (1953a)	-	38
2	Hernandez (1958)	38	-
3	Hicks (1958)	-	19
4	MacGregor (1958)	2	13
5	Sozen et al. (1959)	-	76
6	MacGregor et al. (1960)	5	17

No.	Authors (Year)	Number of Tests	
		With	Without
7	Schumacher (1961)	-	7
8	Bruce Jr (1962)	1	-
9	Hanson and Hulsbos (1964)	30	-
10	Arthur (1965)	-	9
11	Olesen et al. (1965)	4	2
12	Kar (1968)	-	29
13	Calfisch and Thürlimann (1970)	4	-
14	Bennett and Balasooriya (1971)	23	-
15	Regan (1971)	-	8
16	Krauss et al. (1973)	3	-
17	Leonhardt et al. (1973)	3	-
18	Bennett and Debaiky (1974)	4	-
19	Cederwall et al. (1974)	-	12
20	Moayer and Regan (1974)	12	-
21	Lyngberg (1976)	7	-
22	Mahgoub (1976)	-	20
23	Bruggeling et al. (1978)	2	-
24	Nielsen and Braestrup (1978)	-	5
25	Okada et al. (1980)	-	2
26	Funakoshi and Okamoto (1981)	-	3
27	Funakoshi et al. (1982)	-	3
28	Kordina et al. (1983)	1	-
29	Muguruma et al. (1983)	-	3
30	Funakoshi et al. (1984)	-	2
31	Kordina and Weber (1984)	2	-
32	Robertson (1984)	-	1
33	Elzanaty (1985)	2	14
34	Kordina and Teutsch (1986)	11	-
35	Xuan (1986)	5	1
36	Sato (1987)	6	9
37	Hartman et al. (1988)	5	1
38	Kaufman and Ramirez (1988)	6	-
39	Maruyama and Rizkalla (1988)	7	2
40	Kang et al. (1989)	27	-
41	Rangan (1991)	12	-
42	Tan and Mansur (1992)	-	8
43	Public Works Research Institute (1995)	-	10
44	Ito et al. (1996)	-	2
45	Shahawy and de V Batchelor (1996)	34	6
46	Aparicio et al. (1997)	6	-
47	Ito et al. (1997)	-	1
48	Teng et al. (1998a)	10	11



No.	Authors (Year)	Number of Tests	
		With	Without
49	Tan et al. (1999)	9	3
50	Ma et al. (2000)	4	-
51	Ramirez et al. (2000)	2	2
52	Takagi et al. (2000)	-	2
53	Zink (2000)	-	3
54	Hegger et al. (2001)	3	-
55	Mikata et al. (2001)	1	12
56	Reineck et al. (2001)	2	-
57	Meyer (2002)	18	-
58	Teoh et al. (2002b)	6	-
59	Hegger and Görtz (2004)	1	-
60	Hegger and Rauscher (2004)	3	-
61	Haines (2005)	3	-
62	Labonte and Hamilton III (2005)	4	-
63	Naito et al. (2005)	8	-
64	Ramirez and Aguilar (2005)	4	-
65	De Silva and Witchukreangkrai (2006)	4	-
66	Choulli et al. (2007)	-	4
67	Laskar et al. (2007)	7	-
68	Runzell et al. (2007)	2	-
69	Heckmann and Bayrak (2008)	18	-
70	Llanos et al. (2009)	11	-
71	Nakamura et al. (2009)	1	-
72	Saqan and Frosch (2009)	-	6
73	Lee et al. (2010)	7	-
74	Shahrooz (2011)	2	-
75	Labib (2012)	20	
76	Langefeld (2012)	4	-
77	Lin et al. (2012)	3	6
78	Massone et al. (2013)	3	-
79	De Wilder et al. (2015)	6	3
80	Collins et al. (2016)	10	1
81	Garber et al. (2016)	5	-
82	Katz (2016)	4	-
83	Hou et al. (2017)	1	-
84	Kim et al. (2018b)	18	9
85	Haioxiong and Weijian (2020)	9	-
86	Hillebrand and Hegger (2020)	12	-
87	Hillebrand et al. (2020)	10	-

Most of the references were from studies conducted in the United States. However, a few studies conducted in Germany and Japan (only published in the German or Japanese language) are also included through data provided in the database from 2015 ACI-DASb (Dunkelberg et al. 2018).

During the data collection procedures, two criteria were applied: load type and material usage. Only point load data were included in the dataset because continuous load tests showed different trends in shear capacity, such as significantly higher shear capacity compared to point load test results. To maintain consistency, experiments that used external tendons or fiber-reinforced concrete were also excluded from the dataset. These criteria ensured that the collected data were consistent and comparable across different experiments.

Not all of the parameters were available from each document. The values that were not available were not calculated or substituted with other values.

### **3.2.2 Dataset Composition**

The content of the present dataset was primarily based on the ACI-DASb database (Dunkelberg et al. 2018). Data that were reported in SI units were all converted into the U.S. customary units for the purposes of this project. Parameters were categorized per data reference, cross-section properties, beam geometry, concrete properties, longitudinal tension reinforcement properties, longitudinal compression reinforcement properties, prestressing reinforcement properties, prestress, shear reinforcement properties, and test results. The detailed contents of the dataset are summarized in Table 3.2.

**Table 3.2. Content list in dataset.**

<b>Category</b>	<b>Parameter</b>	<b>Unit</b>
Reference	Year	-
	Author	-
	Specimen	-
	Units (SI unit/U.S. customary unit)	-
Cross-Section Properties	Section Type (I/T/Rectangular)	-
	Height	in.
	Top flange width	in.
	Top flange height	in.
	Top haunch height	in.
	Web width	in.
	Web height	in.
	Bottom haunch height	in.
	Bottom flange width	in.
	Bottom flange height	in.
	Concrete section gross area	in. <sup>2</sup>
	Neutral axis to the extreme tension fiber distance	in.
	Section moment of inertia about centroidal axis (neglecting reinforcement)	in. <sup>4</sup>
	Deck slab (yes/no)	-
	Deck slab width	in.
	Deck slab thickness	in.
Beam Geometry	Support plate dimension in direction of beam axis	in.
	Loading plate dimension in direction of beam axis	in.
	Support axis and beam end distance	in.
	Distance between point loads	in.
	Shear span	in.
	Shear-span-to-effective-depth ratio	-
	Minimum concrete cover	in.
Concrete Properties	Aggregate maximum diameter	in.
	Compressive strength test method	ksi
	Compressive strength test size	-
	Compressive strength	-
	Tensile strength test method	-
	Tensile strength	ksi
	MOR	ksi
Longitudinal Tension Reinforcement Properties	Tension reinforcement (yes/no)	-
	Bar type	-
	Tension reinforcement depth	in.
	First type tension reinforcement diameter	in.
	First type tension reinforcement number	-
	Second type tension reinforcement diameter	in.
	Second type tension reinforcement number	-

Category	Parameter	Unit
	Total tension reinforcement area	in. <sup>2</sup>
	Average tension reinforcement diameter	in.
	Tension reinforcement surface	-
	Anchorage coefficient	-
	Tension reinforcement geometrical percentage	%
	Tension reinforcement geometrical percentage based on the width of web	%
	Tension reinforcement nominal MOE	ksi
	Tension reinforcement tested MOE	ksi
	Tension reinforcement nominal yield strength	ksi
	Tension reinforcement tested yield strength	ksi
	Tension reinforcement nominal tensile strength	ksi
	Tension reinforcement tested tensile strength	ksi
	Steel strain at maximum steel stress	-
Longitudinal Compression Reinforcement Properties	Compression reinforcement (yes/no)	-
	Bar type	-
	Compression reinforcement depth	in.
	First type compression reinforcement diameter	in.
	First type compression reinforcement number	-
	Second type compression reinforcement diameter	in.
	Second type compression reinforcement number	-
	Compression reinforcement total area	in. <sup>2</sup>
	Compression reinforcement average diameter	in.
	Compression reinforcement nominal yield strength	ksi
	Compression reinforcement tested yield strength	ksi
Prestressing Reinforcement Properties	Prestressing method (pre/post)	-
	Prestressing bar type	-
	Prestressing reinforcement effective depth at bottom	in.
	Prestressing reinforcement effective depth at web	in.
	Prestressing reinforcement effective depth at top	in.
	Prestressing reinforcement average diameter	in.
	Prestressing reinforcement area at bottom	in. <sup>2</sup>
	Prestressing reinforcement area at web	in. <sup>2</sup>
	Prestressing reinforcement area at top	in. <sup>2</sup>
	Prestressing reinforcement total area	in. <sup>2</sup>
	Total prestressing reinforcement effective depth	in.
	Drape (yes/no)	-
	Draped prestressing reinforcement area	in. <sup>2</sup>
	Draped prestressing reinforcement angle	°
	Prestressing reinforcement nominal MOE	ksi
	Prestressing reinforcement tested MOE	ksi
	Prestressing reinforcement nominal yield strength	ksi
	Prestressing reinforcement tested yield strength	ksi

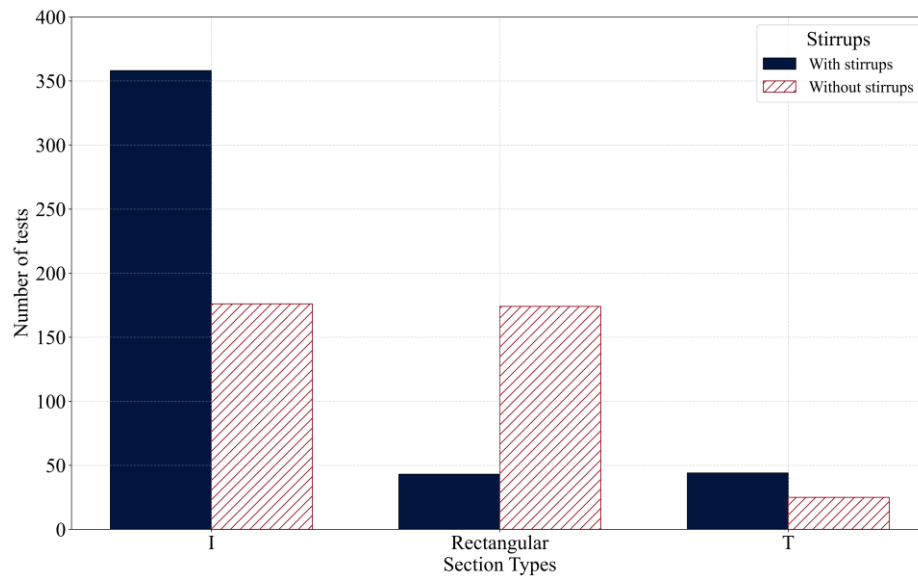
Category	Parameter	Unit
	Prestressing reinforcement nominal tensile strength	ksi
	Prestressing reinforcement tested tensile strength	ksi
Prestress	Bottom tendons effective prestress	kips
	Web tendons effective prestress	kips
	Top tendons effective prestress	kips
	Total effective prestressing force	kips
	Effective prestress in concrete	psi
	Effective prestress in prestress reinforcement	ksi
	Effective prestress in draped prestress reinforcement	ksi
	Effective prestressing force vertical component	kips
Shear Reinforcement Properties	Shear reinforcement (with/without)	-
	Shear reinforcement diameter	in.
	Stirrup legs number	-
	Shear reinforcement total area	in. <sup>2</sup>
	Shear reinforcement surface	-
	Shear reinforcement spacing	in.
	Stirrup spacing over beam height ratio	-
	Stirrup spacing over effective depth ratio	-
	Shear reinforcement geometrical percentage based on the width of web	%
	Shear reinforcement nominal yield strength	ksi
	Shear reinforcement tested yield strength	ksi
	Shear reinforcement nominal tensile strength	ksi
	Shear reinforcement tested tensile strength	ksi
	Steel strain at maximum steel stress	-
Test Results	Load type	-
	Load at diagonal crack	kips
	Shear force at diagonal crack	kips
	Load at failure	kips
	Shear force at failure	kips
	Deflection at midspan at diagonal crack	in.
	Deflection at midspan at failure	in.
	Shear failure (yes/no)	-

### 3.3 EXPLORATORY DATA ANALYSIS

#### 3.3.1 Overview

Exploratory data analysis was conducted to identify preliminary trends, patterns, and correlations between the different parameters in the data. In this analysis, the dataset was often separated into two subsets: one with beams with stirrups and one with beams without stirrups. Figure 3.1 shows

the frequency of section types for the portion of the dataset with beams with stirrups and the portion of the dataset with beams without stirrups. For the dataset with stirrups, most of the specimens were I-shaped sections, while there were under 50 rectangular and T-shaped specimens. For the dataset without stirrups, a similar amount was identified for the I-shaped and rectangular cross sections; about 25 specimens having a T-shaped section were included.



**Figure 3.1. Overview of prestressed concrete shear test dataset.**

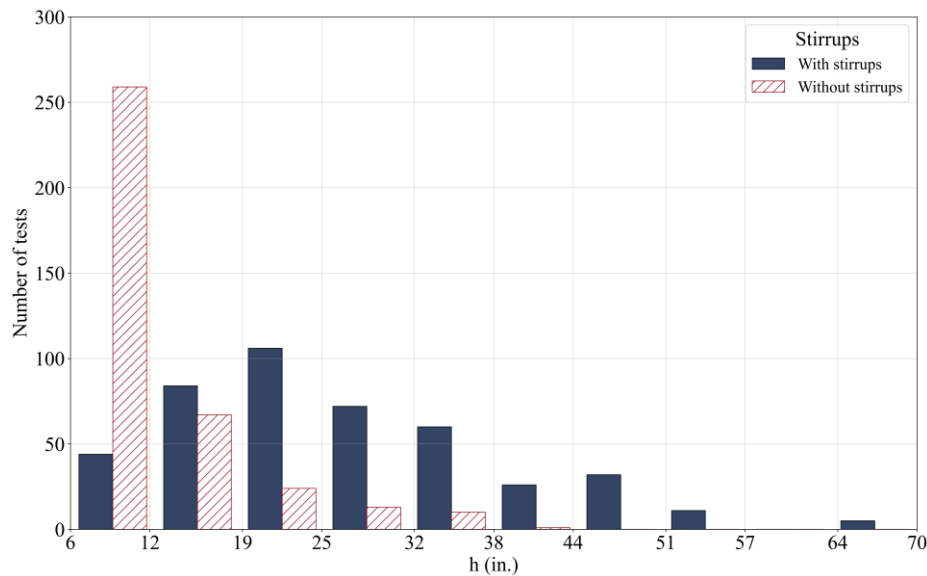
### 3.3.2 Statistical Distribution of Design Variables

Design variables such as beam depth, shear-span-to-depth ratio, concrete compressive strength, level of prestressing, and shear reinforcement properties were plotted as a histogram and are described herein. These design variables largely affect response parameters, such as the shear capacity.

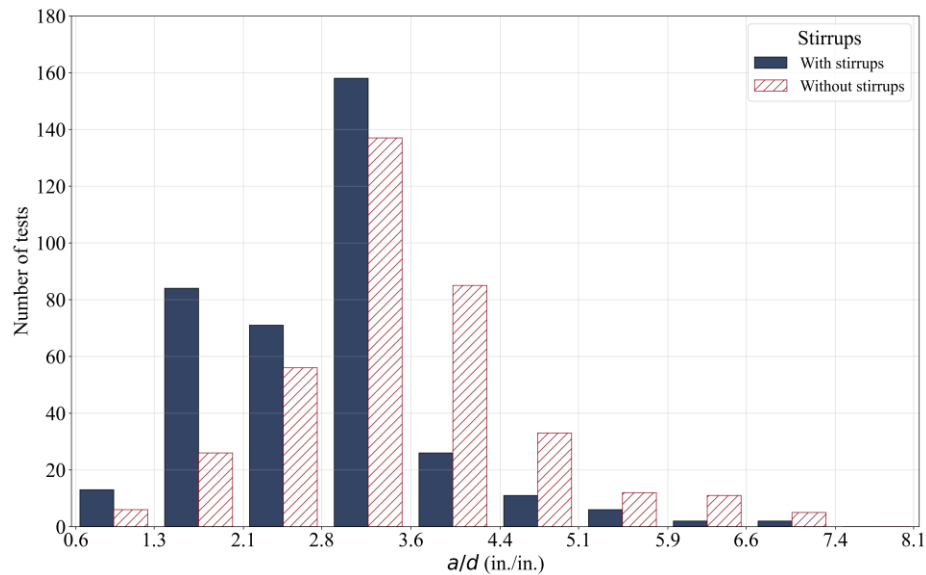
Figure 3.2 shows the distribution of height of the beam cross section. About 75 percent of the specimens without transverse reinforcement have a cross-section height of less than 15.75 in. However, specimens with transverse reinforcement have a mean cross-section height of about 26.75 in. Very few girders have heights that exceed 50 in.

Shear-span-to-effective-depth ratio,  $a/d$ , is correlated with the orientation of principal stress fields and controls the observed shear failure mechanism. It was observed that, for 75 percent of

the specimens, the  $a/d$  is less than 3.6 (see Figure 3.3), while approximately 5 percent of specimens have an  $a/d$  that is more than 5, even though they exhibited shear failure.



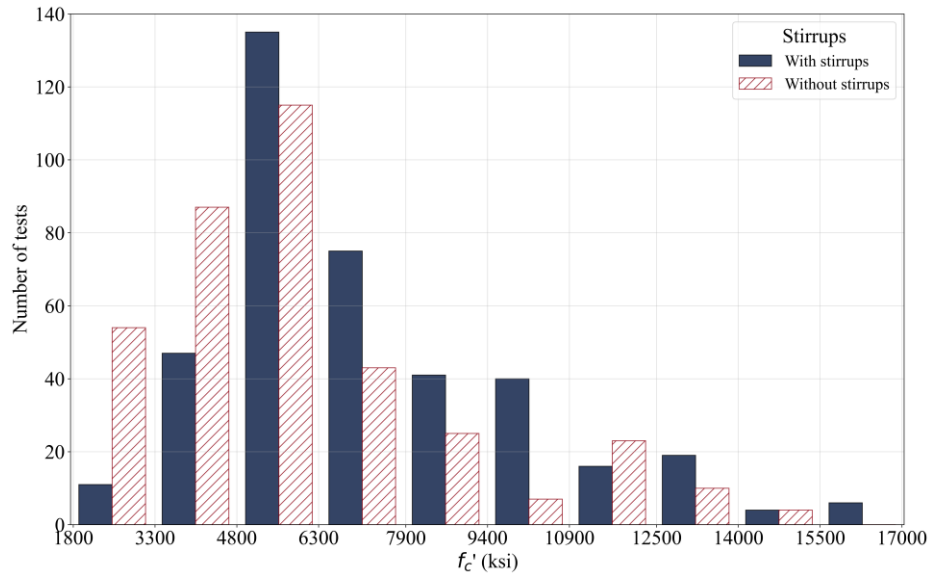
**Figure 3.2. Distribution of cross-section height.**



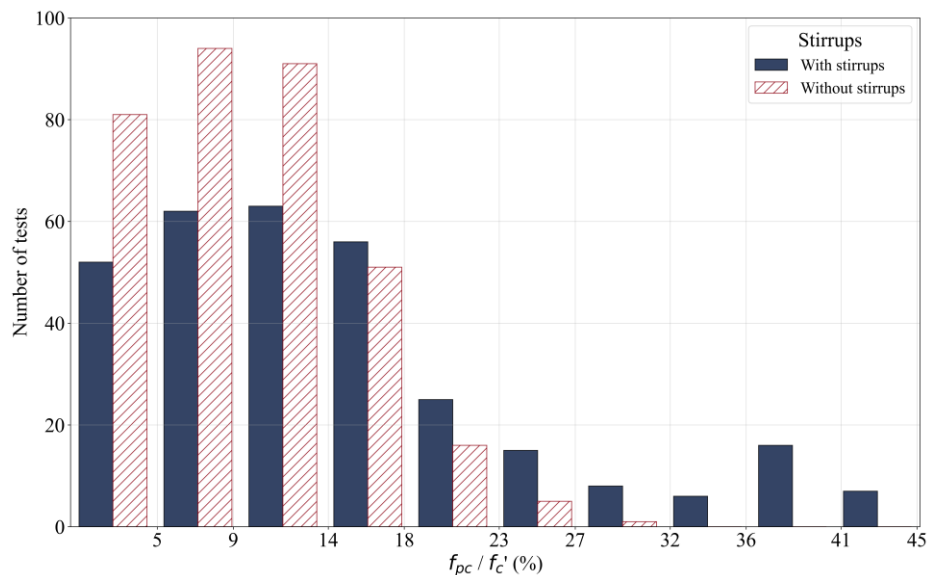
**Figure 3.3. Distribution of shear span over effective depth for total dataset.**

The concrete compressive strength values were collected on the test date and the distribution, as shown on Figure 3.4. It was found that 111 specimens were made with more than 10,000 psi concrete compressive strength and thus were considered high-strength concrete. With the exception of one specimen, the concrete compressive strength of the remaining specimens was above 2,000 psi.

The level of prestressing is known to be related to the delay of diagonal cracking in concrete beams. Approximately 75 percent of the specimens had less than 30 percent of effective prestress over the concrete compressive strength and the maximum effective prestress over the concrete compressive strength was 45 percent, as shown in Figure 3.5.



**Figure 3.4. Distribution of compressive strength of concrete for total dataset.**

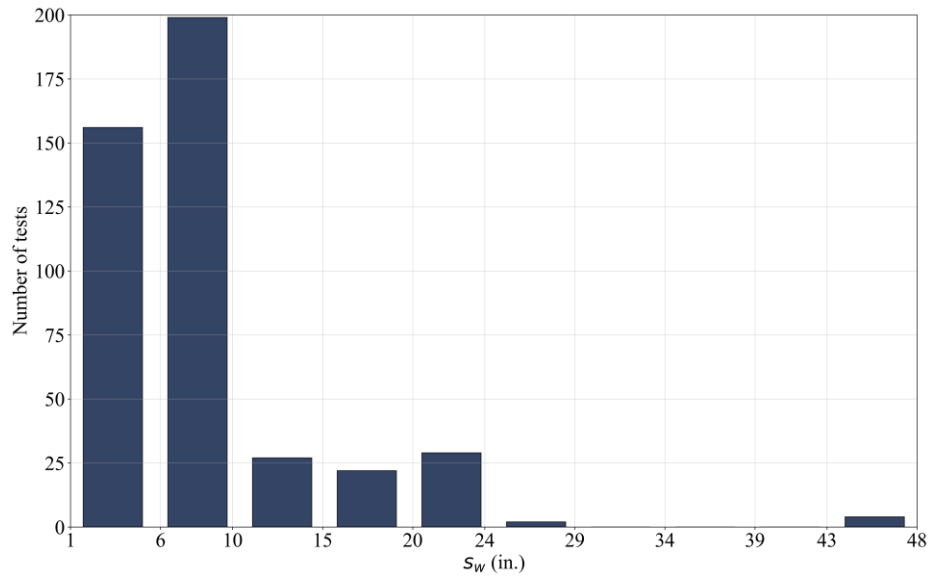


**Figure 3.5. Distribution of effective prestress in concrete for total dataset.**

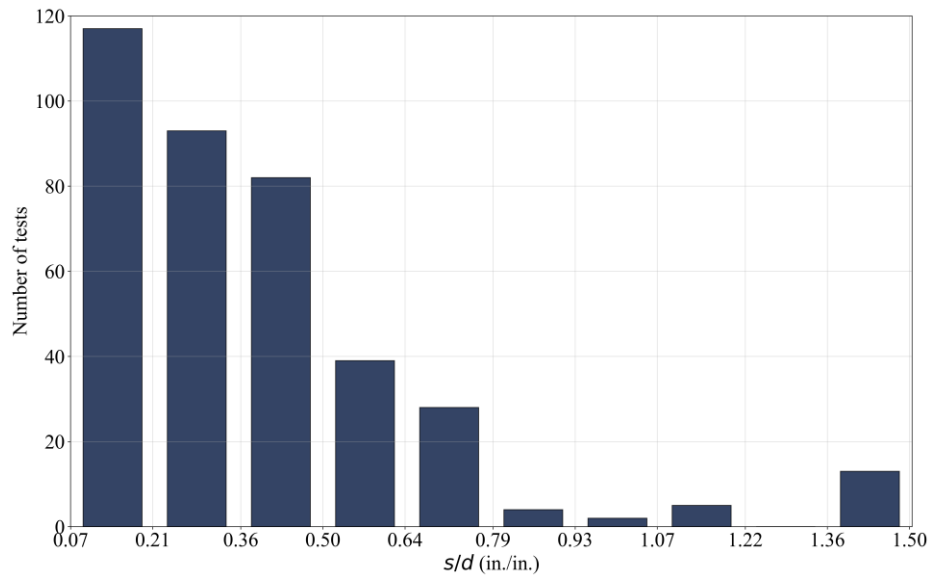
For the specimens with transverse reinforcement, transverse reinforcement properties are additionally described in Figure 3.6 to Figure 3.8. Approximately 80 percent of the stirrups were spaced less than 10 in. apart; however, four specimens had 48 in. of  $s/d$  (Labonte and Hamilton



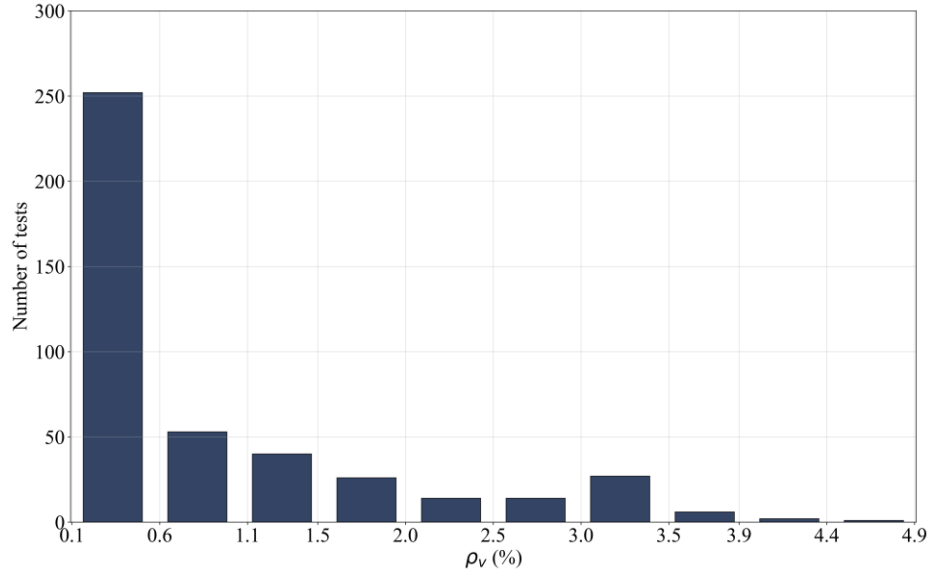
III 2005). When the  $s$  is normalized with the effective depth, 80 percent of specimens'  $s/d$  were less than 1, and about 70 percent of the specimens had 1 percent of shear reinforcement ratio.



**Figure 3.6. Distribution of transverse reinforcement spacing for stirrup dataset.**



**Figure 3.7. Distribution of transverse reinforcement spacing over effective depth for stirrup dataset.**



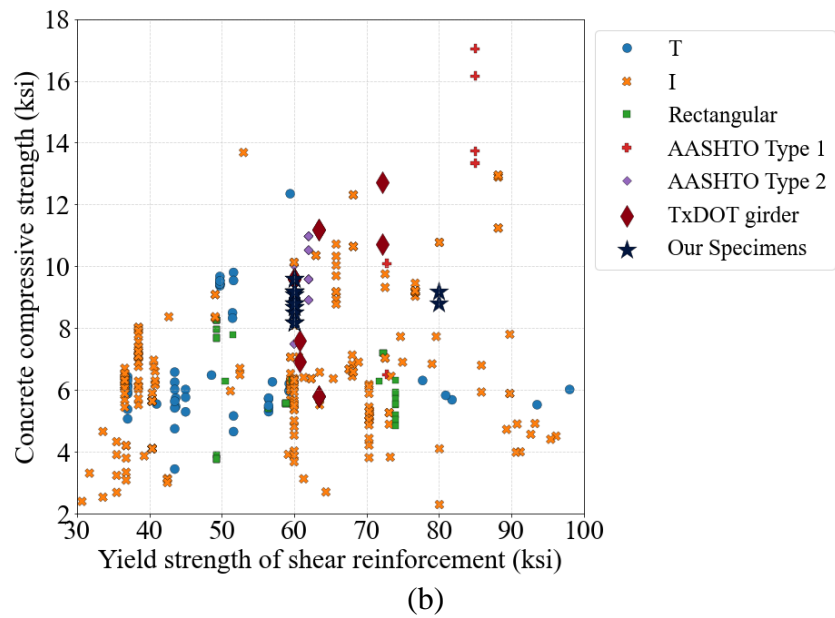
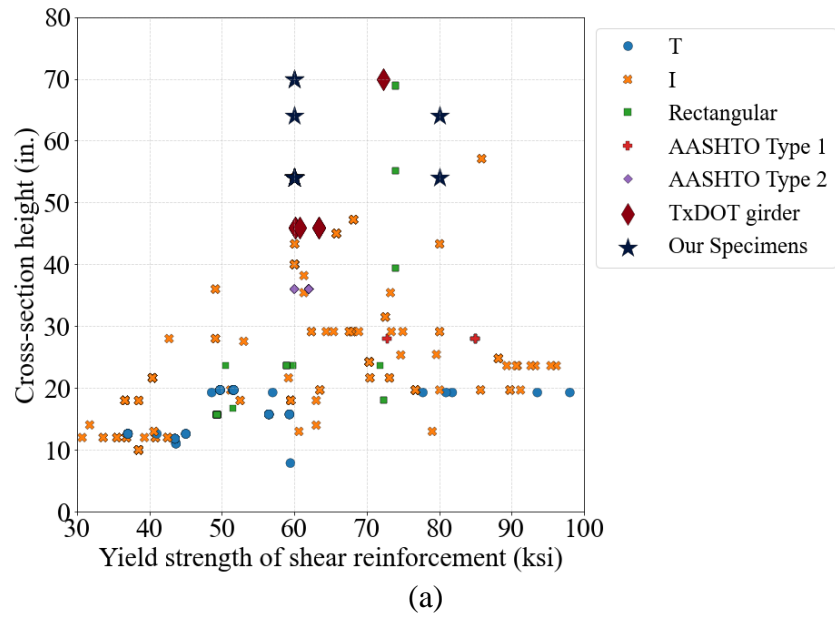
**Figure 3.8. Distribution of stirrup ratio for stirrup dataset.**

### 3.3.3 Determining Experimental Specimens from Dataset Analysis

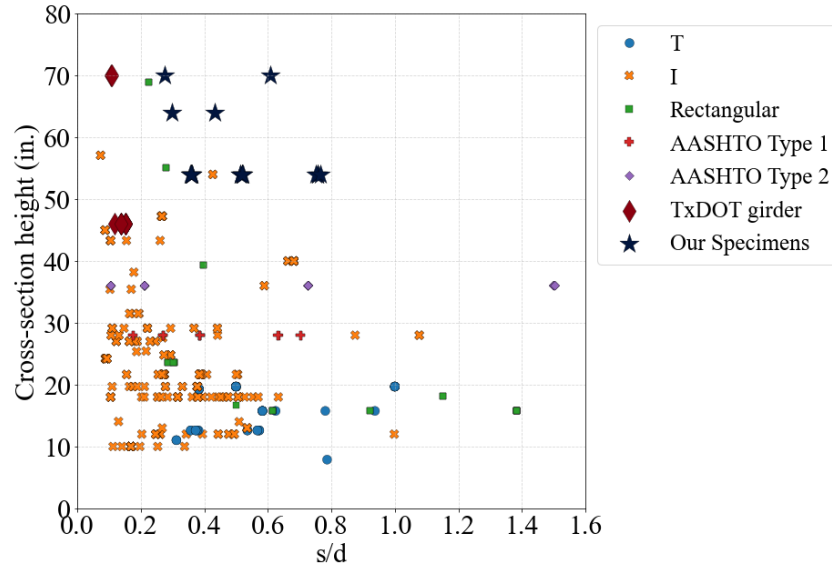
Selecting experimental specimens is vital for complementing the existing dataset with a new design for which no test data are available. Analysis of the generated dataset revealed a combination of design parameters, such as beam dimensions, reinforcement details and material properties, for which test data are scarce.

Inspection of the dataset revealed that there was a very limited number of girders with cross-section heights above 50 in. Also, the limited number of such girders included high-strength reinforcement of yield strength of 75 ksi or 85 ksi, but not 60 ksi. The selected girders for the experimental program (which is discussed in the next chapter) included Tx54 and Tx70 cross sections, as well as stirrup yield strengths of 60 ksi and 80 ksi. As shown in Figure 3.9(a), the dataset does not include combinations of cross-section height and shear reinforcement yield strength. Also, the selected concrete compressive strengths with the 80 ksi stirrups are less common (Figure 3.9[b]).

Moreover, the combination of normalized stirrup spacing and cross-section height of the test specimens (Figure 3.10) is not available in the dataset. Also, the selected  $s/d$  is between 0.25 to 0.75, with its larger values being less common in the dataset.



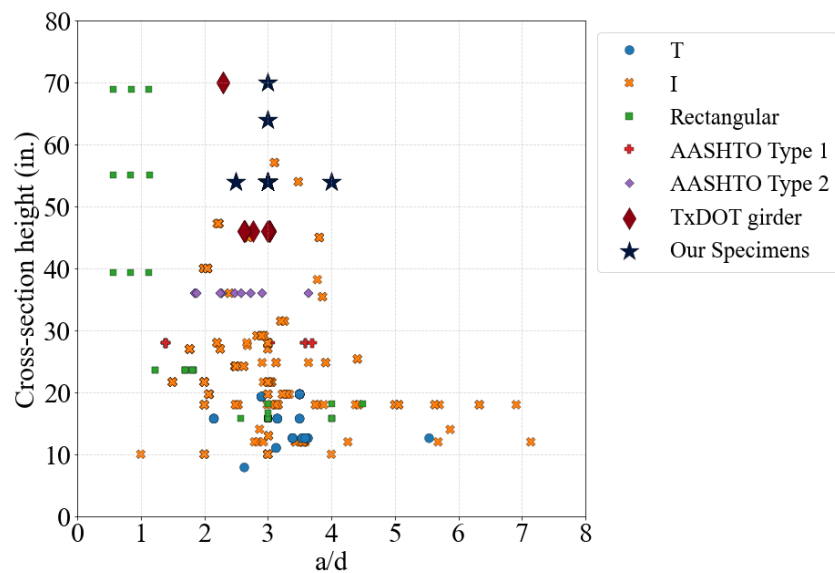
**Figure 3.9. Yield strength of shear reinforcement versus (a) cross-section height and (b) concrete compressive strength.**



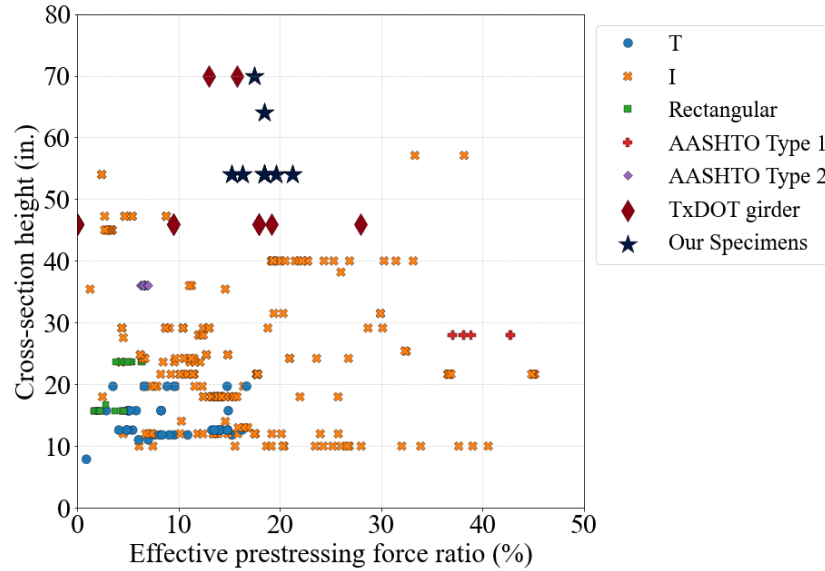
**Figure 3.10. Stirrup spacing ratio versus cross-section height.**

The  $a/d$  is a major factor influencing the shear strength. The selected  $a/d$  range of 2.5 to 4 (Figure 3.11) is representative of a wide range of practical applications, and the resulting combinations of cross-section height and  $a/d$  are not present in the current dataset. Also, the selected prestressing ratio is in a range of 15 percent to 22 percent (Figure 3.12), which is representative of typical designs.

By filling the gaps in the current dataset with new experimental data, the dataset will lead to more representative data-driven models.



**Figure 3.11. Shear span-to-depth ratio versus cross-section height.**

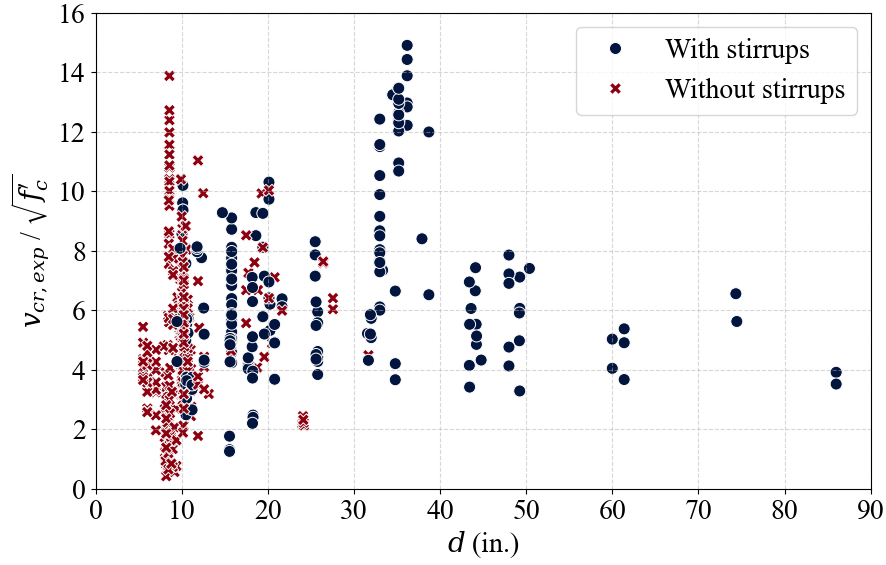


**Figure 3.12. Effective prestressing force ratio versus cross-section height.**

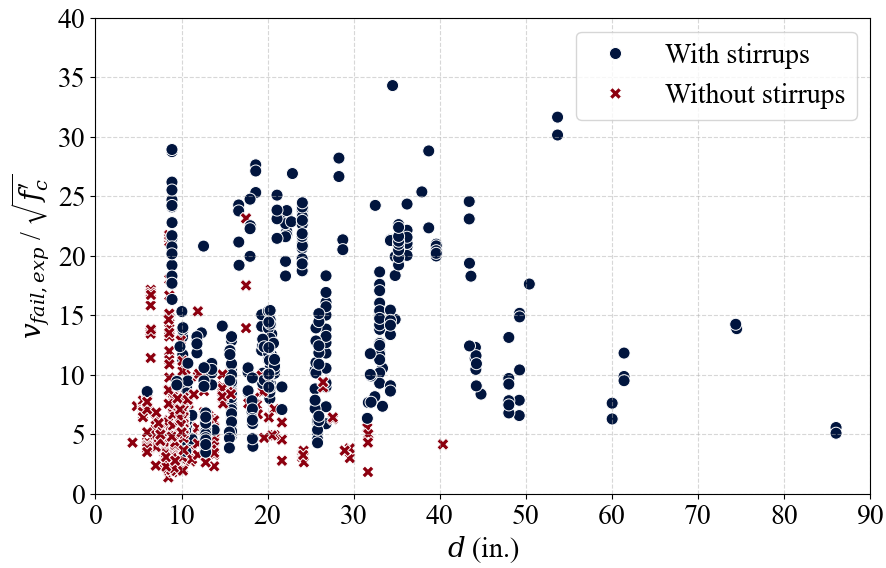
### 3.3.4 Trends between Response Parameters and Design Variables

To find correlations between response parameters and design variables, scatter plots were generated. Such plots can assist in visually exploring whether there is a direct relationship or any trends/patterns (positive or negative, linear or nonlinear, etc.) between two variables. They can also aid in the detection of outliers in the data. Shear stress at the onset of diagonal cracking and shear failure are the key parameters in calculating minimum shear reinforcement requirements. By dividing the shear stress at failure by  $\sqrt{f'_c}$ , the normalized shear stress at onset of cracking and at failure was obtained. It is reasonable to assume that prestressed concrete members will likely have shear strengths that are proportional to  $\sqrt{f'_c}$  (Nakamura 2011).

Smaller cross-section heights appeared to produce higher shear strength (Kani 1967; Shioya 1989). However, as shown in Figure 3.13 and Figure 3.14, the scatterplot does not show a trend for the effective depth with normalized shear stress at the diagonal crack and shear failure for beams with stirrups; conversely, mild correlation for the normalized shear stress at failure seems to be present for the beams without stirrups.

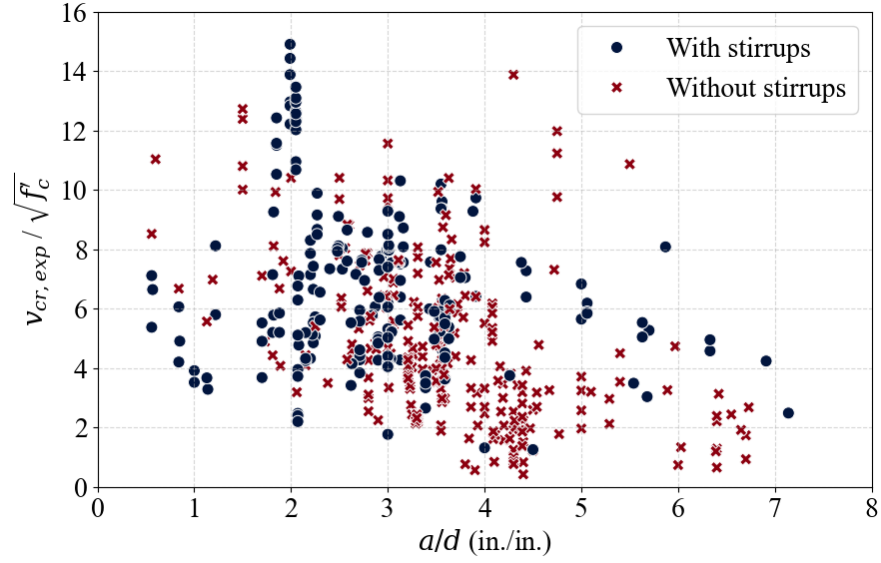


**Figure 3.13. Normalized shear stress at diagonal crack versus effective depth.**

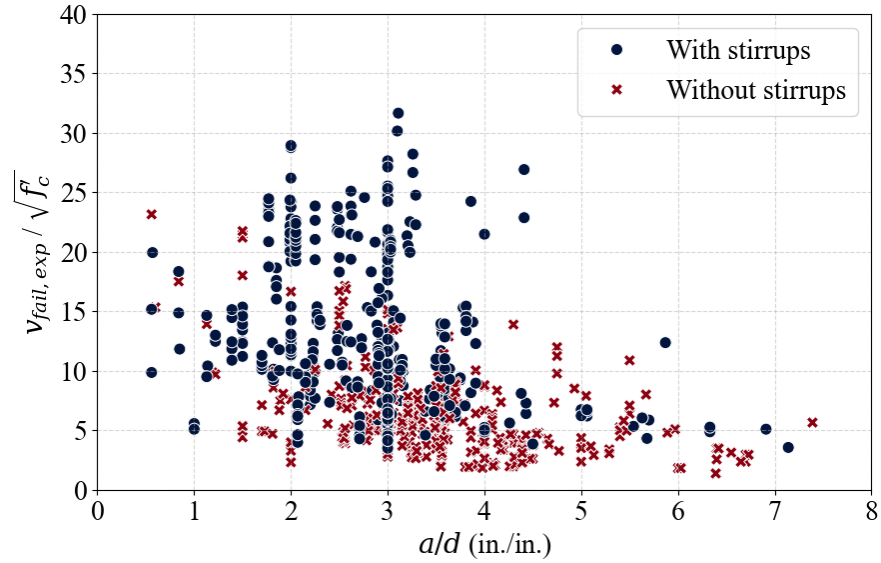


**Figure 3.14. Normalized shear stress at shear failure versus effective depth.**

According to Figure 3.15 and Figure 3.16, the shear-span-to-effective-depth ratio has a significant impact on both shear stress at the diagonal cracking and shear failure of the prestressed concrete elements. The reason for this increase in shear stress at failure is that members with smaller shear-span-to-effective-depth ratios resist the shear force mainly by the arch action, thus, generating larger strength.



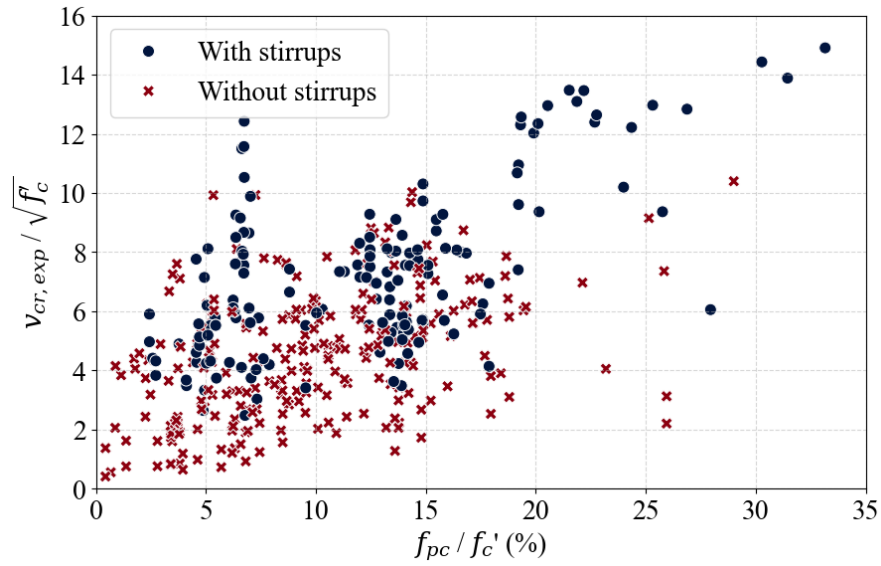
**Figure 3.15. Normalized shear stress at diagonal crack versus shear-span-to-effective-depth ratio.**



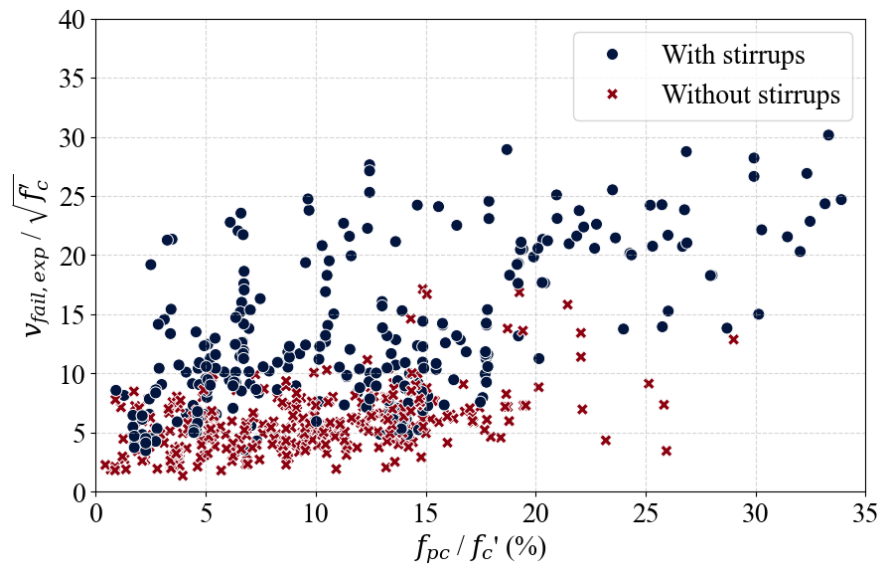
**Figure 3.16. Normalized shear stress at shear failure versus shear-span-to-effective-depth ratio.**

The axial load applied in the section by the tendons in the prestressed concrete beams delays diagonal cracking, thereby enhancing the cracking shear capability of otherwise reinforced concrete parts. In Figure 3.17 and Figure 3.18, the data reveal that it is obvious that when the effective prestress in concrete increases, the normalized shear stress at the diagonal crack and the shear failure increases too.

When effective prestress in concrete increases, both normalized shear stress at the diagonal crack and the shear failure increases, as shown in Figure 3.17 and Figure 3.18. In Figure 3.17, whether the specimens include stirrups or not, they are showing similar trends. However, as seen in Figure 3.18, the specimens are obviously separated based on the stirrups, though still having similar trends related to the increase in the prestress and normalized shear stress at shear failure.



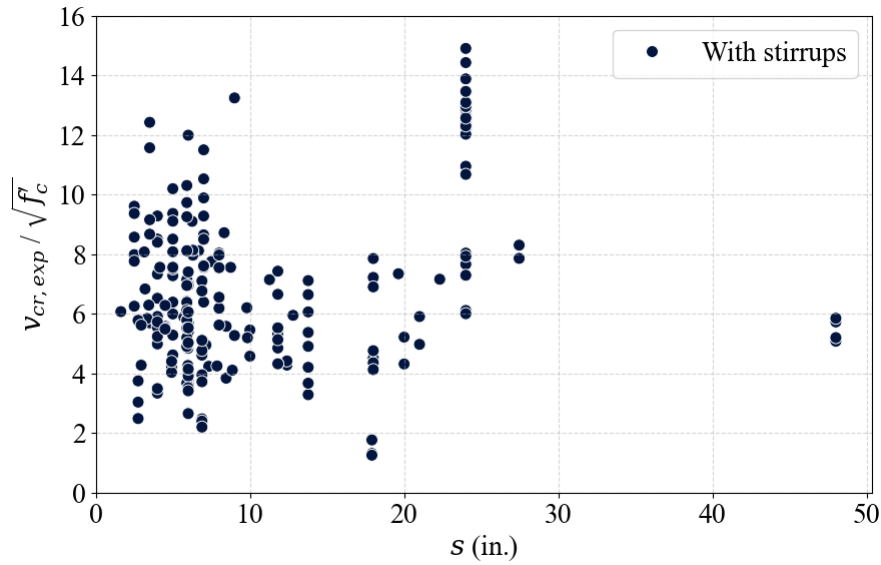
**Figure 3.17. Normalized shear stress at diagonal crack versus effective shear stress in concrete.**



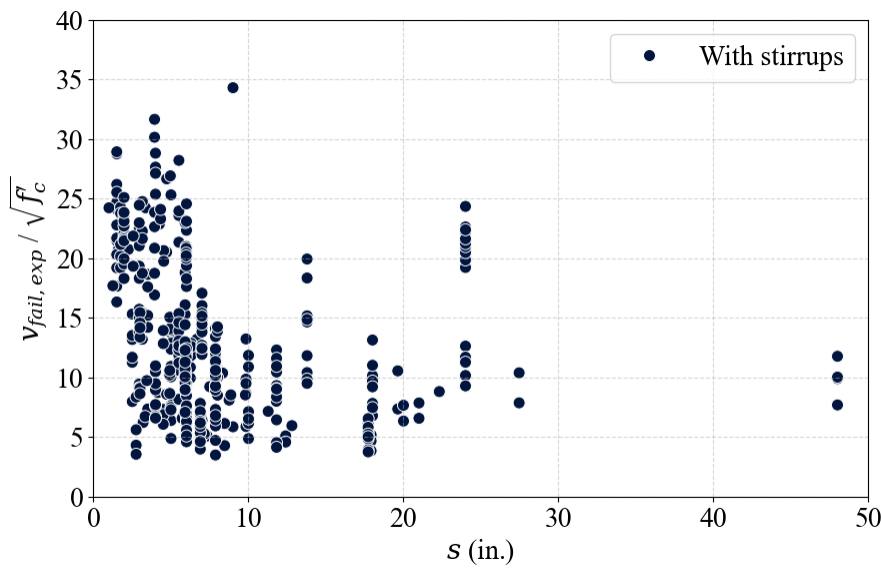
**Figure 3.18. Normalized shear stress at shear failure versus effective shear stress in concrete.**



In Figure 3.19 and Figure 3.20, the  $s/d$  scatterplot trends with the normalized shear stress at the diagonal crack and the shear failure. More specifically, as the  $s/d$  decreases, the shear stress increases, and the phenomenon is more pronounced on the shear stress at shear failure. However, in order to identify the effect of  $s/d$ , the reinforcement ratio should be kept constant for the different spacings, which is not the case for these plots; further, the availability of such tests is limited.

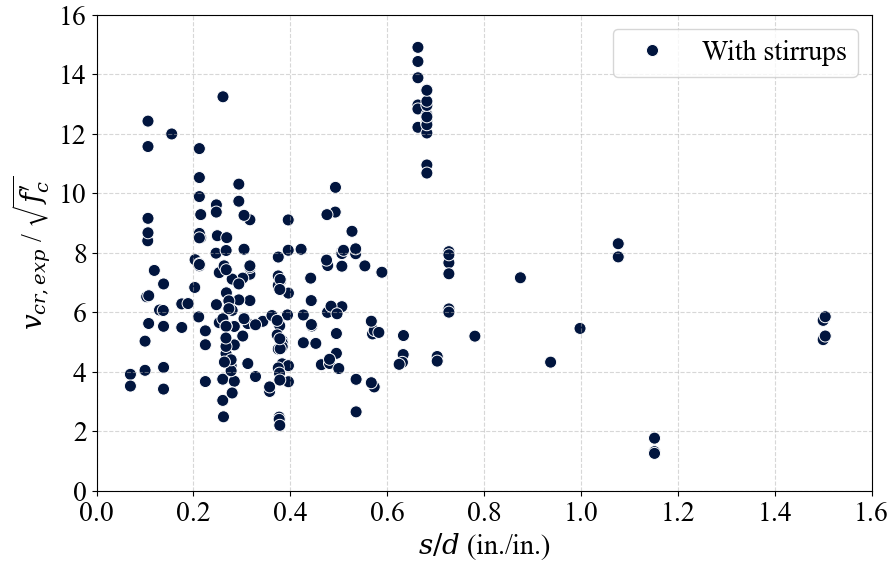


**Figure 3.19. Normalized shear stress at diagonal crack versus stirrup spacing.**



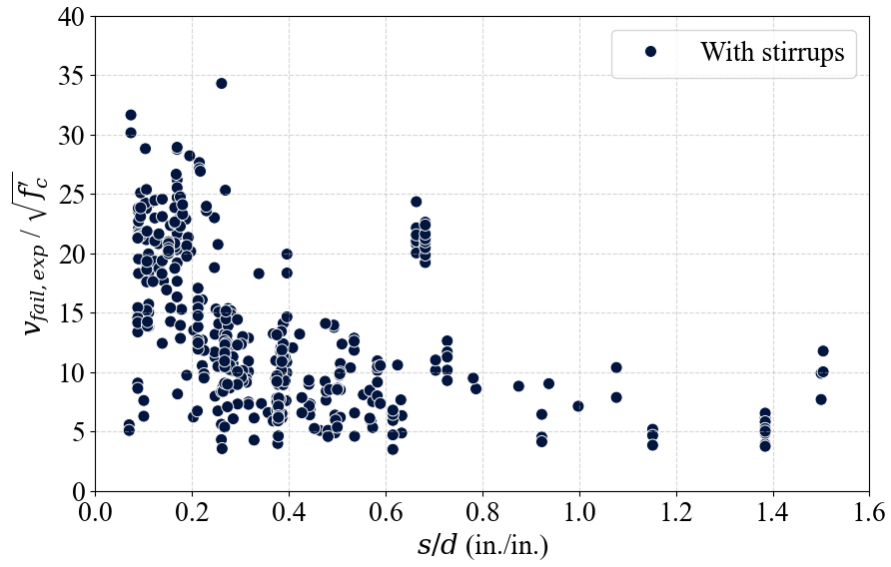
**Figure 3.20. Normalized shear stress at shear failure versus stirrup spacing.**

When the  $s/d$  is normalized with the effective depth, it is harder to find any trends with the normalized shear stress at the diagonal crack. However, normalized shear stress at the shear failure still shows high correlation with the normalized  $s/d$ .

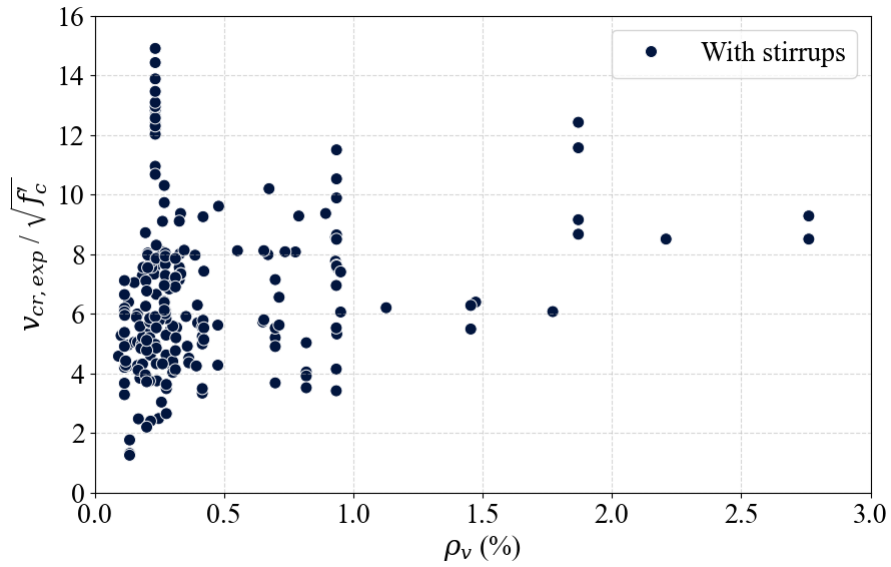


**Figure 3.21. Normalized shear stress at diagonal crack versus stirrup spacing over effective depth ratio.**

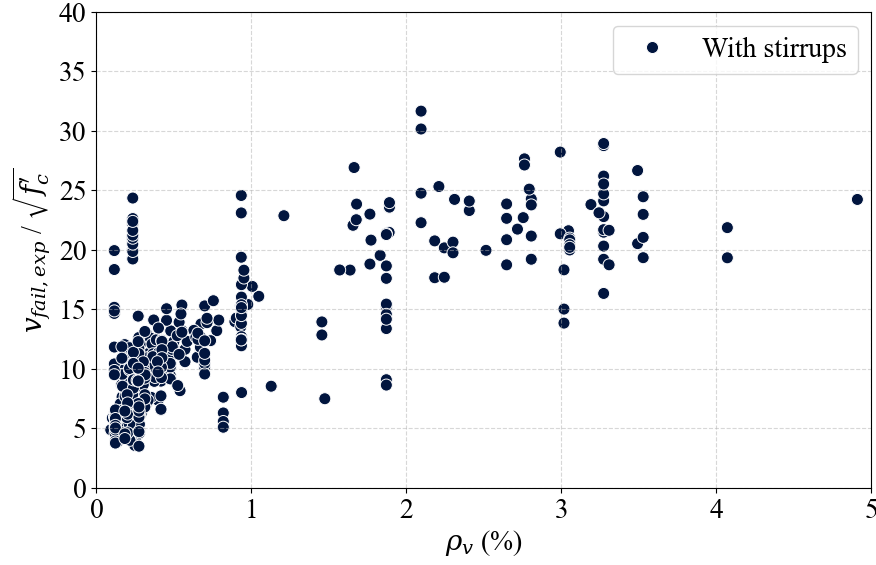
When the shear reinforcement is present, it carries the majority of the shear stress following the onset of diagonal cracking. As shown in Figure 3.22, the shear reinforcement ratio has clear correlation with the normalized shear stress. As the shear reinforcement ratio increases, the normalized shear stress increases. Figure 3.23 shows that normalized shear stress is also correlated with the shear reinforcement ratio.



**Figure 3.22. Normalized shear stress at shear failure versus stirrup spacing over effective depth ratio.**



**Figure 3.23. Normalized shear stress at diagonal crack versus shear reinforcement ratio.**



**Figure 3.24. Normalized shear stress at shear failure versus shear reinforcement ratio.**

### 3.4 NONLINEAR REGRESSION

#### 3.4.1 Overview

The shear force at the onset of diagonal cracking and the shear force at shear failure are the key parameters used to calculate the RSS index. Using the developed dataset, nonlinear regression analysis was performed to develop analytical equations predicting these quantities.

#### 3.4.2 Optimization Problem

Nonlinear regression represents an optimization problem that intends to identify values for a set of coefficients (variables, model parameters) of a given mathematical model that minimize an objective loss/cost function, which is usually an error norm between the model predictions and recorded/measured data. The root mean square error (RMSE) was used as a loss function for optimizing the equation, which can predict the shear stress at the onset of diagonal cracking and the shear stress at shear failure. The RMSE is defined as:

$$RMSE = \sqrt{\frac{1}{N} \sum_{i=1}^n (y_i - \hat{y}_i)^2} \quad (3.1)$$

where  $N$  = the number of data points;  $y_i$  = observed value for the  $i^{th}$  observation in the dataset; and  $\hat{y}_i$  = predicted value for the  $i^{th}$  observation in the dataset.

The error between the data points and the model is measured by residuals, and the spread of these residuals is measured by the RMSE. In other words, it provides information on how tightly the data are clustered around the line/model. The RMSE is frequently used to validate the regression analysis performed and is considered a metrics in this study.

An open-source package called SciPy was used for the optimization that offers a wide variety of quick scientific and numerical capabilities by building on the strengths of Python and Numeric (Virtanen et al. 2020). There are several optimization methods that can be used in the SciPy package, and each method has its own characteristics. Among those methods, the Truncated-Newton Method was selected for this study because it is effective at handling complex nonlinear optimization problems and the equations optimized in this study are nonlinear equations/functions. Also, the parameters that are included in the equations are positively correlated with the results, which means boundaries to the coefficient can be implemented so as not to generate a negative result value.

A model validation technique called *train-test-split* estimates how a model will perform on the new and untested data. It is known as the training dataset used to fit the model. The test dataset is used as the new data and predictions are made. Those predicted values are compared to the actual values, and based on this comparison, the model is evaluated to see if it works for the untested data. Empirical investigation revealed that allocating 20–30 percent of the original data points for testing and the remaining 70–80 percent for training yielded the greatest outcomes (Gholamy et al. 2018). The data were split to 70 percent of train and 30 percent of the test dataset for this nonlinear regression analysis.

### **3.4.3 Shear Force at Onset of Diagonal Crack, $V_{cr}$**

To predict the normalized shear force at the diagonal crack, eight parameters were included in the equation, which was formulated with the prior mechanics knowledge/principles for the shear capacity included in code provisions (ACI 2019; AASHTO 2020). In ACI 318-19, for reinforced concrete, the size modification factor  $\lambda_s$  was considered and was determined as:

$$\lambda_s = \sqrt{\frac{2}{1 + \frac{d}{10}}} \leq 1 \quad (3.2)$$

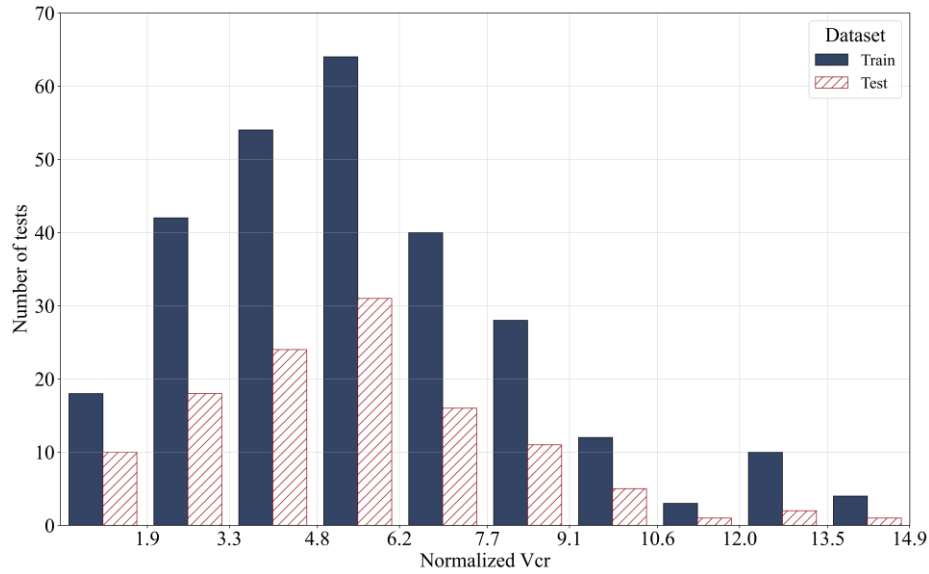
where  $d$  = effective depth of the cross section of beam (in.).

This form was similarly implemented in the predictive proposed equation for the shear force at the diagonal crack. The shear-span-to-effective-depth ratio, which is also known as the ratio of the peak moment over the peak shear times the effective cross-section depth ( $V_u d / M_u$ ), was applied based on the approximate method of calculating  $V_c$ . However, it was inversed in the proposed equation to make it positively correlated with the result. The term for concrete compressive strength has been normalized by dividing it by 5,000 psi, making it dimensionless. For the mild reinforcement ratio, a value of 1 was added to the term to ensure that the equation would not be affected in cases where no mild reinforcement is present (i.e., when the reinforcement ratio is zero). This approach preserves the integrity of the equation across various scenarios, including those with and without mild reinforcement. Moreover, the  $s/d$  over the effective depth was applied similarly to the shear-span-to-effective-depth ratio, which can be correlated with the result. The yield strength of the shear reinforcement and the effective prestress in concrete are divided by 60 ksi and the concrete compressive strength, respectively, to make the term dimensionless. The final equation used for the optimization is provided below:

$$\begin{aligned} \frac{V_{cr}}{\sqrt{f'_c} \cdot b_w \cdot d} = & a_0 \cdot \left( \frac{1}{1 + \frac{d}{10}} \right)^{a_1} \cdot \left( \frac{1}{1 + \frac{a}{d}} \right)^{a_2} \cdot \left( \frac{f'_c}{5,000} \right)^{a_3} \cdot (1 + \rho_w^{a_4}) \\ & + a_5 \cdot \left( \frac{1}{1 + \frac{s}{d}} \right)^{a_6} \cdot \rho_v^{a_7} \cdot \left( \frac{f_{yt}}{60} \right)^{a_8} + a_9 \cdot \left( \frac{f_{pc}}{f'_c} \right)^{a_{10}} \end{aligned} \quad (3.3)$$

where  $a_0, a_1, \dots, a_{10}$  = regression coefficients that will be estimated through optimization;  $d$  = effective depth of the cross section of the beam (in.);  $a/d$  = shear span over effective depth ratio (in./in.);  $f'_c$  = compressive strength of concrete (psi);  $\rho_w$  = ratio of mild reinforcement;  $s/d$  = stirrup spacing over effective depth (in./in.);  $\rho_v$  = ratio of shear reinforcement;  $f_{yt}$  = yield strength of shear reinforcement (ksi); and  $f_{pc}/f'_c$  = effective prestress in concrete over compressive strength of concrete (psi/psi).

The total dataset was split to 70 percent of train and 30 percent of test data, and the distribution of the train and test dataset are plotted in Figure 3.25. Checking the distribution of the train and test dataset is needed since a biased train dataset might influence the model to work for only the train dataset, which means the test dataset might not be predicted well. As Figure 3.25 shows, the train and test dataset is well split since the distribution is similar to each other.



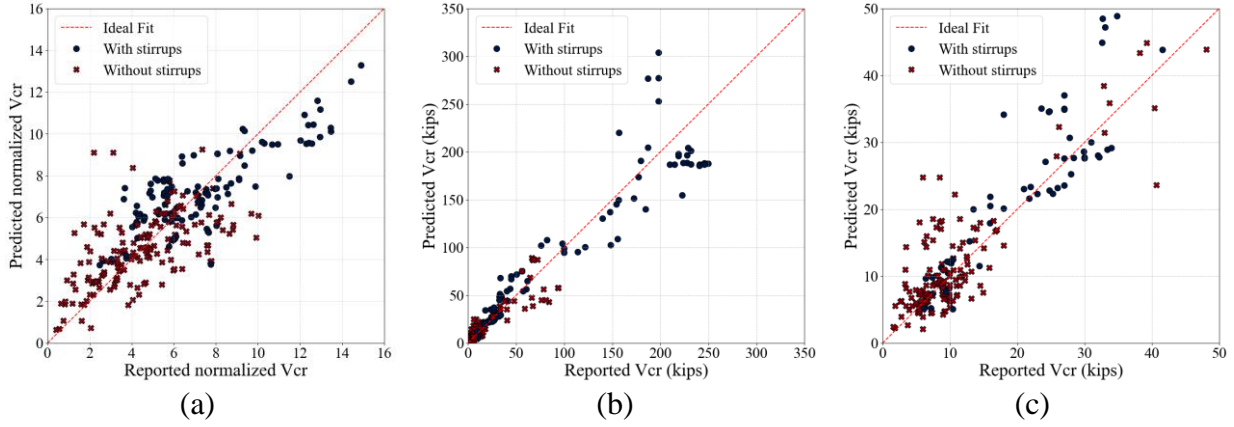
**Figure 3.25. Train, test data split result for normalized shear force at the diagonal crack.**

The results of the optimization, which is finding the coefficients from  $a_0$  to  $a_{10}$  based on the Truncated-Newton Methods, is as follows:

$$\frac{V_{cr}}{\sqrt{f'_c} \cdot b_w \cdot d} = 13.22 \cdot \left( \frac{1}{1 + \frac{a}{d}} \right)^{1.79} \cdot \left( \frac{f'_c}{5,000} \right)^{0.52} + 2.01 \cdot \rho_v^{0.54} \cdot \left( \frac{f_{yt}}{60} \right)^{0.97} + 33.36 \cdot \left( \frac{f_{pc}}{f'_c} \right)^{1.09} \quad (3.4)$$

The terms for the effective depth, mild reinforcement ratio and  $s/d$  over the effective depth are excluded since the coefficient  $a_1$ ,  $a_4$  and  $a_6$  turned out to be zero based on the regression analyses. The scatter plot of the predicted normalized shear stress at the diagonal cracking versus the actual value is presented in Figure 3.26(a). The restored value, shear stress at the diagonal cracking based on the predicted normalized shear stress at the diagonal cracking, is plotted

versus the actual values in Figure 3.26(b), and a zoom-in plot is provided in Figure 3.26(c) to visualize the lower values portion of the graph.



**Figure 3.26. Train dataset: (a) predicted versus actual normalized shear stress at onset of diagonal cracking, (b) predicted versus actual shear force at onset of diagonal cracking, and (c) zoom-in plot of (b) plot up to 50 kips.**

The performance of the optimized model was assessed using the coefficient of determination, also known as  $R^2$ , defined as follows:

$$R^2 = \frac{SSE}{SST} = 1 - \frac{SSR}{SST} \quad (3.5)$$

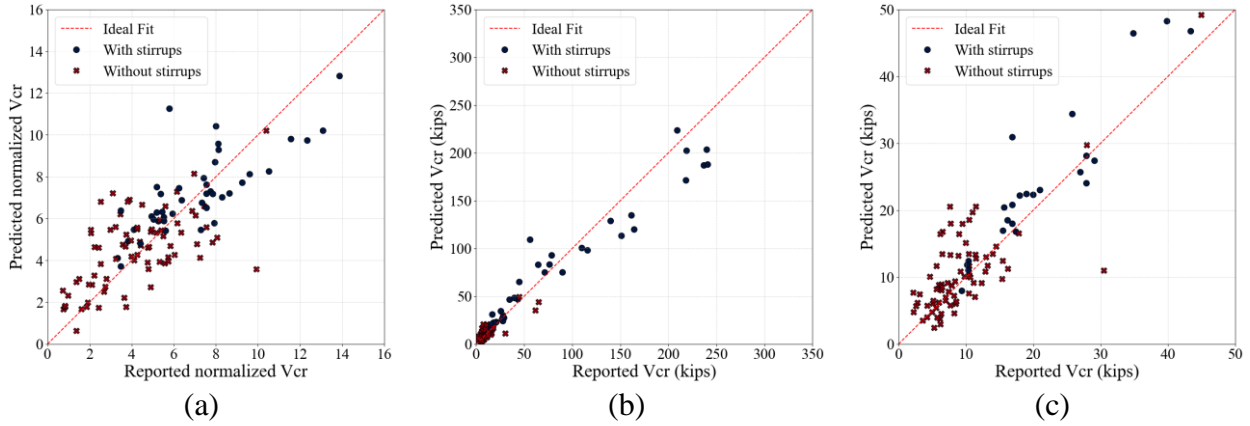
where the total sum of squares ( $SST$ ) =  $\sum_{i=1}^n (y_i - \bar{y})^2$ ; explained sum of squares ( $SSE$ ) =  $\sum_{i=1}^n (\hat{y}_i - \bar{y})^2$ ; sum of squares residual ( $SSR$ ) =  $\sum_{i=1}^n (y_i - \hat{y}_i)^2$ ; and  $\bar{y}$  = mean of the observed value in the dataset.

The greater the coefficient of determination (max = 1), the better the independent variable explains the dependent variable in the regression model.  $R^2$  is a measure of how well the independent variable explains the dependent variable in the regression model. For the train dataset, the  $R^2$  was calculated to be 0.91, which means the independent variables (i.e., the parameters in the proposed equation) are explaining the dependent variable (i.e., the shear stress at the diagonal cracking) well (good accuracy).

To further check how the proposed model works for the new data, the test dataset was used to predict the normalized shear stress, and the results are in Figure 3.27. For the test dataset,  $R^2$  was



calculated to be equal to 0.94. Based on the RMSE and  $R^2$ , it was determined that the optimized model was not overfitted to the train dataset, which means the model works for the new (test) data. The performance evaluations for the train, test, and total datasets are summarized in Table 3.3.



**Figure 3.27. Test dataset: (a) predicted versus actual normalized shear stress at onset of diagonal cracking, (b) predicted versus actual shear force at onset of diagonal cracking, and (c) zoom-in plot of (b) plot up to 50 kips.**

**Table 3.3. Performance evaluations for train, test, and total dataset for the predicted  $V_{cr}$ .**

Metrics	Train dataset	Test dataset	Total dataset
RMSE	18.76	13.48	17.34
$R^2$	0.91	0.94	0.92

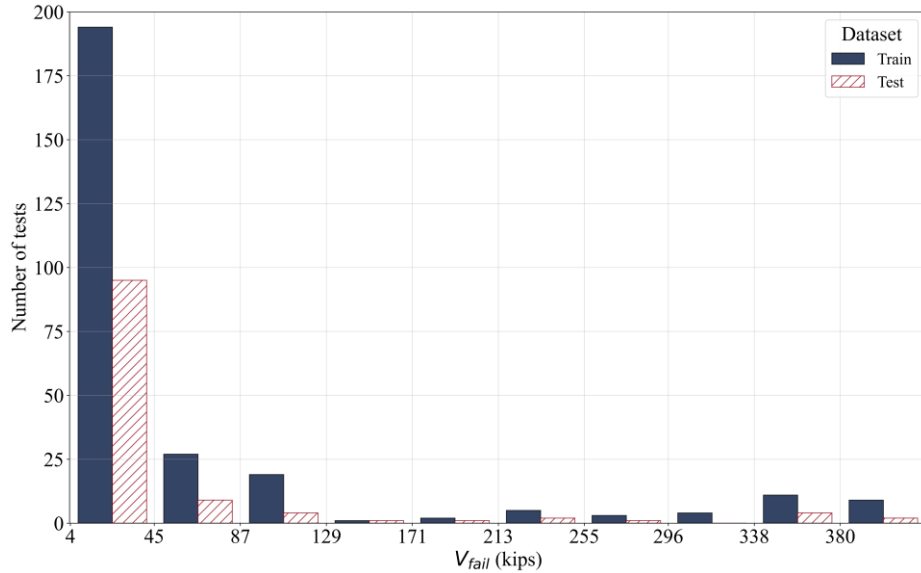
### 3.4.4 Shear Force at Shear Failure, $V_{fail}$

To predict the shear force at shear failure, the shear force contributed from the concrete was predicted and added to the shear contributed from the shear reinforcement. Because the trends observed from the exploratory data analysis for the shear force at onset of cracking and the shear force at failure were fairly similar, the same equation was implemented for the shear force contributed from concrete to the total shear force at shear failure, as:

$$V_{fail} = V_s + \left[ a_0 \cdot \left( \frac{1}{1 + \frac{d}{10}} \right)^{a_1} \cdot \left( \frac{1}{1 + \frac{a}{d}} \right)^{a_2} \cdot \left( \frac{f'_c}{5,000} \right)^{a_3} \cdot (1 + \rho_w^{a_4}) + a_5 \cdot \left( \frac{1}{1 + \frac{s}{d}} \right)^{a_6} \cdot \rho_v^{a_7} \cdot \left( \frac{f_{yt}}{60} \right)^{a_8} + a_9 \cdot \left( \frac{f_{pc}}{f'_c} \right)^{a_{10}} \right] \cdot \frac{\sqrt{f'_c}}{1,000} \cdot b_w \cdot d \quad (3.6)$$

where  $a_0, a_1, \dots, a_{10}$  = regression coefficients that will be estimated through optimization;  $V_s = \frac{A_v f_{yt} (\sin \alpha + \cos \alpha) d}{s}$ ;  $A_v$  = area of shear reinforcement within spacing  $s$  (in.<sup>2</sup>);  $\alpha$  = angle defining the orientation of shear reinforcement (degree);  $d$  = effective depth of the cross section of beam (in.);  $a/d$  = shear span over effective depth ratio (in./in.);  $f'_c$  = compressive strength of concrete (psi);  $\rho_w$  = ratio of mild reinforcement;  $s/d$  = stirrup spacing over effective depth (in./in.);  $\rho_v$  = ratio of shear reinforcement;  $f_{yt}$  = yield strength of shear reinforcement (ksi);  $f_{pc}/f'_c$  = effective prestress in concrete over compressive strength of concrete (psi/psi);  $b_w$  = web width (in.<sup>2</sup>).

The total dataset was divided into 70 percent for the train dataset and 30 percent for the test dataset, and Figure 3.28 shows the distribution of each dataset. The fact that the distributions of the train and test datasets are comparable to one another is seen in Figure 3.28.

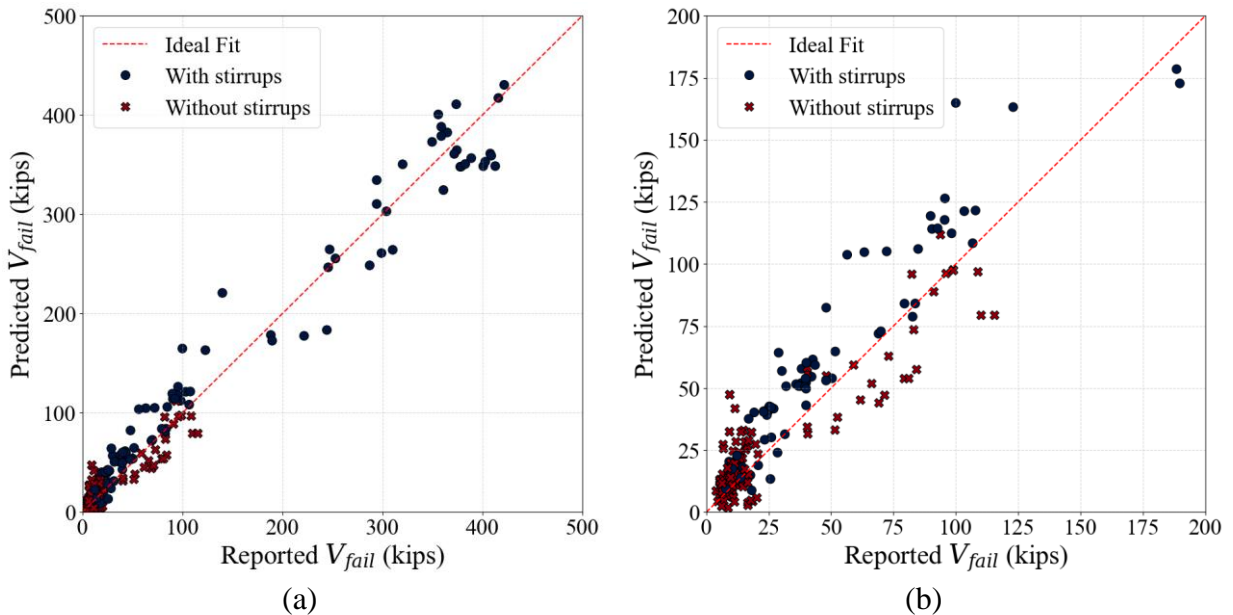


**Figure 3.28. Train, test data split result for shear force at shear failure.**

Equation (3.7) is the result of the optimization, which uses the Truncated-Newton Method to determine the optimal coefficients from  $a_0$  to  $a_{10}$  for the shear force at shear failure.

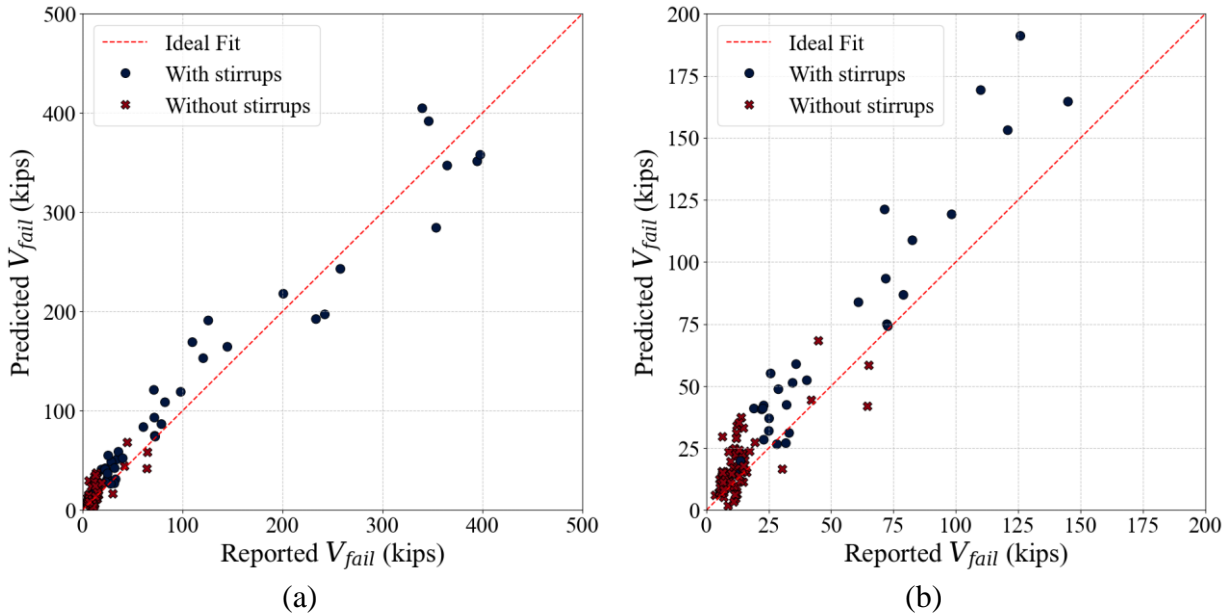
$$V_{fail} = V_s + \left[ 17.54 \cdot \left( \frac{1}{1 + \frac{a}{d}} \right)^{2.09} \cdot \left( \frac{f'_c}{5,000} \right)^{0.02} + 1.85 \cdot \left( \frac{f_{yt}}{60} \right)^{2.29} + 41.20 \cdot \left( \frac{f_{pc}}{f'_c} \right)^{0.91} \right] \cdot \frac{\sqrt{f'_c}}{1,000} \cdot b_w \cdot d \quad (3.7)$$

Since coefficients  $a_1$ ,  $a_4$ ,  $a_6$ , and  $a_7$  turned out to be zero, the terms for the effective depth, mild reinforcement ratio, shear reinforcement ratio, and  $s/d$  over the effective depth are all disregarded. Figure 3.29(a) shows a scatter plot of the predicted shear stress at shear failure versus the measured values, while Figure 3.29(b) zooms in to show the lower values portion of the graph. Compared to the shear force at the onset of diagonal crack prediction, the prediction for the shear force at shear failure shows more predictions of higher values, which means it is less conservative.



**Figure 3.29. (a) Predicted versus actual shear stress at shear failure of train dataset, and (b) zoom-in plot of (a) plot up to 200 kips.**

Figure 3.30 shows the prediction condition for the test dataset and has a similar trend as the train dataset prediction. Based on Figure 3.30, the optimized model works for both train and test datasets similarly, while the  $R^2$  proves that the independent variables are explaining the dependent variable properly.



**Figure 3.30. (a) Predicted versus actual shear stress at shear failure of the test dataset, and (b) zoom-in plot of (a) plot up to 200 kips.**

**Table 3.4. Performance evaluations for the train, test, and total datasets for predicted  $V_{fail}$ .**

Metrics	Train dataset	Test dataset	Total dataset
RMSE	22.92	25.32	23.67
$R^2$	0.95	0.94	0.94

## 3.5 GENETIC PROGRAMMING

### 3.5.1 Overview

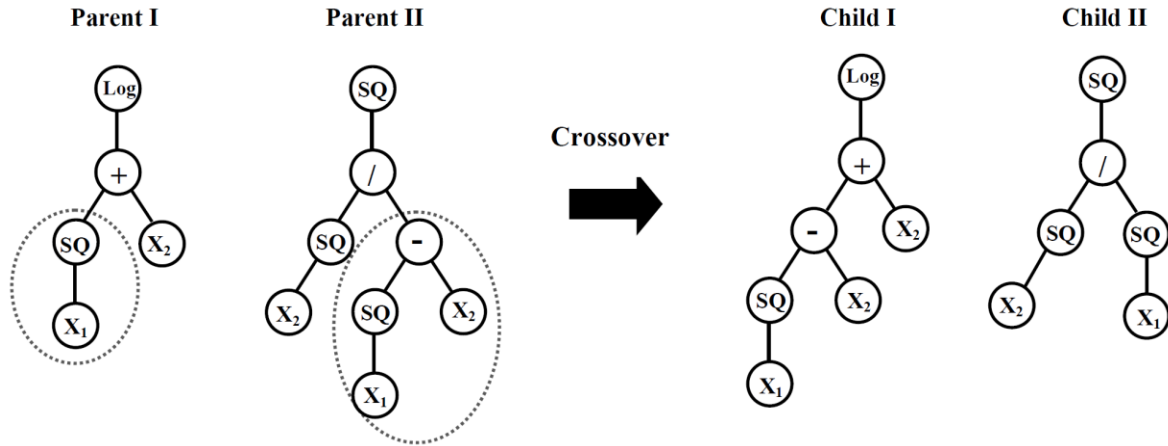
The equations formulated in the previous sections using regression analysis were based on principles and knowledge of mechanics. The proposed equations were developed with a certain form, and then the model's parameters were determined such that they best match the available dataset. This process is one of the main constraints of traditional regression methods, which use a fixed function in the analysis. GP can circumvent this restriction by looking for the optimum form of the functional relationship inside the optimization process (Jeon et al. 2014). Equations

predicting the shear force at the onset of the diagonal crack and shear force at shear failure were developed by implementing GP and are presented in this section.

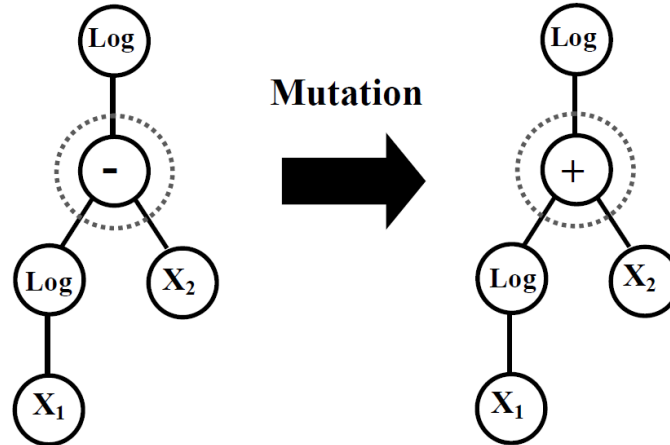
### 3.5.2 Genetic Programming

GP is a symbolic optimization approach that produces computer programs or functional forms to solve problems using the Darwinian natural selection concept (Koza 1994). The distinction between GP and genetic algorithms is based on how the answer is represented. Genetic algorithms create a string of numbers to represent the answer, whereas GP solutions are computer programs that are often represented as tree structures (Gandomi and Alavi 2012).

The GP procedure is as follows: First, create a population of beginning random computer programs made up of the problem's basic terminals and functions. The functions and terminals are chosen from suitable sets. The function set, for example, can include fundamental arithmetic operations (+, -,  $\times$ , /, and so on), Boolean logic functions (AND, OR, NOT, and so on), and any other mathematical functions. The terminal set holds the arguments for the functions, which might be numerical constants, logical constants, variables, and so on. Second, perform each program in the population so that a fitness measurement can be calculated for the program that shows how effectively it solves the issue. Applying the primary operations—which are reproduction, crossover, and mutation—to the programs chosen from the population with a probability based on fitness (i.e., the fitter the program, the more likely it is to be picked) will result in the creation of a new population of programs. *Reproduction* is copying the existing program directly to the new population. *Crossover* is using genetic recombination to genetically combine two current programs to produce two new progeny programs for the new population (shown in Figure 3.31). *Mutation* is a process changing at random in order to increase the fitness of the offspring; it is graphically described in Figure 3.32.



**Figure 3.31. Typical crossover operation in GP (Gandomi et al. 2010).**



**Figure 3.32. Typical mutation operation in GP (Gandomi et al. 2010).**

The output of the GP run is the single best computer program in the population developed during the run. This outcome might be a solution (or an approximation of a solution) to the problem (Koza 1994). The flowchart for GP is shown in Figure 3.33, where  $i$  denotes an individual of size  $M$  in the population.

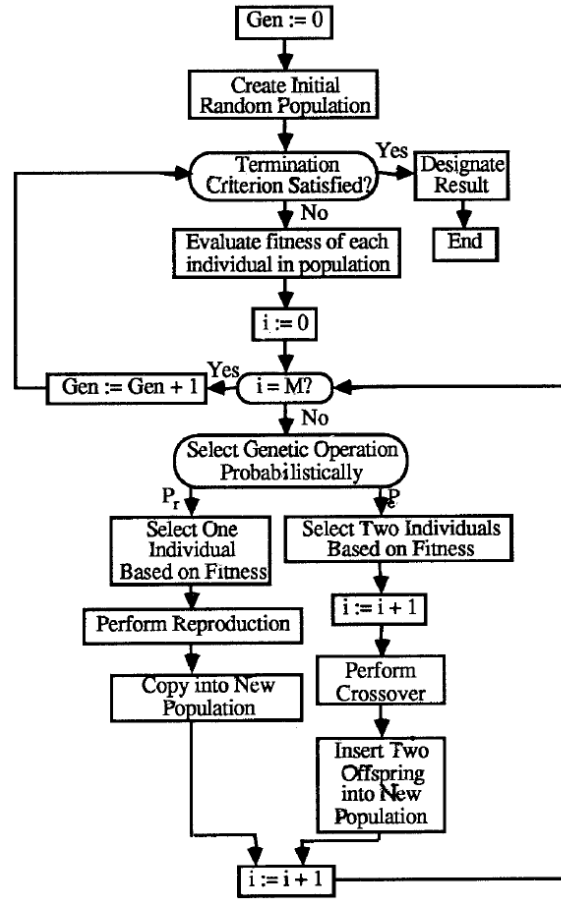


Figure 3.33. Flowchart for GP (Koza 1994).

### 3.5.3 Parameters for Genetic Programming

To apply GP, the GP Learn package in Python was used. The package allows users to modify the parameters that affect the result of the model. The list of parameters considered in this study is provided in Table 3.5. Since GP includes randomness caused from applying random changes to the current model to generate new ones, even though the parameters are fixed, the results are always different. For this reason, the GP procedure was repeated several times while modifying the coefficients.

**Table 3.5. Modifiable parameters on GP Learn package (Stephens 2015).**

<b>Parameters</b>	<b>Description</b>	<b>Default</b>
Population size	Program numbers in each generation.	1000
Generations	Generations number to evolve.	20
Tournament size	Program number that will compete to become a part of next generation.	20
Stopping criteria	The threshold metric value necessary to halt evolution early.	0.0
Initial depth	The range of tree depths for the initial population of naive formulas.	2, 6
Initial method	Methods that decide the priority of nodes or functions.	half and half
Function set	The functions that will be used when evolving the program.	+, -, ×, ÷
Metric	Metric that will be used for evaluating the program for each population.	mean absolute error
Parsimony coefficient	This constant penalizes huge programs by modifying their fitness to make them less acceptable for selection.	0.001
P crossover	Performing crossover probability on a tournament winner.	0.9
P subtree mutation	Performing subtree mutation probability on a tournament winner.	0.01
P hoist mutation	Performing hoist mutation probability on a tournament winner.	0.01
P point mutation	Performing point mutation probability on a tournament winner.	0.01
P point replace	Probability that any given node being mutated for only point mutation.	0.05
Max samples	Sample fraction to evaluate each program.	1.0

### 3.5.4 Shear Force at the Onset of Diagonal Crack, $V_{cr}$

GP was implemented to develop an equation that predicts the normalized shear force at the onset of diagonal cracking. Based on the nonlinear regression, parameters were selected, as summarized in Table 3.6. All of the parameters were transferred to dimensionless terms. Also, parameters such as effective depth and shear span over effective depth ratio were inversed to make them positively correlated with the shear force at the onset of a diagonal crack.



**Table 3.6. Dimensionless variables used for model for shear force at onset of diagonal crack.**

$X_0$	$X_1$	$X_2$	$X_3$	$X_4$	$X_5$	$X_6$	$X_7$
$\frac{d}{10}$	$\frac{d}{a}$	$\frac{f'_c}{5,000 \text{ psi}}$	$\rho_w$	$\frac{1}{1 + \frac{s}{d}}$	$\rho_v$	$\frac{f_{yt}}{60 \text{ ksi}}$	$\frac{f_{pc}}{f'_c}$

Similar to the nonlinear regression, the dataset was split into a training dataset (70 percent of the total dataset) and a test dataset (30 percent of the total dataset) per Figure 3.25. For the function set, functions [*add*, *multiply*, *divide*, *inverse*, *square root*, *log*, *exponential*] were used. Since all the variables were correlated with the shear force at the onset of diagonal cracking, the *subtract* function was excluded from the function set. RMSE was applied as a fitness measurement to evaluate the effectiveness of the model for each population. After a trial-and-error approach, the best equation for calculating the normalized shear force at the onset of diagonal cracking was developed as follows based on the parameters listed in Table 3.6. The interesting point is that similar to the nonlinear regression, the effective depth, mild reinforcement ratio, and the  $s/d$  parameters were excluded from the results, thereby confirming that the three variables are not related to the shear force at the onset of diagonal cracking.

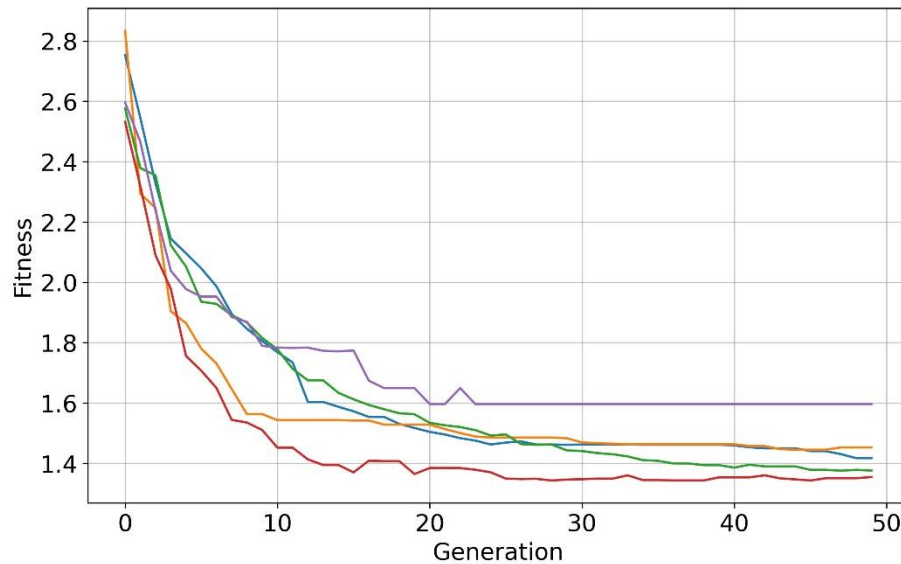
$$y = 0.38X_6X_7^{1.5} + 5.32X_7^{0.5}(5.32X_1 + X_2 + X_5) \quad (3.8)$$

$$\frac{V_{cr}}{\sqrt{f'_c} \cdot b_w \cdot d} = 0.006f_{yt} \left( \frac{f_{pc}}{f'_c} \right)^{1.5} + 5.32 \sqrt{\frac{f_{pc}}{f'_c}} \left( 5.32 \frac{d}{a} + \frac{f'_c}{5,000 \text{ psi}} + \rho_v \right) \quad (3.9)$$

**Table 3.7. Parameter settings of the best result (Vcrack).**

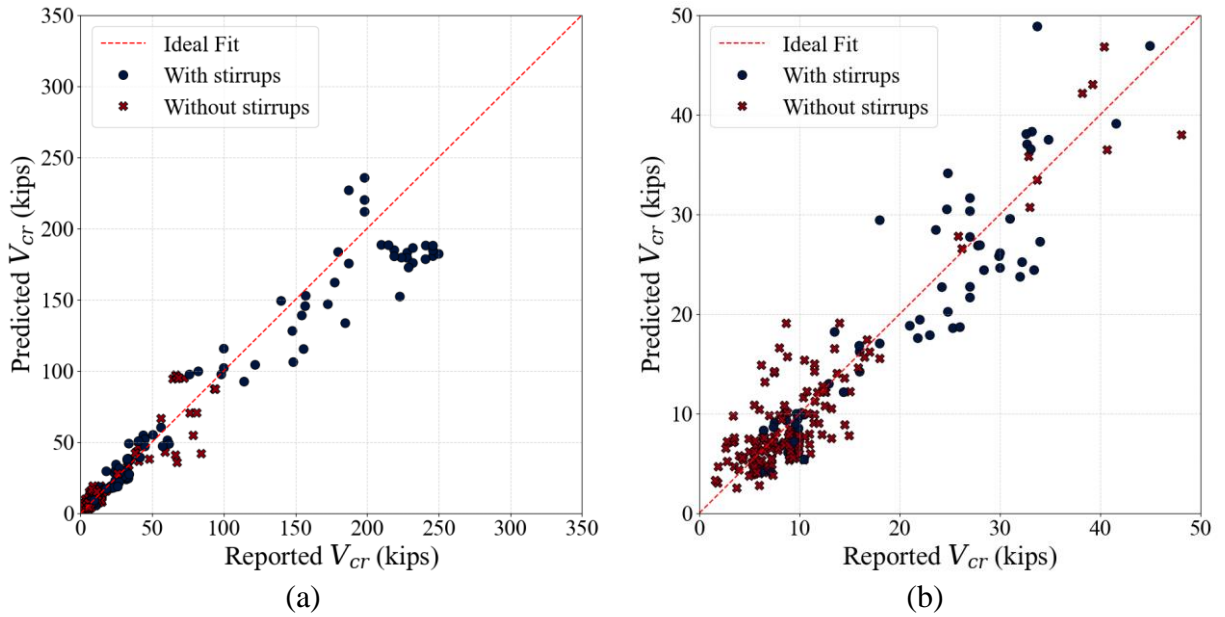
Parameters	Settings	Parameters	Settings
Population size	10,000	Metric	RMSE
Generations	50	Parsimony coefficient	0.004
Tournament size	20	P crossover	0.8
Stopping criteria	0.0	P subtree mutation	0.01
Initial depth	2, 4	P hoist mutation	0.01
Initial method	half and half	P point mutation	0.01
Function set	+, ×, ÷, sqrt, inverse, log, exp	P point replace	0.05

The population size was increased to 10,000 to make the probability increase for the best results. After several iterations of the GP, most of the program's fitness functions were stabilized around the 40th generation. Some trial fitness values are plotted in Figure 3.34. The initial depth, parsimony coefficient, and P hoist mutation were the key parameters used to prohibit bloating the results. In GP, an intriguing phenomenon occurs frequently when the program sizes get larger and larger with no substantial gain in fitness. This is known as *bloat*, because it results in increasingly extended calculation times with minimal value to the solution. The initial depth was decreased to make the result short, and parsimony coefficients were increased to 0.004, which were determined to be the best.

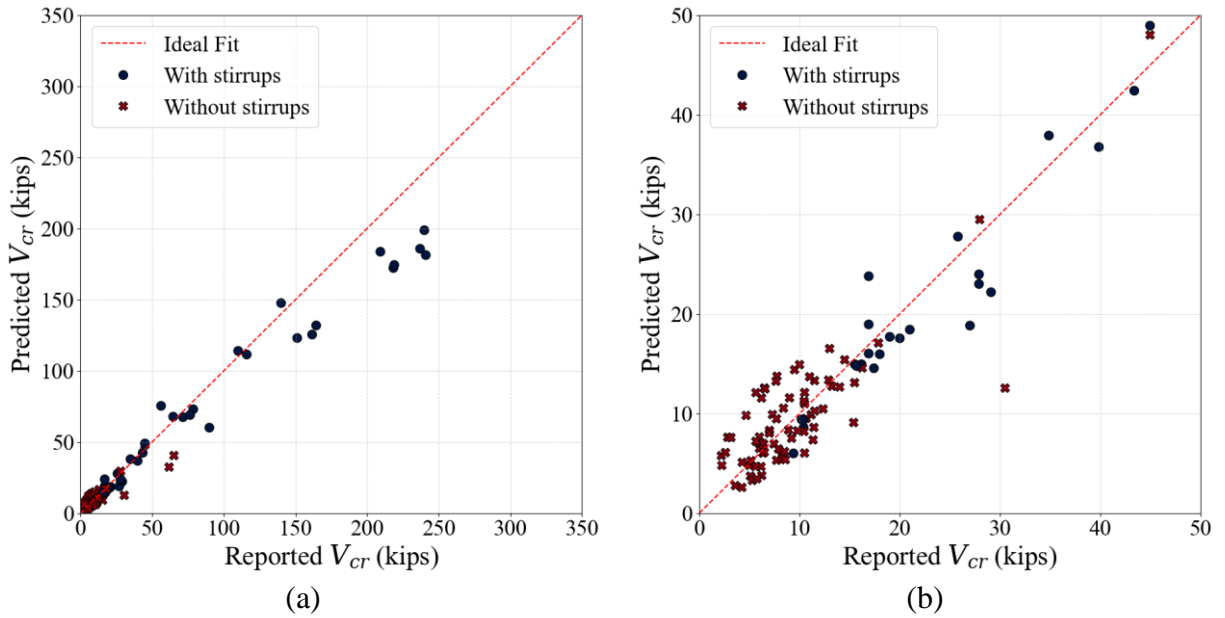


**Figure 3.34. Fitness value change as generation increases ( $V_{cr}$ ).**

Based on the developed equation, the prediction using the training and testing datasets are plotted in Figure 3.35 and Figure 3.36, respectively. Comparing the results with those of the nonlinear regression (Figure 3.26 and Figure 3.27), the GP scatter plot shows less residual from the actual value.



**Figure 3.35. GP results for the train dataset: (a) predicted versus actual shear stress at the onset of diagonal cracking, and (b) zoom-in plot of (a) plot up to 50 kips.**



**Figure 3.36. GP results for the test dataset: (a) predicted versus actual shear stress at the onset of diagonal cracking, and (b) zoom-in plot of (a) plot up to 50 kips.**

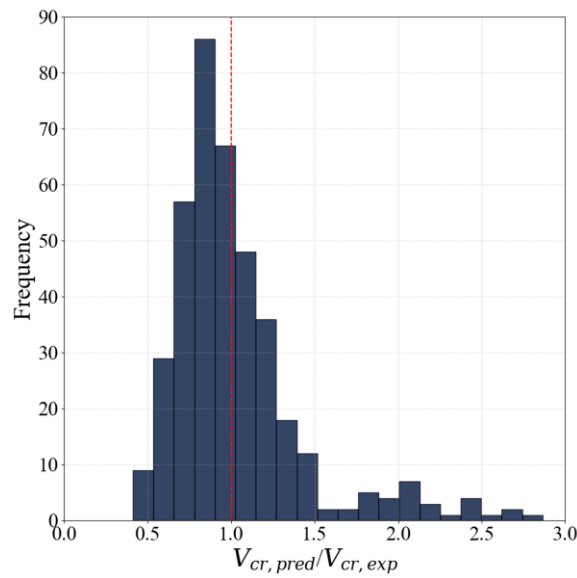
Also, for the RMSE,  $R^2$  and the mean of predicted value over actual value ratio, which are described in Table 3.8, the GP shows better performance than the nonlinear regression.

Figure 3.37 shows the distribution of the ratio of predicted value over actual value of the GP,

which is comparable to the results of the nonlinear regression when using the customized function.

**Table 3.8. GP performance evaluations for train, test, and total dataset for predicted  $V_{cr}$ .**

Metrics	Train dataset	Test dataset	Total dataset
<b>RMSE</b>	11.71	9.07	10.98
<b><math>R^2</math></b>	0.97	0.97	0.97
<b>Mean</b>	-	-	1.07
<b>Std</b>	-	-	0.39
<b>COV</b>	-	-	36.71



**Figure 3.37. Distribution of ratio of predicted over actual shear stress at the onset of diagonal crack of total dataset.**

### 3.5.5 Shear Force at Shear Failure, $V_{fail}$

The shear force at shear failure was predicted by applying the produced GP model to predict the shear force contribution from concrete and adding it to the shear force contribution from the shear reinforcement. Based on the same approach implemented for the nonlinear regression and described in Section 3.4.4, the same variables were used for the GP as the variables used for the nonlinear regression, which is the same as in Table 3.6; additional parameters are presented in Table 3.9. The result was formulated as follows:

$$y = X_4 + 7X_7 + (X_1 + X_7)(X_0 + 2X_2 + 5X_4 + X_6X_7 + 0.892) \quad (3.10)$$

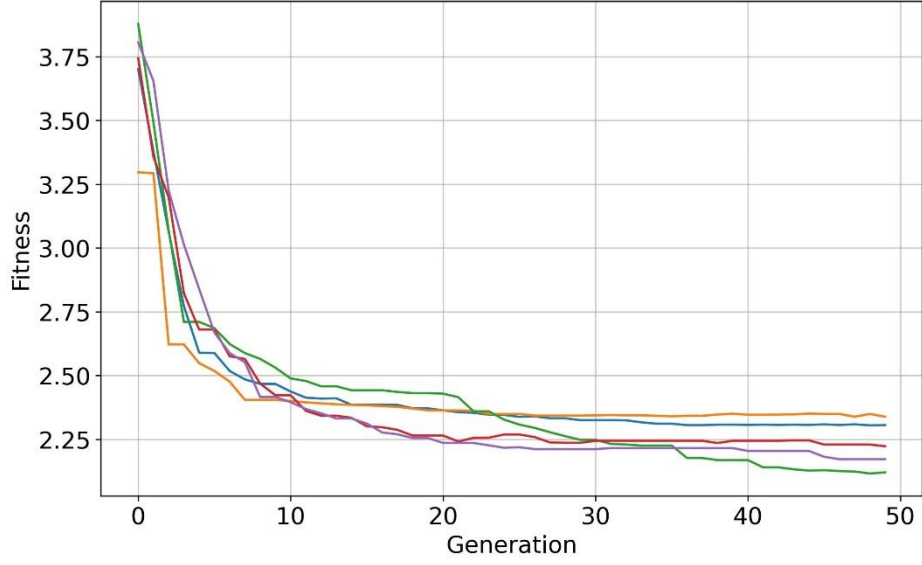
$$V_{fail} = V_s + \left[ \frac{1}{1 + \frac{s}{d}} + 7 \frac{f_{pc}}{f'_c} + \left( \frac{d}{a} + \frac{f_{pc}}{f'_c} \right) \left( \frac{10}{d} + \frac{f'_c}{2,500} + \frac{5}{1 + \frac{s}{d}} + f_{yt} \frac{f_{pc}}{f'_c} + 0.892 \right) \right] \cdot \frac{\sqrt{f'_c}}{1,000} \cdot b_w \cdot d \quad (3.11)$$

The mild reinforcement and shear reinforcement ratios were excluded from the results, which was also the case for the nonlinear regression. During the trial process, there were additional equations with better predictive performances (i.e., RMSE and  $R^2$  values were better than the ones reported here). However, the resulting equation produced by the GP model was overly complicated and thus not practical for real-world application. As a result, Equation (3.11) was selected as the best result.

**Table 3.9. Parameters settings of the best result ( $V_{fail}$ ).**

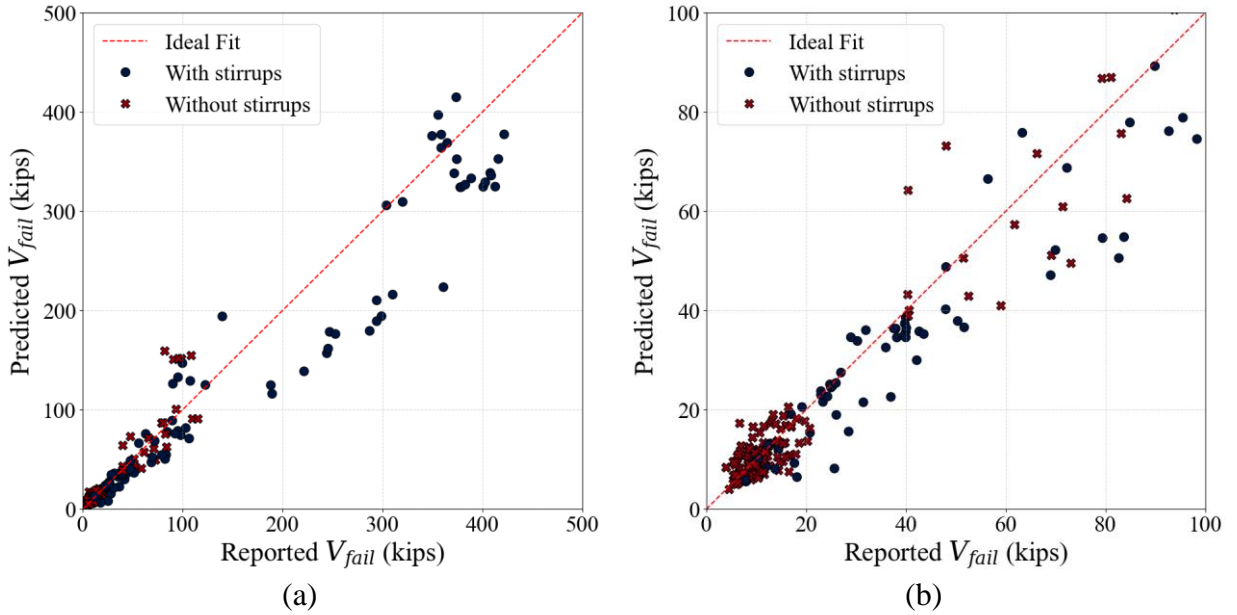
Parameters	Settings	Parameters	Settings
Population size	10,000	Metric	RMSE
Generations	50	Parsimony coefficient	0.005
Tournament size	20	P crossover	0.8
Stopping criteria	0.0	P subtree mutation	0.01
Initial depth	2, 4	P hoist mutation	0.01
Initial method	half and half	P point mutation	0.01
Function set	+, ×, ÷, sqrt, inverse, log, exp	P point replace	0.05

Most of the parameter settings are the same for the GP for predicting the shear force at the onset of diagonal cracking. However, the parsimony coefficients were increased since the results were much more complicated than the GP models for shear force at the onset of diagonal cracking. Figure 3.38 shows that the results begin to converge around the 40th generation.

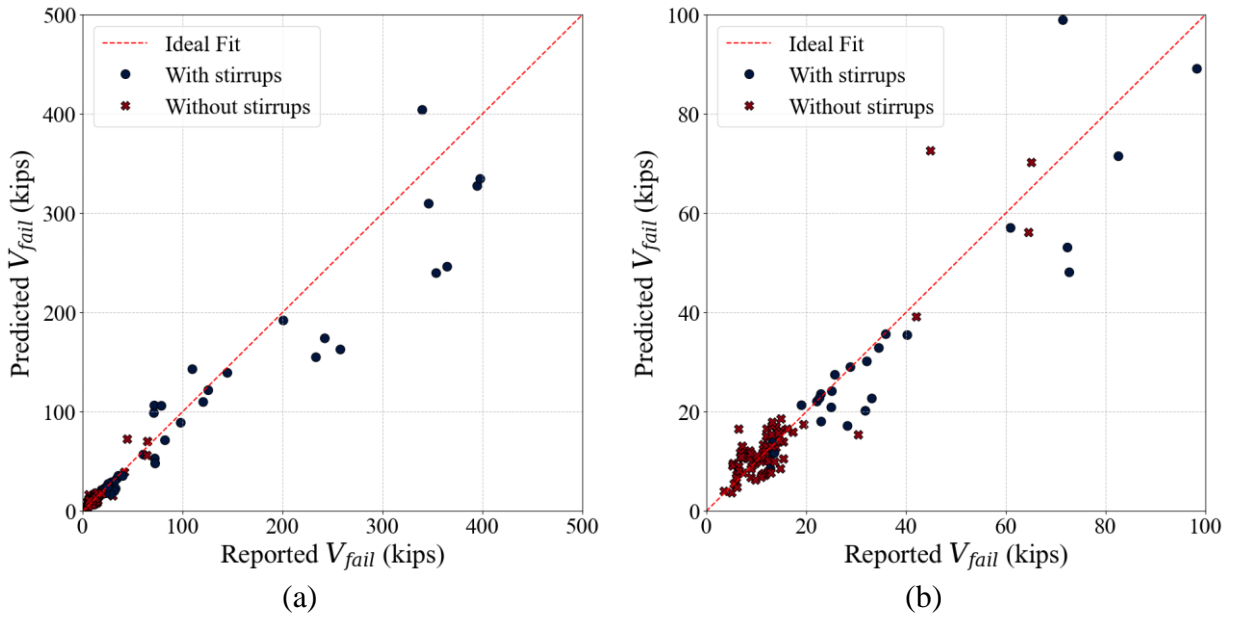


**Figure 3.38. Fitness value change as generation increases ( $V_{fail}$ ).**

Using the proposed Equation (3.11), the shear force at shear failure was calculated and plotted in Figure 3.39 and Figure 3.40 for the training and testing datasets, respectively, where it was observed that, as the reported shear force increases, the residual between the predicted value and the actual value increases.



**Figure 3.39. GP results for (a) predicted versus actual shear stress at shear failure for the train dataset, and (b) zoom-in plot of (a) plot up to 100 kips.**



**Figure 3.40. GP results for (a) predicted versus actual shear stress at shear failure for test dataset, and (b) zoom-in plot of (a) plot up to 100 kips.**

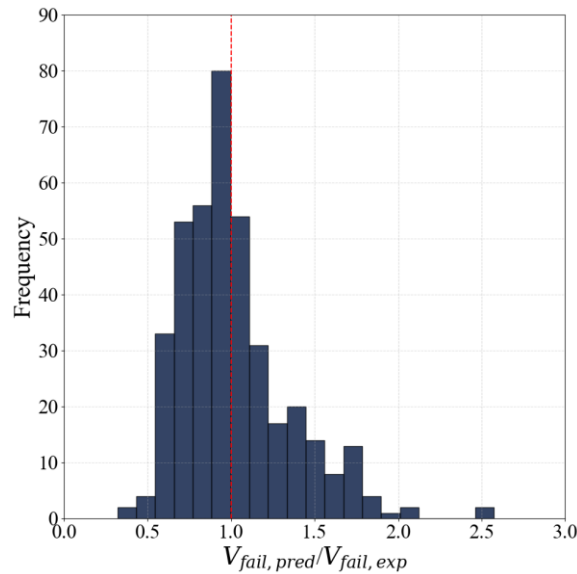
Table 3.10 summarizes the results for the GP implementation for predicting the shear force at shear failure in terms of the performance evaluation criteria. Compared to the nonlinear regression, both RMSE and  $R^2$  showed better values (higher accuracy); thus, it is evident that the GP model results in better predictive performance.

**Table 3.10. GP performance evaluations of the train, test, and total datasets for computing the predicted  $V_{fail}$ .**

Metrics	Train dataset	Test dataset	Total dataset
<b>RMSE</b>	18.54	20.87	19.28
<b><math>R^2</math></b>	0.96	0.97	0.96
<b>Mean</b>	-	-	1.08
<b>Std</b>	-	-	0.31
<b>COV</b>	-	-	29.04

Finally, Figure 3.41 presents the probability density distribution function of the ratio of predicted over actual values. Compared to the nonlinear regression, the ratio is primarily concentrated

around 1.0. Moreover, even when compared to the nonlinear regression, which implements the customized function, the results of the GP model are more conservative.



**Figure 3.41. Distribution of ratio of predicted over actual shear stress at shear failure of total dataset.**

### 3.6 SUMMARY

This chapter presents a comprehensive analysis of the dataset to determine key parameters influencing the shear capacity of prestressed concrete beams. A holistic dataset from 87 past experimental studies served as the foundation for this analysis. Through exploratory data analysis, trends, patterns, and correlations among various design parameters, such as beam depth,  $a/d$ , concrete compressive strength, prestressing level, and shear reinforcement properties were identified. The exploratory analysis also informed the selection of girder specimens that will complement the existing dataset. Nonlinear regression and symbolic regression based on GP were utilized to derive predictive models for shear strength at diagonal cracking and at shear failure. The GP models slightly outperformed the nonlinear regression models.



## **CHAPTER 4:**

### **FULL-SCALE TESTING: DESIGN OF EXPERIMENTAL PROGRAM**

The objective of the experimental program is to support the project goal of re-examining the minimum reinforcement requirements of the AASHTO LRFD Bridge Design Specifications (AASHTO 2020) and the suggested minimum reinforcement requirements from TxDOT standard drawings. The analysis on a wide range of I-girders, ranging from Tx28 to Tx70, has shown that, for the usually selected size, No. 4, of the R-bars of these girders, the minimum shear reinforcement ratio hardly controls. Usually, the maximum spacing of the R-bars controls, which provides transverse steel reinforcement ratios that are higher than the required minimum shear reinforcement ratios. The maximum spacing available in the TxDOT standard drawings is 18 in., while the maximum absolute allowable spacing in the current AASHTO LRFD Bridge Design Specifications is 24 in., which is often much smaller than the maximum cross-section depth-dependent value of  $0.8d_v$ , which is more grounded on the mechanics of shear response and failure.

It is likely that the absolute maximum spacing of 24 in. adopted by AASHTO has resulted from the range of spacings that has been used in available tests rather than from mechanics-based considerations. Our testing program together with data from our database provides information that will likely permit increasing those limits, thus resulting in more economical designs.

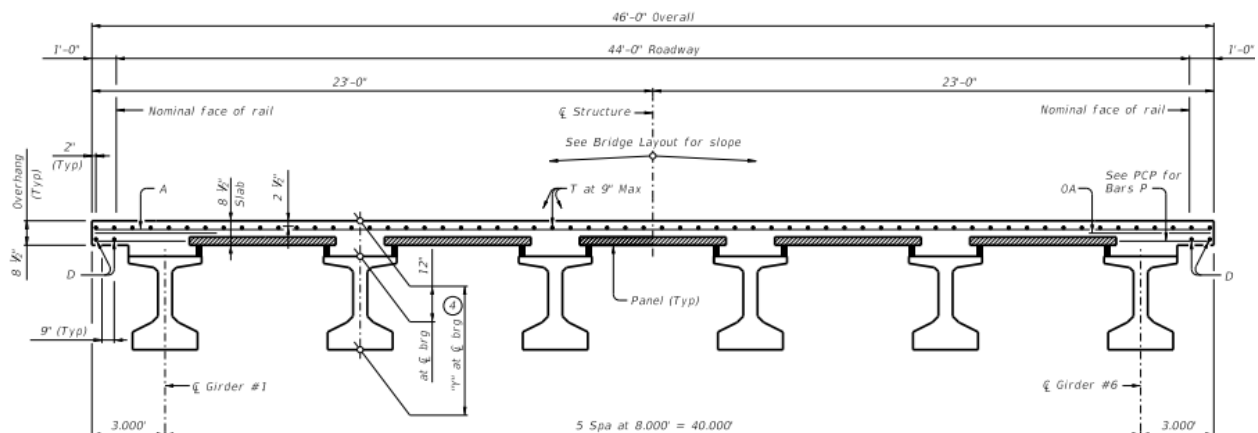
Additionally, the experimental program investigated the effect on shear response and failure of (a) concrete tensile strength, proportional to  $\sqrt{f'_c}$ , (b) steel reinforcement yield strength,  $f_{yt}$ , (c) prestressing ratio,  $\frac{f_{pc}}{f'_c}$ , (d) shear span-to-depth ratio,  $a/d_v$ , (e) harped versus straight tendons, and (f) absolute cross-section height  $h$  (or effective depth,  $d_v$ ).

Given the complexity of effective parameters and various provisions that must be evaluated, the experimental program commenced with the selection of an appropriate prototype girder. However, selecting a prototype girder from the numerous options available in TxDOT's standard designs presented a significant challenge due to the variety of possible combinations. The analysis of the experimental program showed that Tx54 girders were not available in the dataset, and for this reason, were an attractive candidate.

The experimental program started with choosing a suitable prototype girder and thoroughly understanding the factors and equations that influence shear reinforcement spacing and the minimum shear reinforcement zones. Once a prototype girder was selected, the key design parameters were systematically varied to facilitate a comprehensive comparison and provide a deeper understanding of these factors.

## 4.1 PROTOTYPE DESIGN

The process of choosing a prototype girder began by selecting a real-world scenario, such as the construction of a bridge, that will serve as the prototype bridge. The prototype bridge is a simply supported single-span bridge of length 105 ft c/c and of 44 ft wide roadway, with two lanes in each direction. It has six Tx54 girders spaced at 8 ft c/c topped by an 8.5-in. thick concrete slab (Figure 4.1). The bridge has a wearing surface of 2 in. and T501 rails.



**Figure 4.1. Bridge cross section (TxDOT 2022).**

The girders of the prototype bridge have been designed for two nominal (28-day) concrete strengths, 6 ksi and 8 ksi, which cover the range of most used concrete strengths in precast, pretensioned bridge girders in Texas, while the compressive strength of the concrete deck slab is 4 ksi. In all portions of the girders where minimum reinforcement was required, the maximum spacing of 18 in. provided in the TxDOT standard drawings controlled the provided minimum shear reinforcement (R-bars).

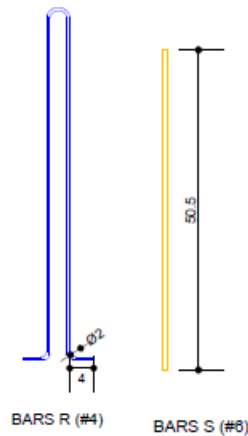
The selected prototype girder was a typical interior girder, and it was designed adhering to the *TxDOT Bridge Design Manual—LRFD* (TxDOT 2023) and AASHTO LRFD provisions

(AASHTO 2020). The variations of this design needed to result in a total of 20 designs for the minimum reinforcement. These 20 designs were included on a total of 10 girders, with each girder including a different design in its left and right halves, denoted as G#-L and G#-R. These variations were selected to complement existing experimental data that are available in a database assembled by the research team.

## **4.2 PARAMETRIC STUDY FOR PROTOTYPE GIRDER**

The design of prestressed concrete girders was based on TxDOT Bridge Design Manual (TxDOT 2023) and AASHTO LRFD Bridge Design Specifications (AASHTO 2020) to follow the design steps and to ensure the safety of girders. The design for shear starts with the basic design principle that the demand should be less than the available shear capacity. If the concrete section itself cannot safely support the shear demand, additional capacity is provided through use of shear reinforcement. The area and spacing of shear reinforcement required must be computed along the entire girder at regularly selected intervals. The next step for the transverse shear design was to check the minimum shear reinforcement and maximum spacing limits. The spacing details for the stirrups should be adjusted in accordance with the limits.

The shear design of the girder should also satisfy interface shear design requirements. The horizontal shear at the interface of the girder and slab in the composite section should be checked in this case. The shear capacity of the interface should be larger than the horizontal shear demand at the interface, otherwise the area of shear reinforcement provided earlier should be increased. The TxDOT standard practice for shear reinforcement contains two types of bars, R and S, shown in Figure 4.2. The R-bars are double-legged and protrude out from the girder like a hook such that the slab can be cast over the hooks, ensuring it crosses the interface. The S-bars are single-legged stirrups which are equal to the height of the girder. The S-bars in prestressed I-girders are bundled with the R-bars and provided in the anchorage zone, where the required area of shear reinforcement might be high due to bursting and spalling requirements. In that case, the bundled bars together provide a higher area of shear reinforcement with the same spacing. Following the interface shear design, the minimum shear reinforcement limits need to be checked, and the provided spacing should be updated.



**Figure 4.2. R-bars and S-bars used for shear reinforcement.**

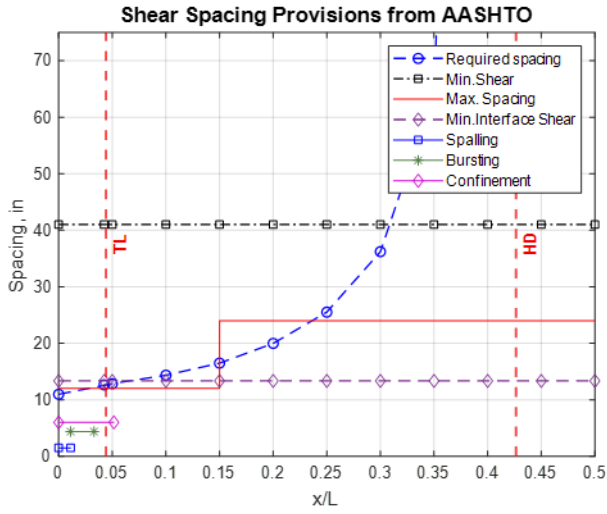
The girder ends must be detailed appropriately in reinforcement to prevent bursting and spalling. However, the primary focus of this project was on the provisions for minimum shear reinforcement, particularly in the central section of the girder where the shear demand tends to be lower. The specific provisions governing the reinforcement spacing depend on both the location along the girder and the design scenario. Critical parameters influencing these provisions for the prototype girders include the girder length and girder depth. Consequently, the selection process should prioritize girders with a longer span in regions where minimum shear reinforcement is a controlling factor. The parametric study behind the selection of these prototype girders is discussed in the following sections.

#### **4.2.1 Size of the Girder**

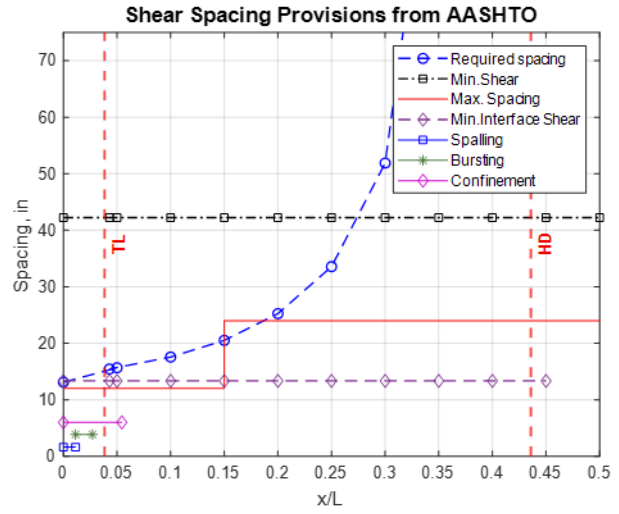
The TxDOT standard girder sizes for a 44-ft-wide bridge span as per TxDOT recommendations are Tx28, Tx34, Tx40, Tx42, Tx54, and Tx62. To make a comparative analysis, plots of reinforcement spacing were developed for #4 R-bars of 60 ksi strength. These plots contain the spacing requirements based on different provisions discussed in the previous section. The length of the region for which the minimum reinforcement controls is then compared for different girder sizes.

The plots were developed based on the economical span length of the girders recommended in the *TxDOT Bridge Design Manual* (TxDOT 2023) and to get an idea on a selected length of the region for which the minimum reinforcement controls. Based on the plots for the economical

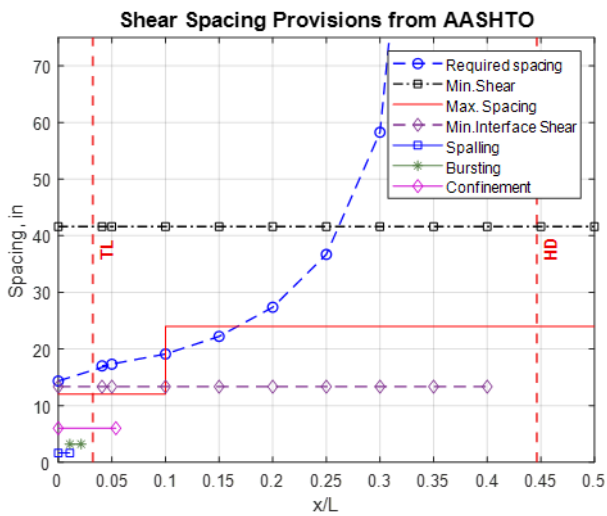
span length, the length of the region having minimum shear reinforcement controlling increases as the girder size increases. The plots can be seen in Figure 4.3, where the  $x$ -axis is the distance from the end of the girder to the midspan, and the  $y$ -axis is the spacing of shear reinforcement based on various provisions.



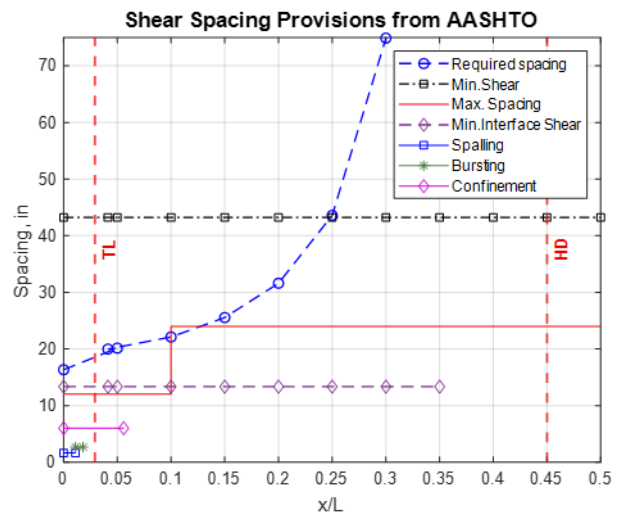
Tx28



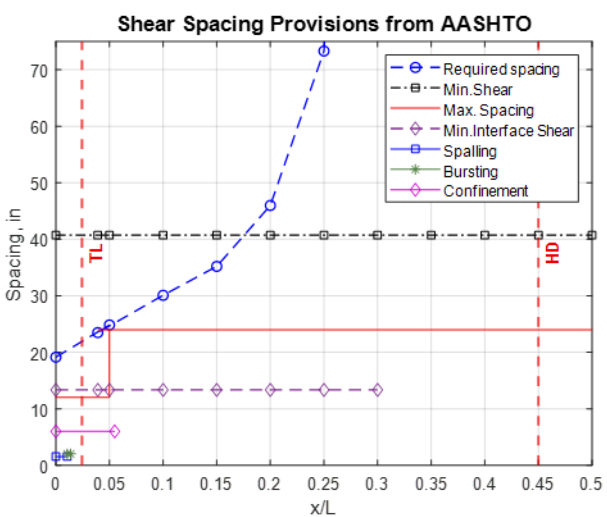
Tx34



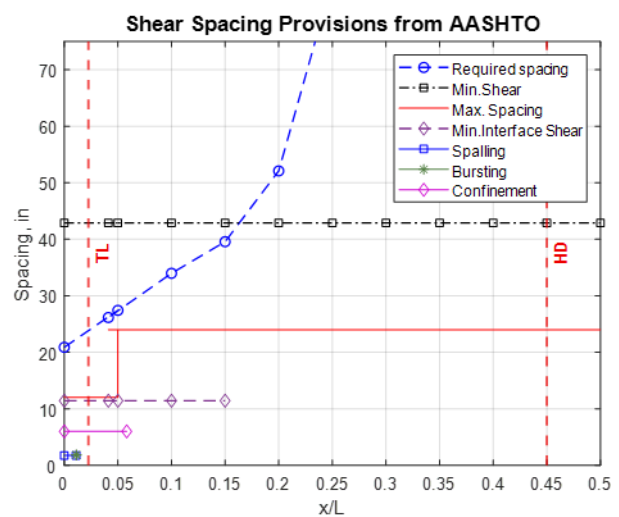
Tx40



Tx46



Tx54



Tx62

Figure 4.3. Spacing plots for economical span lengths for different girder sizes.

The primary objective behind utilizing a larger-sized girder for testing resides in the endeavor to address size-related influences. The shear response of a structure is notably influenced by the proportional relationship between normal and shear stresses, coupled with their distribution across the vertical extent of the cross-sectional profile. However, it is important to recognize that the shear behavior is not exclusively governed by the  $a/d_v$  ratio; the absolute height of the cross section also exerts a considerable influence. Notably, the progression from small-sized to large-sized girders is not marked by a linear scaling of shear behavior solely based on the  $a/d$ .

In the context of the well-established “size effect” phenomenon, it is evident that larger-sized specimens exhibit reduced strength in comparison to their smaller counterparts (Kotsovos and Pavlović 2004). This characteristic differential in strength is a key factor contributing to the inapplicability of directly extrapolating tests conducted on small-sized girders to their larger counterparts. It is important to emphasize that the manifestation of size effects is significant in girders characterized by minimal shear reinforcement. The choice of a Tx70 girder allows for potential extrapolation to the performance of a Tx62 girder during data analysis. This approach is favored over extrapolation because it is cautioned not to reach beyond the range of available test data. Therefore, directly extrapolating the performance of a Tx70 girder from data on a Tx62 girder is not advisable.

#### **4.2.2 Length of the Girder**

The same parametric study is done for the length of the girder by selecting a particular set of girders and developing the spacing plots for each design case. The design case is developed considering the dead load and standard live load according to the *TxDOT Bridge Design Guide* (TxDOT 2023). The calculations are further shown in detail in Figure 4.4. It can be observed that as the span length increases, the length of the region of interest also increases. The plots for Tx54 for different lengths can be seen in Figure 4.4.

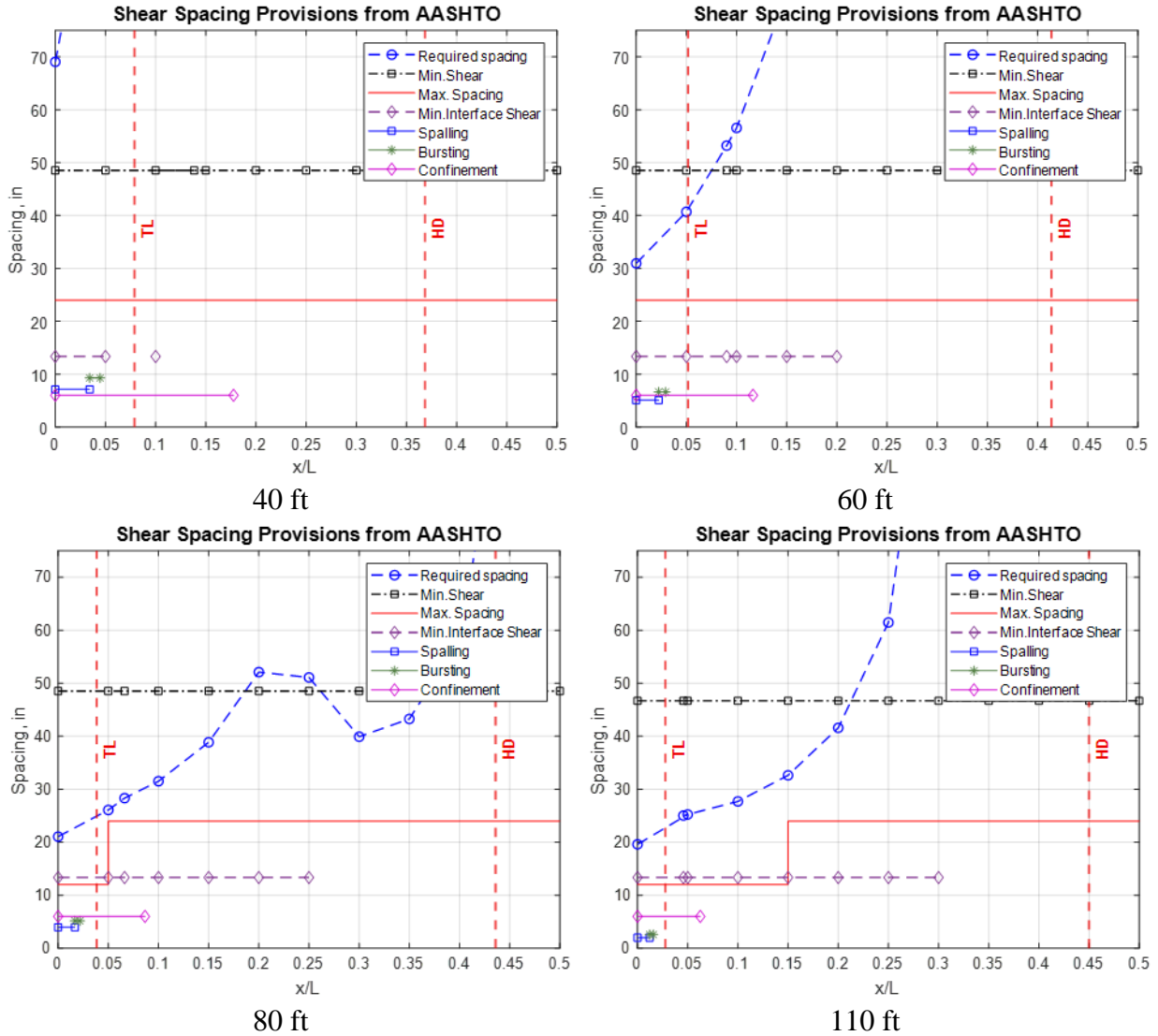


Figure 4.4. Spacing plots for different lengths of Tx54 girder.

### 4.2.3 Remarks

By comparing the spacing plots for both parameters, the key points for selection of the prototype girder are identified. The minimum interface shear requirements control the spacing limit for a longer portion of the girder for smaller girder sizes. The end regions are mainly controlled by additional reinforcement detailing like spalling, bursting, and confinement reinforcement. The smaller girder lengths have regions where no minimum shear reinforcement is needed. In addition, minimum interface shear provisions govern for longer  $x/L$  range as the girder length increases.

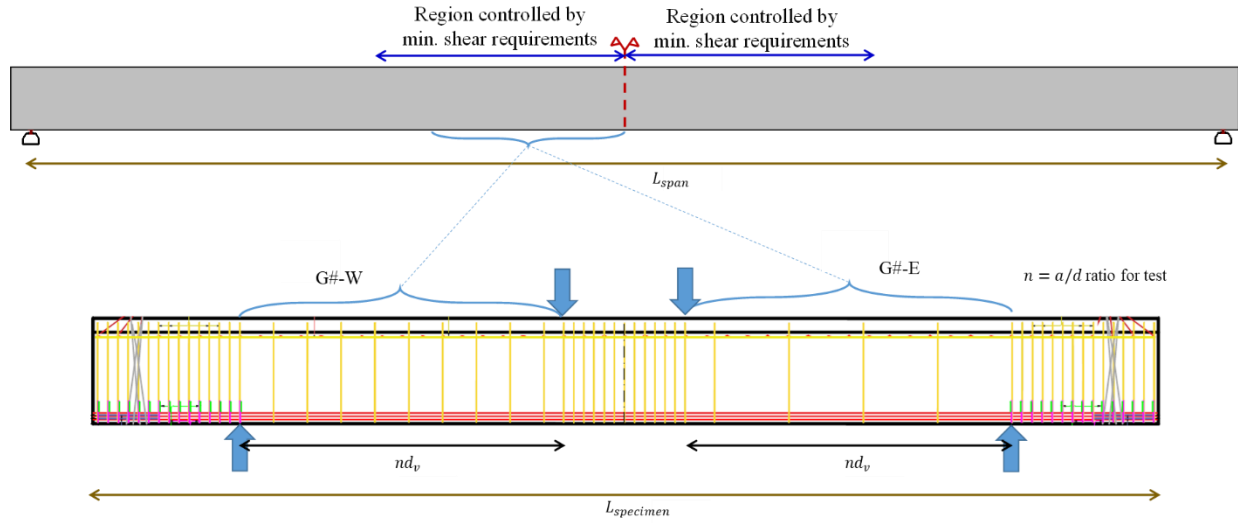


Based on these observations, the prototype with a longer region of interest can be a Tx54 and Tx62. The length of the girder could be between 90 ft and 110 ft. In addition, based on the database analysis from previous literature, the prototype girder was selected to be Tx54 and 105 ft in length, which in turn appends to the potential gaps in terms of girder size and type. In addition, one Tx70 girder specimen was also tested to provide a comparative scenario for girder size effects.

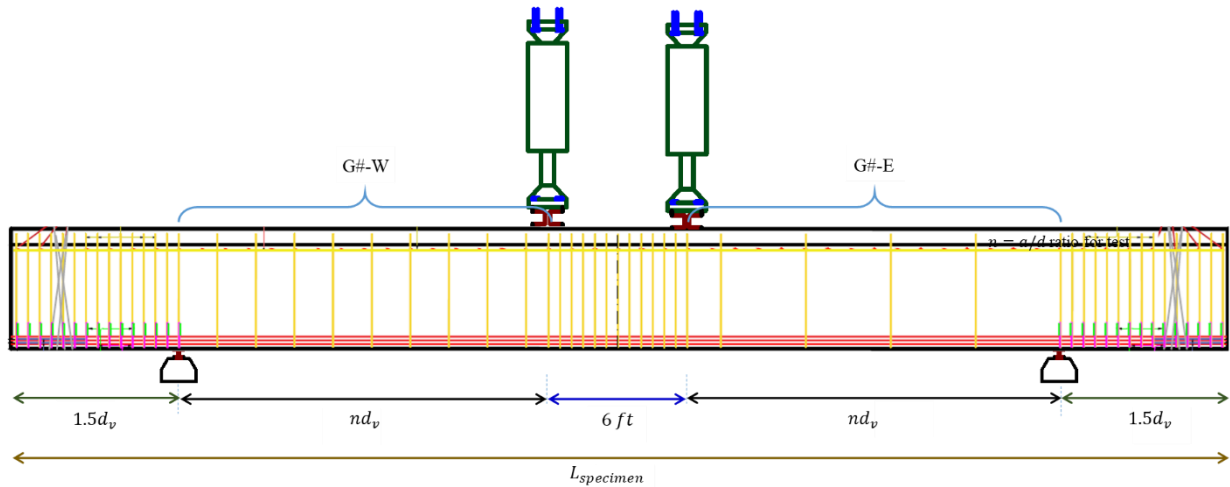
### **4.3 TEST SPECIMENS AND LOADING SYSTEM**

The relationship of the prototype girder to the test specimens is graphically demonstrated in Figure 4.5. Each girder included two specimens, namely, G#-L and G#-R, on the left and right side of the girder. Specimens G#-L and G#-R constitute copies of the relevant portions of the prototype girder. Each of these specimens, G#-L and G#-R, had a different minimum shear reinforcement design. The length of specimens G#-L and G#-R was such that a target  $a/d_v$  was achieved. The overhang regions had a length of about  $1.5d_v$  from each end and were highly reinforced to resist spalling and bursting stresses, achieve strand force transfer, and provide a sufficiently strong anchorage zone overall so that the specimens G#-L and G#-R remained unaffected by such phenomena. Thus, these end/overhang zones were directly designed for the test specimen rather than the prototype girder.

Each girder was subjected to a four-point bending/shear load using two actuators, as shown in Figure 4.6. Loading was applied at a slow rate of 5–10 kips per minute. The loading application was halted periodically to record and mark crack locations and widths.



**Figure 4.5. Example of test specimen extraction from prototype girder.**



**Figure 4.6. Experimental setup of a typical girder specimen.**

#### 4.4 TEST MATRIX

Based on an examination of existing literature, it is advisable to structure the design of experimental specimens in a manner that enables direct comparisons among crucial parameters. Therefore, it becomes essential to define the spacing of the stirrups in accordance with various relationships outlined in earlier studies. By incorporating differences in factors such as concrete strength, yield strength of stirrups, and  $a/d$ , these comparisons can significantly enhance the overall value of the database.

The test matrix, built upon the prototype design and its effective parameters, encompassed 22 variations distributed across 11 girders, ensuring a comprehensive study. Among these variations, the spacing of shear reinforcement emerged as a critical factor under investigation. Additionally, a significant aspect of the testing procedure involves assessing whether to test the girders with or without the deck, introducing another crucial variable to the test matrix. This necessitated casting the prototype design in two identical girders, subsequently facilitating an examination of the impact of the deck, and thereby informing the necessity for its inclusion in subsequent tests.

#### 4.4.1 Shear Reinforcement Spacing in Test Specimens

Based on a review of the design procedure for TxDOT girders, the maximum spacing available in standard drawings is 18 in., whereas the AASHTO LRFD Bridge Design Specifications have a maximum of 24 in. The major question that needed to be addressed is whether increasing the shear reinforcement spacing of 18 in. and 24 in. to larger values to achieve more economical designs without compromising performance was attainable. To answer this question, the experimental program included testing girders with different maximum  $s/d$ , including:

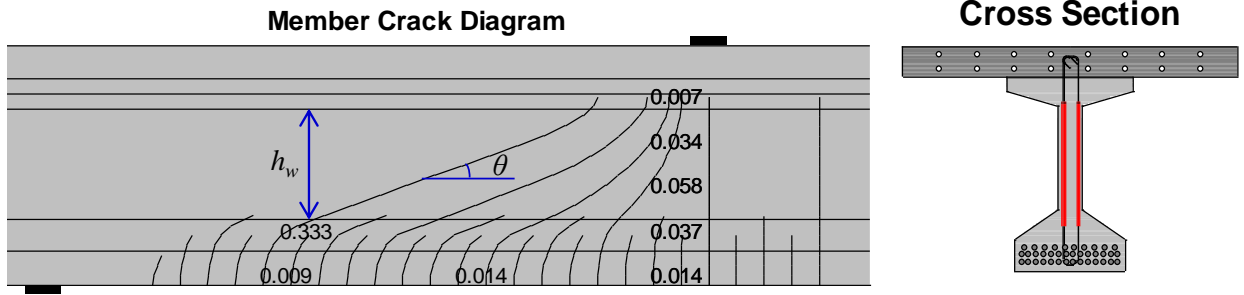
- The maximum spacing of 12 in. for Tx28 and Tx34, 18 in. for Tx40, Tx46, Tx54, Tx62 and Tx70 provided in the standard TxDOT drawings, indicated as  $s_{v,max,TxDOT}$ .
- The spacing indicated as  $s_{v,ACI}$  that results from the minimum shear reinforcement ratio from ACI 318-19 is as follows:

$$\rho_{v,min} f_{yt} = \min \left\{ \frac{A_{ps} f_{pu}}{80d b_w} \sqrt{\frac{d}{b_w}}, \max \left\{ 0.75 \sqrt{f'_c}, 50 \text{ psi} \right\} \right\} \text{ for } A_{ps} f_{se} \geq 0.4(A_{ps} f_{pu} + A_s f_y).$$

This equation includes the effect of prestressing and usually provides a spacing that is slightly larger than AASHTO's 24 in. maximum spacing (Note:  $\rho_{v,min} = A_{v,min}/(b_w s_v)$ ).

- A proposed theoretical peak spacing  $s_{v,max} = h_w / (2 \tan \theta)$  derived as shown in Figure 4.7, which utilizes the angle of cracking over the web and ensures that at least one R-bar crosses each diagonal tension crack. This common rule is typically adopted when selecting the maximum spacing of shear reinforcement. The angle  $\theta$  is directly calculated from the MCFT as adopted in AASHTO (2020).

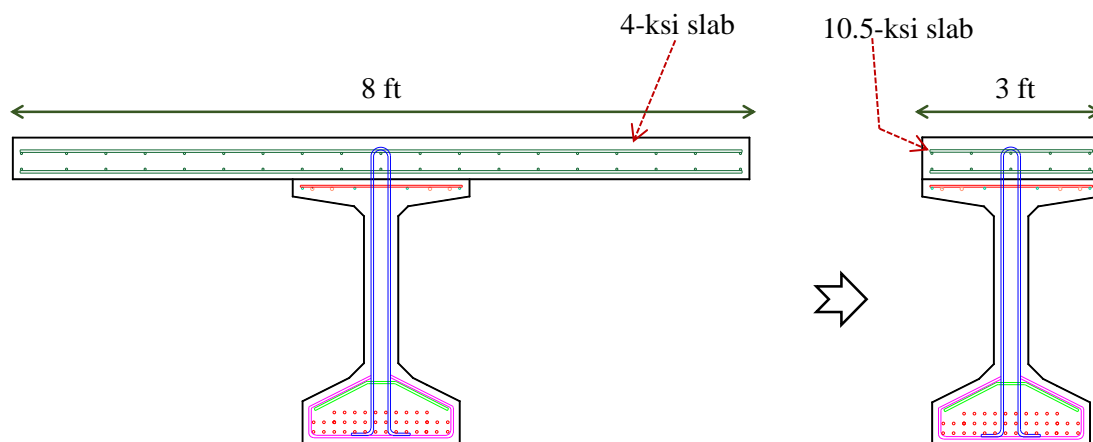
- A spacing resulting from the minimum shear reinforcement ratio of AASHTO,  $\rho_{v,\min} f_{yt} = \lambda \sqrt{f'_c}$ , which usually results in spacings that are larger or much larger than 18 in. or 24 in. but do not exceed the maximum of  $0.8d_v$  of AASHTO. It also needs to be noted that the AASHTO provision does not include the effect of prestressing.



**Figure 4.7.** Parameters for  $s_{v,\max} = h_w / (2 \tan \theta)$ .

#### 4.4.2 Effect of Deck

The effect of the deck slab on the shear response of girders was evaluated by testing two identical girders, one with a cast-in-place deck slab and the other without a slab. To simplify the casting and testing process, instead of the originally intended 8-ft-wide, 8.5-inch-thick concrete slab with a strength of 4 ksi placed atop the girders, an equivalent slab measuring 3 ft in width (with the same 8.5-inch thickness) and a concrete strength of 10.5 ksi was selected, as illustrated in Figure 4.8. Based on analysis, this equivalent slab provides identical tension and compression strains, as well as the same neutral axis position. Consequently, it was expected to induce equivalent stress and strain distributions within the girders, thereby resulting in identical shear responses and shear failure mechanisms. It is worth noting that shear failure predominantly hinges on the stress and strain profiles across the web. This methodology draws from previous applications, notably referenced in Katz (2016) on shear tests.



**Figure 4.8. Equivalent design between 8-ft slab and 3-ft slab.**

### 4.4.3 Experimental Specimens

A list of the 11 girders (i.e., 22 specimens) is shown in Table 4.1. Each girder included two specimens, namely, G#-L and G#-R, on the left and right side of the girder. Girders G1\* and G1 represent the initial variation in the experimental test matrix that were aimed at elucidating the influence of the deck. Within the testing zone, two distinct shear reinforcement configurations were employed, differing in the yield strength of the stirrups. On one side of the girder, 60 ksi bars were spaced at 18 in., while on the other side, an equivalent strength was achieved using 80 ksi bars with a spacing of 26 in. G1\* was outfitted with a deck according to the specifications outlined in Section 4.4.2, whereas G1 did not include a deck. Collectively, these tests offered insights into the impact of the deck while individually highlighting the effects of employing high-strength stirrups in the girder.

Girder G2 was specifically designed to explore variations in shear reinforcement spacing, as detailed in Section 4.4.1. This girder featured two distinct reinforcement zones, each exhibiting different spacing configurations. One side adhered to spacing guidelines derived from the ACI 318-19 minimum shear reinforcement provisions, while the other was determined by the equation for proposed theoretical peak spacing. This setup enabled a direct comparison of different spacing provisions. Additionally, one side of G1 with a spacing of 18 in. complemented this specimen and facilitated a comprehensive comparison across various spacing configurations.

Girder G3 served as a variation of the prototype design, specifically focusing on investigating the impact of harped strands. Designed in accordance with the stress criteria for the prototype

design, this girder incorporated six harped strands, with a harping height of 20.5 in. at the end of the girder. Additionally, to facilitate comprehensive comparisons, both sides of the girder featured variations in shear reinforcement spacing. This approach ensured exploration of the effects of harped strands while considering different shear reinforcement configurations.

Girders G4 and G9 were specifically designed to analyze the impact of the shear span-to-depth ( $a/d$ ) ratio. By comparing them with the G1 girder, which had an  $a/d$  of 3, G4 and G9 provided a range for a more comprehensive comparison. G4 had an  $a/d$  of 2.5, while G9 featured an  $a/d$  of 4. This deliberate variation in  $a/d$  ratios enabled a more thorough exploration of how different span-to-depth ratios affect girder performance, offering valuable insights for comparison and analysis. The  $a/d$  has been found to strongly influence the shear strength of prestressed beams without shear reinforcement, but this influence decreases with the introduction of shear reinforcement (Hawkins 2005).

Girders G5 and G6 were designed to facilitate a comparison of prestressing ratios within the girder design. Achieving this involved modifications to the design of the G1 girder, wherein G5 incorporated fewer prestressing strands, while G6 integrated a higher number of prestressing strands. Despite these variations, both girders successfully met the necessary design and stress criteria. The variation in prestressing ratio is particularly significant since prestressing strands constitute a fundamental difference between a conventional reinforced concrete beam and a prestressed concrete girder. This deliberate alteration allowed for the study of its impact on the minimum shear reinforcement zone, alongside variations in  $s/d$ , thus providing valuable insights into girder behavior under different prestressing conditions.

Girders G7 and G8 were designed with different 28-day concrete compressive strengths and a proportional number of prestressing strands and passed all the stress checks, which ensured that Girder G1 could be compared with a lower strength (G7 with 4 ksi) and higher strength (G8 with 8.5 ksi) girder. Enhancement in concrete tensile strength has been observed to correlate with an augmentation in the transverse reinforcement quantity necessary for effectively countering the shear force that emerges during the initial stages of diagonal cracking. This connection arises because greater tensile stresses correspond to increased forces that need to be redistributed when

diagonal cracks begin to develop. In addition, the concrete tensile strength can be related to the compressive strength of concrete, which is addressed by this effective comparison.

The final girder, G10, was used to explore the effects of the girder depth in terms of absolute cross-section height. Based on the parametric study discussed earlier, a Tx70 girder was chosen, which could ultimately be interpolated to the performance of a Tx62 girder during data processing. This approach was selected because it is not recommended to extrapolate outside the range covered by test data; thus, extrapolation of the performance of a Tx70 girder from data on a Tx62 girder is not recommended. The primary objective behind utilizing a larger-size girder resides in the endeavor to address size-related influences. The selected girder section of Tx70 was designed to provide an effective comparison with a similar Tx54 girder with identical  $a/d$  and prestressing ratio to ensure equivalent testing parameters.

**Table 4.1. Test matrix for girder specimens.**

Test ID	Girder Type	Length (ft)	$f'_{ci}$ (ksi)	$f'_c$ (ksi)	28-day $f'_c$ (ksi)	Spacing (in.)	$f_{yt}$ (ksi)	# of Strands	Top Strands	Harp?	$h$ (Harp)	a/d <sub>v</sub>	$f_{pc}/f'_c$
G1*-W	Tx54	52	6	7	<b>9.2</b>	18	60	34	2	No	0	3	18.42
G1*-E	Tx54	52	6	7	<b>9.2</b>	26	80	34	2	No	0	3	18.42
G1-W	Tx54	51	6	7	<b>8.8</b>	18	60	34	2	No	0	3	18.42
G1-E	Tx54	51	6	7	<b>8.8</b>	26	80	34	2	No	0	3	18.42
G2-W	Tx54	51	6	7	<b>8.2</b>	38	60	34	2	No	0	3	18.42
G2-E	Tx54	51	6	7	<b>8.2</b>	26	60	34	2	No	0	3	18.42
G3-W	Tx54	51	6	7	<b>8.7</b>	26	60	34	2	Yes (6)	20.5	3	18.42
G3-E	Tx54	51	6	7	<b>8.7</b>	18	60	34	2	Yes (6)	20.5	3	18.42
G4-W	Tx54	45	6	7	<b>8.5</b>	38	60	34	2	No	0	2.5	18.42
G4-E	Tx54	45	6	7	<b>8.5</b>	18	60	34	2	No	0	2.5	18.42
G5-W	Tx54	51	6	7	<b>9.2</b>	26	60	26	2	No	0	3	15.23
G5-E	Tx54	51	6	7	<b>9.2</b>	38	60	26	2	No	0	3	15.23
G6-W	Tx54	51	6.3	7	<b>9.1</b>	38	60	40	4	No	0	3	21.24
G6-E	Tx54	51	6.3	7	<b>9.1</b>	18	60	40	4	No	0	3	21.24
G7-W	Tx54	51	4	5	<b>8.2</b>	26	60	24	2	No	0	3	19.66
G7-E	Tx54	51	4	5	<b>8.2</b>	18	60	24	2	No	0	3	19.66
G8-W	Tx54	51	6	8.5	<b>9.6</b>	26	60	38	2	No	0	3	16.31
G8-E	Tx54	51	6	8.5	<b>9.6</b>	18	60	38	2	No	0	3	16.31
G9-W	Tx54	56	6	7	<b>8.8</b>	26	60	34	2	Yes (6)	20.5	4	18.42
G9-E	Tx54	56	6	7	<b>8.8</b>	18	60	34	2	Yes (6)	20.5	4	18.42
G10-W	Tx70	58	6	7	<b>9.2</b>	40	60	40	2	No	0	3	17.51
G10-E	Tx70	58	6	7	<b>9.2</b>	18	60	40	2	No	0	3	17.51

\* Indicates deck on the girder.

$f'_c$  (28-day) is the observed concrete strength based on material testing.



#### 4.4.4 Effect of Major Design Parameters via Experimental Comparisons

The test specimens were selected/designed to enable quantification of the effect of major design parameters on the shear behavior of the girders through direct comparisons of experimental data. These planned comparisons included:

1. Effect of deck slab: Compare G1\*-W versus G1-W and G1\*-E versus G1-E.
2. Effect of  $s/d$ : Compare G1-W versus G2-E versus G2-W; G3-W versus G3-E; G7-W versus G7-E, G8-W versus G8-E; G10-W versus G10-E.
3. Effect of concrete tensile strength: Compare G1-W versus G7-E versus G8-E; G2-E versus G7-W versus G8-W.
4. Effect of stirrup yield strength: Compare G1\*-W versus G1\*-E; G1-W versus G1-E.
5. Effect of  $a/d$ : Compare G1-W versus G4-E versus G9-E; G2-W versus G4-W versus G9-W.
6. Effect of harped tendons: Compare G3-W versus G2-E; G3-E versus G1-W.
7. Effect of prestressing ratio: Compare G6-E versus G5-W versus G2-E, G5-E versus G6-W versus G2-W.
8. Effect of cross-section depth: G10-E versus G1-W; G10-W versus G2-W.

The experimental data also enabled validation of different formulas that address minimum reinforcement requirements, such as:

1. Maximum spacing resulting from  $\rho_{v,\min} f_{yt}$  per ACI 318-19 via G1-W, G1-E, G3-W, G3-E, G4-E, G5-W, G6-W, G7-W, G8-W, G9-W, G10-E.
2. Maximum spacing resulting from  $\rho_{v,\min} f_{yt}$  per AASHTO (2020) via G2-E, G7-E, G8-E, G9-E, G10-W.
3. Maximum spacing resulting from proposed  $s_{v,\max} = h_w / (2 \tan \theta)$  without violating  $\rho_{v,\min} f_{yt}$  from AASHTO (2020) via G2-W, G4-W, G5-E, G6-E, G10-W.
4. Maximum spacing of 18 in. from TxDOT (2023) via G1-W, G4-E, G5-W, G6-W, G7-W, G9-W, G10-E.

## 4.5 SUMMARY

The core aspect of the parametric study of minimum shear reinforcement in this research study lies in the experimental testing. This chapter details the design of the experimental program with key information regarding the test setup, selection of prototype girder, and devising the test matrix based on potential information from the database analysis in the previous chapter. The test specimens and experimental setup were designed to be four-point bending test that enabled two test zones per girder. The minimum shear reinforcement zone of the prototype girder were designed to be in the testing zone of the experimental specimen.

The prototype girder was selected based on designing the TxDOT I-girders and determining the extent of influence of minimum shear reinforcement in the girder. Based on this, girders larger than Tx46 have a significant portion of their length being governed by the minimum shear reinforcement instead of other provisions like anchorage zones and interface shear. The selected girder was Tx54, and the different parameters were identified from literature and varied to develop the test matrix. In addition, a larger girder Tx70 was also added to further understand the size effects. Further, the effect of casting the deck slab was also studied by testing two identical girders with and without the deck. This chapter finally summarizes the resulting effective comparisons from the experimental test specimens.

## **CHAPTER 5:**

### **FULL-SCALE TESTING: CONSTRUCTION OF SPECIMENS**

This chapter provides a detailed account of fabricating the girder specimens as outlined in the test matrix. As previously noted, the design of these girders is intended to enable quantification of the effect of major design parameters on the shear behavior of the girders through direct comparisons of experimental data. Additionally, each girder undergoes stress checks at the ends upon release and is detailed accordingly at the ends and other specified locations, in compliance with TxDOT reinforcement detailing standards (TxDOT 2022). The final shop drawings of these girders are shown in Appendix A. The girders were cast in two phases in 2022 and 2023 at Bexar Concrete Works Inc., Ltd. in San Antonio, Texas. The girders were cast with self-consolidating concrete as per the standards in ASTM C1611-21 (2021).

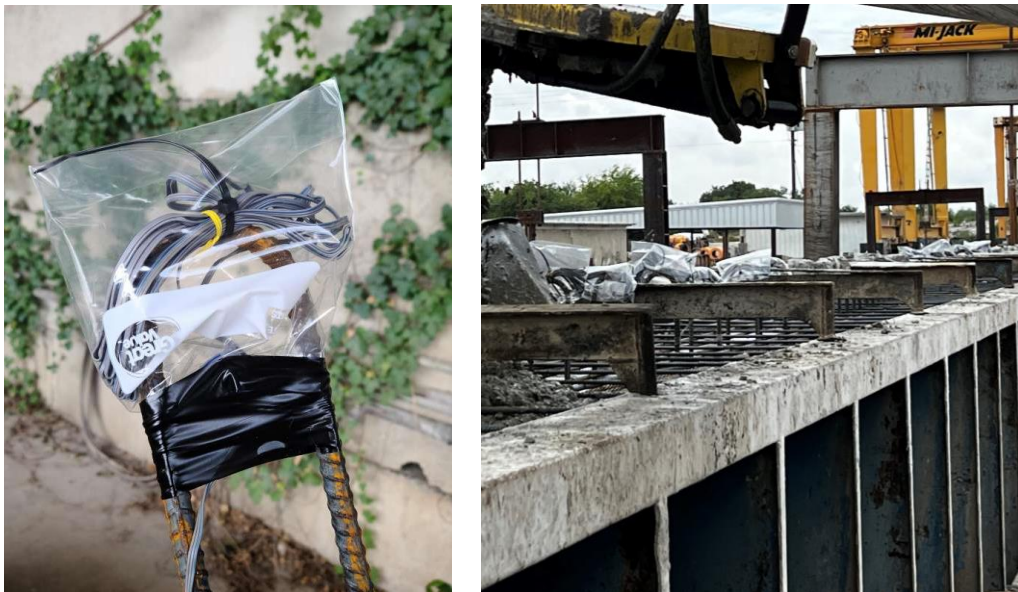
#### **5.1 EMBEDDED GAUGES ON R-BARS**

Before casting the girders, instrumentation plans were developed to detail the placement of embedded strain gauges on the web steel reinforcement bars (R-bars). These gauges were installed at the mid-height of each R-bar and were adequately protected to prevent damage during concrete casting and to avoid water infiltration. The data collected from these strain gauges were instrumental in monitoring the strain in the stirrups throughout the testing process. The specific procedure for attaching the strain gauges to the R-bars is illustrated in Figure 5.1.



**Figure 5.1. Strain gauging of R-bars.**

The instrumented R-bars were further protected by placing plastic airtight bags over them to shield the gauge wires during the concrete pouring process. This precaution ensured that concrete would not directly impact the gauge wires, while also facilitating easier access to these wires for later connection to the data acquisition system (DAQ). It was crucial to ensure that the plastic bags and tape did not cover the sections of the R-bar that would be embedded within the girder. Figure 5.2 demonstrates how this protective measure was implemented and its effectiveness during the casting of the girder.



**Figure 5.2. Protection for the strain gauge wires.**

## 5.2 CASTING OF GIRDERS

The R-bars, with strain gauges attached, were sent to the precast plant ahead of girder fabrication and the placement of gauged bars is verified to be in the testing zone. The installation of reinforcement and verification of the location of instrumented bars are shown in Figure 5.3.



Installation of reinforcement

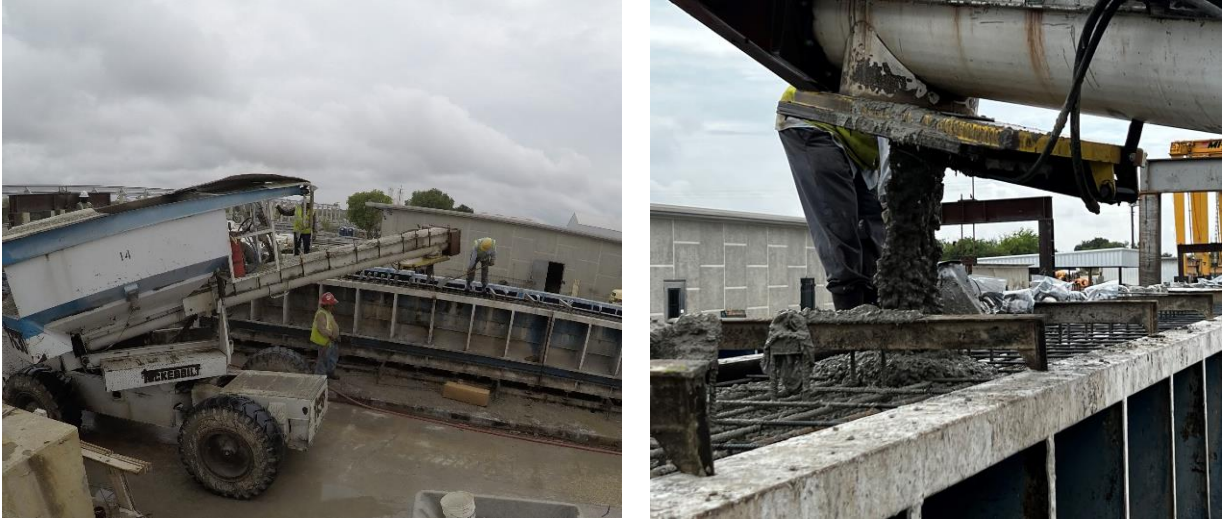


Verifying instrumented bar locations

**Figure 5.3. R-bar installation and verification.**

For each batch, the qualities of the freshly mixed concrete were examined to make sure they met ASTM requirements. As per ASTM C1611-21 (2021), the slump flow test was conducted, and batches were guaranteed to have a slump diameter of at least 20 in.. The temperature of each batch was also measured to make sure it complied with regulations. The concrete was poured into the formwork, as shown in Figure 5.4, after the slump was within the permitted range.





**Figure 5.4. Concrete pouring into the girder formwork.**

Concrete samples were made for each batch of the concrete poured into the girders. The formed concrete cylinders had a diameter of 4 in. and height of 8 in., and the rectangular concrete beams made were 4 in. x 4 in. x 15 in. The concrete samples were prepared based on ASTM-C31 and were later placed in water storage tanks for initial curing based on recommendations in the standards. These samples were further demolded for more than 24 hours and kept in a curing storage space at 23°C and 95 percent humidity. The preparation of samples on-site, demolding of cylinders, and storage in the curing rooms is shown in Figure 5.5.



Preparation of molds



Initial curing at the precast plant



Demolding of cylinders



Storage in curing rooms

**Figure 5.5. Preparation and storage of concrete samples.**

The total number of samples cast for a total of 11 girders was 336 cylinders and 39 beams. The list of samples cast is summarized in Table 5.1.

**Table 5.1. Summary of concrete samples for girders.**

<b>Girder #</b>	<b>Batches</b>	<b>Cylinders</b>	<b>Beams</b>	<b>Date of casting</b>	<b>28-day testing</b>
G1*	E, F, G	36	3	08/23/22	09/19/22
G1	H, I, J	36	3	08/23/22	09/19/22
G2	K, L	30	-	08/23/22	09/19/22
G3	B, C, D	30	3	08/23/22	09/19/22
G4	M, N, O	36	-	08/23/22	09/19/22
G5	P, Q, R	30	-	08/24/22	09/20/22
G6	S, T, U, V	36	6	08/30/22	09/22/22
G7	AA, AB, AC	30	6	06/16/23	07/14/23
G8	BA, BB, BC	30	6	06/26/23	07/21/23
G9	CA, CB, CC	30	6	06/30/23	07/28/23
G10	DA, DB, DC, DD	36	6	07/11/23	08/08/23

The samples were later tested to identify major mechanical properties such as 28-day concrete strength, splitting tensile strength (STS), MOE, and MOR. In addition, the precast plant ensured compliance with the release strength of concrete prescribed in the design documents.

### **5.3 CONCRETE MATERIAL PROPERTIES**

Upon completing the casting of girders, every concrete batch used for the entire set of girders was systematically sampled to ascertain concrete material properties. Adhering to ASTM standards, the fresh concrete properties were rigorously monitored during casting. A slump flow test following ASTM-C1611 (2021) guidelines was conducted on the self-consolidating concrete (SCC) during girder casting to verify a slump flow exceeding a 20 in. diameter, as depicted in Figure 5.6. This test aimed to align with TxDOT specifications, ensuring that the SCC flow adequately navigated the tightly confined reinforcement cage within the girder structure.





**Figure 5.6. Slump flow test for the SCC with more than 20 in.**

Concrete compressive strength evaluations were undertaken for every batch at the 28-day mark in adherence to the ASTM-C39 (2005) standards. These tests involve the application of a compressive load onto cylindrical specimens measuring 4 in. by 8 in. The computed compressive strength,  $f'_c$ , stems from averaging the outcomes of three specimens from each batch. As per the relevant ASTM standards, any anomalous data were expunged from the results. The summarized compressive strength values for the girders are detailed in Table 5.2. A visual representation of a sample compressive strength test is depicted in Figure 5.7.



**Figure 5.7. Sample compressive strength test on a cylinder.**

**Table 5.2. 28-day concrete compressive strength of casted girders.**

<b>Girder</b>	<b>Batch</b>	<b>Avg. Comp. Strength (ksi)</b>
G1*	E	8.99
	F	9.29
	G	9.21
G1	H	8.92
	I	9.07
	J	7.92
G2	K	7.44
	L	8.43
G3	B	8.97
	C	8.51
	D	8.62
G4	M	9.42
	N	9.48
	O	8.05
G5	P	8.07
	Q	8.76
	R	8.98
G6	S	7.93
	T	9.08
	U	8.71
	V	9.4
G7	AA	8.29
	AB	8.11
	AC	8.29
G8	BA	10.17
	BB	9.39
	BC	9.34
G9	CA	8.72
	CB	9.65
	CC	7.94
G10	DA	9.23
	DB	9.11
	DC	9.36
	DD	9.65

In addition to the compressive strength tests at 28 days, MOE tests, STS tests, and MOR tests were carried out following the guidelines specified by ASTM-C469 (2014), ASTM-C496 (2007), and ASTM-C78 (2018), respectively. The comprehensive results for the MOE, STS, and MOR

obtained for the batch corresponding to the web location of the girder are summarized in Table 5.3. The reference photos for each test are also shown in Figure 5.8.

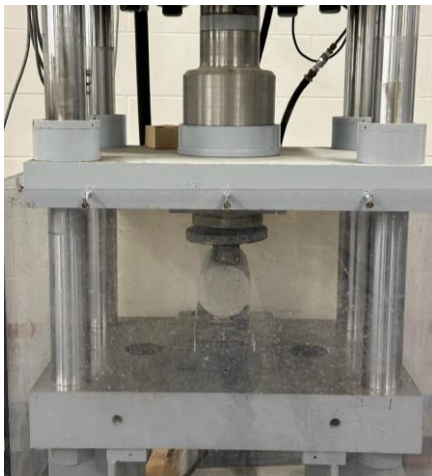
**Table 5.3. 28-day MOE, STS, and MOR results of casted girders.**

<b>Girder</b>	<b>Avg. MOE (ksi)</b>	<b>Avg. STS (ksi)</b>	<b>Avg. MOR (ksi)</b>
G1*	4710	1.02	0.7
G1	4722	0.91	0.72
G2	4675	1.07	*
G3	4573	0.99	0.7
G4	5552	1.04	*
G5	4395	1.11	*
G6	5145	1.09	0.72
G7	4731	0.77	0.57
G8	4323	0.91	0.59
G9	*	0.92	0.47
G10	*	0.83	0.48

\* Indicates no test results for this set.



(a) MOE



(b) STS



(c) MOR

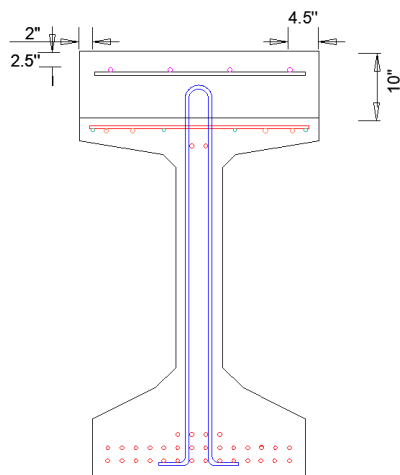
**Figure 5.8. Sample tests for (a) MOE, (b) STS, and (c) MOR.**

#### **5.4 CASTING OF THE DECK FOR GIRDER G1\***

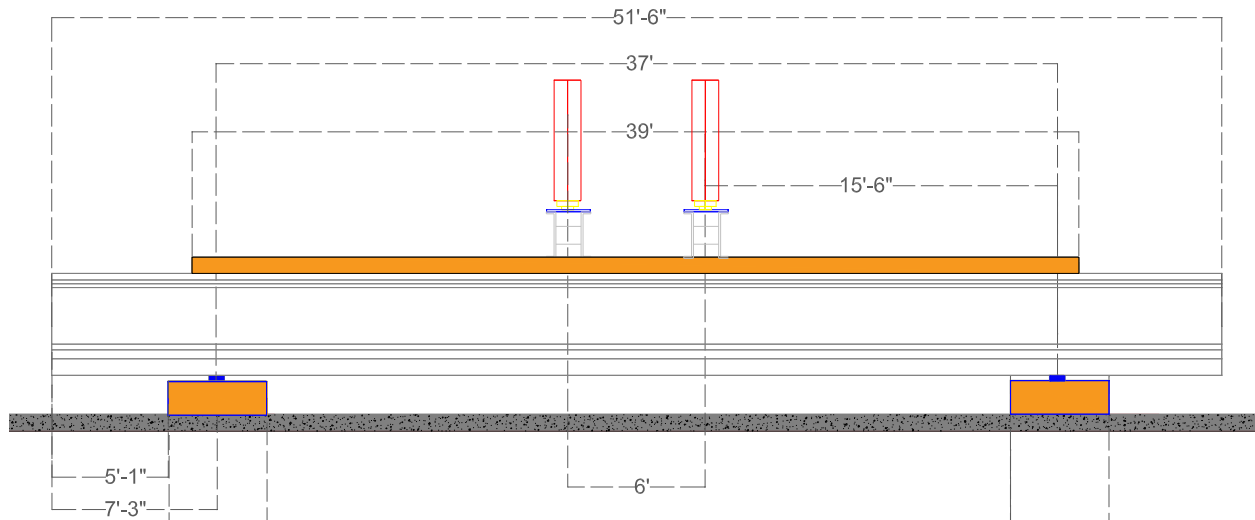
Based on the design of the deck discussed in Section 1.4.2, the first girder, G1\*, included a deck without an overhang on either side. The equivalent slab design has the width of the top flange, and the depth of the slab is 8.5 in. Further, to include the use of bedding strips as done in typical TxDOT bridge construction, a bedding strip of 1.5 in. was added on both sides of the top girder flange along the entire length of the deck. The cross section of the girder along with the deck can be seen in Figure 5.9. In addition, the reinforcement detailing of the deck was formed in accordance with the TxDOT bridge design specifications (TxDOT 2023).

In addition to adjusting the width of the deck, the length of the deck along the girder was specifically reduced to cover only the designated testing zone. This zone encompasses the distance between the girder supports, and the deck was designed to span this entire area, extending an additional foot beyond each support for comprehensive coverage. This modification is based on the specific role the deck plays in the testing process. The portions of the deck on the overhangs of the girder were not involved in the testing and therefore have been omitted. The layout plan for the deck on the girder is illustrated in Figure 5.10.

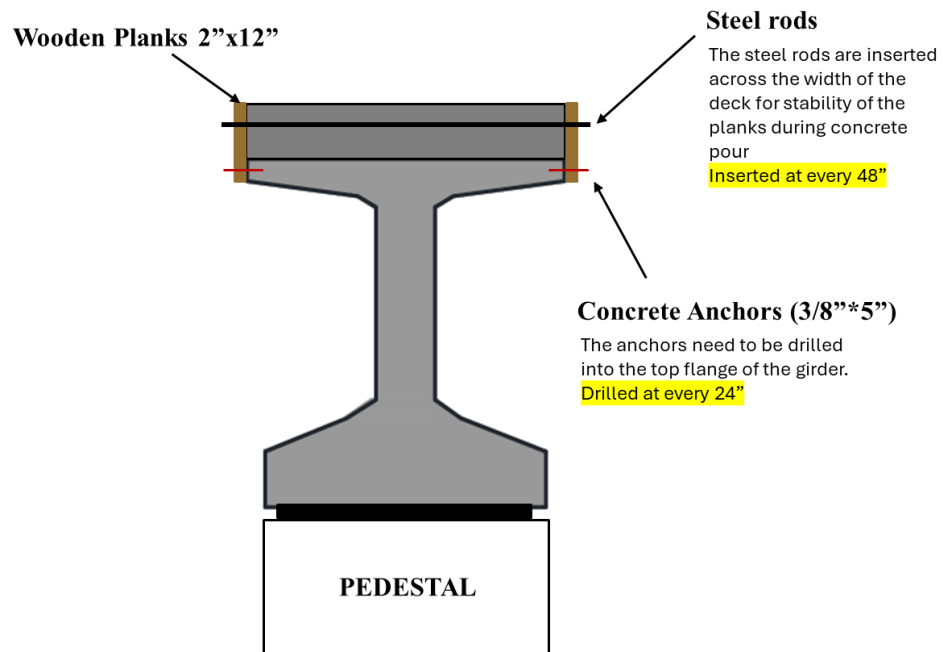
The next phase of the experimental program entailed casting the deck directly onto the girder. This process took place in the high bay lab at the Center for Infrastructure Renewal using concrete specified to meet the required strength, as outlined in Section 4.4.2. Prior to casting, the formwork and reinforcement cage were constructed on top of the girder. The formwork was specifically designed to attach securely to the top flange of the girder using concrete anchors, and it was supported from above with lateral steel threaded rods to prevent outward displacement under the weight of the concrete. Detailed plans for the formwork setup are depicted in Figure 5.11 and Figure 5.12.



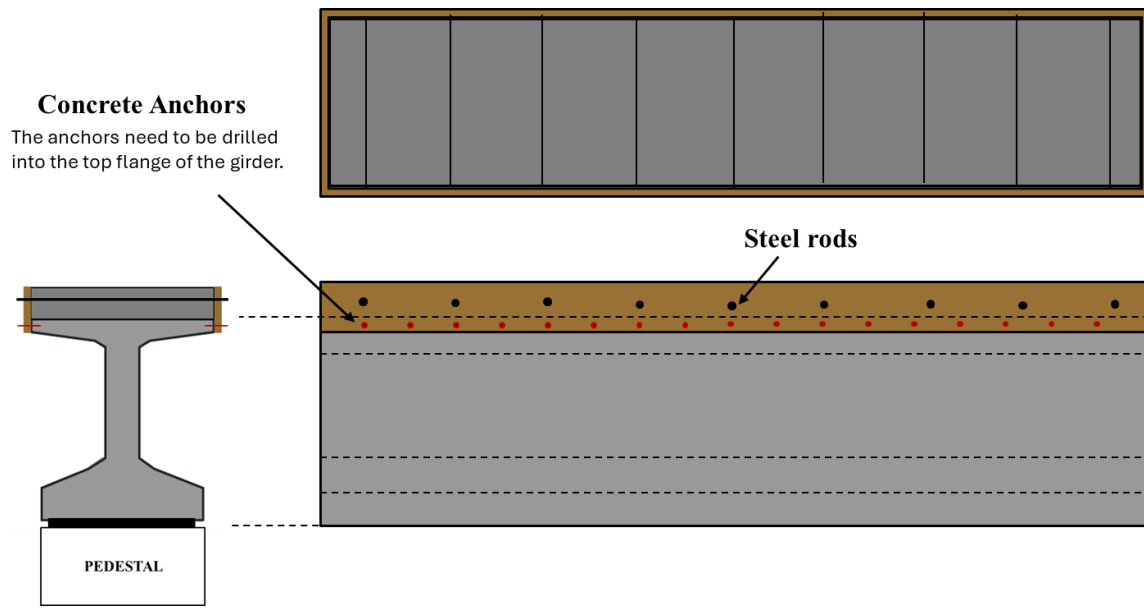
**Figure 5.9. Cross section of Girder G1\* with the deck.**



**Figure 5.10. Elevation view of Girder G1\* showing extent of deck.**

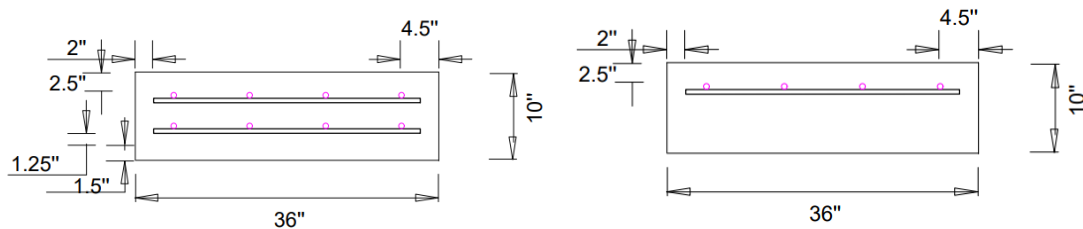


**Figure 5.11. Cross-section view of deck formwork.**

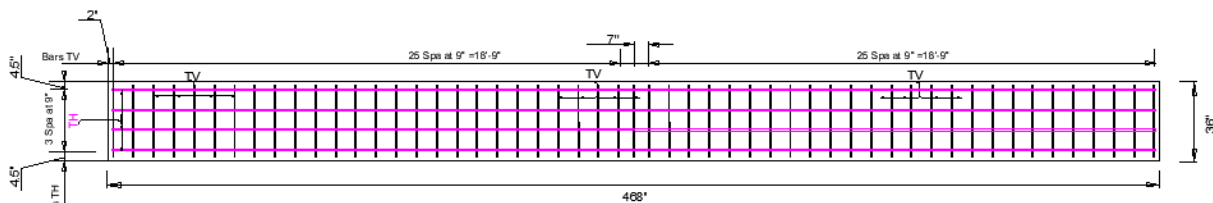


**Figure 5.12. Plan and elevation views for deck formwork.**

The steel reinforcement cage was constructed using No. 4 bars, with the specific detailing provided in Appendix B. The cage was positioned at the correct height using rebar chairs. After consultations with the TxDOT team, it was decided that only a single layer of reinforcement would be used in the deck, rather than two layers with the single layer closer to the tension side. Details of the reinforcement layer are illustrated in Figure 5.13. In addition, the final plan for reinforcement of the deck is shown in Figure 5.14.



**Figure 5.13. Reinforcement detailing in the deck depicting layers.**



**Figure 5.14. Reinforcement detailing plan in the deck.**

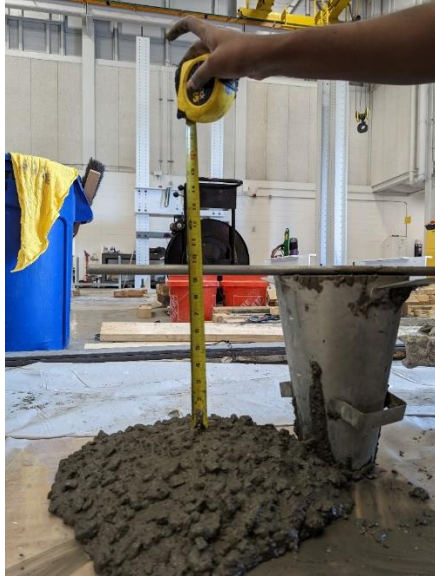
Based on all the detailing, the formwork along with the reinforcement layer was placed above the top flange of the girder. The strain gauge wires from R-bars were held at a higher point using a vertical steel rod and covered with airtight bags to ensure the access and protection of the gauge wires. The final formwork can be seen in Figure 5.15.



**Figure 5.15. Constructed formwork and reinforcement cage for the deck.**

After the reinforcement setup, the next step involved casting the concrete for the deck. The concrete specified for this purpose required a design strength of 10.5 ksi. The concrete ordered was ready-mixed and complied with ASTM C94 specifications. Before pouring, the concrete slump was tested to ensure it was within the appropriate range for optimal placement conditions. The concrete was then poured into the formwork, vibrated to ensure the flow of concrete evenly into the formwork, and carefully screeded to achieve a smooth surface. Additionally, concrete samples were collected to test mechanical properties such as strength, MOE, MOR, and STS, as outlined in Section 5.3, to ensure consistency with the properties tested in the girder. Figure 5.16 depicts the slump test, casting of the deck, final finished deck surface, and the samples collected.





(a) Slump test



(b) Screeding of concrete surface



(c) Finished deck



(d) Cylinders in the curing room

**Figure 5.16. Casting of the deck.**

The deck was subjected to a curing process to maintain its moisture and hydration levels, during which it was covered with a plastic tarp. Curing is essential for concrete decks because it ensures optimal strength and durability by maintaining moisture necessary for the hydration process, which is critical for hardening and strengthening the concrete. This process also controls temperature to prevent improper hydration speeds, thus reducing the risk of surface cracking due to rapid moisture loss. The formwork was removed after 7 days to ensure that the deck had achieved sufficient strength. Additionally, the concrete samples taken from the deck were tested

on the 28th day to assess their mechanical properties. The results of these tests are presented in Table 5.4.

**Table 5.4. 28-day concrete material testing results for deck.**

<b>Sample</b>	<b>Compressive strength (ksi)</b>	<b>MOE (ksi)</b>	<b>MOR (ksi)</b>	<b>STS (ksi)</b>
<b>G1*-Deck-28 day</b>	13.40	7391	1.13	1.28
	13.22	7321	1.31	1.29
	12.97	7394	1.19	1.40
<b>Average (ksi)</b>	13.20	7368	1.21	1.32

## 5.5 SUMMARY

This chapter discusses the construction of the test specimens along with the cast-in-place deck slab. The preparation of R-bars for strain gauges and verification of reinforcement placement was conducted before the casting of girders. The chapter also includes a description of the construction of formwork and reinforcement for the deck cast on top of the girder. In addition, concrete samples were cast for material properties that were tested on the 28th day and the day of test. The chapter summarizes the material properties—including compressive strength, MOE, MOR, and STS—for all the batches of concrete that were cast.

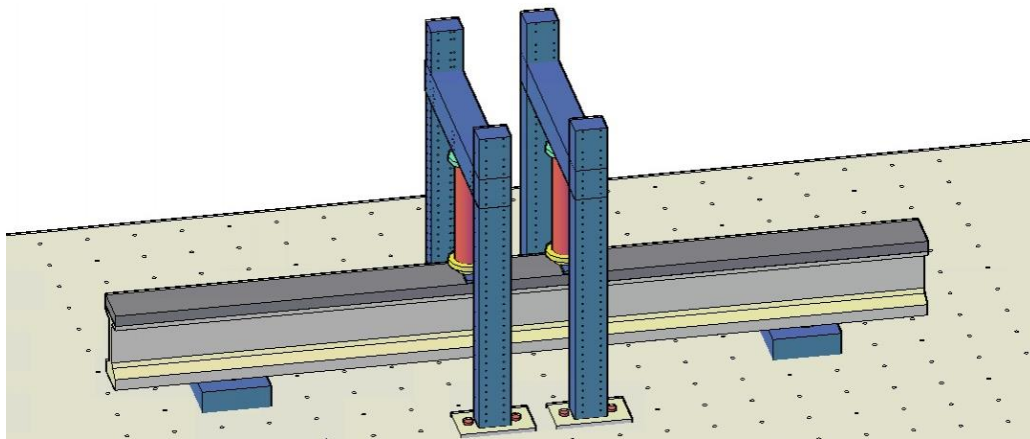
## **CHAPTER 6:**

### **FULL-SCALE TESTING: EXPERIMENTAL TESTING OF GIRDERS**

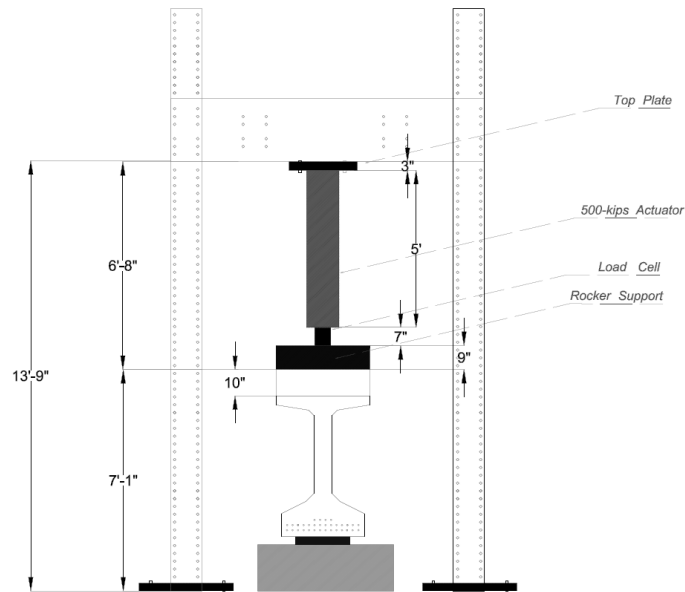
The core part of the experimental program included the extensive large-scale testing of the girders. The test setup encompassed various aspects, including the loading configuration, the load protocol, and the intricate aspects of instrumentation and data acquisition. The large-scale testing also involved detailed instrumentation plans to capture vital data that can later help in the effective comparison and parametric study. This chapter details the complete experimental setup used to test each girder.

#### **6.1 TEST SETUP**

Implementation of the test setup for each girder specimen was initiated by positioning the specimen and the loading frames on the strong floor of the high bay structural testing lab. The girder specimen and the actuators were positioned in accordance with the selected shear-span-to-depth ratio. The loading setup included use of two pressure-driven 600-kip actuators that were used to load the girders close to a point of failure. The actuators were positioned such that a four-point bending configuration was achieved with the specimens G#-L and G#-R in the span between the actuator and pedestal on each side. The three-dimensional model of the test setup is shown in Figure 6.1. The end/side elevation view of the actuator on the frame is also shown in Figure 6.2.



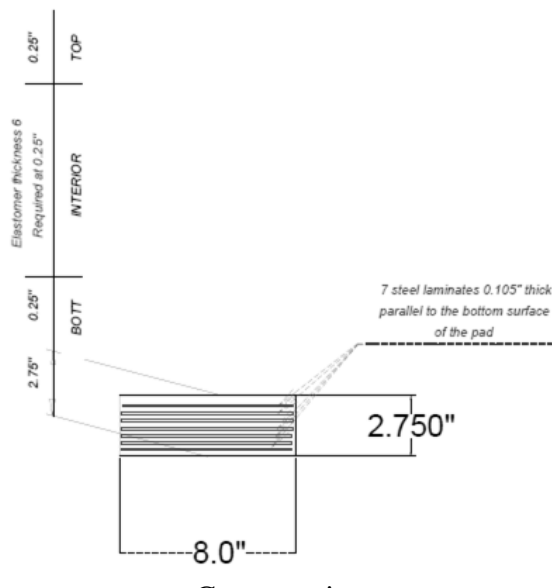
**Figure 6.1. Test setup of a typical girder specimen.**



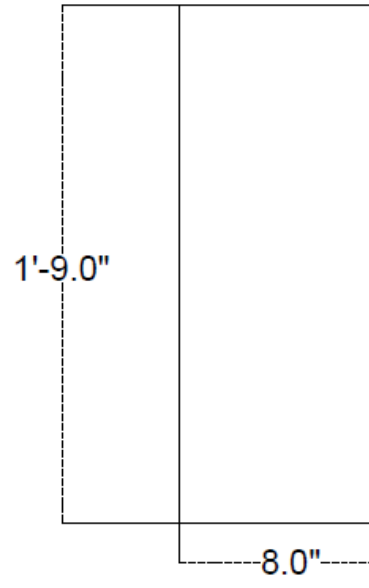
**Figure 6.2. End elevation of actuator position with respect to a girder specimen.**

The two actuators were positioned 6 ft apart and in symmetry with respect to the midspan. Each actuator was aligned with the centerline of the girder section. The support locations were chosen relative to the actuator positioning, which collectively yields the targeted  $a/d_v$  ratio as per the planned specifications for each individual test. The shear span, which is the region of interest, lies between the actuator and the corresponding support. These regions correspond to the zones where variations in shear reinforcement were introduced. The girders were supported on concrete pedestals, positioned on the strong floor of the lab. On top of each pedestal, a standard steel bearing pad was carefully positioned, forming the foundational surface upon which the girder was mounted (see Figure 6.3).

Figure 6.4 shows the girder setup on the pedestal and bearing pad and the girder specimen with the actuator frames in the lab in accordance with the testing plan.



Cross section



Plan dimensions

**Figure 6.3. Drawings of standard bearing pad used at each support pedestal.**



Girder positioned on pedestal and bearing pad



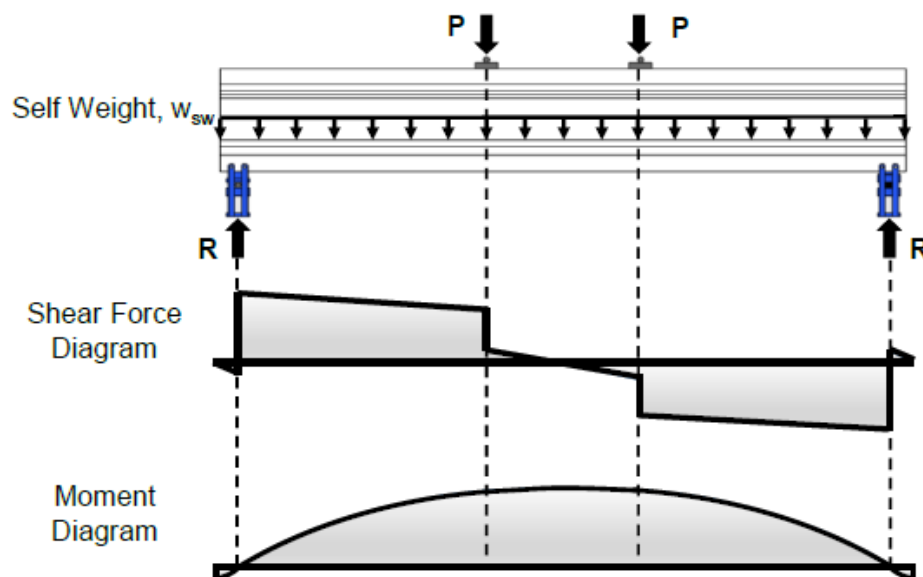
Loading frame and positioned girder before instrumentation

**Figure 6.4. Girder test setup in the lab.**



## 6.2 LOADING PROTOCOL

The test setup is a four-point bending system with the girder simply supported on the pedestals. The application of two-point loads placed symmetrically with respect to the midspan ensures an almost constant shear in the regions of interest along with low shear force in the center portion of the girder span. This configuration also ensures the maximum moment occurs at the midspan region of the girder, while the girders were designed to fail in shear before showing any cracks or distress in flexure. A similar loading setup was also used in prestressed concrete girder testing by Katz (2016), and the relevant shear force diagram and bending moment diagram are shown in Figure 6.5.



**Figure 6.5. Shear force and bending moment diagrams for 4-point bending system (from Katz (2016)).**

Nevertheless, due to the presence of two distinct regions of interest within each girder, each characterized by differing shear reinforcement patterns, the estimated nominal capacity (AASHTO 2020) on either side varies. To account for this difference, the loading protocol was devised to effectively mitigate the impact of varying shear reinforcement by introducing a differential loading strategy for the two girder ends. As a result of this approach, the required loads in the actuators, aiming to reach nearly simultaneous shear failure of both ends of the girder, were computed. These computed loads subsequently informed the determination of the incremental actuator load steps across the course of the experimental timeline.

The loading protocol for each test was developed beforehand to carefully identify the formation of cracks. The protocol also includes various estimated values like the service limit and strength limit used in the design, cracking shear force by AASHTO, nominal shear capacity by AASHTO, a factored value (such as 1.25 times the nominal shear capacity), and the estimated ultimate shear force from the ABAQUS model. A sample loading protocol is shown in Table 6.1. Each step is associated with a halt of about 5 minutes to visually assess the girder, mark cracks, and document the girder condition with images.

**Table 6.1. Sample loading protocol developed for the girder test.**

<b>Step no.</b>	<b>Shear force West (kips)</b>	<b>Shear force East (kips)</b>	<b>Actuator load West (kips)</b>	<b>Actuator load East (kips)</b>	<b>Comment</b>
1	183	183	175	175	Service Limit
2	198	198	190	190	$V_c$ from AASHTO
3	228	228	220	220	Strength Limit
4	253	253	245	245	
5	285	276	300	245	
6	325	316	340	285	$V_n$ from AASHTO
7	357	345	380	305	
8	383	369	410	325	
9	408	394	435	350	1.25* $V_n$ AASHTO
10	424	408	455	360	Failure (ABAQUS)
11	443	428	475	380	
12	463	448	495	400	
13	<i>Unload to 0 kips</i>				

### 6.3 INSTRUMENTATION AND DATA ACQUISITION

The experimental tests need to be instrumented with potential sensors and data acquisition that can further be studied for making key effective comparisons. These data can also be utilized for the validation of the FE analysis and to further develop different cases of loading for the FE model. The experimental data assume a pivotal role in the subsequent phase of data analysis, offering a foundational platform for the validation of the FE models that have been

conceptualized and calibrated. These models have their ultimate need in a variety of contexts, each contributing to the objective of formulating comprehensive design guidelines in alignment with the intended project objectives.

The instrumentation included embedded strain gauges for R-bars, concrete surface strain gauges, linear variable differential transformers (LVDTs), string potentiometers (string pots) and digital image correlation (DIC) systems, and Optotrak motion capture systems. Furthermore, the actuators were outfitted with pressure sensors to monitor the hydraulic oil pressure, while load cells were integrated to precisely quantify the load applied by each actuator. The detailed instrumentation plan with drawings is included in Appendix C.

### **6.3.1 Embedded Rebar Strain Gauges**

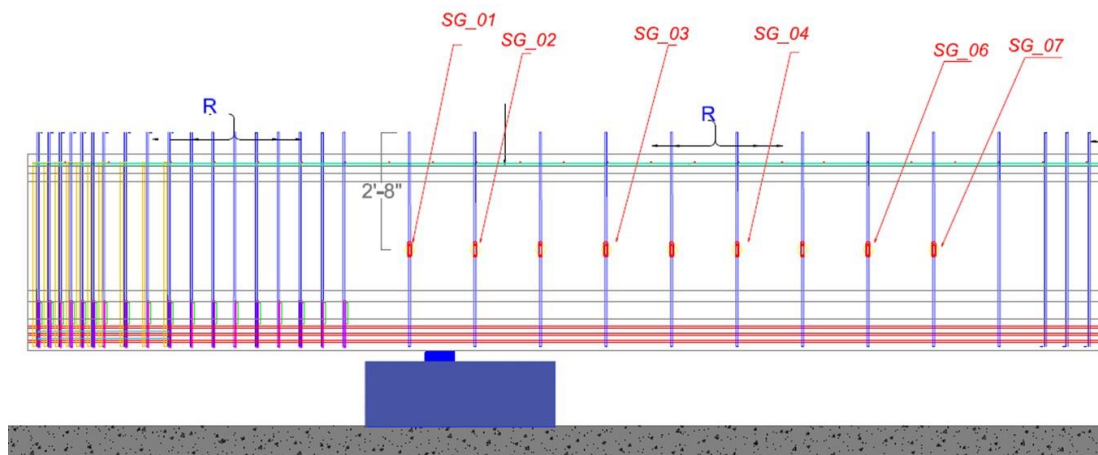
Embedded strain gauges were installed on the stirrups to monitor the strain in the shear reinforcement as the loading increases. Since the research is more focused on the impact of the shear reinforcement, the strain gauges were attached to the R-bars only in the testing region. One strain gauge was attached to one of the legs of the R-bars that are in the region where the  $s/d$  is varied. The R-bars were collected from the precast plant before casting the girders, and then the strain gauges were attached. Later, when the concrete was cast for the girder specimen, the strain gauges were embedded in the concrete section. Figure 6.6 shows instrumented strain gauges on the stirrups.

The plan for embedded strain gauges for one side of the girder is shown in Figure 6.7. The strain gauges were only in the region where the shear was being monitored. Each girder contained 8–12 strain gauges on each half of the length because there were two testing regions. These strain gauges were used for monitoring the strain in the transverse reinforcement. Table 6.2 shows the list of the strain gauges and the type of strain gauges used.





**Figure 6.6. Strain gauges attached to R-bars.**



**Figure 6.7. Embedded strain gauge layout for half of a girder specimen.**

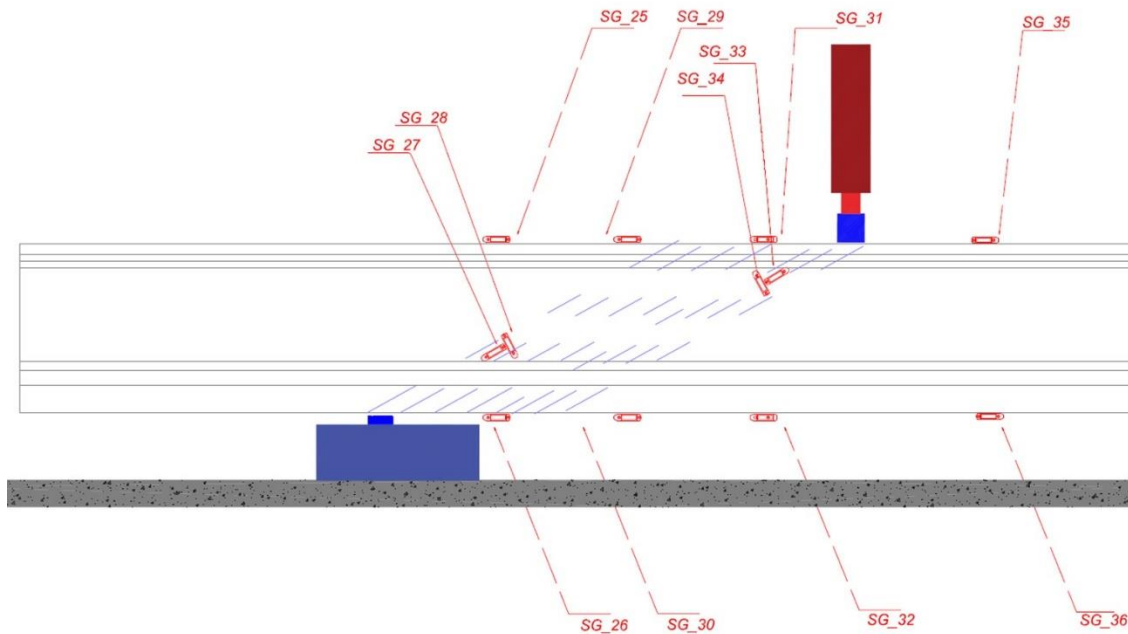
**Table 6.2. Summary of embedded strain gauges.**

<b>Location</b>	<b>Module</b>	<b>Type</b>	<b>Purpose</b>
E	6_0	FLAB-5-350-11-5LJCT-F	Strains in transverse reinforcement
E	6_1	FLAB-5-350-11-5LJCT-F	Strains in transverse reinforcement
E	6_2	FLAB-5-350-11-5LJCT-F	Strains in transverse reinforcement
E	6_3	FLAB-5-350-11-5LJCT-F	Strains in transverse reinforcement
E	6_4	FLAB-5-350-11-5LJCT-F	Strains in transverse reinforcement
E	6_5	FLAB-5-350-11-5LJCT-F	Strains in transverse reinforcement
E	6_6	FLAB-5-350-11-5LJCT-F	Strains in transverse reinforcement
E	6_7	FLAB-5-350-11-5LJCT-F	Strains in transverse reinforcement
E	7_0	FLAB-5-350-11-5LJCT-F	Strains in transverse reinforcement
E	7_1	FLAB-5-350-11-5LJCT-F	Strains in transverse reinforcement
W	7_2	FLAB-5-350-11-5LJCT-F	Strains in transverse reinforcement
W	7_3	FLAB-5-350-11-5LJCT-F	Strains in transverse reinforcement
W	7_4	FLAB-5-350-11-5LJCT-F	Strains in transverse reinforcement
W	7_5	FLAB-5-350-11-5LJCT-F	Strains in transverse reinforcement
W	7_6	FLAB-5-350-11-5LJCT-F	Strains in transverse reinforcement

### 6.3.2 Concrete Surface Strain Gauges

The next set of strain gauges are the surface strain gauges that were installed on the concrete girder surface. These gauges were used to obtain the strain profile at the critical section of the girder during various loading steps. The surface strain gauges have a longer gauge length than the embedded rebar strain gauges. Figure 6.8 shows the plan for the locations of surface strain gauges for half of the girder length, and it was the same for the other side as well.

The concrete surface strain gauges are intended to monitor the strain in the extreme top fiber and the extreme bottom fiber of the girder cross section. Additional gauges were installed on the web, thereby allowing determination of a strain profile from the extreme top to extreme bottom of the girder cross section. Table 6.3 shows a summary of the surface strain gauges planned for each girder test.



**Figure 6.8. Concrete surface strain gauge layout for half of a girder specimen.**

**Table 6.3. Summary of concrete surface strain gauges.**

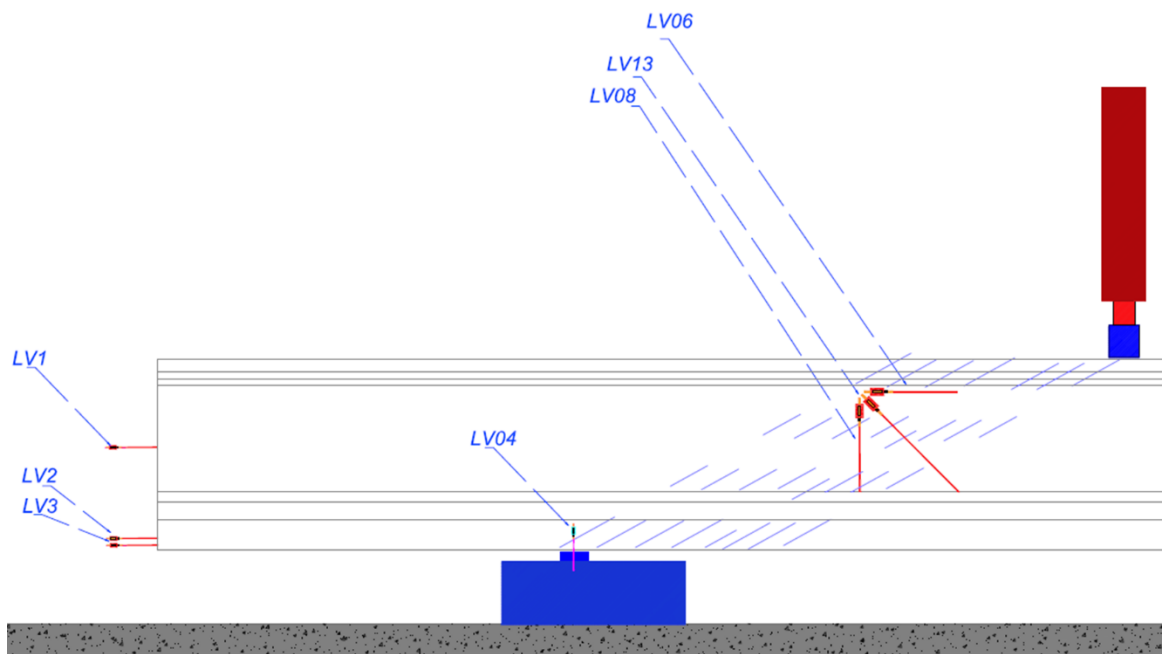
Location	Type	Purpose
Top_E	PL-60-11-5LJCT-00	Strain in extreme top fiber
Bottom_E	PL-60-11-5LJCT-00	Strain in extreme bottom fiber
Top_E	PL-60-11-5LJCT-00	Strain in extreme top fiber
Bottom_E	PL-60-11-5LJCT-00	Strain in extreme bottom fiber
Top_E	PL-60-11-5LJCT-00	Strain in extreme top fiber
Bottom_E	PL-60-11-5LJCT-00	Strain in extreme bottom fiber
Top_E	PL-60-11-5LJCT-00	Strain in extreme top fiber
Bottom_E	PL-60-11-5LJCT-00	Strain in extreme bottom fiber
Top_W	PL-60-11-5LJCT-00	Strain in extreme top fiber
Bottom_W	PL-60-11-5LJCT-00	Strain in extreme bottom fiber
Top_W	PL-60-11-5LJCT-00	Strain in extreme top fiber
Bottom_W	PL-60-11-5LJCT-00	Strain in extreme bottom fiber
Top_W	PL-60-11-5LJCT-00	Strain in extreme top fiber
Bottom_W	PL-60-11-5LJCT-00	Strain in extreme bottom fiber
SW	PL-60-11-5LJCT-00	Strain in web
SW	PL-60-11-5LJCT-00	Strain in web
SW	PL-60-11-5LJCT-00	Strain in web
SW	PL-60-11-5LJCT-00	Strain in web
SE	PL-60-11-5LJCT-00	Strain in web
SE	PL-60-11-5LJCT-00	Strain in web
SE	PL-60-11-5LJCT-00	Strain in web
SE	PL-60-11-5LJCT-00	Strain in web

### 6.3.3 Linear Variable Differential Transformers

LVDTs are used to measure relative displacement between the two points to which it is attached. They can also be used to measure average strain as it covers a larger dimension. In this project, LVDTs were used for various purposes, including monitoring displacement, strand slip, and relative displacement between surfaces. The plan for attaching the LVDTs for half of the girder length is shown in Figure 6.9.

The LVDTs give out the output as a displacement that changes at all the installed locations as the loading increases. In total, 20 LVDTs were installed, of which two of them were at either end of the girder monitoring the horizontal movement of the girder as the test proceeded. There were a set of three LVDTs on each end of the girder monitoring one strand in each row (three rows in total) to identify the strand slippage during the test. There was a set of four LVDTs to monitor the horizontal, vertical, and diagonal tensile and shear displacement, and they were installed on the web face of the girder. Finally, there were four LVDTs monitoring the relative displacement between the top flange and the deck to obtain information regarding the interface shear.

Table 6.4 summarizes all the LVDTs that were installed and their individual purposes.



**Figure 6.9. LVDT layout for half of a girder specimen.**

**Table 6.4. Summary of LVDTs.**

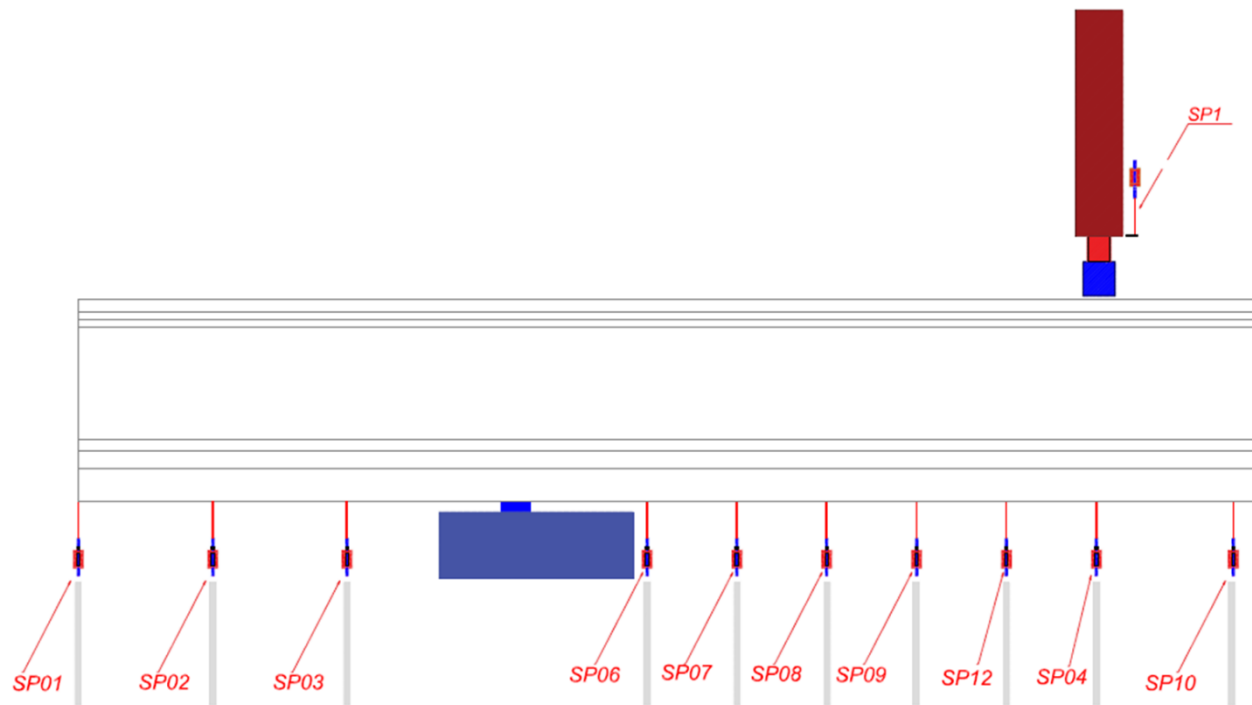
<b>Location</b>	<b>Type</b>	<b>Purpose</b>
SE	LVDT	Horizontal movement of the girder
SE	LVDT	Strand slip
SE	LVDT	Strand slip
SE	LVDT	Strand slip
SE	LVDT	Horizontal tensile and shear displacement in web
SE	LVDT	diagonal tensile and shear displacement in web
SE	LVDT	Vertical tensile and shear displacement in web
SE	LVDT	diagonal tensile and shear displacement in web
SW	LVDT	Horizontal movement of the girder
SW	LVDT	Strand slip
SW	LVDT	Strand slip
SW	LVDT	Strand slip
SW	LVDT	Horizontal tensile and shear displacement in web
SW	LVDT	diagonal tensile and shear displacement in web
SW	LVDT	Vertical tensile and shear displacement in web
SE	LVDT	diagonal tensile and shear displacement in web
SE	LVDT	Interface slip between deck slab and girder
SE	LVDT	Interface slip between deck slab and girder
SW	LVDT	Interface slip between deck slab and girder
SW	LVDT	Interface slip between deck slab and girder

#### 6.3.4 String Potentiometers

String potentiometers are another type of sensor that also measure displacement. Unlike LVDTs, these measurements are taken from a constant origin or a fixed surface where the string is attached to a moving surface. The string pots were attached along the length of the girder to the bottom face, and the measurement was done relative to the strong floor of the slab. This created a deformation profile along the length of the girder during testing. The plan of positions of the string pots along the length of the girder is shown in Figure 6.10 for half of the girder.

The string pots attached along the length of the girder included one at the extreme end to monitor the vertical movement of the end. Since there was an initial camber in the girder as it was prestressed, the displacement computed should be calibrated carefully based on the initial positions. Two string pots were also attached to the actuator to monitor the displacement of the actuator during the experiment.

Table 6.5 shows a summary of the string pots used in the test setup.



**Figure 6.10. Plan for string potentiometers for one of the girders.**

**Table 6.5. Summary of string potentiometers.**

<b>Location</b>	<b>Type</b>	<b>Purpose</b>
MID	String Potentiometers (stroke: 50 in.)	Actuator Displacement
MID	String Potentiometers (stroke: 50 in.)	Actuator Displacement
E	String Potentiometers (stroke: 4 in.)	Displacement of bottom girder face relative to strong floor
E	String Potentiometers (stroke: 4 in.)	Displacement of bottom girder face relative to strong floor
E	String Potentiometers (stroke: 4 in.)	Displacement of bottom girder face relative to strong floor
E	String Potentiometers (stroke: 4 in.)	Displacement of bottom girder face relative to strong floor
E	String Potentiometers (stroke: 4 in.)	Displacement of bottom girder face relative to strong floor
E	String Potentiometers (stroke: 4 in.)	Displacement of bottom girder face relative to strong floor
E	String Potentiometers (stroke: 4 in.)	Displacement of bottom girder face relative to strong floor
E	String Potentiometers (stroke: 4 in.)	Displacement of bottom girder face relative to strong floor
E	String Potentiometers (stroke: 4 in.)	Displacement of bottom girder face relative to strong floor
MID	String Potentiometers (stroke: 4 in.)	Displacement of bottom girder face relative to strong floor
W	String Potentiometers (stroke: 4 in.)	Displacement of bottom girder face relative to strong floor
W	String Potentiometers (stroke: 4 in.)	Displacement of bottom girder face relative to strong floor
W	String Potentiometers (stroke: 4 in.)	Displacement of bottom girder face relative to strong floor
W	String Potentiometers (stroke: 4 in.)	Displacement of bottom girder face relative to strong floor
W	String Potentiometers (stroke: 4 in.)	Displacement of bottom girder face relative to strong floor
W	String Potentiometers (stroke: 4 in.)	Displacement of bottom girder face relative to strong floor
W	String Potentiometers (stroke: 4 in.)	Displacement of bottom girder face relative to strong floor
W	String Potentiometers (stroke: 4 in.)	Displacement of bottom girder face relative to strong floor
W	String Potentiometers (stroke: 4 in.)	Displacement of bottom girder face relative to strong floor

### 6.3.5 Data Acquisition for Sensor Arrays

The DAQ for the sensor arrays, along with the actuator control, is connected to a standard National Instruments DAQ (Figure 6.11) with all channels calibrated according to the sensor. The strain gauges in each test were shunt calibrated before the test for correct results. The string pots and LVDTs were also calibrated using the standard procedure listed in their respective manuals. The main DAQ system captured test data at a frequency of 1 Hz, commencing from the initiation of the test and encompassing the entire duration until ultimate failure, including the subsequent unloading phase.



**Figure 6.11. DAQ system for sensor arrays.**

### 6.3.6 Digital Image Correlation

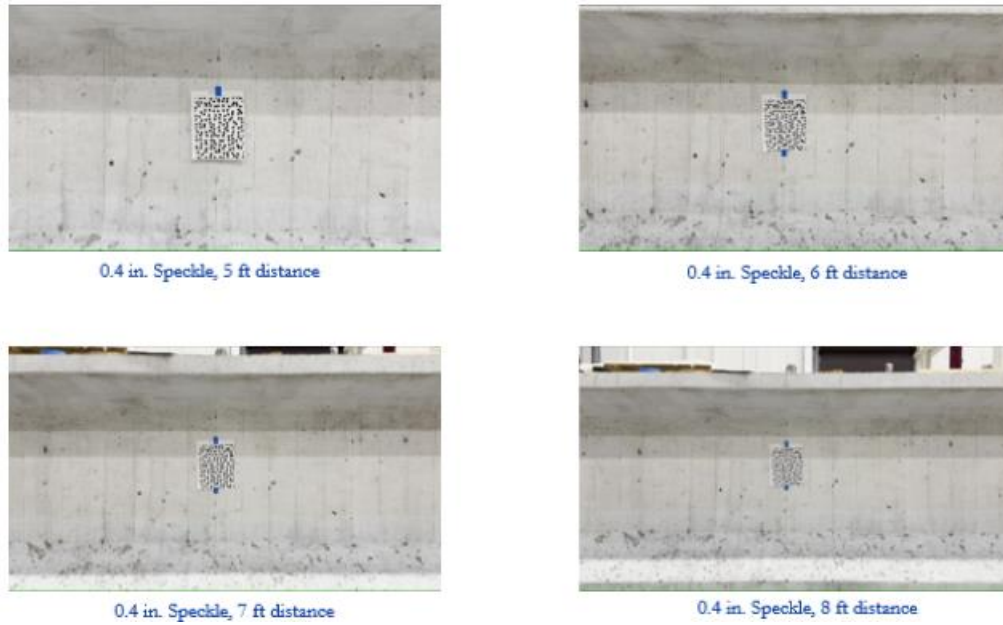
The DIC is an optical method used to monitor the experiment. DIC and target tracking systems have been used in several research projects to monitor surface strains and identify cracks. The study by Chehab et al. (2018) on shear testing for AASHTO Type II girders used a target tracking system to measure (average) concrete strains at peak load. The DIC method used 60 frames per second (fps) cameras to record video of the face of the girder pointed at, and later, when processed, each frame or every alternate frame was taken and processed to identify propagation of cracks. The DIC uses Sony Handycam CX405 type cameras to record the web of



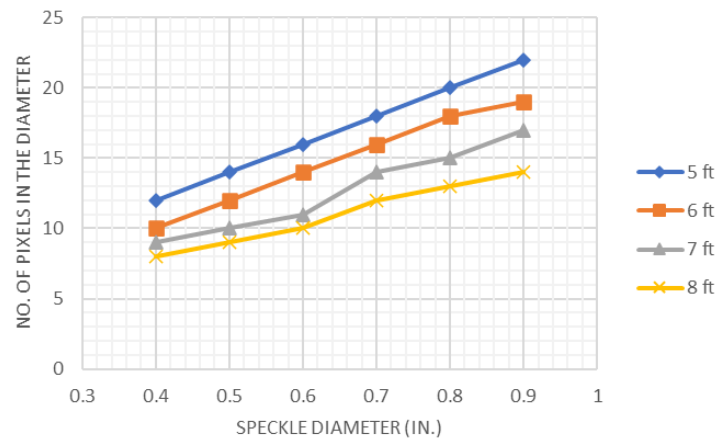
the girder during the entire test duration. A total of four cameras were used to record the shear span length of half of the girder. The DIC method is a technique that involves registering a series of images of a surface with a randomized speckle pattern. Further, the movement of the speckle map is used to calculate the deformation and later for strain and stress fields.

The next step in DIC is to select the appropriate speckle size and the distance of the cameras from the web surface. This step is accomplished through a concise parametric study grounded in the fundamental principles of DIC processing. Lecompte et al. (2007) and Yaofeng and Pang (2007) studied the quality assessment of speckle patterns for DIC and looked into an appropriate number of pixels in the diameter of each speckle for better quality results. The studies indicated that an optimal count of 8–10 pixels within the diameter of each speckle yields superior results. However, the position of the cameras and speckle size still needs to be identified. The parametric study involves generating a speckle pattern with speckle diameters varying between 0.4 in., 0.5 in., 0.6 in., 0.7 in., 0.8 in., and 0.9 in. and observation distance ranging from 5 ft to 8 ft. The random speckle pattern is generated using a software named Speckle Generator, and the sample testing is shown in Figure 6.12.

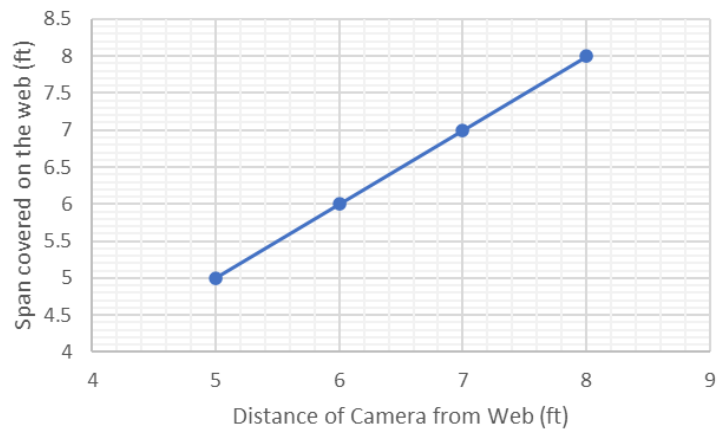
The speckle diameter, as well as the camera distance, collectively determine the number of pixels along the diameter. The coverage spans of each camera, in turn, hinges on the camera distance from the web surface. Given that the entirety of the span is comprehensively observed using multiple cameras, it becomes imperative for the view frames of neighboring cameras to overlap by approximately 30 percent at the extremities. This strategic overlap is essential to mitigate concerns related to blurred and smoothed image resolution encountered at the frame edges. The parametric comparison is shown in the plots in Figure 6.13 and Figure 6.14.



**Figure 6.12. Parametric study for DIC speckle pattern.**



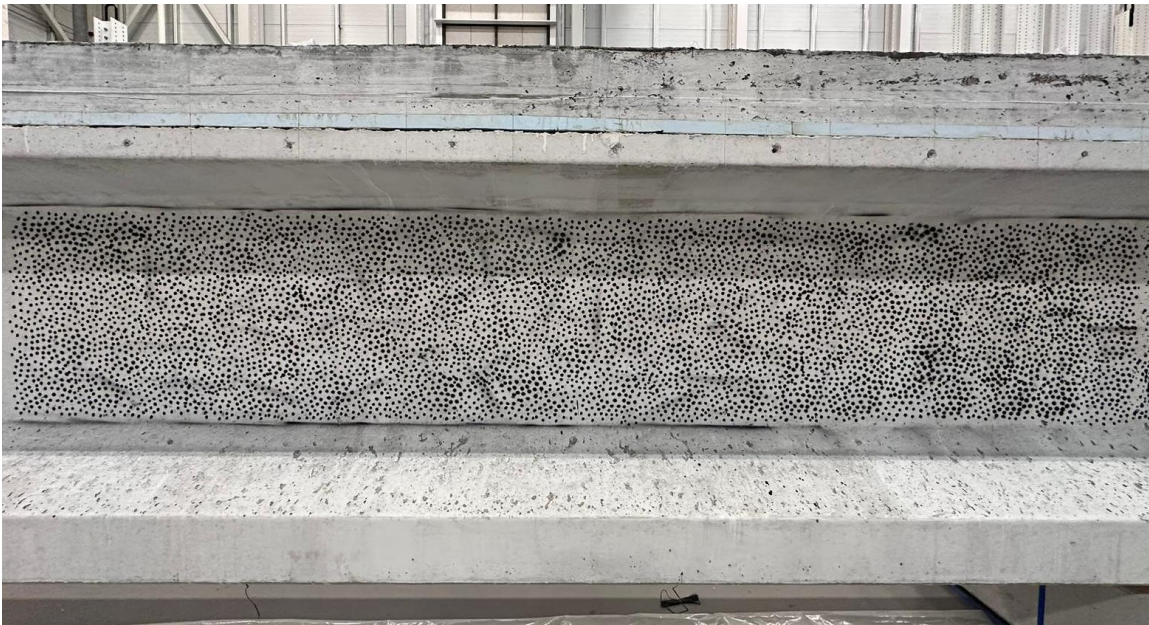
**Figure 6.13. Pixels versus speckle diameter for DIC.**



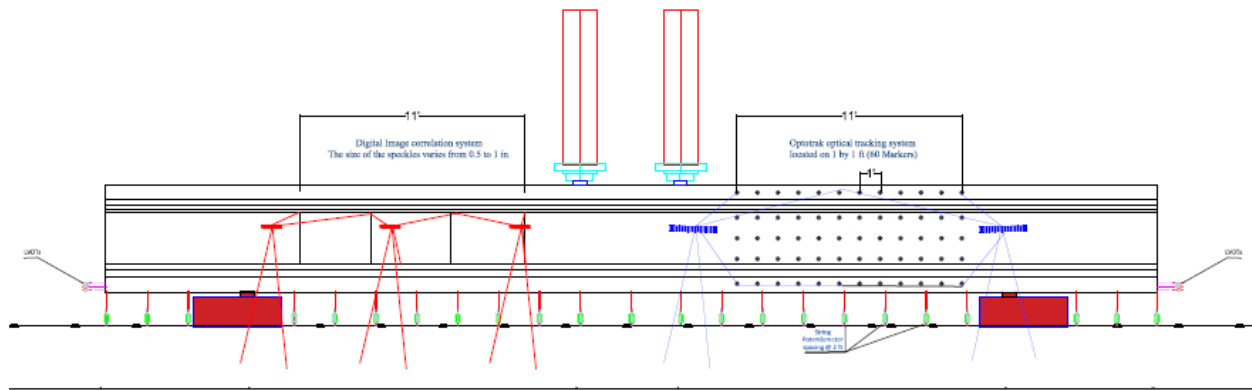
**Figure 6.14. Camera distance versus span covered for DIC.**

Consequently, the outcome materialized in a speckle diameter of 0.5 in., a configuration that aligns with cameras positioned at 6 ft from the web surface. This configuration yielded a total of 10–12 dark pixels within each individual speckle. Considering an individual camera’s coverage span of 6 ft, in conjunction with the requisite 30 percent overlap between adjacent cameras, a four-camera setup efficiently encompassed the entire span for one face of the girder. Operating at a resolution of 1080p and a frame rate of 60 frames per second, the cameras continuously recorded data that are subsequently fine-tuned for post-processing of outcomes. A visual representation of the developed speckle pattern for a girder is presented in Figure 6.15, while Figure 6.16 shows the plan of the DIC and Optotrak systems on the girder.

The DIC system and the Optotrak system were used to monitor the face of the girder in the region where shear reinforcement is varied. These data support identification of crack initiation and propagation, as well as girder deflection.



**Figure 6.15. Speckle pattern painted on the web surface.**



**Figure 6.16. Plan for the DIC and Optotrak systems.**

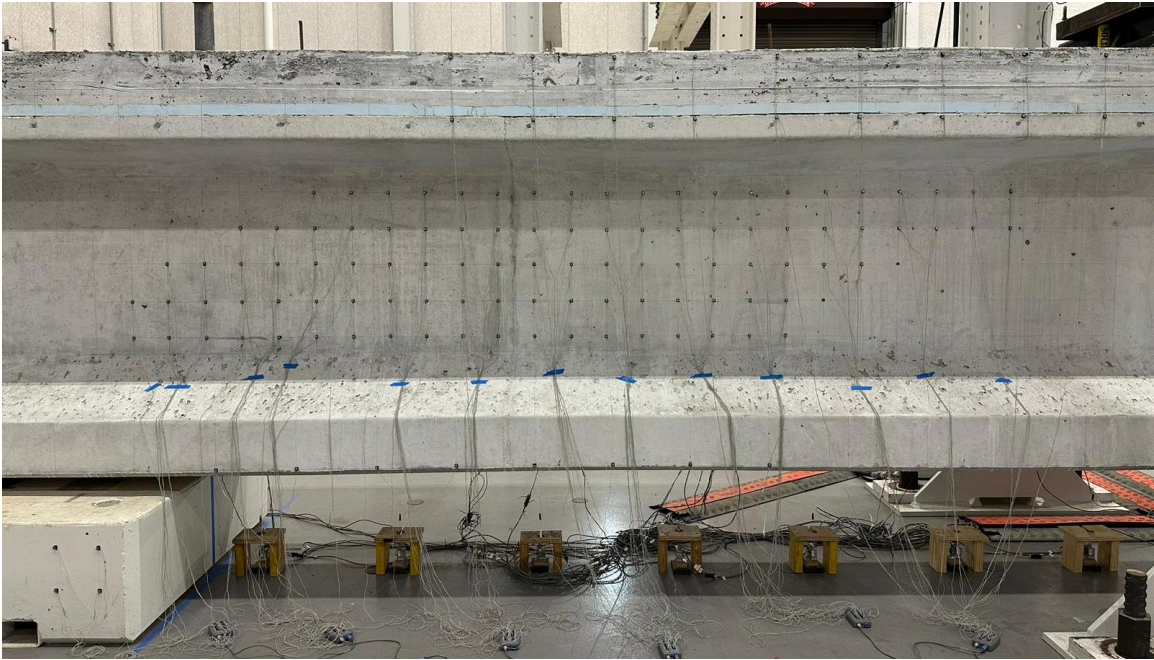
### 6.3.7 Optotrak Motion Capture System

Optotrak is an optical-based recording system developed by Northern Digital Inc. (NDI). The Optotrak system uses LED targets that are attached to the face of the girder specimen and monitors the locations of the targets. As the test progresses, the system measures the movement of these targets in real time, and displacements can be obtained when compared with a fixed position. The data from Optotrak are also used to build a strain profile of the girder face as it is configured in a grid pattern.

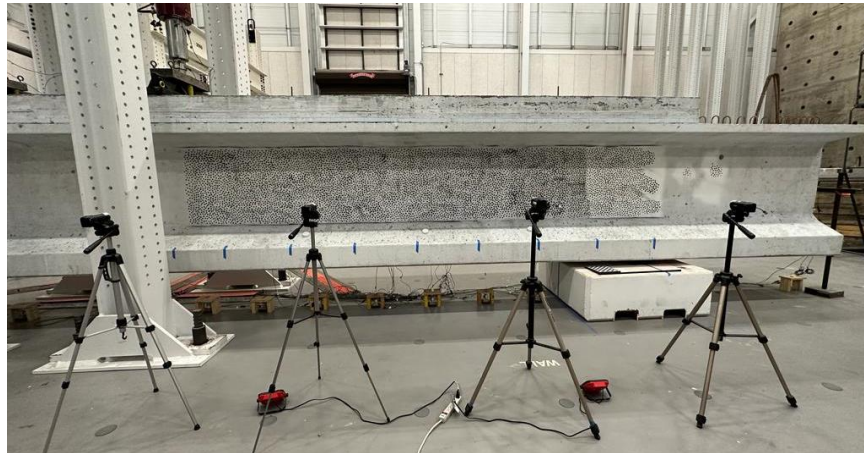
The Optotrak motion capture system constitutes another optical technique seamlessly integrated into the testing framework and specifically applied to the opposite half of the girder. This method employed wired LED targets affixed to the surface under observation. Through the deployment of two Optotrak Certus cameras, each aligned and calibrated, the real-time positions of the targets were recorded. As the test unfolded, the system continuously tracked the target positions, referencing the initial calibration and establishing a consistent coordinate system. The resultant output data encompassed X, Y, and Z coordinates in relation to the passage of time. In this context, data were recorded at 10 Hz, capitalizing on the capacity of the optical system for elevated frame rates. To formulate the target layout, the anticipated damage derived from the FE model was superimposed onto the actual girder. Subsequently, targets were positioned to envelop all foreseen cracks on the girder web surface. Additionally, some targets were placed on the pedestal that were used as a reference origin for analysis, and some targets were placed on the girder flanges to develop an overall strain profile. A sample target layout is shown in Figure 6.17.



The final setup of the DIC and Optotrak systems can be seen in Figure 6.18 and Figure 6.19. As the test progressed, all the instrumentation and visual systems recorded the data at selected frequencies. In addition, GoPro cameras were installed to document the entire test in video for later reference. Further, 3D images were also captured using a LiDAR sensor in an iPhone camera through Polycam software.



**Figure 6.17. Sample Optotrak target layout.**



**Figure 6.18. Final DIC setup for one side of the girder.**



**Figure 6.19. Final Optotrak setup for one side of girder.**

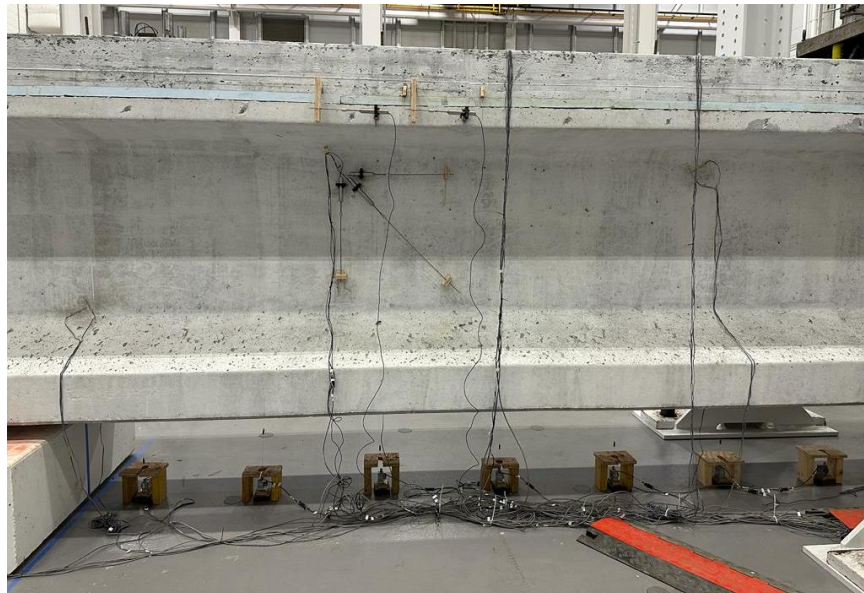
## **6.4 TESTING PROCEDURE**

The testing procedure described below serves as a consolidated overview of the key steps and phases discussed in the preceding sections. Following the complete connection of all sensors and comprehensive validation checks, along with meticulous confirmation of accurate data capture through optical methods, the test was initiated. For the DIC cameras, specific configurations and settings had to be consistently employed across all tests. The Optotrak system required calibration and alignment to ensure precise data recording by both cameras. Additionally, existing cracks on the girders were identified and marked prior to commencement of testing; the cracks were predominantly concentrated at the girder extremities. Figure 6.20 and Figure 6.21 offers a visual representation of the girder equipped with an array of integrated sensors.

The girders were systematically subjected to loading by the actuators, adhering precisely to the sequence detailed in Table 6.1. Within this load protocol, a 5-minute halt was strategically incorporated between steps. This pause facilitated the research team's thorough examination of factors, including crack development, progression of crack widths, and visual documentation, as the test unfolded. The experiment advanced gradually, proceeding until the defined service limit was reached through incremental steps. At this juncture, the widths of all visible cracks were recorded in detail. The test was then further advanced until the initial appearance of the first shear crack in the girder accompanied by the annotation of the corresponding loads for future reference. Throughout the duration of the experiment, cracks were systematically marked and



meticulously monitored, ensuring a comprehensive assessment as the loading protocol ended with the ultimate failure of the girder.



**Figure 6.20. Instrumented girder with sensor arrays.**



**Figure 6.21. Final setup of the girder before testing.**

## **6.5 SUMMARY**

After the casting of experimental specimens, the loading protocol was developed as a part of the testing procedure. Because there are two different shear reinforcement spacings for each girder, the difference in the shear capacities of both the sides need to be considered to develop a differential loading protocol. Further, the detailed instrumentation plan and data acquisition for each test of the girder were developed to record and document data during the experiment. The sensor arrays included strain gauges, LVDTs, string potentiometers, and load cells, along with optical tracking methods like DIC and Optotrak for crack visualization. The chapter describes the location of each of these sensors and potential outcomes from the collected data. Furthermore, the testing procedure is summarized by detailing each individual step followed during the experiment.



## CHAPTER 7:

### FULL-SCALE TESTING: OBSERVATIONS AND RESULTS

The testing regimen encompasses the systematic application of shear loads to the girders, coupled with observation of key events, such as the occurrence of cracks and eventual failure. The load protocol outlined in Section 6.2 mirrors this approach and is tailored to facilitate this comprehensive study. This chapter provides a detailed description of observations made from each individual test as well as girder-to-girder comparisons.

#### 7.1 GIRDER TESTING AND OBSERVATIONS

##### 7.1.1 G1\* Test

The G1\* girder is a Tx54 type girder and features two distinct shear reinforcements within the designated testing zones. This girder is cast with a deck measuring 8.5 in. in thickness and 3 ft in width, which aligns with the length of the top flange of the girder. The concrete's intended 28-day compressive strength was designed to be 10.5 ksi, computed through the equivalent deck design methodology, which facilitated the reduction of the width from the original 8 ft to 3 ft. Further insights into the deck's design and its construction on the girder can be found in a succinct manner within Section 5.4. The major design parameters of this girder are shown in Table 7.1.

**Table 7.1. Design parameters for G1\* girder.**

Test ID	Girder Type	Length (ft)	$f'_{ci}$ (ksi)	$f'_c$ (ksi)	28-day $f'_c$ (ksi)	Spacing (in.)	$f_{yt}$ (ksi)	# of Strands	Harp	$a/d$
G1*-W	Tx54	52	6	7	9.2	18	60	34 (2 Top)	No	3
G1*-E	Tx54	52	6	7	9.2	26	80	34 (2 Top)	No	3

The west side of the girder has an 18 in. spacing of 60 ksi R-bars, which is used in the TxDOT standard drawings, and the east side of the girder has 26 in. spacing of 80 ksi strands with equivalent shear strength. The initial load increments applied in this test primarily induced extensions of pre-existing cracks at the girder's ends resulting from prestress transfer. A significant diagonal shear crack emerged on the east side of the girder with multiple cracks corresponding to a recorded shear force of 229 kips. This force surpasses the girder's required

strength, which is calculated at 220 kips based on factored dead and live loads for design. The advent of diagonal cracking manifested as a reduction in overall specimen stiffness accompanied by a decrease in actuator load. Subsequently, the test progressed, leading to the appearance of the first diagonal cracking with multiple cracks on the west side of the girder at 252 kips. Figure 7.1 and Figure 7.2 show the first diagonal crack formation on both sides.



**Figure 7.1. West side of G1\* at cracking load.**



**Figure 7.2. East side of G1\* at cracking load.**

Further, the test was incrementally advanced toward the predicted ultimate load in accordance with the prescribed loading protocol. Each progressive step accompanied an escalation in the widths of the formed cracks, occasionally leading to additional diagonal cracking. After each step, crack widths were meticulously measured and closely monitored, ensuring safe progression. Owing to the notably brittle and abrupt nature of shear failure, crack width measurements were

suspended toward the later stages of the test for safety reasons. However, it is important to note that the spacing between cracks and the angles of the cracks were recorded after the completion of the test. These data hold relevance in the context of determining the minimum shear reinforcement and guiding the shear design for the girders.

The ultimate failure occurred on the west side of the girder, occurring at a shear force of 360 kips, which prompted the cessation of the test. Notably, the east side of the girder had nearly reached a comparable stage of cracking, registering a recorded shear force of 352 kips. However, due to the interconnectivity between both regions, the decision was made to halt the test after substantial failure had transpired on either side of the girder. This approach was underpinned by the loading protocol's design, ensuring that both sides of the girder closely approached the predicted ultimate shear force. The ultimate failure of the girders can be seen in Figure 7.3 and Figure 7.4. The ultimate failure on the east side had compression diagonal failure along with a large area of concrete spalled from the web of the girder.



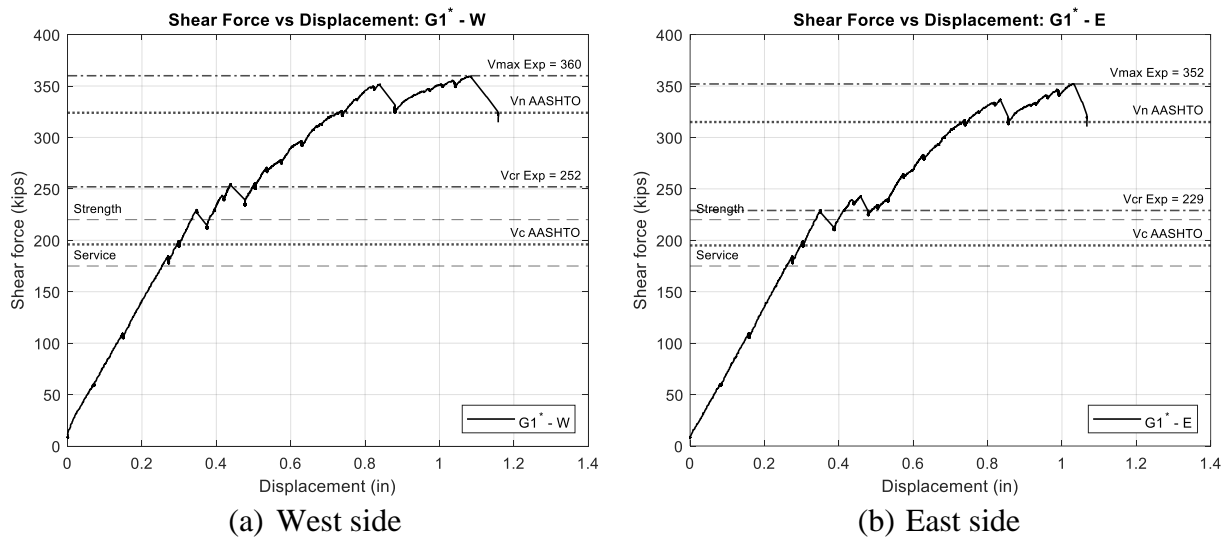
**Figure 7.3. West side of G1\* after ultimate failure.**



**Figure 7.4. East side of G1\* after ultimate failure (after unloading).**

As part of the preliminary processing of the test data, the crack maps were developed to identify the crack angles of the diagonal cracks and the spacing between the diagonal cracks. The spacing between the diagonal cracks relates to the MCFT in terms of number of stirrups passed intercepting the cracks. The observed crack widths at the first cracking shear were in the range of 0.15 mm to 0.7 mm on the west side and 0.2 mm to 0.4 mm on the east side.

The preliminary investigation also encompassed the generation of a shear force versus displacement plot for the entirety of the test alongside a displacement profile illustrating the girder's behavior during both cracking and ultimate stages. The shear force versus displacement plot was constructed by calculating support reactions through load cell data collected from the actuators, coupled with displacement measurements derived from the deflection of the string pot located beneath the load point. The shear force plot was further enriched by notations of the experimentally determined cracking and ultimate shear force values, annotated with corresponding AASHTO specifications. For a comprehensive overview, both the service limit and strength limit were also delineated. Figure 7.5 shows the shear force (kips) versus deflection under load point (in.) for both sides of G1\* girder.



**Figure 7.5. Shear force versus displacement plots for G1\* girder (west and east sides).**

### 7.1.2 G1 Test

The girder G1 is also of the Tx54 type, and it shares identical design parameters with the G1\* girder, with one exception—the presence of a deck. In the case of the G1 girder, no deck is cast, which allows for a focused investigation into the influence of deck presence on girder testing. This investigation sought to elucidate the role of the deck in influencing the shear strength of the girder. The key design parameters for this girder are summarized in Table 7.2.

**Table 7.2. Design parameters for G1 girder.**

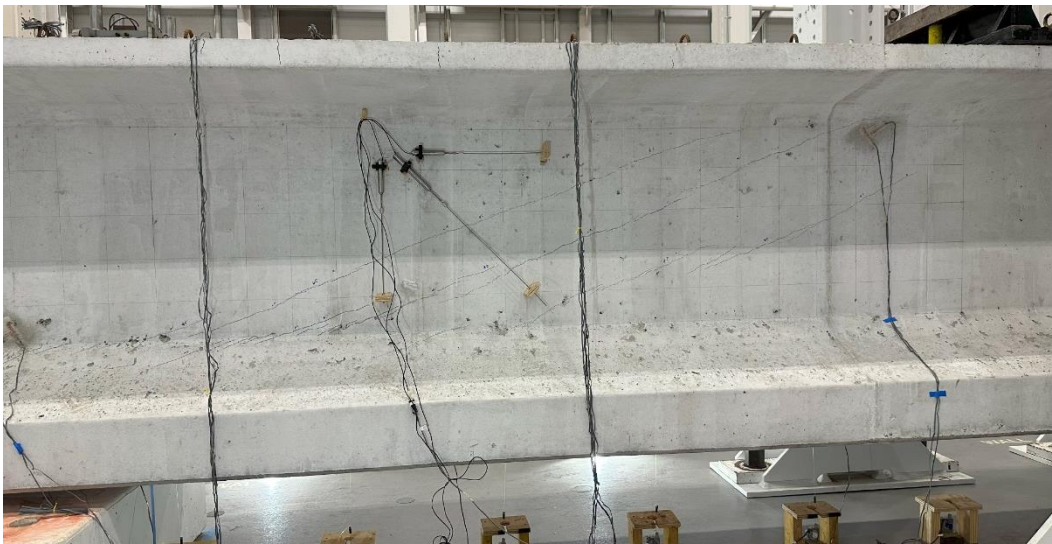
Test ID	Girder Type	Length (ft)	$f'_{ci}$ (ksi)	$f'_c$ (ksi)	28-day $f'_c$ (ksi)	Spacing (in.)	$f_{yt}$ (ksi)	# of Strands	Harp ?	$a/d$
G1-W	Tx54	52	6	7	8.8	18	60	34 (2 Top)	No	3
G1-E	Tx54	52	6	7	8.8	26	80	34 (2 Top)	No	3

This girder has identical shear reinforcement characteristics as the G1\* girder within the specified testing zones. The omission of a deck in the G1 specimen resulted in a notable decrease of 30 kips in the computation of the cracking shear force when employing the guidelines provided by AASHTO (2020). Similarly, in the calculation of the ultimate shear force, this reduction was even more prominent, amounting to 50 kips. However, it is worth highlighting that the disparity between the west and east sides of the G1 girder closely resembled that observed in the G1\* girder. Consequently, the loading methodology closely follows that of the G1\*



specimen, albeit with adjusted values to accommodate the reductions. The experimental procedure followed a similar progression to the preceding test—an examination of crack formation at intermediate stages, conducted before the onset of diagonal cracking.

Initial diagonal cracking was observed on the west side of the girder, becoming evident when subjected to a shear force of 215 kips. Similar to the preceding test, the onset of diagonal cracking was characterized by the emergence of multiple cracks at the specified shear force level. These cracks led to a slight reduction in the load on the actuator due to the resulting deflection in the girder's structure. As the test progressed, a comparable diagonal cracking pattern was observed on the east side of the girder, occurring at the same recorded shear force of 215 kips. This consistency aligns well with the expected design behavior because both the eastern and western side designs exhibited equivalence. The cracking pattern on the east side also resembled that on the west side, with multiple cracks appearing simultaneously. Figure 7.6 and Figure 7.7 provide a visual representation of the girder's condition at the cracking stage.



**Figure 7.6. West side of G1 girder at cracking load.**

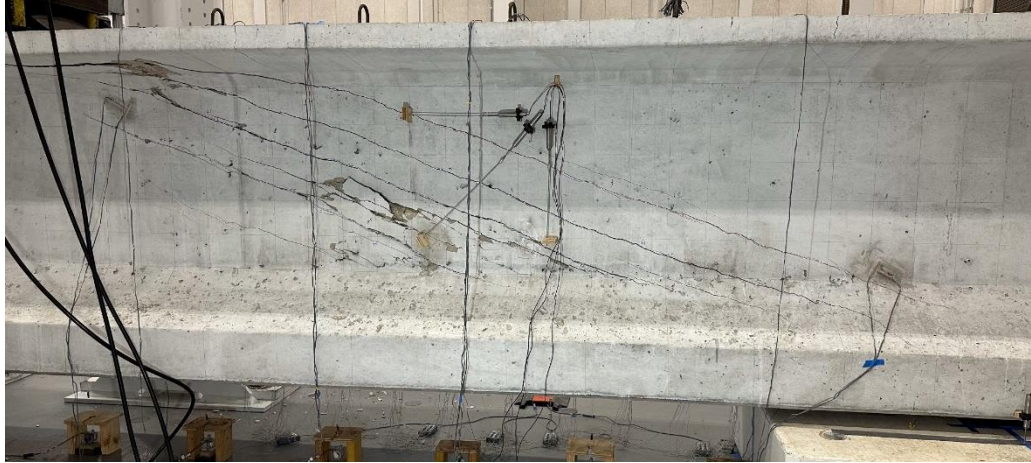


**Figure 7.7. East side of G1 girder at cracking load.**

The initiation of the cracking stage occurred prior to reaching the strength limit of 220 kips. As the test advanced, continuous monitoring of crack widths was conducted until a point deemed safe for further approach to the girder. The girder experienced its ultimate failure on the east side, specifically at a shear force of 351 kips. In accordance with the earlier outlined procedure, the test was promptly halted at this juncture, with the recorded shear force on the west side amounting to 361 kips. Figure 7.8 and Figure 7.9 depict the damage on the girder at the ultimate failure.

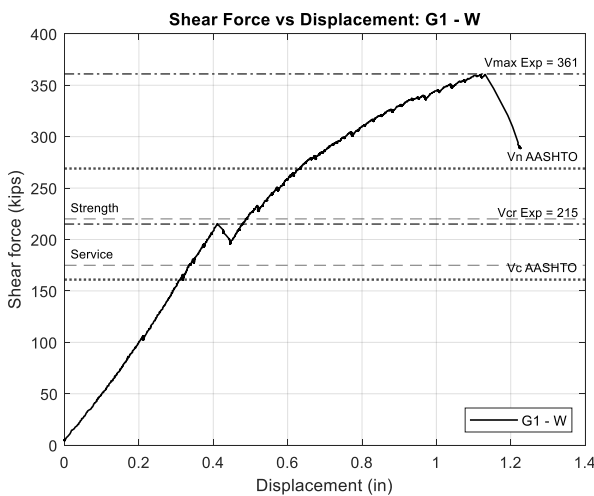


**Figure 7.8. West side of G1 girder at ultimate failure.**

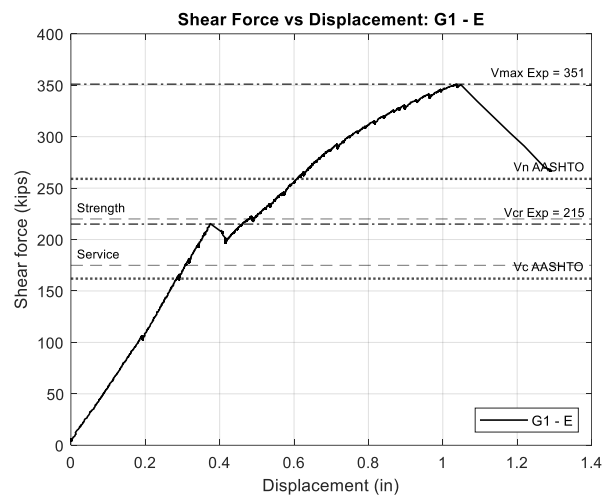


**Figure 7.9. East side of G1 girder at ultimate failure.**

The girder's ultimate failure exhibited a compression diagonal failure mode accompanied by evident damage to the top flange. This damage beneath the top flange evolved along the trajectory of the inclined diagonal shear cracks, advancing progressively toward the actuator plates. During the initial cracking stage, the measured crack widths ranged from 0.15 to 0.2 mm on the west side and from 0.25 to 0.3 mm on the east side. Similar to previous preliminary results, the shear force versus displacement plots were developed. These plots were eventually combined for effective comparison analysis, as mentioned in Section 7.2.1. Figure 7.10 shows the plots for the G1 girder for both sides.



(a) West side



(b) East side

**Figure 7.10. Shear force versus displacement plots for G1 girder (west and east).**



### 7.1.3 G2 Test

Following the determination to exclude decks discussed in 7.2.1 from the testing of the remaining girders, the subsequent girder, G2 was tested. This test involved the same girder type, specifically the Tx54, which adheres to the same prestressed design and maintains an equivalent shear-span-to-depth ratio. The key design parameters for the G2 girder are shown in Table 7.3.

**Table 7.3. Design parameters for G2 girder.**

Test ID	Girder Type	Length (ft)	$f'_{ci}$ (ksi)	$f'_c$ (ksi)	28-day $f'_c$ (ksi)	Spacing (in.)	$f_{yt}$ (ksi)	# of Strands	$a/d$
G2-W	Tx54	52	6	7	8.2	38	60	34 (2 Top)	3
G2-E	Tx54	52	6	7	8.2	26	60	34 (2 Top)	3

A key difference between this girder, designated G2, and the earlier comparable girder G1 resides in the configuration of shear reinforcement within the designated testing zones. Specifically, the west side of the girder features a 26 in. spacing of 60 ksi R-bars. This spacing was determined by  $h_w / (2 * \tan \theta)$ , which considers the web height ( $h_w$ ) and the angle ( $\theta$ ) of diagonal cracks. It was predicated on the principle that each crack should be crossed by at least one stirrup. Conversely, the east side of the girder was equipped with a 38 in. spacing of 60 ksi R-bars; this spacing was derived from the minimum shear reinforcement formula as per the AASHTO (2020).

The testing procedure detailed in Section 6.4 was adhered to for this test as well. The initial appearance of diagonal cracking was observed on the east side of the girder and corresponded to a recorded shear force of 191 kips. In this specific step, a collection of cracks emerged in closer proximity to the support. Subsequently, upon the restoration of the load in the actuators, the west side of the girder also experienced cracking at a similar shear force of 190 kips. Notably, on the west side, this occurrence involved the formation of a singular significant crack during the initial onset of diagonal cracking. Figure 7.11 and Figure 7.12 display a visual representation of cracks at the first diagonal cracking step.



**Figure 7.11. West side of G2 girder at cracking load.**

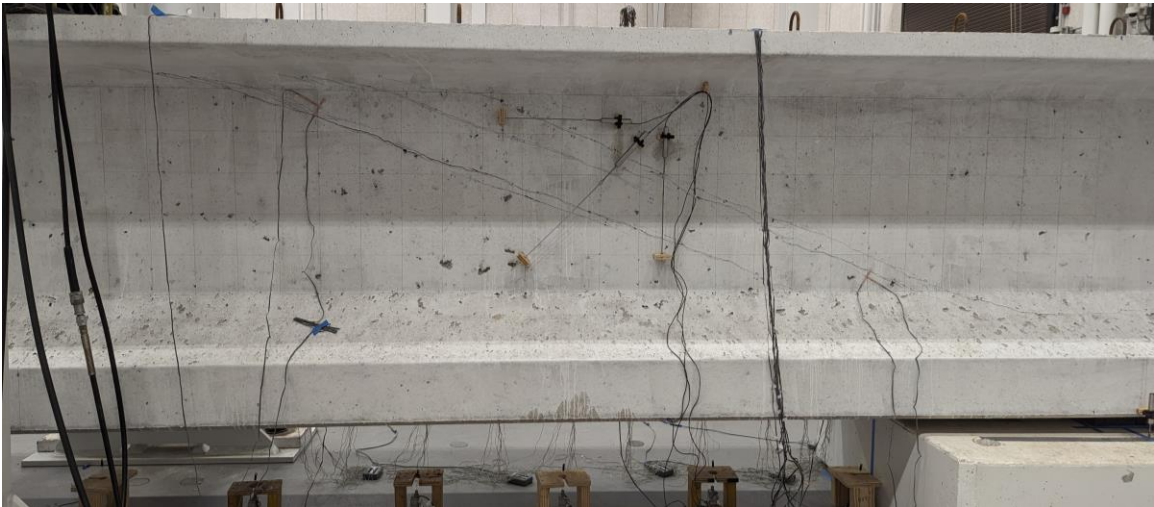


**Figure 7.12. East side of G2 girder at cracking load.**

The post-cracking loading protocol for this girder was devised by taking into consideration the substantial disparity in nominal strengths between its two sides. Due to a notable difference of 20 kips and the presence of minimal reinforcement on the west side, the testing team exercised cautious progression toward the ultimate failure stage. Ultimately, the west side of the girder experienced failure at a recorded shear force of 292 kips, accompanied by extensive damage within the girder. The damage manifested primarily along the shear cracks, coupled with the rupture of two R-bars. Notably, the concrete near the support on the west side suffered crushing, leading to an abrupt release of force after the ultimate failure. On the east side of the girder, a shear force of 302 kips was recorded, accompanied by clearly visible compression diagonal cracks. Figure 7.13 and Figure 7.14 depict the damage to the girder at ultimate failure.



**Figure 7.13. West side of G2 girder at ultimate failure.**



**Figure 7.14. East side of G2 girder at ultimate failure.**

The presence of minimal reinforcement, where the R-bars are spaced approximately 3 ft apart, rendered the task of supporting the girder's dead weight after reaching the cracking load quite challenging. The considerable load imposed under such conditions led to the rupture of two R-bars within this region. The sudden release of force culminated in the girder experiencing crushing near the support and visible sagging of the prestressing strands in the bottom flange. Additionally, the top flange of the girder suffered significant damage seen as an overlap of the two halves, a consequence of the two halves being thrust against each other. Figure 7.15 shows the detailed images from the test.





(a) Fractured R-bar



(b) Top flange



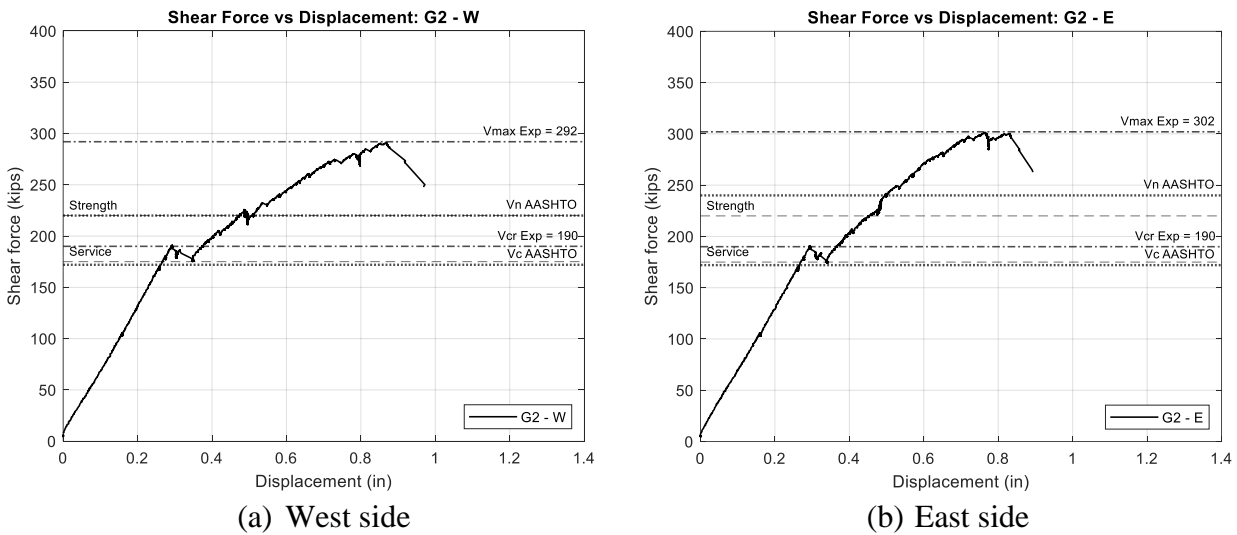
(c) Crushing near support

**Figure 7.15. Detailed damage at ultimate failure in G2 west.**

At the cracking stage, the observed crack widths fell within the range of 1.25–1.50 mm on the west side of the girder and 0.35–0.50 mm on the east side. The relatively higher crack widths witnessed on the west side can be directly attributed to the significantly reduced reinforcement within that zone. Because of this low reinforcement, each crack typically accommodated a maximum of two to three stirrups, resulting in considerable stress concentration on the R-bars.

This dynamic is vividly illustrated in the failure mode observed on the west side marked by the fracture of these stirrups.

The preliminary processing involves developing the shear force versus displacement plots of the girder. These plots will assist in making an initial understanding of the test data and post-cracking behavior of the girder. Figure 7.16 depicts the respective plots for both sides of G2 girder.



**Figure 7.16. Shear force versus displacement plots for G2 girder (west and east).**

#### 7.1.4 G3 Test

Moving forward, the subsequent girder subjected to testing is denoted as G3. This girder adheres to the same prestressing design principles as G1 and G2 yet features a significant difference in strand arrangement. G3 is configured with six harped strands extending to a height of 20.5 in. from the bottom flange, with their terminations situated within the web at the girder's ends. The design of these harped strands follows the established standard protocol determining the hold-down point in accordance with AASHTO (2020). The testing of this girder presented a valuable opportunity for an insightful comparison, owing to the inclusion of the harped strands giving a vertical force component because of the prestressing arrangement. The key design parameters for this girder are shown in Table 7.4.

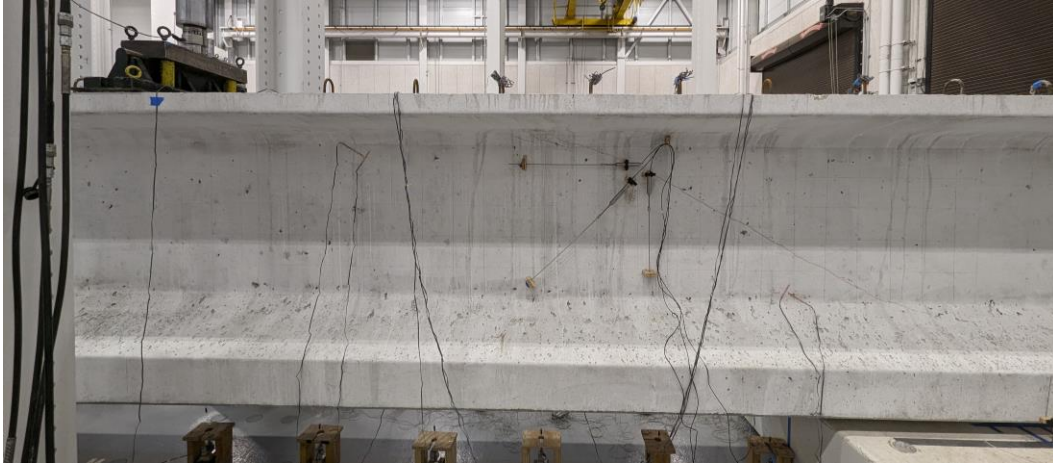
**Table 7.4. Design parameters for G3 girder.**

Test ID	Girder Type	L (ft)	$f'_{ci}$ (ksi)	$f'_c$ (ksi)	28-day $f'_c$ (ksi)	Spacing (in.)	$f_{yt}$ (ksi)	# of Strands	Harp	$a/d$
G3-W	Tx54	52	6	7	8.7	18	60	34 (2 Top)	6 (20.5 in.)	3
G3-E	Tx54	52	6	7	8.7	26	60	34 (2 Top)	6 (20.5 in.)	3

The shear reinforcement design mirrors that of G1-W (18 in. spacing of 60 ksi) and G2-W (26 in. spacing of 60 ksi). The test data and findings from testing this girder facilitated a meaningful comparison, particularly in relation to the influence of the harped strands on the same shear reinforcement configuration. The girder was subjected to loading in a manner that adheres to the devised loading protocol specifically designed for this girder. The initial appearance of diagonal cracking was observed on the west side, manifesting as two distinct cracks extending from the support to the actuator. This occurrence transpired at a recorded shear force of 205 kips. Subsequently, following the restoration of load, the east side of the girder also experienced cracking at the same recorded shear force of 205 kips. On the east side, a single crack emerged closer to the support, characterized by a steeper angle. During this phase, halt periods were instituted for crack width measurements and documentation of other pertinent images. Figure 7.17 and Figure 7.18 showcase the extent of cracking damage sustained by this girder.



**Figure 7.17. West side of G3 girder at cracking load.**



**Figure 7.18. East side of G3 girder at cracking load.**

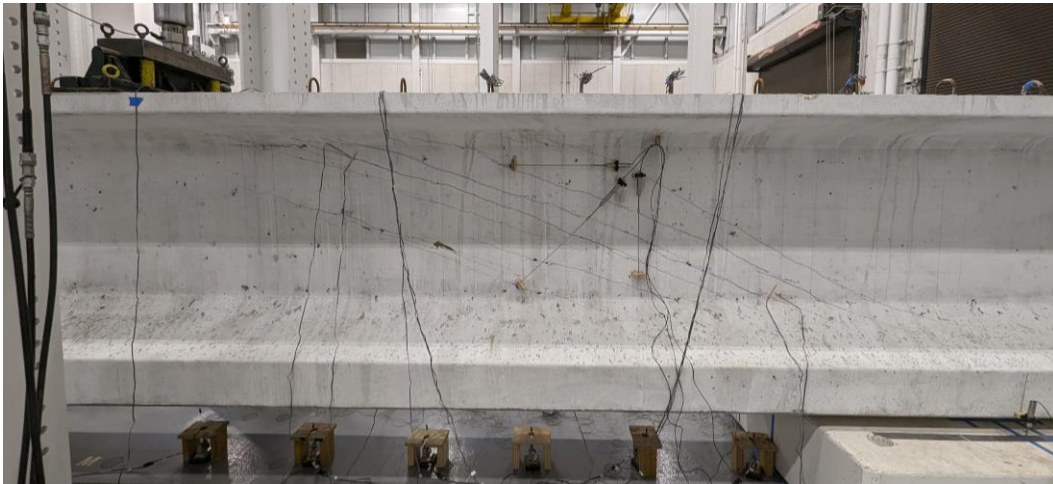
The test progressed in alignment with the load protocol, steadily approaching the ultimate failure of the girder. On the west side, the progression entailed the emergence of multiple cracks in close proximity to the initially formed cracks. These new cracks were characterized by a nearly identical angle and direction as their predecessors. In contrast, the east side of the girder experienced the development of new cracks adjacent to the initial crack, demonstrating a gradual decrease in angle toward the actuator. The observed variation in crack pattern development necessitated further scrutiny through additional data analysis.

Ultimately, the west side of the girder succumbed to failure at a recorded shear force of 341 kips. This failure was accompanied by notable damage to the top flange alongside instances of concrete spalling at certain compression diagonals. Concurrently, on the east side, a shear force of 354 kips was recorded at this stage. Figure 7.19 and Figure 7.20 show the cracks at the ultimate failure stage of the test.





**Figure 7.19. West side of G3 girder at ultimate failure.**

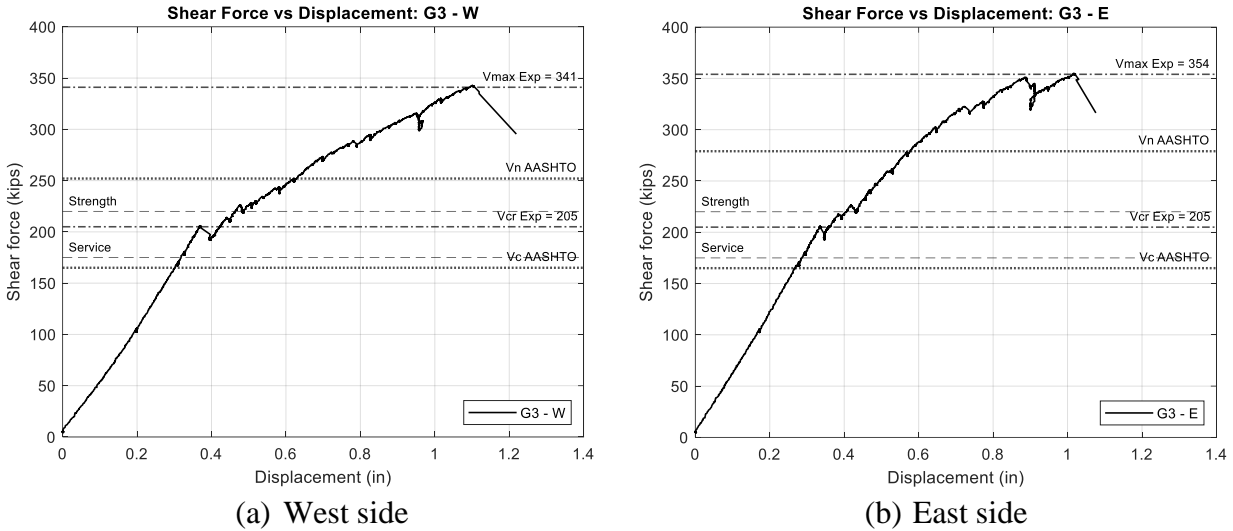


**Figure 7.20. East side of G3 girder at ultimate failure.**

The observed crack widths at the cracking stage for the west side of the girder are in the range of 0.6–1.0 mm, while on the side they are in the range of 0.3–0.4 mm.

In the preliminary analysis, shear force versus displacement offers an initial understanding of the test data and post-cracking behavior. Figure 7.21 illustrates these plots for both sides of the G3 girder.





**Figure 7.21. Shear force versus displacement plots for G3 girder (west and east).**

### 7.1.5 G4 Test

The next girder in the testing matrix is G4 which was a variation in shear-span-to-depth ratio with  $a/d$  of 2.5. The prestressing design of the girder was the same as the prototype girder G1. The testing of this girder is an insightful comparison in understanding higher shear capacity and more concentrated shear zone due to a shorter testing span. This girder G4, along with another comparison with girder G9 having an  $a/d$  of 4, provides a broader understanding of its effect. The key design parameters for this girder are shown in Table 7.5.

**Table 7.5. Design parameters for G4 girder.**

Test ID	Girder Type	Length (ft)	$f'_{ci}$ (ksi)	$f'_c$ (ksi)	28-day $f'_c$ (ksi)	Spacing (in.)	$f_{yt}$ (ksi)	# of Strands	$a/d$
G4-W	Tx54	45	6	7	8.5	38	60	34 (2 Top)	2.5
G4-E	Tx54	45	6	7	8.5	18	60	34 (2 Top)	2.5

The shear reinforcement design mirrors that of G1-W (18 in. spacing of 60 ksi) and G2-E (38 in. spacing of 60 ksi). The setup changed for this girder owing to a shorter shear span, which brought the pedestals closer to the actuators. The girder was subjected to loading in a manner that adheres to the devised loading protocol specifically designed for this girder. The initial appearance of diagonal cracking was observed on the east side, manifesting as one distinct crack

extending from the support to the actuator. This occurrence transpired at a recorded shear force of 175 kips. Subsequently, following the restoration of load, the west side of the girder also experienced cracking at the same recorded shear force of 214 kips. On that side, the crack formed is a single crack thicker in the crack width and also characterized by a steeper angle. During this phase, halt periods were used for crack width measurements and documentation of other pertinent images. Figure 7.22 and Figure 7.23 showcase the extent of cracking damage sustained by this girder.



**Figure 7.22. West side of G4 girder at cracking load.**



**Figure 7.23. East side of G4 girder at cracking load.**

Ultimately, the west side of the girder succumbed to failure at a recorded shear force of 335 kips. This failure was accompanied by notable damage to the top flange alongside instances of

concrete spalling at certain compression diagonals, with many shear cracks forming and merging. Concurrently, on the east side, a shear force of 380 kips was recorded at this stage. Figure 7.24 and Figure 7.25 show the cracks at the ultimate failure stage of the test.

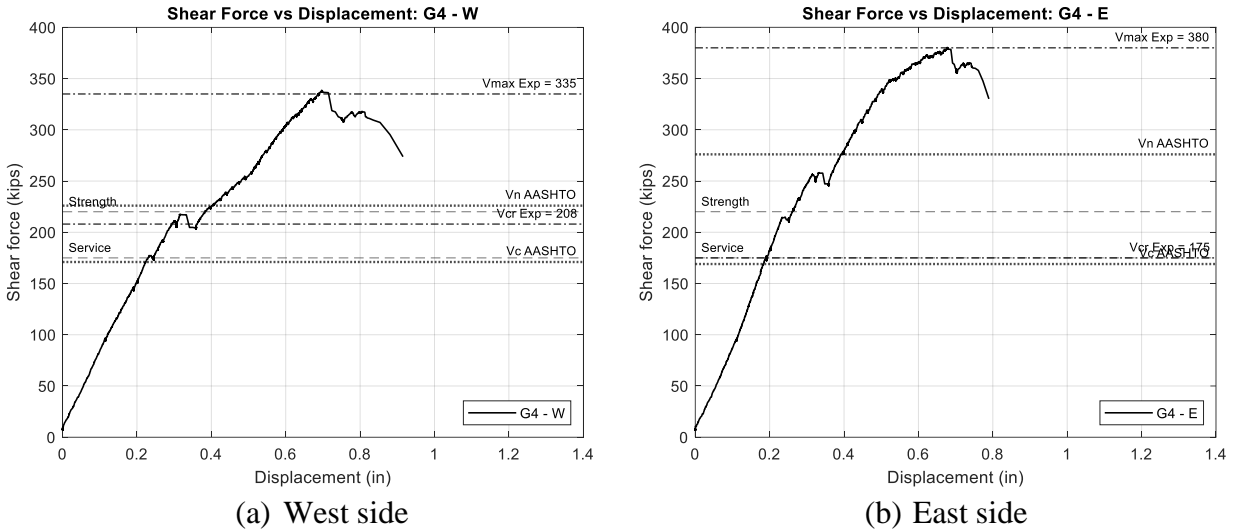


**Figure 7.24. West side of G4 girder at ultimate failure.**



**Figure 7.25. East side of G4 girder at ultimate failure.**

The observed crack widths at the cracking stage for the west side of the girder are in the range of 2.0 mm, while on the east side they are in the range of 0.5–0.6 mm. In the preliminary analysis, shear force versus displacement plots offer an initial understanding of the test data and post-cracking behavior. Figure 7.26 illustrates these plots for both sides of the G4 girder.



**Figure 7.26. Shear force versus displacement plots for G4 girder (west and east).**

#### 7.1.6 G5 Test

Girder G5 is the next one in the test matrix representing a variation in the prestressing ratio. The prestressing design of this girder is a variation of the prototype girder G1, with a lower number of prestressing strands— 26 in G5 compared to 34 in G1. Despite the reduction in the number of prestressing strands the girder was verified to pass all the stress checks in the design aspects. The testing of this girder is an insightful comparison because the prestressing ratio is the key difference between a regular RC beam and PC beam. This variation helps in determining the role of the prestressing ratio in minimum shear reinforcement provisions. The key design parameters for this girder are shown in Table 7.6.

**Table 7.6. Design parameters for G5 girder.**

Test ID	Girder Type	Length (ft)	$f'_{ci}$ (ksi)	$f'_c$ (ksi)	28-day $f'_c$ (ksi)	Spacing (in.)	$f_{yt}$ (ksi)	# of Strands	$a/d$
G5-W	Tx54	52	6	7	9.2	26	60	26 (2 Top)	3
G5-E	Tx54	52	6	7	9.2	38	60	26 (2 Top)	3

The shear reinforcement design in this girder was obtained from the ACI equation (26 in. of 60 ksi) and proposed spacing of  $h_w/(2\tan\theta)$  (38 in. of 60 ksi).

The setup of the test was the same as G1 because the shear-span-to-depth ratio is kept constant to understand the sole effects of the prestressing ratio. The girder was subjected to loading in a manner that adheres to the devised loading protocol specifically designed for this girder. The initial appearance of diagonal cracking was observed on the west side, manifesting as two distinct cracks extending from the support to the actuator. This occurrence transpired at a recorded shear force of 162 kips. Subsequently, following the restoration of load, the east side of the girder also experienced cracking at the same recorded shear force of 188 kips. On the east side, a single crack thicker in crack width and characterized by a steeper angle formed closer to the support. During this phase, halt periods were used for crack width measurements and documentation of other pertinent images. Figure 7.27 and Figure 7.28 showcase the extent of cracking damage sustained by this girder.



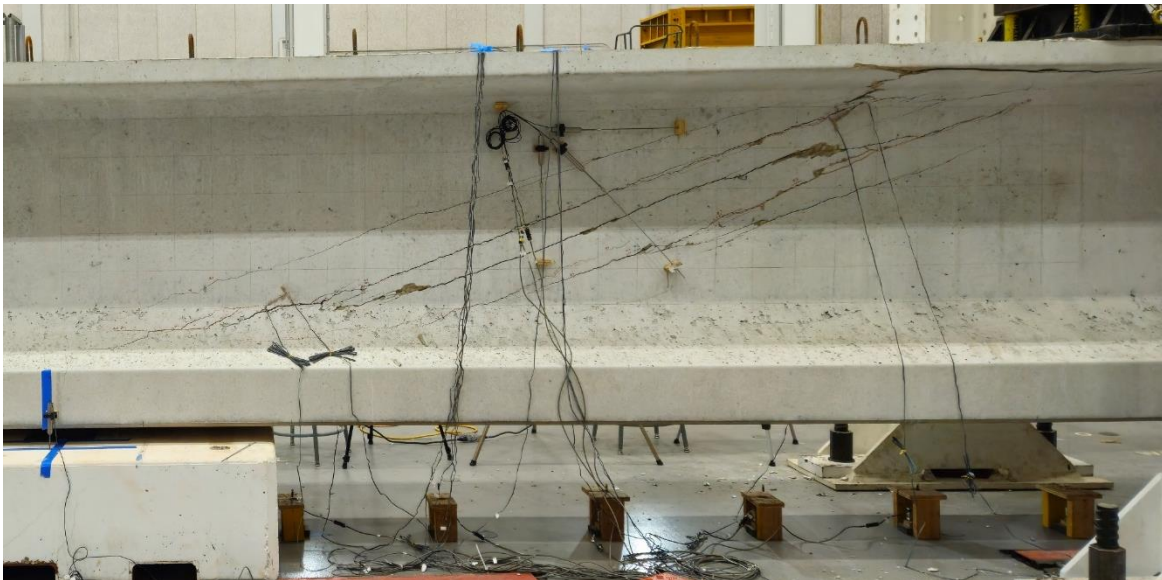
**Figure 7.27. West side of G5 girder at cracking load.**



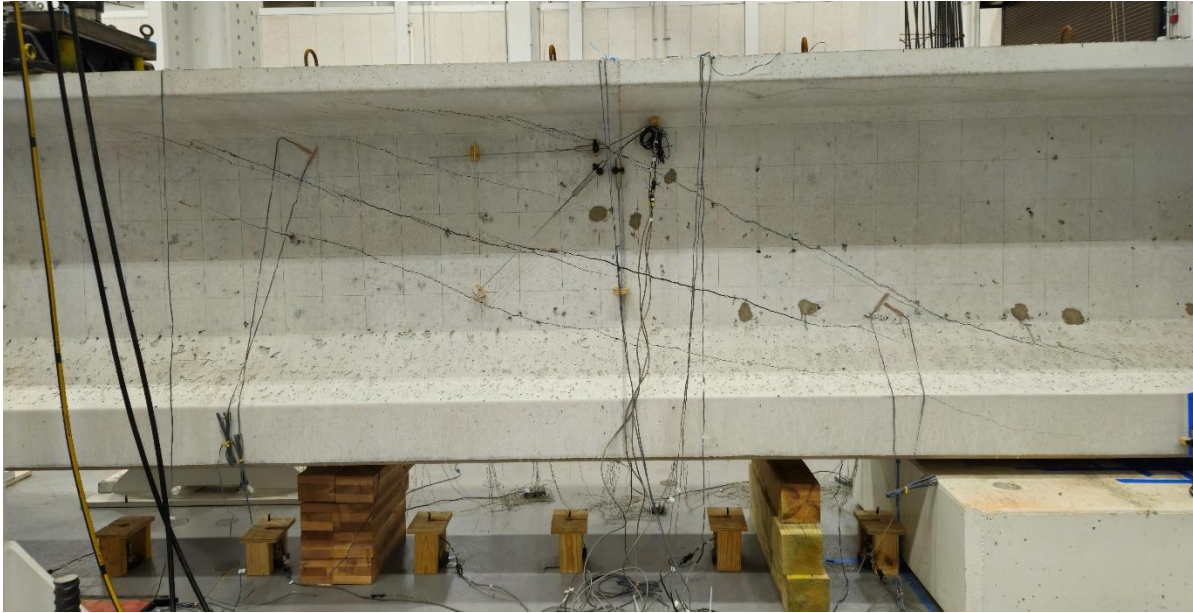


**Figure 7.28. East side of G5 girder at cracking load.**

Ultimately, the west side of the girder succumbed to failure at a recorded shear force of 293 kips. This failure was accompanied by notable damage to the top flange, with some shear cracks merging together. Concurrently, on the east side, a shear force of 262 kips was recorded at this stage, revealing more cracks formed on this side as well. Figure 7.29 and Figure 7.30 show the cracks at the ultimate failure stage of the test.

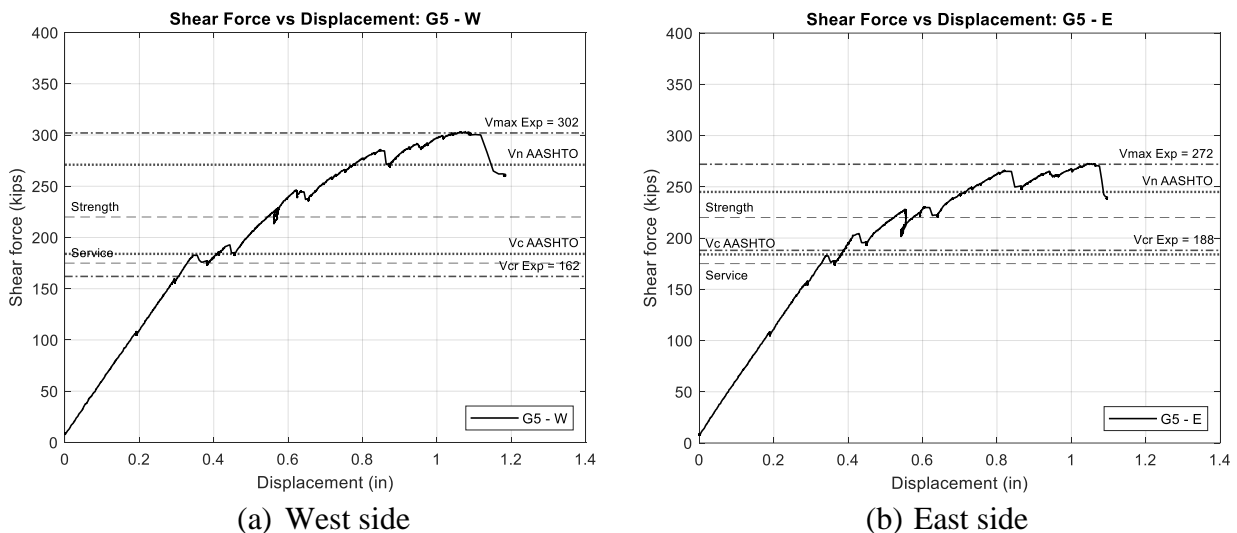


**Figure 7.29. West side of G5 girder at ultimate failure.**



**Figure 7.30. East side of G5 girder at ultimate failure.**

The observed crack widths at the cracking stage for the west side of the girder are in the range of 0.4–0.7 mm, while on the east side they are in the range of 1.5 mm. In the preliminary analysis, shear force versus displacement plots offer an initial understanding of the test data and post-cracking behavior. Figure 7.31 illustrates these plots for both sides of the G5 girder.



**Figure 7.31. Shear force versus displacement plots for G5 girder (west and east).**

### 7.1.7 G6 Test

The next girder tested was G6; like G5, this girder is also a variation in the prestressing ratio in the girder design. The prototype G1 had 34 strands; G5 had 26 strands due to a lower prestressing ratio; and G6 was designed to have 40 strands because of a higher prestressing ratio. This test together with the G1 and G5 provides an effective comparison of prestressing ratio over a broad range. In addition, it is another vital comparison since the ACI minimum shear reinforcement equation includes a prestressing ratio, so the effect of prestressing ratio in minimum shear reinforcement can also be studied. The key design parameters for this girder are shown in Table 7.7.

**Table 7.7. Design parameters for G6 girder.**

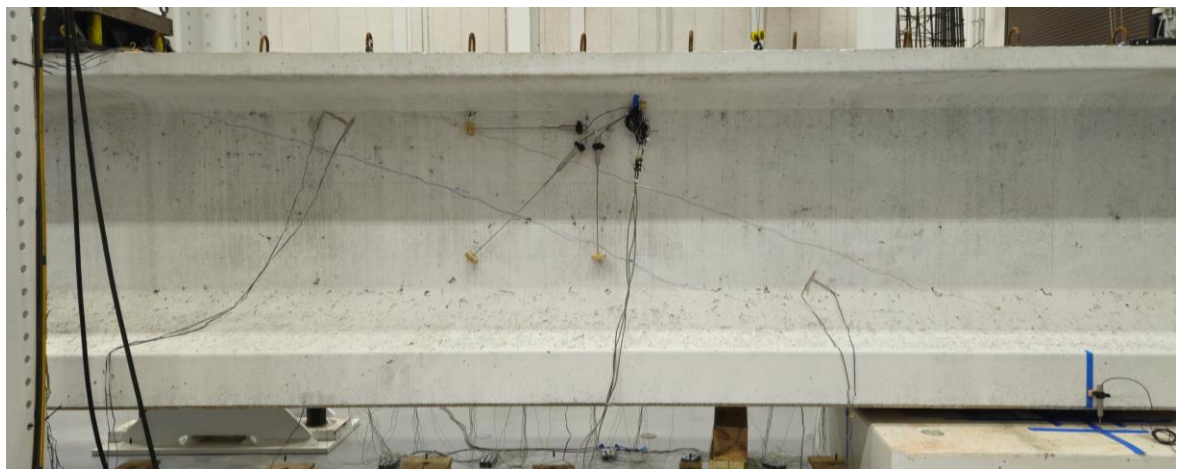
Test ID	Girder Type	Length (ft)	$f'_{ci}$ (ksi)	$f'_c$ (ksi)	28-day $f'_c$ (ksi)	Spacing (in.)	$f_{yt}$ (ksi)	# of Strands	$a/d$
G6-W	Tx54	52	6	7	9.1	38	60	40 (2 Top)	3
G6-E	Tx54	52	6	7	9.1	18	60	40 (2 Top)	3

The shear reinforcement design mirrors that of G1-W (18 in. spacing of 60 ksi) and G2-E (38 in. spacing of 60 ksi). The setup for this girder remains the same as for G5; the only key parameter that varies is the prestressing in the girder. The loading protocol developed for this girder was based on design estimates and FE prediction, and the girder was loaded in accordance. The first appearance of shear cracking on the east side occurred at a shear force of 219 kips, which caused two distinct cracks on that side. Then, the west side of the girder cracked at 211 kips with a significantly bigger crack. The cracks were marked, and the crack measurements were documented right after the appearance. Figure 7.32 and Figure 7.33 show the extent of cracking damage sustained by this girder.





**Figure 7.32. West side of G6 girder at cracking load.**



**Figure 7.33. East side of G6 girder at cracking load.**

Ultimately, the west side of the girder succumbed to failure at a recorded shear force of 306 kips. This failure was brittle, with the web of girder completely damaged and the concrete near the bottom flange at the support blown into pieces. In addition, two of the stirrups in the shear failure zone yielded at a height corresponding to the formation of shear cracks. Concurrently, on the east side, a shear force of 374 kips was recorded at this stage. Figure 7.34 and Figure 7.35 show the cracks at the ultimate failure stage of the test.

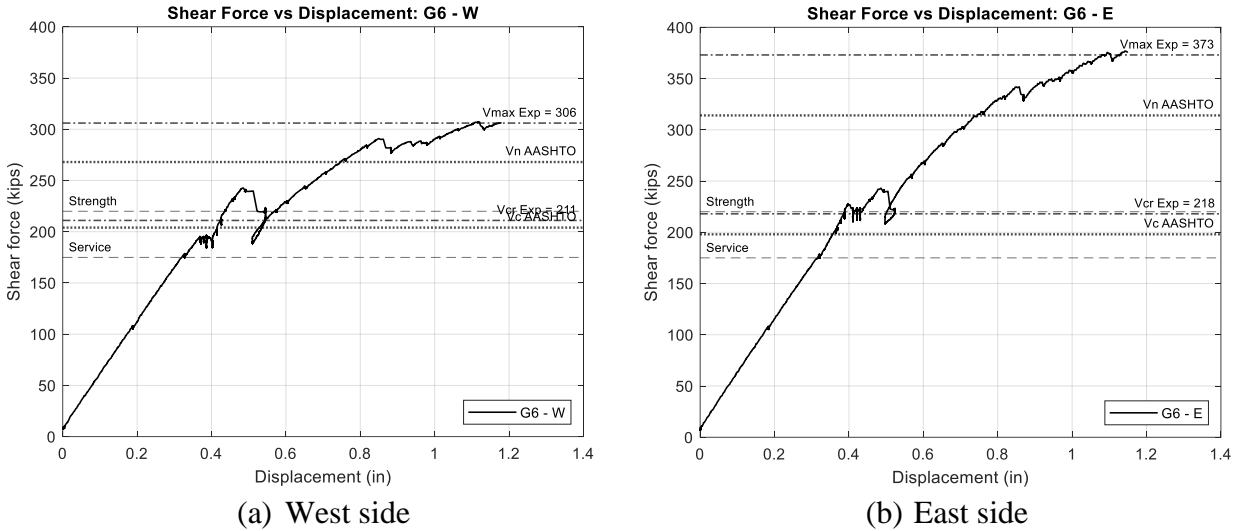


**Figure 7.34. West side of G6 girder at ultimate failure.**



**Figure 7.35. East side of G6 girder at ultimate failure.**

The observed crack widths at the cracking stage for the west side of the girder are in the range of 3.5 mm, while on the east side they are in the range of 0.45 mm. The larger crack widths on the west side can be related to wider spacing of stirrups. In the preliminary analysis, shear force versus displacement plots offer an initial understanding of the test data and post-cracking behavior. Figure 7.36 illustrates these plots for both sides of the G6 girder.



**Figure 7.36. Shear force versus displacement plots for G6 girder (west and east).**

### 7.1.8 G7 Test

G7 is the next girder in this testing program with a key variation of concrete strength in the design of girder. The prototype girder G1 is designed with a compressive strength of 7 ksi and the corresponding prestressing strands were 34, thereby passing all the stress checks based on AASHTO provisions. Thus, the G7 girder is a variation in the design compressive strength of concrete, and the girder design was revised to 24 prestressing strands. This effective comparison helps in studying the effect of concrete tensile strength, which is proportional to compressive strength in shear reinforcement design. The key design parameters for this girder are shown in Table 7.8.

**Table 7.8. Design parameters for G7 girder.**

Test ID	Girder Type	Length (ft)	$f'_{ci}$ (ksi)	$f'_c$ (ksi)	28-day $f'_c$ (ksi)	Spacing (in.)	$f_{yt}$ (ksi)	# of Strands	$a/d$
G7-W	Tx54	52	4	5	8.2	26	60	24 (2 Top)	3
G7-E	Tx54	52	4	5	8.2	18	60	24 (2 Top)	3

The shear reinforcement design mirrors that of G1-W (18 in. spacing of 60 ksi) and G2-W (26 in. spacing of 60 ksi). This girder compares effectively to G1 and G2, so the shear-span-to-depth ratio was kept similar, which is 3. The loading protocol was developed for this girder based on



design estimates and FE prediction, and the girder was loaded in accordance. The first appearance of shear cracking was almost at the same time for both sides of the girder. The recorded shear force was 176 kips on both sides, and the west side featured one distinct crack, while the east side had 2 widely separated cracks. The cracks were marked, and the crack measurements were documented right after the appearance. Figure 7.37 and Figure 7.38 show the extent of cracking damage sustained by this girder.



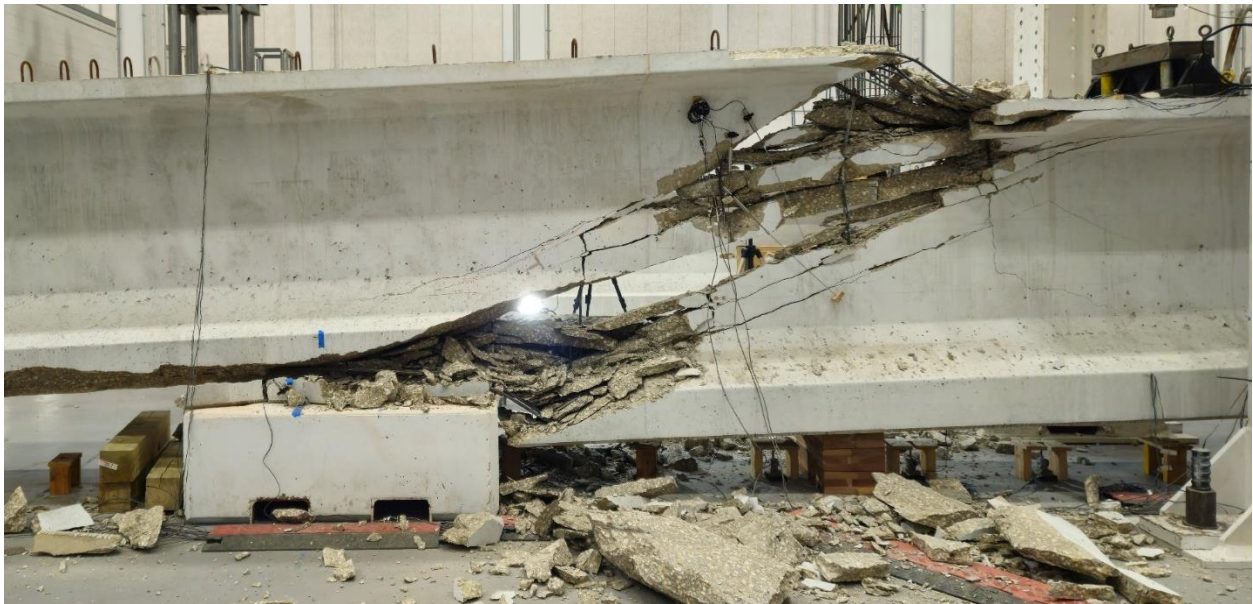
**Figure 7.37. West side of G7 girder at cracking load.**



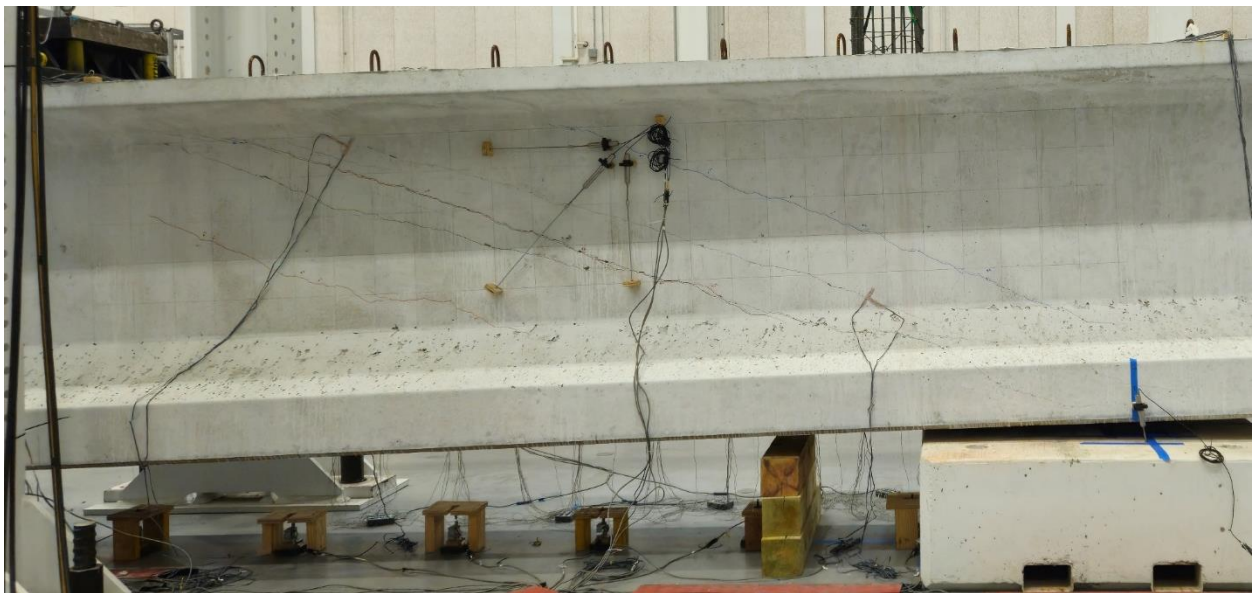
**Figure 7.38. East side of G7 girder at cracking load.**

Ultimately, the west side of the girder succumbed to failure at a recorded shear force of 282 kips. This failure was brittle, with the web of girder completely damaged, and the concrete near the bottom flange at the support blown into pieces. In addition, two of the stirrups in the shear failure zone yielded at a height corresponding to the formation of shear cracks. Concurrently, on the east

side, a shear force of 306 kips was recorded at this stage. Figure 7.39 and Figure 7.40 show the cracks at the ultimate failure stage of the test.



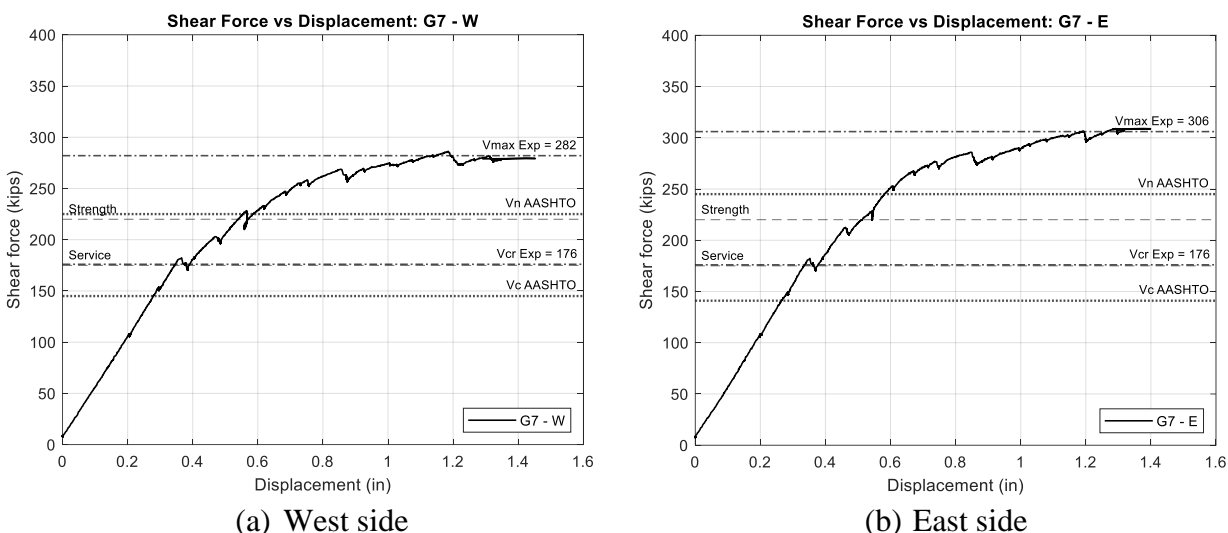
**Figure 7.39. West side of G7 girder at ultimate failure.**



**Figure 7.40. East side of G7 girder at ultimate failure.**

The observed crack widths at the cracking stage for the west side of the girder were in the range of 0.65 mm, while on the side they were in the range of 0.3 mm. The larger crack widths on the west side can be related to wider spacing of stirrups. In the preliminary analysis, shear force

versus displacement plots offer an initial understanding of the test data and post-cracking behavior. Figure 7.41 illustrates these plots for both sides of the G7 girder.



**Figure 7.41. Shear force versus displacement plots for G7 girder (west and east).**

### 7.1.9 G8 Test

The next girder in the test matrix is G8 is also a variation of concrete strength like G7. However, this girder is designed with a higher concrete strength of 8.5 ksi, as opposed to 5 ksi in G7. This girder—together with the prototype G1 and G7 girders—provides a comprehensive understanding of the effects of concrete compressive strength. This girder has 38 prestressing strands based on the design compressive strength. The key design parameters for this girder are shown in Table 7.9.

**Table 7.9. Design parameters for G8 girder.**

Test ID	Girder Type	Length (ft)	$f'_{ci}$ (ksi)	$f'_c$ (ksi)	28-day $f'_c$ (ksi)	Spacing (in.)	$f_{yt}$ (ksi)	# of Strands	$a/d$
G8-W	Tx54	52	4	5	8.5	26	60	38 (2 Top)	3
G8-E	Tx54	52	4	5	8.5	18	60	38 (2 Top)	3

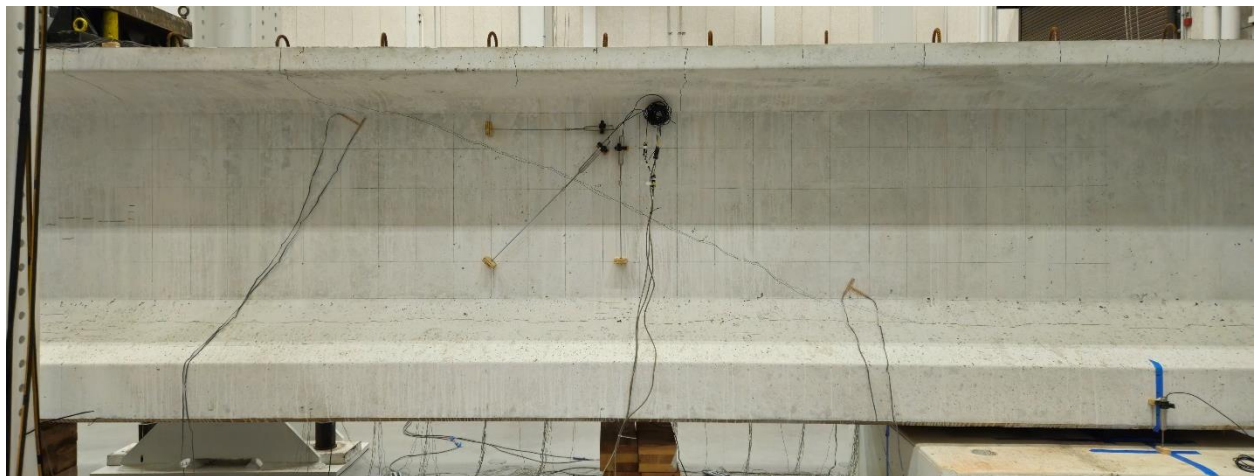
The shear reinforcement design for this girder is similar to the G7. The effective comparison for this girder aligns with G1 and G2, maintaining a similar shear-span-to-depth ratio of 3. The loading protocol for this girder is based on design estimates and predictions from FE analysis,



and the girder was loaded accordingly. The first cracking appeared on the west side of the girder, with two distinct cracks and one partially formed crack at a recorded shear force of 218 kips. After gaining the load, the east side of the girder cracked eventually at a shear force of 214 kips on that side. The cracks were marked, and the crack measurements were documented right after the appearance. Figure 7.42 and Figure 7.43 show the extent of cracking damage sustained by this girder.



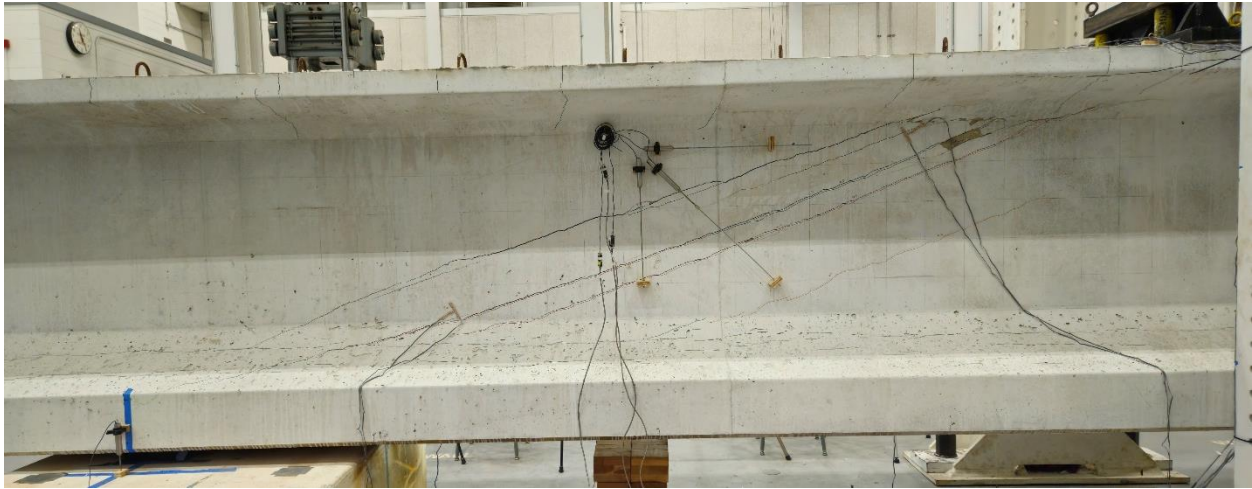
**Figure 7.42. West side of G8 girder at cracking load.**



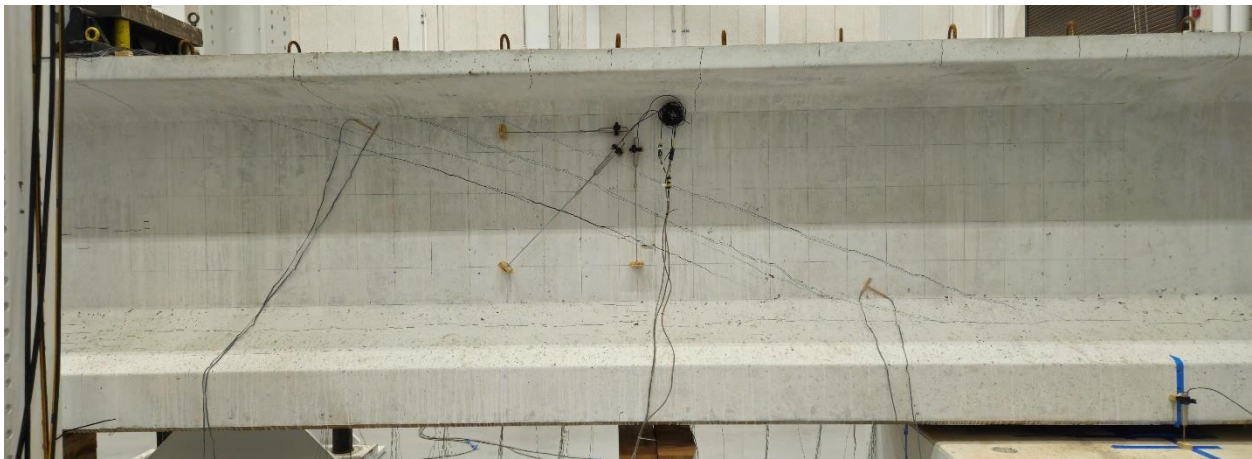
**Figure 7.43. East side of G8 girder at cracking load.**

Ultimately, the west side of the girder succumbed to failure at a recorded shear force of 328 kips. The failure was demonstrated by damage to the top flange of the girder, with loss of load and also damage at the web-top flange interaction zone. Concurrently, on the east side, a shear force

of 334 kips was recorded at this stage. Figure 7.44 and Figure 7.45 show the cracks at the ultimate failure stage of the test.



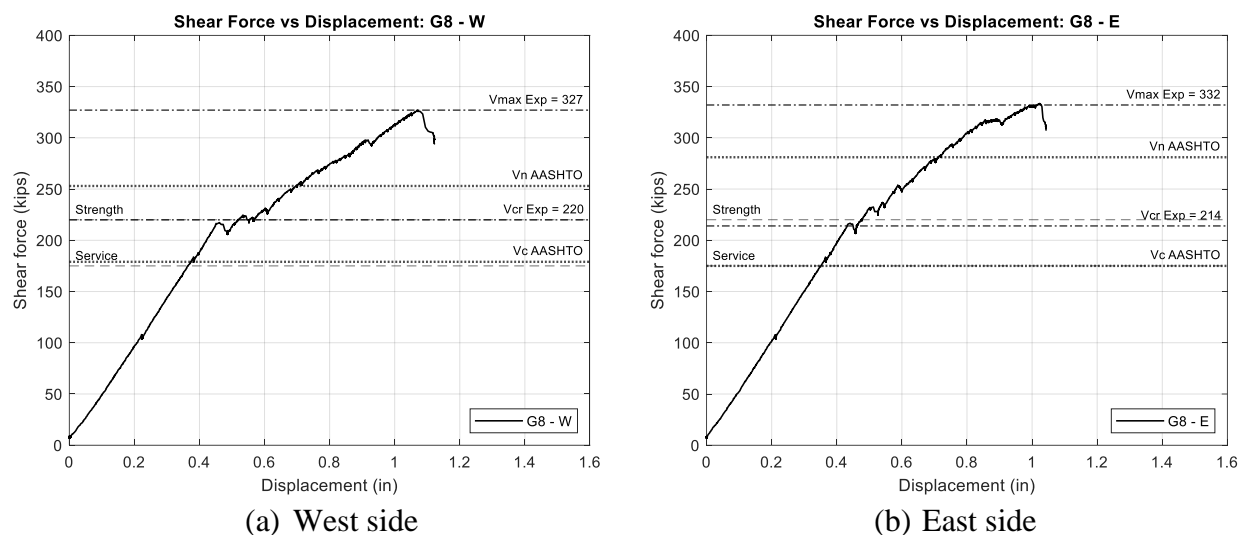
**Figure 7.44. West side of G8 girder at ultimate failure.**



**Figure 7.45. East side of G8 girder at ultimate failure.**

The observed crack widths at the cracking stage for the west side of the girder were in the range of 0.7 mm, while on the side they were in the range of 0.4 mm. The larger crack widths on the west side can be related to wider spacing of stirrups, as in the case of G7. In the preliminary analysis, shear force versus displacement plots offer an initial understanding of the test data and post-cracking behavior. Figure 7.46 illustrates these plots for both sides of the G7 girder.





**Figure 7.46. Shear force versus displacement plots for G8 girder (west and east).**

### 7.1.10 G9 Test

The next girder in the testing matrix is G9; this girder is a variation in shear-span-to-depth ratio in the test setup like G4. The prestressing design of the girder is same as the prototype girder G1 and the other comparative girder G4. The testing of this girder is an insightful comparison in understanding the shear capacity due to the longer testing span. This girder—with an  $a/d$  of 4 combined with G4 having an  $a/d$  of 2.5—provides a broad understanding of effect of shear-span-to-depth ratio. The key design parameters for this girder are shown in Table 7.10.

**Table 7.10. Design parameters for G9 girder.**

Test ID	Girder Type	L (ft)	$f'_{ci}$ (ksi)	$f'_c$ (ksi)	28-day $f'_c$ (ksi)	Spacing (in.)	$f_{yt}$ (ksi)	# of Strands	Harp	$a/d$
G9-W	Tx54	56	6	7	8.5	26	60	34 (2 Top)	Yes (6)	3
G9-E	Tx54	56	6	7	8.5	18	60	34 (2 Top)	Yes (6)	3

The girder also features 6 harped strands, which allows a comparative understanding of  $a/d$  in the presence of harped strands. The shear reinforcement design mirrors that of G1-W (18 in. spacing of 60 ksi) and G2-W (26 in. spacing of 60 ksi). The setup changed for this girder owing to a longer shear span, which meant that the pedestals had to be moved away from the actuators. The girder was subjected to loading in a manner that adhered to the devised loading protocol

specifically designed for this girder. The initial appearance of diagonal cracking was observed on the west side, manifesting as one distinct crack extending from the support and ending at half the distance of the test zone. This occurrence transpired at a recorded shear force of 143 kips. Subsequently, following the restoration of load, the east side of the girder also experienced cracking at the same recorded shear force of 175 kips. On the east side, the cracking formed was a single crack with a steeper crack angle and away from the actuator. During this phase, halt periods were used for crack width measurements and documentation of other pertinent images. Figure 7.47 and Figure 7.48 showcase the extent of cracking damage sustained by this girder.



**Figure 7.47. West side of G9 girder at cracking load.**



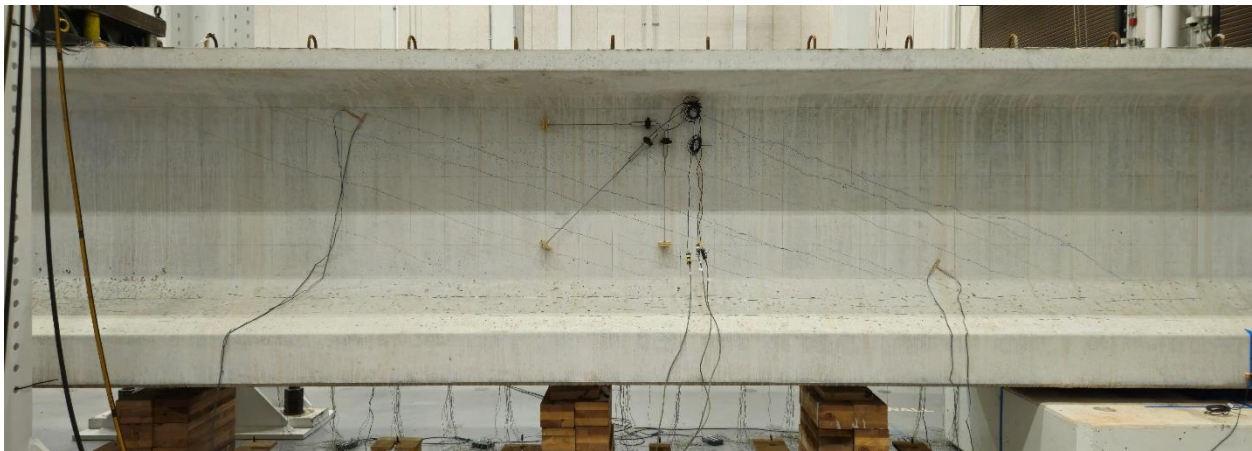
**Figure 7.48. East side of G9 girder at cracking load.**

Ultimately, the west side of the girder succumbed to failure at a recorded shear force of 280 kips. This failure was accompanied by a significant number of shear cracks at a steeper angle ranging

along the entire testing zone. In addition, the shear cracks coalesced in the bottom flange, causing a significant drop in the force. Concurrently, on the east side, a shear force of 30.8 kips was recorded at this stage. Figure 7.49 and Figure 7.50 show the cracks at the ultimate failure stage of the test.

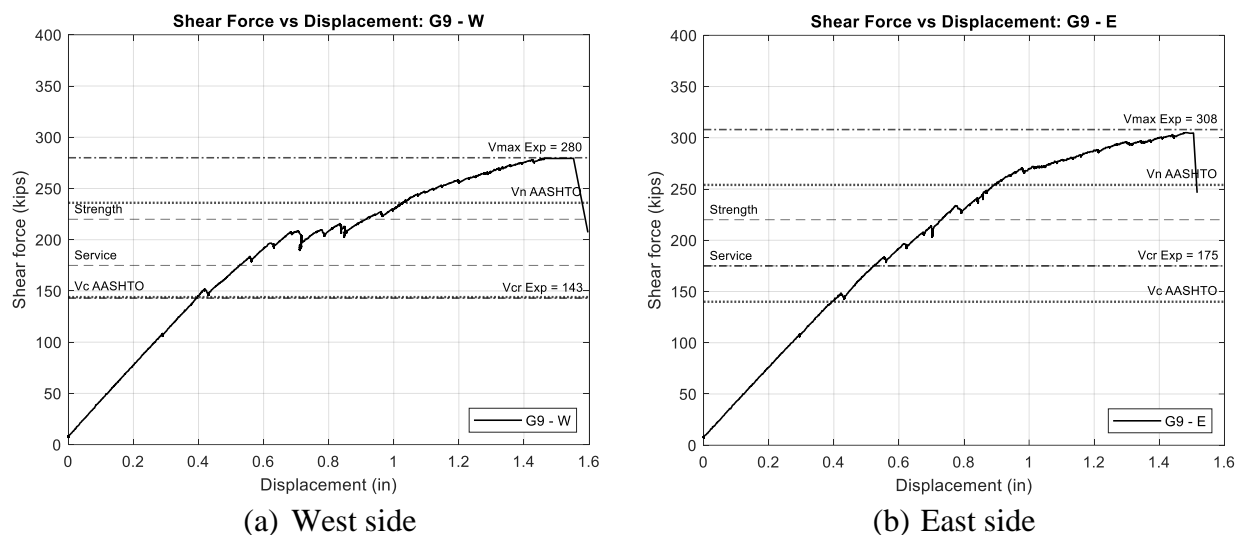


**Figure 7.49. West side of G9 girder at ultimate failure.**



**Figure 7.50. East side of G9 girder at ultimate failure.**

The observed crack widths at the cracking stage for the west side of the girder are in the range of 0.4 mm, while on the east side they are in the range of 0.25 mm. In the preliminary analysis, shear force versus displacement plots offer an initial understanding of the test data and post-cracking behavior. Figure 7.51 illustrates these plots for both sides of the G9 girder.



**Figure 7.51. Shear force versus displacement plots for G9 girder (west and east).**

### 7.1.11 G10 Test

The final girder in this testing program is G10. This Tx70 girder was selected to study the effect of girder depth. The prototype girder is a Tx54 selected based on a detailed study looking into various equations that govern the shear reinforcement spacing and ultimately identify the girder with the major minimum shear reinforcement zone. The size effect phenomenon shows that larger girders exhibit reduced strength compared to smaller ones, making it problematic to extrapolate results from small to large girders directly. This effect is particularly pronounced in girders with minimal shear reinforcement. The key design parameters for this girder are shown in Table 7.11.

**Table 7.11. Design parameters for G10 girder.**

Test ID	Girder Type	Length (ft)	$f'_{ci}$ (ksi)	$f'_c$ (ksi)	28-day $f'_c$ (ksi)	Spacing (in.)	$f_{yt}$ (ksi)	# of Strands	$a/d$
G10-W	Tx70	58	6	7	8.7	40	60	40 (2 Top)	3
G10-E	Tx70	58	6	7	8.7	18	60	40 (2 Top)	3

The shear reinforcement design in the two testing zones of this girder is 18 in. spacing of 60 ksi, as from the TxDOT spacing, and 40 in. spacing of 60 ksi from  $hw/2tan$ . In this setup, the pedestals were positioned further from the actuators to maintain a constant  $a/d$  while changes in



the girder depth adjusted the shear span accordingly. The girder was subjected to loading in a manner that adheres to the devised loading protocol specifically designed for this girder. The initial appearance of diagonal cracking was observed on the east side, manifesting as two distinct widely spaced cracks spanning along the length of the testing zone. This occurrence transpired at a recorded shear force of 285 kips. Subsequently, following the restoration of load, the west side of the girder also experienced cracking at a recorded shear force of 251 kips. On that side, the cracking formed was a single crack with a steeper crack angle and wider crack which can be related to very wide spacing of stirrups. During this phase, halt periods were used for crack width measurements and documentation of other pertinent images. Figure 7.52 and Figure 7.53 showcase the extent of cracking damage sustained by this girder.



**Figure 7.52. West side of G10 girder at cracking load.**



**Figure 7.53. East side of G10 girder at cracking load.**

Ultimately, the west side of the girder succumbed to failure at a recorded shear force of 351 kips. This failure was accompanied by a significant number of shear cracks at a steeper angle ranging along the entire testing zone. In addition, the shear cracks coalesced in the bottom flange, causing significant damage in the bottom flange and web interaction zone along with severe damage to the top flange at the loading point. Concurrently, on the east side, a shear force of 388 kips was recorded at this stage. Figure 7.54 and Figure 7.55 show the cracks at the ultimate failure stage of the test.



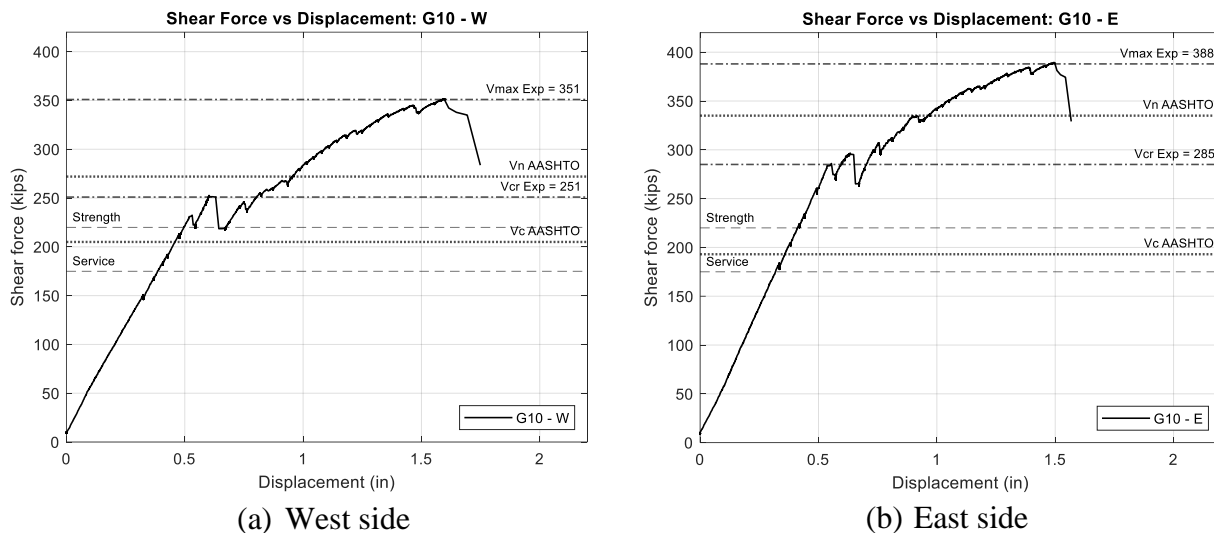
**Figure 7.54. West side of G10 girder at ultimate failure.**



**Figure 7.55. East side of G10 girder at ultimate failure.**

The observed crack widths at the cracking stage for the west side of the girder are in the range of 4.5 mm, while on the east side they are in the range of 0.8 mm. In the preliminary analysis, shear

force versus displacement plots offer an initial understanding of the test data and post-cracking behavior. Figure 7.56 illustrates these plots for both sides of the G9 girder.



**Figure 7.56. Shear force versus displacement plots for G10 girder (west and east).**

### 7.1.12 Full-Scale Testing Observations

The testing phase was completed, with all girders undergoing ultimate failure. The testing phase involved careful planning and detailed instrumentation setup for data acquisition that can be used to make quantifiable conclusions. Each test was preceded by an analytical and computational estimation to devise an appropriate loading protocol such that both sides of the girders approximately reached the maximum shear capacity around the same time and ultimately one side of the girder failed in significant damage. The test program and process were also drafted with various aspects in mind such that careful documentation was necessary for key parameters, such as crack width at the first cracking shear. The tests were also documented with various camera recordings, pictures, and 3D point cloud captures for later investigations and review.

The initial analysis highlights the prominent distinctions among the girders, thereby facilitating insightful comparisons. The shear force versus displacement plots and displacement profile plots serves as the foundational elements in the ensuing comparison study phase, with additional sensor data being integrated to reinforce any potential observations. The preliminary effective comparisons were studied based on the visual observation of the crack pattern; crack

measurements such as crack angles, crack widths, and crack spacing; and shear force versus displacement plots. Based on the observed cracking shear and ultimate shear capacities, the initial point for the trend or effect of the parameter can be gauged. However, these measurements should further be reinforced with additional sensor data and an outcome parametric study.

Table 7.12 shows a summary of these girders that compares the numerical data of cracking and ultimate shear force from the experiments to other computed and analyzed values. The table also shows 1.25 times the cracking and nominal capacities from ACI and AASHTO for understanding the range of observed values. In addition, the ultimate shear capacity predicted by FE models are also listed for comparison which are discussed in detail in Chapter 8. Figure 7.57 and Figure 7.58 show a comparison of experimental strengths to ACI and AASHTO estimates. It should be noted that ACI 318-19 and AASHTO LRFD calculations use  $V_c$  as the estimate for cracking shear strength,  $V_{cr}$ . And for nominal capacity  $V_n$  to compare with the ultimate strength for the code estimates it is used as  $V_c + V_s$  without any reduction factor.

The next section in this chapter reviews the investigation of the necessary effective comparisons of the parameters on which the test matrix was developed.



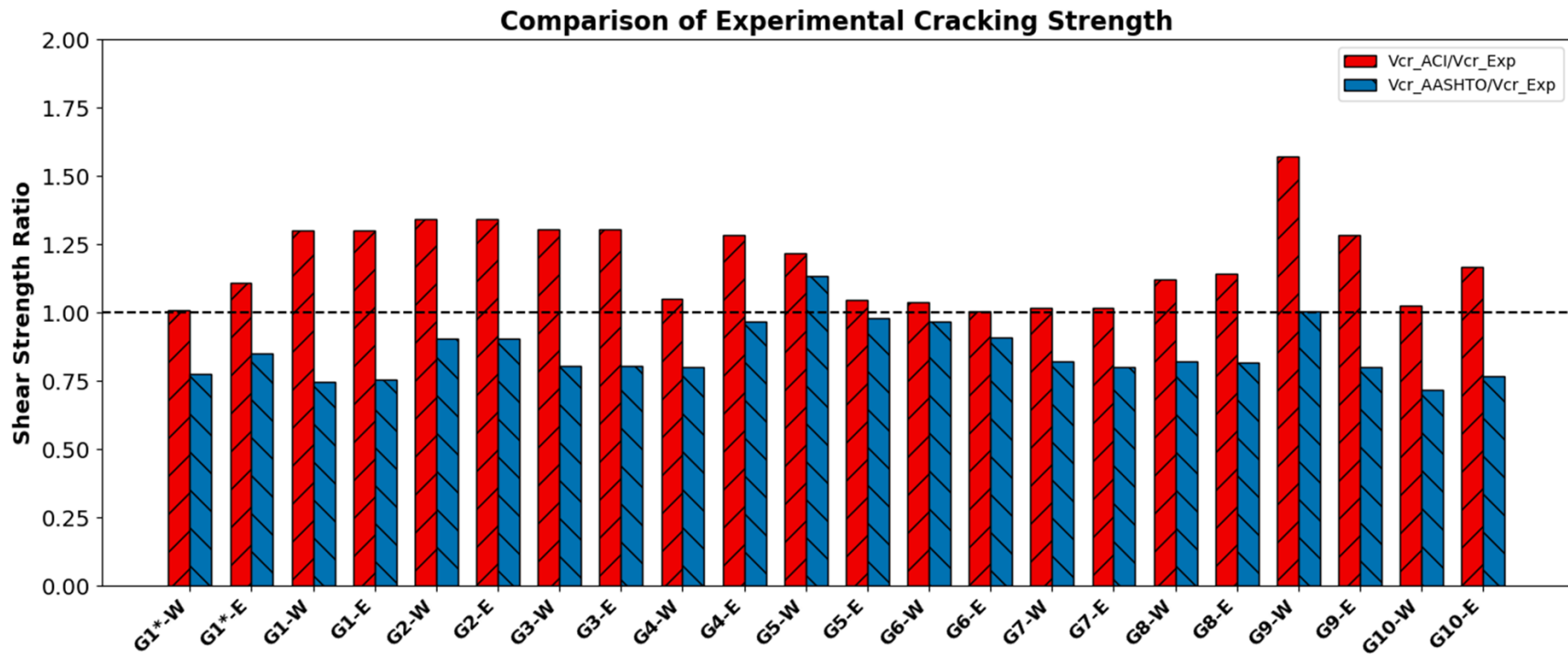
**Table 7.12. Summary of shear force results for all the girders.**

Specimens	G1*-W	G1*-E	G1-W	G1-E	G2-W	G2-E	G3-W	G3-E	G4-W	G4-E	G5-W	G5-E	G6-W	G6-E	G7-W	G7-E	G8-W	G8-E	G9-W	G9-E	G10-W	G10-E
<b>Cracking</b>																						
$V_{cr, exp}$	252	229	215	215	190	190	205	205	214	175	162	188	211	218	176	176	218	214	143	175	285	251
$V_c, AASHTO$	196	195	161	162	172	172	165	165	171	169	184	184	204	198	145	141	179	175	144	140	205	193
$1.25 * V_c, AASHTO$	246	244	203	205	215	215	206	206	218	210	230	230	255	247	181	176	223	218	180	175	256	241
$V_c, ACI$	254	254	280	280	255	255	268	268	225	225	197	197	219	219	179	179	245	245	225	225	293	293
$1.25 * V_c, ACI$	318	318	350	350	319	319	335	335	281	281	246	246	274	274	225	225	306	306	281	281	366	366
<b>Ultimate / Maximum</b>																						
Failure Side	✓			✓	✓		✓		✓		✓		✓		✓		✓		✓		✓	
$V_{max, exp}$	360	352	361	351	292	302	341	354	335	380	292	262	306	373	282	306	325	332	280	308	351	388
$V_{max, FE}$	331	318	334	330	297	304	330	341	291	347	302	286	339	372	289	304	337	350	293	310	367	427
$V_n, AASHTO$	324	315	269	259	220	240	252	279	226	276	271	245	268	314	225	245	253	281	226	254	272	335
$1.25 * V_n, AASHTO$	405	394	336	323	280	300	315	349	283	345	338	306	335	392	282	307	317	351	282	316	340	419
$V_n, ACI$	329	323	343	338	299	285	331	312	255	288	251	235	256	294	223	243	288	308	269	288	331	377
$1.25 * V_n, ACI$	411	404	429	422	374	357	414	389	319	361	313	293	320	368	280	303	361	385	336	360	414	472
<b>Limits</b>																						
Service Limit	175	175	175	175	175	175	175	175	175	175	175	175	175	175	175	175	175	175	175	175	175	175
Strength Limit	220	220	220	220	220	220	220	220	220	220	220	220	220	220	220	220	220	220	220	220	220	220

✓: Failure side which reached the ultimate failure in each girder test.

Note:

- $V_{cr, exp}$  = Cracking shear force of the girder in the test.
- $V_c, AASHTO$  = Contribution of concrete computed using AASHTO (2020) equations.
- $V_c, ACI$  = Contribution of concrete computed using ACI 318-19 (2019) equations.
- $V_{max, exp}$  = Ultimate/maximum load of girder failure in the test.
- $V_{max, FE}$  = Ultimate/maximum load from the analysis of FE models.
- $V_n, AASHTO$  = Nominal strength of girder computed using AASHTO (2020) equations.
- $V_n, ACI$  = Nominal strength of girder computed using ACI 318-19 (2019) equations.



**Figure 7.57. Cracking shear strength ratio comparison between experimental tests, ACI, and AASHTO.**

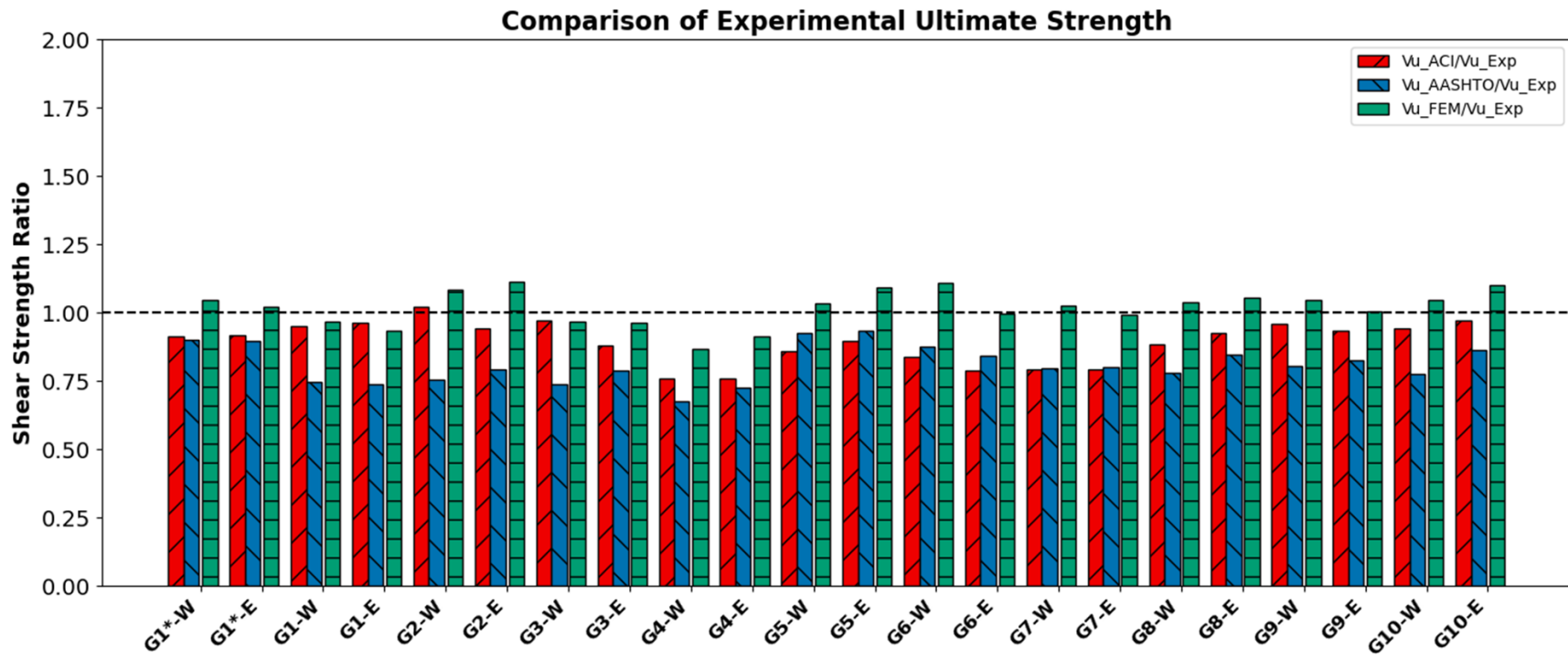


Figure 7.58. Ultimate shear strength ratio comparison between experimental tests, ACI, AASHTO, and finite element method (FEM).

## 7.2 EFFECTIVE COMPARISONS

Following the testing phase, the next step was to utilize the various data collected from the experiments for detailed parametric study and effective comparisons. Preliminary understanding began with the comparison of the key parameters varied in terms of design and testing of the girder. Further, the shear force versus displacement plot along with the cracking and ultimate shear capacities of the girder were compared to understand the change in the capacity with respect to the parameters. In addition, the RSS was also compared to give a quantified comparison of these effects. The RSS is defined as the ratio of shear strength at shear failure over the shear strength at the onset of first diagonal/shear cracking. The preliminary effective comparison also looked into the visual comparison of the cracks at both first cracking and failure stage because it provides an understanding of crack spacing and density.

Of all the effective comparisons, the effect of deck was studied first and in detail due to its critical nature in the decision-making process of the remaining girder testing. The key points and observations from this effective comparison were used to decide whether the testing of other girders would continue with or without a deck. This process is detailed in the following section, and the other effective comparisons are presented with preliminary observations and details.

### 7.2.1 Effect of Deck

The first two girder tests, G1\* and G1, held the principal objective of determining whether the subsequent girders should be tested with or without a deck. A decision was reached through a comprehensive comparison of various responses that encompassed factors such as the observed failure mechanisms, girder strengths, and notable discrepancies between the two testing scenarios. Table 7.13 details the design parameters in both girders.

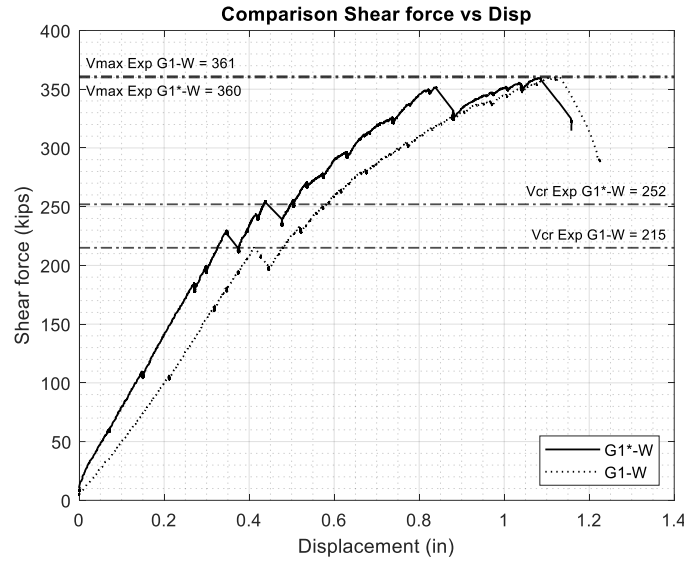
**Table 7.13. Comparison of design parameters between G1\* and G1.**

Test ID	Girder Type	Length (ft)	$f'_{ci}$ (ksi)	$f'_c$ (ksi)	28-day $f'_c$ (ksi)	Spacing (in.)	$f_{yt}$ (ksi)	# of Strands	Harp ?	$a/d$
G1*-W	Tx54	52	6	7	9.2	18	60	34 (2 Top)	No	3
G1*-E	Tx54	52	6	7	9.2	26	80	34 (2 Top)	No	3
G1-W	Tx54	52	6	7	8.8	18	60	34 (2 Top)	No	3
G1-E	Tx54	52	6	7	8.8	26	80	34 (2 Top)	No	3

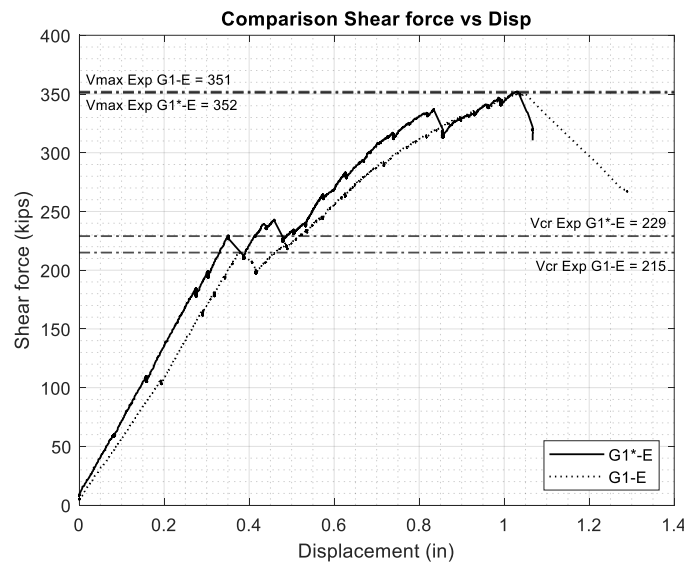
As evident from the Table 7.13, the design parameters for the two girders are identical, including having the same prestressing ratio, shear reinforcement, and strand layout. Nevertheless, a crucial divergence arises in relation to the shear-span-to-depth ratio,  $a/d_v$ . The “ $d$ ” in the shear-span-to-depth ratio undergoes alteration with the inclusion of a deck, given that it affects the overall effective depth of the girder if the deck acts as a composite section. To enable a meaningful comparison pertaining to the presence of the deck, a decision was made to maintain a consistent  $a/d$ , thus resulting in different span lengths within the testing zones.

The adapted span lengths for the girders were 15.5 ft for the G1\* girder and 13 ft for the G1 girder. This necessitated a minor recalibration of the pedestal positions involving their closer alignment to the actuators for the G1 girder test. Although the instrumentation design remained largely unaltered, some adjustments were made to the positions of the string potentiometers, a consequence of the pedestal repositioning. It is worth noting that the spacing of the string potentiometers remained consistent at 2 ft, extending from the load point to the end of the girder, thus facilitating the acquisition of the displacement profile.

In this manner, the process yielded two distinct comparative cases to scrutinize the impact of the deck’s presence: G1\*-W versus G1-W and G1\*E versus G1-E. To identify key disparities, a comprehensive analysis involved a comparison of the shear force versus displacement plots, coupled with an examination of crack measurements. This approach served as a reliable means to identify any notable discrepancies that may arise between the two scenarios. Figure 7.59 and Figure 7.60 show the comparison between shear force versus displacement plots of west and east sides.



**Figure 7.59. Shear force versus displacement comparison of G1\*-W versus G1-W.**


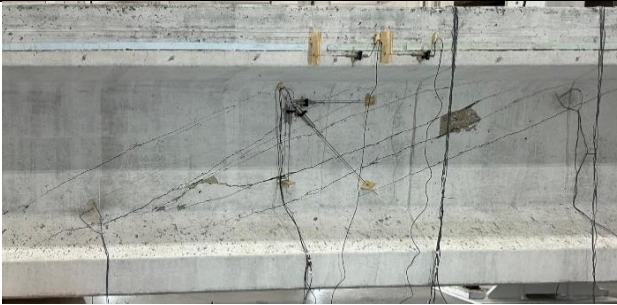

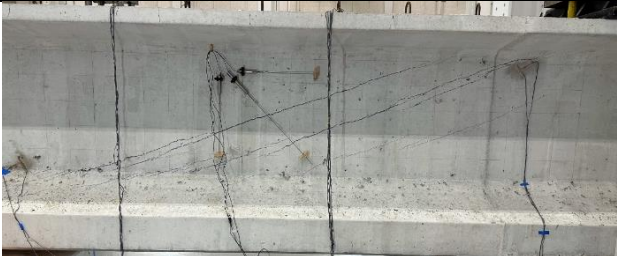


**Figure 7.60. Shear force versus displacement comparison of G1\*-E versus G1-E.**


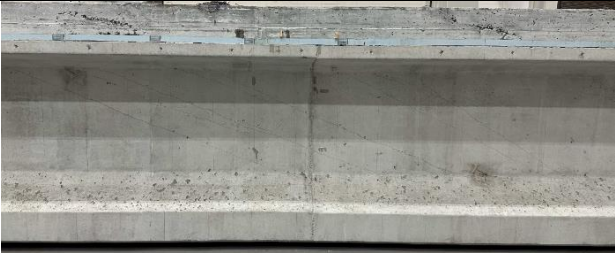
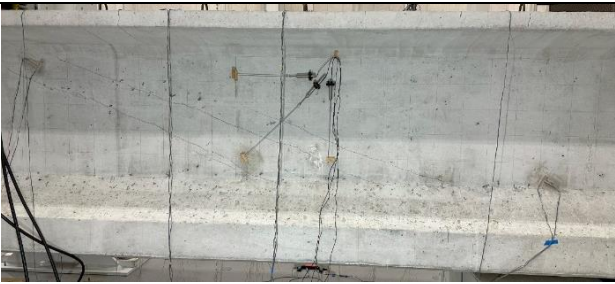

Notably, the girder equipped with a deck exhibited higher cracking shear strength in both scenarios, suggesting a possible manifestation of complete composite action facilitated by the presence of the deck. The girder with the deck slab was stiffer, which is evident before the first cracking owing to composite cross section. However, it is noteworthy that the observed ultimate shear strengths are remarkably similar for both spacings with 1 kip difference. This element could be attributed to the potential limitation in achieving full composite action of the deck, given the minimal shear reinforcement present within these specific testing regions.

For G1\*-W versus G1-W, the RSS is 1.43 and 1.68, respectively, indicating a higher RSS value for the girder without the deck. Similarly, for G1\*-E versus G1-E, the RSS is 1.54 and 1.63, respectively, indicating a similar pattern of a higher RSS for the girder without the deck. It is noted that the 26-inch spacing configuration had a similar or larger RSS than the 18-in. spacing. Also, all achieved RSS values were larger than 1.30 to 1.35, which are the values used in the calculation of the minimum shear reinforcement. Table 7.14 and Table 7.15 show the visual comparison of cracking patterns on the girder.

**Table 7.14. Visual comparison of G1\*-W versus G1-W.**

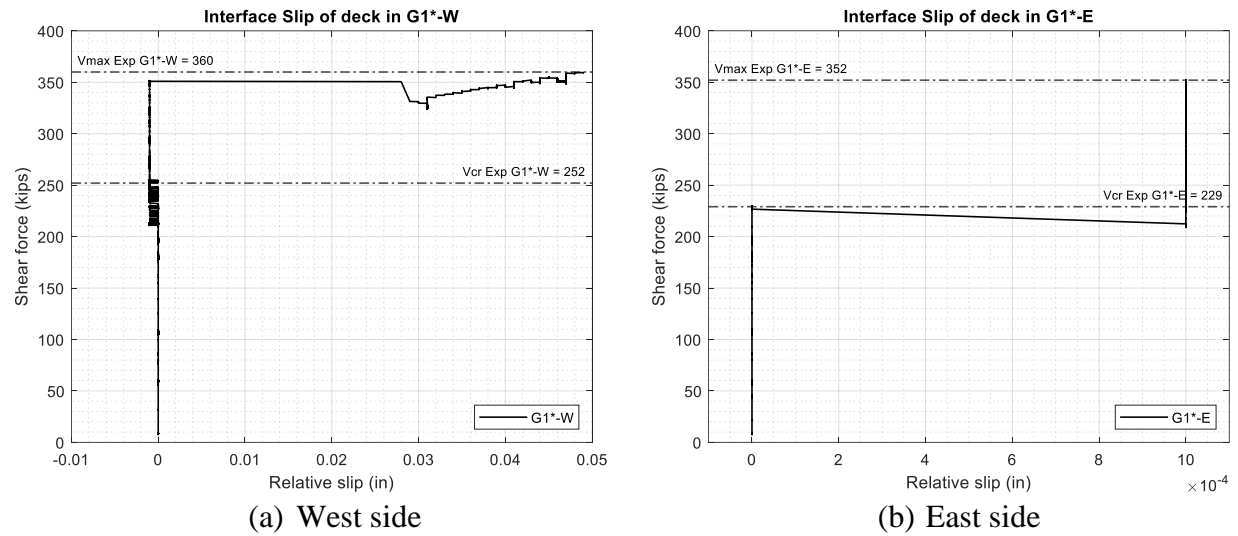
<b>G1*-W</b>	<b>Cracking</b>	
	<b>Ultimate/Maximum</b>	
<b>G1-W</b>	<b>Cracking</b>	
	<b>Ultimate/Maximum</b>	

**Table 7.15. Visual comparison of G1\*-E versus G1-E.**

<b>G1*-E</b>	<b>Cracking</b>	
	<b>Ultimate/Maximum</b>	
<b>G1-E</b>	<b>Cracking</b>	
	<b>Ultimate/Maximum</b>	

Furthermore, the data from the LVDTs, which monitored the relative displacement between the deck and the girder, indicated a degree of slippage after the cracking load. This slippage intensified considerably as the ultimate load was reached, culminating in noticeable sliding between the components. Figure 7.61 shows the relative sliding between the girder and the deck on both west and east sides.





**Figure 7.61. Interface slip of deck in G1\* girder.**

This observation strengthens the notion that post-cracking behavior of the G1\* girder involved deck slip. Moreover, a comprehensive comparison involves scrutinizing crack measurements such as crack widths at the cracking stage, crack angles, and spacings. This analysis aims to shed light on the influence of the deck on the girder's failure mechanisms. The visual crack comparison for both cracking and ultimate stages of the girder were compared individually for east and west sides in Table 7.16. In addition, the summary of the crack measurements is presented in Table 7.16.

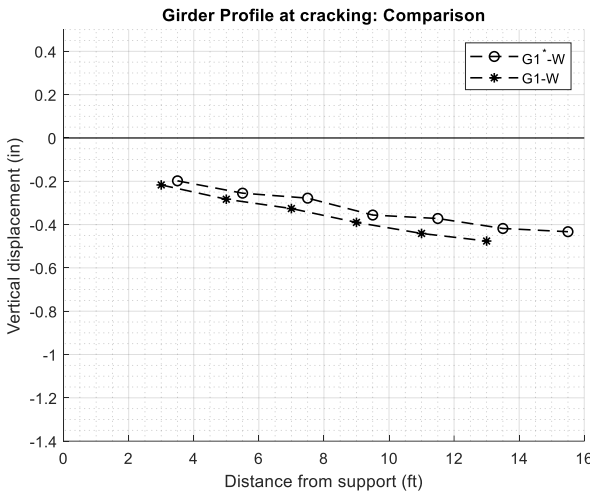
**Table 7.16. Comparison of crack measurement for G1\* versus G1.**

Level	Crack Properties	G1*-W	G1*-E	G1-W	G1-E
<b>Cracking</b>	Crack Angles (deg.)	17-30	20-28	17-27	20-22
	Crack width (mm)	0.15-0.7	0.2-0.4	0.15-0.2	0.25-0.2
	Crack spacing (in.)	7.1-16	5.4-13.4	7.1-10.8	5.1-7.6
<b>Ultimate/Maximum</b>	Crack Angles (deg.)	17-30	20-28	17-27	18-22
	Crack spacing (in.)	3.1-7.4	5.4-13.4	7.1-10.8	3.8-7.6

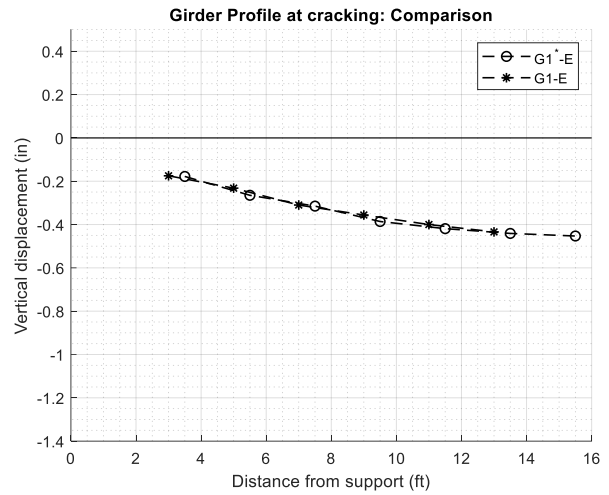
The crack measurements reveal larger crack widths for the deck-equipped girder in both instances. This result can be attributed to the extra dead load of the deck, which prompts wider crack openings. Remarkably, crack angles were nearly identical on the west side of the girder, whereas slightly steeper cracks were observed for G1\* on the east side. This variation could

potentially lead to fewer R-bars intercepting the cracks. However, it is noteworthy that this discrepancy did not translate into any observable disparity in ultimate strength outcomes.

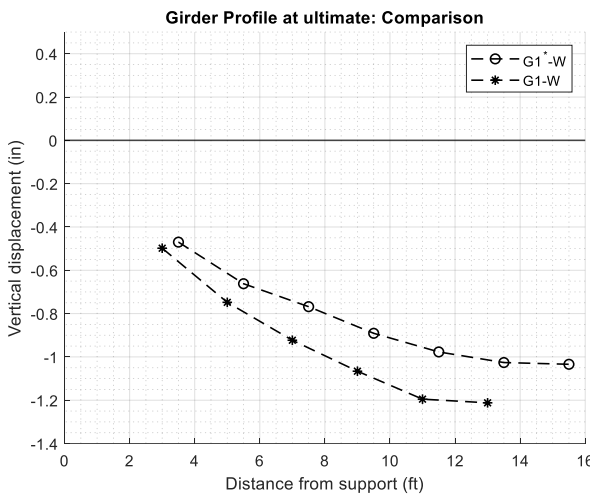
The girder's profile was constructed utilizing the girder displacement data acquired from the string pots strategically positioned beneath the girder, which spanned from the support to the load point. To ensure accuracy, this deflection was normalized and factored in the support deformation, as quantified by the LVDT measurements taken from the underlying bearing pad. The resultant girder profile offers insights into the displacement distribution during both cracking and ultimate stages. This depiction effectively captures the decrease in stiffness exhibited by the girder in its post-cracking behavior. In addition, the girder displacement profile is also compared (Figure 7.62) at the cracking and ultimate stages to identify potential differences.



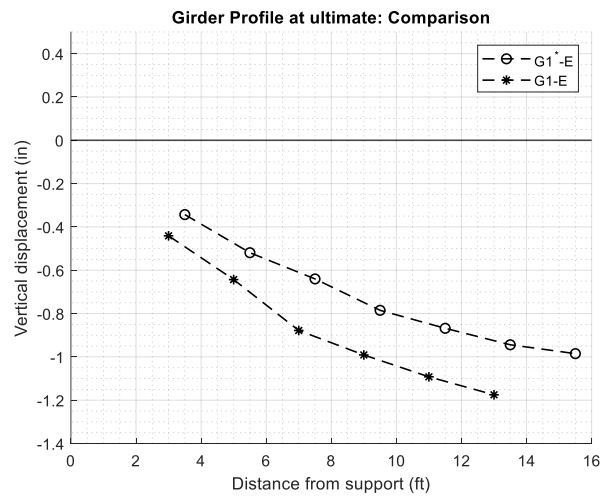
(a) West side



(b) East side



(c) West side



(d) East side

**Figure 7.62. Comparison of girder profile at cracking and ultimate: G1\* versus G1.**

The girder profile for both the west and east side remained largely consistent regardless of the presence of the deck. Minor variations are noticeable, particularly during the post-cracking phase at the ultimate failure stage. Notably, these disparities do not exert any credible impact on the ultimate strength of the girder. Following deliberations within the project team and in consultation with the TxDOT team, it was decided that, given the closely resembling failure mechanisms and ultimate strengths, future girder tests will not involve the inclusion of a deck. These conclusions are substantiated by the outcomes of FE analyses applied to the G1\* and G1 models, which have been extensively detailed in Section 8.3.

## 7.2.2 Effect of Shear Reinforcement Spacing

The spacing of shear reinforcement is one of the major aspects studied in effective comparisons. This factor influences the number of stirrups intercepting the diagonal cracks during the post-cracking behavior of the girder, as well as the strength provided by the stirrups. The TxDOT girder designs typically use 60 ksi bars and a spacing of 18 in. in the minimum shear reinforcement zones. However, as a part of the effective comparison, the other two spacing provisions were obtained using the ACI 318-19 (2019) equations and  $h_w/2 \tan(\theta)$  or maximum spacing by AASHTO (2020) equations. Table 7.17 and Table 7.18 depict the design parameters for these effective comparisons.

**Table 7.17. Comparison of design parameters for G1-W versus G2-W versus G2-E.**

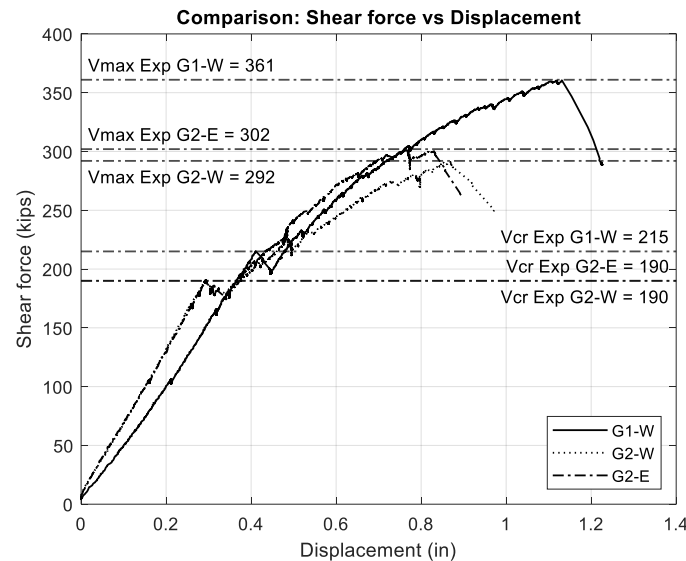
Test ID	Girder Type	$f'_{ci}$ (ksi)	$f'_c$ (ksi)	28-day $f'_c$ (ksi)	Spacing (in.)	$f_{yt}$ (ksi)	# of Strands	Harp?	$a/d_v$
G1-W	Tx54	6	7	8.8	18	60	34	No	3
G2-W	Tx54	6	7	8.2	38	60	34	No	3
G2-E	Tx54	6	7	8.2	26	60	34	No	3

**Table 7.18. Comparison of design parameters for G3-W versus G3-E.**

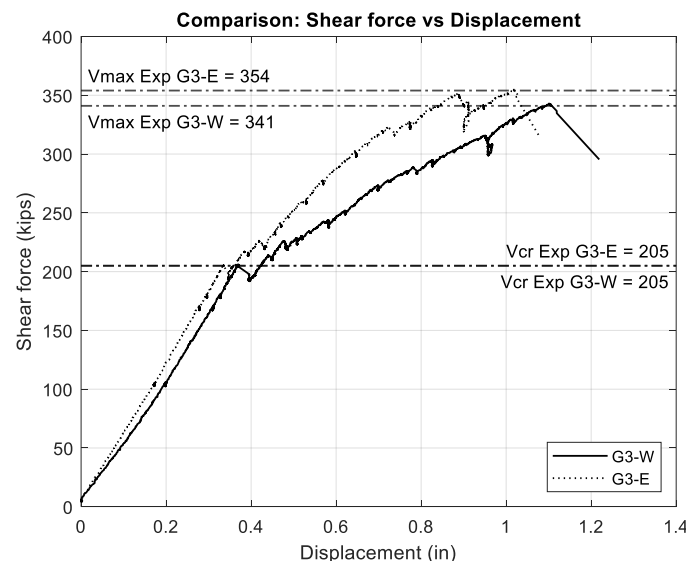
Test ID	Girder Type	$f'_{ci}$ (ksi)	$f'_c$ (ksi)	28-day $f'_c$ (ksi)	Spacing (in.)	$f_{yt}$ (ksi)	# of Strands	Harp?	$a/d_v$
G3-W	Tx54	6	7	8.7	26	60	34	Yes (6)	3
G3-E	Tx54	6	7	8.7	18	60	34	Yes (6)	3

The comprehensive assessment involving G1-W, G2-W, and G2-E pertains to a comparative exploration of girder designs sharing identical prestressing parameters without harped tendons. The uniformity of the  $a/d_v$  ratio across all three specimens ensures a consistent basis for evaluating diverse spacing provisions. This assessment investigated the variances associated with the 60 ksi bars, notably manifesting as 18 in. spacing in G1-W, 26 in. spacing in G2-W, and 38 in. spacing in G2-E. The subsequent analysis, G3-W versus G3-E, addressed a parallel investigation involving girder designs featuring harped tendons. These design variants scrutinize two distinct spacing configurations for 60 ksi bars: 18 in. spacing in G3-E and 26 in. spacing in G3-W. The examination meticulously investigated the influence of shear reinforcement spacing in both scenarios—those with and without harped tendons. Subsequently, in Section 7.2.4, a comprehensive evaluation of the impact of harped tendons is undertaken with due diligence. The

comparison is analyzed with the shear force versus displacement plots of the different test specimens in Figure 7.63 and Figure 7.64.



**Figure 7.63. Shear force versus displacement comparison: G1-W versus G2-W versus G2-E.**



**Figure 7.64. Shear force versus displacement comparison: G3-W versus G3-E.**

The initial comparison reveals notable differences, with the 18 in. spacing specimen exhibiting significantly higher cracking shear force (25 kips) and ultimate shear force (60 kips) when juxtaposed with the other two spacing provisions. In contrast, the performance of the 26 in. spacing specimen, as per ACI provisions, aligns closely with the  $h_w/2 \tan(\theta)$  spacing.

However, in the second comparison, which considers the influence of harped strands, the discrepancy between the cracking strengths is notably reduced to a lower margin of 13 kips. This intriguing outcome suggests that while the 18 in. spacing configuration exhibits superior strength, the effects of harped strands warrant further in-depth investigation. In terms of RSS, the 18 in. spacing configuration achieved an RSS of 1.68, while the 26 in. spacing configuration and the 38 in. spacing configuration achieved an RSS of 1.59 and 1.54, respectively. Interestingly, all designs appear to have acceptable RSS, since most RSS values adopted in the literature are in the range of 1.3 to 1.35.

In addition to these, the comparisons of G7-W versus G7-E, G8-W versus G8-E, and G10-W versus G10-E can also be used for some understanding of the effect of  $s/d$ . G7-W versus G7-E is designed to be a low concrete strength girder with the spacings from ACI 318-19 equations (26 in.) and TxDOT standard usage (18 in.). G8-W versus G8-E is a similar girder in terms of spacing but designed to be a higher-strength girder compared to the prototype girder design strength. G10-W versus G10-E is larger depth girder, Tx70, with two spacings from TxDOT standard usage (18 in.) and  $h_w/(2 * \tan \theta)$  equation spacing. The design parameters for these comparisons are detailed in Table 7.19, Table 7.20, and Table 7.21.

**Table 7.19. Comparison of design parameters for G7-W versus G7-E.**

Test ID	Girder Type	$f'_{ci}$ (ksi)	$f'_c$ (ksi)	28-day $f'_c$ (ksi)	Spacing (in.)	$f_{yt}$ (ksi)	# of Strands	Top Strands	Harp?	a/ $d_v$
G7-W	Tx54	4	5	8.2	26	60	24	2	No	3
G7-E	Tx54	4	5	8.2	18	60	24	2	No	3

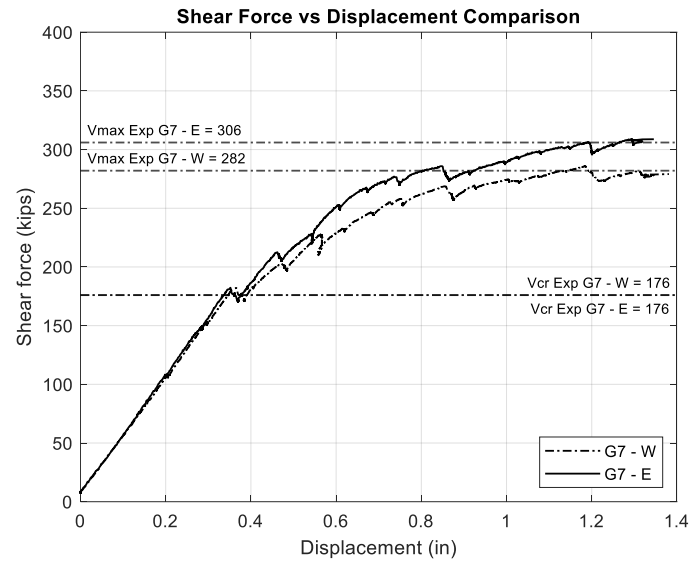
**Table 7.20. Comparison of design parameters for G8-W versus G8-E.**

Test ID	Girder Type	$f'_{ci}$ (ksi)	$f'_c$ (ksi)	28-day $f'_c$ (ksi)	Spacing (in.)	$f_{yt}$ (ksi)	# of Strands	Top Strands	Harp?	a/ $d_v$
G8-W	Tx54	6	8.5	<b>9.6</b>	26	60	38	2	No	3
G8-E	Tx54	6	8.5	<b>9.6</b>	18	60	38	2	No	3

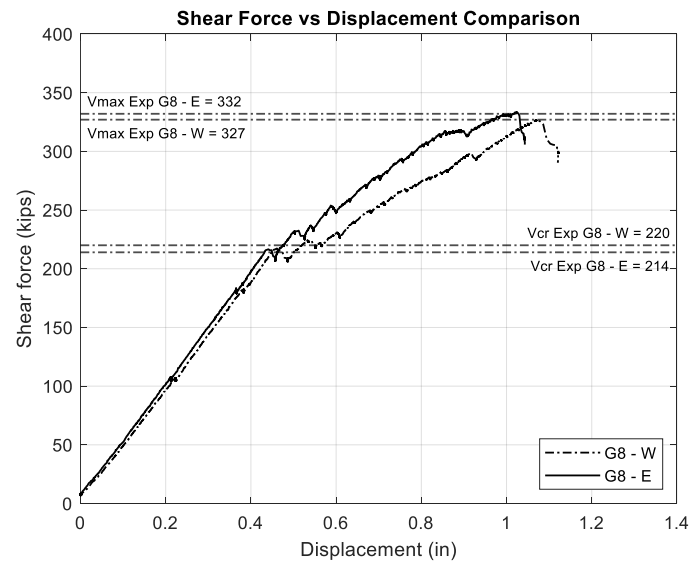
**Table 7.21. Comparison of design parameters for G10-W versus G10-E.**

Test ID	Girder Type	$f'_{ci}$ (ksi)	$f'_c$ (ksi)	28-day $f'_c$ (ksi)	Spacing (in.)	$f_{yt}$ (ksi)	# of Strands	Top Strands	Harp?	a/ $d_v$
G10-W	Tx70	6	7	<b>9.2</b>	40	60	40	2	No	3
G10-E	Tx70	6	7	<b>9.2</b>	18	60	40	2	No	3

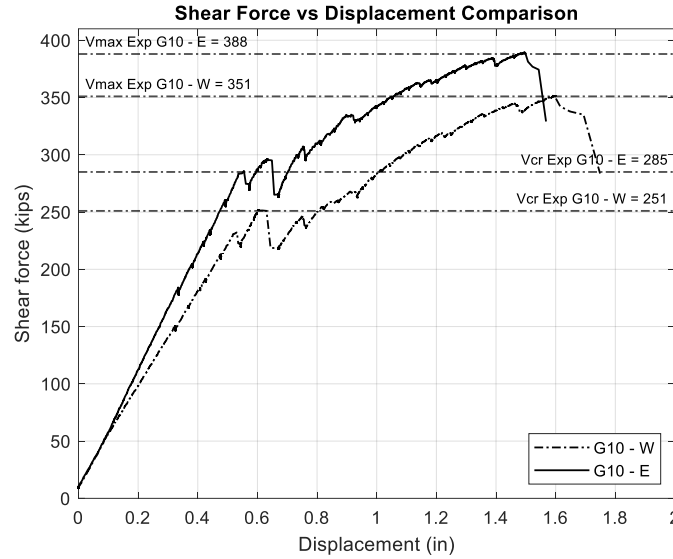
The comparison was analyzed with the shear force versus displacement plots of the different test specimens in Figure 7.65, Figure 7.66, and Figure 7.67.



**Figure 7.65. Shear force versus displacement comparison: G7-W versus G7-E.**



**Figure 7.66. Shear force versus displacement comparison: G8-W versus G8-E.**



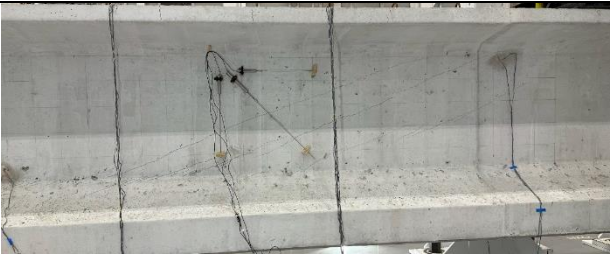
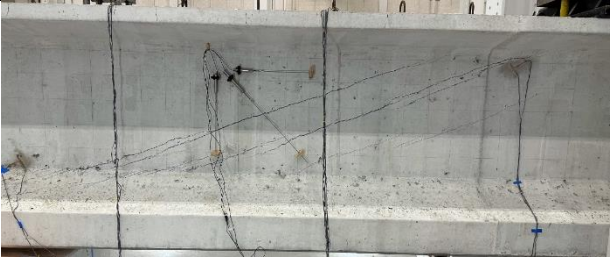
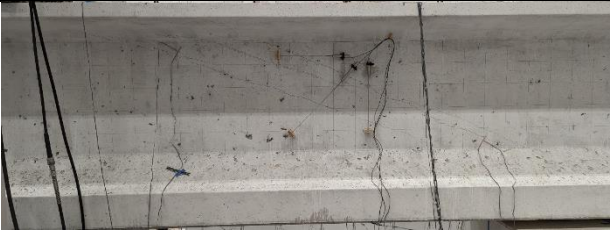
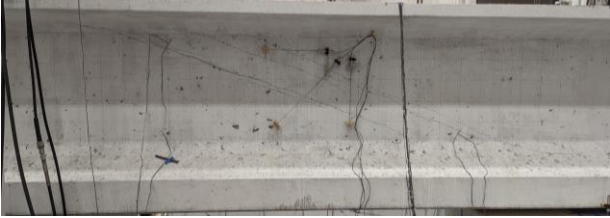


**Figure 7.67. Shear force versus displacement comparison: G10-W versus G10-E.**

For G7-W versus G7-E, the first cracking shear was the same for both the sides, which is 176 kips, while the ultimate shear capacity was 282 kips for the 26 in. spacing and 306 kips for the 18 in. spacing. For G8-W versus G8-E, a similar pattern is observed, with the first cracking shear occurring at almost the same shear capacity—218 kips and 214 kips, and the ultimate shear capacity is 325 kips for 26 in. and 332 kips for 18 in. spacing. Similarly, for G10-W versus G10-E, the first cracking shear for 40 in. spacing is 285 kips while for 18 in. spacing it is 251 kips, marking a higher cracking shear for larger spacing. However, for the ultimate shear capacity, the significant difference in the spacing is clearly seen because the 40 in. side failed at a shear of 351 kips while the other side held up at 388 kips.

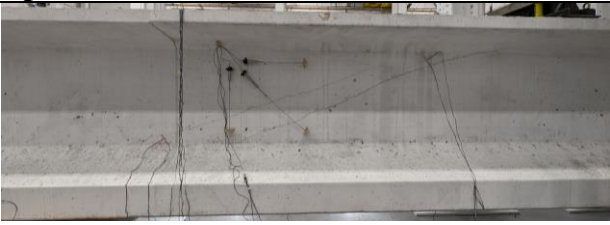



For these cases, the RSS values for G7-W versus G7-E were 1.60 and 1.74, respectively, indicating a higher value for the 18 in. spacing. In the case of G8-W versus G8-E, the RSS values were 1.49 and 1.55, respectively, also depicting a higher ratio for the 18 in. spacing. In the comparison for Tx70 for G10-W versus G10-E, the RSS values were 1.24 and 1.55, respectively. However, almost all the RSS values are higher than 1.3. So, further detailed investigation is needed to check the effect of spacing for each individual scenario. A more comprehensive understanding can be achieved through an examination of crack measurements and crack maps (Table 7.22, Table 7.23, Table 7.24, Table 7.25, and Table 7.26).






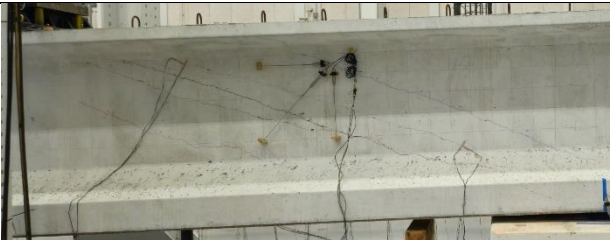
**Table 7.22. Visual comparison of G1-W versus G2-E versus G2-W.**

<b>G1-W</b>	<b>Cracking</b>	
	<b>Ultimate/Maximum</b>	
<b>G2-E</b>	<b>Cracking</b>	
	<b>Ultimate/Maximum</b>	
<b>G2-W</b>	<b>Cracking</b>	
	<b>Ultimate/Maximum</b>	

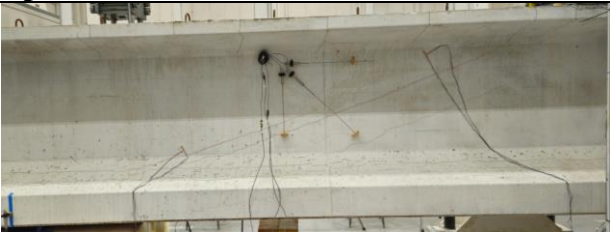
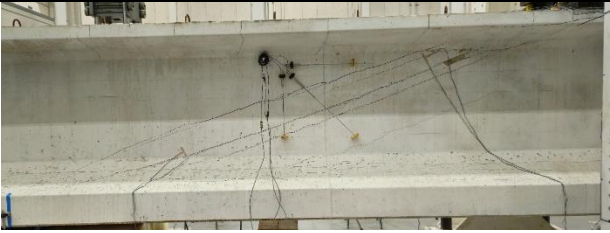
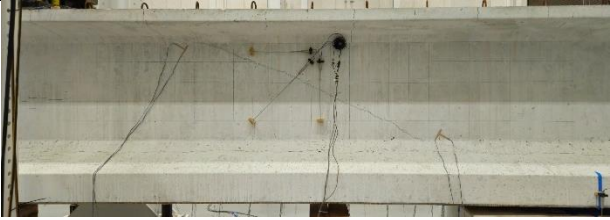

**Table 7.23. Visual comparison of G3-W versus G3-E.**

<b>G3-W</b>	<b>Cracking</b>	
	<b>Ultimate/Maximum</b>	
<b>G3-E</b>	<b>Cracking</b>	
	<b>Ultimate/Maximum</b>	



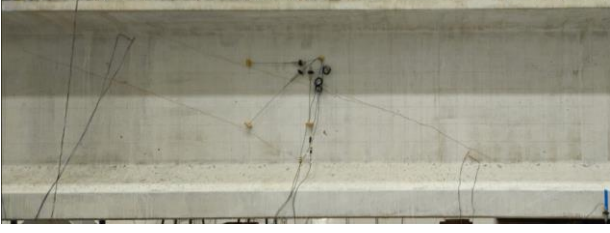

**Table 7.24. Visual comparison of G7-W versus G7-E.**

<b>G7-W</b>	<b>Cracking</b>	
	<b>Ultimate/Maximum</b>	
<b>G7-E</b>	<b>Cracking</b>	
	<b>Ultimate/Maximum</b>	

**Table 7.25. Visual comparison of G8-W versus G8-E.**

<b>G8-W</b>	<b>Cracking</b>	
	<b>Ultimate/Maximum</b>	
<b>G8-E</b>	<b>Cracking</b>	
	<b>Ultimate/Maximum</b>	

**Table 7.26. Visual comparison of G10-W versus G10-E.**

<b>G10-W</b>	<b>Cracking</b>	
	<b>Ultimate/Maximum</b>	
<b>G10-E</b>	<b>Cracking</b>	
	<b>Ultimate/Maximum</b>	

The analysis of crack measurements in the first comparison involving  $s/d$  without harped tendons reveals that the 18-inch spacing exhibited lower crack angles and narrower crack widths than the other spacing provisions. Furthermore, the crack distribution was denser in the other two spacing provisions, contrasting with the more spaced-out cracking in the 18-inch spacing. However, when comparing girder behavior with harped strands, the crack spacing was nearly identical, with slightly wider cracks observed in the 26-inch spacing. Nevertheless, the crack angles are steeper for the 18-inch spacing in this comparison. However, in-depth analysis of the data needs to be performed, and the effective comparisons for different provisions or equations used to select the shear reinforcement spacing also need to be analyzed.

### 7.2.3 Effect of Yield Strength of R-Bars

The yield strength of the R-bars plays a significant role in determining the shear resistance provided by the shear reinforcement. Typically, TxDOT girder designs utilize 60 ksi bars for shear reinforcement. The experiments explore the impact of using higher-strength stirrups, which can affect the girder's performance in two ways. One way is through spacing considerations; higher-strength stirrups may result in greater spacing between them or reach the maximum spacing provision given by AASHTO. This factor can influence the girder's performance by reducing the number of stirrups intercepting diagonal cracks. The second consideration is the lower deformation capacity of high-strength steel, which might result in reduced ductility of the girder. The design parameters for these effective comparisons are shown in Table 7.27 and Table 7.28.

**Table 7.27. Comparison of design parameters for G1\*-W versus G1\*-E.**

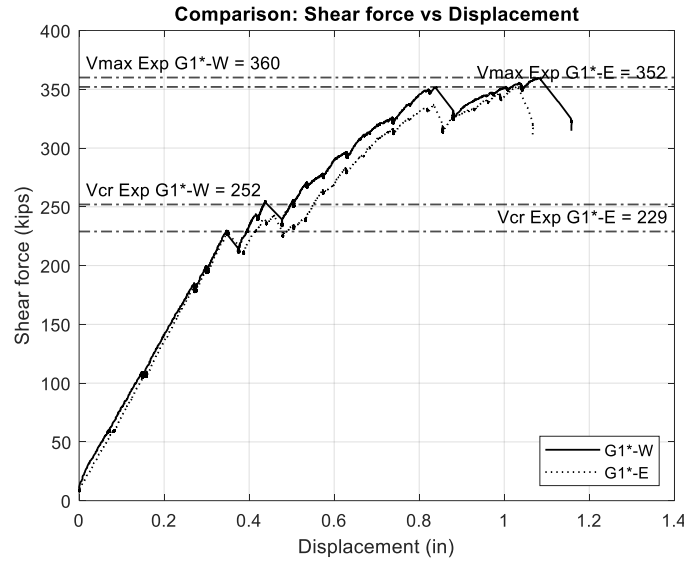
Test ID	Girder Type	$f'_{ci}$ (ksi)	$f'_c$ (ksi)	28-day $f'_c$ (ksi)	Spacing (in.)	$f_{yt}$ (ksi)	# of Strands	$a/d_v$
G1*-W	Tx54	6	7	9.2	18	60	34	3
G1*-E	Tx54	6	7	9.2	26	80	34	3

**Table 7.28. Comparison of design parameters for G1-W versus G1-E.**

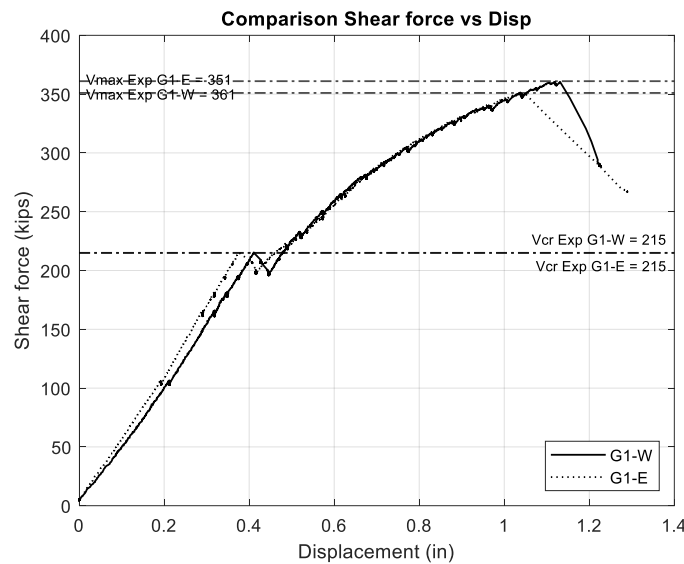
Test ID	Girder Type	$f'_{ci}$ (ksi)	$f'_c$ (ksi)	28-day $f'_c$ (ksi)	Spacing (in.)	$f_{yt}$ (ksi)	# of Strands	$a/d_v$
G1-W	Tx54	6	7	8.8	18	60	34	3
G1-E	Tx54	6	7	8.8	26	80	34	3

The effective comparisons of G1\*-W versus G1\*-E and G1-W versus G1-E investigated the impact of varying stirrup strength from 60 ksi to 80 ksi. To ensure an equivalent overall strength contributed by the stirrups, spacing was adjusted accordingly. Specifically, the comparison examined the effects of 18 in. spacing of 60 ksi bars versus 26 in. spacing of 80 ksi bars. The comparative analysis began with an examination of shear force versus displacement plots for the two sides being compared (Figure 7.68 and Figure 7.69).





**Figure 7.68. Shear force versus displacement comparison: G1\*-W versus G1\*-E.**







**Figure 7.69. Shear force versus displacement comparison: G1-W versus G1-E.**

In both cases, the girder's stiffness appears to be almost identical. However, the reinforcement with 18 in. spacing yielded a higher maximum strength than the higher-strength bars, with a difference in the range of 8–10 kips. In a comparison of RSS, for G1\*-W versus G1\*-E, the ratio was 1.43 for 60 ksi bars and 1.54 for 80 ksi bars, thus showing a higher ratio for the high-strength stirrups. For G1-W versus G1-E, the ratio was 1.68 for 60 ksi bars and 1.63 for 80 ksi bars, thereby indicating a slightly lower ratio. The effect of high-strength stirrups seems to be significant for the comparison in the case of the deck, and the difference reduces for the

comparison without the deck. This outcome requires further investigation into these effective comparisons. The next aspect of comparison will involve examining crack measurements and their distribution in Table 7.29 and Table 7.30.


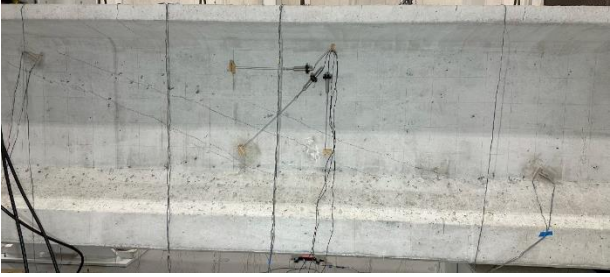

**Table 7.29. Visual comparison of G1\*-W versus G1\*-E.**

<b>G1*-W</b>	<b>Cracking</b>	
	<b>Ultimate/Maximum</b>	
<b>G1*-E</b>	<b>Cracking</b>	
	<b>Ultimate/Maximum</b>	

**Table 7.30. Visual comparison of G1-W versus G1-E.**

<b>G1-W</b>	<b>Cracking</b>	
-------------	-----------------	--



	<b>Ultimate/Maximum</b>	
<b>G1-E</b>	<b>Cracking</b>	
	<b>Ultimate/Maximum</b>	

Based on the observations, it is noted that the crack angles are lower on the side with 26 in. spacing, leading to an equivalent number of stirrups intercepting the diagonal cracks. Additionally, the crack distribution appears denser in the case of the G1 girder with 26 in. spacing. However, crack widths are similar in both cases for the G1 girder, while the G1\* girder exhibits higher crack widths on the side with 18 in. spacing. To draw more definitive conclusions, further investigation incorporating strain data from the concrete and R-bars for a comprehensive analysis is required.

#### **7.2.4 Effect of Harped Strands**

The girder designs incorporate a comparison aimed at studying the impact of harped strands. Harped strands contribute significantly to the shear capacity of the girder due to the vertical component of the prestressing force generated by the inclined angle of the harped prestressing tendons. In terms of design, this contribution from the prestressing force is factored into the cracking shear strength of the girder, as opposed to stirrups, which contribute post-cracking. The comparisons of G1-W versus G3-E and G2-E versus G3-W delved into the impact of harped

strands on girder behavior. In both comparisons, the spacing of the R-bars, along with other parameters such as shear-span-to-depth ratio and concrete strength, remains consistent, with the sole variation being the presence of harped strands. The design parameters are shown in Table 7.31 and Table 7.32.

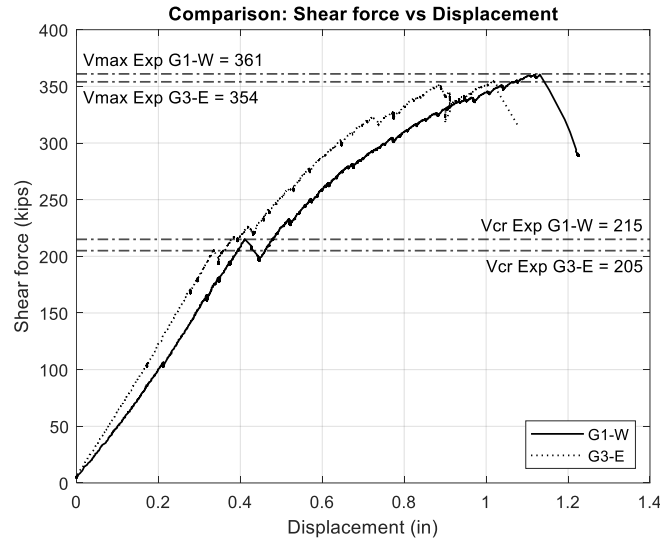
**Table 7.31. Comparison of design parameters for G1-W versus G3-E.**

Test ID	$f'_{ci}$ (ksi)	$f'_c$ (ksi)	28-day $f'_c$ (ksi)	Spacing (in.)	$f_{yt}$ (ksi)	# of Strands	Harp?	$h$ (Harp)	$a/d_v$
G1-W	6	7	8.8	18	60	34	No	0	3
G3-E	6	7	8.7	18	60	34	Yes (6)	20.5	3

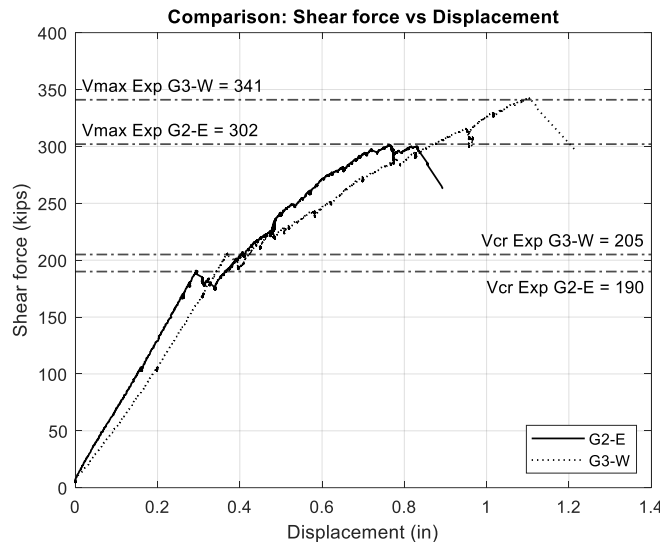
**Table 7.32. Comparison of design parameters for G2-E versus G3-W.**

Test ID	$f'_{ci}$ (ksi)	$f'_c$ (ksi)	28-day $f'_c$ (ksi)	Spacing (in.)	$f_{yt}$ (ksi)	# of Strands	Harp?	$h$ (Harp)	$a/d_v$
G2-E	6	7	8.2	26	60	34	No	0	3
G3-W	6	7	8.7	26	60	34	Yes (6)	20.5	3

In the G1-W versus G3-E comparison, the focus is on the effect of harped strands in conjunction with a shear reinforcement spacing of 18 in. using 60 ksi bars, adhering to the standard TxDOT spacing in the minimum shear reinforcement zone. On the other hand, the G2-E versus G3-W comparison investigates the scenario of 26 in. spacing with 60 ksi bars, determined based on the minimum shear reinforcement spacing specified by ACI 318-19 (2019). These comparisons aim to shed light on how harped strands influence girder behavior under these specific conditions. The comparative analysis begins with an evaluation of shear force versus displacement plots for the two sides under consideration, as seen in Figure 7.70 and Figure 7.71.



**Figure 7.70. Shear force versus displacement comparison: G1-W versus G3-E.**





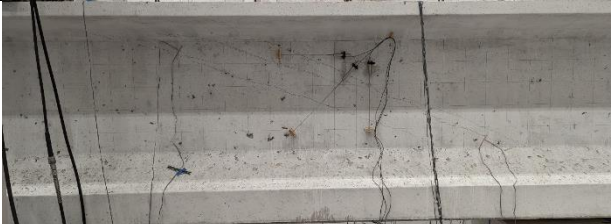
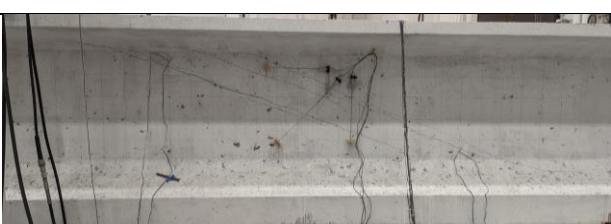
**Figure 7.71. Shear force versus displacement comparison: G2-E versus G3-W.**

In the first comparison, G1-W versus G3-E, where the shear reinforcement spacing is 18 in. and G3-E has harped strands, the additional contribution from prestressing force is not evident in both cracking and ultimate shear forces. Surprisingly, the girder with harped strands exhibited a slightly lower capacity (10 kips at cracking and 7 kips at ultimate) than expected. However, in the second comparison, G2-E versus G3-W, where the shear reinforcement spacing is 26 in. and G3 has harped strands, the effect of harped strands becomes more apparent. The girder with harped strands displayed a slightly higher concrete shear force at cracking (15 kips) and a significantly higher force at the ultimate state (39 kips). Indeed, it seems that the tighter spacing





of 18 in. had an unexpected impact on the contribution of prestressing force in the girder with harped tendons.

For the comparison of RSS, the first case of G1-W versus G3-E revealed an RSS of 1.68 and 1.73, respectively. In both ratios, the girder with the harped strands showed better performance in terms of these metrics. For the second case of G2-E versus G3-W, the RSS was 1.59 and 1.66, respectively, depicting similar behavior of a higher ratio for the harped strands. This feature should be further studied with the help of crack maps and crack measurements in Table 7.33 and Table 7.34.

**Table 7.33. Visual comparison of G3-W versus G2-E.**

<b>G3-W</b>	<b>Cracking</b>	
	<b>Ultimate/Maximum</b>	
<b>G2-E</b>	<b>Cracking</b>	
	<b>Ultimate/Maximum</b>	

**Table 7.34. Visual comparison of G3-E versus G1-W.**

<b>G3-E</b>	<b>Cracking</b>	
	<b>Ultimate/Maximum</b>	
<b>G1-W</b>	<b>Cracking</b>	
	<b>Ultimate/Maximum</b>	

The analysis of crack patterns in the G1-W versus G3-E comparison indicates denser cracking and lower crack angles in the girder with harped strands. In contrast, the G2-E versus G3-W comparison shows similar crack angles and spacing at both the cracking and ultimate stages. Additionally, when considering crack widths at the cracking stage, the 18-inch spacing comparison reveals wider cracks in the girder with harped tendons, while the 26-inch spacing comparison results in nearly identical crack widths. These findings substantiate the earlier observation from the shear force versus displacement plots, thus highlighting the counterintuitive effect of 18-inch spacing on girder behavior with harped tendons. Further investigation is warranted to fully comprehend this phenomenon.

## 7.2.5 Effect of Prestressing Ratio

The next effective comparison was the prestressing ratio in the design of prestressed girders, which is varied in terms of prestressing strands in the girder. The prestressing in the girder is the key differentiation in a prestressed concrete girder, and this effect is vital in understanding how the girder performs if all the other design and testing parameters are kept constant. The ACI equations for minimum shear reinforcement include the prestressing component, as opposed to the AASHTO equations, which do not, so this reflects another key outcome from this comparison. The two comparisons G5-E versus G2-W versus G6-W and G5-W versus G2-E versus G6-E investigated the effect of prestressing ratio. The prestressing ratio varies by using the same design concrete compressive strength along with variation in the number of prestressing strands in the girder. Overall, this factor gave a range of three different prestressing ratios for a set of two shear reinforcement spacings in the testing zone. The comparison of the design parameters for these two effective comparisons are shown in Table 7.35 and Table 7.36.

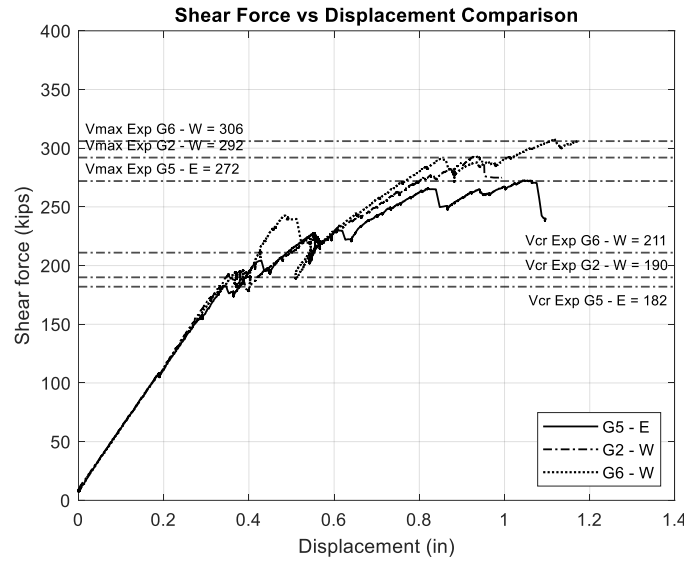
**Table 7.35. Comparison of design parameters for G5-E versus G2-W versus G6-W.**

Test ID	$f'_{ci}$ (ksi)	$f'_c$ (ksi)	28-day $f'_c$ (ksi)	Spacing (in.)	$f_{yt}$ (ksi)	# of Strands	Top Strands	$a/d_v$	$f_{pc}/f'_c$
G5-E	6	7	<b>9.2</b>	38	60	26	2	3	15.23
G2-W	6	7	<b>8.2</b>	38	60	34	2	3	18.42
G6-W	6.3	7	<b>9.1</b>	38	60	40	4	3	21.24

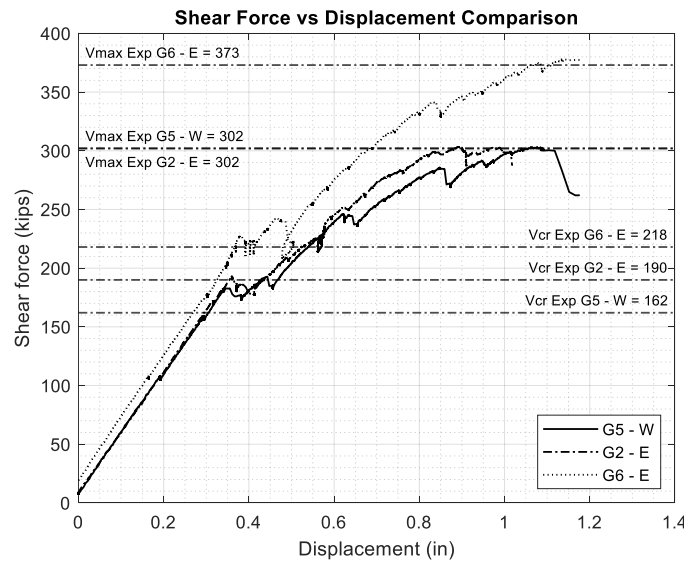
**Table 7.36. Comparison of design parameters for G5-W versus G2-E versus G6-E.**

Test ID	$f'_{ci}$ (ksi)	$f'_c$ (ksi)	28-day $f'_c$ (ksi)	Spacing (in.)	$f_{yt}$ (ksi)	# of Strands	Top Strands	$a/d_v$	$f_{pc}/f'_c$
G5-W	6	7	<b>9.2</b>	26	60	26	2	3	15.23
G2-E	6	7	<b>8.2</b>	26	60	34	2	3	18.42
G6-E	6.3	7	<b>9.1</b>	18	60	40	4	3	21.24

The first comparison investigated the spacing determined by the minimum shear reinforcement equation from ACI 318 for the respective girder design, and the second comparison investigated the effects of  $h_w/(2 * \tan \theta)$  spacing. The comparative analysis began with an evaluation of shear force versus displacement plots for the two sides under consideration, as shown in Figure 7.72 and Figure 7.73.



**Figure 7.72. Shear force versus displacement comparison: G5-E versus G2-W versus G6-W.**






**Figure 7.73. Shear force versus displacement comparison: G5-W versus G2-E versus G6-E.**

In both the comparisons for G5 versus G2 versus G6, the prestressing ratio varied in the range of 15.2 percent, 18.4 percent, and 21.2 percent, respectively. For the first case, the spacing was determined by  $h_w/(2 * \tan \theta)$ , and the cracking shear was 162 kips, 190 kips, 218 kips, respectively, which shows an increase in the cracking shear owing to higher prestressing in the girder. When the ultimate shear was compared, it was 292 kips, 302 kips and 373 kips, respectively, clearly depicting a trend with respect to the higher prestressing ratio. In the second comparison, in which the spacing derived from minimum shear reinforcement equations from




ACI 318-19 the first cracking shear was 188 kips, 190 kips and 211 kips, respectively. This result shows clearly that the cracking shear increases with respect to an increase in the prestressing ratio, that is, the number of prestressing strands. For the same comparison, the maximum shear capacity was 262 kips, 292 kips, and 306 kips, respectively, which also shows a higher maximum capacity for the highest prestressing.

For the first comparison of  $h_w/(2 * \tan \theta)$  spacing, the RSS values were 1.39 for G5-E, 1.54 for G2-W and 1.45 for G6-W, indicating a decrease in the value as the prestressing ratio increases. For the second comparison of ACI minimum shear reinforcement spacing, the RSS values were 1.80 for G5-W, 1.59 for G2-E and 1.71 for G6-E. This comparison also indicates a higher ratio value for the lower prestressing ratio, indicating a more ductile behavior. In addition to the shear capacity, the crack pattern and crack measurements need to be compared for a comprehensive understanding (see Table 7.37 and Table 7.38).

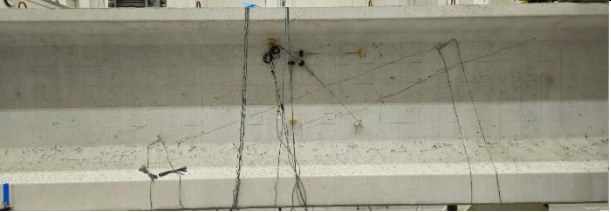


**Table 7.37. Visual comparison of G5-E versus G2-W versus G6-W.**

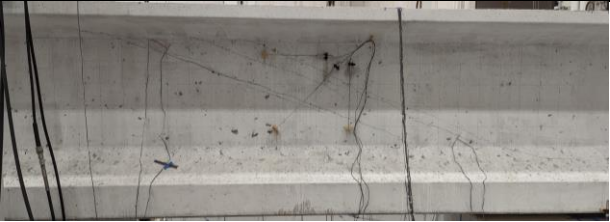

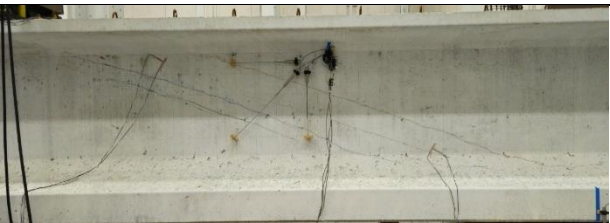
<b>G5-E</b>	<b>Cracking</b>	
	<b>Ultimate/Maximum</b>	
<b>G2-W</b>	<b>Cracking</b>	



	<b>Ultimate/Maximum</b>	
<b>G6-W</b>	<b>Cracking</b>	
	<b>Ultimate/Maximum</b>	

**Table 7.38. Visual comparison of G5-W versus G2-E versus G6-E.**

<b>G5-W</b>	<b>Cracking</b>	
	<b>Ultimate/Maximum</b>	
<b>G2-E</b>	<b>Cracking</b>	

	<b>Ultimate/Maximum</b>	
<b>G6-E</b>	<b>Cracking</b>	
	<b>Ultimate/Maximum</b>	

Visual observation of crack patterns can bring in additional points for the effective comparison. For the first comparison, G5-E versus G2-W versus G6-W, the first shear crack is a single distinct crack in all the cases of prestressing. This result is related to the number of stirrups covering the shear span. In addition, all the cases have similar tightly spaced cracks with larger crack widths, and the last two cases show brittle failure of the girder. However, the failure mode is also related to the very low shear reinforcement in this zone, and the force values are a better comparison in this scenario. For the second comparison, G5-W versus G2-E versus G6-E, the cracks formed at the first crack seem to increase in the angle and become more widely spaced as the prestressing ratio increases. However, not much can be determined about the ultimate state comparison from observation, and thus the prestressing ratio needs further analysis.

### 7.2.6 Effect of Concrete Strength

The effect of concrete strength is another vital factor in this parametric study since the increase in concrete tensile strength is linked to a need for increased transverse reinforcement to effectively counter shear forces during early diagonal cracking. This relationship is due to higher tensile stresses requiring redistribution as cracks form to correlate tensile strength with the concrete's compressive strength. In the test matrix design, the parameter of design concrete

strength was varied, and the girder design, including the arrangement of prestressing strands, was also adjusted to ensure that the stress checks align with the specified design concrete strength. The two comparisons derived from the test matrix were G1-W versus G7-E versus G8-E and G2-E versus G7-W versus G8-W. Both comparisons were designed to have three variations in the design concrete strength, with a range of 5 ksi, 7 ksi, and 8.5 ksi. The design parameters are shown in Table 7.39 and Table 7.40.

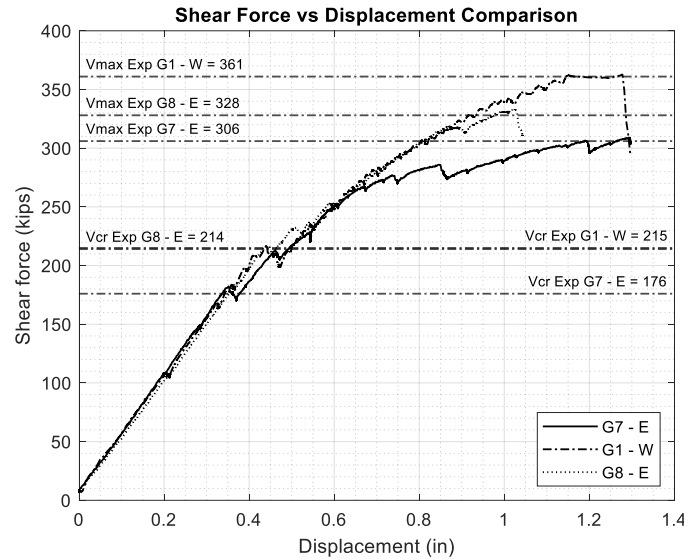
**Table 7.39. Comparison of design parameters for G1-W versus G7-E versus G8-E.**

Test ID	$f'_{ci}$ (ksi)	$f'_c$ (ksi)	28-day $f'_c$ (ksi)	Spacing (in.)	$f_{yt}$ (ksi)	# of Strands	Top Strands	$a/d_v$	$f_{pc}/f'_c$
G1-W	6	7	8.8	18	60	34	2	3	18.42
G7-E	4	5	8.2	18	60	24	2	3	19.66
G8-E	6	8.5	9.6	18	60	38	2	3	16.31

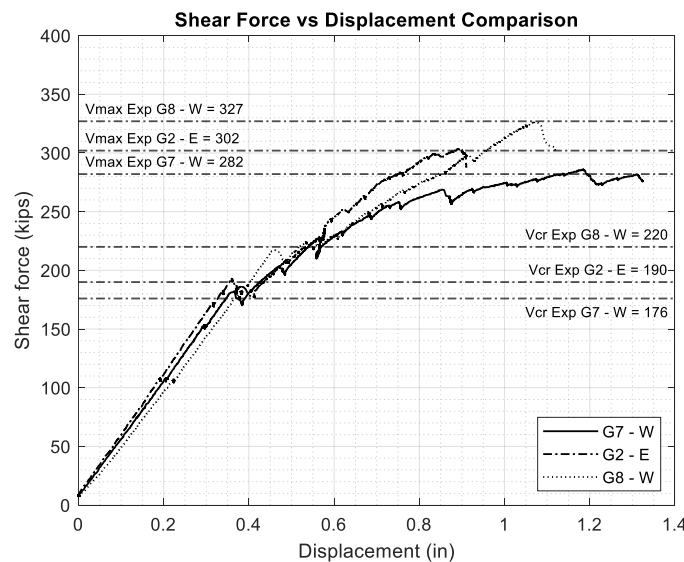
**Table 7.40. Comparison of design parameters for G2-E versus G7-W versus G8-W.**

Test ID	$f'_{ci}$ (ksi)	$f'_c$ (ksi)	28-day $f'_c$ (ksi)	Spacing (in.)	$f_{yt}$ (ksi)	# of Strands	Top Strands	$a/d_v$	$f_{pc}/f'_c$
G2-E	6	7	8.2	26	60	34	2	3	18.42
G7-W	4	5	8.2	26	60	24	2	3	19.66
G8-W	6	8.5	9.6	26	60	38	2	3	16.31

The 5 ksi and 8.5 ksi limits are based on the *TxDOT LRFD Bridge Design Manual* for the design concrete compressive strength. Girder G7 is the 5 ksi girder, G1-W and G2-E are the 7 ksi girders, and G8 is the 8.5 ksi girder. The effective comparison, however, arises in terms of the spacing of shear reinforcement in the testing zone. The first comparison, G1-W versus G7-E versus G8-E, has a spacing of 18 in., coming from the TxDOT standard usage, and the second comparison, G2-E versus G7-W versus G8-W, has a spacing of 26 in. derived from the ACI 318-19 minimum shear reinforcement provisions. The comparative analysis began with an evaluation of shear force versus displacement plots for the two sides under consideration, as seen in Figure 7.74 and Figure 7.75.



**Figure 7.74. Shear force versus displacement comparison: G1-W versus G7-E versus G8-E.**






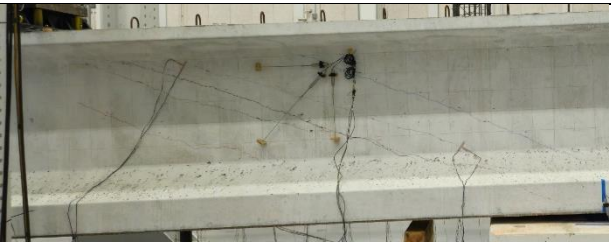
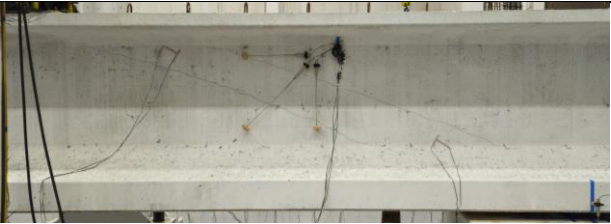
**Figure 7.75. Shear force versus displacement comparison: G2-E versus G7-W versus G8-W.**

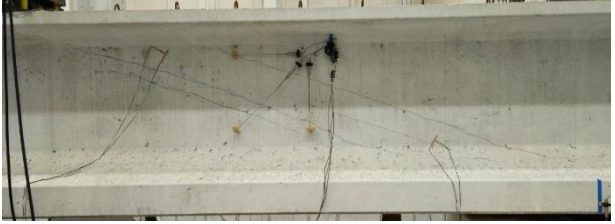
In the first comparison, G1-W versus G7-E versus G8-E, the concrete strength varies—G7-E of 5 ksi, G1-W of 7 ksi, and G8-E of 8.5 ksi. The comparison of first cracking shear strength gave 176 kips for G7-E, 215 kips for G1-W, and 214 kips for G8-E. The significant difference between the low strength to higher-strength girder can be clearly seen in this case; however, the comparison between 7 ksi and 8.5 ksi yields the same. For the ultimate shear capacity, it was 306 kips for G7-E, 361 kips for G1-W, and 332 kips for G8-E. The lower-strength girder marks a

significant difference for ultimate capacity as well; however, G8-E is not entirely damaged and might yield a higher capacity; therefore, it cannot be entirely relied on for effective comparison.

The RSS values for this comparison are 1.68 for G1-W, 1.74 for G7-E and 1.55 for G8-E, which does not indicate a clear pattern of increase in design concrete strength. Consequently, further investigation into the design parameters that might cause the variation in RSS is needed. Further, the visual comparison for this case can be seen in Table 7.41.

**Table 7.41. Visual comparison of G1-W versus G7-E versus G8-E.**

<b>G1-W</b>	<b>Cracking</b>	
	<b>Ultimate/Maximum</b>	
<b>G7-E</b>	<b>Cracking</b>	
	<b>Ultimate/Maximum</b>	
<b>G8-E</b>	<b>Cracking</b>	


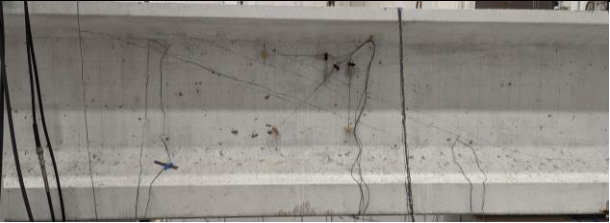


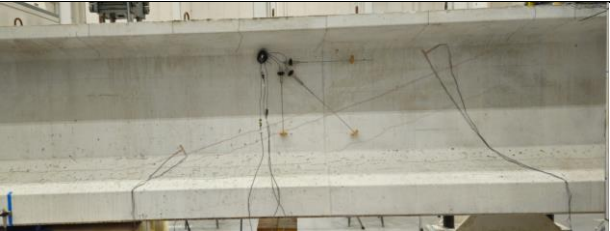
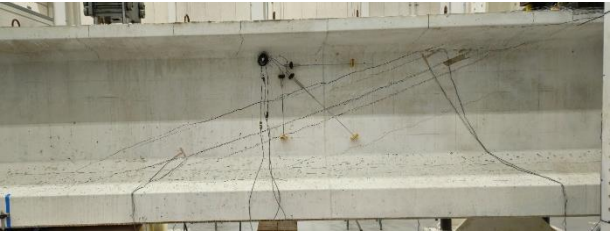
	<b>Ultimate/Maximum</b>	
--	-------------------------	--

For the second comparison, G2-E versus G7-W versus G8-W, the concrete strength varied—G7-W of 5 ksi, G2-E of 7 ksi, and G8-W of 8.5 ksi. A comparison of the first cracking shear strength gave 176 kips for G7-W, 190 kips for G2-E, and 218 kips for G8-W, thus depicting a clear increase with the concrete strength. The ultimate shear capacity was 282 kips for G7-W, 302 kips for G2-E, and 325 kips for G8-W, which also details a similar trend. Therefore, the use of higher concrete strength helps in both the cracking and ultimate shear capacity based on the preliminary observations.

The RSS values for this comparison were 1.59 for G2-E, 1.60 for G7-W, and 1.49 for G8-W, which did not indicate a distinctive pattern. However, for all the design concrete strength values, the RSS values are higher than 1.3, with the higher design strength close to the lower end. Furthermore, analysis needs to be done on the crack pattern shown in Table 7.42.



**Table 7.42. Visual comparison of G2-E versus G7-W versus G8-W.**

<b>G2-E</b>	<b>Cracking</b>	
	<b>Ultimate/Maximum</b>	
<b>G7-W</b>	<b>Cracking</b>	
	<b>Ultimate/Maximum</b>	
<b>G8-W</b>	<b>Cracking</b>	
	<b>Ultimate/Maximum</b>	

The visual comparison also depicts a change in the density of cracks and crack widths at the formation of the first shear crack. At the ultimate stage, the lower-strength girder showed

significantly more damage for both the cases. In addition, the density of the cracks can be seen to increase with the increase in concrete strength. However, the role of concrete strength is quite evident from the shear capacities, and further data analysis is needed to identify any other variations in parameters.

### 7.2.7 Effect of Shear Span-to-Depth Ratio

The next factor that was studied as a part of this preliminary study is the shear-span-to-depth ratio. The  $a/d$  has been found to strongly influence the shear strength of prestressed beams without shear reinforcement, but this influence decreases with the introduction of shear reinforcement. Thus, for the minimum shear reinforcement zone, the effect of this ratio can be significant. Typically, lower  $a/d$  tends to yield higher shear capacity, and it reduces with the increase of this ratio. The role of this ratio needs to be studied for the minimum shear reinforcement provisions to understand this trend and the significance. In this effective comparison, two cases that arose were G4-E versus G1-W versus G9-E and G4-W versus G2-W versus G9-W. Both the cases yielded an effective comparison of  $a/d$  ratios over the values 2.5, 3, and 4. The design parameters are summarized in Table 7.43 and Table 7.44 for the effective comparisons mentioned above.

**Table 7.43. Comparison of design parameters for G4-E versus G1-W versus G9-E.**

Test ID	Length (ft)	$f'_{ci}$ (ksi)	$f'_c$ (ksi)	28-day $f'_c$ (ksi)	Spacing (in.)	$f_{yt}$ (ksi)	# of Strands	$a/d_v$	$f_{pc}/f'_c$
G4-E	45	6	7	8.5	18	60	34	2.5	18.42
G1-W	51	6	7	8.8	18	60	34	3	18.42
G9-E	56	6	7	8.8	18	60	34	4	18.42

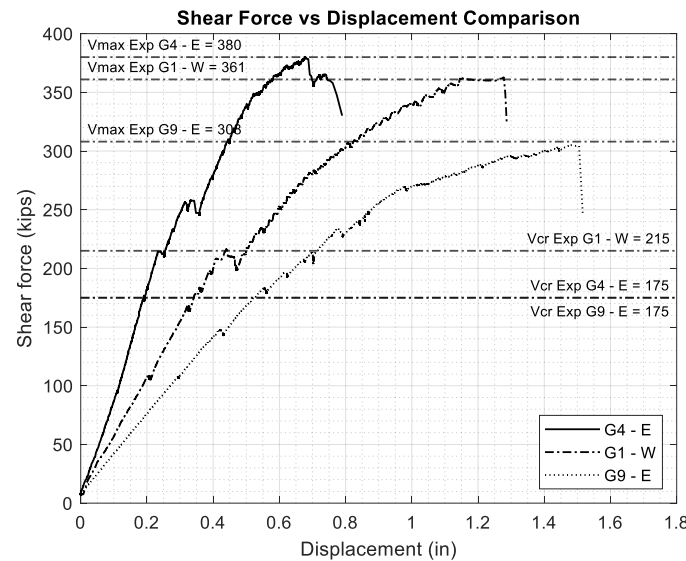
**Table 7.44. Comparison of design parameters for G4-W versus G2-W versus G9-W.**

Test ID	Length (ft)	$f'_{ci}$ (ksi)	$f'_c$ (ksi)	28-day $f'_c$ (ksi)	Spacing (in.)	$f_{yt}$ (ksi)	# of Strands	$a/d_v$	$f_{pc}/f'_c$
G4-W	45	6	7	8.5	38	60	34	2.5	18.42
G2-W	51	6	7	8.8	38	60	34	3	18.42
G9-W	56	6	7	8.8	38	60	34	4	18.42

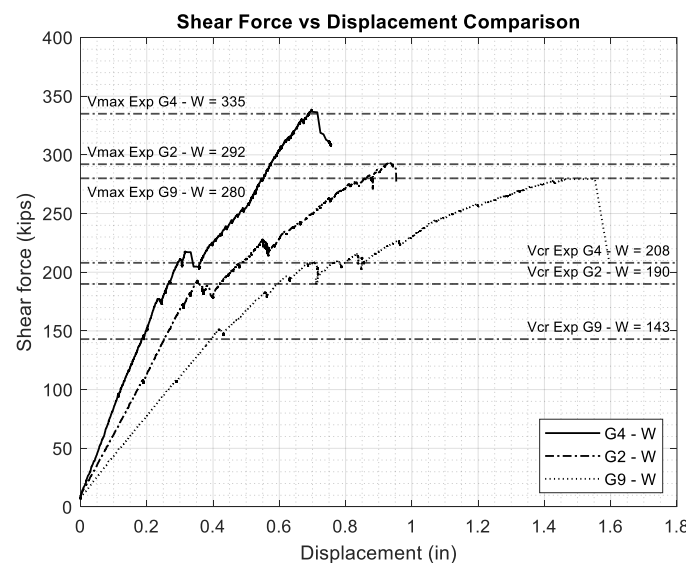
The girder G4 was tested with 2.5 ratio, and G1 and G2 were tested with a ratio of 3, and the girder G9 with a higher  $a/d$  of 4. The effective comparison is different for both the cases in terms of shear reinforcement spacing in the testing zone. The first comparison had a spacing of 18 in.,



which is from the TxDOT standard usage, and the second comparison had a spacing from the  $h_w/(2 * \tan \theta)$  equation. On a broader scale, both these comparisons give an understanding of the influence of  $a/d$  with the change in shear reinforcement spacing. The initial comparison of the shear force versus displacement plots can be seen in Figure 7.76 and Figure 7.77.



**Figure 7.76. Shear force versus displacement comparison: G4-E versus G1-W versus G9-E.**





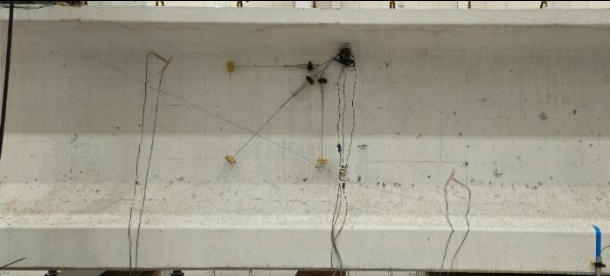

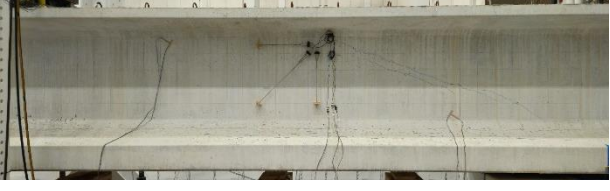

**Figure 7.77. Shear force versus displacement comparison: G4-W versus G2-W versus G9-W.**

For the first comparison, G4-E versus G1-W versus G9-E, the  $a/d$  for the respective tests was 2.5, 3, and 4. The recorded cracking shear strength for these tests was 175 kips for G4-E, 215



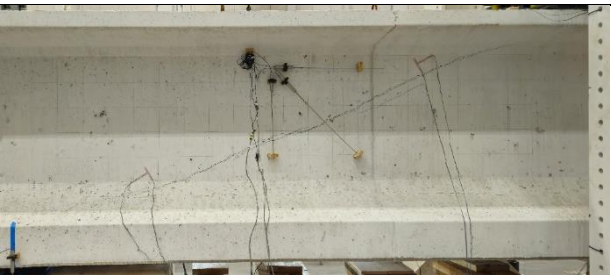



kips for G1-W, and 175 kips for G9-E, which is not showing any appropriate trend with respect to  $a/d$  ratio to make significant comments. However, the ultimate shear strength is 380 kips for G4-E, 361 kips for G1-W, and 308 kips for G9-E, which shows a significant decrease in the shear capacity for the higher shear span. However, for the other case, G4-W versus G2-W versus G9-W, with larger spacing than the first case, the effect of  $a/d$  with the variation in  $s/d$  can be found. The first cracking shear strength was 214 kips for G4-W, 190 kips for G2-W, and 143 kips for G9-W showing a clear decrease in the cracking strength with an increase in  $a/d$ . For the ultimate shear capacity, it was 335 kips for G4-W, 292 kips for G2-W, and 280 kips for G9-W, all of which also depicted a decrease in strength. Consequently, both cases show a significant decrease in the shear capacity with the decrease in the  $a/d$ .

The G4-E versus G1-W versus G9-E comparison yielded an RSS ratio of 2.17, 1.68, and 1.76, respectively. For this case of 18 in. spacing, the RSS did not show a pattern for all the cases of shear-span-to-depth ratios. For the second comparison, G4-W versus G2-W versus G9-W, the RSS values were 1.57, 1.54 and 1.96, respectively. This case of wider spacing shows a higher RSS for the higher shear-span-to-depth ratio, thereby depicting more ductile behavior. Further, the visual comparison for both the cases can be seen in Table 7.45 and Table 7.46.

**Table 7.45. Visual comparison of G1-W versus G4-E versus G9-E.**

<b>G1-W</b>	<b>Cracking</b>	
	<b>Ultimate/Maximum</b>	
<b>G4-E</b>	<b>Cracking</b>	
	<b>Ultimate/Maximum</b>	
<b>G9-E</b>	<b>Cracking</b>	
	<b>Ultimate/Maximum</b>	

**Table 7.46. Visual comparison of G2-W versus G4-W versus G9-W.**

<b>G2-W</b>	<b>Cracking</b>	
	<b>Ultimate/Maximum</b>	
<b>G4-W</b>	<b>Cracking</b>	
	<b>Ultimate/Maximum</b>	
<b>G9-W</b>	<b>Cracking</b>	
	<b>Ultimate/Maximum</b>	

Based on the visual observations and comparisons, the first cracking in the girder started at a higher distance from the actuator for the longer shear span. The longer shear spans also depicted formation of a higher number of cracks as opposed to the shorter shear span, with the cracks densely appearing close to the major crack connecting the actuator and the support. The crack patterns clearly depict the change of the shear-span-to-depth ratio, and further crack measurements need to be compared for productive results.

### 7.2.8 Effect of Cross-Section Depth

The cross-section depth of the girder is one other key parameter studied by changing the girder size from Tx54 to Tx70. The prototype girder selected was a Tx54, chosen after a comprehensive analysis of the equations that determine shear reinforcement spacing, with a particular focus on girders that predominantly feature minimal shear reinforcement zones. The selection was influenced by the “size effect” phenomenon, which reveals that larger girders tend to have lower strength than smaller ones, thereby complicating the direct extrapolation of test results from smaller to larger girders. This effect is more significant in girders with lower shear reinforcement, necessitating careful consideration in scaling up test results to ensure structural reliability and safety. The two comparisons based on this effect are G10-E versus G1-W and G10-W versus G2-W, with the G10 girder being a Tx70 and G1 and G2 being Tx54 girders. The design parameters are listed in Table 7.47 and Table 7.48.

**Table 7.47. Comparison of design parameters for G10-E versus G1-W.**

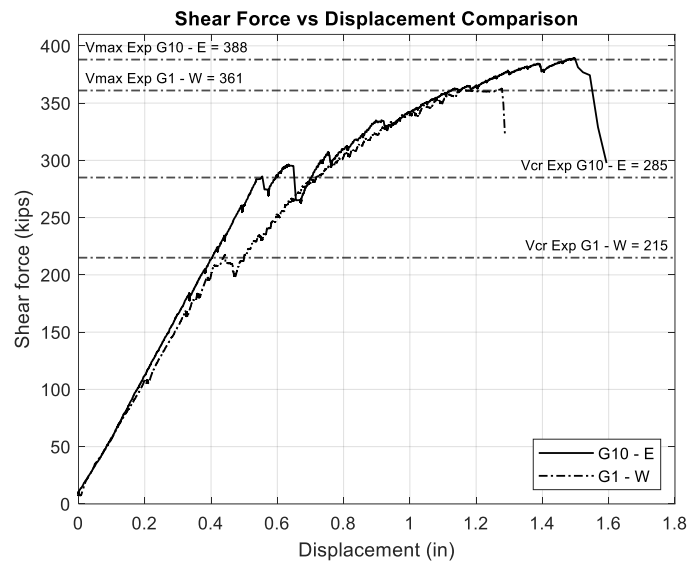
Test ID	Girder Type	Length (ft)	$f'_{ci}$ (ksi)	$f'_c$ (ksi)	28-day $f'_c$ (ksi)	Spacing (in.)	$f_{yt}$ (ksi)	# of Strands	$a/d_v$
G10-E	Tx70	58	6	7	9.2	18	60	40	3
G1-W	Tx54	51	6	7	8.8	18	60	34	3

**Table 7.48. Comparison of design parameters for G10-W versus G2-W.**

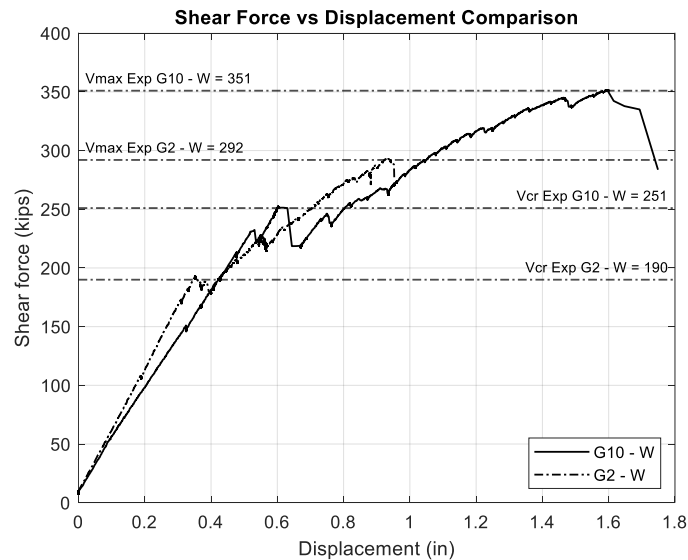
Test ID	Girder Type	Length (ft)	$f'_{ci}$ (ksi)	$f'_c$ (ksi)	28-day $f'_c$ (ksi)	Spacing (in.)	$f_{yt}$ (ksi)	# of Strands	$a/d_v$
G10-W	Tx70	58	6	7	9.2	40	60	40	3
G2-W	Tx54	51	6	7	8.8	38	60	34	3

The shear reinforcement spacing is also a variation between both the comparisons; the first comparison had an 18 in. spacing that depicted the TxDOT standard usage, and the second comparison had a spacing from the  $h_w/(2 \tan \theta)$  equation. The broader comparison between

both the cases depicts the effect of size of the girder on a tighter spacing compared to the low shear reinforcement. The preliminary step involved developing the shear force versus displacement plots for both the cases, as shown in Figure 7.78 and Figure 7.79.



**Figure 7.78. Shear force versus displacement comparison: G10-E versus G1-W.**



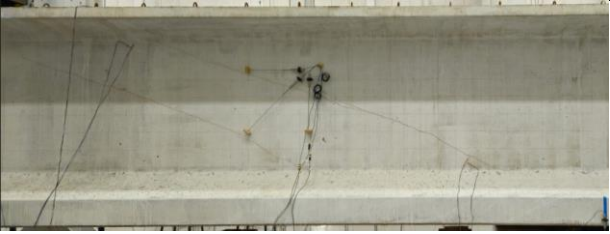
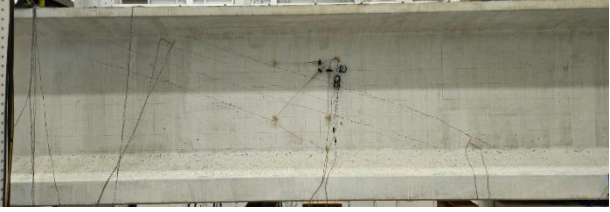


**Figure 7.79. Shear force versus displacement comparison: G10-W versus G2-W.**

For the first comparison, the first cracking shear recorded was 285 kips for G10-E and 215 kips for G1-W, as is clearly depicted by the larger cross section of the Tx70 girder. However, the ultimate strength of G10-E is 388 kips; for G1-W, it is 361 kips, with the G10-E having further capacity based on visual observations. Similarly, for the second comparison, the first cracking

shear for G10-W was 251 kips and for G2-W was 190 kips. The ultimate shear for G10-W was 351 kips and for G2-W was 292 kips. However, all the significant differences in the capacities can be accounted for in the larger girder cross section, so further study into additional parameters from the test data is required.





The RSS values for G10-E versus G1-W with the 18 in. spacing are 1.55 and 1.54, respectively. Both the ratios are almost similar for both the Tx54 and Tx70 girders. For the second comparison of G10-W versus G2-W, the RSS values are 1.23 and 1.68, respectively. This comparison shows a higher ratio for the Tx54 girder despite the higher shear capacity values for Tx70. Furthermore, the visual comparison of the cracking stages for both the cases can be seen in Table 7.49 and Table 7.50.

**Table 7.49. Visual comparison of G10-E versus G1-W.**

<b>G10-E</b>	<b>Cracking</b>	
	<b>Ultimate/Maximum</b>	
<b>G1-W</b>	<b>Cracking</b>	
	<b>Ultimate/Maximum</b>	



**Table 7.50. Visual comparison of G10-W versus G2-W.**

<b>G10-W</b>	<b>Cracking</b>	
	<b>Ultimate/Maximum</b>	
<b>G2-W</b>	<b>Cracking</b>	
	<b>Ultimate/Maximum</b>	

Based on the crack pattern observations, the larger cross-section girder has widely spaced cracks for the 18 in.  $s/d$  in both the cracking and ultimate stages. For the comparison in the case of larger  $s/d$ , the formation of cracks is almost similar owing to the low shear reinforcement. However, in the second case, the girder showed significant brittle failure for the Tx54 girder despite having a smaller cross section, which brings out the need for detailed study of additional parameters. The role of size effects can be clearly observed in the deeper girders with wider spacings where the RSS reduces for deeper girders.



### 7.3 SUMMARY

This chapter discusses major observations during each girder testing. Further, the testing data are summarized in terms of observed strength and predicted capacities. Next, the individual tests were utilized for the resulting effective comparisons.

The full-scale testing enabled a comprehensive study of girder performance under varying design parameters and minimum shear reinforcement spacing by utilizing a four-point bending test to create zones of constant shear. This approach facilitated a detailed parametric study that examined the impact of factors such as the presence or absence of a deck, concrete strength, yield strength and spacing of stirrups, shear-span-to-depth ratio, prestressing strands, harped strands, and girder depth. Key findings indicated that AASHTO LRFD's minimum shear reinforcement equation often underestimates spacing due to a limited number of considered factors. The study found that closer  $s/d$  significantly enhances shear strength, particularly in designs without harped tendons, while higher-grade shear reinforcement and increased prestressing ratios improve performance but may result in more brittle behavior. Additionally, the effectiveness of harped strands varies with reinforcement spacing, and increasing concrete strength consistently enhances both cracking and ultimate shear capacities.

Further findings highlighted that the shear-span-to-depth ratio significantly affects shear strength, with lower ratios resulting in higher capacities and more ductile behavior. Deeper girders, such as Tx70, exhibited higher cracking and ultimate shear capacities than Tx54 girders, and also showed different failure modes and crack patterns. The experimental observations revealed that girder performance, characterized by RSS and serviceability criteria like crack measurements, is significantly influenced by these varied parameters. Detailed instrumentation plans utilizing strain gauges, string potentiometers, load cells, LVDTs, DIC, and Optotrak provided critical data for effective comparisons. The data obtained from the experiments, supplemented with FE modeling and machine learning models, aim to refine design guidelines by quantifying the impact of various factors on minimum shear reinforcement and enhancing the reliability and safety of prestressed concrete girders.



## **CHAPTER 8:**

### **FINITE ELEMENT ANALYSIS PARAMETRIC STUDY**

#### **8.1 INTRODUCTION**

FE modeling is an effective numerical technique in engineering that is used to study and simulate the behavior of complicated structures such as prestressed concrete elements. Engineers can use this method to design and optimize structures by properly predicting their response to various loads and environmental conditions. The FE technique requires the structure to be segmented into several smaller, interconnected pieces that are capable of being mathematically modeled. The findings from these various aspects are then merged to produce an overall representation of the system's response.

The accuracy of FE modeling for reinforced and prestressed concrete elements is one of its primary advantages. The model can capture the structure's behavior in detail, allowing researchers to predict how the structure will behave when facing varied loads and environmental circumstances. This knowledge helps to optimize the structure's design and verify that it meets the necessary performance and safety standards. FE modeling also provides the ability to visualize the structure and detect potential stress or failure points. This representation enables informed decisions about the structure's design and implementation, ensuring that it is both safe and efficient.

Another advantage of FE modeling is its adaptability. The model is easily modifiable to represent changes in design, loads, or climatic conditions, thereby allowing researchers to examine the impact of these changes on the structure fast and efficiently. Because of its versatility, FE modeling is a valuable tool for engineers and the construction industry, allowing for a high level of collaboration and flexibility in the design and execution processes.

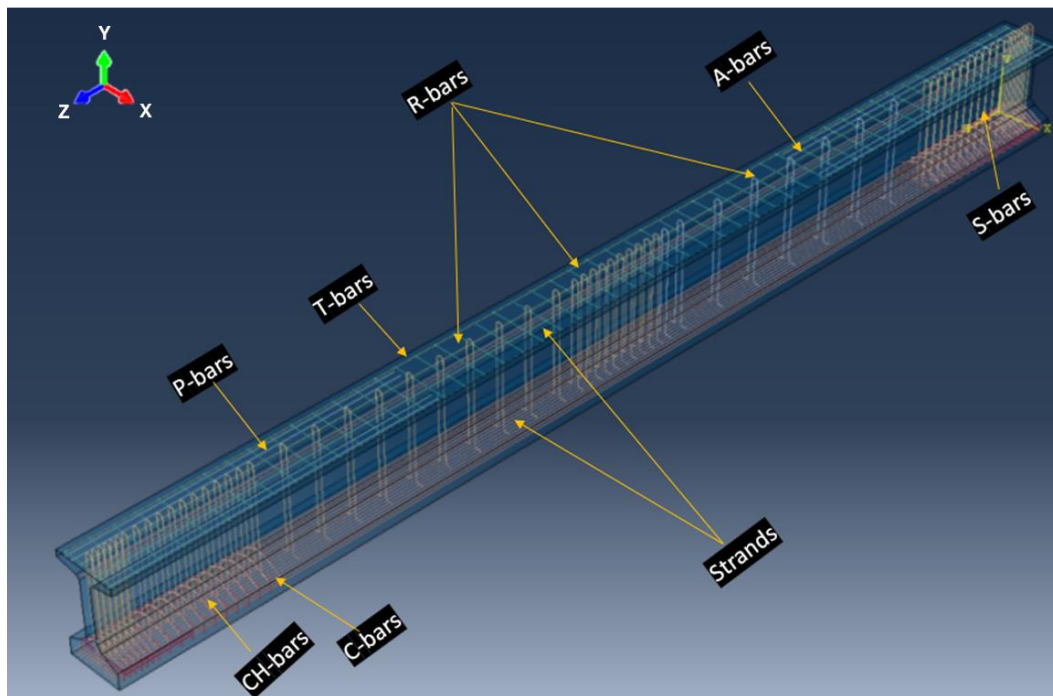
The ABAQUS FE (Abaqus (2012)) program was employed because of its capacity to mimic various concrete, steel, and tendon components. This chapter discusses the development and validations of an FE model to simulate the response of prestressed concrete girders as well as apply this model in a parametric study that investigates the effect of significant design

parameters on the performance of prestressed concrete girders with low levels of shear reinforcement.

## 8.2 MODEL DESCRIPTION

### 8.2.1 Geometry and Meshing

The geometry in FE models is represented by discrete elements with distinct properties connected at shared nodes to form the desired structure. First, the geometry is generated, and then different portions/parts are seeded to guide the size and distribution of meshing. The different parts created in the model were the girder, deck slab, strands, R-bars, S-bars, T-bars, A-bars, C-bars, CH-bars, and P-bars, as shown in Figure 8.1.

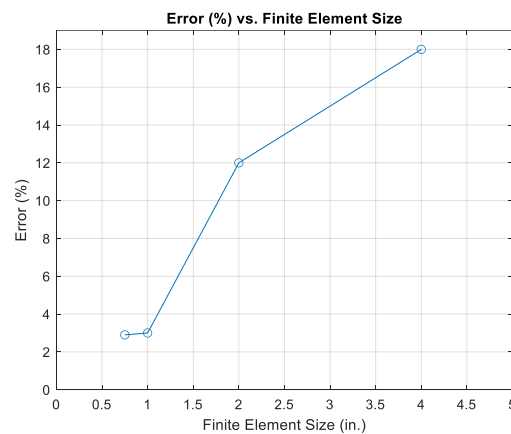


**Figure 8.1. Three-dimensional view of the girder with strands and reinforcement.**

The girder and deck slab were modeled via the eight-node solid elements and by adopting reduced integration, enhanced hourglass control, and distortion control (C3D8R). Reduced integration combines a low computational cost with the ability to prevent shear locking and maintain reasonable stiffness. Hourglass control is used to prevent element instabilities produced by stress-free/energy-free element-deformed shapes, whereas distortion control is used to prevent

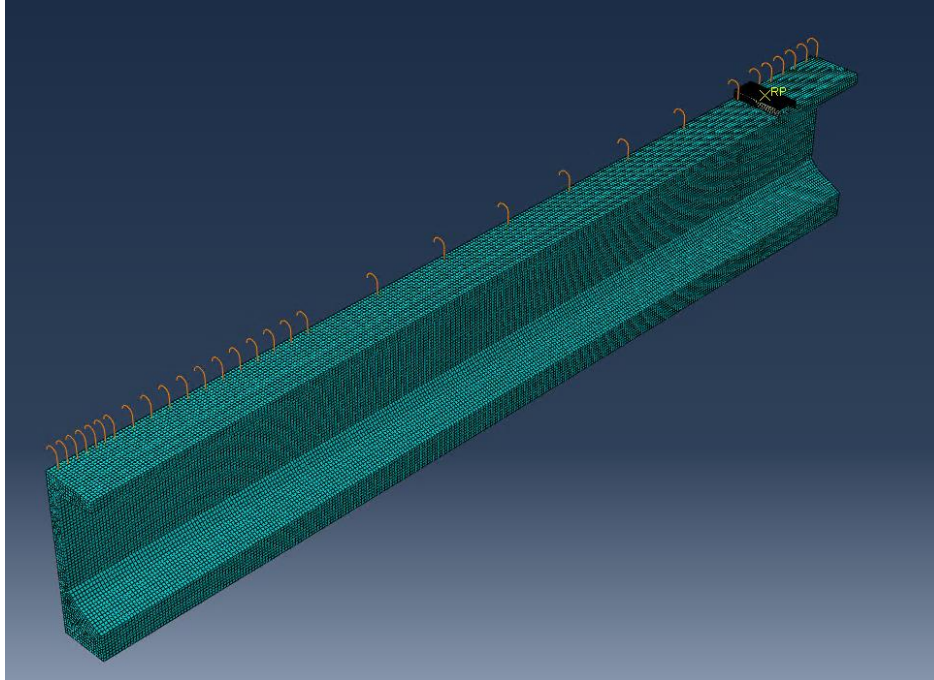
overly distorted deformed shapes that may lead to negative stiffnesses. The distortion control is activated when deformed shapes contradict the element's geometric convexity. A mesh size of 1 in. is used in all girders and deck slabs. The mesh size for the model was selected by considering a balance between accuracy and time constraints.

Below is a chart showing the dependence between error computed between the experimental and FE model along with FE size; Figure 8.2 specifically refers to the error between FE results and experimental results. It is evident that adopting an FE size of 1 in. proves to be the most advantageous choice. This conclusion was drawn from a thorough examination of both FE sizes of 0.75 in., 1 in., 2 in., and 4 in., considering data from FM, and experimental results.

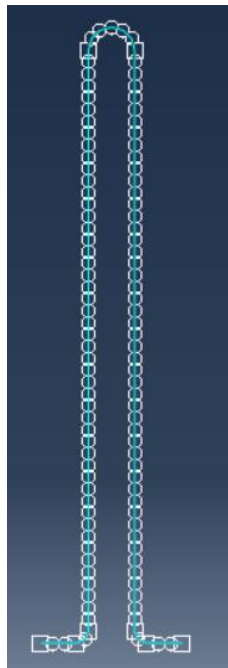


**Figure 8.2. Relationship between FE size and error.**

To reduce the analysis cost, only one-fourth of the original girder is analyzed, taking advantage of two planes of symmetry. The final model geometry and mesh for the specimen are presented in Figure 8.3. Strands and mild steel are modeled by two-node linear truss elements embedded in the concrete (T3D2). The T3D2 elements are three-dimensional truss elements having 2 degrees of freedom per node. The mesh size used for both S-bars and R-bars is 1 in., as shown in Figure 8.4.



**Figure 8.3. 3-D view of model mesh.**



**(a)**



**(b)**

**Figure 8.4. Meshing of steel reinforcement: (a) R-bars and (b) S-bars.**

## 8.2.2 Material Modeling

Accurate material modeling of concrete under tension and compression and reinforcing bars is essential to accurate predictions in simulations. Test properties' results have been used in the simulation to ensure accuracy.

### 8.2.2.1 Concrete

The concrete damage plasticity (CDP) model was created to simulate the response of the concrete material. The CDP model uses a combination of non-associated multi-hardening plasticity and scalar-damaged elasticity. The CDP model considers two failure processes: tensile cracking and compressive crushing of the concrete. When compared to the experimental results, the CDP model implemented in ABAQUS provided a stable response with reasonable accuracy for modeling the nonlinear and post-peak behavior of concrete.

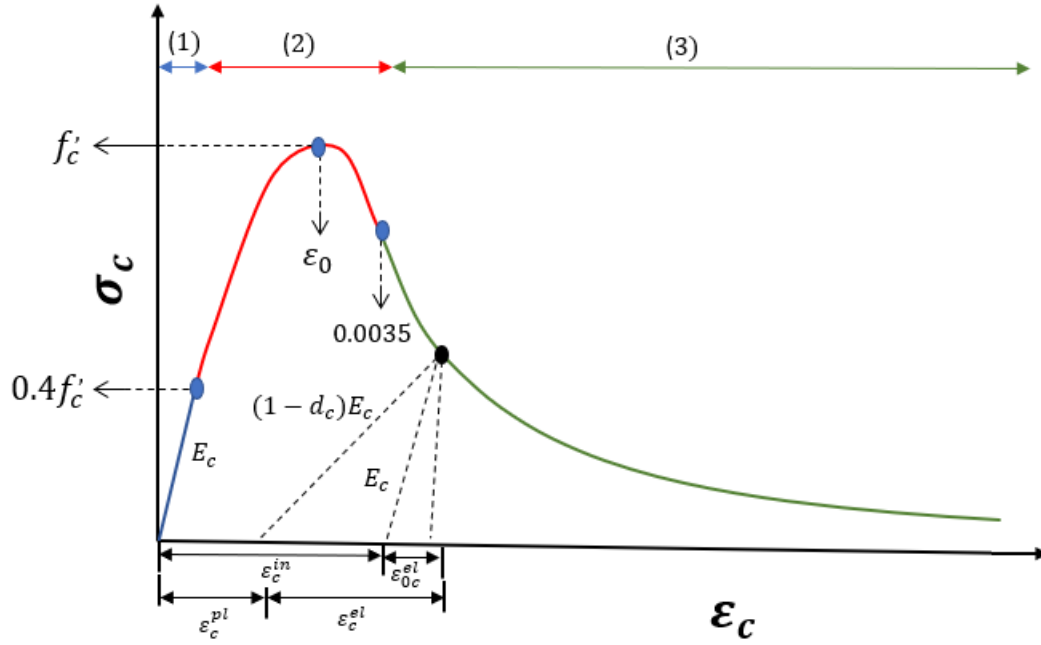
Yielding is modeled via the Drucker-Prager hyperbolic function that includes five parameters: the dilation angle,  $\psi$ , measured in the p-q plane at high confining pressure; eccentricity,  $\varepsilon$ , to adjust the shape of the plastic potential surface; equi-biaxial compressive yield stress to uniaxial compressive yield stress ratio,  $\frac{\sigma_{bo}}{\sigma_{co}}$ ; the ratio of the cracking stress in triaxial tension to the yield stress in triaxial compression,  $K_c$ ; and the viscosity parameter that defines visco-plastic regularization,  $\mu$ , representing the relaxation time of the visco-plastic system. These parameters are provided in Table 8.1.

**Table 8.1. Plastic damage parameters.**

<b>Dilation angle, <math>\psi</math></b>	50°
<b>Eccentricity, <math>\varepsilon</math></b>	0.1
<b><math>\frac{\sigma_{bo}}{\sigma_{co}}</math></b>	1.16
<b><math>K_c</math></b>	0.6667
<b>Viscosity Parameter, <math>\mu</math></b>	0.00001

In the CDP model, the *uniaxial compressive behavior* of concrete follows the general stress–strain curve shown in Figure 8.5. There are three stages to the stress–strain behavior:

1. Linear elastic response until the initial yield stress is reached.
2. The plastic response following first yields stress and strain-hardening behavior till ultimate stress.
3. Softening beyond the maximum stress.



**Figure 8.5. Compressive stress–strain relationship (Behnam et al. 2018).**

The compressive stress and inelastic strain values at different intervals are necessary to model the behavior beyond the elastic region. The stress–strain behavior of concrete in compression can be determined experimentally or numerically. Instead of relying on experimental results, the numerical technique is applied in this study, and is as follows:

$$\varepsilon_c^{pl} = \varepsilon_c - \frac{1}{(1 - d_c)} \frac{\sigma_c}{E_c} \quad (8.1)$$

where:

$\varepsilon_c^{pl}$ : the plastic strain.

$\varepsilon_c$ : the total compressive strain.

$\sigma_c$ : the compressive stress



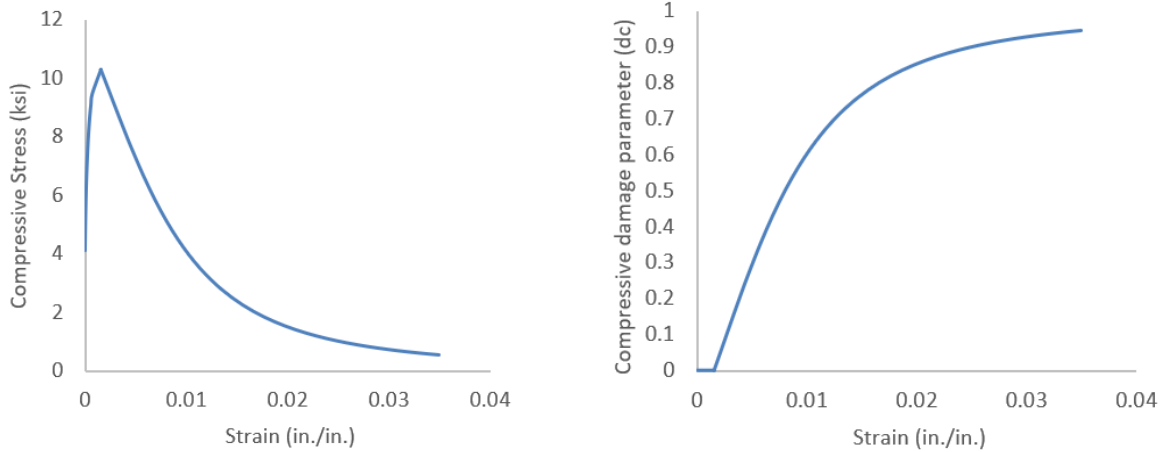
$E_c$  : Young's modulus of concrete.

$d_c$  : the concrete damage in compression determined as:  $d_c = 1 - \frac{\sigma_c}{f'_c}$ .

The concrete stress–strain behavior under compression was modeled in three stages using the equations from Jankowiak and Lodygowski (2005), as shown in equation (8.2). The variable defines the linear elastic branch of the curve,  $\epsilon_c$ , which ranges from zero to  $0.4 \frac{f'_c}{E_c}$ . The linear branch comes to an end at  $0.4f'_c$ . The appropriate peak stress–strain level is defined as  $\epsilon_c = 1.75 \frac{f'_c}{E_c}$ , where  $\eta_c$  is the material constant. The stress and strain compatibility at the strain level of  $\epsilon_c = 0.4 \frac{f'_c}{E_c}$  gives the value of  $\eta_c$ . The  $k_c$  represents the constant crushing energy as a material attribute. The value of  $\lambda_c$  can be calculated by using the stress and strain compatibility at the strain level of  $\epsilon_c = 0.0035$  in. To avoid numerical issues, the ultimate concrete strain  $\epsilon_u$  is set to a large value of 0.035.

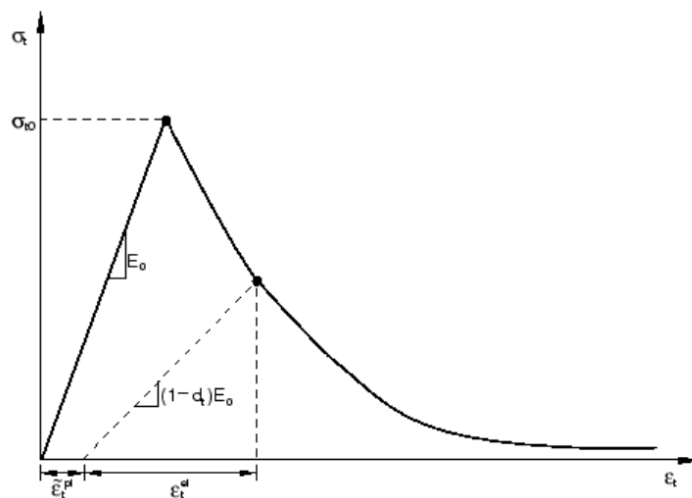
$$\sigma_c = \begin{cases} E_c \epsilon_c, & \text{when } \epsilon_c < 0.4 \frac{f'_c}{E_c} \\ \frac{\eta_c \left( \frac{\epsilon_c}{\epsilon_0} \right) - \left( \frac{\epsilon_c}{\epsilon_0} \right)^2}{1 + (\eta_c - 2) \left( \frac{\epsilon_c}{\epsilon_0} \right)} f'_c, & \text{when } 0.4 \frac{f'_c}{E_c} \leq \epsilon_c \leq 0.0035 \\ \left( \frac{2 + \lambda_c f'_c \epsilon_0}{2f'_c} - \lambda_c \epsilon_0 + \frac{\lambda_c \epsilon_c^2}{2\epsilon_0} \right)^{-1}, & \text{when } 0.0035 \leq \epsilon_c \leq 0.035 \end{cases} \quad (8.2)$$

Based on data obtained from testing of concrete cylinders taken during the casting of the girder, the strength of the concrete and the MOE (testing day) for the first girder was found to be approximately 10.3 ksi and 5541 ksi, respectively. The Poisson's ratio of concrete varies between 0.15 and 0.22. The Poisson's ratio for concrete in this investigation is taken as 0.2. The stress–strain relationship is presented in Figure 8.6.

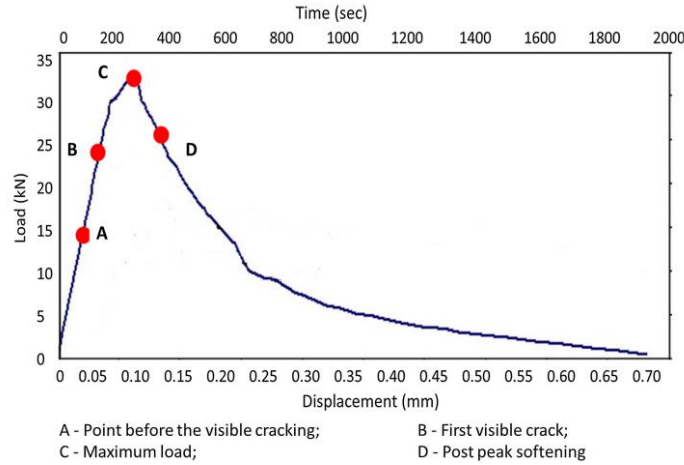


(a) Compressive Stress–Strain Relationship      (b) Compressive Damage–Strain Relationship  
**Figure 8.6. Compressive behavior for concrete.**

For the tensile response of concrete, the cracking load, a crucial factor, was not accounted for in the previous model. To bridge this gap, adjustments were introduced to the original model. The previous model assumed that concrete has a linear elastic behavior before reaching the concrete tensile strength, as shown in Figure 8.7. However, experimental testing on concrete cylinders and beams in tension revealed that noticeable cracks emerged between load levels of 0.65 to 0.8 of the ultimate loads. In a recent study, Mirgal et al. (2023) monitored how tension damage progresses and assessed fracture in plain concrete beams subjected to three-point bending, as shown in Figure 8.8. This realization prompted the researchers to calculate the cracking stress of the concrete and include it in the new model to address this limitation.



**Figure 8.7. Uniaxial tensile-stress–strain relationship for concrete.**



**Figure 8.8. Transition points along the three-point bending beam load-displacement curve ((Mirgal et al. 2023).**

For the *tensile response of concrete*, linear elastic behavior is assumed up to the cracking stress.

Zad and Melhem (2023) suggested the following equation to estimate the cracking stress:

$$f_{cr} = 4.56f'_c{}^{0.5} \text{ with } f'_c \text{ in (psi)} \quad (8.3)$$

Incorporating the post-peak tensile response, which indicates the onset of cracking, requires either a softening stress versus inelastic strain curve or a stress versus cracking opening curve, both of which are based on the concept of fracture energy.

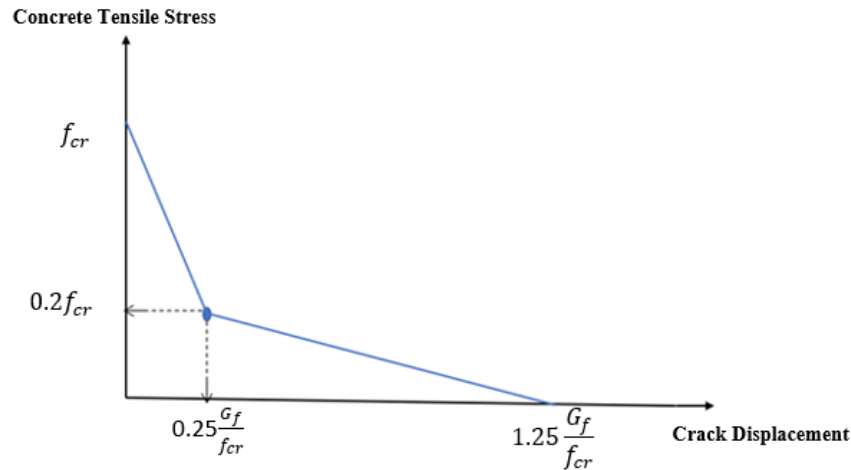
The concept of fracture energy,  $G_f$ , established by Hillerborg et al. (1976), is used to characterize the post-peak tensile response in the present work. Hillerborg et al. defined  $G_f$  as the crack opening energy release rate per unit fracture area, making it a material property. Several factors affect  $G_f$ , including the water-to-cement ratio, the aggregate size, the age of concrete, and the curing conditions (Mercan et al. 2010; Okumus et al. 2012). The *fib* Model Code 2010 suggested the following estimate of the fracture energy in the absence of physical testing:

$$G_f = 0.17f'_c{}^{0.18} \text{ with } G_f \text{ in } \left(\frac{\text{ib}}{\text{in}}\right) \text{ and } f'_c \text{ in (psi)} \quad (8.4)$$

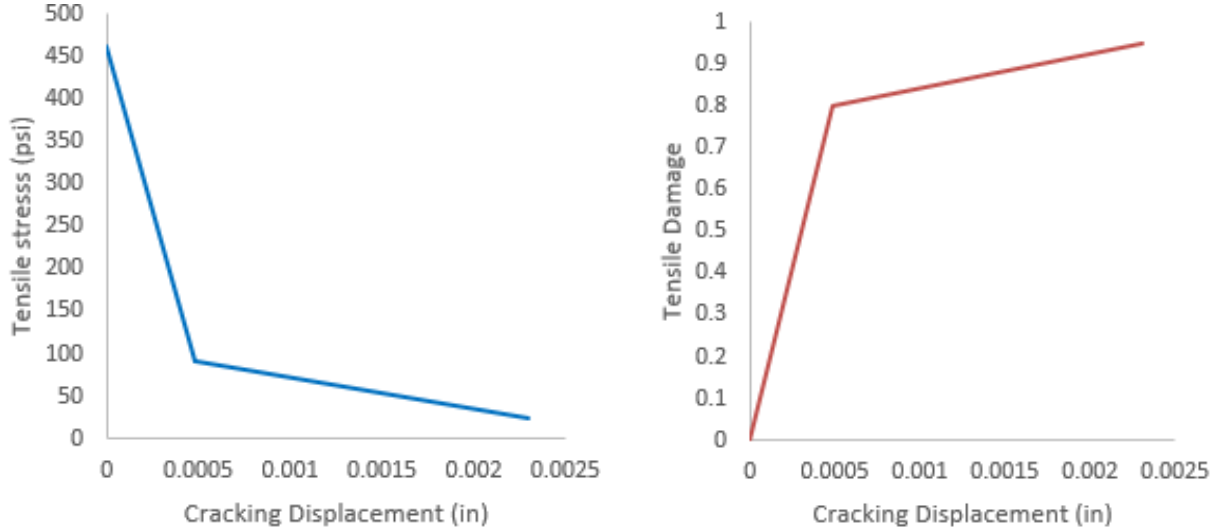
To obtain the cracked pattern in concrete, modified bilinear softening, proposed by the *fib* Model Code 2010, is used to describe the softening response. Figure 8.9 and Figure 8.10 display the

modified bilinear forms as functions of cracking strength,  $f_{cr}$ , and the total fracture energy,  $G_f$ . Tensile damage,  $d_t$ , was also considered based on the following equation:

$$d_t = 1 - \frac{\sigma_t}{f_{cr}} \quad (8.5)$$



**Figure 8.9. Modified post-peak tensile stress versus cracking displacement (fib Model Code 2010).**

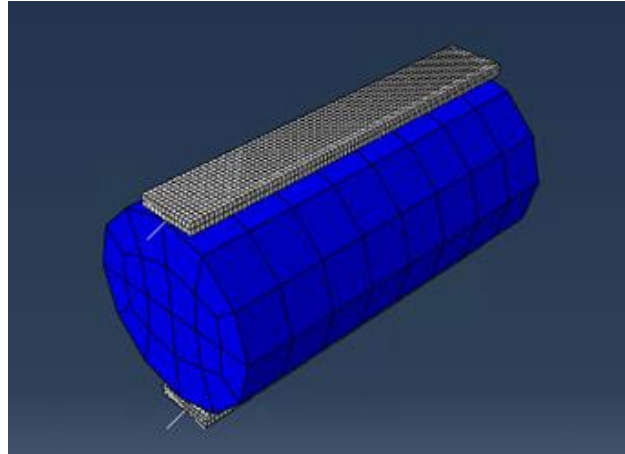


(a) Tensile stress-cracking displacement (b) Tensile damage-cracking displacement

**Figure 8.10. Tensile behavior of concrete.**

A splitting tensile test was simulated using ABAQUS to verify the accuracy of the updated model in capturing the ultimate load. The mesh size used was the same as the one employed for the girders, as depicted in Figure 8.11. Based on data obtained from testing of concrete cylinders

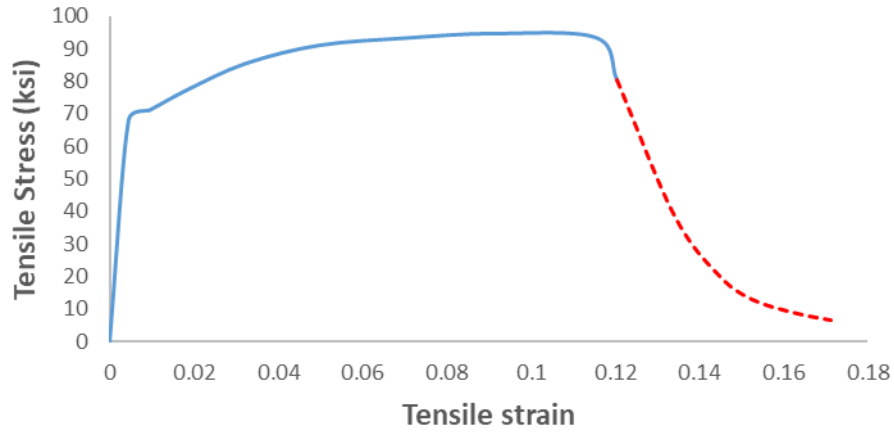
taken during the girder casting, the STS was 1.16 ksi, while the result from FE was 1.13 ksi. The variance between the predicted and experimental failure loads was approximately 3 percent, indicating a strong level of agreement between the two.



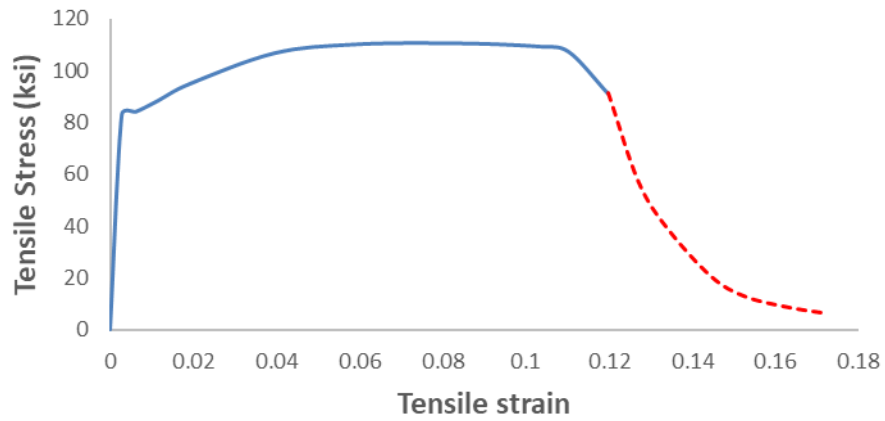
**Figure 8.11. ABAQUS model geometry for splitting tensile test.**

#### *8.2.2.2 Steel Rebar*

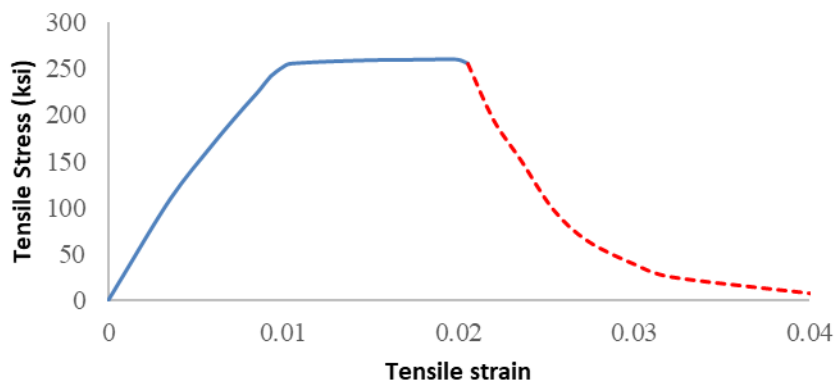
Three steel material models were considered in this study: models of the mild steel of Grade 60 and Grade 80 reinforcing bars and a model for the Grade 270 low relaxation strands. The elastic modulus and Poisson's ratio were taken as 29,000 ksi and 0.29, respectively. The stress–strain curves for the steel material are presented in Figure 8.12, Figure 8.13, and Figure 8.14. These curves are divided into two branches, namely the hardening and softening branches, which are indicated by blue and red, respectively, as shown in the figures. The inclusion of the softening branch represented by the red curve in the simulations is not intended real-world material behavior but was used for convergence and numerical stability purposes.



**Figure 8.12. Stress versus strain curve for mild steel Grade 60.**



**Figure 8.13. Stress versus strain curve for mild steel Grade 80.**



**Figure 8.14. Stress versus strain curve for low relaxation strands Grade 270.**

### 8.2.3 Defining Loading Steps

The simulation of a structure may include one or more loading steps. All analyses included two loading steps. The initial stresses in tendons and the gravity loads were applied in the first step. In the second step, vertical loading was applied. All analyses were conducted using the explicit solver provided by ABAQUS/Explicit. Explicit analysis can be used for dynamic problems or quasi-static problems with a low loading rate. The explicit solver is computationally efficient for large problems and models with high nonlinearities (material and geometric) as well as for extremely discontinuous events (e.g., contact/impact amongst rigid or deformable bodies).

The explicit solver uses a central-difference integration scheme, which is conditionally stable, and the maximum stable time increment is a function of the highest frequency of the model. An approximation of the maximum stable time increment is provided by the smallest transit time of a dilatational (volumetric) wave across any of the elements of the model. This transit time,  $\Delta t_{\text{tran},e}$ , for a given element is estimated as:

$$\Delta t_{\text{tran},e} = L_{e,\min} \sqrt{\left(\frac{\rho}{E}\right)} \quad (8.6)$$

where  $L_{e,\min}$  is the minimum of the equivalent element length,  $\rho$  is the mass density, and  $E$  is the current stiffness modulus (function of the deformation). Thus, this transit time is larger for elements of larger size, larger mass, and smaller stiffness. As a result, the critical stable time increment for a model is controlled by the smallest, stiffest, and lightest element, while mesh refinement may significantly reduce this increment. To ensure that the time increment was never smaller than a prescribed minimum value, targeted mass scaling was utilized, resulting in an equivalent mass increase for very small elements, which otherwise would lead to time increments smaller than the prescribed minimum value of  $9 \times 10^{-5}$  s. Displacement was applied at a rate of 0.05 in./s. To ensure that quasi-static conditions were achieved, the kinetic energy of the model over time was monitored to confirm that it remained orders of magnitude smaller than the strain energy.

#### **8.2.4 Constraints and Contact between Elements**

Steel rebar truss elements were embedded into the concrete elements. This approach enforces the nodal displacement of these truss elements to be obtained from the displacement shape functions of the concrete solid elements, which constitute the host region.

Displacement at the girder midspan was applied by a rectangular steel piece, while the girders were sitting on pedestals to mimic the actual supports. These contacts were modeled using a pair of driving and dependent surfaces through a tie constraint. The structural system was modeled using ABAQUS software, with external contacts defined between the supports, loading plates, deck slab, and girder. The top surface of the supports was assigned as the driving surface, while the bottom slave of the girder was assigned as the dependent surface. Similarly, the top surface of the girder was assigned as the driving component in the model, while the bottom surface of the deck slab was assigned as the dependent component.

Additionally, the deck slab was assigned as the driving component on its top surface, while the loading plates were assigned as the dependent components on its bottom surface. By assigning appropriate driving and dependent components in the model, accurate simulation of the physical interactions between different components of the structural system was achieved. This enabled the transfer of forces and deformations between the components, which is crucial for accurately analyzing the structural behavior. To reduce the number of numerical errors, the dependent surface should be made of a more deformable material and have a finer mesh than the driving surface. For this reason, the dependent/dependent surface was assigned to the surfaces of the concrete. By utilizing these tie constraints, the displacements of the nodes on the dependent surface are interpolated from the nodes on the driving surface, which results in the elimination of the relative slip that existed between these two surfaces.

#### **8.2.5 Boundary Conditions and Loading**

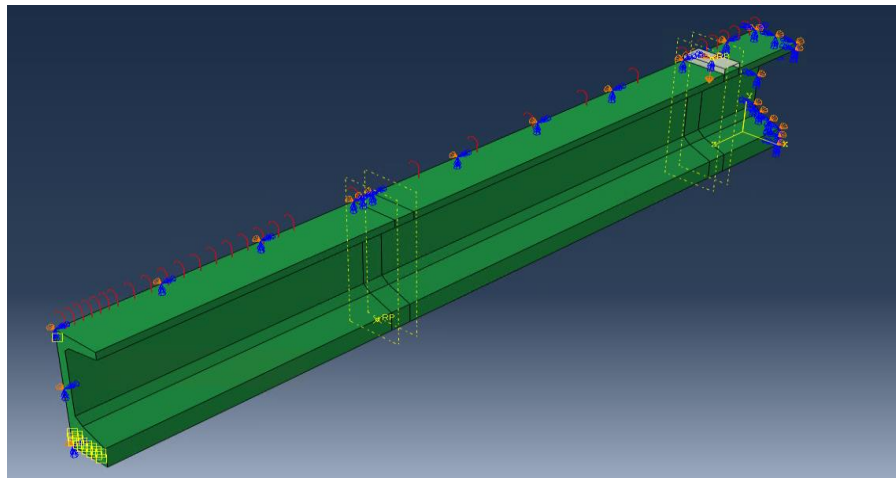
For boundary conditions, in the experimental test, a simply supported beam was tested.

Additionally, because the beam that was tested had a symmetrical design, we were able to model a fourth of the beam. Therefore, to mimic the support conditions situated 7.5 ft from the ends of the beam, the displacement was constrained in the X and Y directions and was represented by U2



$= U3 = 0$ . On the other side, the symmetry boundary condition was implemented when the symmetry line was found, which was 25 ft and 9 ft away. They contained a restriction on movement along the horizontal axis (in the direction Z), as well as a restriction on rotation about an out-of-plane axis (in the directions X and Y), each of which was represented by the values  $U3 = 0$ ,  $UR1 = 0$ , and  $UR2 = 0$  in the proper location. Also, the restriction of movement in directions X and the rotation about out-of-plane axes (direction Z and Y) are indicated by  $U1 = 0$ ,  $UR3 = 0$ , and  $UR2 = 0$ , accordingly. These values indicate that the movement cannot occur in those directions.

Displacement-controlled loading at midspan was used. To illustrate, a particular value of displacement was applied at the loading plate. The value that was used was 3 in. To replicate these loading conditions, the permissible displacement was set to 3 in. along the vertical axis (in the direction Y),  $U2 = 3$  in., and the location was set to 22.75 ft from the end. The boundary conditions and the applied loads are shown in Figure 8.15.



**Figure 8.15. Boundary conditions and applied loads on FE models.**

### **8.2.6 Simulation with Element Deletion**

This study also employed element deletion as a means of more accurately predicting failure mechanisms. Although it should be noted that achieving a perfect replication of experiments was challenging due to simplifications in the simulations, element deletion was found to be essential to quantifying how prestressed girders exhibit shear failure. By removing elements when 95 percent of the total damage was reached, the formation of cracks could more naturally be

captured. Furthermore, this approach predicted sudden drops in the shear force-displacement curve, resembling those observed in the laboratory experiments during shear failure. This graphical representation enhanced the failure process.

The removal of elements in ABAQUS software results in the exclusion of these elements from all analysis, leading to the loss of associated information such as stress and strain data. This step can provide significant challenges, especially when dealing with complex structures or systems. The loss of information might present a significant disadvantage and impede thorough post-processing and analysis. In addition, the removal of elements in a model creates a discontinuity that has the potential to generate stress concentrations that are not representative of real-world conditions. This action can lead to less accurate results, especially when the eliminated elements are actively engaged in supporting significant loads or experiencing high levels of stress (Saykin et al. 2017).

### **8.3 MODEL COMPARISON WITH THE EXPERIMENTAL DATA**

In this section, a comparison of the FE model predictions with experimental data for girders G1\* and G1 is performed to verify the accuracy of the FE models and ensure that these models and the related modeling assumptions can be used with confidence to predict the shear behavior of prestressed concrete girders in real-world situations.

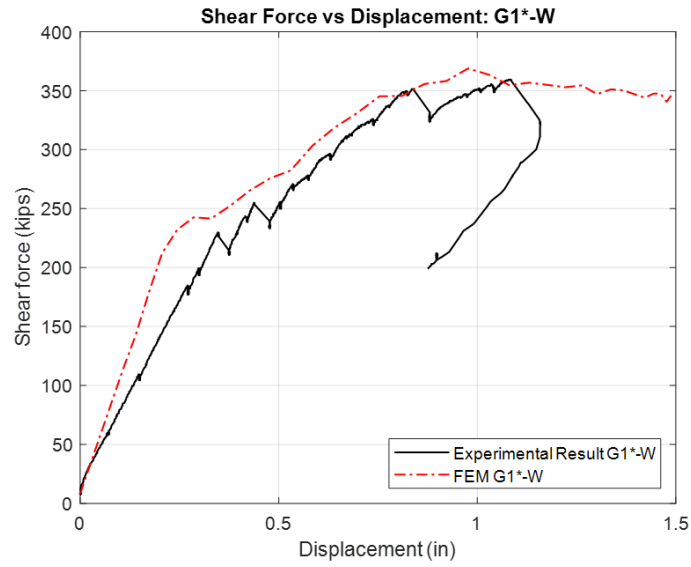
#### **8.3.1 G1\* Test**

##### *8.3.1.1 G1\* Test without Element Deletion*

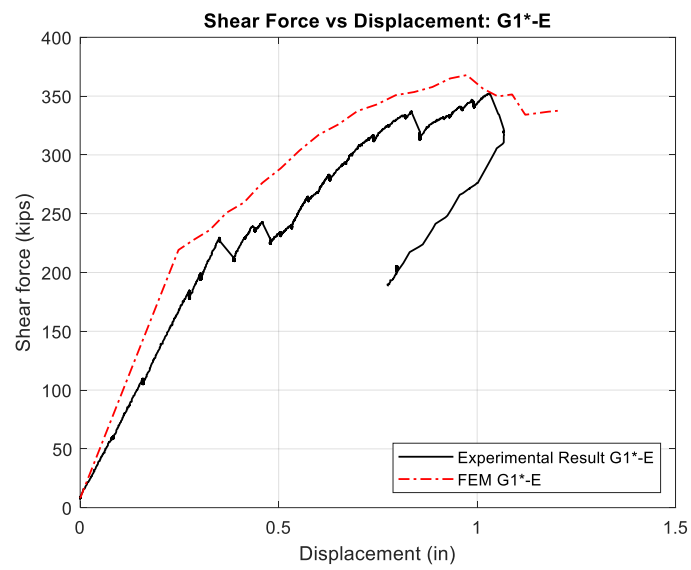
The G1\* girder is a Tx54 type girder and has two different shear reinforcements in specific test areas. This girder is cast with a deck of 10 in. in thickness and 3 ft in width. The west side of the girder has 18 in. spacing of 60 ksi R-bars, and the east side of the girder has 26 in. spacing of 80 ksi R-bars with equivalent shear strength.

In Figure 8.16, a comparison is made between the test data and the FE model predictions for the shear force versus deflection at the point of load application. Also, Figure 8.17 and Figure 8.18 compare the observed damage and crack patterns and orientation observed experimentally with the damage predicted via FE analyses on the west and east sides of the G1\* girder, respectively.

These figures also include the computationally predicted stresses in R-bars. As observed, the shear force versus deflection curves, as well as the failures of the two girders, were reproduced accurately by the FE analyses. In the case of the west side, the experimental occurrence of cracking and the ultimate shear force took place at 252 kips and 360 kips, respectively, whereas in the FE analysis, these values were 238 kips for cracking and 370 kips for ultimate shear force. On the other side, the cracking and ultimate shear force occurred at 229 kips and 352 kips, respectively, while the corresponding values predicted by the FE analyses were 240 kips for cracking and 350 kips for ultimate shear force. The comparison between the predicted and experimental crack loads revealed close agreement, with a difference of only 6 percent and 5 percent for the west and east sides, respectively, of girder G1\*. Additionally, a close agreement was found in the response between the predicted and experimental failure loads, with differences of only 3 percent for the west side and 0.6 percent for the east side. This result indicates that the FE models were able to reasonably predict the failure loads of the specimens. Moreover, the FE models accurately replicated the web shear failure mode that was observed in the experiments, indicating that the models were able to capture the essential failure mechanisms of the specimens with good fidelity (Figure 8.17 and Figure 8.18).

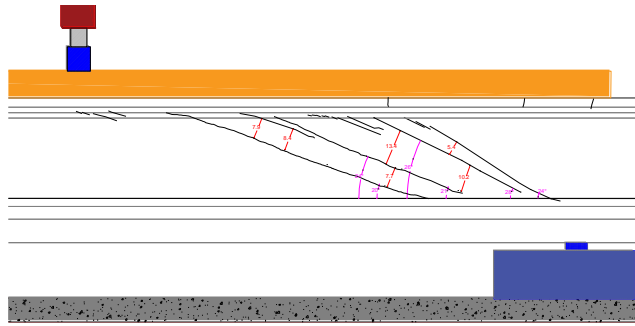


(a)

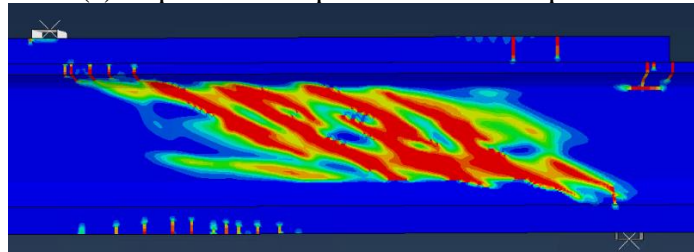


(b)

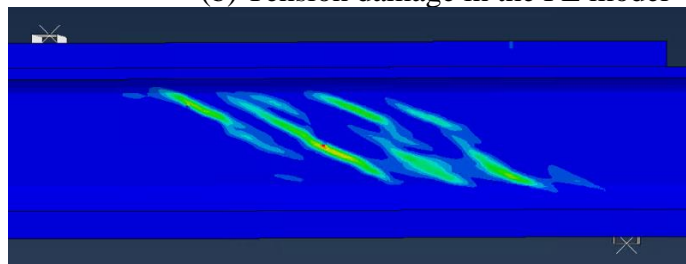
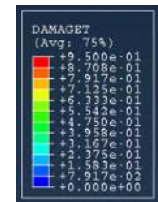
**Figure 8.16. Shear force versus displacement comparison between tests and FE models for G1\* girder: (a) west side, (b) east side.**



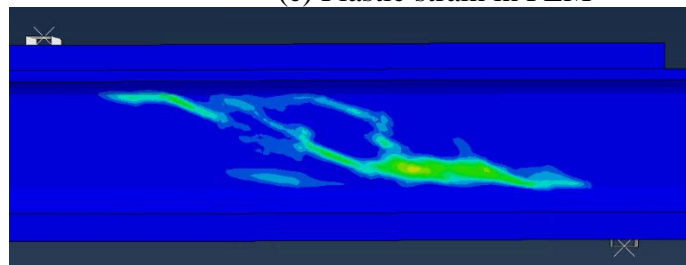
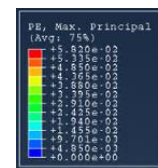
(a) Experimental specimen crack map at ultimate failure



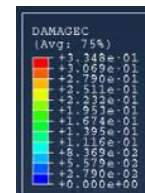
(b) Tension damage in the FE model



(c) Plastic strain in FEM



(d) Compression damage in FEM



(e) Axial stress in R-bars in FEM

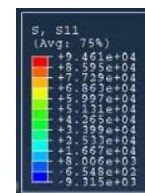
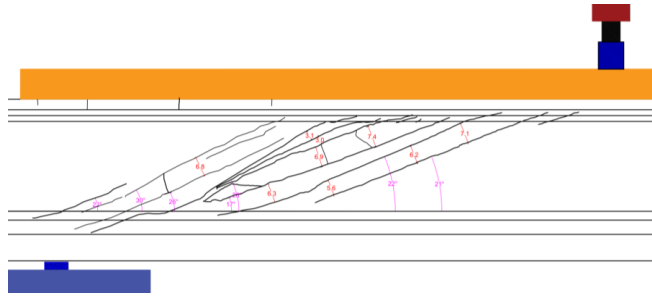
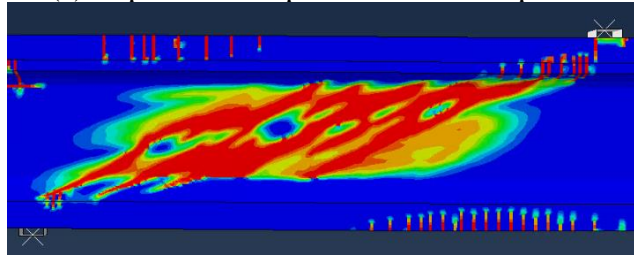


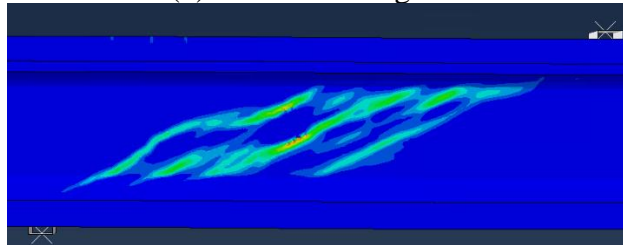
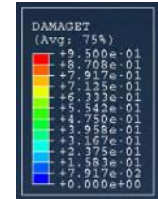
Figure 8.17. Results of FE model at peak load of G1\* east.



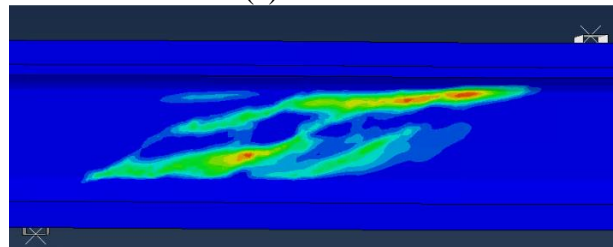
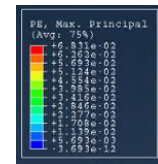
(a) Experimental specimen crack map at ultimate failure



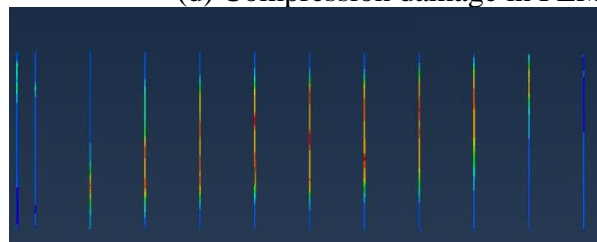
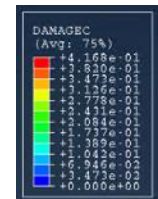
(b) Tension damage in the FE model



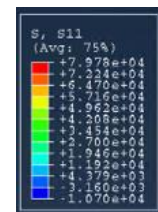
(c) Plastic strain in FEM



(d) Compression damage in FEM



(e) Axial stress in R-bars in FEM



**Figure 8.18. Results of FE model at peak load of G1\* west.**

### 8.3.1.2 G1\* Test with Element Deletion

In Figure 8.19, a comparison is made between the test data and the predictions from FE models, both with and without element deletion. This comparison is focused on the shear force versus

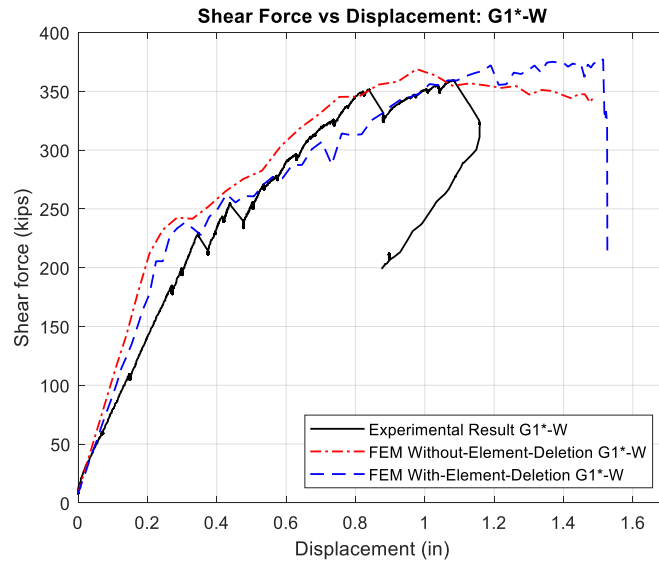
deflection at the point of load application. Additionally, Figure 8.20 and Figure 8.21 present comparisons of the observed damage, crack patterns, and orientations found experimentally with the damages predicted via FE analyses on the west and east sides of the G1\* girder, respectively.

On the west side, the occurrence of cracking and the ultimate shear force were recorded at 252 kips and 360 kips, respectively, in the experimental data. The FE analysis without element deletion estimated these values at 238 kips for cracking and 370 kips for ultimate shear force, whereas, with element deletion, the predictions stood at 232 kips and 377 kips, respectively.

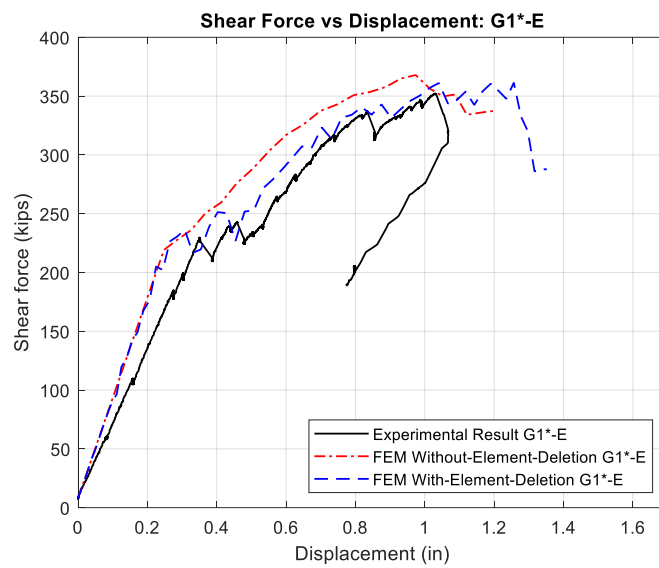
For the east side, the experimentally observed values for cracking and ultimate shear force were 229 kips and 352 kips, respectively. The corresponding values predicted by the FE analysis without element deletion were 240 kips and 350 kips, whereas the FE analysis with element deletion forecasted 230 kips for cracking and 361 kips for ultimate shear force.

Comparing the FE models with and without element deletion, the model with element deletion exhibited a 2.5 percent decrease in the predicted cracking value and a 1.9 percent increase in the ultimate shear force on the west side. Similarly, on the east side, the application of element deletion resulted in a 4.2 percent reduction and a 3.1 percent increase in the estimated cracking and ultimate shear force values, respectively.

Furthermore, both FE models, with and without element deletion, effectively replicated the web shear failure mode observed in the experiments, signifying that the models could capture the essential failure mechanisms of the specimens with high fidelity (as depicted in Figure 8.20 and Figure 8.21).



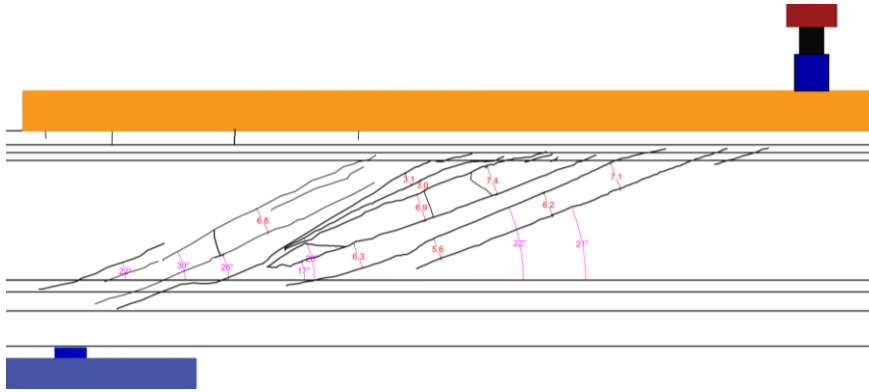
(a)



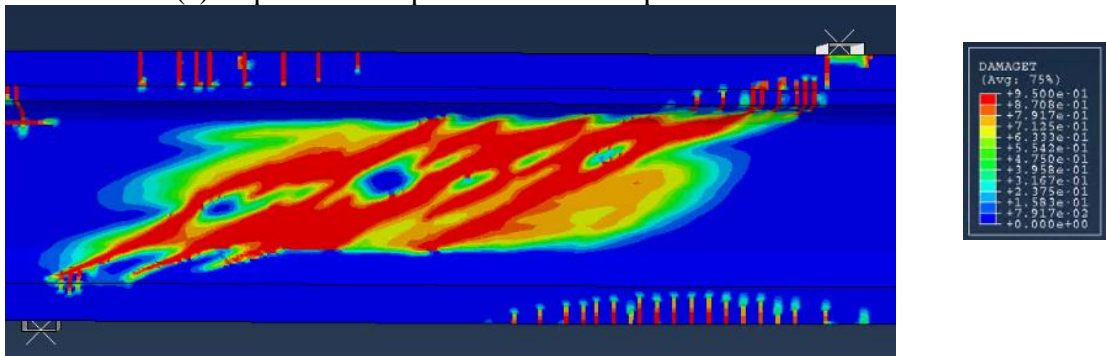
(b)

**Figure 8.19. Shear force versus displacement comparison between tests and FE models for G1\* girder: (a) west side, (b) east side**

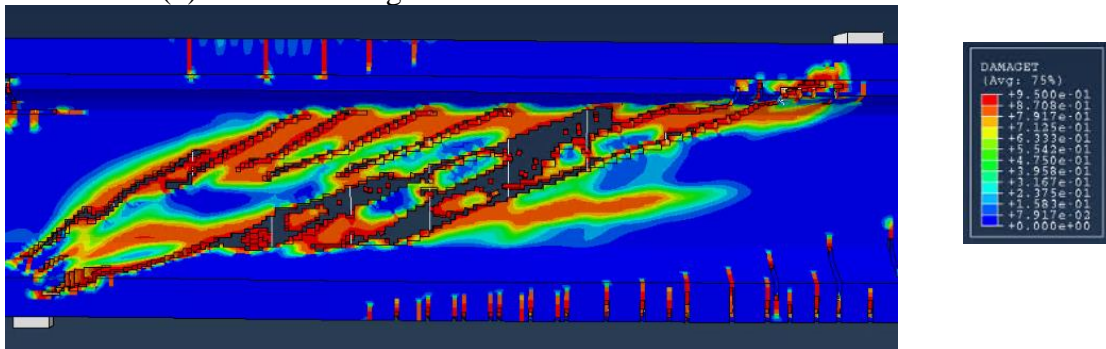




(a) Experimental specimen crack map at ultimate failure

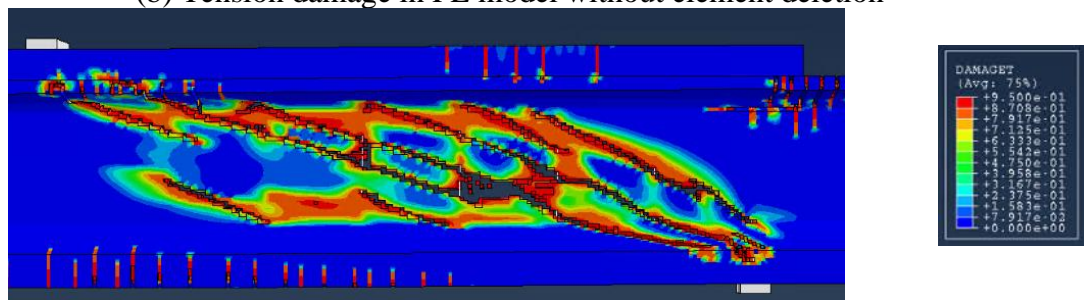
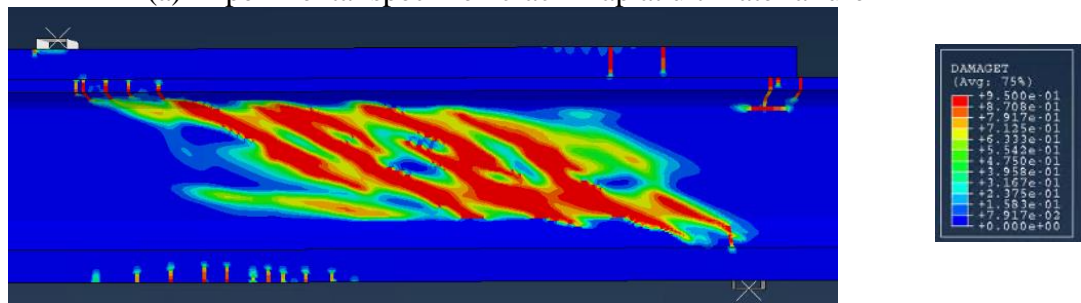
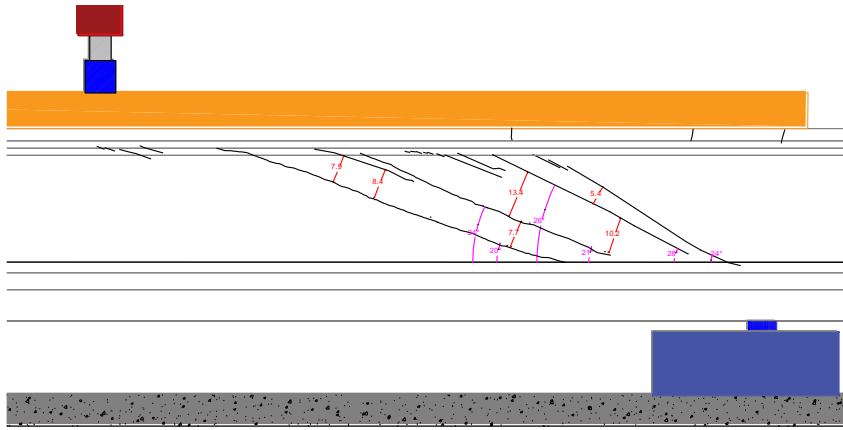


(b) Tension damage in FE model without element deletion



(c) Tension damage in FE model with element deletion

**Figure 8.20. Results of FE model at peak load of G1\* west side.**



(c) Tension damage in FE model with element deletion  
**Figure 8.21. Results of FE model at peak load of G1\* east side.**

### 8.3.2 G1 Test

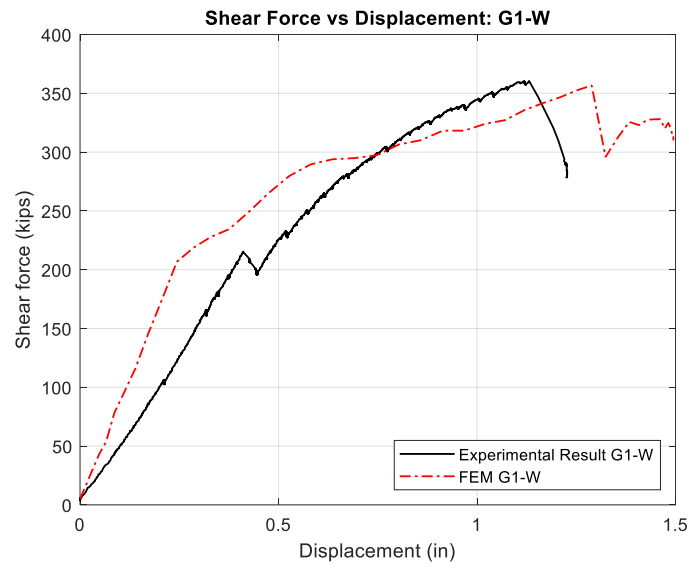
#### 8.3.2.1 G1 Test without Element Deletion

The G1 girder possesses identical design parameters as the G1\* girder, but differs in one aspect: the inclusion of a deck. The west side of the girder has an 18 in. spacing of 60 ksi R-bars, and the east side of the girder has a 26 in. spacing of 80 ksi strands with equivalent shear strength.

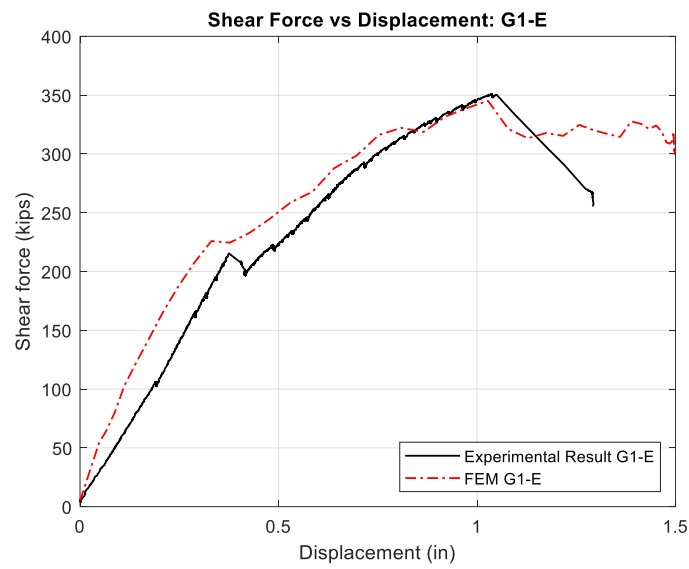
In Figure 8.22, a comparison of experimental versus computationally predicted shear force versus deflection at the point load application curves is presented. Figure 8.23 and Figure 8.24

compare the observed damage and crack patterns and orientation observed experimentally with the damage predicted via FE analyses on the west and east sides of the G1 girder, respectively. These figures also include the computationally predicted stresses in R-bars.

Figure 8.22 demonstrates that the shear force versus deflection curves, as well as the failures of the two girders, were reproduced accurately by the FE models. The experimental cracking and ultimate shear forces for the west side were experimentally measured to be 215 kips and 361 kips, respectively, while the FE analyses predicted 206 kips and 357 kips, respectively. On the east side, the experimental cracking and ultimate shear forces occurred at 215 kips and 351 kips, respectively, while the FE analyses predicted 221 kips and 349 kips, respectively.

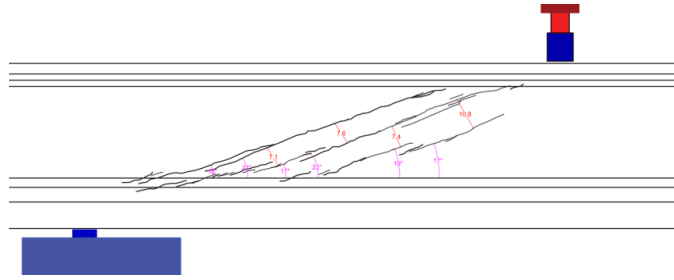


(a)

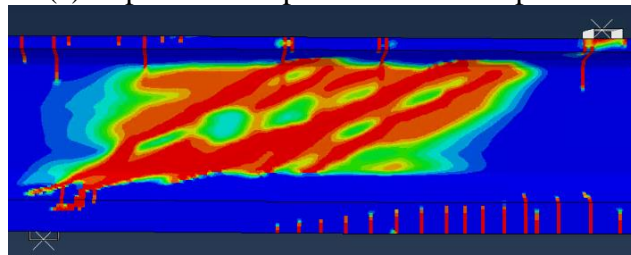


(b)

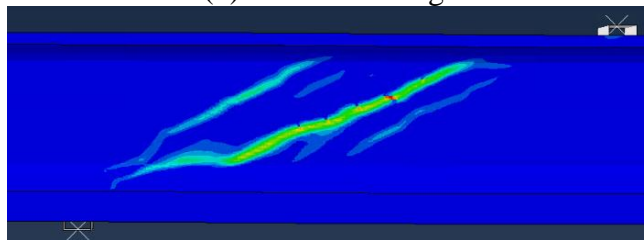
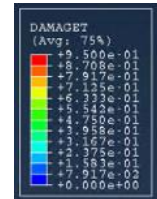
**Figure 8.22. Shear force versus displacement comparison between tests and FE models for G1 girder: (a) west side, (b) east side.**



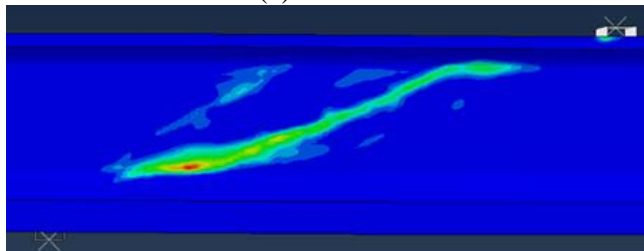
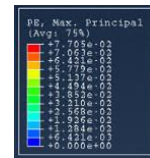
(a) Experimental specimen crack map at ultimate failure



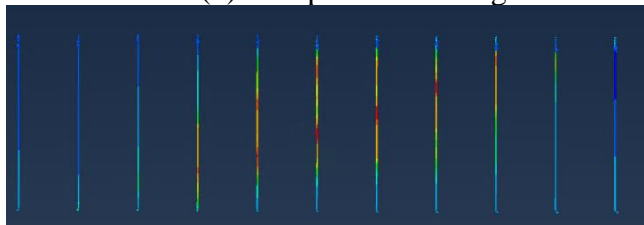
(b) Tension damage in FE model



(c) Plastic strain in FEM



(d) Compression damage in FEM



(e) Axial stress in R-bars in FEM

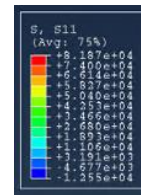
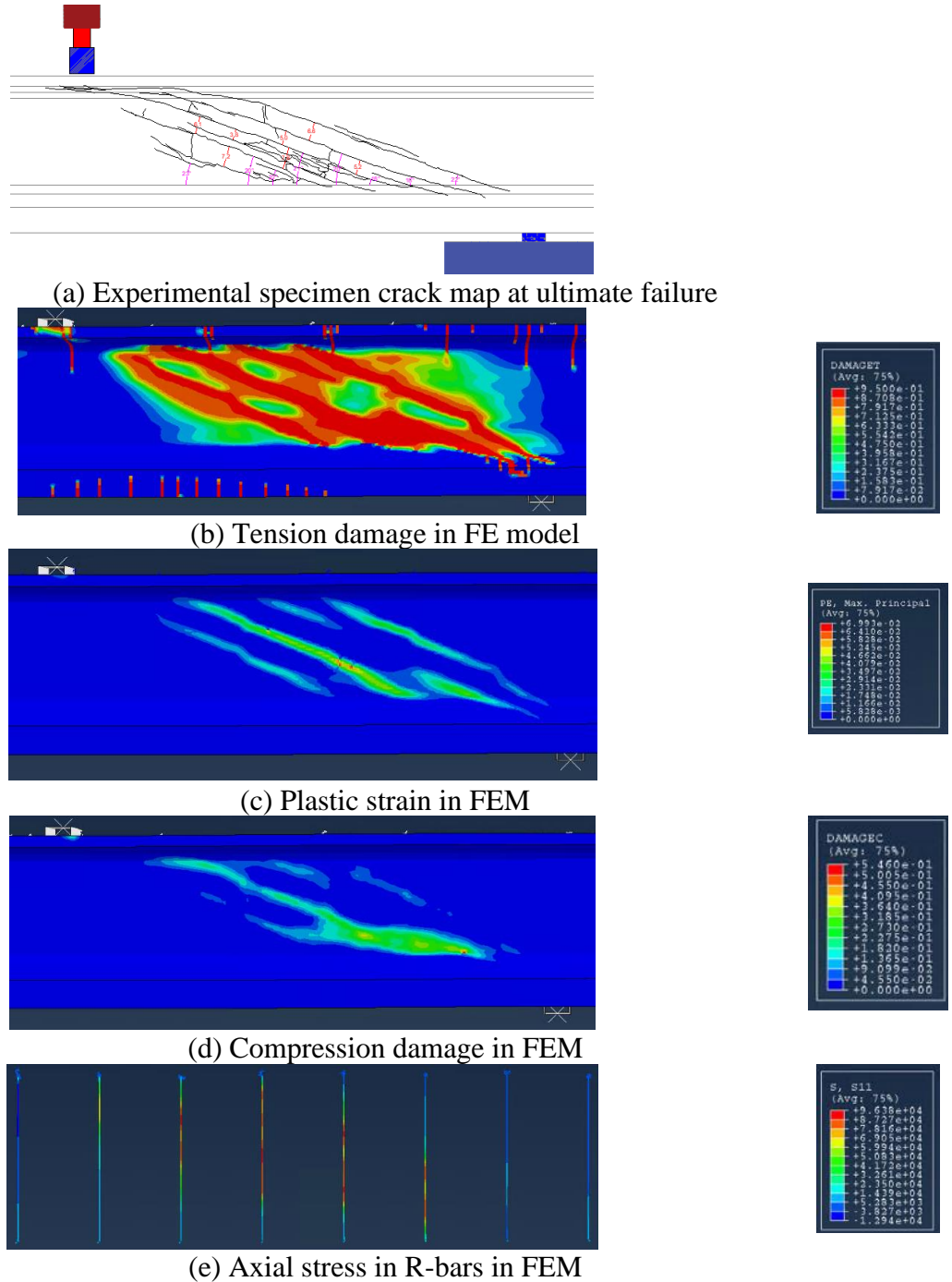


Figure 8.23. Results of FE model at peak load of G1 west side.



**Figure 8.24. Results of FE model at peak load of G1 east side.**

### 8.3.2.2 G1 Test with Element Deletion

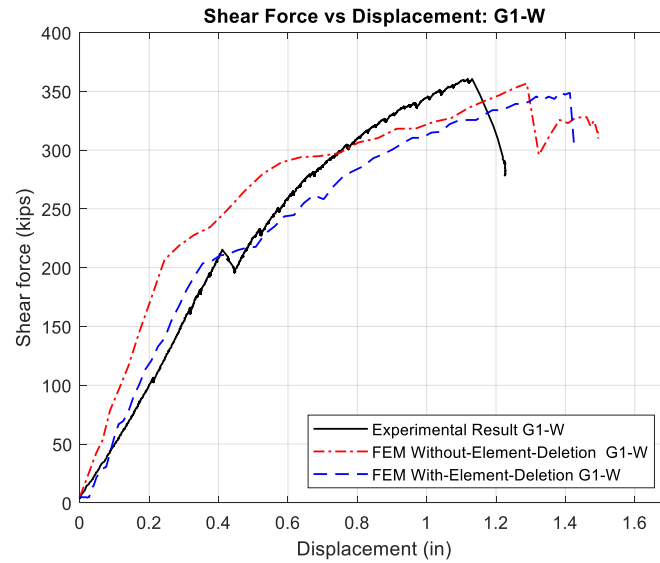
In Figure 8.25, a comparative study utilizing both the presence and absence of element deletion is presented between the test data and the predictions derived from FE models. Subsequently, Figure 8.26 offers insights into the observed damages, including the patterns and orientations of

cracks found experimentally and those predicted through FE analyses on the west and east sides of the G1 girder, respectively.

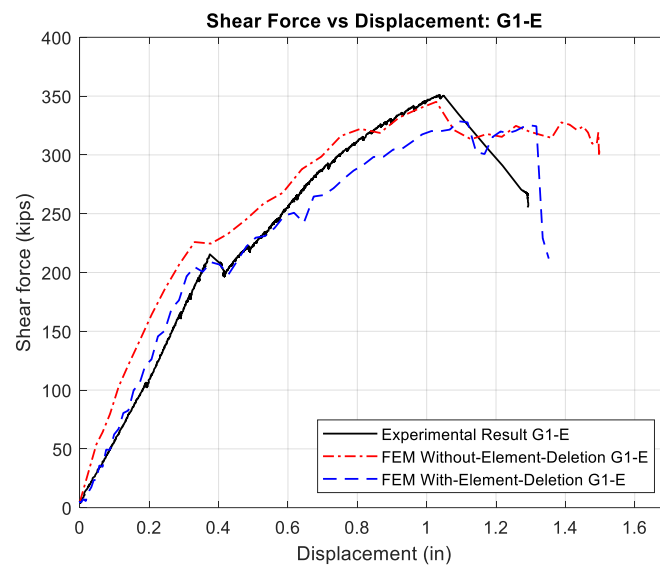
On the west side, the experimental data recorded the onset of cracking and the ultimate shear force at 215 kips and 361 kips, respectively. The FE model without element deletion estimated these figures at 206 kips and 357 kips, while incorporating element deletion adjusted the predictions to 204 kips and 349 kips, respectively. This outcome implies that the introduction of element deletion resulted in a 0.98 percent decrease in the predicted value for cracking and a 2.24 percent decrease in the value for ultimate shear force on the west side.

For the east side, cracking and ultimate shear force were experimentally observed at 215 kips and 351 kips, respectively. The FE model, without implementing element deletion, predicted values of 221 kips and 349 kips. Conversely, applying element deletion yielded forecasted values of 204 kips and 328 kips for cracking and ultimate shear force, respectively. Thus, on the east side, the utilization of element deletion led to a 7.7 percent reduction in the predicted cracking value and a 6.01 percent decrease in the ultimate shear force.

Moreover, both FE models—with and without element deletion—were successful in replicating the web shear failure mode observed in the experiments, thereby demonstrating their ability to accurately capture the fundamental failure mechanisms of the specimens. Nonetheless, it warrants emphasis that there were discernible differences in the fidelity of the models on either side of the G1 girder. On the west side, the model incorporating element deletion demonstrated a closer resemblance to the web shear failure mode observed experimentally than to its counterpart without element deletion. Conversely, on the east side, the model without element deletion yielded a more accurate reflection of the observed failure mode, as depicted in Figure 8.27.



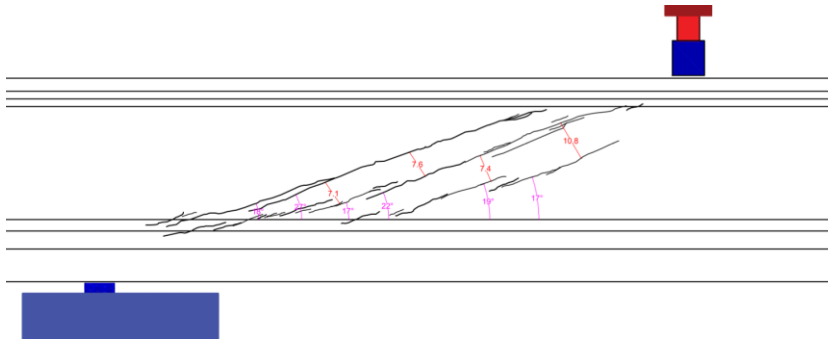
(a) West side



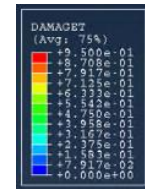
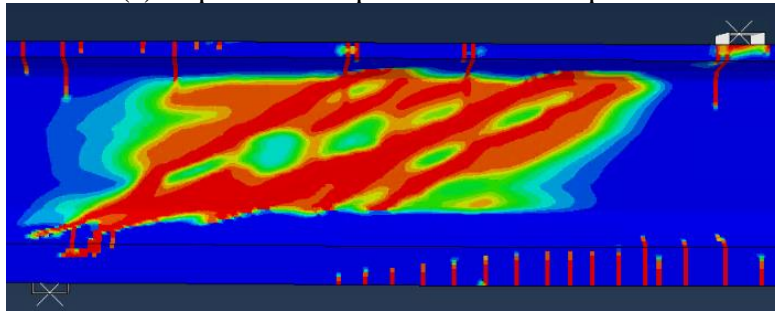
(b) East side

**Figure 8.25. Shear force versus displacement comparison between tests and FE models for G1 girder: (a) west side, (b) east side.**

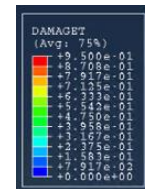
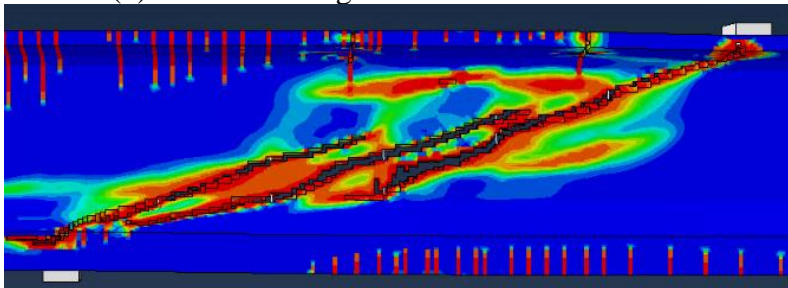




(a) Experimental specimen crack map at ultimate failure

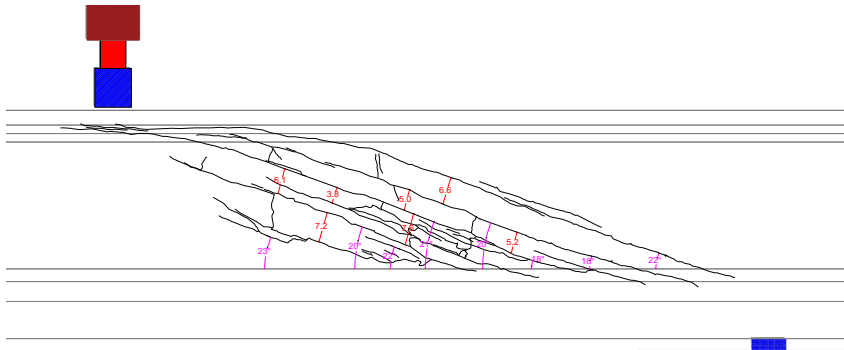


(b) Tension damage in FE model without element deletion

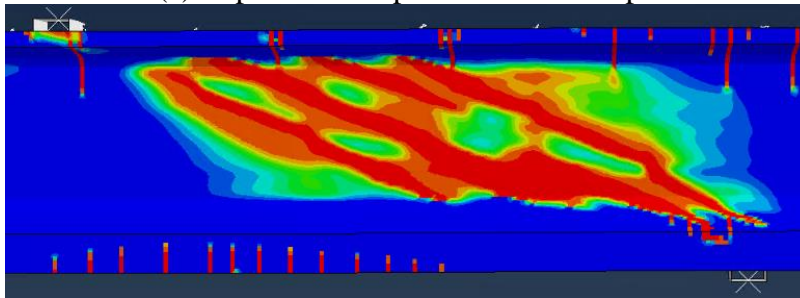


(c) Tension damage in FE model with element deletion

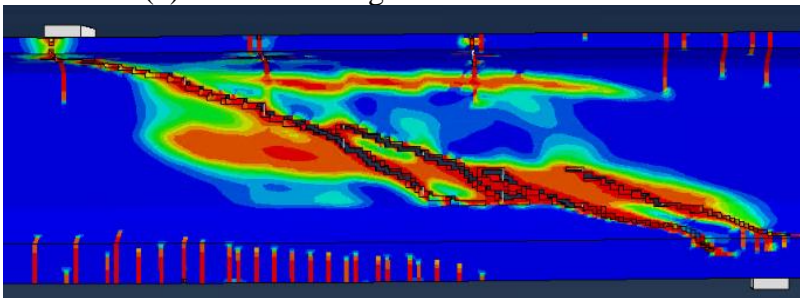
**Figure 8.26. Results of FE model at peak load of G1 west side.**



(a) Experimental specimen crack map at ultimate failure



(b) Tension damage in FE model without element deletion



(c) Tension damage in FE model with element deletion

**Figure 8.27. Results of FE model at peak load of G1 east side.**

## 8.4 EXTRACTING DATA FROM FINITE ELEMENT ANALYSIS

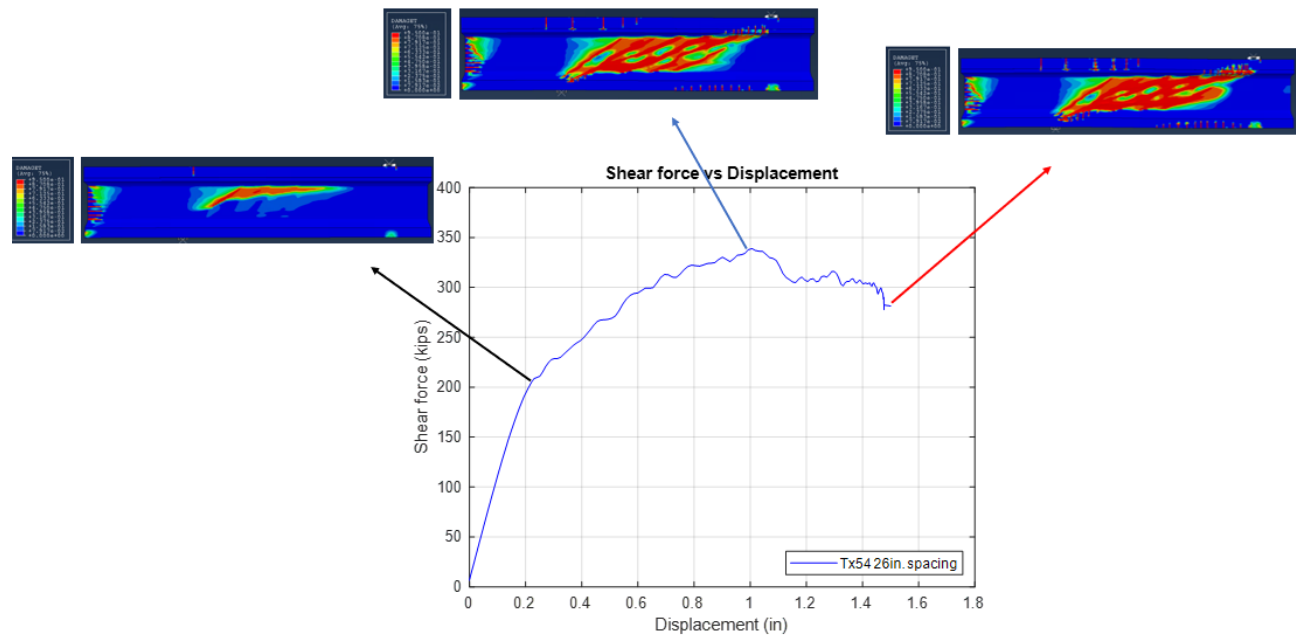
The data extraction process for assessing the structural behavior of the analyzed components involved retrieving crucial parameters such as cracking force, maximum force, and inclination angle. Figure 8.28, Figure 8.29, and Figure 8.30 illustrate the progression of tension damage, plastic strain, and axial stress across different stages of shear force. The methodology for obtaining each of these critical data points is outlined next.

### 8.4.1 Cracking Shear Force

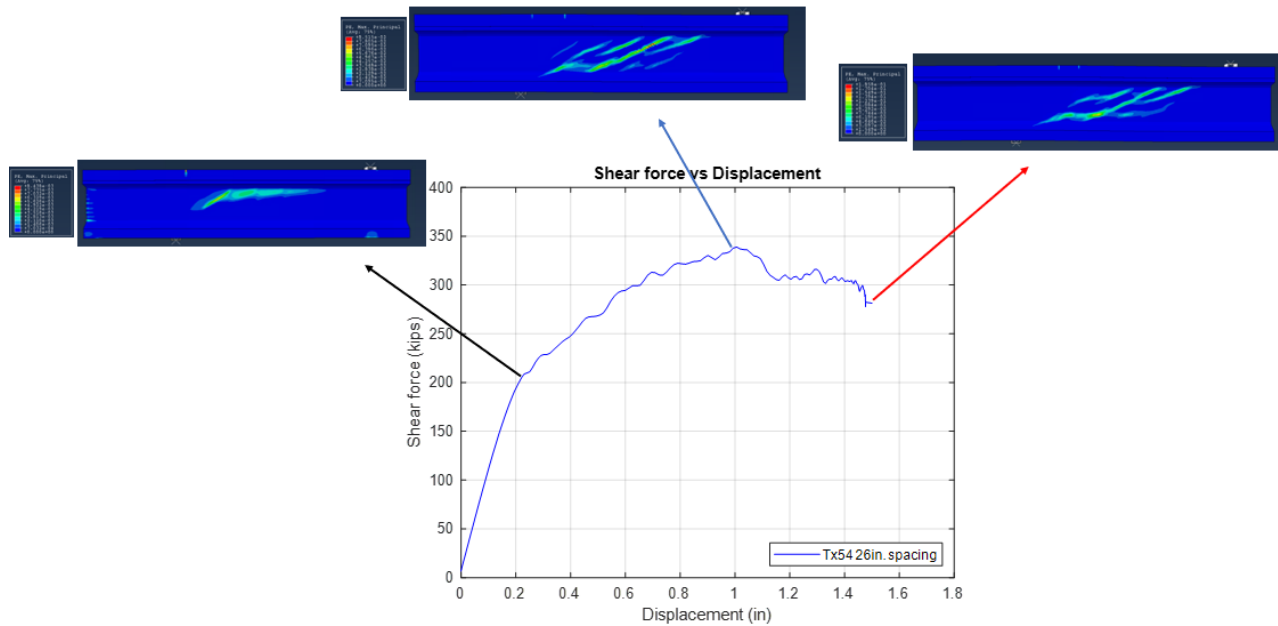
The cracking force represents the point at which the material initially begins to exhibit signs of cracking or failure. This value was derived from the force-displacement analysis of the simulated model at the point where the curve deviates from linear behavior.

### 8.4.2 Maximum Shear Force

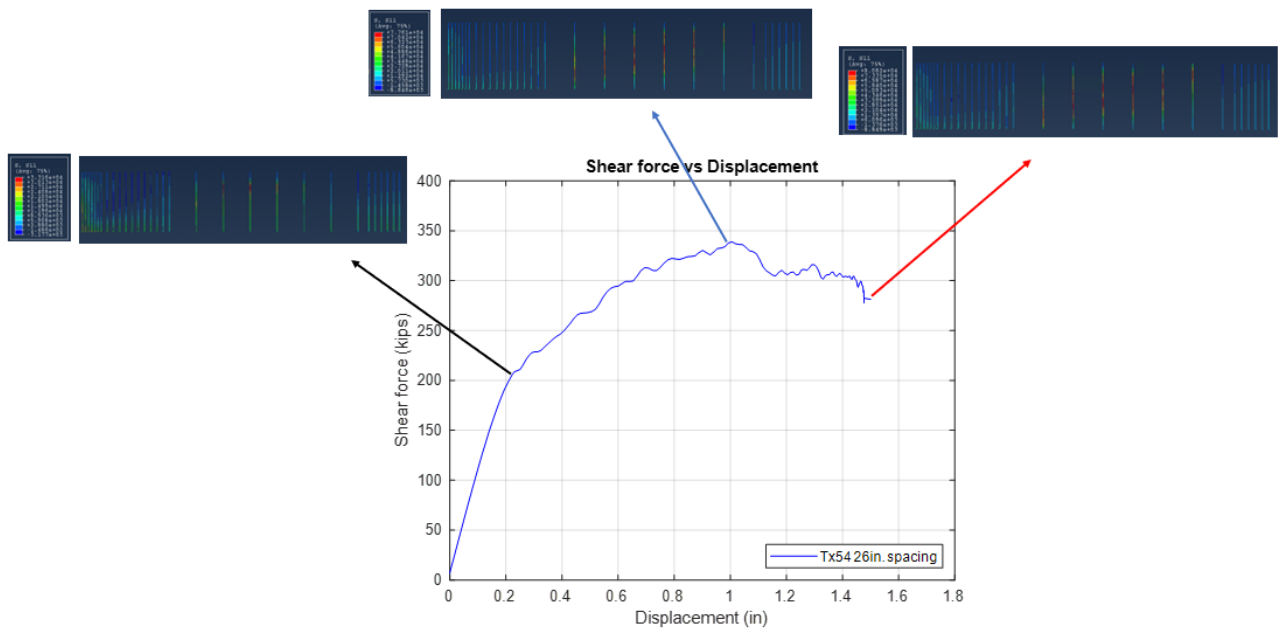
The maximum force, signifying the highest load value that the structure successfully sustained during the simulations, was also obtained through force-displacement analysis of the simulated model.



**Figure 8.28. Tension damage at various stages of loading.**



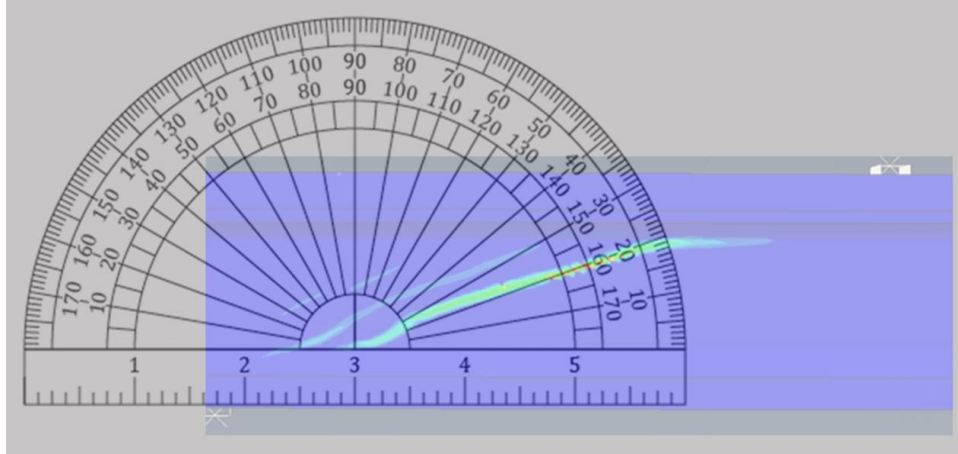
**Figure 8.29. Plastic strain at various stages of loading.**



**Figure 8.30. Axial stress in R-bars at various stages of loading.**

### 8.4.3 Inclination Angle Measurement

As illustrated in Figure 8.31, an online protractor accurately measured the inclination angle.



**Figure 8.31. Inclination angle measurement using an online protractor.**

## 8.5 PARAMETRIC STUDY

The influence of various configurations on the shear behavior of prestressed concrete bridge girders was investigated through numerical modeling and simulation techniques. The parameters considered in this study encompassed:

- Influence of shear reinforcement spacing. The researchers studied the influence of shear reinforcement spacing on the behavior of Tx54 and Tx70 girders. Specifically, five different spacing configurations were examined, namely 18 in., 26 in., 38 in., 48 in., and without shear reinforcement.
- The effect of the slab presence. The research focused on four different girders: Tx46, Tx54, Tx62, and Tx70.
- The effect of the slab width. The simulations were executed on Tx54 and Tx70 girders, each with 3-ft and 8-ft deck slab widths.
- Influence of shear reinforcement grade. The researchers investigated the impact of two different grades of shear reinforcement: 60 ksi and 100 ksi.
- The effect of the size of shear reinforcement on the shear behavior of reinforced concrete bridge girders. The study considered three different sizes for R-bars: No. 3, No. 4, and No. 5.
- The effect of  $a/d$ . The influence of shear reinforcement spacing on the behavior of Tx54 and Tx70 girders was studied. Specifically, three different  $a/d$  values were examined, namely 2.5, 3, and 4.

- The effect of concrete strength. Numerical simulations were conducted on Tx54 and Tx70 girders specimens with varying concrete compressive strengths of 5 ksi, 8.5 ksi, and 14 ksi.
- The effect of prestressing force. The researchers studied the influence of three values of  $f_{pc}/f'_c$ , 13.2 percent, 16.6 percent, and 23.7 percent, which are representative of the range considered in many field applications, on the behavior of Tx54 and Tx70 girders.
- The effect of the tendon path. The researchers also investigated the influence of different types of strands on the shear behavior of Tx54 and Tx70 girders. Specifically, two types of strands were considered: harped strands and straight strands.

These factors were selected due to their potential impact on the shear capacity and overall performance of the bridge girders.

### 8.5.1 Effect of Shear Reinforcement Spacing

The numerical simulations assessed how the spacing of shear reinforcement impacted the shear behavior of reinforced concrete bridge girders. The goal was to evaluate the shear capacity, crack pattern, and overall performance of Tx54 and Tx70 girders with low levels of shear reinforcement. Five different spacing configurations were considered: 18 in., 26 in., 38 in., 48 in., and without shear reinforcement. The 18 in. spacing adhered to TxDOT standards. The 26 in. spacing was determined by calculating the web height for Tx54 ( $h_w$ ) and the angle ( $\theta$ ) of diagonal cracks, ensuring that each crack was adequately reinforced by at least one stirrup by using the formula  $h_w/(2 * \tan \theta)$ . Furthermore, the 38 in. spacing was derived from the minimum shear reinforcement formula,  $A_{V,min} \geq 0.0316\lambda\sqrt{f'_c} \frac{b_v s}{f_y}$ , as specified in the AASHTO (2020) specifications. The 48 in. spacing represented twice the maximum allowable spacing set by AASHTO (2020), which set the maximum at 24 in. Other parameters were kept constant to ensure consistent results.

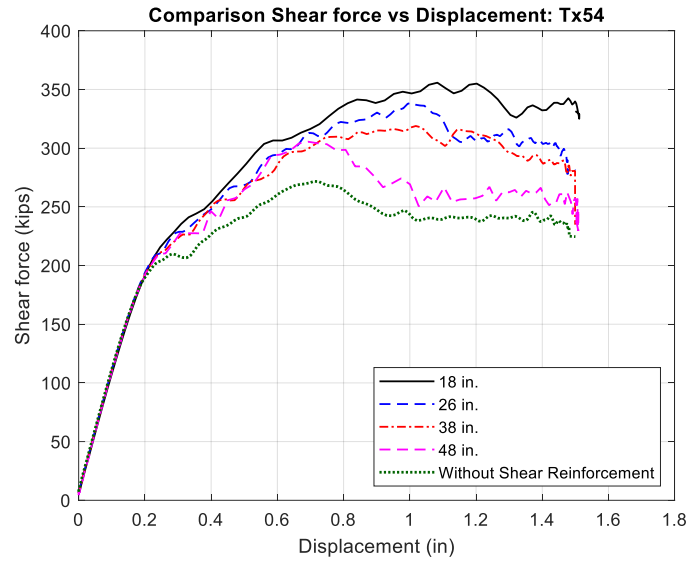
The shear behavior of the bridge girders was influenced by the spacing of shear reinforcement, as indicated by the results presented in Figure 8.32 and Figure 8.33 for Tx54 and Tx70, respectively. For the Tx54 girders, specimens without shear reinforcement exhibited a cracking force of 199 kips. As for the shear-reinforced specimens, the cracking force increased with the

introduction of shear reinforcement. Specifically, for a shear reinforcement spacing of 18 in., the cracking force elevated to 217 kips, indicating a positive effect of reinforcement in delaying shear cracking initiation. Likewise, for 26 in., 38 in., and 48 in. spacing configurations, the cracking force elevated to approximately 211 kips.

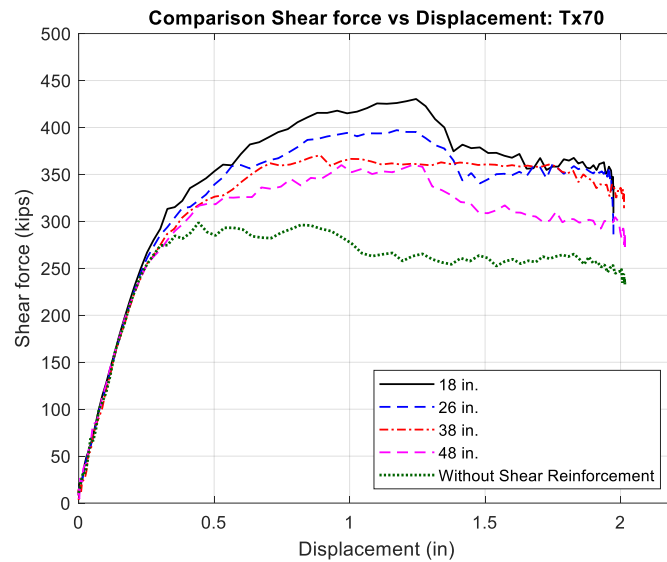
Turning to the Tx70 girders, the cracking force without shear reinforcement was 265 kips. Upon incorporating shear reinforcement with spacings of 18 in., 26 in., 38 in., and 48 in., the cracking loads progressively rose to 313 kips, 293 kips, 292 kips, and 286 kips, respectively. These increments in cracking force signify the reinforcement's efficacy in enhancing girder shear resistance and mitigating shear cracking.

For Tx54 girders, the shear capacity was 272 kips for the absence of shear reinforcement. When shear reinforcement was spaced at 18 in., the shear capacity increased to 354 kips, reflecting a load gain of 30.1 percent compared to the no-shear configuration. Similarly, with a shear reinforcement spacing of 26 in., the capacity reached 336 kips, marking a load gain of 23.5 percent. With a spacing of 38 in., the capacity rose to 317 kips, resulting in a load gain of 16.5 percent. For a spacing of 48 in., the capacity increased to 305 kips, resulting in a load gain of 12.1 percent.

In the case of Tx70 girders without shear reinforcement, the ultimate shear was 295 kips. Upon incorporating shear reinforcement at 18 in., the capacity escalated to 427 kips, representing a load gain of 46.7 percent over the no-shear condition. Similarly, shear reinforcement spaced at 26 in. increased capacity to 397 kips, indicating a load gain of 34.6 percent. With a spacing of 38 in., the shear capacity reached 367 kips, leading to a load gain of 24.4 percent. For a spacing of 48 in., the capacity increased to 360 kips, resulting in a load gain of 22.0 percent.



**Figure 8.32. Shear force versus displacement plots for Tx54.**



**Figure 8.33. Shear force versus displacement plots for Tx70.**

Table 8.2 provides a comprehensive comparative analysis of the calculated values obtained from different design guides and provisions, including ACI, AASHTO specifications, and the FEM for Tx54 and Tx70. The “ $V_{cr-FEM}$ ” indicates the shear cracking force, measured in kips, representing the force level at which shear cracking initiates, as predicted by the FEM. Furthermore, the “ $V_{u-FEM}$ ” denotes the shear force capacity, measured in kips, as predicted by the FEM. On the other hand, the “ $V_{c-AASHTO}$ ” and “ $V_{c-ACI}$ ” indicate the concrete shear contribution according to AASHTO and ACI standards, respectively. These values are also measured in kips. Moreover,



Table 8.2 provides ultimate shear force ( $V_u$ ) values, measured in kips, for both AASHTO and ACI standards. Last, Table 8.2 provides information about the inclination angle and RSS index.

When comparing the FEM with AASHTO and ACI shear cracking force, the FEM tends to yield higher values than AASHTO, indicating a potentially conservative design approach. On the other hand, the comparison between the FEM and ACI results reveals a more harmonious alignment. The ratios of the FEM shear cracking load to AASHTO shear cracking load range from approximately 1.11 to 1.2 for the Tx54 specimens and from 1.09 to 1.29 for the Tx70 specimens. Similarly, the ratios of the FEM shear cracking load to ACI shear cracking load fall within the range of 0.94 to 1.03 for Tx54 and 0.98 to 1.20 for Tx70. A noteworthy observation is that both AASHTO and ACI specifications did not indicate any significant increase in the cracking load when the spacing of shear reinforcement was reduced.

For the shear capacity, the shear strengths obtained through the FEM consistently surpass those computed by the ACI and AASHTO across all test scenarios. The ratios of ultimate shear force from the FEM to AASHTO range approximately from 1.13 to 1.51 for Tx54 and from 1.03 to 1.21 for Tx70. A trend of increased ratios in ultimate shear forces, as predicted by the FEM, compared to AASHTO, was observed as the spacing of shear reinforcement was reduced. Similarly, the ratios of the FEM shear capacity to ACI shear capacity fall within the range of 1.23 to 1.29 for Tx54 and 1.13 to 1.21 for Tx70.

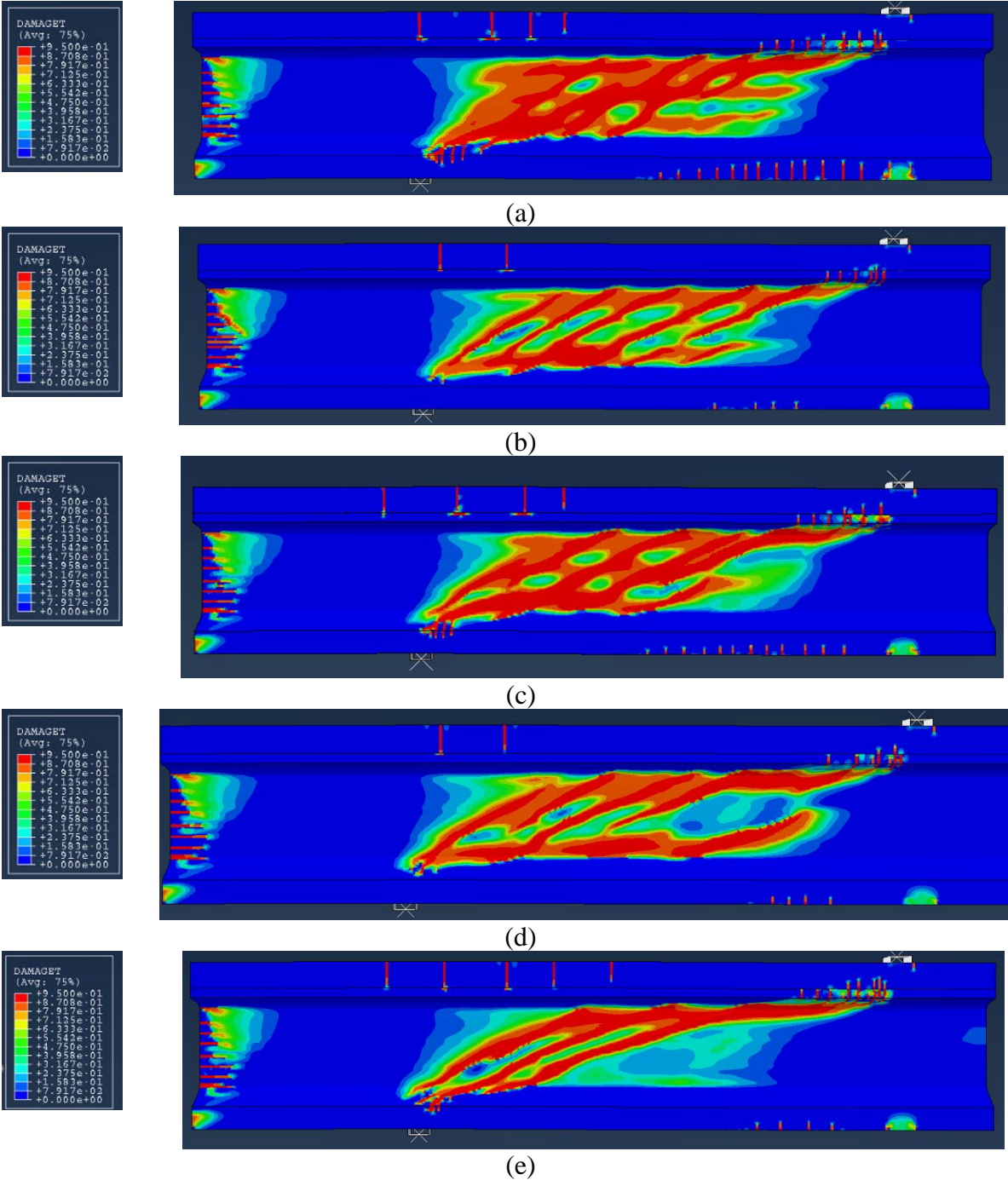
Notably, the RSS and inclination angle values increased in both cases as the number of transverse reinforcement intercepts along the inclined crack increased. When considering similar spacing conditions, it was evident that the RSS values were greater for Tx54 than for Tx70.

**Table 8.2. R-bars spacing comparison of Tx54 and Tx70 results with different code results.**

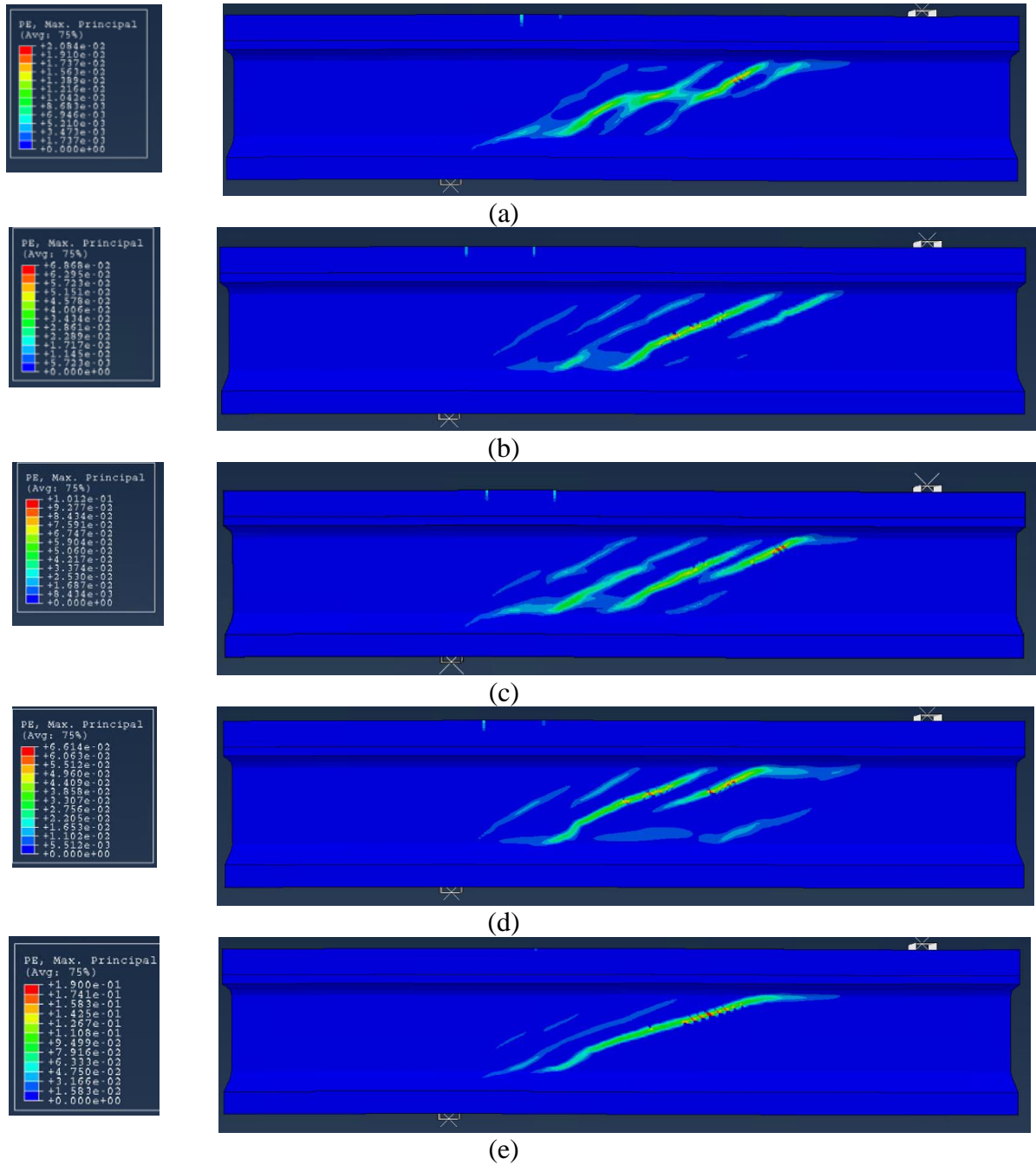
Model	$V_{cr-FEM}$ (kips)	$V_{c-AASHTO}$ (kips)	$V_{c-ACI}$ (kips)	$V_{u-FEM}$ (kips)	$V_{u-AASHTO}$ (kips)	$V_{u-ACI}$ (kips)	RSS	Crack Angle
<b>Tx54_18</b>	217	180	211	354	314	287	1.63	27-30
<b>Tx54_26</b>	211	180	211	336	272	264	1.59	22-28
<b>Tx54_38</b>	211	180	211	317	243	247	1.5	22-26
<b>Tx54_48</b>	210	180	211	305	230	239	1.45	22-26
<b>Tx54_w/o shear</b>	199	180	211	272	180	211	1.37	18-22
<b>Tx70_18</b>	313	243	260	427	415	357	1.36	23-30
<b>Tx70_26</b>	293	243	260	397	362	327	1.35	19-29
<b>Tx70_38</b>	292	243	260	367	324	306	1.26	18-27
<b>Tx70_48</b>	286	243	260	360	306	297	1.26	18-22
<b>Tx70_w/o shear</b>	265	243	260	295	243	260	1.11	17-22

Figure 8.34, Figure 8.35, Figure 8.37, and Figure 8.38 compare the failure mode and concrete damage at the peak force for Tx54 and Tx70 girders, as analyzed using numerical models. The schematic drawings of the tension and maximum plastic strain crack patterns for Tx54 and Tx70 specimens indicated that they exhibited approximately the same crack pattern at peak load. All specimens failed in diagonal tension failure in the web; no flexural or bond failure was observed. The inclination angles of the diagonal cracks in the web with the horizontal direction increased with decreasing R-bars' spacing. However, the shear crack width was not able to be measured. It can be observed that the plastic strain increases with increasing  $s/d$ .

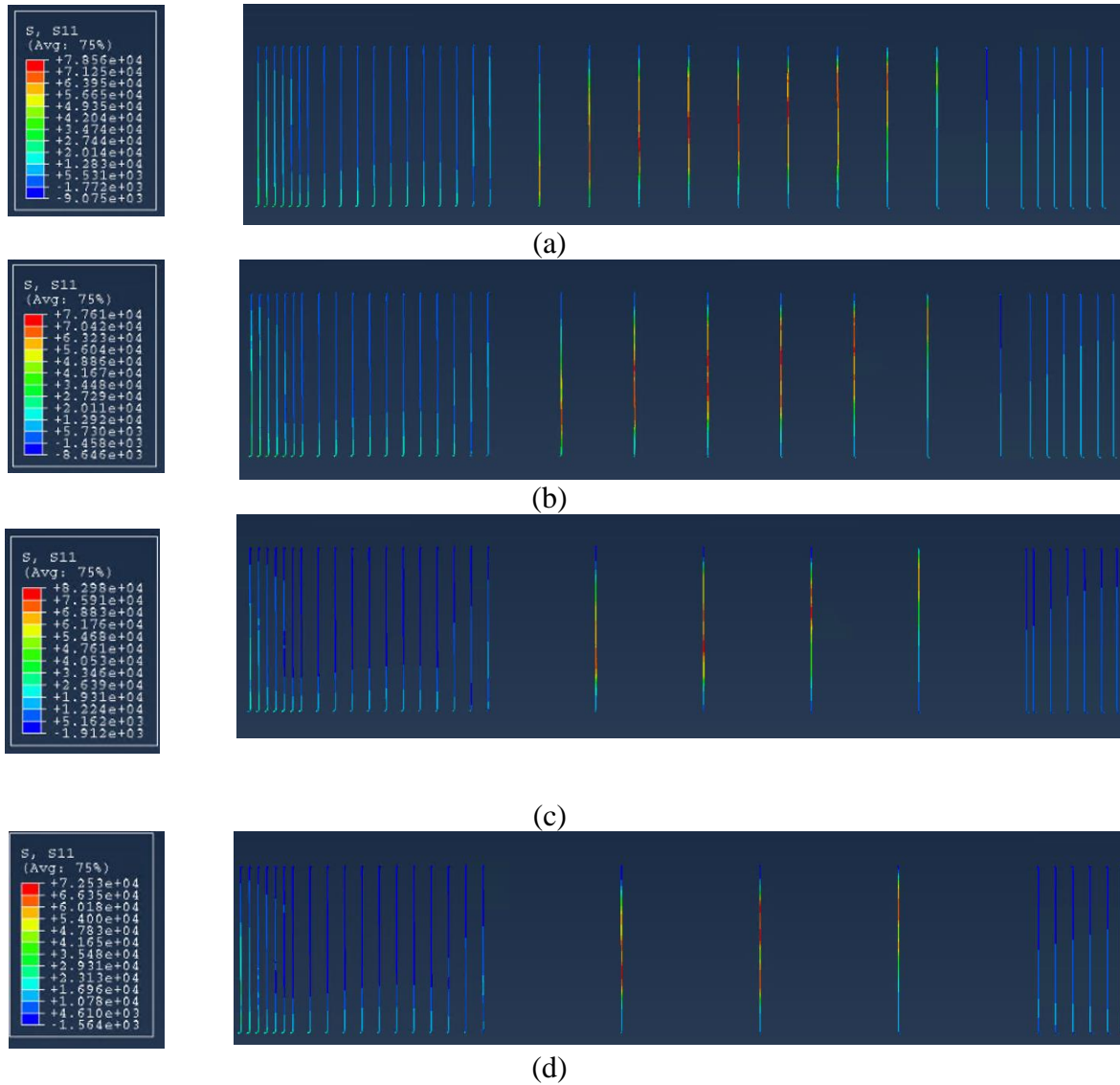
It is clear that for Tx54 and Tx70 specimens in Figure 8.36 and Figure 8.39, reducing the  $s/d$  resulted in a decrease in the axial stress in R-bars at ultimate force, which can be attributed to the shear force being distributed among a more significant number of stirrups, thus consequently reducing the axial stresses.



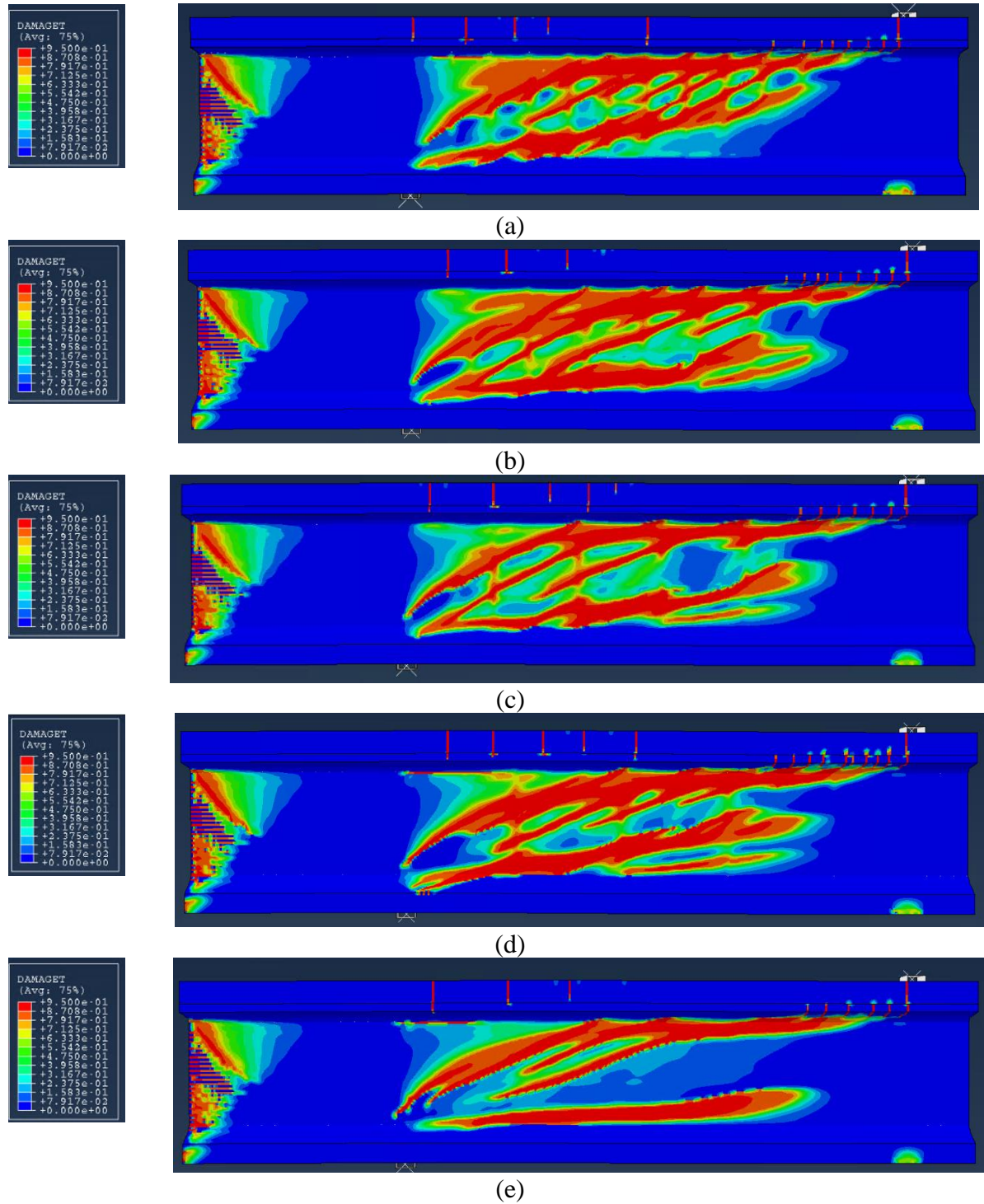
**Figure 8.34. Tension damage in FE model at peak load for Tx54: (a) 18 in., (b) 26 in., (c) 38 in., (d) 48 in., and (e) without shear reinforcement.**



**Figure 8.35. Plastic strain in FE model at peak load for Tx54: (a) 18 in., (b) 26 in., (c) 38 in., (d) 48 in., and (e) without shear reinforcement.**

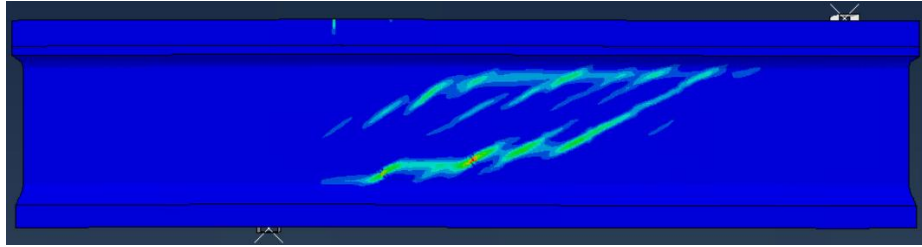
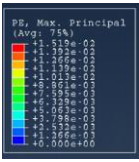


**Figure 8.36. Axial stress in R-bars in FEM at peak load for Tx54: (a) 18 in., (b) 26 in., (c) 38 in., and (d) 48 in.**

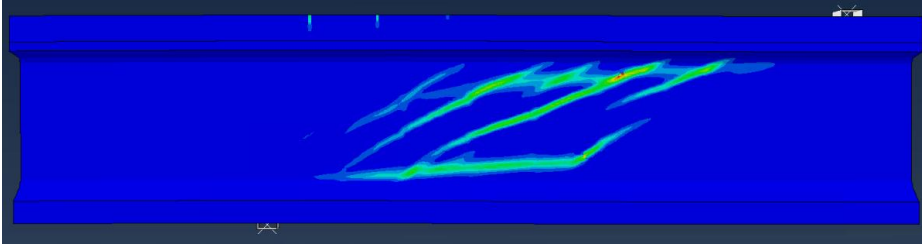
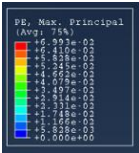


**Figure 8.37. Tension damage in FE model at peak load for Tx70: (a) 18 in., (b) 26 in., (c) 38 in., (d) 48 in., and (e) without shear reinforcement.**

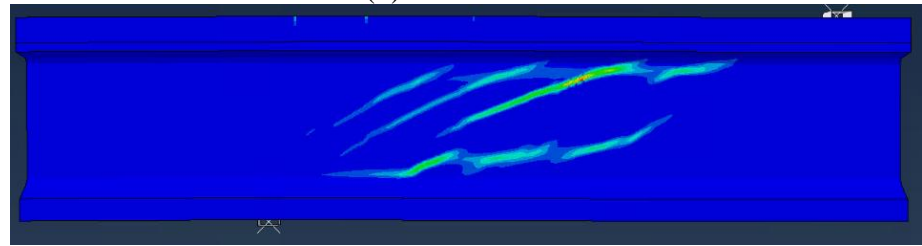
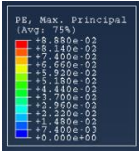




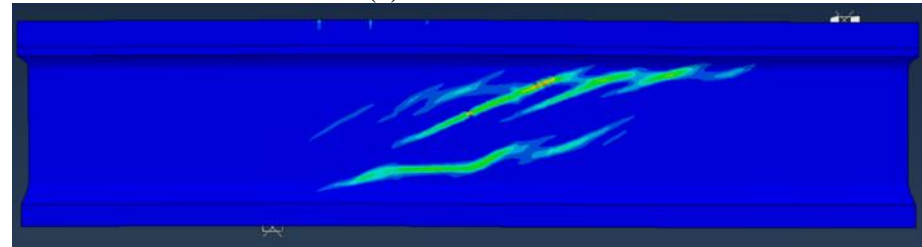
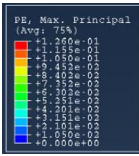
(a)



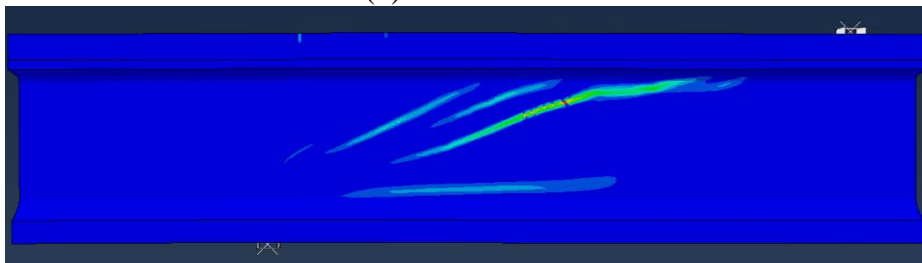
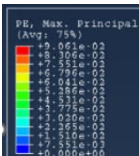
(b)



(c)

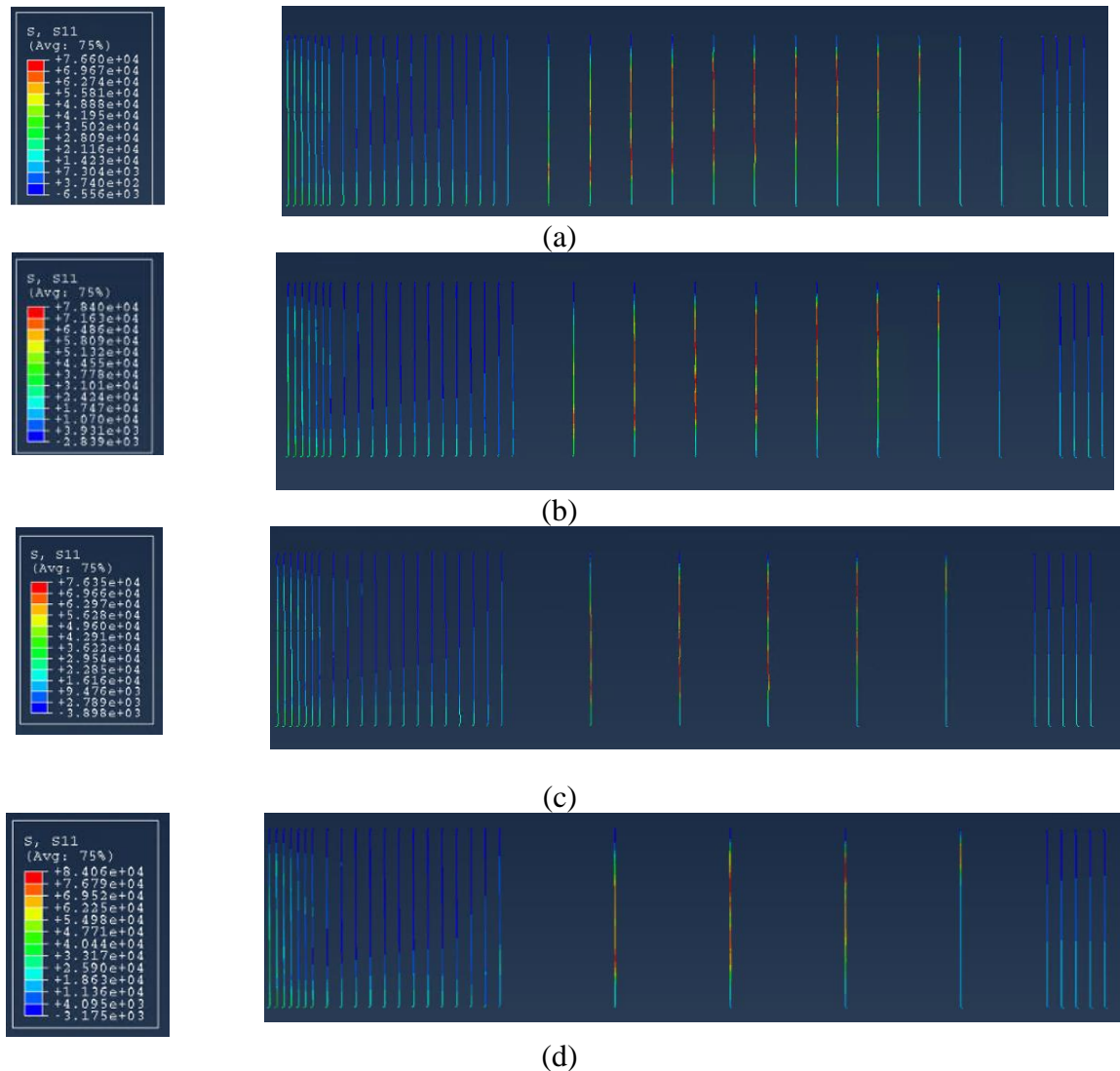


(d)



(e)

**Figure 8.38. Plastic strain in FE model at peak load for Tx70: (a) 18 in., (b) 26 in., (c) 38 in., (d) 48 in., and (e) without shear reinforcement.**



**Figure 8.39. Axial stress in R-bars in FEM at peak load for Tx70: (a) 18 in., (b) 26 in., (c) 38 in., and (d) 48 in.**

A comparative study was carried out to consider the element deletion. The findings from this study are illustrated in Figure 8.40 and Figure 8.41 for Tx70.

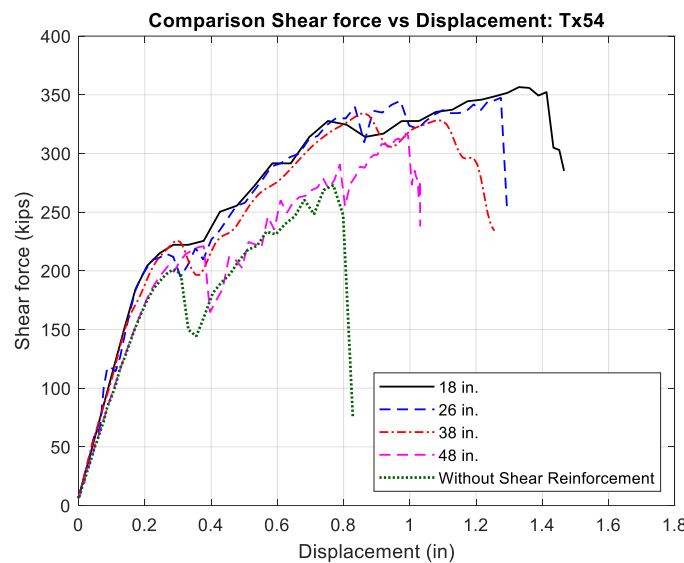
For the Tx54 girders, specimens without shear reinforcement exhibited a cracking force of 201 kips. As for the shear-reinforced specimens, the cracking force increased with the introduction of shear reinforcement. Specifically, for a shear reinforcement spacing of 18 in., the cracking force elevated to 218 kips, indicating a positive effect of reinforcement in delaying shear cracking initiation. Likewise, for both 26-in. and 38-in. spacing configurations, the cracking force elevated to 215 kips. Furthermore, for a spacing of 48 in., the cracking force increased to 204 kips.



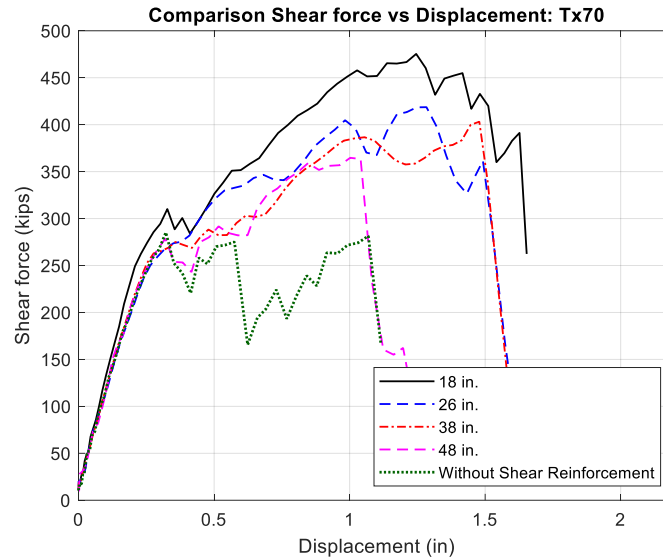
Turning to the Tx70 girders, the cracking force without shear reinforcement was 257 kips. Upon incorporating shear reinforcement with spacings of 18 in., 26 in., 38 in., and 48 in., the cracking loads progressively rose to 295 kips, 257 kips, 257 kips, and 257 kips, respectively. These increments in cracking force signify the reinforcement's efficacy in enhancing the girders' shear resistance and mitigating shear cracking.

For Tx54 girders, the shear capacity was 273 kips in the absence of shear reinforcement. When shear reinforcement was spaced at 18 in., the shear capacity increased to 357 kips, reflecting a load gain of 30.8 percent over the no-shear configuration. Similarly, with a shear reinforcement spacing of 26 in., the capacity reached 347 kips, marking a load gain of 27.1 percent. With a spacing of 38 in., the capacity rose to 332 kips, resulting in a load gain of 21.6 percent. For a spacing of 48 in., the capacity increased to 317 kips, resulting in a load gain of 16.1 percent.

In the case of Tx70 girders without shear reinforcement, the ultimate shear was 285 kips. Upon incorporating shear reinforcement at 18 in., the capacity escalated to 465 kips, representing a load gain of 63.2 percent over the no-shear condition. Similarly, shear reinforcement spaced at 26 in. increased capacity to 419 kips, indicating a load gain of 47 percent. With a spacing of 38 in., the shear capacity reached 403 kips, leading to a load gain of 41.4 percent. For a spacing of 48 in., the capacity increased to 363 kips, resulting in a load gain of 27.4 percent.



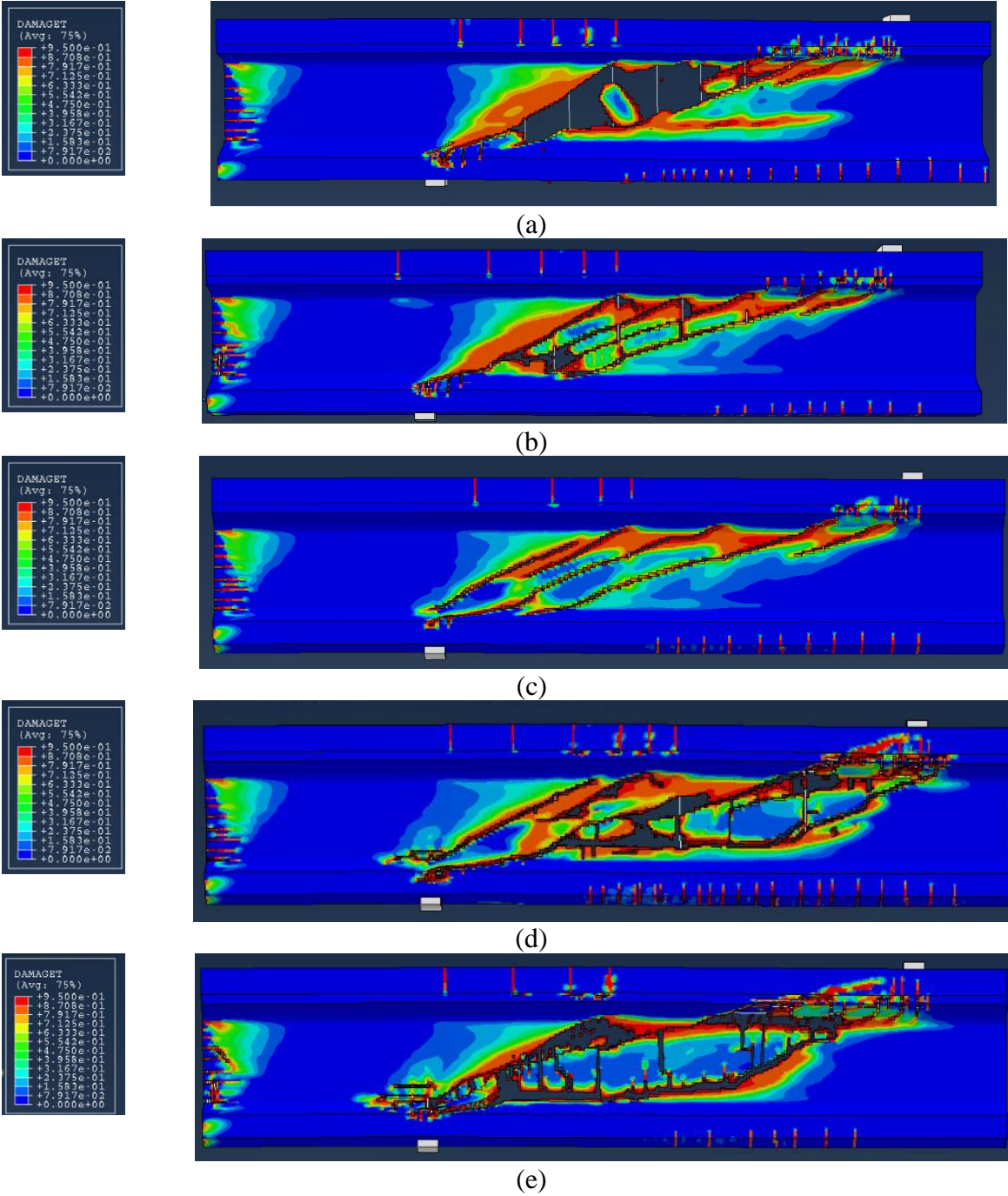
**Figure 8.40. Shear force versus displacement plots for Tx54 with element deletion.**



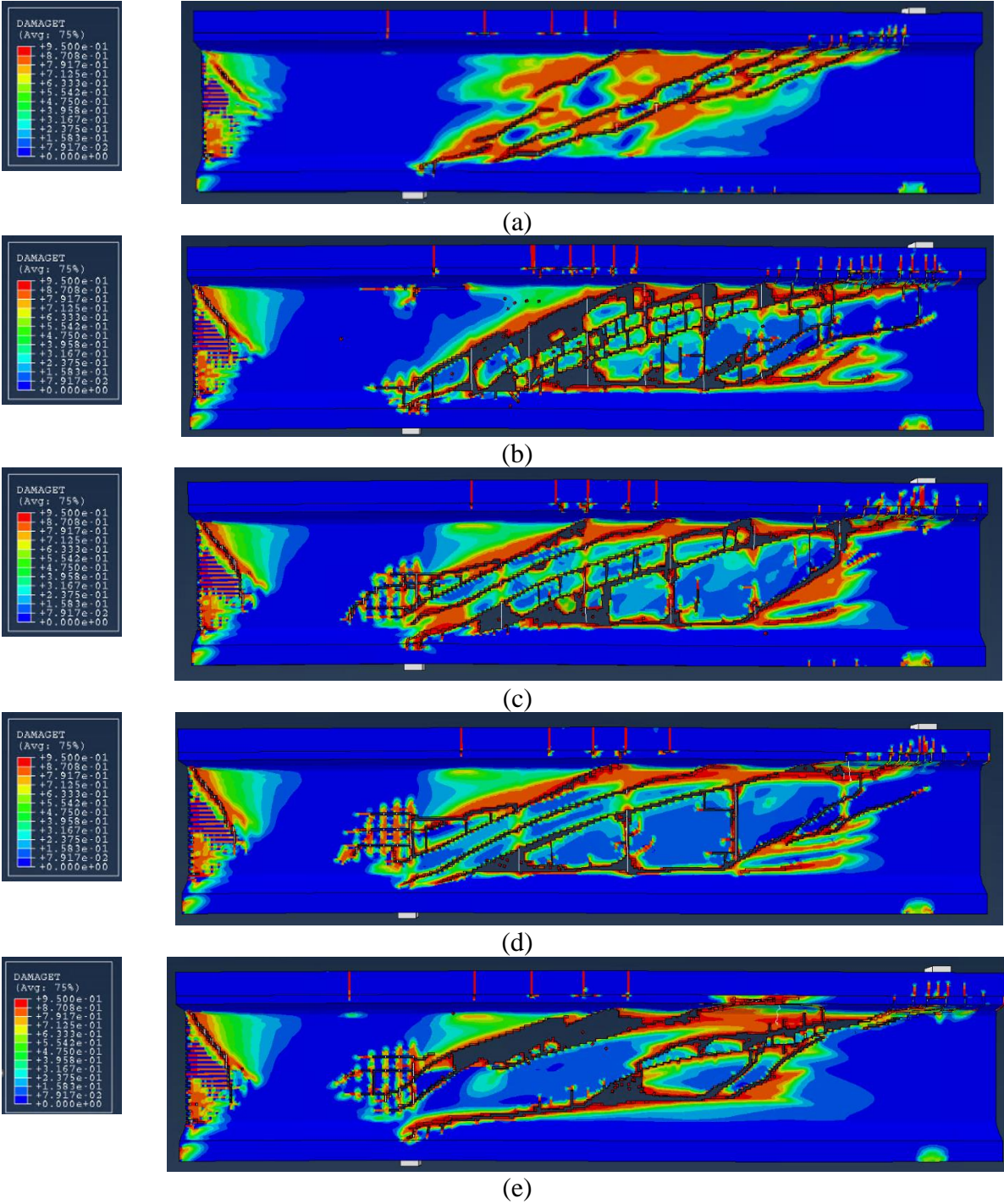
**Figure 8.41. Shear force versus displacement plots for Tx70 with element deletion.**

In comparing the results of two studies—one without element deletion and the other with element deletion—on the Tx54 girders, cracking forces showed variations of 1.01 percent increase without shear reinforcement, 0.46 percent for 18-in. spacing, 1.9 percent for both 26 and 38-in. spacings, and a decrease of 2.86 percent for the 48-in. spacing. Shear capacities had alterations of 0.37 percent increase without shear reinforcement, 0.85 percent for 18 in., 3.27 percent for 26 in., 4.73 percent for 38 in., and 3.93 percent for 48 in. For the Tx70 girders, the cracking force reductions were 3.02 percent without shear reinforcement, 5.75 percent for 18 in., and an average decrease of about 12.21 percent for spacings of 26, 38, and 48 in. Shear capacities presented a 3.39 percent decrease without reinforcement, but increases of 8.9 percent for 18 in., 5.54 percent for 26 in., 9.81 percent for 38 in., and 0.83 percent for 48 in.

Figure 8.42 and Figure 8.43 compare the failure mode and concrete damage at the peak force for Tx54 and Tx70 girders, as analyzed using numerical models.



**Figure 8.42. Tension damage in FE with element deletion model at peak load for Tx54:**  
 (a) 18 in., (b) 26 in., (c) 38 in., (d) 48 in., and (e) without shear reinforcement.



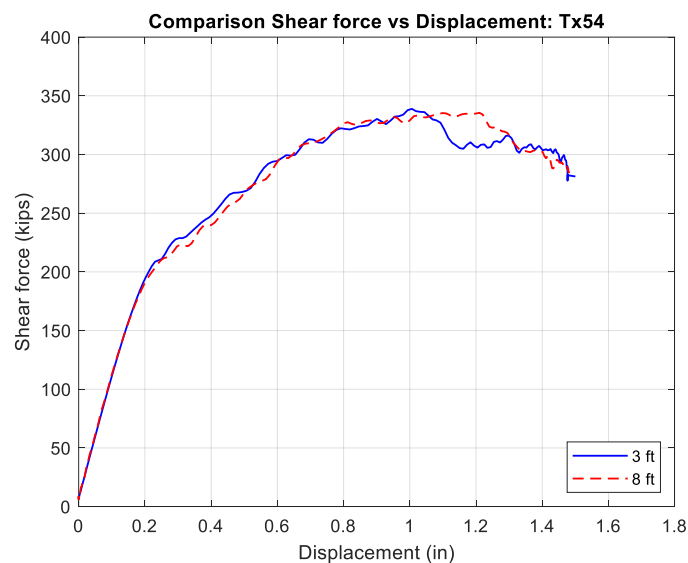
**Figure 8.43. Tension damage in FE with element deletion model at peak load for Tx70: (a) 18 in., (b) 26 in., (c) 38 in., (d) 48 in., and (e) without shear reinforcement.**

### 8.5.2 Effect of Deck Slab Width

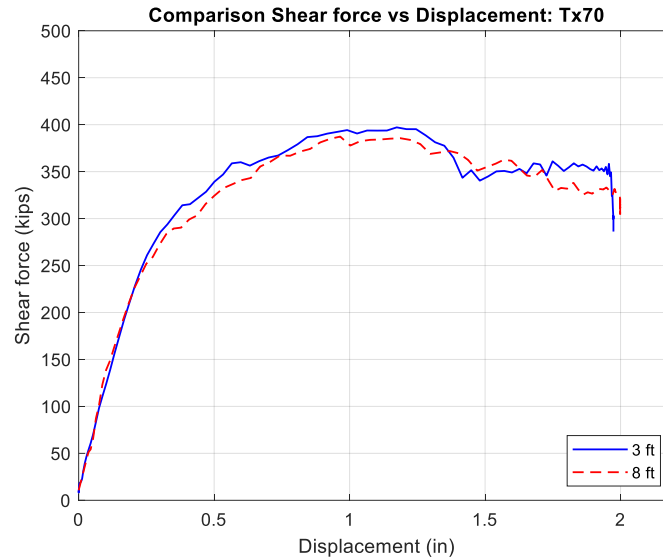
This study conducted numerical simulations to examine the impact of varying deck slab widths with different compressive strengths on the structural response of bridge girders. Two girders,

Tx54 and Tx70, were subjected to these simulations. Specifically, the 3-ft deck slab had a compressive strength of 10 ksi, while the 8-ft slab had a compressive strength of 4 ksi. It is important to emphasize that the deck slab, which had a width of 3 ft, had a stiffness comparable to that of the 8 ft slab. This finding indicates that, although different in width, the two slabs demonstrated similar levels of rigidity.

The outcomes of this analysis are graphically depicted in Figure 8.44 and Figure 8.45. Remarkably, the 3-ft and 8-ft deck slab in both specimens exhibited nearly identical crack force and shear strengths. In the case of Tx54, both specimens showed the same cracking force of 211 kips. However, for the Tx70 specimens, the 3-ft deck slab displayed a cracking force of 293 kips, while the 8-ft deck slab demonstrated a cracking force of 284 kips, representing a difference of approximately 3 percent. Regarding shear capacity, the disparity between the 3-ft and 8-ft deck slabs was nearly 0.3 percent and 2.3 percent for specimens Tx54 and Tx70, respectively.



**Figure 8.44. Shear force versus displacement plots for Tx54.**



**Figure 8.45. Shear force versus displacement plots for Tx70.**

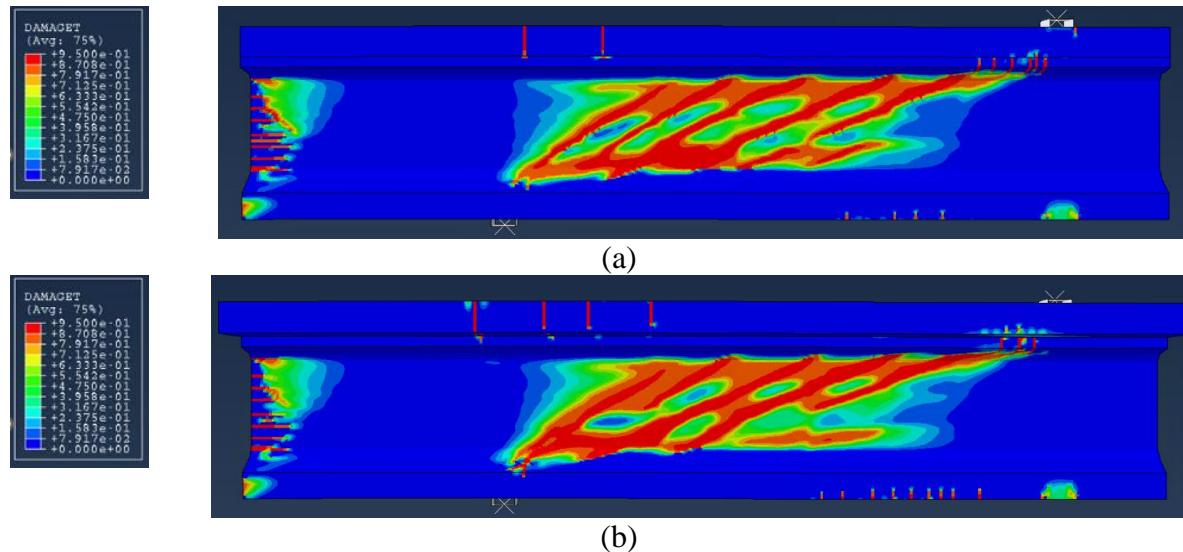
Table 8.3 provides a comprehensive comparative analysis of the predicted values obtained from different design guides and provisions, including ACI, AASHTO specifications, and the FEM for Tx54 and Tx70. Notably, the FEM consistently showed higher shear strengths than those computed by both the ACI and AASHTO standards, regardless of the width of the slab. Indeed, the results also highlight an interesting trend related to the depth of the girders. Notably, as the depth of the girders increases, the differences between the FEM-predicted values and the AASHTO and ACI-predicted values tend to decrease. Moreover, it is worth highlighting that the RSS and inclination angle displayed nearly identical values for the 3-ft and 8-ft deck slabs in both specimens.

**Table 8.3. Slab width comparison of Tx54 and Tx70 results with different code results.**

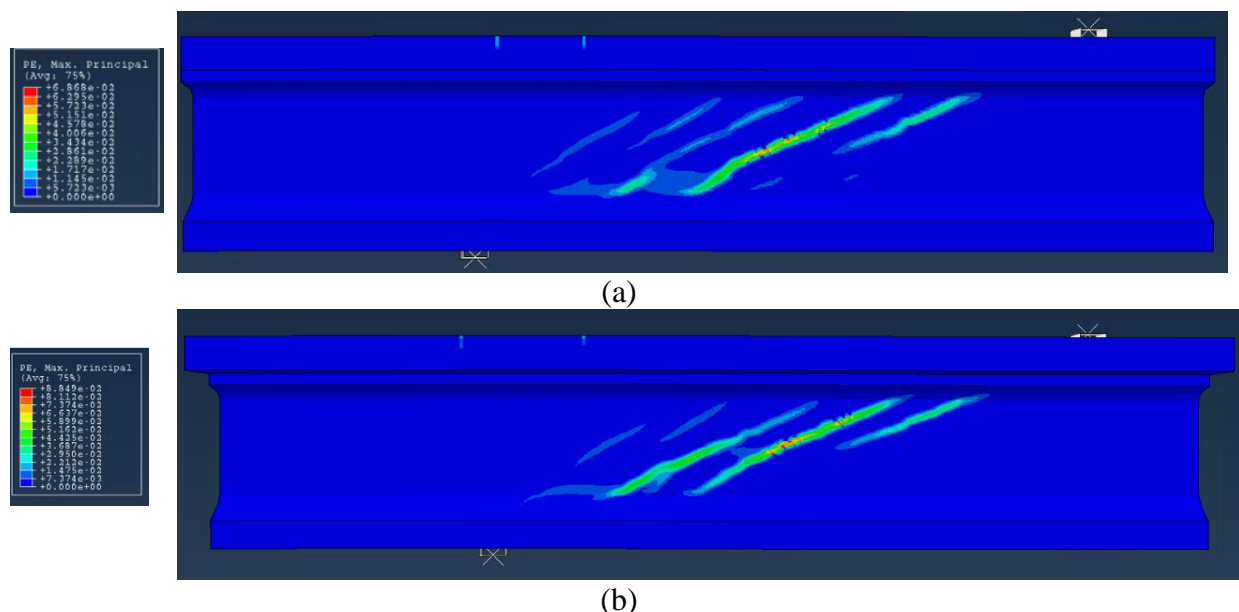
Model	$V_{cr-FEM}$ (kips)	$V_{c-AASHTO}$ (kips)	$V_{c-ACI}$ (kips)	$V_{u-FEM}$ (kips)	$V_{u-AASHTO}$ (kips)	$V_{u-ACI}$ (kips)	RSS	Crack Angle
<b>Tx54_3ft</b>	211	180	211	336	272	264	1.59	22-28
<b>Tx54_8ft</b>	211	180	211	337	272	264	1.6	23-27
<b>Tx70_3ft</b>	293	243	260	397	362	327	1.35	19-29
<b>Tx70_8ft</b>	284	243	260	388	362	327	1.37	20-29



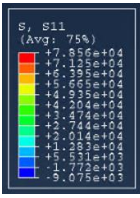
Figure 8.46, Figure 8.47, Figure 8.49, and Figure 8.50 compare the failure mode and concrete damage at the peak force for Tx54 and Tx70 girders, as analyzed using numerical models. The schematic drawings of the tension and maximum plastic strain crack patterns for Tx54 and Tx70 specimens indicated that they exhibited approximately identical crack patterns at peak force. Moreover, the axial stress in R-bars at ultimate force is also almost identical for both Tx54 and Tx70, as shown in Figure 8.48 and Figure 8.51.



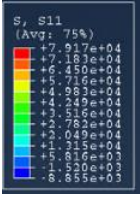
**Figure 8.46. Tension damage in FE model at peak load for Tx54: (a) 3-ft deck slab, and (b) 8-ft deck slab.**



**Figure 8.47. Plastic strain in FE model at peak load for Tx54: (a) 3-ft deck slab, and (b) 8-ft deck slab.**

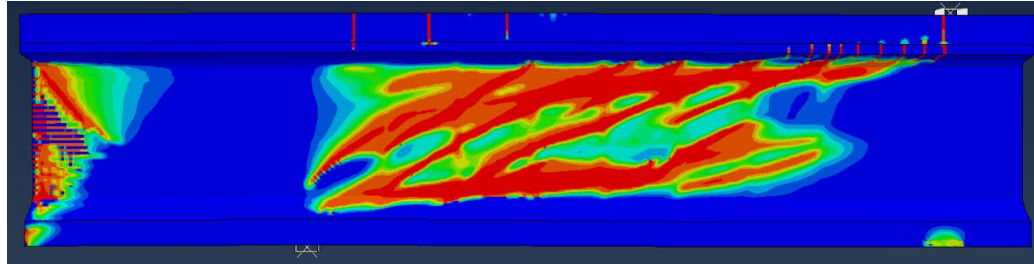
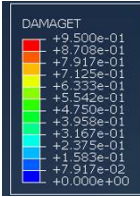


(a)

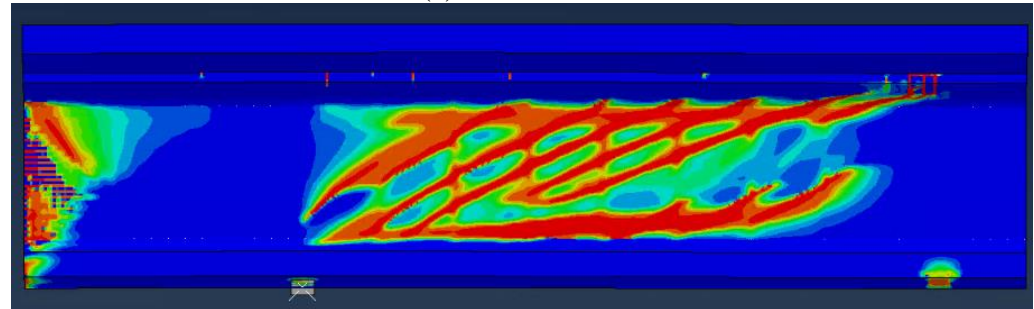
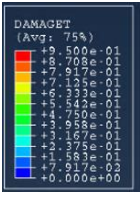


(b)

**Figure 8.48. Axial stress in R-bars in FE model at peak load for Tx54: (a) 3-ft deck slab, and (b) 8-ft deck slab.**



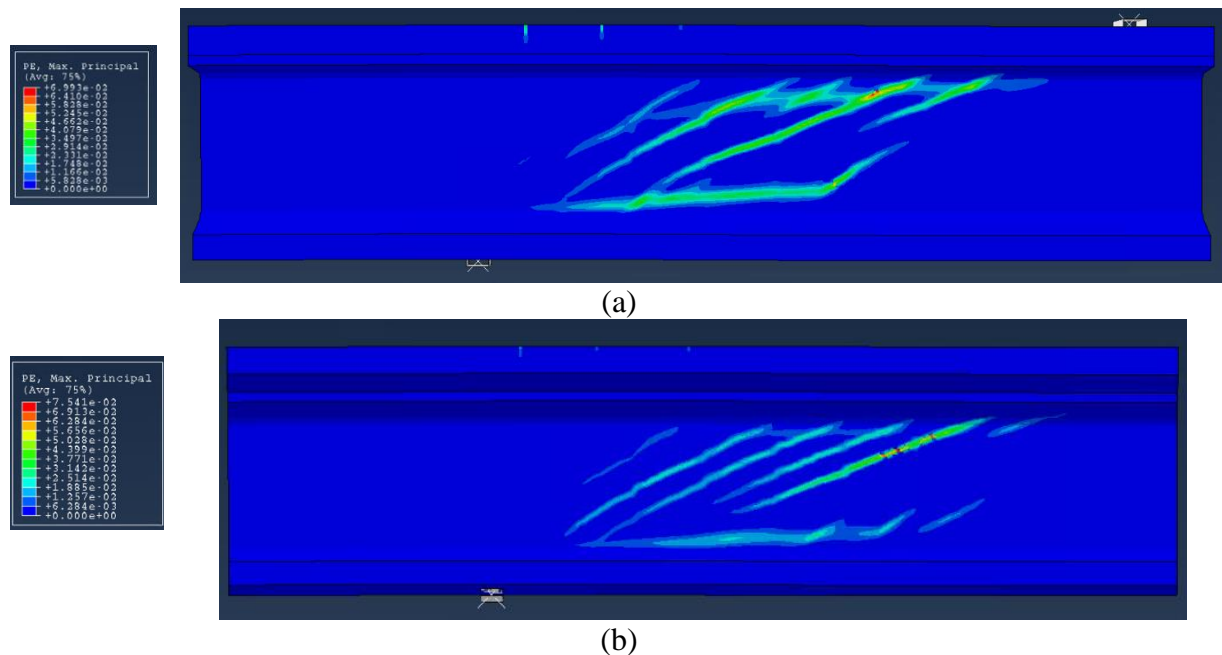
(a)



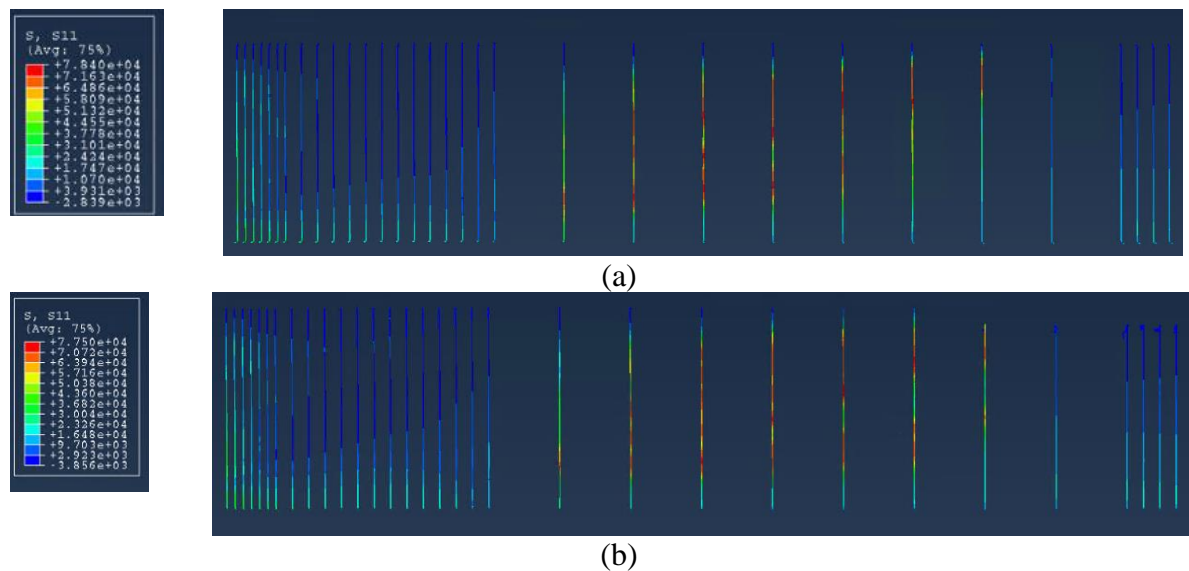
(b)

**Figure 8.49. Tension damage in FE model at peak load for Tx70: (a) 3-ft deck slab, and (b) 8-ft deck slab.**





**Figure 8.50. Plastic strain in FE model at peak load for Tx54: (a) 3-ft deck slab, and (b) 8-ft deck slab.**



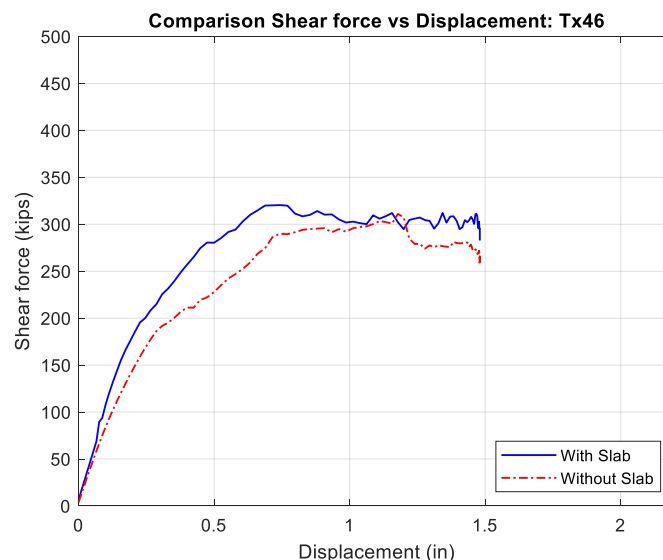
**Figure 8.51. Axial stress in R-bars in FE model at peak load for Tx70: (a) 3-ft deck slab and (b) 8-ft deck slab.**

### 8.5.3 Effect of Presence or Not of Deck Slab

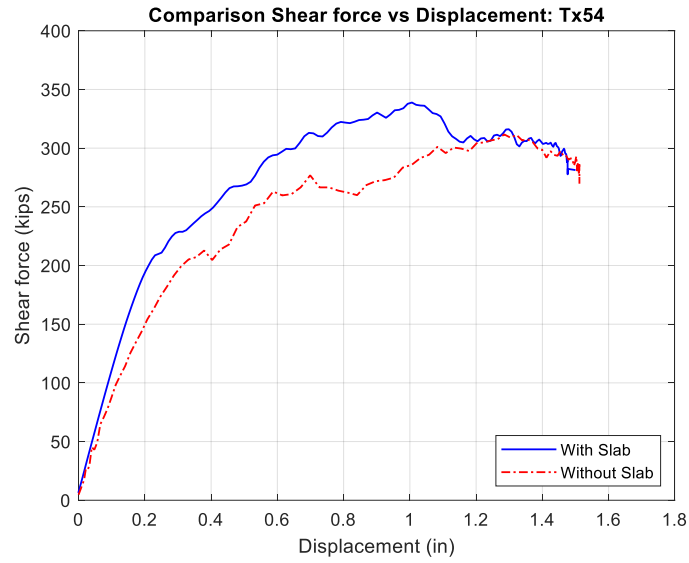
To investigate the influence of a deck slab on the behavior of bridge girders, numerical simulations were conducted on specimens of Tx46, Tx54, Tx62, and Tx70 girders with and without a deck slab. The shear-span-to-depth ratio for all specimens was maintained at 3, and

shear reinforcement with a spacing of 26 in. was used. The results of this evaluation are presented graphically in Figure 8.52, Figure 8.53, Figure 8.54, and Figure 8.55. It was observed that the specimens with a deck slab exhibited higher cracking forces than those specimens without a deck slab. Specifically, the specimens with a deck slab had cracking forces of 193 kips for Tx46, 211 kips for Tx54, 265 kips for Tx62, and 293 kips for Tx70. In contrast, the specimens without a deck slab could only sustain cracking forces of 189 kips for Tx46, 205 kips for Tx54, 232 kips for Tx62, and 272 kips for Tx70. These results indicate cracking force ratios of approximately 1.02, 1.03, 1.14, and 1.08 for Tx46, Tx54, Tx62, and Tx70 when comparing specimens with a deck slab to those without a deck slab.

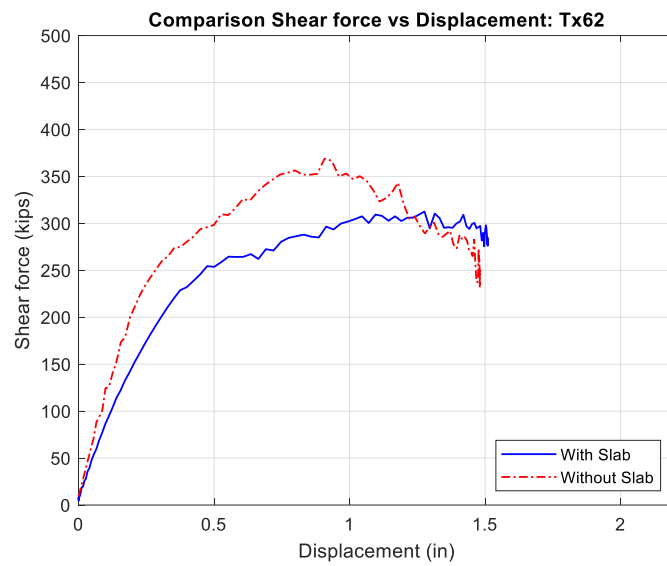
Furthermore, it was observed that the specimens with a deck slab exhibited higher load capacities than those specimens without a deck slab. Specifically, the specimens with a deck slab had maximum loads of 318 kips for Tx46, 336 kips for Tx54, 366 kips for Tx62, and 397 kips for Tx70. In contrast, the specimens without a deck slab could only sustain maximum shear forces of 304 kips for Tx46, 312 kips for Tx54, 323 kips for Tx62, and 363 kips for Tx70. These results indicate shear capacity ratios of approximately 1.05, 1.08, 1.13, and 1.09 for Tx46, Tx54, Tx62, and Tx70, respectively, when comparing specimens with a deck slab to those without a deck slab. Although these differences are small for the Tx46 and Tx54 girders (~ 5-8 percent), they become larger for Tx62 and Tx70 girders (~ 9-13 percent) and appear to increase with the cross-section height.



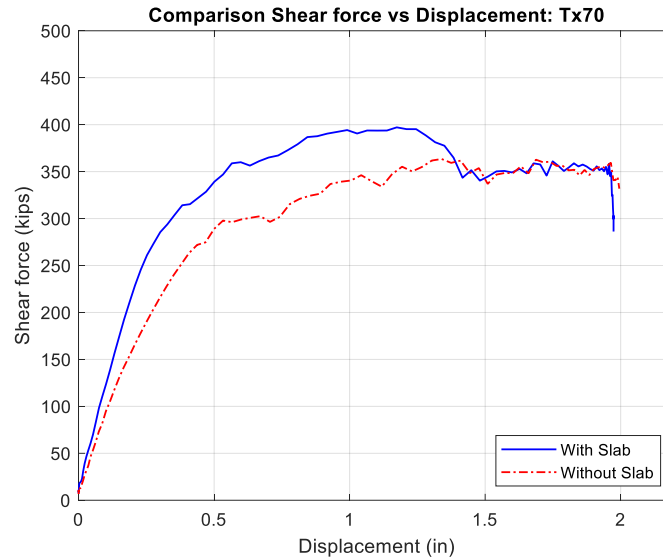
**Figure 8.52. Shear force versus displacement plots for Tx46.**



**Figure 8.53. Shear force versus displacement plots for Tx54.**



**Figure 8.54. Shear force versus displacement plots for Tx62.**



**Figure 8.55. Shear force versus displacement plots for Tx70.**

Table 8.4 provides a comprehensive comparative analysis encompassing projected values derived from various design guides and provisions. Upon scrutinizing results between AASHTO and the FEM, it becomes evident that AASHTO generally underestimates both cracking and ultimate shear forces. However, AASHTO's results for ultimate shear forces for specimens with deck slabs align more closely with the FEM's projections than with those specimens without deck slabs.

Similarly, within the ACI versus FEM comparison, a clear pattern emerges. For specimens without slabs, ACI predicts significantly higher shear cracking forces than the FEM. Conversely, ACI indicates lower shear cracking forces for specimens with slabs than the FEM. Additionally, ACI's results exhibit lower shear capacity than results from the FEM. However, an interesting reversal of this pattern occurs when considering ultimate shear forces. Here, ACI's results align more closely with the FEM's projections in contrast to the corresponding values predicted by AASHTO.

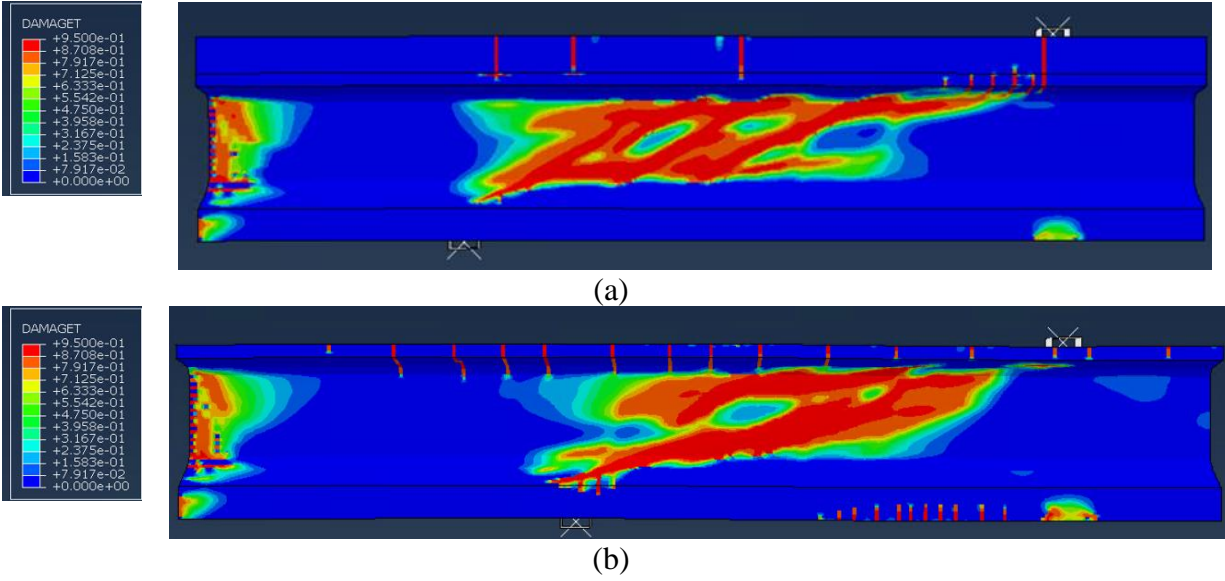
Additionally, the RSS values are higher for girders with slabs than for those girders without slabs. Interestingly, these RSS values decrease as the cross-section height increases, indicating a noteworthy trend. Remarkably, the crack angles are steeper for girders with slabs than for those girders without slabs.

**Table 8.4. Presence of slab comparison of Tx46, Tx54, Tx62, and Tx70 results with different code results.**

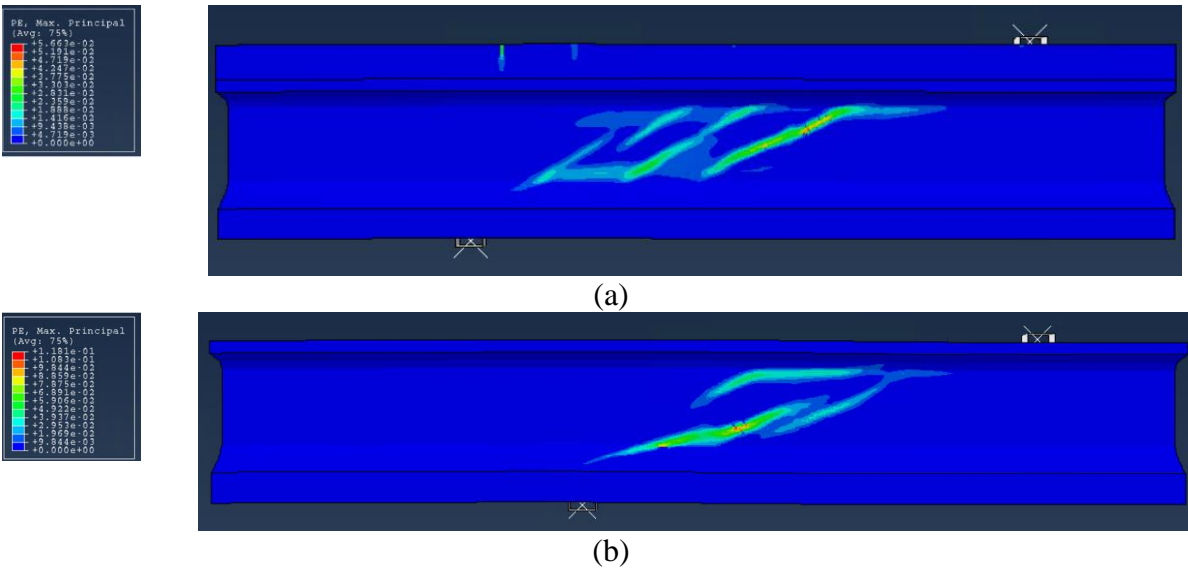
<b>Model</b>	<b><math>V_{cr-FEM}</math> (kips)</b>	<b><math>V_{c-AASHTO}</math> (kips)</b>	<b><math>V_{c-ACI}</math> (kips)</b>	<b><math>V_{u-FEM}</math> (kips)</b>	<b><math>V_{u-AASHTO}</math> (kips)</b>	<b><math>V_{u-ACI}</math> (kips)</b>	<b>RSS</b>	<b>Crack Angle</b>
<b>Tx46_With Slab</b>	193	157	183	318	236	228	1.65	25-28
<b>Tx46_Without Slab</b>	189	121	206	304	182	242	1.61	19-24
<b>Tx54_With Slab</b>	211	180	211	336	272	264	1.59	22-28
<b>Tx54_Without Slab</b>	205	144	237	312	217	281	1.52	18-26
<b>Tx62_With Slab</b>	265	207	234	366	314	294	1.38	24-29
<b>Tx62_Without Slab</b>	232	166	261	323	251	312	1.39	20-26
<b>Tx70_With Slab</b>	293	243	260	397	362	327	1.35	19-29
<b>Tx70_Without Slab</b>	272	177	270	363	269	326	1.33	21-24

Figure 8.56, Figure 8.57, Figure 8.59, Figure 8.60, Figure 8.62, Figure 8.63, Figure 8.65, and Figure 8.66 provide a comparison of the failure mode and plastic strain at the peak force for Tx46, Tx54, Tx62, and Tx70 girders with and without a deck slab, as analyzed using numerical models. It can be observed that the plastic strain was higher for specimens without slab compared to specimens with slab.

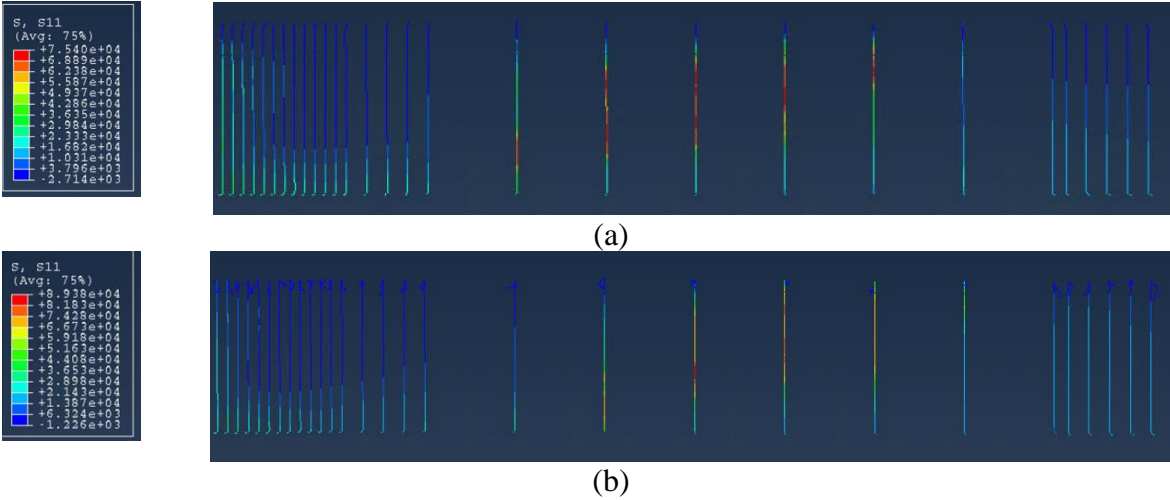
It is evident that for Tx46, Tx54, Tx62, and Tx70 girders, as depicted in Figure 8.58, Figure 8.61, Figure 8.64, and Figure 8.67, the presence of a deck slab led to a reduction in the axial stress experienced by the R-bars at the ultimate force. This reduction can be attributed to the shear force being distributed among a greater number of stirrups, thereby reducing the axial stresses.



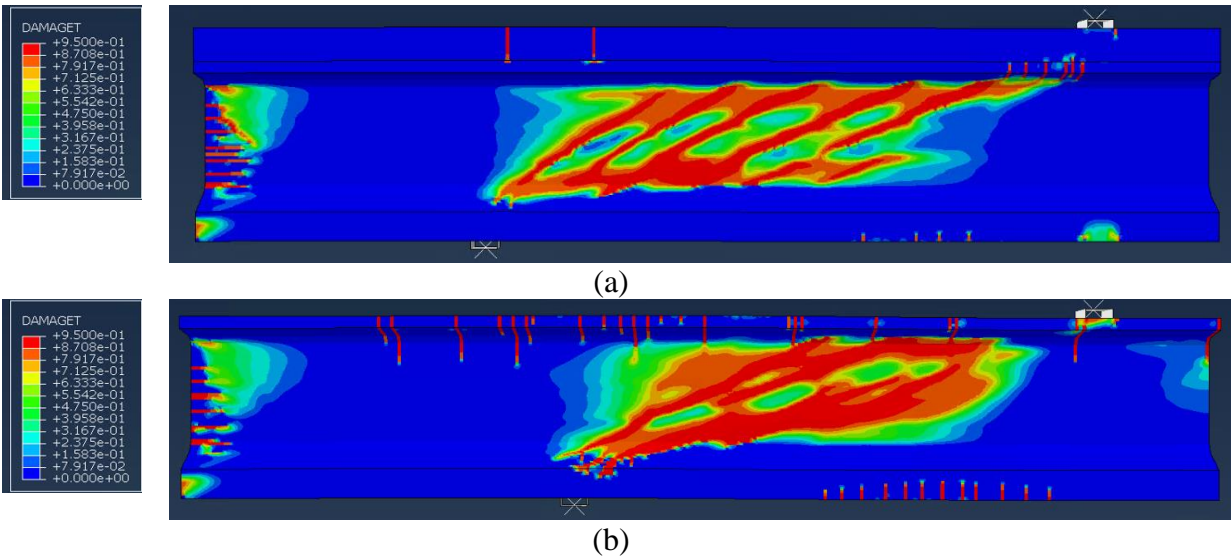
**Figure 8.56. Tension damage in FE model at peak load for Tx46: (a) with deck slab, and (b) without deck slab.**



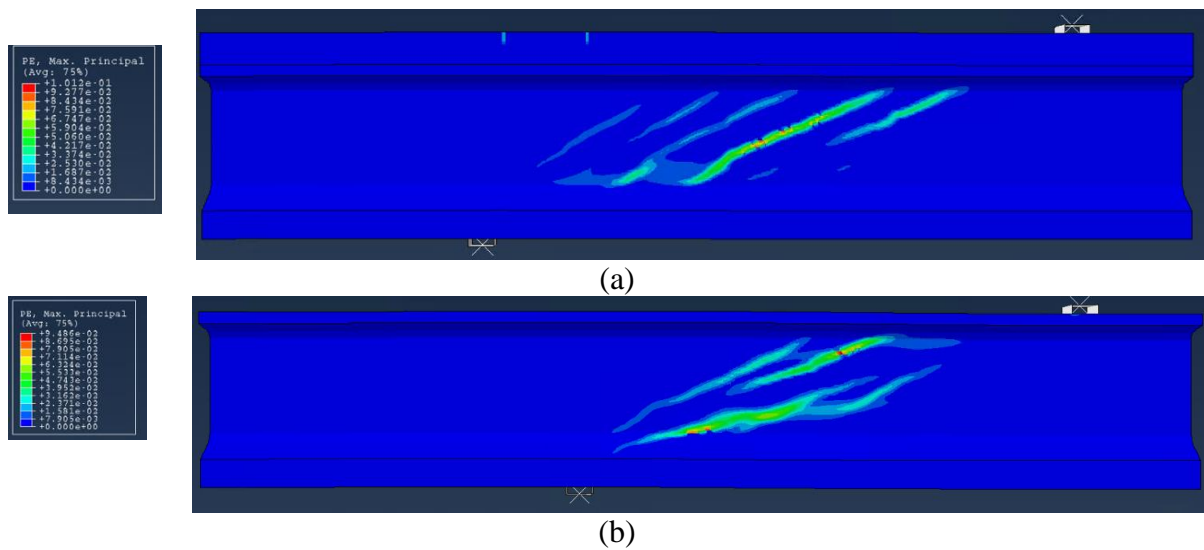
**Figure 8.57. Plastic strain in FE model at peak load for Tx46: (a) with deck slab, and (b) without deck slab.**



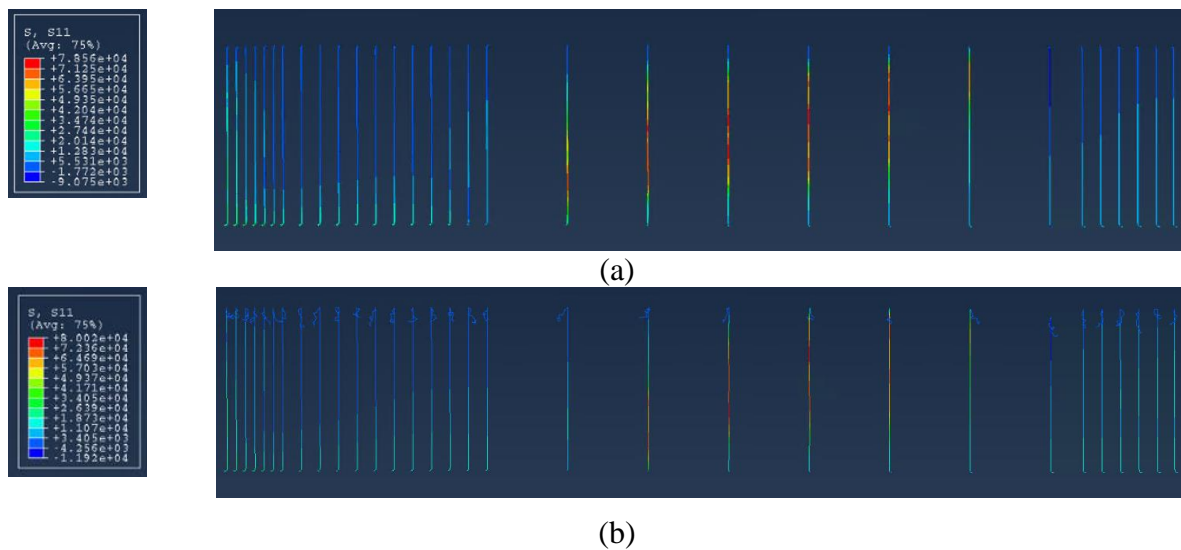
**Figure 8.58. Axial stress in R-bars in FE model at peak load for Tx46: (a) with deck slab, and (b) without deck slab.**



**Figure 8.59. Tension damage in FE model at peak load for Tx54: (a) with deck slab, and (b) without deck slab.**

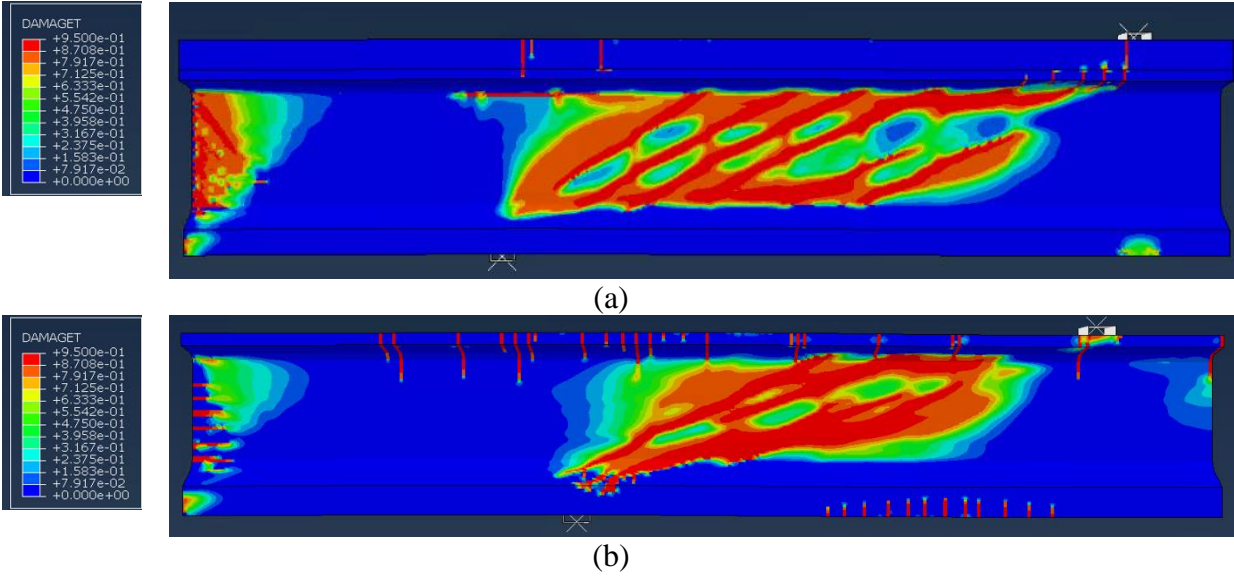


**Figure 8.60. Plastic strain in FE model at peak load for Tx54: (a) with deck slab, and (b) without deck slab.**

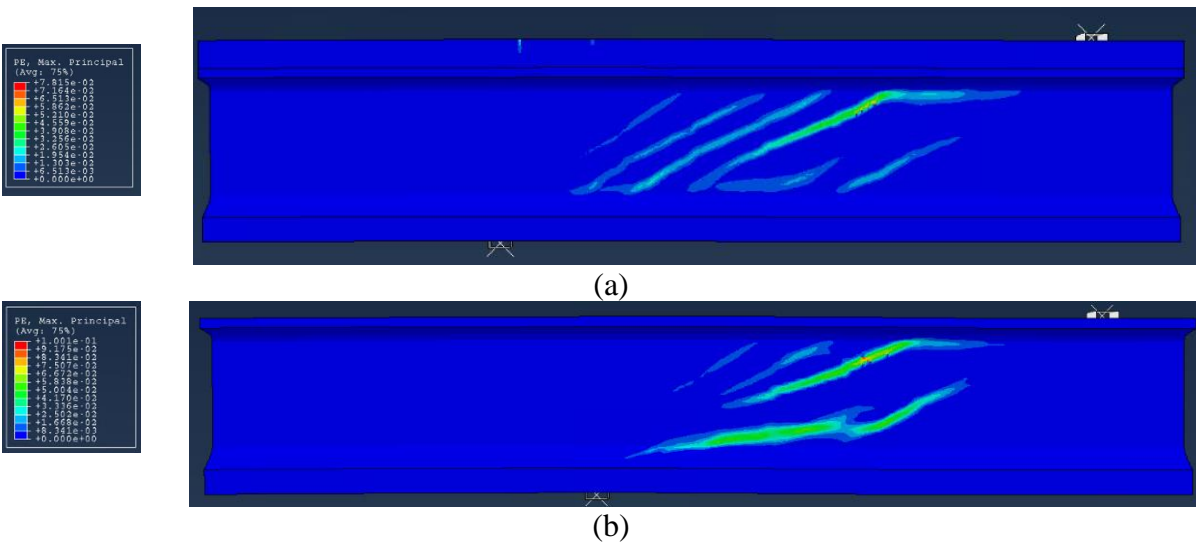


**Figure 8.61. Axial stress in R-bars in FE model at peak load for Tx54: (a) with deck slab, and (b) without deck slab.**

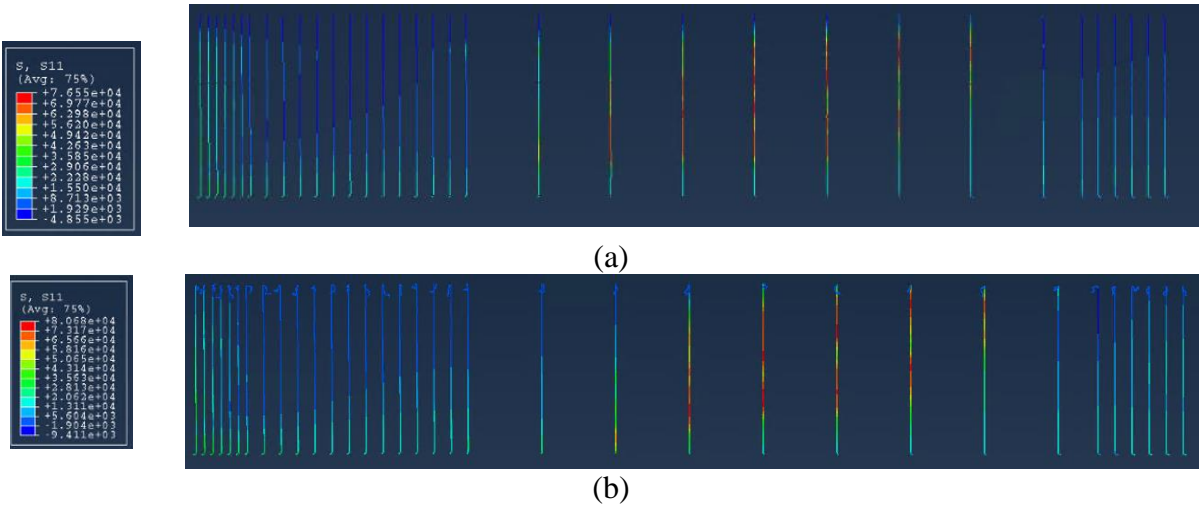




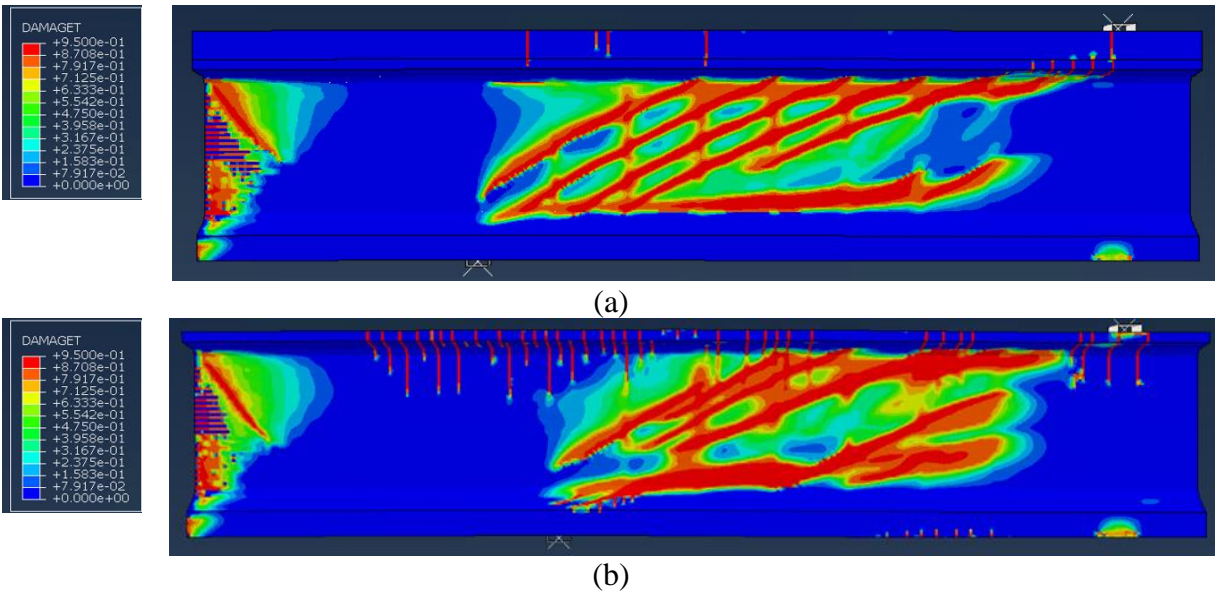
**Figure 8.62. Tension damage in FE model at peak load for Tx62: (a) with deck slab, and (b) without deck slab.**



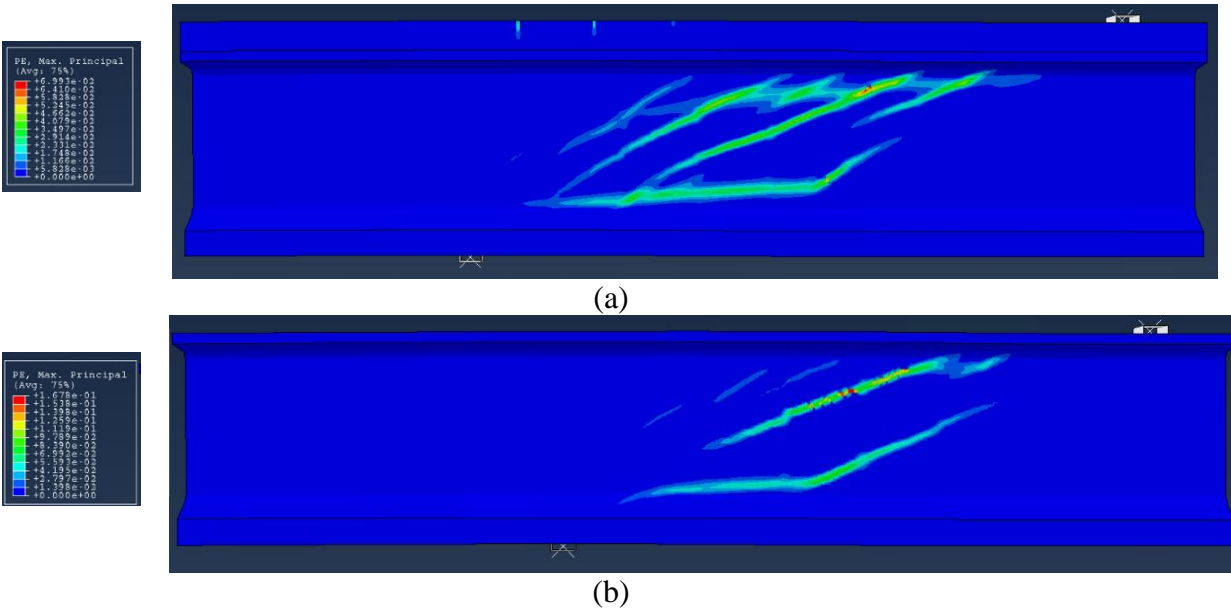
**Figure 8.63. Plastic strain in FE model at peak load for Tx62: (a) with deck slab, and (b) without deck slab.**



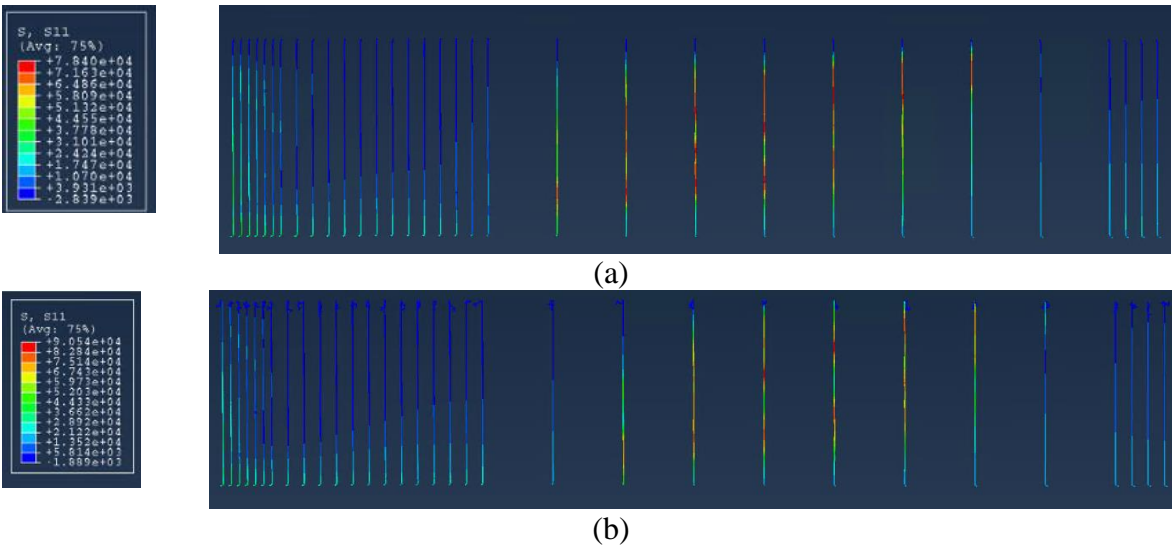
**Figure 8.64. Axial stress in R-bars in FE model at peak load for Tx62: (a) with deck slab, and (b) without deck slab.**



**Figure 8.65. Tension damage in FE model at peak load for Tx70: (a) with deck slab, and (b) without deck slab.**



**Figure 8.66. Plastic strain in FE model at peak load for Tx70: (a) with deck slab, and (b) without deck slab.**



**Figure 8.67. Axial stress in R-bars in FE model at peak load for Tx70: (a) with deck slab and (b) without deck slab.**

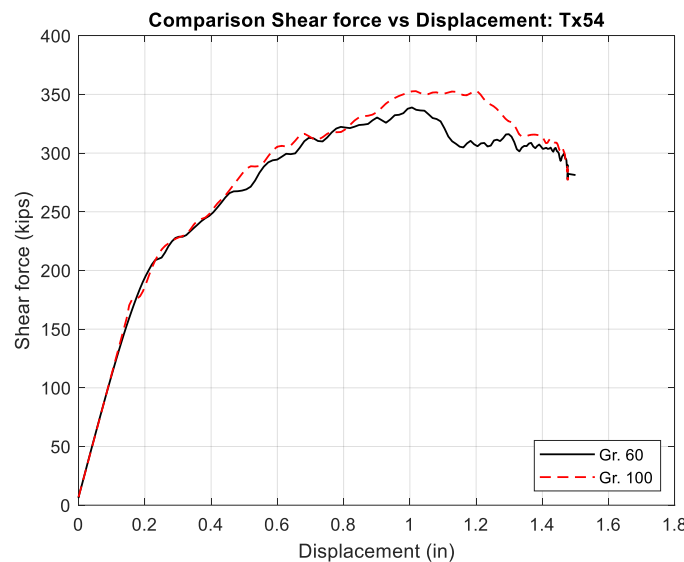
### 8.5.4 Effect of Grade of Shear Reinforcement

Numerical simulations were executed to investigate the influence of shear reinforcement grade on the shear behavior of reinforced concrete bridge girders. The objective was to assess the shear capacity, crack pattern, and overall performance of Tx54 and Tx70 girders when subjected to low levels of shear reinforcement. Two distinct grades were considered: 60 ksi and 100 ksi, with

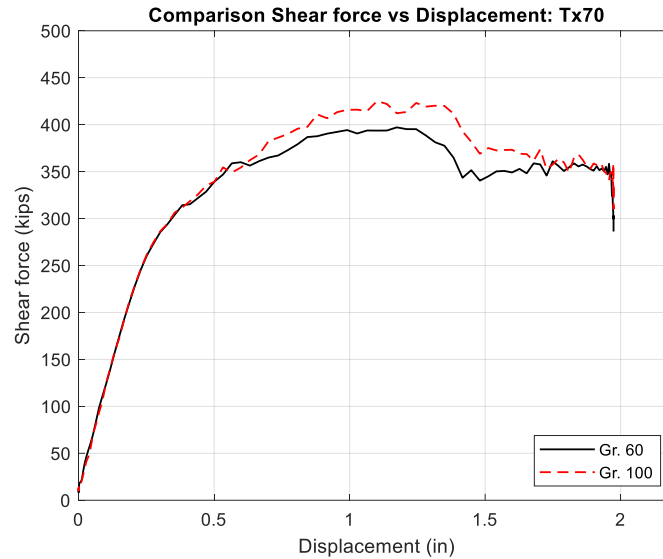
a spacing of 26 in. Moreover, other design parameters, such as concrete strength,  $a/d$ , and prestressing force, were maintained consistently throughout the study.

The grade of shear reinforcement distinctly influenced how the bridge girders responded to shear forces, a conclusion drawn from the findings depicted by the results presented in Figure 8.68 and Figure 8.69 for Tx54 and Tx70, respectively. Notably, the shear cracking load remains consistent across different grades for both Tx54 and Tx70 girders. This finding indicates that the reinforcement grade does not influence the initiation of shear cracking. However, increasing the reinforcement grade led to higher ultimate shear loads for both girders. For instance, Tx54\_Gr. 60 demonstrated an ultimate shear force of 336 kips, whereas Tx54\_Gr. 100 showcased a slightly higher load capacity of 353 kips, marking an approximate 5 percent increase.

Similarly, for the Tx70 specimens, Tx70\_Gr. 60 exhibited an ultimate shear load of 397 kips, while Tx70\_Gr. 100 exhibited a higher ultimate shear load of 423 kips, indicating roughly a 6.5 percent increase. Notably, girders with a higher grade of shear reinforcement exhibited larger deflections at ultimate load.



**Figure 8.68. Shear force versus displacement plots for Tx54.**



**Figure 8.69. Shear force versus displacement plots for Tx70.**

Table 8.5 presents a comprehensive comparative analysis of predicted values from ACI, AASHTO specifications, and the FEM for Tx54 and Tx70. These numerical trends reaffirm earlier observations: higher-grade reinforcement enhances shear strength, and the FEM consistently predicts higher shear capacity than AASHTO and ACI provisions.

Comparing AASHTO and the FEM results, it is clear that AASHTO generally underestimates shear cracking and ultimate shear loads, but in the case of Tx70 girders, the ultimate shear load results provided by AASHTO for Grade 100 reinforcement are higher than the corresponding values predicted by the FEM. Similarly, in the ACI versus the FEM comparison, ACI results tend to underestimate shear cracking and ultimate shear loads, while the FEM consistently offers higher estimates for both girders.

Furthermore, it is essential to note that the RSS values are higher in girders with Grade 100 reinforcement than in Grade 60. Remarkably, the crack angles are steeper in girders with Grade 100 reinforcement than in Grade 60.

**Table 8.5. Grade of R-bars comparison of Tx54 and Tx70 results with different code results.**

Model	$V_{cr-FEM}$ (kips)	$V_{c-AASHTO}$ (kips)	$V_{c-ACI}$ (kips)	$V_{u-FEM}$ (kips)	$V_{u-AASHTO}$ (kips)	$V_{u-ACI}$ (kips)	RSS	Crack Angle
<b>Tx54_Gr. 60</b>	211	180	211	336	272	264	1.59	22-28
<b>Tx54_Gr. 100</b>	211	180	211	353	334	299	1.67	24-31
<b>Tx70_Gr. 60</b>	293	243	260	397	362	327	1.35	19-29
<b>Tx70_Gr. 100</b>	293	243	260	423	442	372	1.44	24-34

Figure 8.70, Figure 8.71, Figure 8.73, and Figure 8.74 compare the failure mode and concrete damage at the peak load for Tx54 and Tx70 girders, as analyzed using numerical models. The schematic drawings depicting crack patterns in tension, and the maximum plastic strain for Tx54 and Tx70 specimens reveals notable findings. First, in girders with Grade 100 reinforcement, there is an evident increase in crack intensity over girders with Grade 60 reinforcement. However, there were distinct differences in the plastic strain behavior. Specifically, for Tx54, the plastic strain was higher in girders with Grade 100 reinforcement than in girders with Grade 60 reinforcement. On the other hand, for Tx70 specimens, the plastic strain was higher in girders with Grade 60 reinforcement than in girders with Grade 100 reinforcement.

It is clear from Figure 8.72 and Figure 8.75 that when the shear reinforcement grade increased, there was a corresponding increase in the axial stress experienced by the reinforcement bars (R-bars) at the ultimate force for both Tx54 and Tx70 specimens.

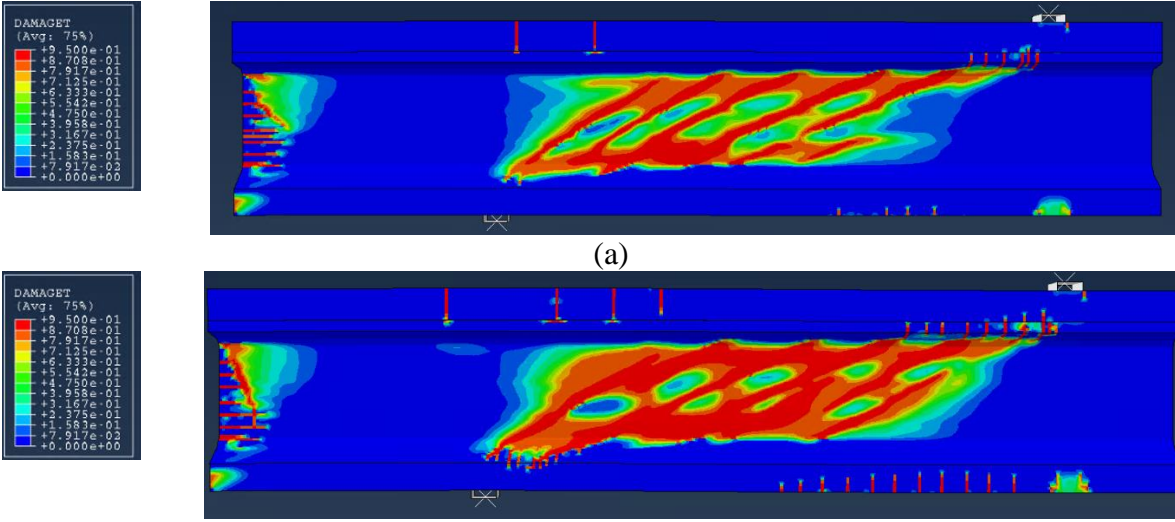


Figure 8.70. Tension damage in FE model at peak load for Tx54: (a) Grade 60 ksi, and (b) Grade 100 ksi.

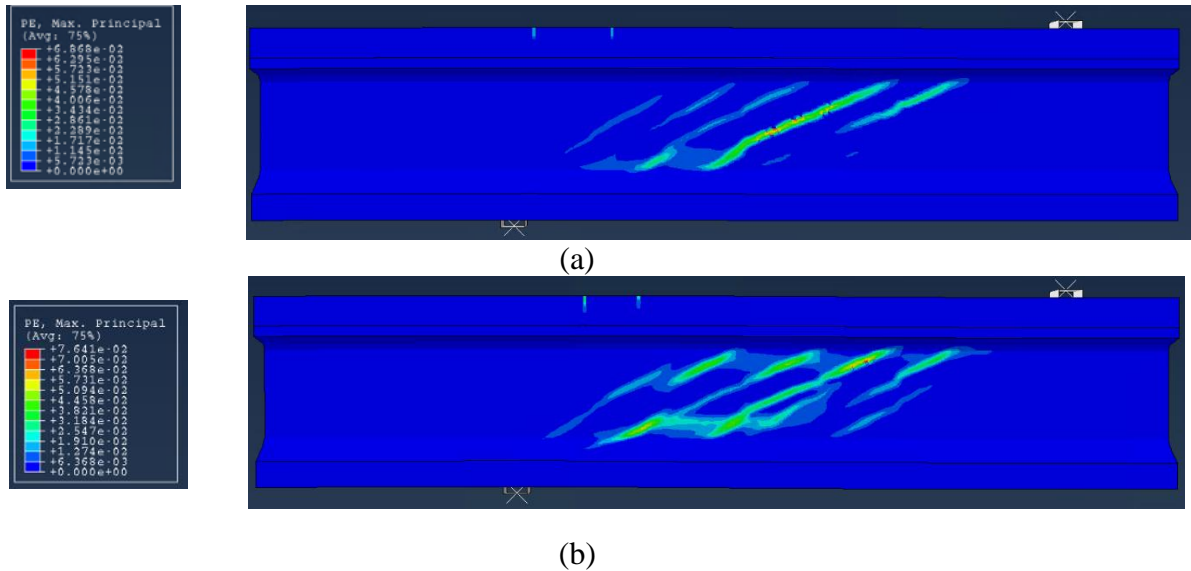
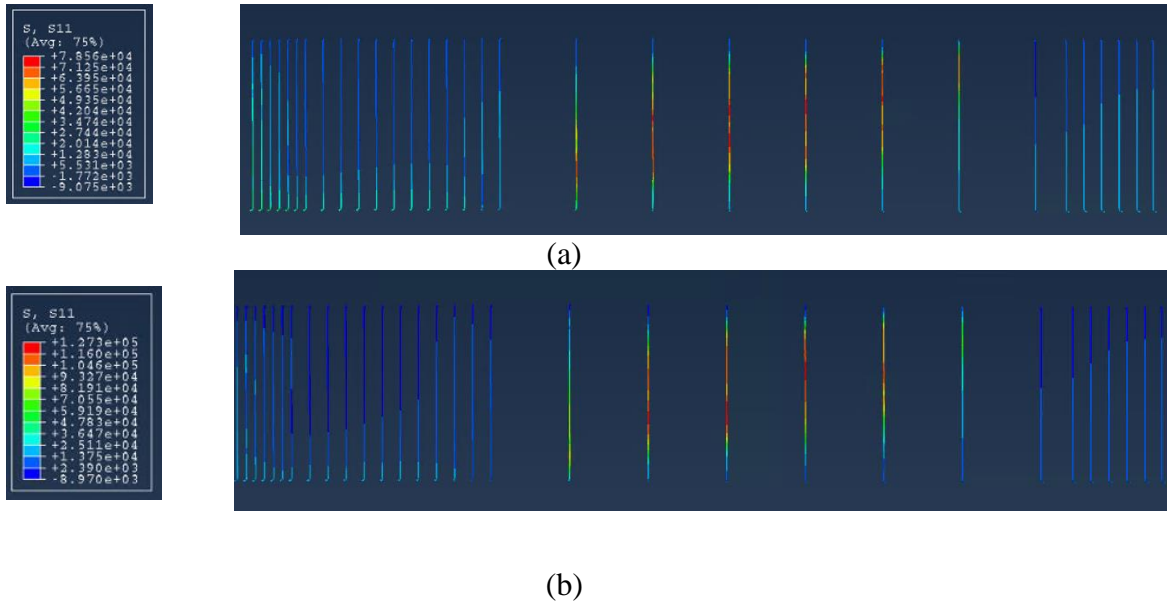
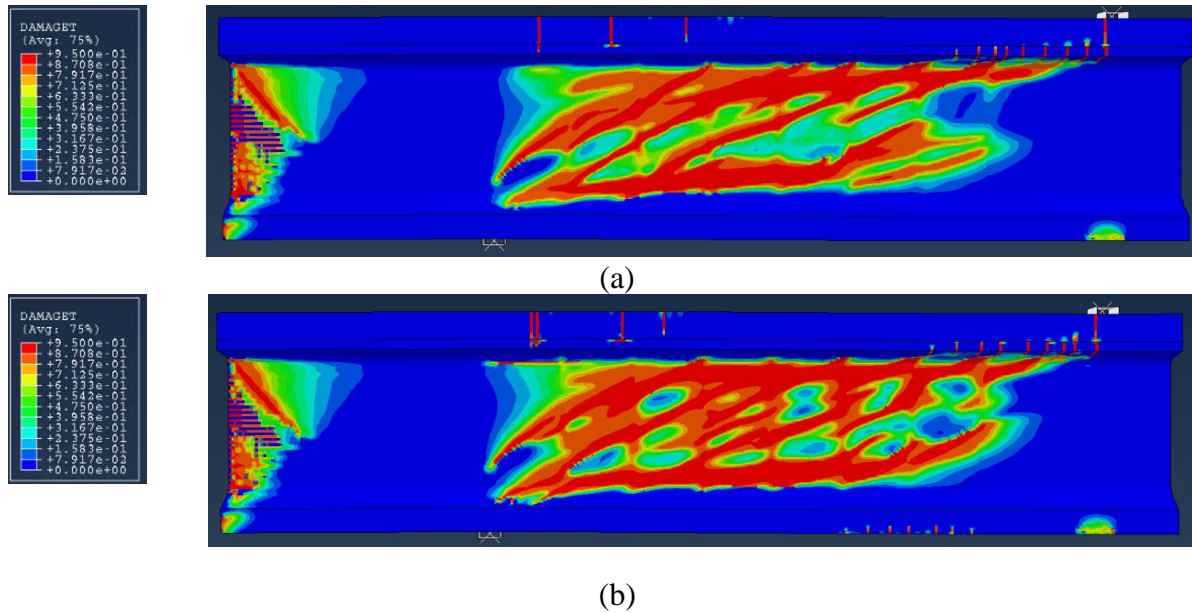


Figure 8.71. Plastic strain in FE model at peak load for Tx54: (a) Grade 60 ksi, and (b) Grade 100 ksi.



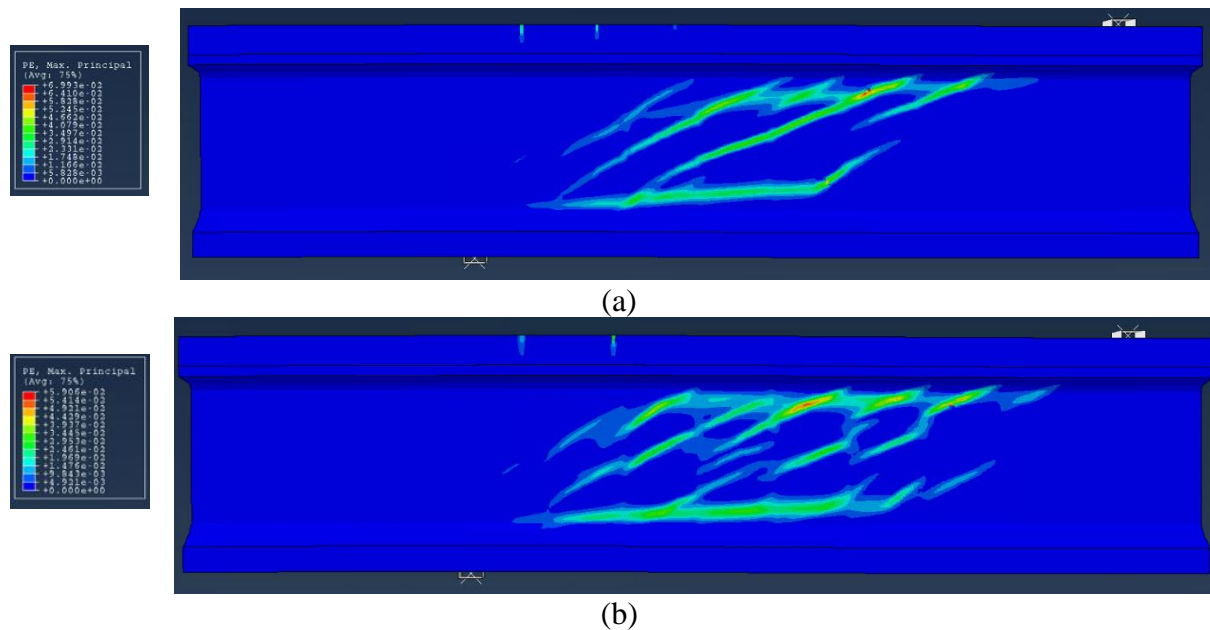


**Figure 8.72. Axial stress in R-bars in FEM at peak load for Tx54: (a) Grade 60 ksi, and (b) Grade 100 ksi.**

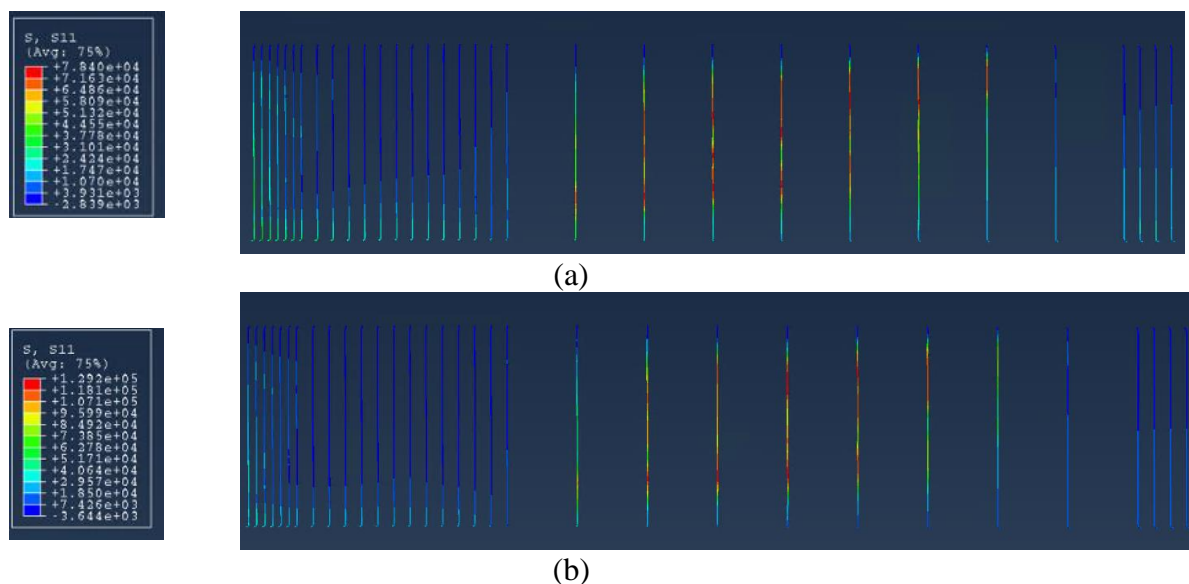


**Figure 8.73. Tension damage in FE model at peak load for Tx70: (a) Grade 60 ksi, and (b) Grade 100 ksi.**





**Figure 8.74. Plastic strain in FE model at peak load for Tx70: (a) Grade 60 ksi, and (b) Grade 100 ksi.**



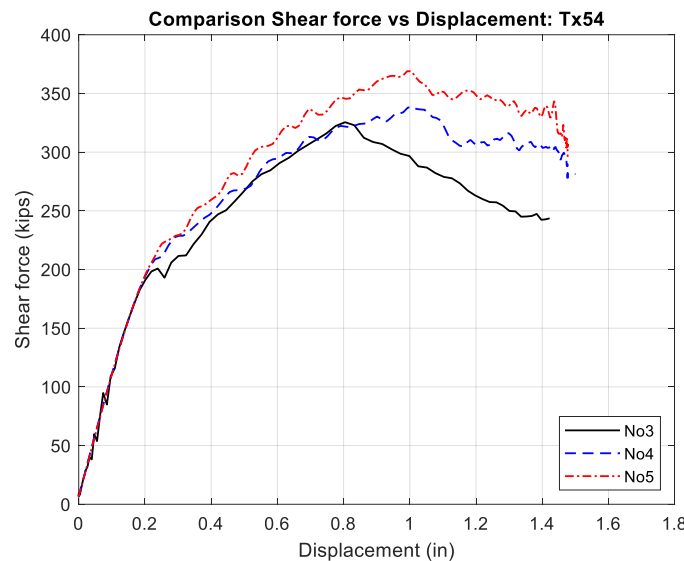
**Figure 8.75. Axial stress in R-bars in FEM at peak load for Tx70: (a) Grade 60 ksi and (b) Grade 100 ksi.**

### 8.5.5 Effect of Shear Reinforcement Size

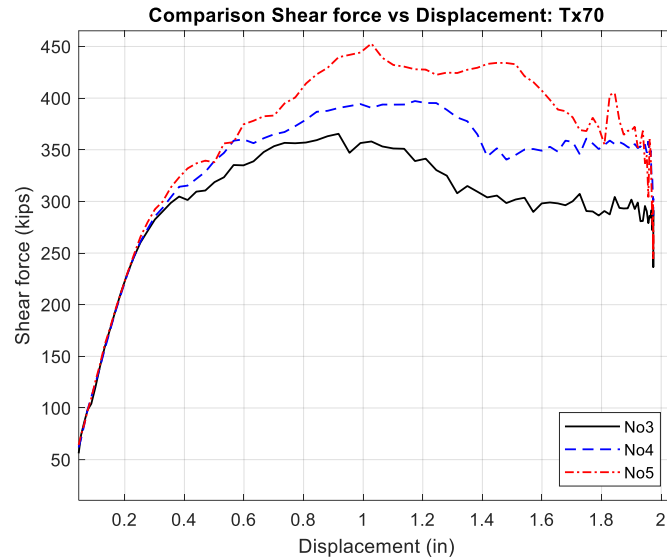
Numerical simulations were conducted to analyze how the size of shear reinforcement affects the shear behavior of reinforced concrete bridge girders. The study considered three different sizes for R-bars: No. 3, No. 4, and No. 5, with a spacing of 26 in. in both Tx54 and Tx70 girders.

The results of this evaluation are presented graphically in Figure 8.76 and Figure 8.77. In the Tx54 series, the cracking force of specimens showed a range between 198 kips (No. 3) and 222 kips (No. 5), representing an increase of approximately 12 percent. Additionally, there was an increase in shear capacity from 325 kips (No. 3) to 368 kips (No. 5), indicating an elevation of roughly 13 percent. The inclusion of No. 4 resulted in a cracking shear of 211 kips and an ultimate capacity of 336 kips.

Similarly, in the Tx70 series, the cracking force varied between 291 kips (No. 3) and 323 kips (No. 5), highlighting an approximate increase of 11 percent. Furthermore, shear capacity ranged from 366 kips (No. 3) to 453 kips (No. 5), indicating a rise of around 24 percent. The utilization of No. 4 yielded a cracking force of 293 kips and an ultimate capacity of 397 kips.



**Figure 8.76. Shear force versus displacement plots for Tx54.**



**Figure 8.77. Shear force versus displacement plots for Tx70.**

Table 8.6 compares the FEM results and the standards set by AASHTO and ACI for shear cracking force and ultimate shear force across various specimens. These comparisons help highlight where the analytical approaches align and where there are disparities.

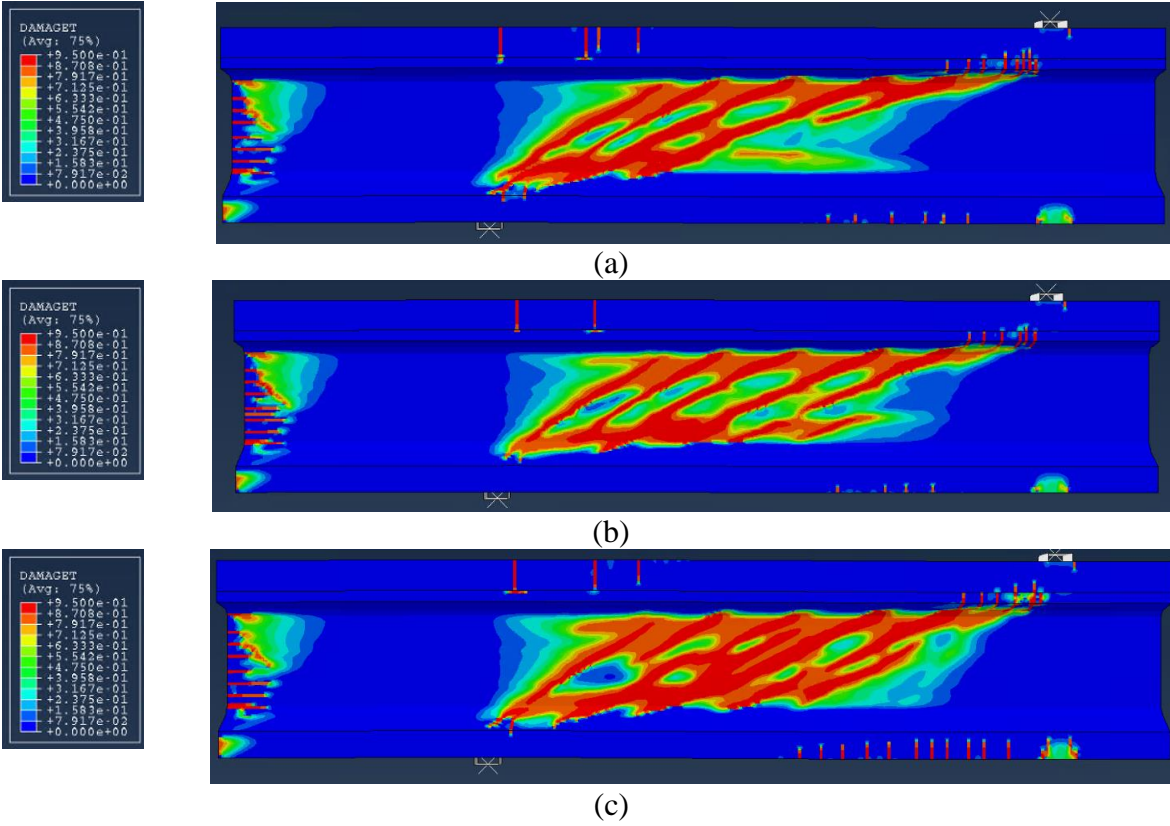
The FEM results showed variations when compared to the AASHTO and ACI standards regarding shear cracking load and shear capacity. The FEM results indicated higher shear cracking loads than those estimated by AASHTO and ACI for most specimens. Furthermore, the FEM's estimation of the ultimate shear load significantly exceeded the results made by ACI and AASHTO. Across the various specimens, the ratio of the FEM's ultimate shear force to AASHTO's ranged from 1.06 to 1.41. In parallel, the ratio of the FEM's  $V_u$  to ACI's  $V_u$  spanned from 1.21 to 1.35. Additionally, it is worth noting that as the size of shear reinforcement increased, there was a trend of higher RSS values and inclination angles.

**Table 8.6. Size of R-bar comparison of Tx54 and Tx70 results with different code results.**

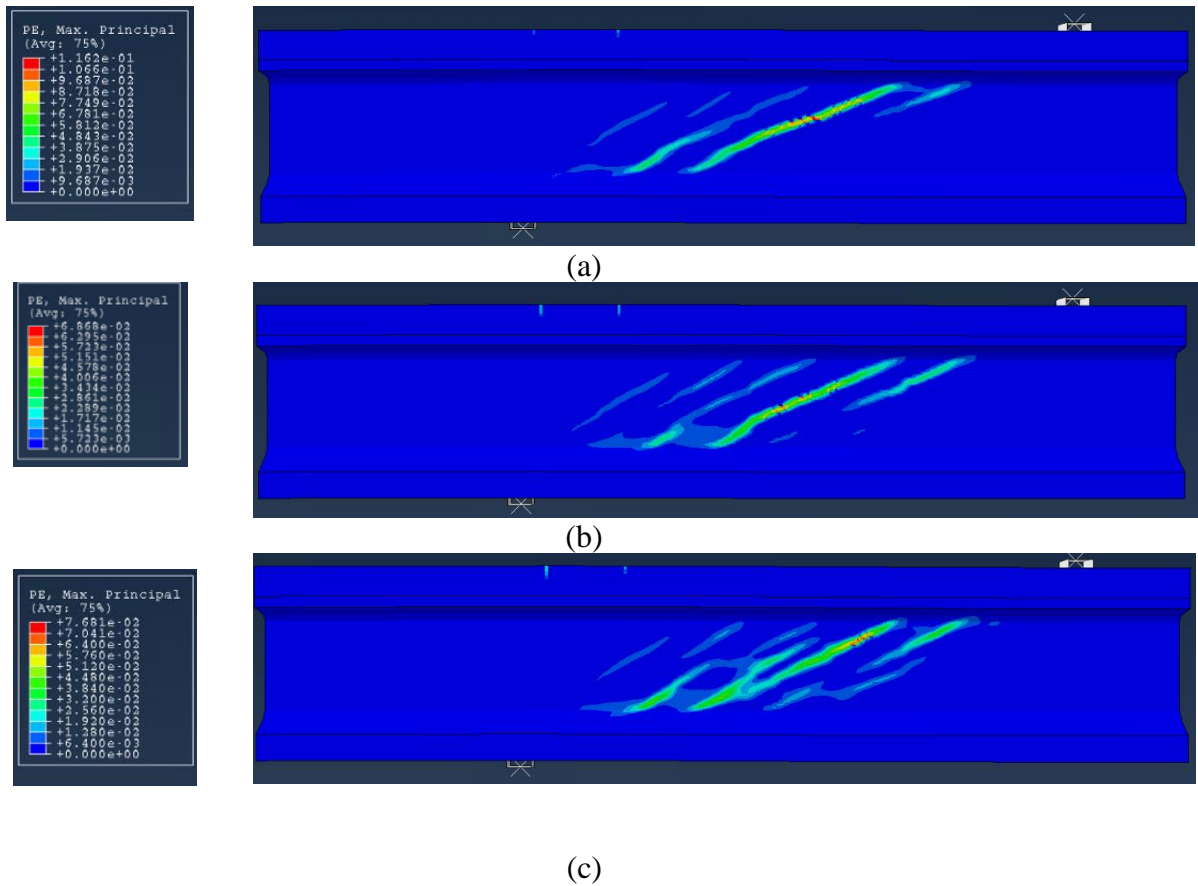
Model	$V_{cr-FEM}$ (kips)	$V_{c-AASHTO}$ (kips)	$V_{c-ACI}$ (kips)	$V_{u-FEM}$ (kips)	$V_{u-AASHTO}$ (kips)	$V_{u-ACI}$ (kips)	RSS	Crack Angle
<b>Tx54_No. 3</b>	198	180	211	325	231	240	1.64	21-23
<b>Tx54_No. 4</b>	211	180	211	336	272	264	1.59	22-28
<b>Tx54_No. 5</b>	222	180	211	368	323	293	1.66	26-29
<b>Tx70_No. 3</b>	291	243	260	366	309	297	1.26	18-27
<b>Tx70_No. 4</b>	293	243	260	397	362	327	1.35	19-29
<b>Tx70_No. 5</b>	323	243	260	453	428	364	1.4	26-30

Figure 8.78, Figure 8.79, Figure 8.81, and Figure 8.82 provide a comparison of the failure mode and concrete damage at the peak load for Tx54 and Tx70 girders, as analyzed using numerical models. The schematic drawings depicting crack patterns in tension and the maximum plastic strain for Tx54 and Tx70 specimens reveal notable findings. First, there is a clear trend of increased crack intensity as the size of shear reinforcement increases. Second, it is evident that as the size of the shear reinforcement increased, there was a corresponding reduction in the plastic strain at the ultimate force for both Tx54 and Tx70 specimens.

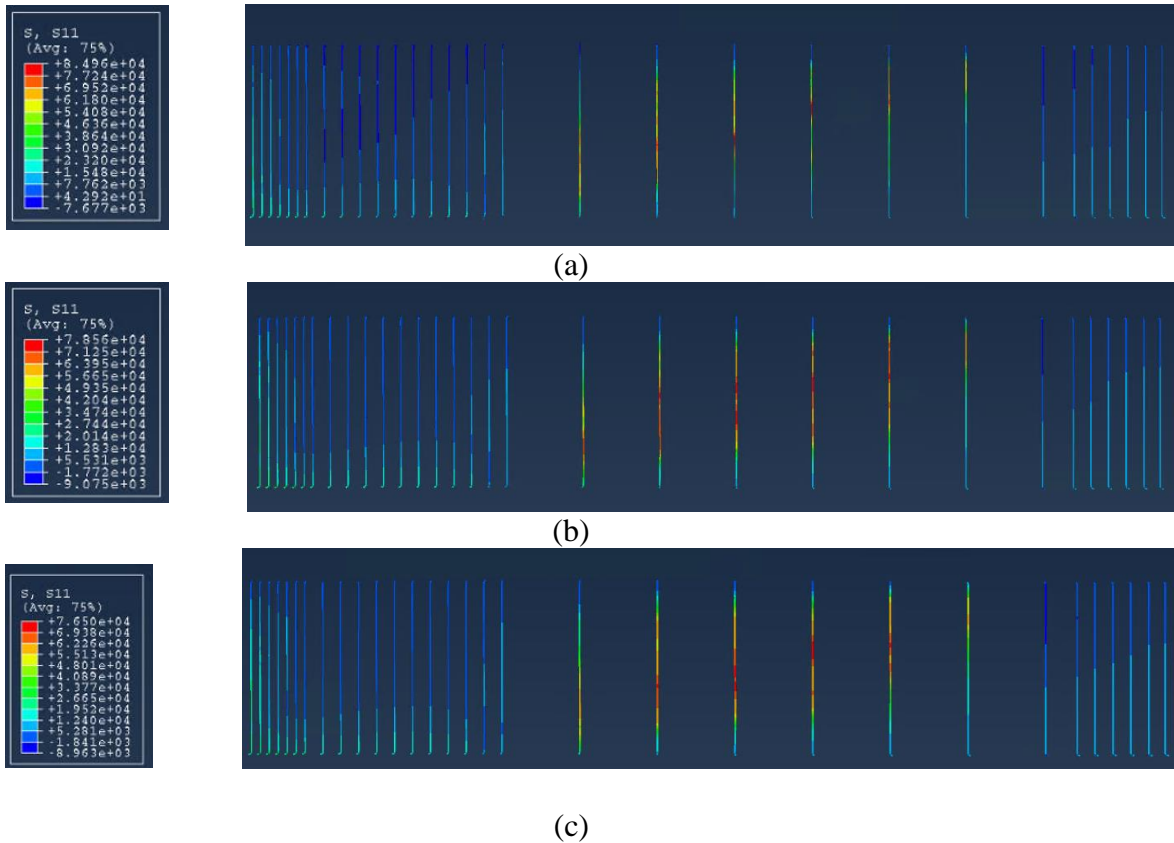
It is clear from Figure 8.72, and Figure 8.80 that when the shear reinforcement size increased, there was a corresponding decrease in the axial stress experienced by the reinforcement bars (R-bars) at the ultimate force for both Tx54 and Tx70 specimens.



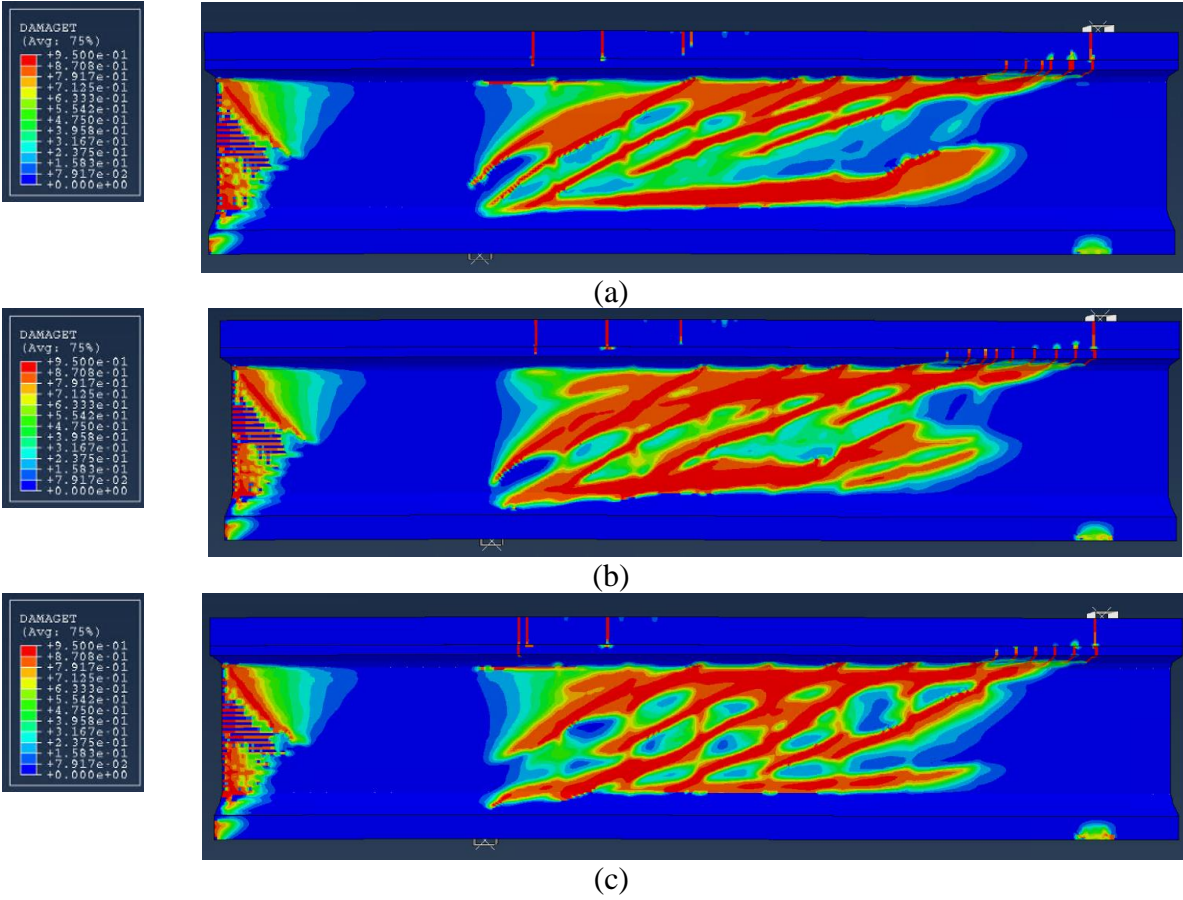
**Figure 8.78. Tension damage in FE model at peak load for Tx54: (a) No. 3, (b) No. 4, and (c) No. 5.**



**Figure 8.79. Plastic strain in FE model at peak load for Tx54: (a) No. 3, (b) No. 4, and (c) No. 5.**

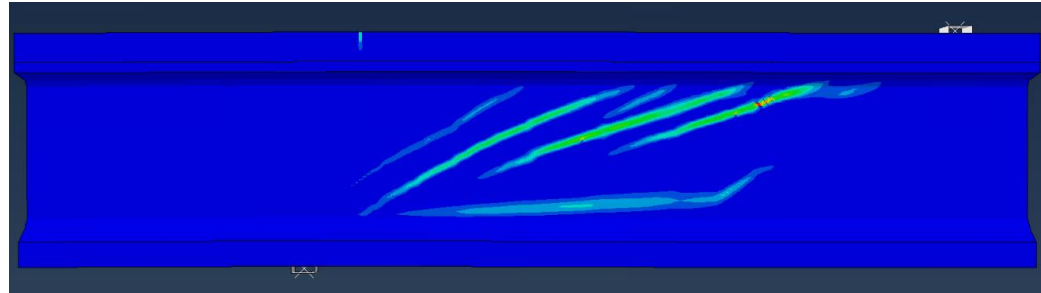
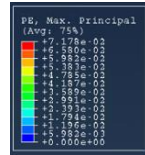


**Figure 8.80. Axial stress in R-bars in FEM at peak load for Tx54: (a) No. 3, (b) No. 4, and (c) No. 5.**

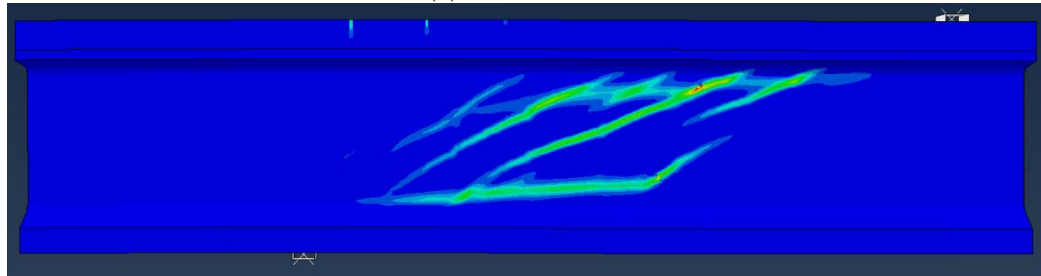
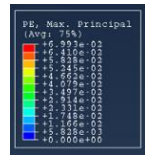


**Figure 8.81. Tension damage in FE model at peak load for Tx70: (a) No. 3, (b) No. 4, and (c) No. 5.**

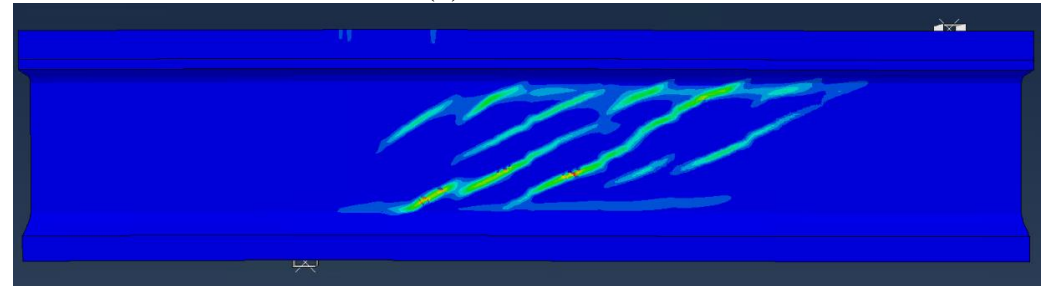
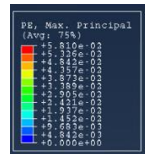




(a)

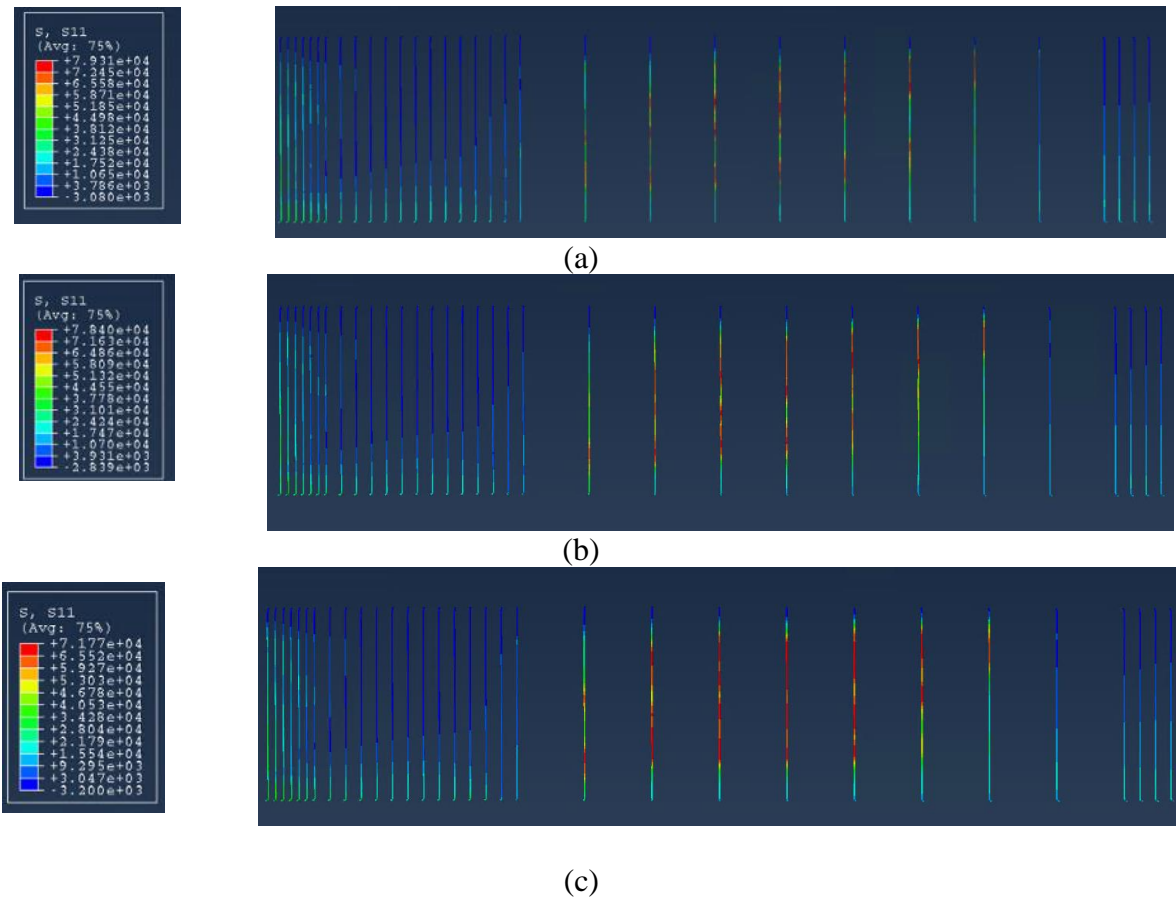


(b)



(c)

**Figure 8.82. Plastic strain in FE model at peak load for Tx70: (a) No. 3, (b) No. 4, and (c) No. 5.**



**Figure 8.83. Axial stress in R-bars in FEM at peak load for Tx70: (a) No. 3, (b) No. 4, and (c) No. 5.**

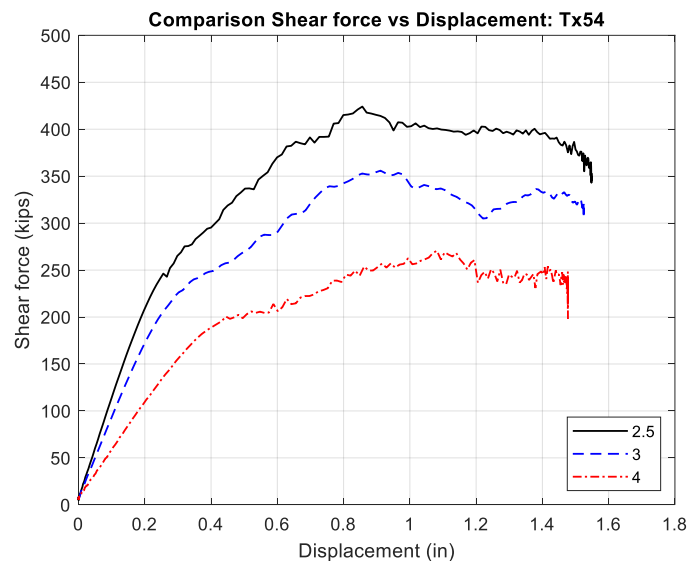
### 8.5.6 Effect of Shear Span-to-Depth Ratio

Numerical simulations were performed on specimens of Tx54 and Tx70 girders with  $a/d$  of 2.5, 3, and 4 to evaluate their impact on girder behavior. The specimens maintained a compressive strength of 7.5, employing a shear reinforcement spacing of 26 in.

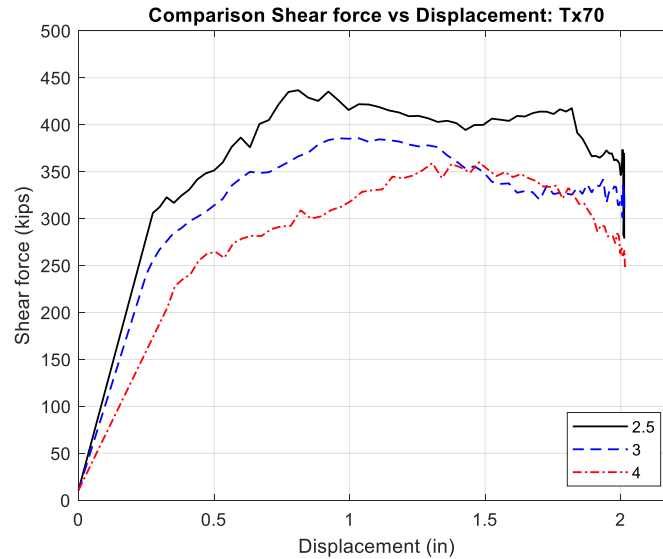
The shear force versus deformation graph obtained from the results illustrates significant variations in the maximum force capacities of Tx54 and Tx70 girders for different  $a/d$ , as depicted in Figure 8.84 and Figure 8.85. The cracking force values for Tx54 girders exhibit a discernible pattern across different  $a/d$ . At 4, 3, and 2.5 ratios, the respective cracking force values are 185 kips, 211 kips, and 235 kips. Calculating the force gains underscores the impact of these ratios on cracking force capacity. There is an increase of about 14.6 percent when comparing a ratio of 3 to a ratio of 4. Moreover, a more substantial gain of approximately 27.0 percent is observed when comparing a ratio of 2.5 to a ratio of 4.

Likewise, a similar trend emerges for Tx70 girders. At  $a/d$  of 4, 3, and 2.5, the cracking force values are 254 kips, 293 kips, and 304 kips, respectively. The force increases by around 15.4 percent when comparing a ratio of 3 to a ratio of 4 and experiences a gain of about 19.7 percent when comparing a ratio of 2.5 to 4. This consistent trend emphasizes the significance of  $a/d$  in determining the cracking force capacity of Tx70 girders.

For Tx54 girders, maximum force values of 266 kips, 336 kips, and 421 kips were observed for  $a/d$  of 4, 3, and 2.5, respectively. This indicates force gains of approximately 26.3 percent and 58.3 percent when comparing the lower span-to-depth ratios (3 and 2.5) to the ratio of 4. Similarly, for Tx70 girders, maximum force values of 354 kips, 397 kips, and 434 kips were recorded for the corresponding  $a/d$ . These values translate to force gains of approximately 12.4 percent and 22.6 percent when comparing the lower span-to-depth ratios (3 and 2.5) to the ratio of 4. Notably, the girder with higher  $a/d$  was less stiff and exhibited larger deflections under loading.



**Figure 8.84. Shear force versus displacement plots for Tx54.**



**Figure 8.85. Shear force versus displacement plots for Tx70.**

The comparative analysis in Table 8.7 highlights the disparities between the shear strength results obtained from the FEM, the AASHTO specifications, and the ACI provisions for Tx54 and Tx70 specimens. Notably, the FEM consistently produces higher ultimate force values than those calculated by both AASHTO and ACI across various test scenarios.

The FEM-predicted shear cracking forces for Tx54 and Tx70 specimens are notably higher than their respective AASHTO and ACI counterparts for the  $a/d$  of 2.5. The ratios of FEM shear cracking force to AASHTO shear cracking force range from approximately 1.13 to 1.24 for the Tx54 specimens and from 1.14 to 1.21 for the Tx70 specimens. Similarly, the ratios of FEM shear cracking force to ACI shear cracking force fall within the range of 0.88 to 1.11 for Tx54 and 0.98 to 1.17 for Tx70. This discrepancy is attributed to ACI's omission of the influence of the  $a/d$ .

For the ultimate shear forces, a similar trend is observed. The FEM-predicted ultimate shear forces for Tx54 and Tx70 are consistently higher than the forces predicted by AASHTO and ACI. The ratios of the FEM ultimate shear force to AASHTO ultimate shear force range from 1.04 to 1.49 for Tx54 and 1.04 to 1.16 for Tx70. Similarly, the ratios of the FEM ultimate shear force to ACI ultimate shear force fall within the range of 1.01 to 1.59 for Tx54 and 1.08 to 1.33 for Tx70. These ratios further affirm the tendency of the FEM to provide higher ultimate shear force results than AASHTO and ACI. Interestingly, for both specimens, it is notable that

AASHTO and ACI ultimate shear forces results more closely align with the FEM values as the shear-span-to-depth increases.

Additionally, it is worth noting that as the  $a/d$  decreased, there was a trend of higher RSS values and inclination angles.

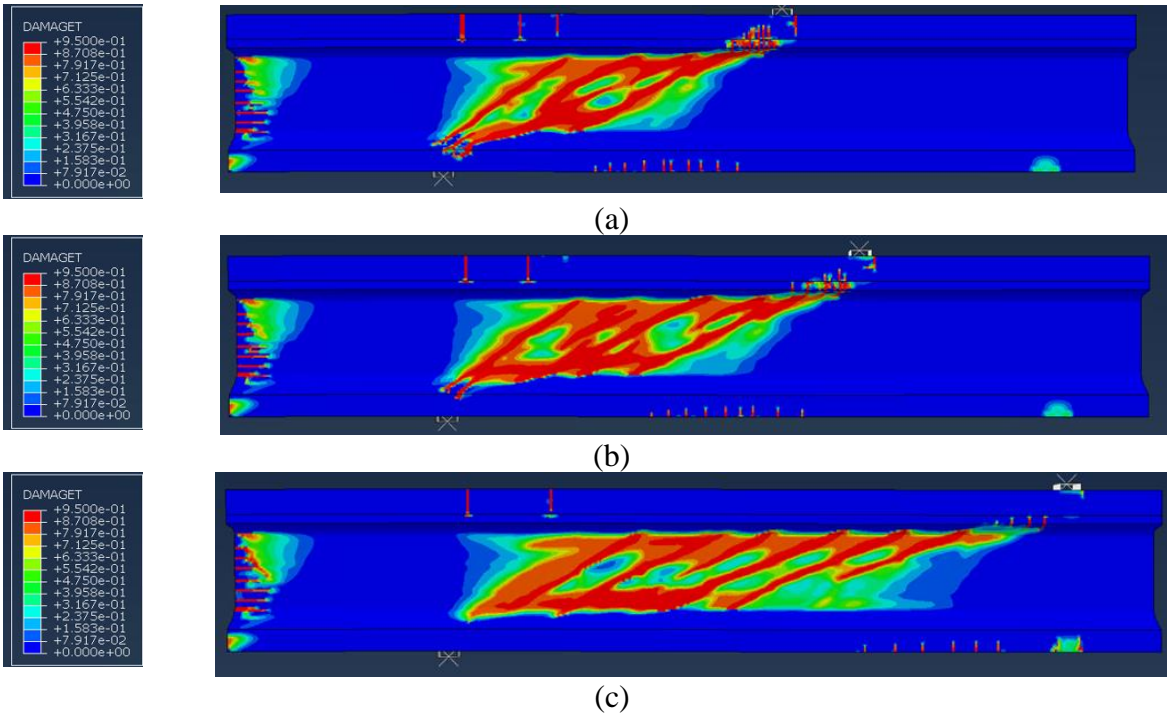
**Table 8.7. Shear-span-to-depth comparison of Tx54 and Tx70 results with different code results.**

Model	$V_{cr-FEM}$ (kips)	$V_{c-AASHTO}$ (kips)	$V_{c-ACI}$ (kips)	$V_{u-FEM}$ (kips)	$V_{u-AASHTO}$ (kips)	$V_{u-ACI}$ (kips)	RSS	Crack Angle
<b>Tx54_2.5</b>	235	189	211	421	283	264	1.79	24-30
<b>Tx54_3</b>	211	180	211	336	272	264	1.59	22-28
<b>Tx54_4</b>	185	164	211	266	255	264	1.44	22-24
<b>Tx70_2.5</b>	304	255	260	434	375	327	1.43	23-27
<b>Tx70_3</b>	293	243	260	397	362	327	1.35	20-26
<b>Tx70_4</b>	254	223	260	354	340	327	1.39	18-23

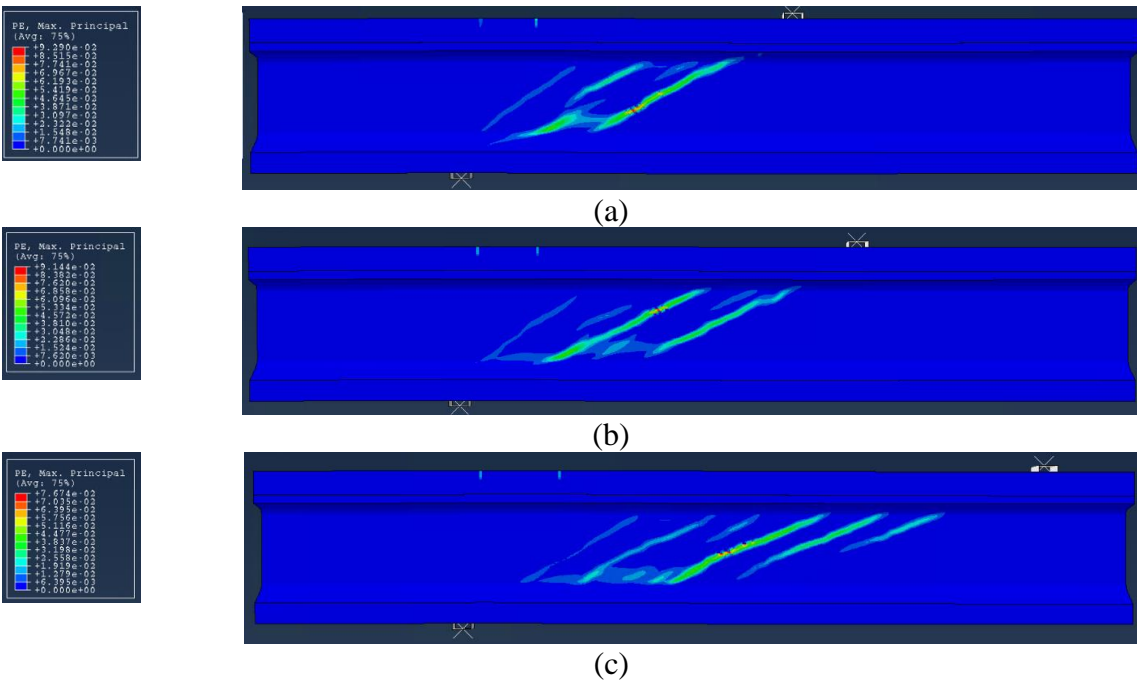
Figure 8.86, Figure 8.87, Figure 8.89, and Figure 8.90 provide a comparison of the failure mode and concrete damage at the peak force for Tx54 and Tx70 girders, as analyzed using numerical models at various  $a/d$  ratios.

The schematic diagrams for Tx54 and Tx70 specimens illustrate that those girders with smaller  $a/d$  ratios tend to exhibit increased strains in concrete and a higher inclined cracking angle, leading to shear failure. This phenomenon is attributed to enhanced confinement within the compression zone in structures with lower  $a/d$ s, resulting in a higher contribution from the concrete to the overall shear strength. The  $a/d$  significantly impacts the orientation of principal stress fields and the formation of inclined cracks, subsequently influencing the shear failure mechanism of the girder, thus making it crucial in determining the structural behavior.

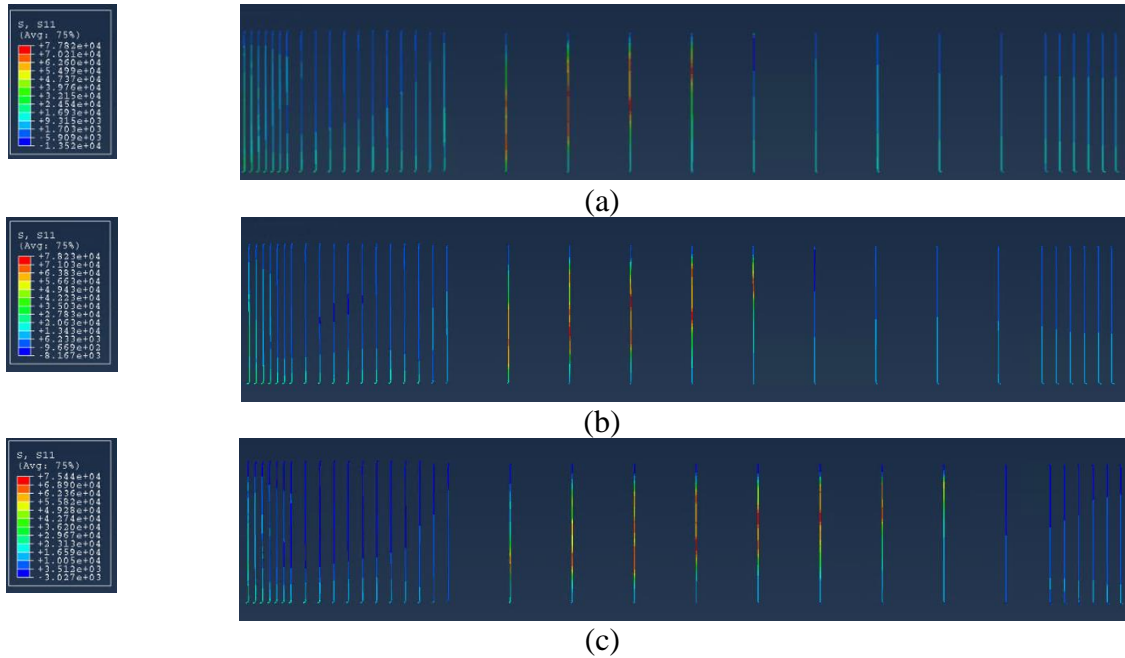
Furthermore, the axial stress in R-bars at ultimate force remained consistently similar for Tx54 and Tx70 girders across various  $a/d$  ratios, as demonstrated in Figure 8.88 and Figure 8.91.



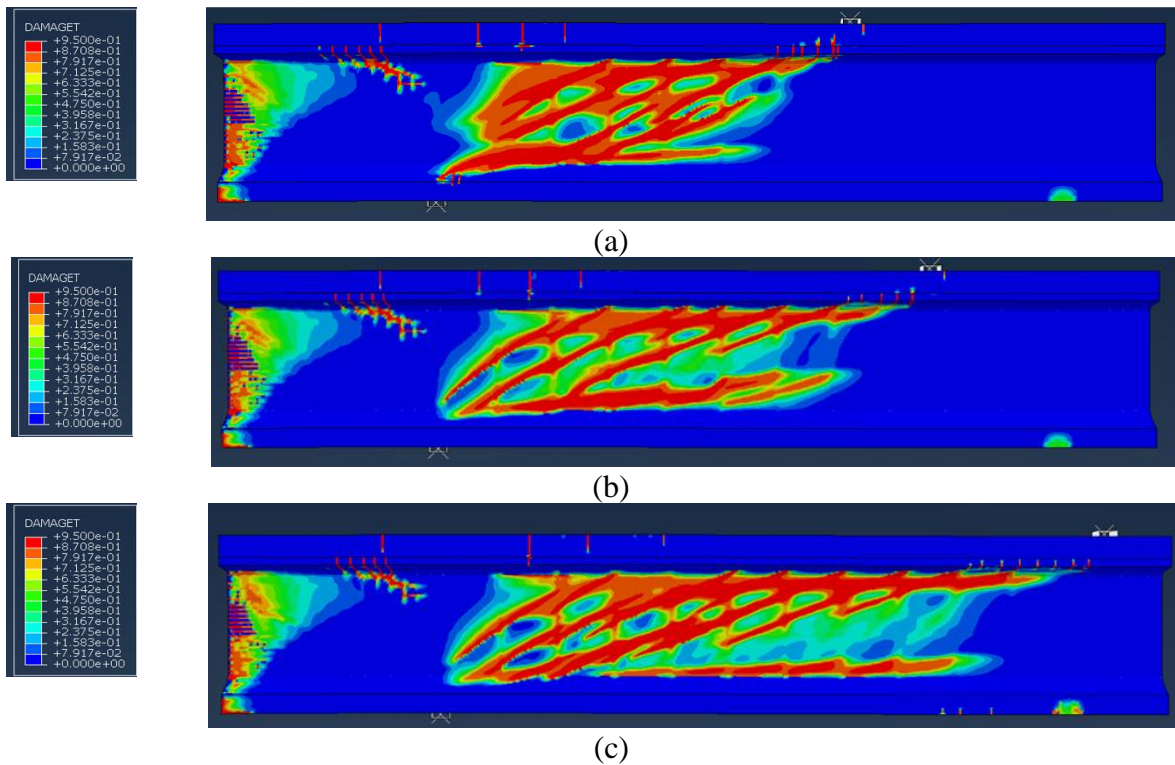
**Figure 8.86. Tension damage in FE model at peak load for Tx54: (a) 2.5, (b) 3, and (c) 4.**



**Figure 8.87. Plastic strain in FE model at peak load for Tx54: (a) 2.5, (b) 3, and (c) 4.**

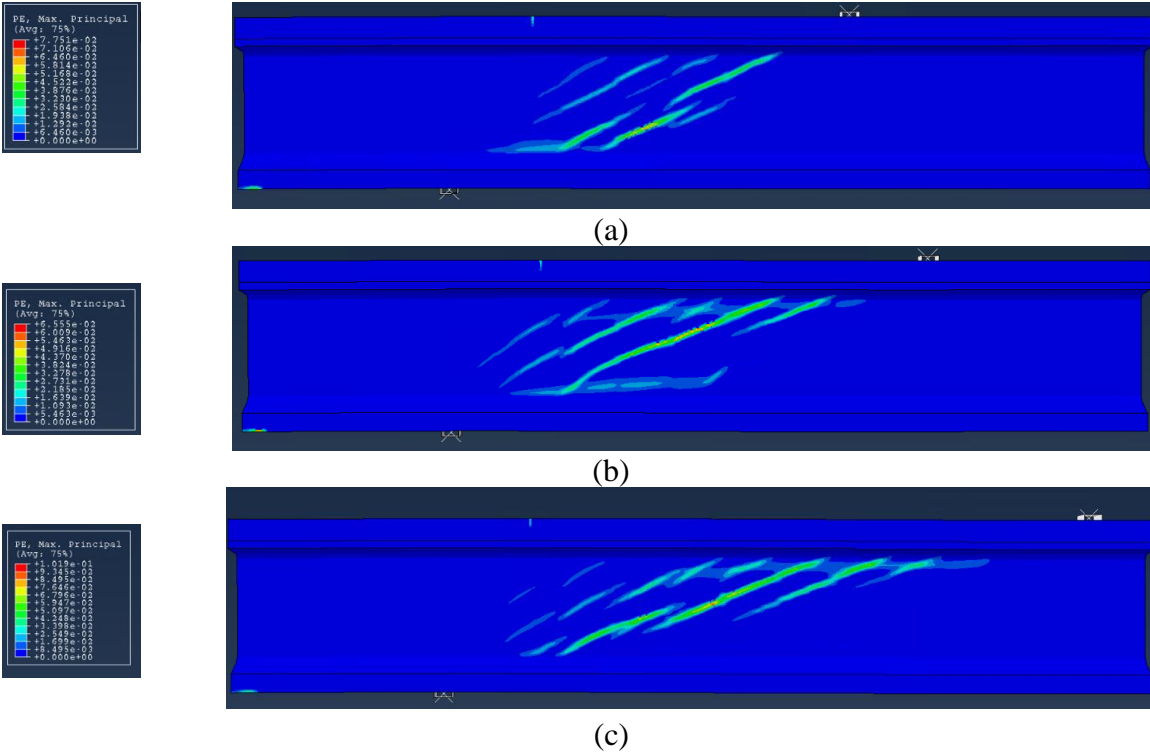


**Figure 8.88. Axial stress in R-bars in FE model at peak load for Tx54: (a) 2.5, (b) 3, and (c) 4.**

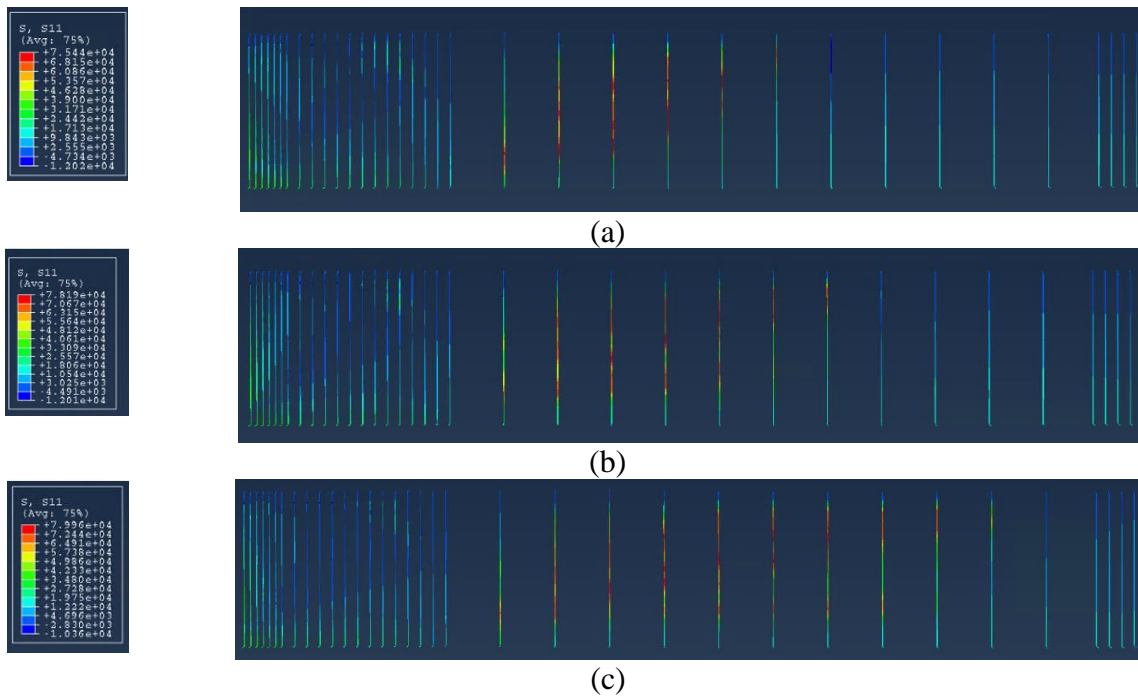


**Figure 8.89. Tension damage in FE model at peak load for Tx70: (a) 2.5, (b) 3, and (c) 4.**





**Figure 8.90. Plastic strain in FE model at peak load for Tx70: (a) 2.5, (b) 3, and (c) 4.**



**Figure 8.91. Axial stress in R-bars in FE model at peak load for Tx70: (a) 2.5, (b) 3, and (c) 4.**



### 8.5.7 Effect of Concrete Strength

Tx54 and Tx70 girders with varying concrete compressive strengths of 5 ksi, 8.5 ksi, and 14 ksi were used to assess the effect of concrete strength. The shear-to-depth ratio was maintained at 3 for all specimens, and a shear reinforcement spacing of 26 in. was used. Table 8.8 summarizes concrete material properties considered in the model.

**Table 8.8. Material properties for concrete.**

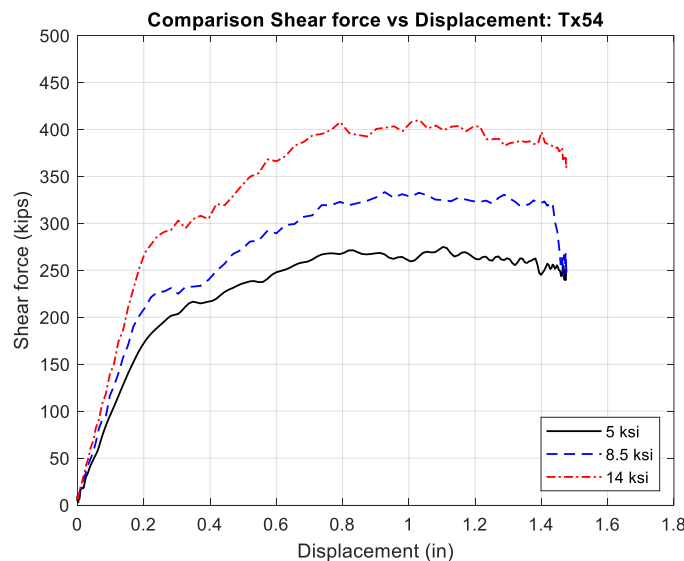
Property		Value
$f'_c = 5 \text{ ksi}$	Elastic modulus, $E_c$	4087 ksi
	Cracking tensile strength, $f_{cr}$	315 psi
	Fracture energy, $G_f$	0.79 lb/in
$f'_c = 8.5 \text{ ksi}$	Elastic modulus, $E_c$	5329 ksi
	Cracking tensile strength, $f_{cr}$	411 psi
	Fracture energy, $G_f$	0.87 lb/in
$f'_c = 14 \text{ ksi}$	Elastic modulus, $E_c$	6829 ksi
	Cracking tensile strength, $f_{cr}$	527 psi
	Fracture energy, $G_f$	0.95 lb/in

The shear force versus deformation graph obtained from the results illustrates significant variations in the maximum force capacities of Tx54 and Tx70 girders for different concrete compressive strengths, as depicted in Figure 8.92 and Figure 8.93.

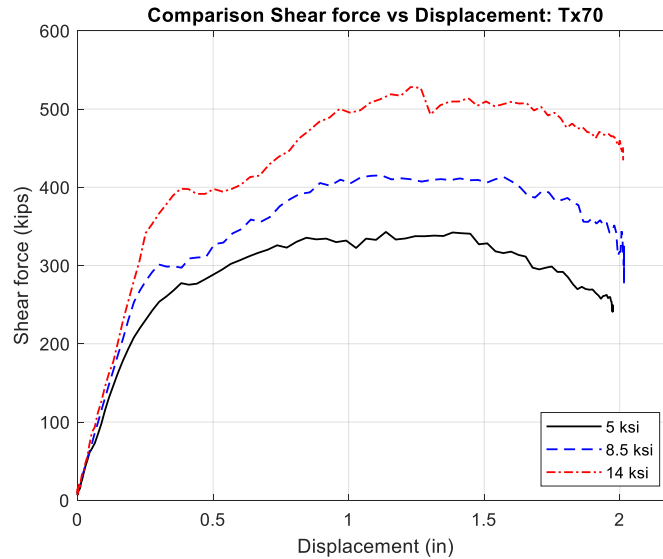
In analyzing shear cracking force across different specimens, a clear trend highlights the impact of varying concrete compressive strengths. For the Tx54 girders, as the concrete compressive strength increased from 5 ksi to 8.5 ksi, there was a noticeable percentage increase of around 37 percent in cracking force, with 164 kips and 226 kips, respectively. Similarly, when comparing 5 ksi to 14 ksi concrete compressive strength, cracking force experiences a substantial rise of approximately 75 percent, with 164 kips and 287 kips, respectively. The Tx70 girders follow a similar pattern. Transitioning from 5 ksi to 8.5 ksi concrete compressive strength leads

to a cracking force increase of roughly 33 percent, with values of 220 kips and 292 kips. Moreover, the highest concrete compressive strength of 14 ksi results in a cracking force of 398 kips, showcasing a significant growth of around 81 percent compared to 5 ksi concrete.

The ultimate shear force for the different specimens and their concrete compressive strengths reveals a compelling relationship between concrete strength and shear capacity. For the Tx54 girders, as the concrete compressive strength increases from 5 ksi to 8.5 ksi, there is an approximate force gain of 36 percent, with shear capacity values of 272 kips and 370 kips, respectively. Similarly, when comparing 5 ksi to 14 ksi concrete compressive strength, there is a substantial increase of about 51 percent, with shear capacity values of 272 kips and 411 kips, respectively. The trend persists for the Tx70 girders. Transitioning from 5 ksi to 8.5 ksi concrete compressive strength yields a capacity increase of around 22 percent, with values of 340 kips and 415 kips. Moreover, the highest concrete compressive strength of 14 ksi results in a capacity of 528 kips, representing a remarkable growth of approximately 58 percent compared to 5 ksi concrete.



**Figure 8.92. Shear force versus displacement plots for Tx54.**



**Figure 8.93. Shear force versus displacement plots for Tx70.**

The comparative analysis presented in Table 8.9 highlights the disparities between the shear strength results obtained from the FEM, the AASHTO specifications, and the ACI provisions for both Tx54 and Tx70 specimens. Notably, the FEM consistently produces higher ultimate force values than those calculated by AASHTO and ACI across various test scenarios.

The ratios of the FEM shear cracking force to AASHTO shear cracking force range from approximately 1.07 to 1.2 for the Tx54 specimens and from 1.2 to 1.36 for the Tx70 specimens. Similarly, the ratios of the FEM shear cracking force to ACI shear cracking force fall within the range of 0.94 to 1.07 for Tx54 and 1.06 to 1.27 for Tx70.

For the ultimate shear forces, a similar trend is observed. The FEM-predicted ultimate shear forces for Tx54 and Tx70 are consistently higher than those forces predicted by AASHTO and ACI. The ratios of the FEM ultimate shear force to AASHTO ultimate shear force range from 1.11 to 1.30 for Tx54 and from 1.13 to 1.30 for Tx70. Similarly, the ratios of the FEM ultimate shear force to ACI ultimate shear force fall within the range of 1.20 to 1.36 for Tx54 and 1.25 to 1.39 for Tx70. These ratios further affirm the tendency of the FEM to provide higher ultimate shear force results than AASHTO and ACI. Interestingly, for both specimens, it is notable that AASHTO and ACI ultimate shear forces results more closely align with the FEM values as the compressive strength decreases.

Furthermore, it is worth noting that with the increase in compressive strength, there is a trend of lower RSS values. This increase in compressive strength also reduces the angle of the critical diagonal shear crack.

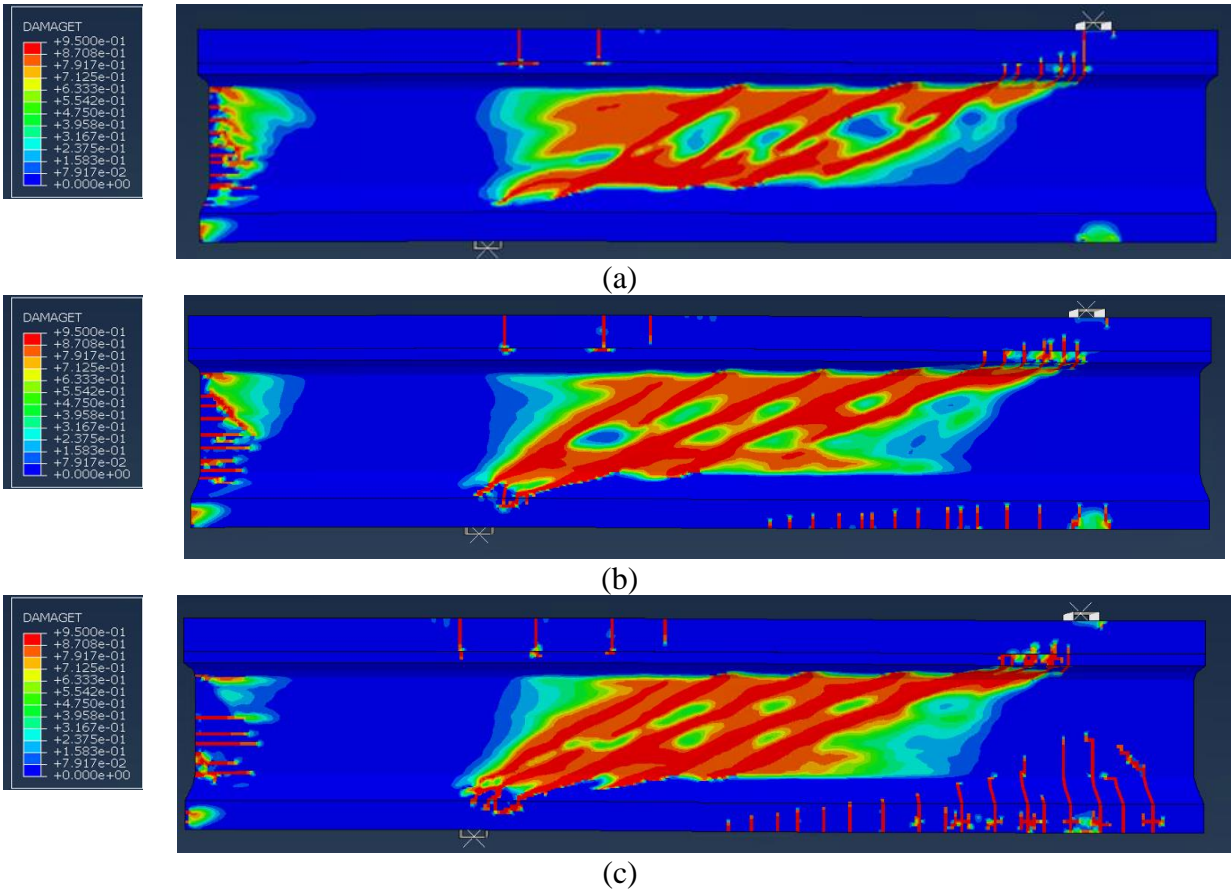
**Table 8.9. Compressive strength comparison of Tx54 and Tx70 results with different code results.**

Model	$V_{cr-FEM}$ (kips)	$V_{c-AASHTO}$ (kips)	$V_{c-ACI}$ (kips)	$V_{u-FEM}$ (kips)	$V_{u-AASHTO}$ (kips)	$V_{u-ACI}$ (kips)	RSS	Crack Angle
<b>Tx54_5</b>	164	153	174	272	246	227	1.66	23-31
<b>Tx54_8.5</b>	226	192	219	370	284	272	1.64	23-24
<b>Tx54_14</b>	287	239	268	411	331	321	1.43	22-23
<b>Tx70_5</b>	220	183	207	340	300	273	1.55	21-29
<b>Tx70_8.5</b>	292	232	258	415	348	323	1.42	23-27
<b>Tx70_14</b>	398	292	314	528	407	379	1.33	17-24

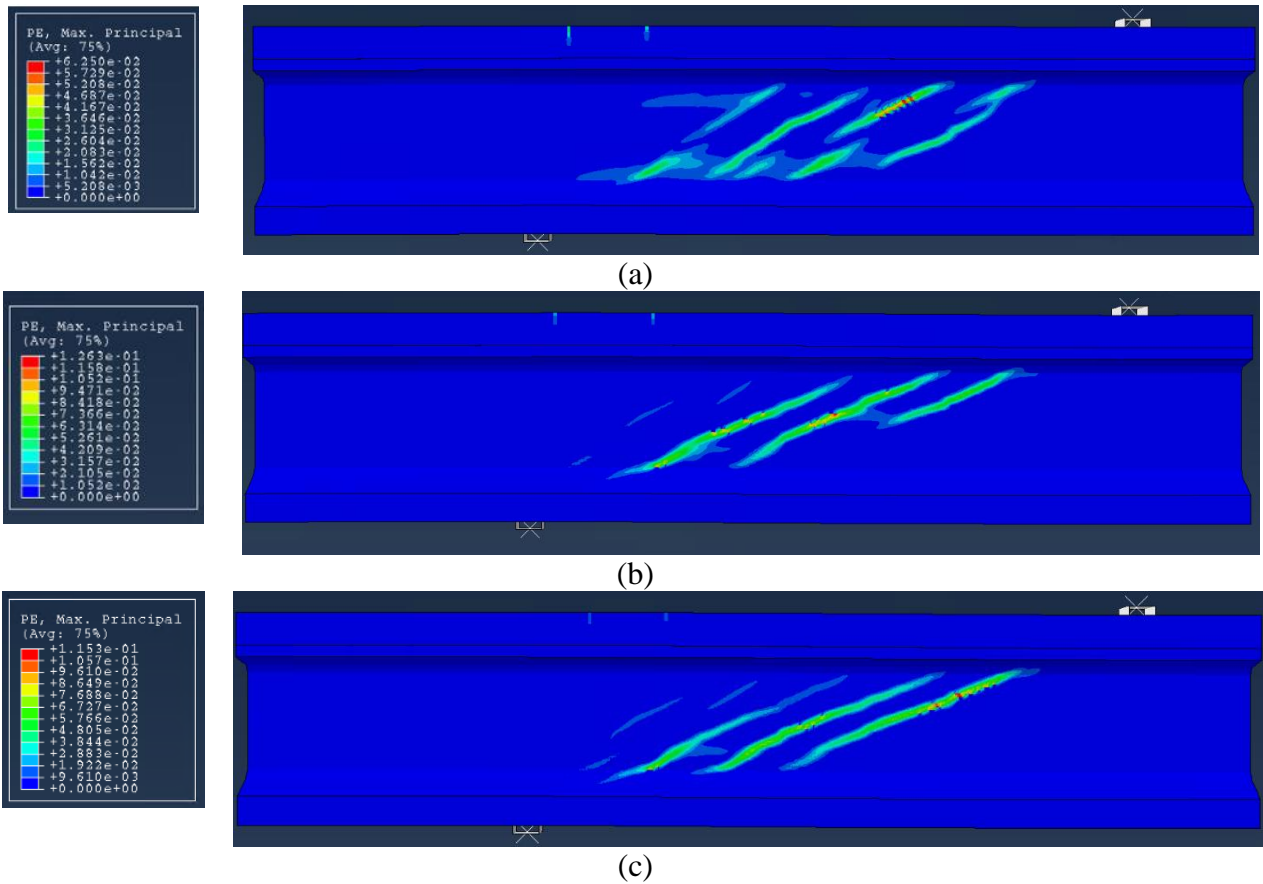
Figure 8.94, Figure 8.95, Figure 8.97, and Figure 8.98 provide a comparison of the failure mode and concrete damage at the peak force for Tx54 and Tx70 girders, as analyzed using numerical models at various compressive strengths.

The schematic drawings of the tension and maximum plastic strain crack patterns for Tx54 and Tx70 specimens reveal that an increase in compressive strength leads to a higher intensity of diagonal tension cracking. This observation aligns with previous research, indicating that as the tensile strength of concrete increases, there is a corresponding need for an increase in the amount of shear reinforcement. High-strength concrete tends to exhibit smoother crack surfaces compared to its lower-strength counterparts, resulting in a reduction in the shear carried by aggregate interlock.

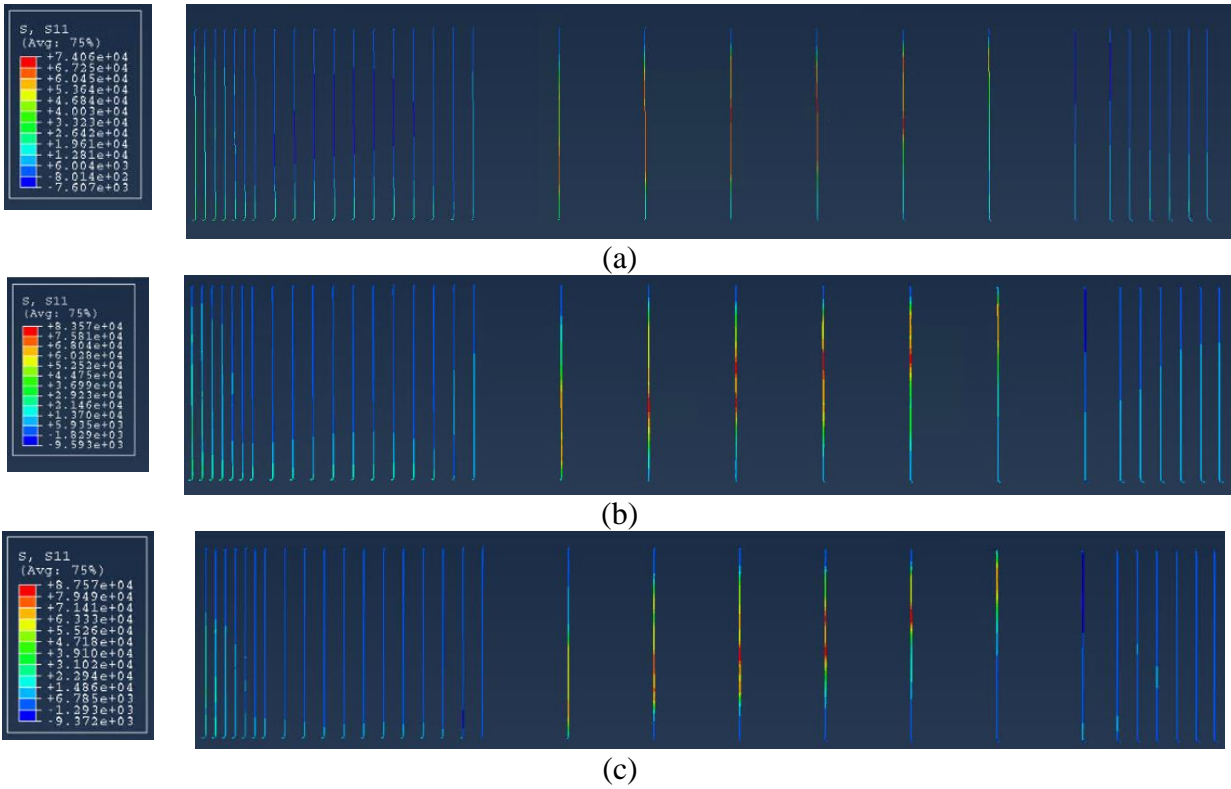
Furthermore, increasing the compressive strength increased axial stress within the R-bars at the ultimate force for both Tx54 and Tx70 girders, as illustrated in Figure 8.96 and Figure 8.99.



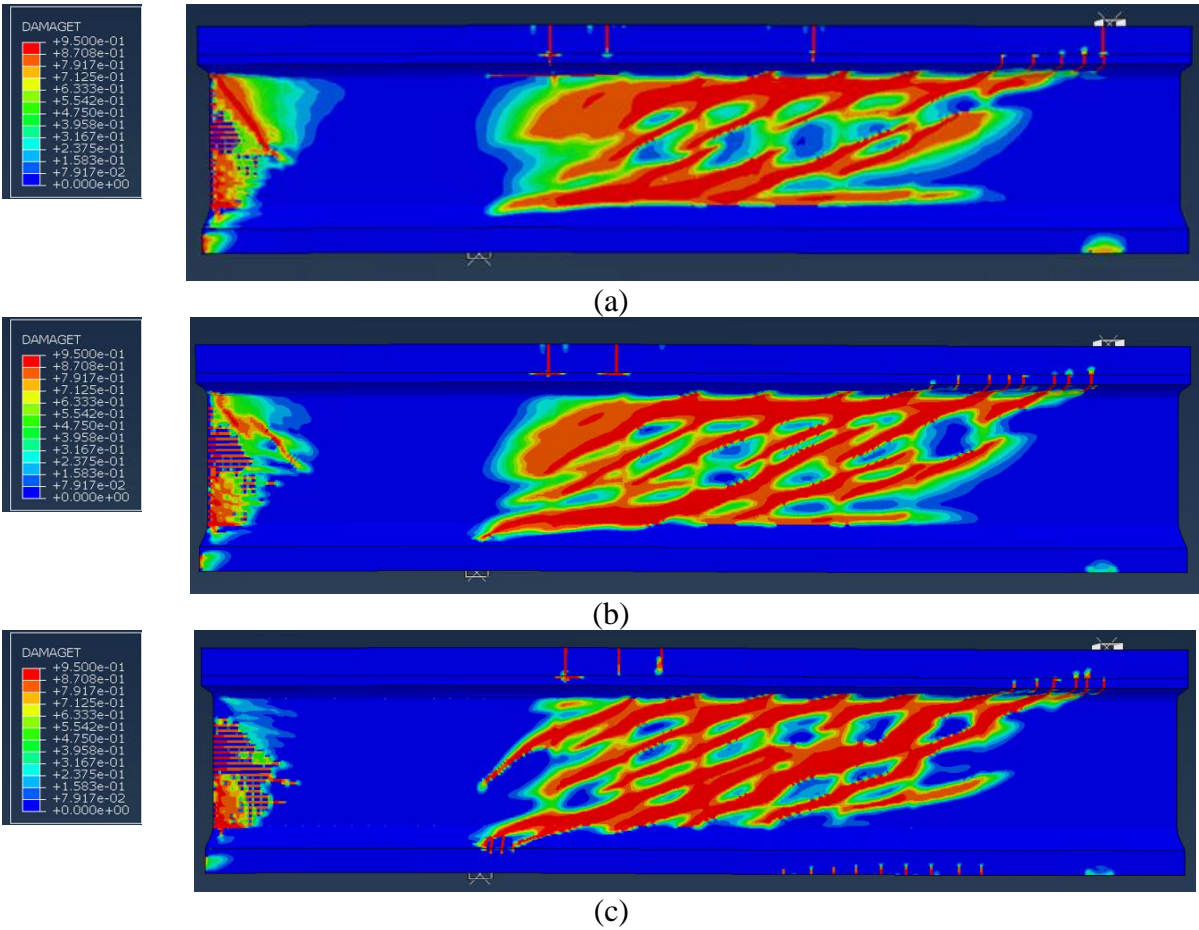
**Figure 8.94. Tension damage in FE model at peak load for Tx54: (a) 5 ksi, (b) 8.5 ksi, and (c) 14 ksi.**



**Figure 8.95. Plastic strain in FE model at peak load for Tx54: (a) 5 ksi, (b) 8.5 ksi, and (c) 14 ksi.**

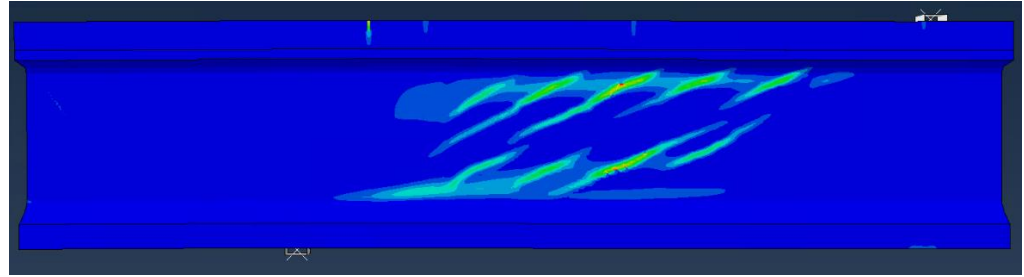
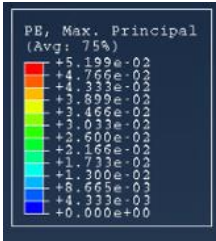


**Figure 8.96. Axial stress in R-bars in FE model at peak load for Tx54: (a) 5 ksi, (b) 8.5 ksi, and (c) 14 ksi.**

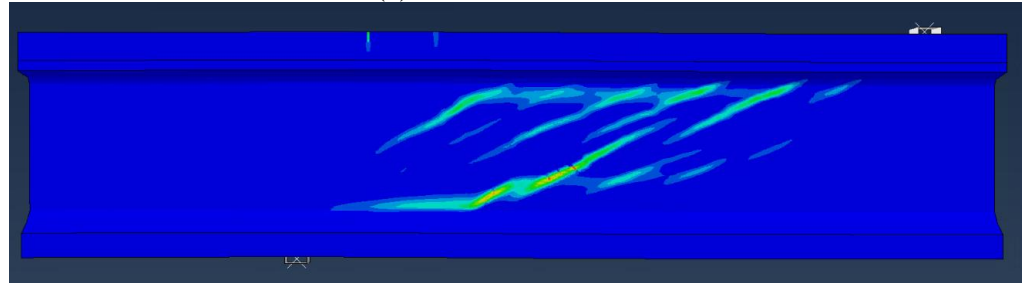
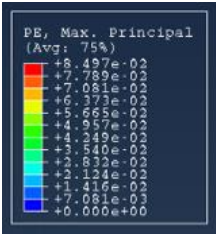


**Figure 8.97. Tension damage in FE model at peak load for Tx70: (a) 5 ksi, (b) 8.5 ksi, and (c) 14 ksi.**

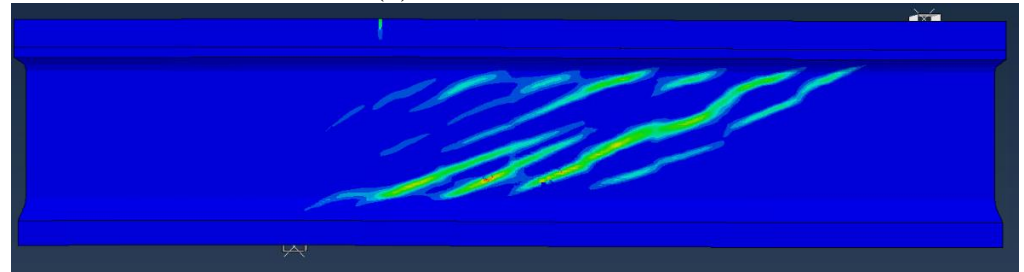
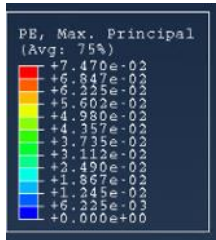




(a)

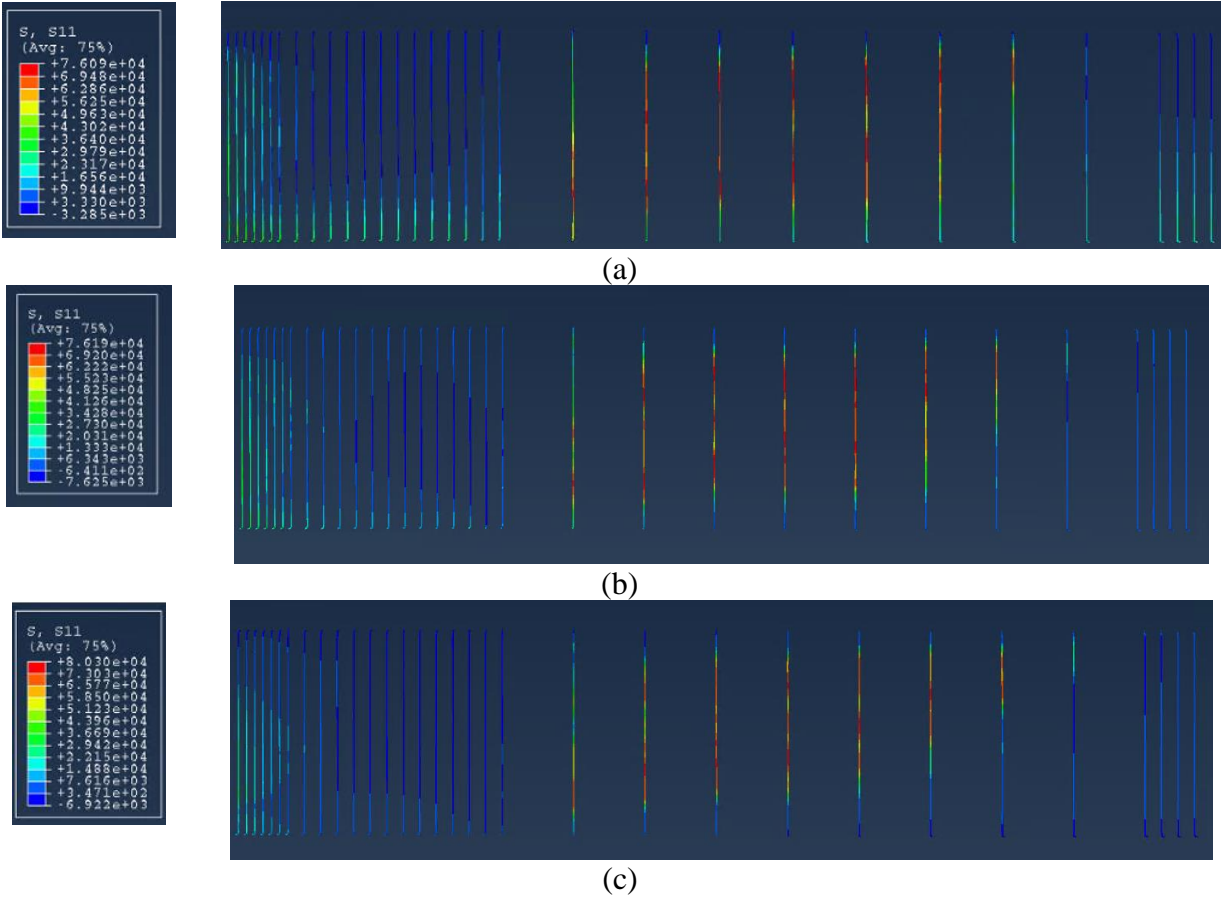


(b)



(c)

**Figure 8.98. Plastic strain in FE model at peak load for Tx70: (a) 5 ksi, (b) 8.5 ksi, and (c) 14 ksi.**



**Figure 8.99. Axial stress in R-bars in FE model at peak load for Tx70: (a) 5 ksi, (b) 8.5 ksi, and (c) 14 ksi.**

### 8.5.8 Effect of Prestressing Force

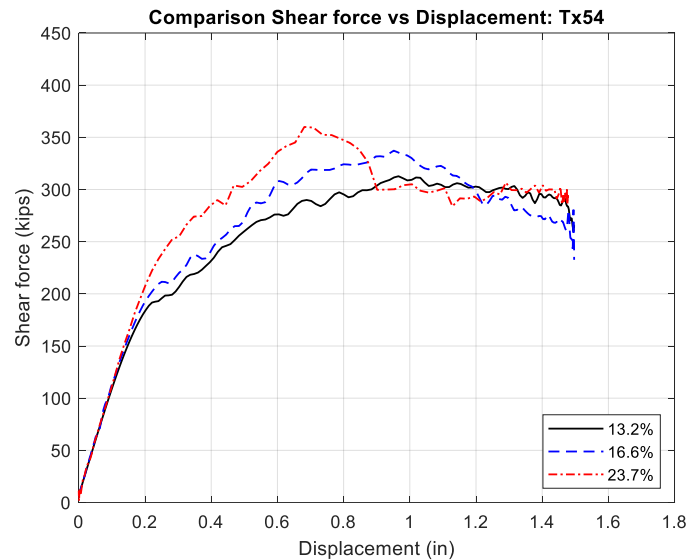
Numerical simulations were conducted to assess the effects of prestressing force on the shear behavior of reinforced concrete bridge girders. The goal was to evaluate the shear capacity, crack pattern, and overall performance of Tx54 and Tx70 girders with low levels of shear reinforcement. The simulations involved varying the number of strands and using three different values of  $f_{pc}/f'_c$  (13.2 percent, 16.6 percent, and 23.7 percent).

The shear force versus deformation graph obtained from the results clearly illustrates significant variations in the maximum force capacities of Tx54 and Tx70 girders, depending on the different  $f_{pc}/f'_c$  values. This finding can be seen in Figure 8.100 and Figure 8.101.

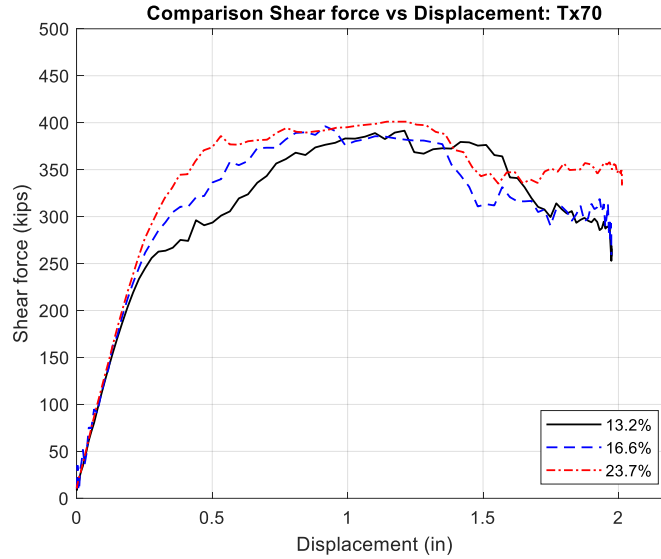
The comparison of cracking forces among the girder specimens reveals a consistent trend: as the percentage of  $f_{pc}/f'_c$  increases, there is a corresponding increase in the cracking force. For

instance, in the Tx54 series, the cracking force rises from 185 kips for Tx54\_13.2% to 212 kips for Tx54\_16.6% and further to 253 kips for Tx54\_23.7%. This pattern continues within the Tx70 series, where the cracking force escalates from 247 kips (Tx70\_13.2%) to 287 kips (Tx70\_16.6%) and finally to 344 kips (Tx70\_23.7%).

Similarly, the comparison of shear capacity among the girder specimens demonstrates a consistent correlation: an increase in the percentage of  $f_{pc}/f'_c$  instigates a subsequent increase in the shear capacity. Within the Tx54 series, the ultimate force progresses from 312 kips for Tx54\_13.2% to 335 kips for Tx54\_16.6% and further to 361 kips for Tx54\_23.7%. This trend is similarly observed in the Tx70 series as the capacity increases from 388 kips (Tx70\_13.2%) to 391 kips (Tx70\_16.6%) and ultimately to 401 kips (Tx70\_23.7%).



**Figure 8.100. Shear force versus displacement plots for Tx54.**



**Figure 8.101. Shear force versus displacement plots for Tx70.**

The comparative analysis presented in Table 8.10 highlights the disparities between the shear strength results obtained from the FEM, the AASHTO specifications, and the ACI provisions for both Tx54 and Tx70 specimens. Notably, the FEM consistently produces higher ultimate force values than those values calculated by AASHTO and ACI across various test scenarios.

The ratios of the FEM shear cracking force to AASHTO shear cracking force range from approximately 1.16 to 1.21 for the Tx54 specimens and from 1.14 to 1.37 for the Tx70 specimens. Similarly, the ratios of the FEM shear cracking force to ACI shear cracking force fall within the range of 0.98 to 1.08 for Tx54 and 1.04 to 1.13 for Tx70.

For the ultimate shear forces, a similar trend is observed. The FEM-predicted ultimate shear forces for Tx54 and Tx70 are consistently higher than those predicted by AASHTO and ACI. The ratios of the FEM ultimate shear force to AASHTO ultimate shear force range from 1.17 to 1.25 for Tx54 and 1.09 to 1.16 for Tx70. Similarly, the ratios of the FEM ultimate shear force to ACI ultimate shear force fall within the range of 1.26 to 1.31 for Tx54 and 1.10 to 1.27 for Tx70. Interestingly, for both specimens, it is notable that AASHTO and ACI ultimate shear forces results more closely align with FEM values as the  $f_{pc}/f'_c$  decreases.

Furthermore, it is worth noting that with the increase in  $f_{pc}/f'_c$ , there is a trend of lower RSS values. This increase in the  $f_{pc}/f'_c$  ratio also increases the inclination angle values.

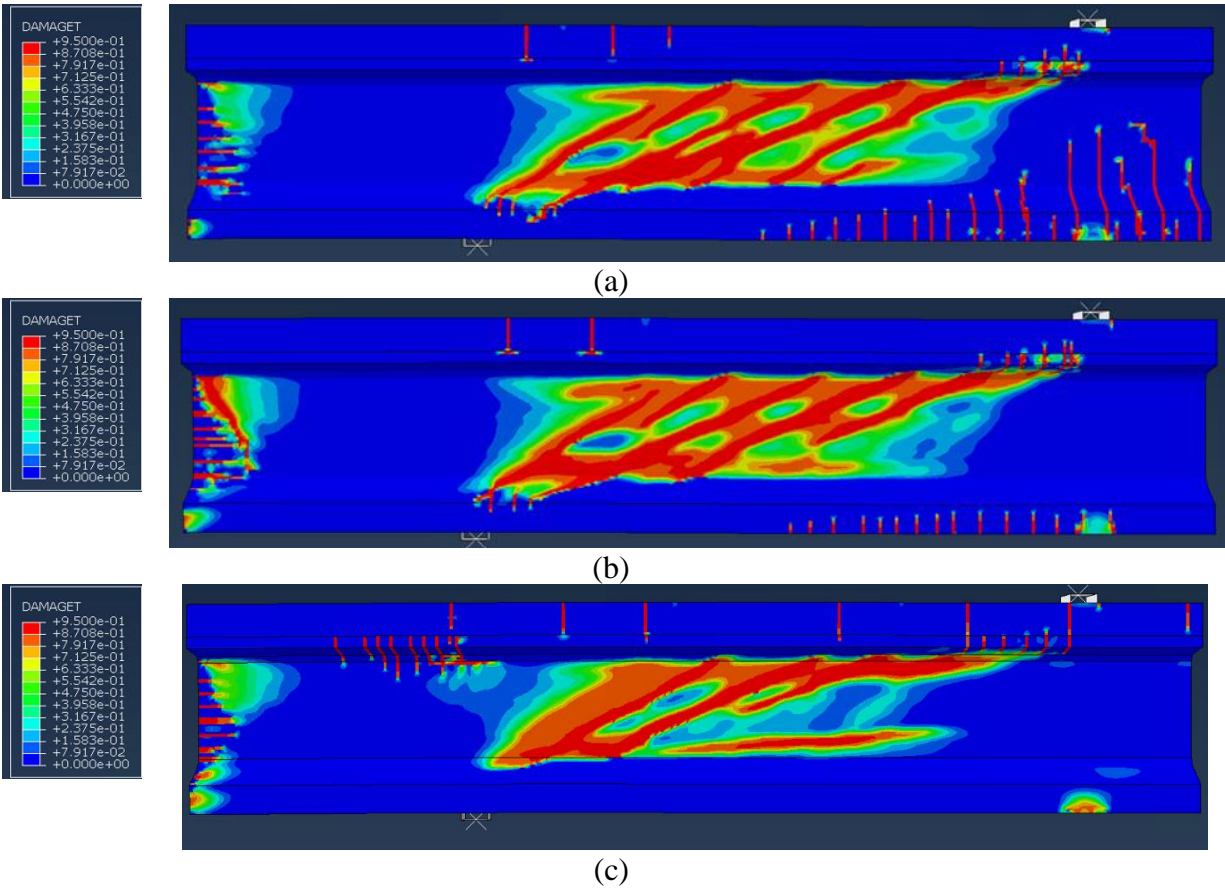
**Table 8.10. Prestressing force comparison of Tx54 and Tx70 results with different code results.**

Model	$V_{cr-FEM}$ (kips)	$V_{c-AASHTO}$ (kips)	$V_{c-ACI}$ (kips)	$V_{u-FEM}$ (kips)	$V_{u-AASHTO}$ (kips)	$V_{u-ACI}$ (kips)	RSS	Crack Angle
<b>Tx54_13.2%</b>	185	160	188	312	251	240	1.69	23-25
<b>Tx54_16.6%</b>	212	175	202	335	268	255	1.58	21-26
<b>Tx54_23.7%</b>	253	217	234	361	308	286	1.43	24-27
<b>Tx70_13.2%</b>	247	217	238	388	335	305	1.57	25-26
<b>Tx70_16.6%</b>	287	241	256	391	360	323	1.36	22-28
<b>Tx70_23.7%</b>	344	251	305	401	357	365	1.17	23-34

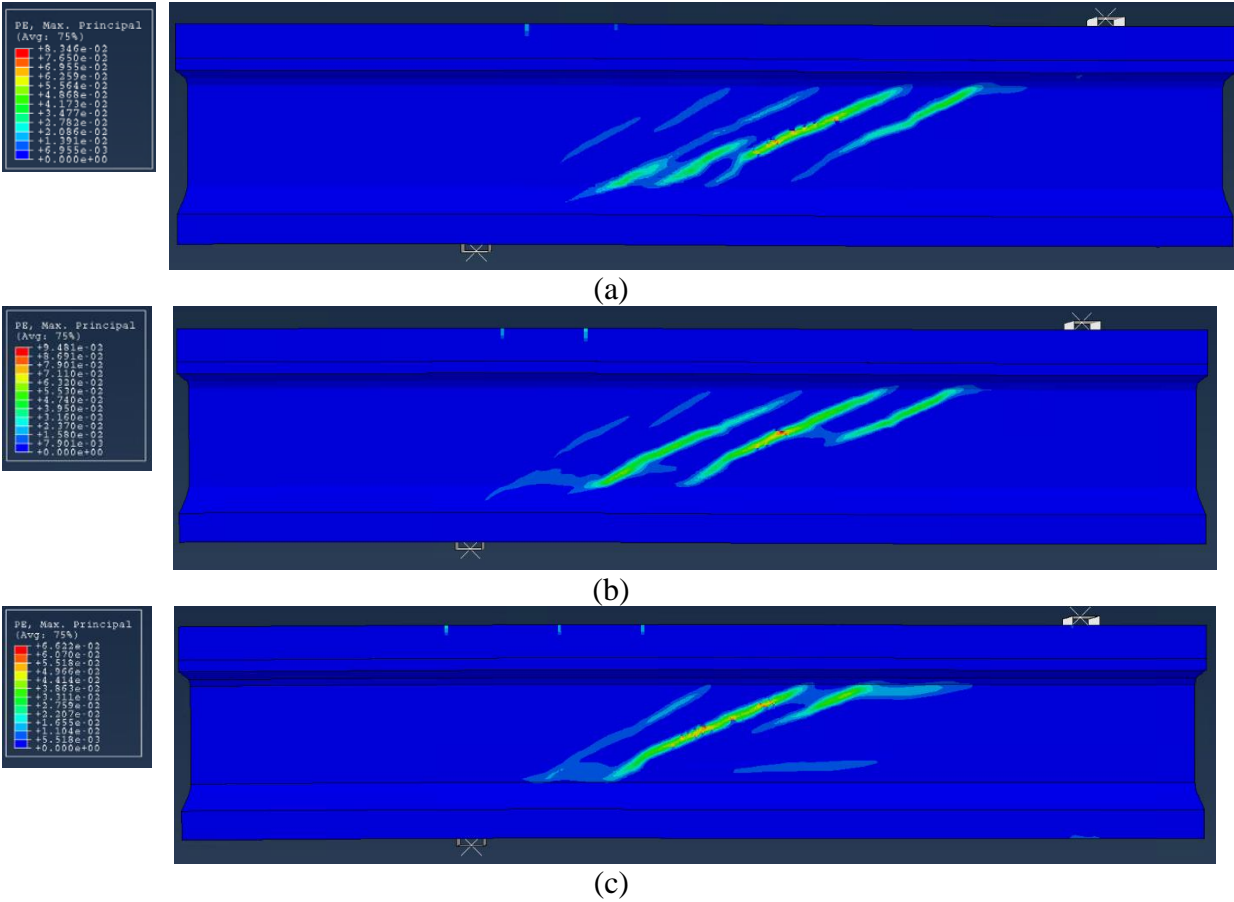
Figure 8.102, Figure 8.103, Figure 8.105, and Figure 8.106 provide a comparison of the failure mode and concrete damage at the peak force for Tx54 and Tx70 girders, as analyzed using numerical models at various  $f_{pc}/f'_c$ . The results indicate that an increase in the ratio of  $f_{pc}/f'_c$  hinders the expansion of cracks. This increase in the ratio leads to increased friction between cracked surfaces, contributing to the overall shear strength of the structure.

In the specific case of Tx70, with a prestress level of 23.7 percent, prestressing induces internal forces that significantly impact stress distribution within the girder. When shear forces are applied, the interaction between flexural and shear behavior can result in high stresses at the flange-web junction. This stress concentration can exceed the concrete's tensile strength, leading to the formation of cracks.

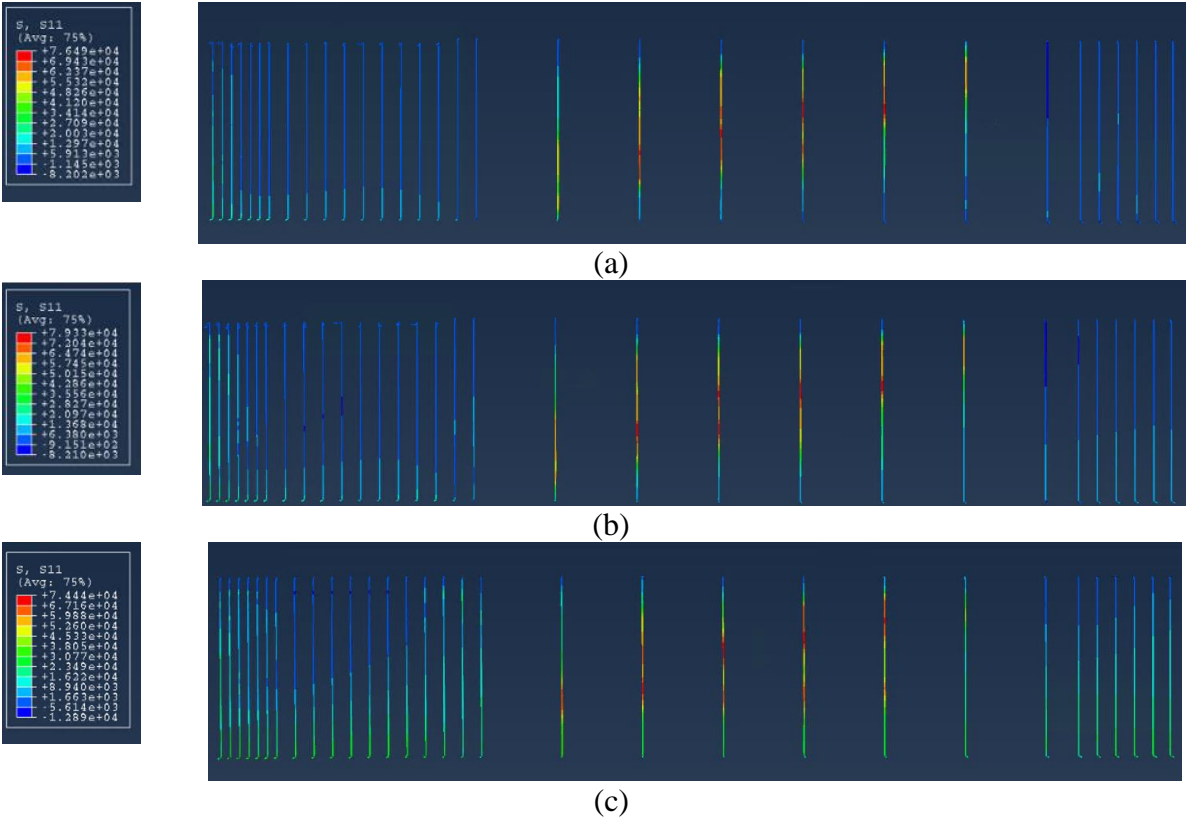
Furthermore, increasing the  $f_{pc}/f'_c$  slightly affected the axial stress within the R-bars at the ultimate force for both Tx54 and Tx70 girders, as illustrated in Figure 8.104 and Figure 8.107.



**Figure 8.102. Tension damage in FE model at peak load for Tx54: (a) 13.2 percent, (b) 16.6 percent, and (c) 23.7 percent.**

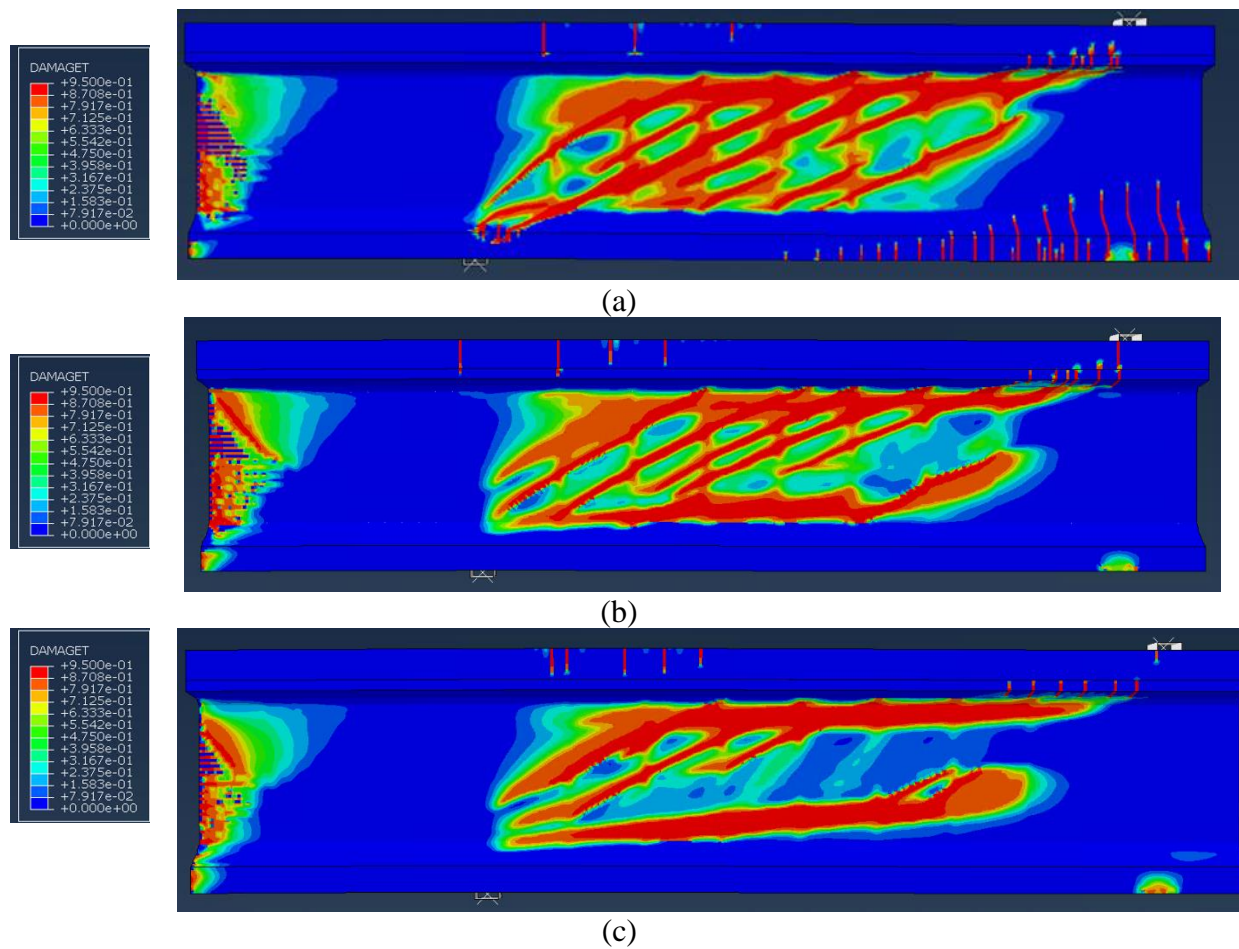


**Figure 8.103. Plastic strain in FE model at peak load for Tx54: (a) 13.2 percent, (b) 16.6 percent, and (c) 23.7 percent.**

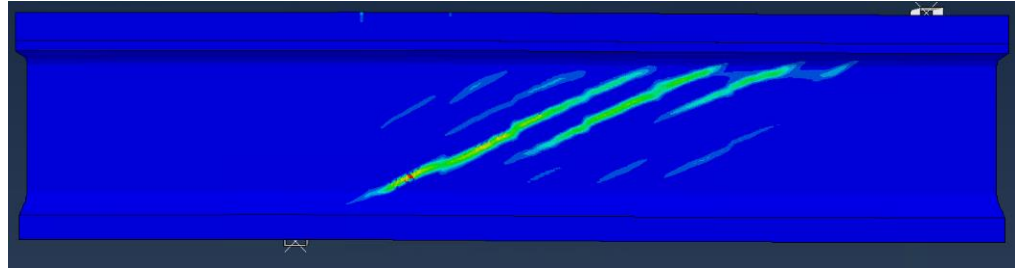
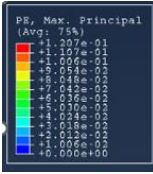


**Figure 8.104. Axial stress in R-bars in FE model at peak load for Tx54: (a) 13.2 percent, (b) 16.6 percent, and (c) 23.7 percent.**

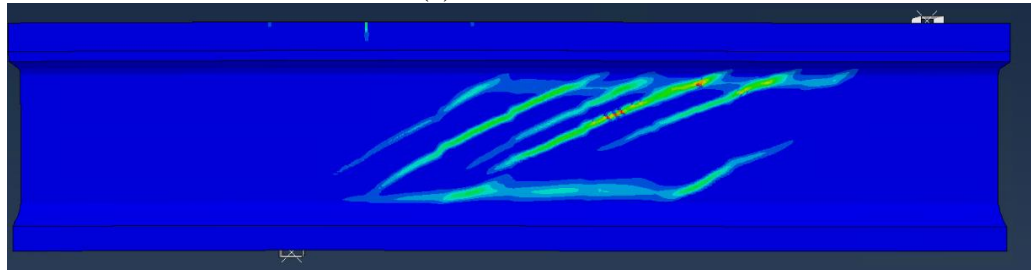
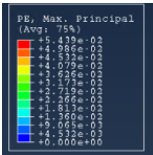




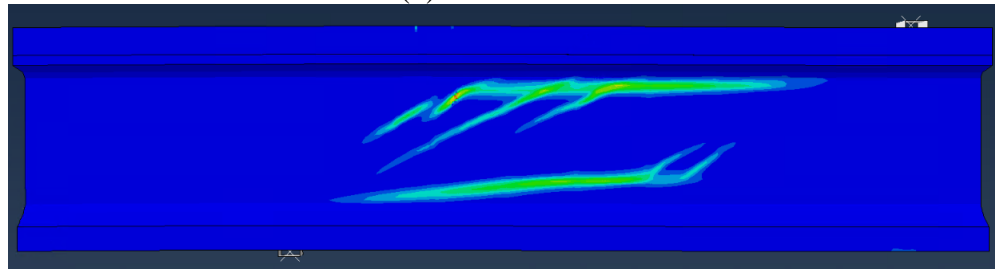
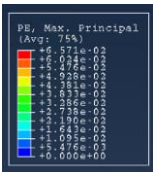
**Figure 8.105. Tension damage in FE model at peak load for Tx70: (a) 13.2 percent, (b) 16.6 percent, and (c) 23.7 percent.**



(a)

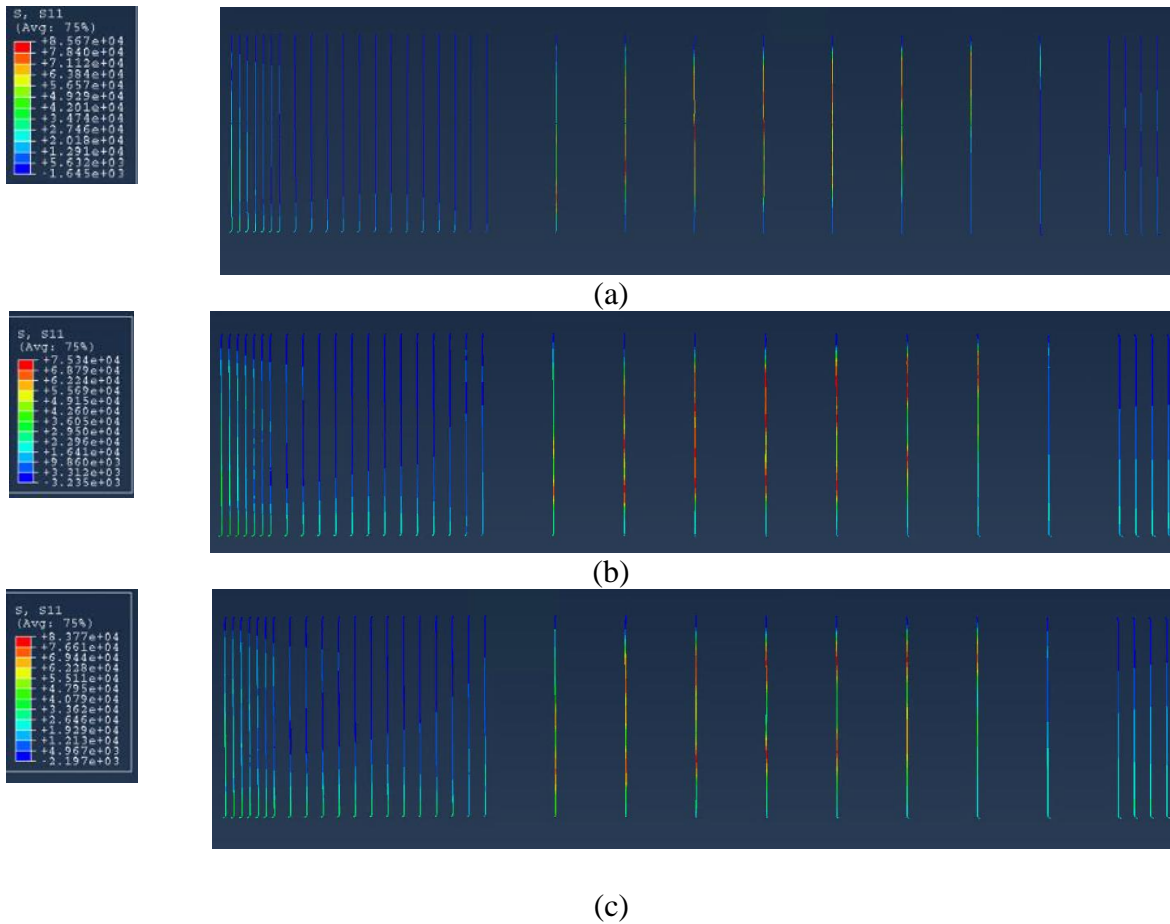


(b)



(c)

**Figure 8.106. Plastic strain in FE model at peak load for Tx70: (a) 13.2 percent, (b) 16.6 percent, and (c) 23.7 percent.**

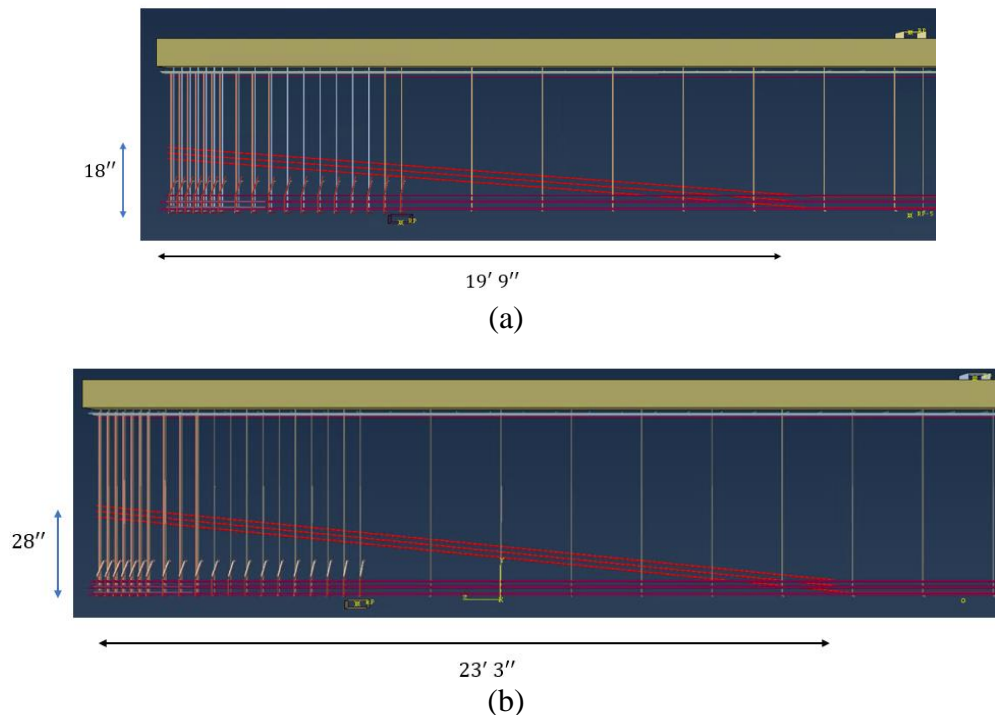


**Figure 8.107. Axial stress in R-bars in FE model at peak load for Tx70: (a) 13.2 percent, (b) 16.6 percent, and (c) 23.7 percent.**

### 8.5.9 Effect of Tendon Path

Numerical simulations were conducted to assess the effects of tendon path on Tx54 and Tx70 girders on the shear behavior of reinforced concrete bridge girders. The goal was to evaluate the shear capacity, crack pattern, and overall performance of Tx54 and Tx70 girders with low levels of shear reinforcement. The simulations were conducted by comparing straight path and harped path configurations. The two harped girders were configured with six harped strands extending to heights of 18 in. and 28 in. from the bottom flange for Tx54 and Tx70, respectively. The terminations of these strands were situated within the web at the girder's ends, as shown in Figure 8.108. The design of these harped strands follows the established standard protocol, which determines the hold-down point using AASHTO (2020).

For Tx54, the eccentricity at the end equals 13.7 in., and at midspan, it equals 16.89 in. As for Tx70, the eccentricity at the end equals 20.3 in., and at midspan, it equals 24.54 in. This is illustrated in Figure 8.108.

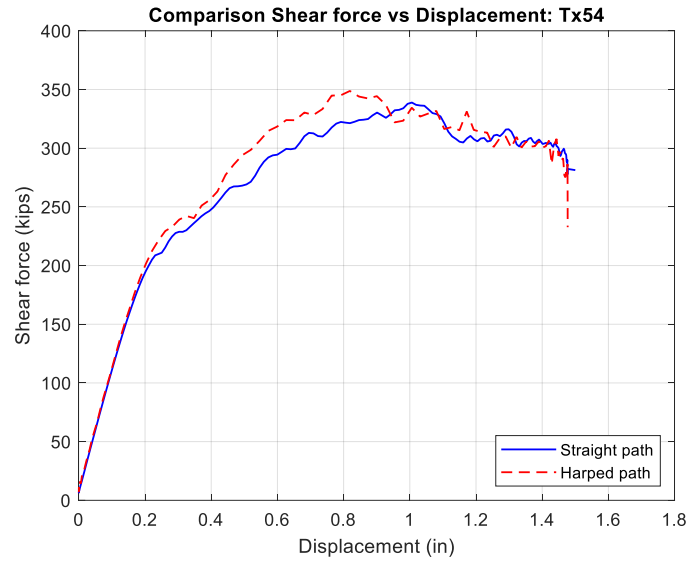


**Figure 8.108. ABAQUS model geometry and reinforcement location for (a) Tx54 specimen and (b) Tx70 specimen.**

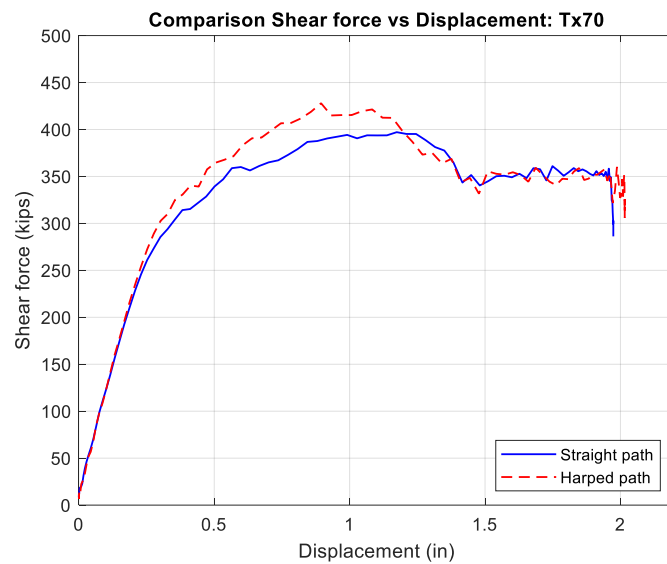
The shear force versus deformation graph derived from the results demonstrates significant variations in the cracking force and shear capacity of Tx54 and Tx70 girders, depending on the chosen tendon path. This fact is illustrated in Figure 8.109 and Figure 8.110.

It was observed that specimens with harped strands exhibited significantly higher cracking forces than specimens with straight strands. Specifically, the specimens with harped strands had cracking forces of 231 kips for Tx54 and 302 kips for Tx70, representing an approximate increase of 9 percent and 3 percent, respectively, over specimens without harped strands.

Furthermore, specimens with harped strands showed higher load capacities than specimens without harped strands. Specifically, the specimens with harped strands sustained maximum shear forces of 350 kips for Tx54 and 428 kips for Tx70, indicating an approximate increase of 4 percent and 7 percent, respectively, in shear capacity over specimens without harped strands.



**Figure 8.109. Shear force versus displacement plots for Tx54.**



**Figure 8.110. Shear force versus displacement plots for Tx70.**

The comparative analysis in Table 8.11 highlights the disparities between the shear strength results obtained from the FEM, the AASHTO specifications, and the ACI provisions for Tx54 and Tx70 specimens. Notably, the FEM consistently produces higher cracking and ultimate force values than those calculated by both AASHTO and ACI across various test scenarios.

The ratios of FEM shear cracking force to AASHTO shear cracking force range from approximately 1.17 to 1.27 for the Tx54 specimens and from 1.21 to 1.23 for the Tx70

specimens. Similarly, the ratios of FEM shear cracking force to ACI shear cracking force fall within the range of 0.94 to 1.00 for Tx54 and 1.04 to 1.13 for Tx70.

For the ultimate shear forces, a similar trend is observed. The FEM-predicted ultimate shear forces for Tx54 and Tx70 are consistently higher than those predicted by AASHTO and ACI. The ratios of FEM ultimate shear force to AASHTO ultimate shear force range from 1.13 to 1.24 for Tx54 and 1.08 to 1.10 for Tx70. Similarly, the ratios of FEM ultimate shear force to ACI ultimate shear force fall within the range of 1.52 to 1.59 for Tx54 and 1.35 to 1.42 for Tx70.

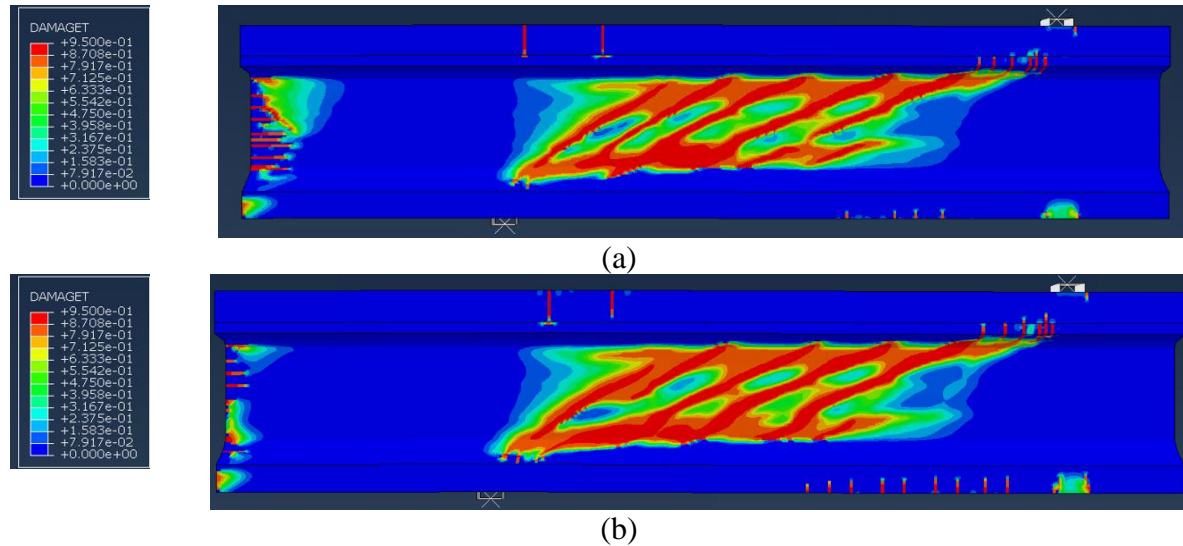
Additionally, it is noteworthy that the inclination angle values are slightly greater for girders with harped strands than for girders without them. Furthermore, in the case of Tx54 with harped strands, there is a tendency toward lower RSS values when contrasted with Tx54 without harped strands, whereas in Tx70 with harped strands, there is a trend toward higher RSS values when compared to Tx70 without harped strands.

**Table 8.11. Tendon path comparison of Tx54 and Tx70 results with different code results.**

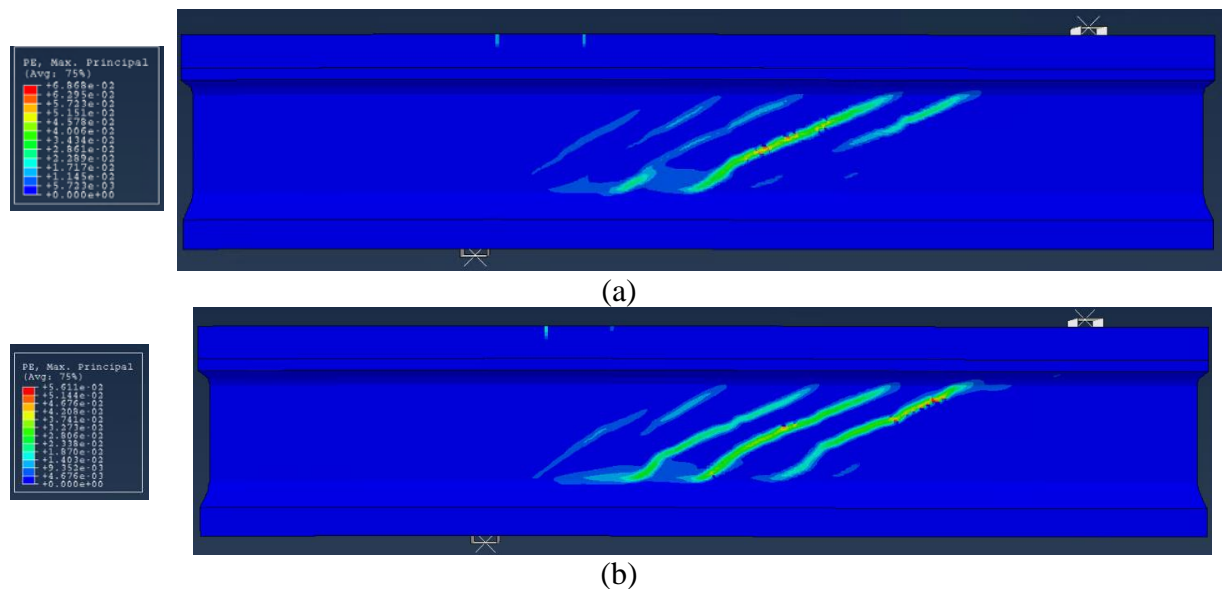
Model	$V_{cr-FEM}$ (kips)	$V_{c-AASHTO}$ (kips)	$V_{c-ACI}$ (kips)	$V_{u-FEM}$ (kips)	$V_{u-AASHTO}$ (kips)	$V_{u-ACI}$ (kips)	RSS	Crack Angle
<b>Tx54_ Straight path</b>	211	180	211	336	272	264	1.59	22-28
<b>Tx54_ Harped path</b>	231	182	245	350	309	298	1.52	23-29
<b>Tx70_ Straight path</b>	293	243	260	397	362	327	1.35	19-29
<b>Tx70_ Harped path</b>	302	245	291	428	395	358	1.42	22-31

Figure 8.111, Figure 8.112, Figure 8.114, and Figure 8.115 compare the failure mode and plastic strain at the peak force for Tx54 and Tx70 girders with and without harped strands, as analyzed using numerical models. It can be observed that the plastic strain was higher for specimens without harped strands than for specimens with harped strands.

It is evident that for Tx54 and Tx70 girders, as depicted in Figure 8.113 and Figure 8.116, the presence of harped strands led to a reduction in the axial stress experienced by the R-bars at the ultimate force as opposed to specimens without harped strands.

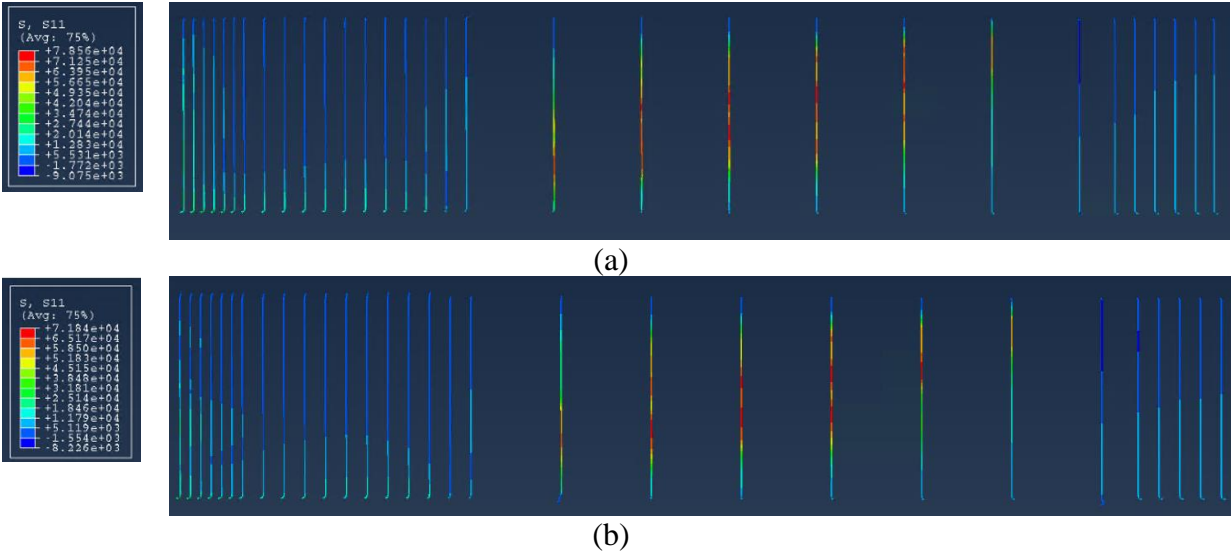


**Figure 8.111. Tension damage in FE model at peak load for Tx54: (a) straight path, and (b) harped path.**

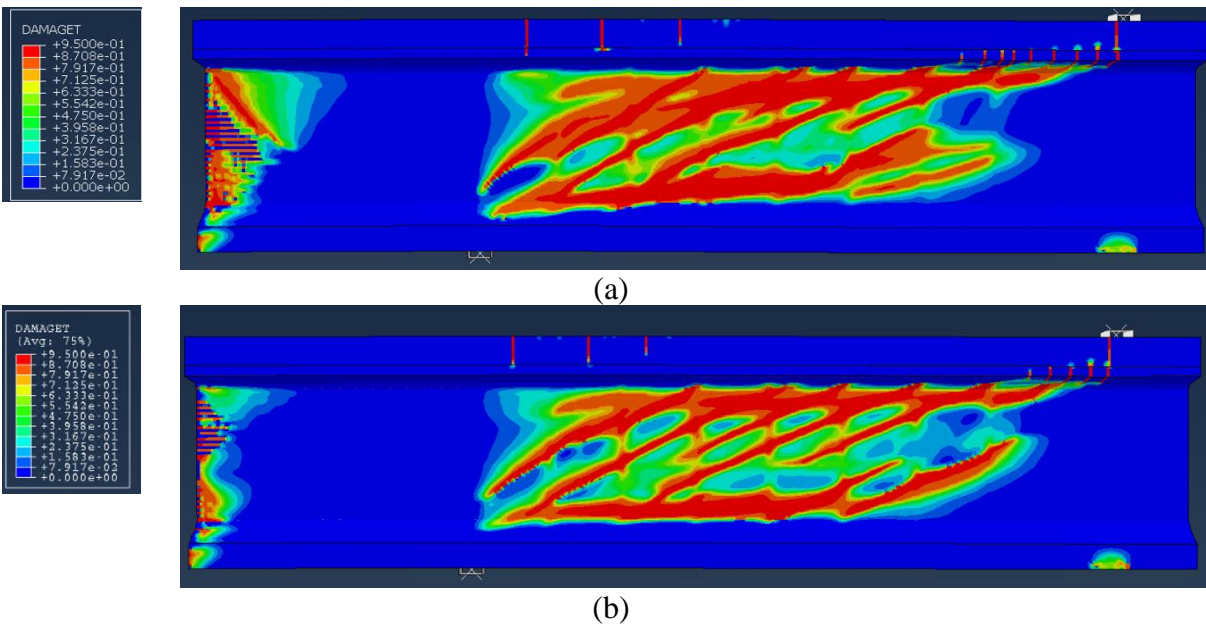


**Figure 8.112. Plastic strain in FE model at peak load for Tx54: (a) straight path, and (b) harped path.**



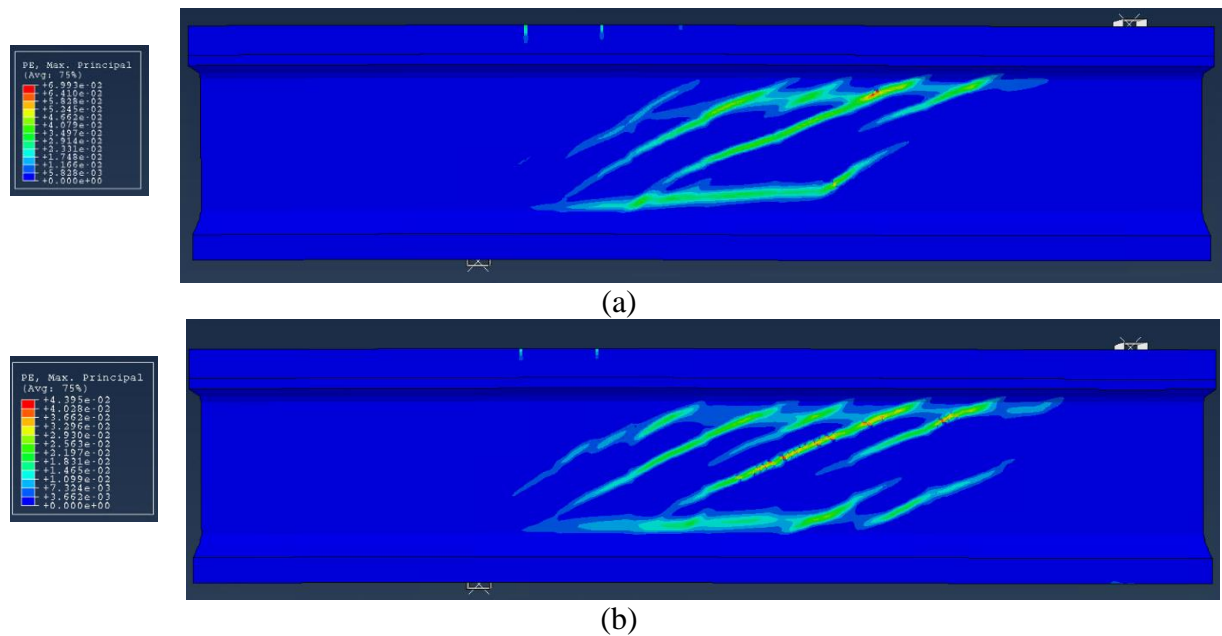


**Figure 8.113. Axial stress in R-bars in FE model at peak load for Tx54: (a) straight path, and (b) harped path.**

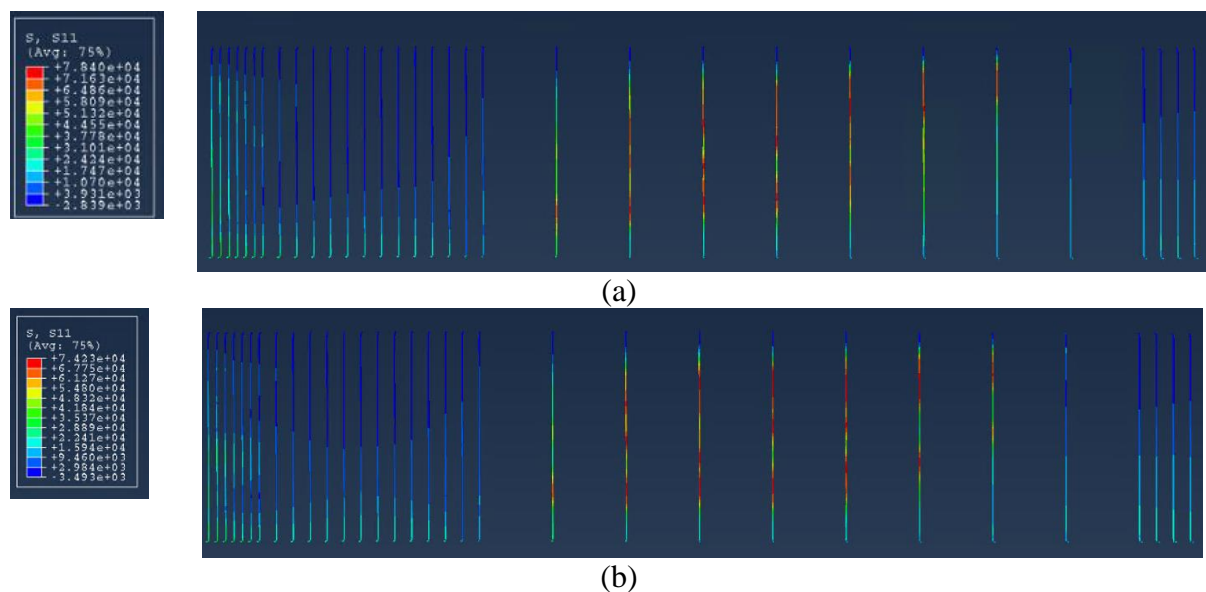


**Figure 8.114. Tension damage in FE model at peak load for Tx70: (a) straight path, and (b) harped path.**





**Figure 8.115. Plastic strain in FE model at peak load for Tx54: (a) straight path, and (b) harped path.**



**Figure 8.116. Axial stress in R-bars in FE model at peak load for Tx70: (a) straight path and (b) harped path.**

## 8.6 SUMMARY

This chapter describes the FE modeling that played a crucial role in the analysis of TxDOT girders by replicating failure outcomes from experimental tests. The modeling phase involved developing appropriate FE models in terms of geometry, material parameters, and FE

parameters. These models were validated against existing literature and experimental results, reinforcing their reliability for studying key factors, such as shear reinforcement spacing, deck slab presence, concrete strength variations, prestressing force levels, tendon path types (harped and straight strands), and  $a/d$  ratios. Comprehensive numerical simulations provided detailed insights into the specific influences of each factor on shear behavior, including parameters like cracking load, ultimate load, RSS index, concrete damage percentage, and stress distribution within shear reinforcement.

Key findings from the FE analysis revealed that the presence of a deck slab significantly enhances shear performance, with girders exhibiting higher cracking forces, load capacities, RSS values, steeper crack angles, and lower concrete strain and axial stress at ultimate force. This outcome was not in agreement with the experimental data that showed the slab experienced slippage at the interface with the girder (even when designed with sufficient interfacial reinforcement), thus losing some of its composite action. This anomaly was probably because the FE model did not explicitly account for interfacial effects. Studies on shear reinforcement grade indicated that higher-grade reinforcement (Grade 100) increased ultimate shear force, deflections, RSS values, and crack angles, with varying strain behaviors between Tx54 and Tx70 girders. Increasing the size of shear reinforcement also enhanced cracking force and shear capacity, resulting in higher RSS values, steeper crack angles, increased crack intensity, and reduced plastic strain. FEM predictions consistently showed higher shear loads compared to AASHTO and ACI standards, highlighting their conservative nature.

Further, the analysis demonstrated that lower  $a/d$  ratios significantly increase cracking and ultimate shear forces, with improved shear capacities and higher RSS values. Increasing concrete compressive strength and prestressing ratios also boosted cracking and ultimate shear capacities, though with lower RSS values and higher axial stress in reinforcement bars. Specimens with harped strands showed higher cracking forces and shear capacities than specimens with straight strands, with greater crack angles and reduced concrete strain. The combined parametric study from experimental and FE analyses identified key parameters that should be included in the minimum shear reinforcement equation that will be utilized in data-driven model development for creating refined design equations based on the developed database.

## **CHAPTER 9:**

### **EVALUATION OF PARAMETERS AFFECTING MINIMUM SHEAR REINFORCEMENT**

Using the findings from the experimental program and the parametric FE studies (as well as the findings of the literature review), this chapter provides an evaluation of the effect of major design parameters on the shear behavior of prestressed girders and their relevant minimum shear reinforcement requirements.

#### **9.1 EFFECT OF DECK SLAB PRESENCE**

The primary objective of the initial girder tests, G1\* and G1, was to evaluate the impact of a deck slab on girder performance through a comparative analysis. Both girders shared identical design parameters with different shear-span-to-depth ratio due to the presence or absence of the deck. The inclusion of the deck altered the effective girder depth and span lengths, necessitating adjustments in testing configurations. Despite these variations, both specimens exhibited similar ultimate shear strengths, suggesting that the presence of the deck did not significantly influence the girder's capacity to resist shear forces.

Crack measurements indicated larger crack widths in the presence of the deck, which could be attributed to the additional dead loads from the slab. However, this occurrence did not translate into notable differences in ultimate strength between girders with and without the deck. Post-cracking behavior, including observed deck slippage, was consistent across both configurations, reaffirming the similarity in failure mechanisms and supporting the decision not to include a deck in future tests. These findings were further validated through FE analyses.

The FE analyses provided significant insights into the impact of deck slabs on girder behavior. Results consistently showed that girder specimens with a deck slab exhibited higher cracking forces and shear capacities than girders without a deck slab as long as interface slippage does not occur. Specifically, the presence of a deck slab led to increased (a) cracking force ratio between a girder with a deck and without a deck (approximately 1.02 to 1.14) and (b) ultimate shear capacity ratios (approximately 1.05 to 1.13) across different girder types. Additionally, girders

with slabs demonstrated higher RSS values and steeper crack angles, indicating enhanced structural performance under load. The FE analyses demonstrated a change in the RSS with the presence of a deck compared to the experimental findings. The contrast in the observations might be due to the slippage of deck clearly depicted in the experiments that might not have been demonstrated in the computation analysis.

Concrete strains were generally higher in specimens without a deck slab, suggesting greater deformation and potential structural vulnerability. Furthermore, the presence of a deck slab redistributed shear forces more effectively among stirrups, resulting in reduced axial stress on the reinforcement bars at ultimate loads. Comparisons with established design guidelines revealed that the FE models tended to predict higher shear capacities than design standards, such as AASHTO LRFD Specifications (2020) and ACI 318-19, suggesting a potentially conservative approach in current design practices.

## **9.2 EFFECT OF SHEAR REINFORCEMENT SPACING**

The study on shear reinforcement spacing examined how the distance between stirrups affects the strength of girders. Girders with closer  $s/d$  (18 in.) consistently showed higher shear strength than those with wider spacing (26 in. and 38 in.), especially in designs without harped tendons (like G1-W, G2-W, G2-E). This higher strength also resulted from the higher shear reinforcement ratio that resulted from the smaller spacing. This smaller spacing helped control cracks better and increased overall girder strength. However, girders with harped tendons (G3-W, G3-E) had less difference in shear strength between spacing configurations, indicating that harped tendons could compensate for wider  $s/d$  to some extent. Overall, the research finding emphasized the critical role of  $s/d$  in optimizing girder design to withstand shear forces effectively.

The FE analyses provided critical insights into the effects of shear reinforcement on girder behavior. In fact, larger shear reinforcement ratios effectively delayed the initiation of shear cracking in both Tx54 and Tx70 girders, and increased the cracking force in the girders by up to about 18 percent, depending on the girder type and spacing configuration, thereby improving overall structural integrity. Moreover, the FE analyses showed substantial increase in the ultimate shear strength, ranging from approximately 12.1 percent to 46.7 percent for Tx54 and

Tx70 girders with varying  $s/ds$ . This underscores the importance of proper spacing in shear reinforcement to control crack propagation, as indicated by increased inclination angles of diagonal cracks and higher RSS values at closer spacing. Additionally, closer spacing of shear reinforcement reduced axial stress in reinforcement bars at ultimate force, highlighting its role in distributing shear forces effectively among more stirrups across cracks. Finally, comparisons with design guidelines revealed that the FE analyses tended to predict higher shear capacities compared to AASHTO and ACI guidelines, thus demonstrating the conservative nature of these standards.

### **9.3 EFFECT OF GRADE OF SHEAR REINFORCEMENT**

Higher-strength shear reinforcement, such as using 80 ksi bars instead of 60 ksi bars, significantly influences girder behavior. The experiments compared girder designs with different stirrup strengths while adjusting spacing to maintain overall strength equivalence. For instance, when comparing G1\*-W (using 60 ksi bars with 18 in. spacing) and G1\*-E (using 80 ksi bars with 26 in. spacing), both girders showed nearly identical stiffness. However, the 60 ksi bars with 18 in. spacing exhibited slightly higher maximum strength, about 8–10 kips more than the girders with 80 ksi bars and wider spacing (with the same shear steel reinforcement index).

In terms of the RSS, the girders with 80 ksi bars generally showed higher ratios compared to those with 60 ksi bars, indicating better reserve strength. Specifically, G1\*-W versus G1\*-E had an RSS ratio of 1.43 for 60 ksi bars and 1.54 for 80 ksi bars, showing the advantage of higher-strength stirrups in maintaining shear capacity but with a lower cracking strength. Further analysis of crack measurements revealed differences in crack angles and distribution, suggesting that stirrup grade affects crack characteristics, which has implications for structural performance and durability.

In analyzing the impact of shear reinforcement grade on girder performance using FE analyses, several key findings emerge. The initiation of shear cracking in Tx54 and Tx70 girders was consistent regardless of the reinforcement grade (Grade 60 or Grade 100), suggesting that initial cracking loads were unaffected by the strength of the shear reinforcement similar to the behavior observed in experiments. However, increasing the reinforcement grade from Grade 60 to Grade 100 resulted in notable enhancements in ultimate shear force. Specifically, there was a 5 percent

increase observed for Tx54 girders and a 6.5 percent increase for Tx70 girders, thus underscoring the role of higher-grade reinforcement in improving structural resilience to shear forces.

Furthermore, girders reinforced with Grade 100 shear reinforcement exhibited larger deflections at ultimate load than those with Grade 60 reinforcement, indicating differences in structural behavior and ductility. This higher-grade reinforcement also led to higher RSS values, indicating greater RSS and steeper crack angles, which can affect crack propagation characteristics.

Differences in concrete strain behavior were also noted, with Tx54 girders experiencing higher strains when reinforced with Grade 100 and Tx70 girders showing higher strains with Grade 60 reinforcement. These findings collectively suggest that while higher-grade shear reinforcement enhances ultimate shear capacity and reserve strength, it also influences structural behavior and performance characteristics under loading conditions.

#### **9.4 EFFECT OF SIZE OF SHEAR REINFORCEMENT**

The FE analyses on Tx54 and Tx70 girders with shear reinforcement of different sizes/diameters highlights several significant findings. Increasing the size/diameter of shear reinforcement resulted in notable improvements in both cracking force and shear capacity across both girder types as a result of the larger steel reinforcement ratios. Specifically, in the Tx54 series, upgrading from #3 to #5 shear reinforcement led to approximately 12 percent higher cracking force and a 13 percent increase in shear capacity. Similarly, for Tx70 specimens, there was an approximately 11 percent increase in cracking force and a substantial 24 percent boost in shear capacity with larger reinforcement sizes.

As shear reinforcement size increased, there was a trend toward higher RSS values and steeper crack inclination angles, indicating greater variability in performance and crack propagation characteristics. Concrete damage analysis revealed intensified cracking patterns with larger reinforcement sizes coupled with reduced plastic strain in concrete at ultimate load. Interestingly, despite these enhancements, the axial stress experienced by reinforcement bars decreased as shear reinforcement size increased, reflecting a redistribution of forces and improved structural behavior under load. Comparative analysis with AASHTO and ACI standards demonstrated that FE analyses consistently predicted higher ultimate shear loads compared to code standards, highlighting potential conservatism in the design guidelines.

## 9.5 EFFECT OF HARPED STRANDS

The experimental study on the impact of harped strands on girder behavior reveals significant effects on shear capacity and crack propagation. Harped strands, designed to enhance shear capacity through prestressing force contributions, were evaluated in two comparative scenarios: G1-W versus G3-E and G2-E versus G3-W. In the first scenario, with 18-inch shear reinforcement spacing, girder G3 equipped with harped strands surprisingly exhibited slightly lower capacities at both cracking and ultimate states than the G1 girder without harped strands. This unexpected outcome suggests potential complexities in how harped strands interact with standard reinforcement configurations.

Conversely, in the second scenario, with 26-inch spacing, girder G3 with harped strands demonstrated improved shear performance, showing higher capacities at both cracking and ultimate stages compared to the G2 girder without harped strands. This result indicates that the effectiveness of harped strands may be more pronounced in girders with larger  $s/d$ s and have a greater influence on shear force distribution and crack propagation characteristics. Analysis of RSS further supported these observations, showing generally better performance metrics for girder configurations incorporating harped strands.

However, crack pattern analysis revealed denser cracking and wider crack widths in girders with harped tendons at tighter spacing, contrasting with more uniform crack characteristics at wider spacing. This underscores the need for further investigation into how spacing influences the effectiveness of harped strands in enhancing girder performance.

The FE analyses comparing girder specimens with and without harped strands revealed significant enhancements in cracking forces and shear capacities with the inclusion of harped strands. In both Tx54 and Tx70 girder types, specimens equipped with harped strands demonstrated higher cracking forces, with increases of approximately 9 percent and 3 percent, respectively, over specimens with straight strands. Similarly, shear capacities were notably elevated, showing approximately 4 percent and 7 percent increases for Tx54 and Tx70, respectively. This finding underscores the effectiveness of harped strands in improving the structural performance of girders under shear loading conditions.

Furthermore, the presence of harped strands influenced other structural behaviors: inclination angles of cracks were slightly greater, indicating potential differences in crack propagation patterns. Concrete strains were generally lower in specimens with harped strands, suggesting improved ductility and strain distribution within the concrete. Interestingly, while harped strands reduced the axial stress experienced by reinforcement bars at ultimate load, they showed varied effects on RSS values between Tx54 and Tx70 specimens. Additionally, comparative analyses against AASHTO LRFD specifications and ACI 318-19 standards consistently showed that FE analysis predictions tended to estimate higher shear cracking and ultimate shear forces. However, the FE models are closer in prediction of the experimental values.

## **9.6 EFFECT OF PRESTRESSING**

The experimental study on prestressing in girder design highlights significant effects on structural performance under shear loading conditions. Two key comparisons, G5-E versus G2-W versus G6-W and G5-W versus G2-E versus G6-E varied the prestressing ratio by altering the number of prestressing strands while keeping other design parameters constant. In both comparisons, higher prestressing ratios corresponded to increased cracking forces and ultimate shear capacities. For instance, in the first comparison using  $h_w/(2 \tan\theta)$  spacing, cracking shear forces increased from 162 kips to 218 kips as the prestressing ratio increased from 15.23 percent to 21.24 percent. Similarly, maximum shear capacities rose from 292 kips to 373 kips, indicating a clear trend of improved structural performance with higher prestressing.

Analysis of RSS values revealed that higher prestressing ratios generally resulted in lower RSS values, suggesting that for higher prestressing ratios, higher shear reinforcement is needed to achieve the same RSS (and vice versa), or, higher prestressing ratios lead to more brittle behaviors. Visual inspections of crack patterns further supported these findings, showing tighter, more concentrated cracking in high prestressing scenarios compared to wider, less frequent cracks in lower prestressing scenarios.

The finite element (FE) study on the effect of increasing the prestressing ratio in prestressed concrete girders reveals significant impacts on structural behavior under shear loading conditions. Across both Tx54 and Tx70 girder series, increasing this ratio led to notable increases in cracking forces and ultimate shear capacities. The study also found that



higher prestressing ratios contributed to reduced RSS values, indicating improved shear strength and less variability in performance. Increased ratios were associated with higher inclination angles of cracks, suggesting a more pronounced shear transfer mechanism. Although axial stresses within the reinforcement bars showed slight variations with changing prestressing ratios, the overall trend pointed toward optimized stress distributions enhancing structural integrity.

In terms of predictive accuracy, FE analyses consistently projected higher shear cracking and ultimate shear forces than AASHTO and ACI standards. Ratios of FE-predicted forces to AASHTO were approximately 1.16 to 1.37 for Tx54 and 1.09 to 1.27 for Tx70, while ratios to ACI ranged from 0.98 to 1.13 for Tx54 and 1.04 to 1.27 for Tx70. These findings underscore the significance of higher prestressing ratios in enhancing shear performance beyond conventional code-based expectations and highlight the potential for optimizing girder designs.

## **9.7 EFFECT OF CONCRETE STRENGTH**

The experimental study investigated the impact of varying concrete strength on prestressed concrete girder performance, focusing on two key comparisons: G1-W versus G7-E versus G8-E and G2-E versus G7-W versus G8-W. In these comparisons, concrete strength levels of 5 ksi, 7 ksi, and 8.5 ksi were tested, with consistent design parameters except for concrete compressive strength. For the first comparison at an 18-inch shear reinforcement spacing, increasing concrete strength showed a clear trend of enhancing both cracking and ultimate shear capacities. Cracking forces rose from 176 kips for G7-E (5 ksi) to 215 kips for G1-W (7 ksi) but remained at 214 kips for G8-E (8.5 ksi). Ultimate shear capacities similarly increased from 306 kips (G7-E) to 361 kips (G1-W), with G8-E yielding 332 kips. The relative spacing of reinforcement did not show a consistent pattern in terms of RSS, indicating a need for further investigation into these parameters.

In the second comparison, using a 26-inch spacing as per ACI 318-19 standards, similar trends were observed with concrete strength variations. Cracking shear strengths increased from 176 kips (G7-W) to 190 kips (G2-E) to 218 kips (G8-W), clearly illustrating the influence of higher concrete strength on girder performance. Ultimate shear capacities followed suit, with values of 282 kips (G7-W), 302 kips (G2-E), and 325 kips (G8-W), reinforcing the beneficial effect of

stronger concrete in enhancing structural resilience. Despite these improvements in shear capacities, the RSS values did not consistently reflect the strength variations.

Increasing concrete compressive strength led to significant improvements in both cracking force and ultimate shear force capacities for Tx54 and Tx70 girders. For Tx54, transitioning from 5 ksi to 8.5 ksi concrete resulted in a cracking force increase of approximately 37 percent, and up to 75 percent when transitioning to 14 ksi concrete. Similarly, Tx70 girders showed a 33 percent increase in cracking force at 8.5 ksi and an 81 percent increase at 14 ksi concrete strength. The ultimate shear capacities also saw substantial gains with higher concrete strengths, with Tx54 experiencing increases of 36 percent at 8.5 ksi and 51 percent at 14 ksi, and Tx70 showing increases of 22 percent at 8.5 ksi and 58 percent at 14 ksi.

Increasing concrete strength correlated with lower RSS values, indicating improved cracking shear strength, but not showing as much increase in the ultimate strength, which is similar to the behavior observed in experimental study. It also resulted in higher axial stresses within the R-bars at ultimate forces for both girder types. Furthermore, FE-predicted shear cracking and ultimate force ratios consistently exceeded those calculated by AASHTO and ACI standards for both Tx54 and Tx70 specimens. The FE-predicted to AASHTO-predicted ratios ranged from approximately 1.07 to 1.36 for shear cracking forces and 1.11 to 1.39 for ultimate shear forces, while against ACI, these ratios varied from 0.94 to 1.27 for shear cracking forces and 1.20 to 1.36 for ultimate shear forces. These results underscore the effectiveness of higher concrete compressive strengths in enhancing the structural performance and strength predictions of prestressed concrete girders.

## **9.8 EFFECT OF SHEAR SPAN-TO-DEPTH RATIO**

The shear-span-to-depth ratio,  $a/d_v$ , significantly influences the shear strength of prestressed concrete girders, particularly in zones with minimal shear reinforcement. Lower  $a/d_v$  generally results in higher shear capacities. Two comparative studies—G4-E versus G1-W versus G9-E and G4-W versus G2-W versus G9-W—explored  $a/d_v$  of 2.5, 3, and 4 across different girder configurations. In both comparisons, shear force versus displacement plots indicated clear trends: higher  $a/d_v$  correlated with reduced cracking and ultimate shear strengths. For instance, in G4-W versus G2-W versus G9-W, the first cracking shear strengths decreased from 214 kips ( $a/d_v =$

2.5) to 143 kips ( $a/d_v = 4$ ), and ultimate shear capacities decreased from 335 kips ( $a/d_v = 2.5$ ) to 280 kips ( $a/d_v = 4$ ).

Moreover, the comparisons revealed different RSS values across different  $a/d_v$  and shear reinforcement spacings. Higher  $a/d_v$  generally exhibited higher RSS values, implying that larger minimum shear reinforcement may be needed for smaller  $a/d_v$ . Visual inspections of crack patterns confirmed these findings, with longer shear spans exhibiting more cracks and broader distributions than shorter spans. Overall, the study underscores the critical role of the shear-span-to-depth ratio in determining the shear performance and ductility of prestressed concrete girders, especially in zones without adequate shear reinforcement.

In FE analyses of Tx54 and Tx70 girders, lower  $a/d_v$  consistently demonstrated higher cracking and ultimate shear forces. For Tx54 girders, the transition from  $a/d_v$  of 4 to 2.5 resulted in a significant 27 percent increase in cracking force and a substantial 58.3 percent increase in maximum force capacity. Similarly, Tx70 girders showed a 19.7 percent increase in cracking force and a 22.6 percent increase in maximum force capacity under similar transitions. These findings underscored the critical role of  $a/d_v$  in influencing structural behavior, in which smaller ratios enhanced shear resistance, likely due to more effective shear transfer mechanisms and reduced susceptibility to diagonal cracking. In terms of RSS, the FE analyses demonstrated an increase in the RSS as the  $a/d_v$  decreased.

Moreover, the study highlighted that as  $a/d_v$  decreased, the orientation of principal stress fields shifted, leading to a more pronounced formation of inclined cracks. This change in cracking behavior at different ratios underscores the importance of optimizing structural designs to achieve higher shear capacities while managing crack propagation effectively. Additionally, FE analysis predictions consistently exceeded those by AASHTO and ACI standards, with ratios ranging from 1.01 to 1.59 for Tx54 and 1.04 to 1.33 for Tx70, indicating potential for more accurate predictions under varying  $a/d$  ratios.

## **9.9 EFFECT OF CROSS-SECTION DEPTH**

The experimental study investigated the influence of girder cross-section depth on the shear performance of prestressed concrete girders by comparing Tx54 and Tx70 girders. The transition

from Tx54 to Tx70, representing larger cross sections, revealed notable differences in cracking and ultimate shear capacities. For instance, in the comparison between G10-E (Tx70) and G1-W (Tx54), the Tx70 girder exhibited higher cracking and ultimate shear forces, with recorded values of 285 kips and 388 kips, respectively, compared to 215 kips and 361 kips for the Tx54 girder. Similarly, in the G10-W (Tx70) versus G2-W (Tx54) comparison, the Tx70 girder displayed superior shear capacities, with first cracking forces of 251 kips and ultimate shear forces of 351 kips, compared to 190 kips and 292 kips for the Tx54 girder.

The study highlighted that larger cross-section girders tend to achieve higher shear capacities but also exhibit different failure modes when compared to smaller girders. Visual inspections of crack patterns revealed that the larger cross-section girder experienced widely spaced cracks, especially evident under smaller  $s/d$  conditions. Conversely, the Tx54 girder, despite its smaller cross section, showed brittle failure characteristics under larger  $s/d$  conditions, underscoring the complexity of shear behavior influenced by both girder size and shear reinforcement spacing. For the larger spacing, the RSS reduced as the cross-section depth increased despite higher ultimate shear strength depicting the role of size effects in larger beams. Analysis of RSS values further indicated variations in crack resistance between the different girder sizes and reinforcement configurations, suggesting a need for enhanced design considerations in larger girder applications to ensure structural reliability and safety.

## **9.10 SUMMARY**

This chapter investigates the effects of various factors on the shear performance of prestressed concrete girders through full-scale testing and FE analysis. The role of minimum shear reinforcement in restraining the growth of inclined cracking is emphasized in an effort to improve ductility, maintain concrete shear resistance, and control crack widths. Key parameters such as the presence of a deck slab, shear reinforcement spacing, shear reinforcement grade, reinforcement size, harped strands, prestressing force, concrete strength,  $a/d$ , and cross-section depth are evaluated to understand their influence on shear capacity and girder performance.

## CHAPTER 10:

### REFINEMENTS TO DATA-DRIVEN MODELING AND ESTIMATION OF THE RESERVE SHEAR STRENGTH INDEX

In earlier dataset analyses, models developed through nonlinear regression and GP successfully predicted the shear force at both the onset of diagonal cracking and at shear failure. Despite their high accuracy, using these models to calculate the RSS index resulted in significantly lower accuracy. This chapter advances the previously nonlinear regression techniques by (a) including the error in the RSS predictions in the loss/cost objective function, (b) weighting the error norm with respect to the cross-section size, and (c) including physics-based inequality constraints. Using the refined models, a reliability-based strategy is devised to estimate appropriate RSS values.

#### 10.1 REFINED NONLINEAR REGRESSION

##### 10.1.1 Refinements to Nonlinear Regression Process

The selected function for  $V_{cr}$  and  $V_{fail}$  are those used in the earlier dataset analysis (Chapter 3), specifically Equations (10.1), (10.2) and (10.3), which are shown below:

$$V_{cr} = \left[ a_0 \cdot \left( \frac{1}{1 + \frac{d}{10}} \right)^{a_1} \cdot \left( \frac{1}{1 + \frac{a}{d}} \right)^{a_2} \cdot \left( \frac{f'_c}{5,000\text{psi}} \right)^{a_3} \cdot (1 + \rho_w^{a_4}) + a_5 \right. \\ \left. \cdot \left( \frac{1}{1 + \frac{s}{d}} \right)^{a_6} \cdot \rho_v^{a_7} \cdot \left( \frac{f_{yt}}{60\text{ksi}} \right)^{a_8} + a_9 \cdot \left( \frac{f_{pc}}{f'_c} \right)^{a_{10}} \right] \frac{\sqrt{f'_c}}{1,000\text{psi}} b_w d \quad (10.1)$$

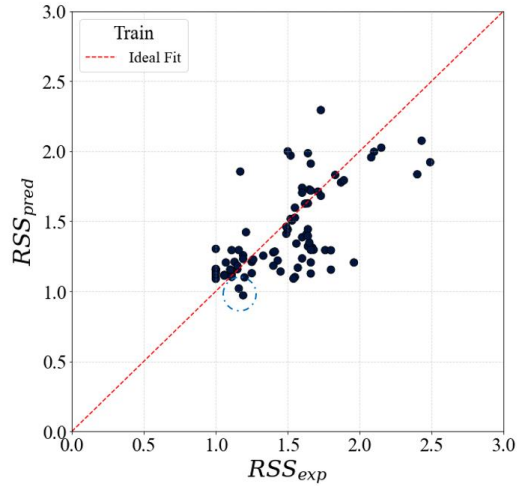
$$V_{fail} = V_s + \left[ b_0 \cdot \left( \frac{1}{1 + \frac{d}{10}} \right)^{b_1} \cdot \left( \frac{1}{1 + \frac{a}{d}} \right)^{b_2} \cdot \left( \frac{f'_c}{5,000\text{psi}} \right)^{b_3} \cdot (1 + \rho_w^{b_4}) + b_5 \right. \\ \left. \cdot \left( \frac{1}{1 + \frac{s}{d}} \right)^{b_6} \cdot \rho_v^{b_7} \cdot \left( \frac{f_{yt}}{60\text{ksi}} \right)^{b_8} + b_9 \cdot \left( \frac{f_{pc}}{f'_c} \right)^{b_{10}} \right] \frac{\sqrt{f'_c}}{1,000\text{psi}} b_w d \quad (10.2)$$

$$RSS = \frac{V_{fail}}{V_{cr}} \quad (10.3)$$

where  $a_0, a_1, \dots, a_{10}$  = coefficients that will be estimated through optimization;  $V_s = \frac{A_v f_{yt} d}{s}$ , which is the same or smaller than  $8\sqrt{f'_c} b_w d$  to minimize the likelihood of diagonal compression failure (ACI 2019);  $A_v$  = area of shear reinforcement within spacing  $s$  (in.<sup>2</sup>);  $\alpha$  = angle defining the orientation of shear reinforcement (degree);  $d$  = effective depth of the cross section of beam (in.);  $a/d$  = shear span over effective depth ratio (in./in.);  $f'_c$  = compressive strength of concrete (psi);  $\rho_w$  = ratio of mild reinforcement;  $s/d$  = stirrup spacing over effective depth (in./in.);  $\rho_v$  = ratio of shear reinforcement;  $f_{yt}$  = yield strength of shear reinforcement (ksi);  $f_{pc}/f'_c$  = effective prestress in concrete over compressive strength of concrete (psi/psi); and  $b_w$  = web width (in.<sup>2</sup>).

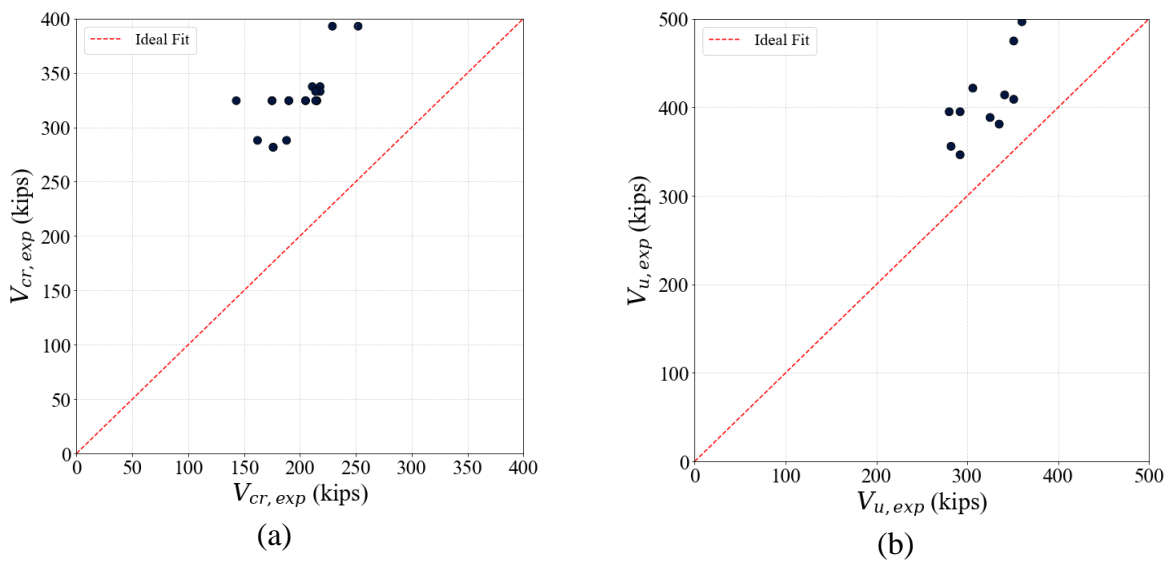
Based on the challenges identified during the early dataset analyses, a *first refinement* is using an RMSE that includes error norms for  $V_{cr}$ ,  $V_{fail}$ , and RSS, simultaneously. This approach will calibrate the equations for  $V_{cr}$  and  $V_{fail}$  simultaneously while searching for optimal calibration that also minimizes the error in RSS. To ensure that no norm will overshadow the other norms, the RMSE will be expressed in terms of normalized errors (as opposed to absolute error), as shown later. In fact, because  $V_{cr}$  and  $V_{fail}$  are measured in units of force, with values reaching into the hundreds, as opposed to the much smaller values of RSS, which are usually between 0.5 and 2.5, it is certain that unnormalized error norms are unfavorable to the RSS predictions.

An examination of the optimization results revealed instances where the predicted  $V_{cr}$  values exceeded  $V_{fail}$ , resulting in RSS values of less than 1, which is shown in Figure 10.1. This is physically implausible since shear failure cannot occur before the onset of diagonal cracking. Such predictions arose because the optimization process lacked physical constraints, leading to results that violated fundamental principles of structural behavior. Thus, a *second refinement* will include the introduction of a physical constraint, enforcing using  $V_{cr} \leq V_{fail}$ .



**Figure 10.1. Predicting  $V_{cr}$  higher than  $V_{fail}$  problem (see dashed circle).**

The early regression models also showed lower prediction accuracy for girders with larger depth because of the limited number of tests on large girders. As Figure 10.2 shows, both  $V_{cr}$  and  $V_{fail}$  are predicted higher than the actual value, and it seems to be shifted to the upper side from the ideal fit line. This issue was primarily due to the skewness in the dataset, which contained a relatively high number of smaller specimens and fewer larger specimens, such as those used in the field. This imbalance adversely affected the model's predictive performance for real-world applications. Thus, a *third refinement* will include the introduction of larger weights for large-size girders and the exclusion of test data on girders with very small cross-section heights.

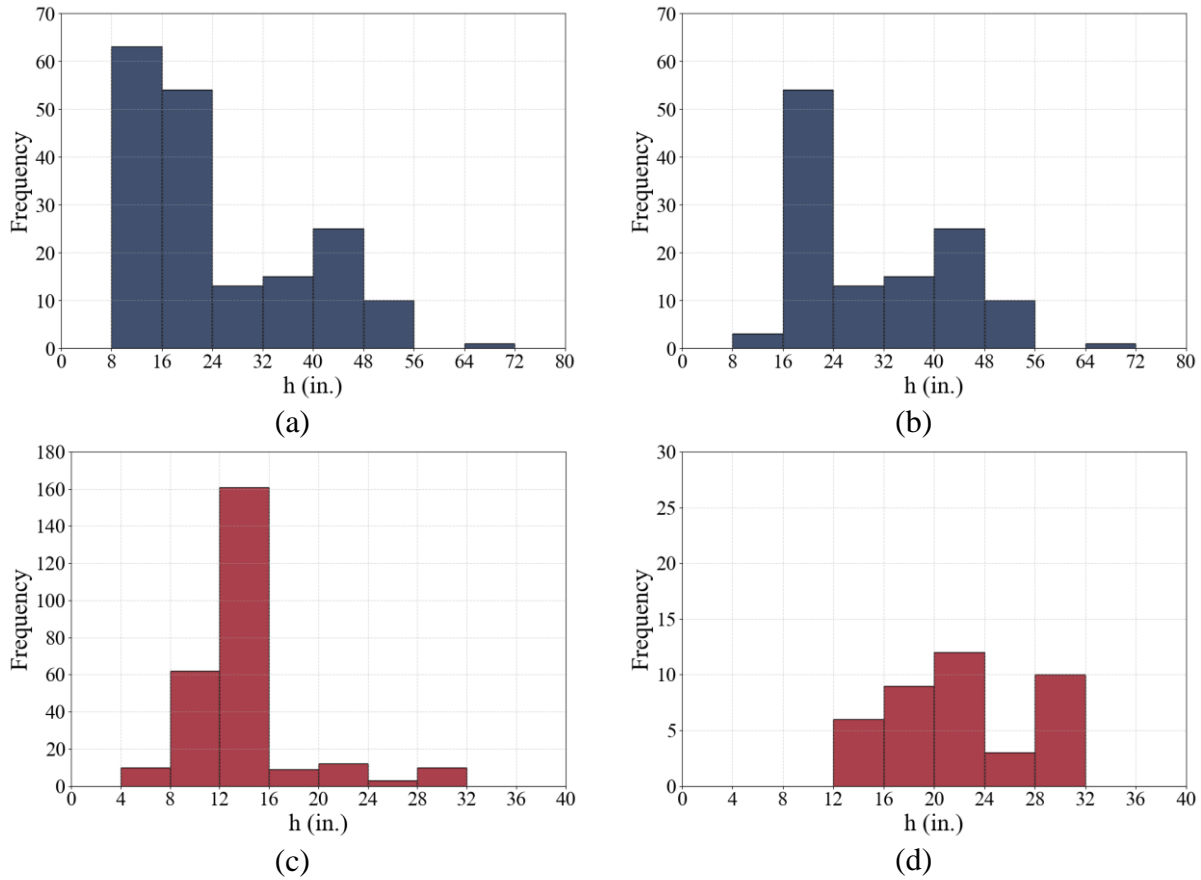


**Figure 10.2. Predicting  $V_{cr}$  and  $V_{fail}$  for experimental value problem.**

### **10.1.2 Final Nonlinear Optimization Process**

Initially, the data were loaded and then filtered according to specific conditions. Data missing essential input variables required for the analysis were removed. Since the dataset includes experimental data from 1950 onward, it contains many results from scaled-down experiments, resulting in numerous data with small section heights for prestressed concrete beams. To better align with the actual types of girders used by TxDOT, data with section heights less than 15 in. were excluded. This exclusion significantly reduced the amount of data without transverse reinforcement, revealing that the model was not well-optimized for these data. Therefore, only data with transverse reinforcement were included in the optimization process. Figure 10.3 illustrates how the data distribution is affected when the section height is limited to 15 in. or more. In cases where data excluding transverse reinforcement were used, the number of data points significantly decreased after filtering. Consequently, the range of the y-axis label in the histogram was adjusted and reduced to reflect this change.





**Figure 10.3. Data distribution, (a) including transverse reinforcement, (b) including transverse reinforcement after filtering, (c) not including transverse reinforcement, and (d) not including transverse reinforcement after filtering.**

In the modeling stage, two models, the shear force at the onset of diagonal cracking,  $V_{cr}$  model, and the shear force at shear failure,  $V_{fail}$  model, were defined to predict shear strength, respectively, as Equation (10.1) and Equation (10.2). During the optimization process, the primary goal was to adjust the model parameters to minimize the prediction error. The loss function aimed to minimize the error between the predicted values from the  $V_{cr}$  model and the  $V_{fail}$  model and the actual values,  $V_{cr}$ ,  $V_{fail}$ , and  $RSS$ . The final loss function employed in nonlinear optimization is as follows:

$$\begin{aligned}
\text{Loss function} = & \sqrt{\frac{\sum_i w_i \left( \frac{V_{cr,exp,i} - V_{cr,pred,i}}{V_{cr,exp,i}} \right)^2}{\sum_i w_i}} \\
& + \sqrt{\frac{\sum_i w_i \left( \frac{V_{fail,exp,i} - V_{fail,pred,i}}{V_{u,exp,i}} \right)^2}{\sum_i w_i}} + \sqrt{\frac{\sum_i w_i \left( \frac{RSS_{exp,i} - RSS_{pred,i}}{RSS_{exp,i}} \right)^2}{\sum_i w_i}}
\end{aligned} \tag{10.4}$$

$$w_i = \frac{d_i}{d_{ref}} \tag{10.5}$$

where  $w_i$  = term assigning weight based on the height of the member cross section;  $V_{cr,exp}$  = observed shear force at the onset of diagonal cracking for the  $i^{th}$  observation in the dataset;  $V_{cr,pred}$  = predicted shear force at the onset of diagonal cracking for the  $i^{th}$  in the dataset;  $V_{fail,exp}$  = observed shear force at shear failure for the  $i^{th}$  observation in the dataset;  $V_{fail,pred}$  = predicted shear force at shear failure for the  $i^{th}$  in the dataset;  $RSS_{exp}$  = observed RSS index for the  $i^{th}$  observation in the dataset;  $RSS_{pred}$  = predicted RSS index for the  $i^{th}$  in the dataset;  $d$  = effective depth for the  $i^{th}$  in the dataset (in.);  $d_{ref}$  = reference effective depth (in.)

The distinguishing feature of this loss function, as shown in Equation (10.4), is its ability to equally consider the accuracy of the key parameters in this study:  $V_{cr}$ ,  $V_{fail}$ , and  $RSS$ . This outcome is achieved by using the root mean square percentage error rather than the more commonly used RMSE in regression analysis and optimization. Furthermore, this loss function incorporates a  $w_i$  term that assigns weights according to the height of the cross section of the data, and it is defined as the Equation (10.5). The variable  $d_i$  represents the effective depth of the  $i$ -th girder, and  $d_{ref}$  is a specific reference value set to 54 in. for this analysis. This reference value, chosen as the height of TxDOT girders, ensures that the  $w_i$  term remains within a reasonable range, preventing it from becoming excessively small or large. Despite filtering out data below 15 in., the majority of the data remains within the 16 to 24 inch girder range, as shown in Figure 10.3. The reference value,  $d_{ref}$ , of 54 in. helps prevent overfitting to these smaller datasets, ensuring that those data points receive less weight.

Optimization was conducted using the SciPy library via a method—*trust-constr*—that combines trust-region techniques with sequential quadratic programming (SQP) and interior point methods, allowing for efficient solutions to large-scale problems with both equality and inequality constraints. For equality-constrained problems, it employs the Byrd-Omojokun Trust-Region SQP method, which iteratively solves quadratic subproblems to ensure strict constraint satisfaction while minimizing the objective function (Nocedal and Wright 2006). When inequality constraints are present, the method switches to a trust-region interior point approach. This approach introduces slack variables to transform inequality constraints into equality constraints, solving a series of equality-constrained barrier problems and progressively reducing the barrier parameter to converge to the optimal solution (Byrd et al. 1999). The *trust-constr* method offers several key advantages, making it an ideal choice for nonlinear optimization problems with constraints. First, it is well-suited for large-scale problems due to its efficient handling of trust regions and its ability to work with both sparse and dense constraints. This capability makes it particularly effective in scenarios involving a large number of variables and constraints because it can manage computational complexity and memory usage efficiently (Conn et al. 2000). Second, the method is versatile and robust. It is one of the most flexible constrained minimization algorithms implemented in SciPy, capable of adapting to a wide range of problem types. It switches between the Byrd-Omojokun Trust-Region SQP method for equality-constrained problems and the trust-region interior point method for problems that also include inequality constraints. This adaptability ensures that the algorithm can find optimal solutions across different types of constraint structures (Wendorff et al. 2016). Additionally, the *trust-constr* method uses finite difference schemes to approximate gradients and Hessians, which is particularly useful when exact derivatives are not available. This feature enhances its accuracy and reliability in solving complex optimization problems (Nocedal and Wright 2006).

The constraint required that  $V_{fail}$  be greater than or equal to  $V_{cr}$ , ensuring the physical validity of the model. This constraint guarantees that the shear force at shear failure is always greater than or equal to shear force at the onset of diagonal cracking. This condition is integrated into the training process. However, due to the nature of data-driven methods, even if this condition is fully met during training, there is no guarantee it will be satisfied during testing with new data. To improve this process, the test data and additional TxDOT girder design values (Table 10.1)

were incorporated into the training process. Crucially, these values were not used to optimize the model but solely to verify that the constraint was satisfied over a much broader design space. Although this approach does not ensure the constraint is 100 percent satisfied with new data, it reduces the likelihood of violating the constraint compared to previous methods.

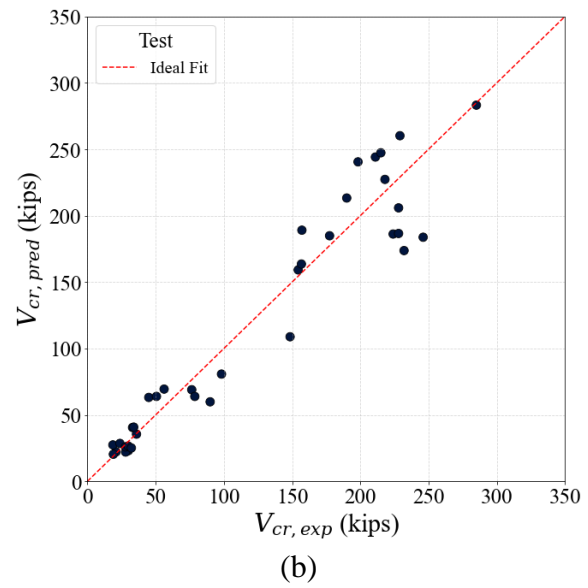
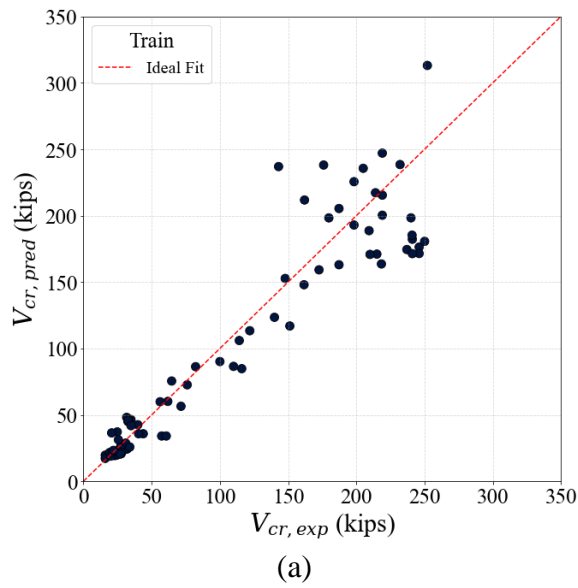
### 10.1.3 Comprehensive Regression Model

The results of the nonlinear optimization produced Equations (10.6) and (10.7). In both equations, the coefficient related to the spacing of shear reinforcement was optimized to zero. This result implies that for the shear force at the onset of diagonal cracking the spacing of shear reinforcement has no effect. Similarly, for the shear force at shear failure, the spacing has no effect except for the component involving  $V_s$ .

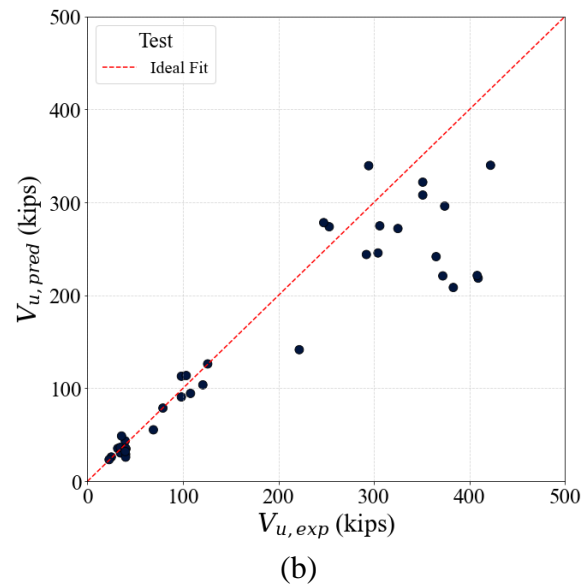
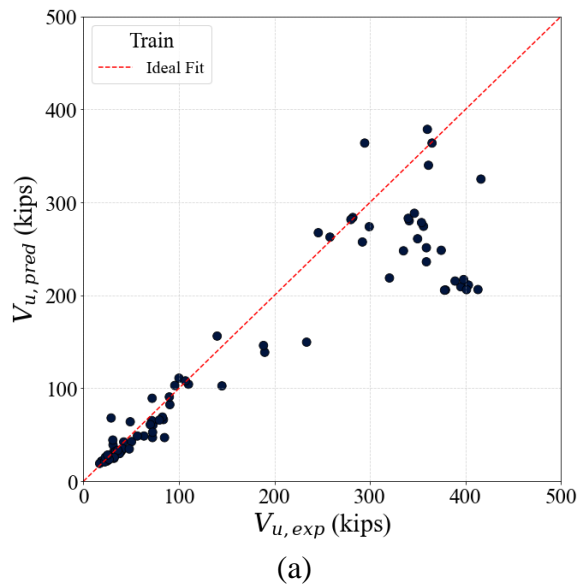
$$V_{cr} = \left[ 6.95 \left( \frac{1}{1 + \frac{d}{10}} \right)^{8.8} \left( \frac{1}{1 + \frac{a}{d}} \right)^{8.47} \left( \frac{f'_c}{5,000\text{psi}} \right)^{4.42} (1 + \rho_w^{1.61}) + 7.56 \rho_v^{0.29} \left( \frac{f_{yt}}{60\text{ksi}} \right)^{0.23} + 98.98 \left( \frac{f_{pc}}{f'_c} \right)^{2.12} \right] \frac{\sqrt{f'_c} b_w d}{1,000\text{psi}} \quad (10.6)$$

$$V_{fail} = V_s + \left[ 5.87 \left( \frac{1}{1 + \frac{d}{10}} \right)^{5.5} \left( \frac{1}{1 + \frac{a}{d}} \right)^{10.29} \left( \frac{f'_c}{5,000\text{psi}} \right)^{4.12} (1 + \rho_w^{2.61}) + 7.54 \rho_v^{0.29} \left( \frac{f_{yt}}{60\text{ksi}} \right)^{0.23} + 98.97 \left( \frac{f_{pc}}{f'_c} \right)^{2.12} \right] \frac{\sqrt{f'_c} b_w d}{1,000\text{psi}} \quad (10.7)$$

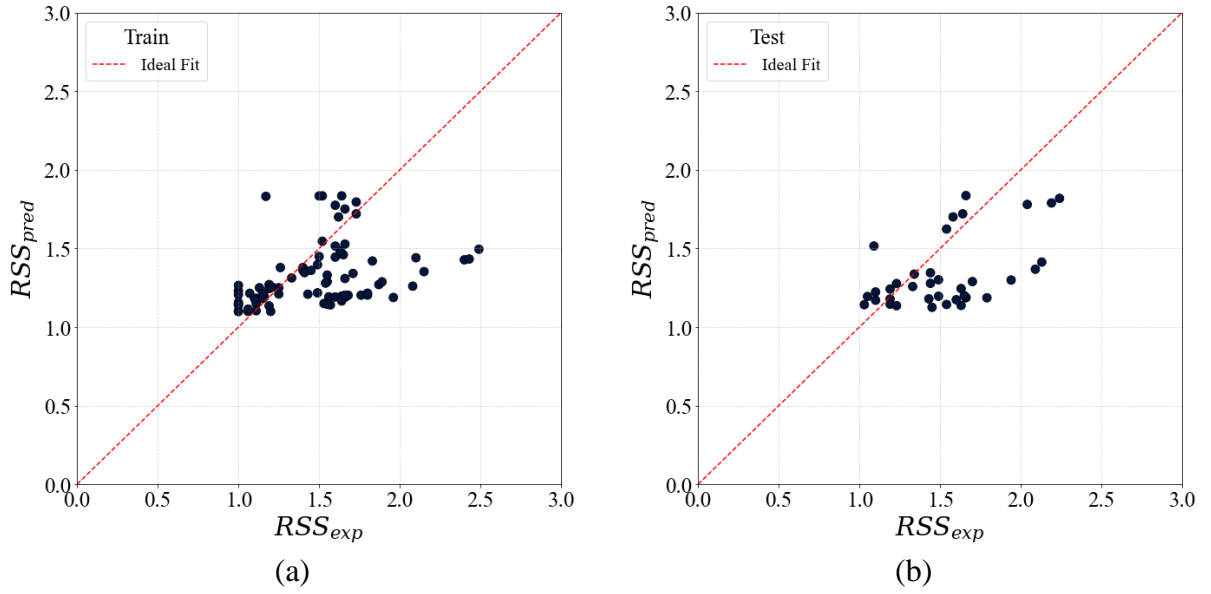
Figure 10.4 through Figure 10.6 show the results of  $V_{cr}$ ,  $V_{fail}$ , and the RSS index for both the training and test data. It is observed that  $V_{cr}$  and  $V_{fail}$  display results that are somewhat close to the ideal fit. However, the RSS plot reveals that the predicted values are overall lower than the actual values.



**Figure 10.4. Predicted versus actual shear force at the onset of diagonal cracking: (a) train dataset, and (b) test dataset.**



**Figure 10.5. Predicted versus actual shear force at the shear failure: (a) train dataset, and (b) test dataset.**



**Figure 10.6. Predicted versus actual RSS index: (a) train dataset and (b) test dataset.**

The Root Mean Square Percentage Error (RMSPE), which was used in the loss function, was employed to evaluate the model's performance. The RMSPE was calculated as follows:

$$RMSPE = \sqrt{\frac{\sum_i w_i \left( \frac{y_i - \hat{y}_i}{y_i} \right)^2}{\sum_i w_i}} \quad (10.8)$$

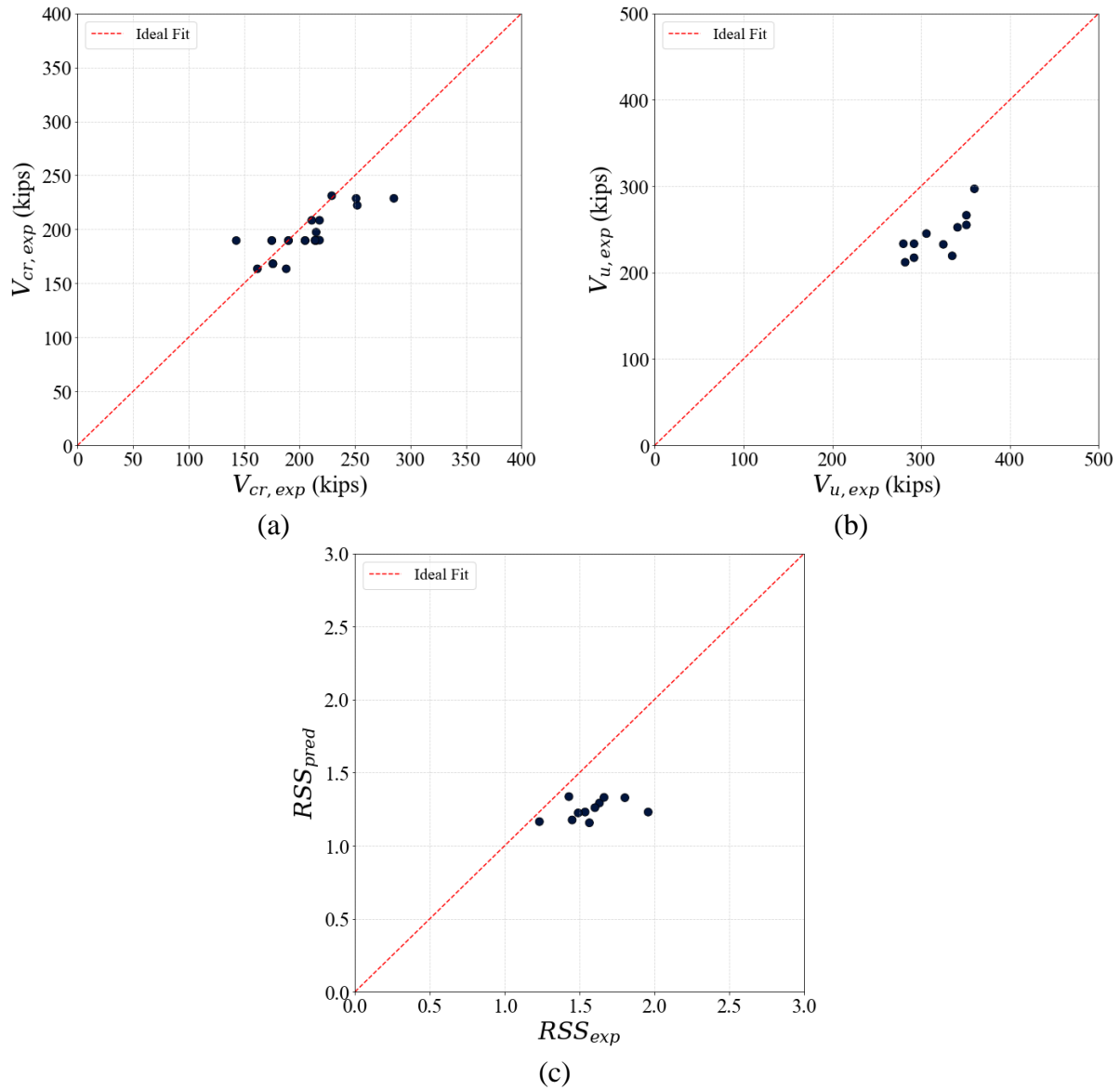
where  $w_i$  = term assigning weight based on the height of the member cross section (calculated from Equation (10.5));  $y_i$  = observed value for the  $i^{th}$  observation in the dataset;  $\hat{y}_i$  = predicted value for the  $i^{th}$  observation in the dataset.

As indicated in Table 10.1, the three key parameters exhibit similar RMSPE values overall. This result suggests that the model consistently performs well across each key parameter without bias toward any particular one. It is further noted that for all three quantities,  $V_{cr}$ ,  $V_{fail}$ , and RSS, the RMSPE is a little over 20 percent.

**Table 10.1. Performance evaluation for comprehensive complex model.**

Performance Metric	$V_{cr}$		$V_{fail}$		$RSS$	
	Train	Test	Train	Test	Train	Test
RMSPE	0.23	0.2	0.28	0.22	0.21	0.2

Figure 10.7 illustrates the developed model's predictions for the girders of the experiments of this study (Chapter 6). In Figure 10.7(a), the predicted shear force at the onset of diagonal cracking displays data points closely aligned with the ideal fit line, indicating accurate model predictions for  $V_{cr}$ . This close alignment suggests that the model effectively captures the critical parameters influencing shear force at diagonal cracking onset, demonstrating its robustness and reliability for practical applications in prestressed concrete beam design. Figure 10.7(b) shows the predicted shear force at shear failure. The data points here are slightly below the ideal fit line, indicating the model tends to predict  $V_{fail}$  conservatively. This conservative bias provides an additional safety margin in structural engineering design, reducing the risk of unexpected shear failures. Despite the slight shift, predictions remain within an acceptable range, validating the model's effectiveness in estimating the shear capacity of prestressed concrete beams. Figure 10.7(c) presents the predicted RSS index. The RSS index predictions do not align as closely with the ideal fit line as do  $V_{cr}$  and  $V_{fail}$ , indicating relatively lower accuracy. Since the RSS index is derived from both  $V_{cr}$  and  $V_{fail}$ , the compounded nature of these predictions may contribute to the observed discrepancies. Further refinement of the model may be necessary to enhance predictive accuracy for the RSS index.



**Figure 10.7. Predicted versus actual experimental value: (a) shear force at the onset of diagonal cracking, (b) shear force at shear, and (c) RSS index.**

#### 10.1.4 Simplified Regression Model

The development of a simplified explicit model was driven by the need to use hand calculations to predict the  $A_v/s$ . The goal was to create a model that maintains predictive accuracy while being simple enough for manual calculation. This ability enhances the model's usability, allowing engineers to efficiently determine the minimum shear reinforcement needed without relying on complex computational tools. The complexity of the existing model (Equations (10.1) and (10.2)) results from the fact that the stirrup spacing,  $s$ , appears in two nonlinear terms.



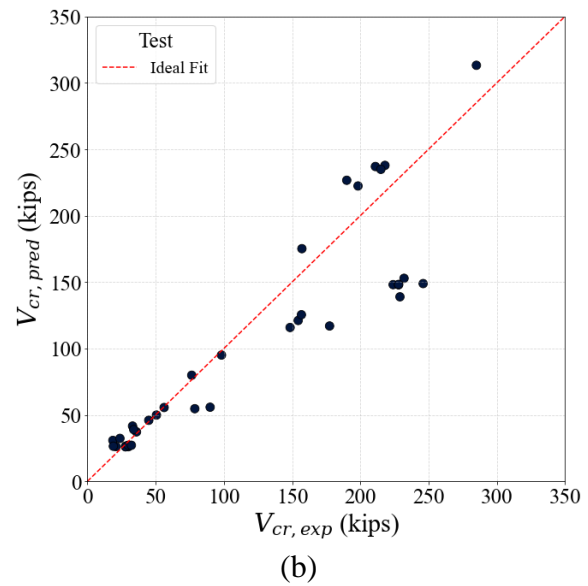
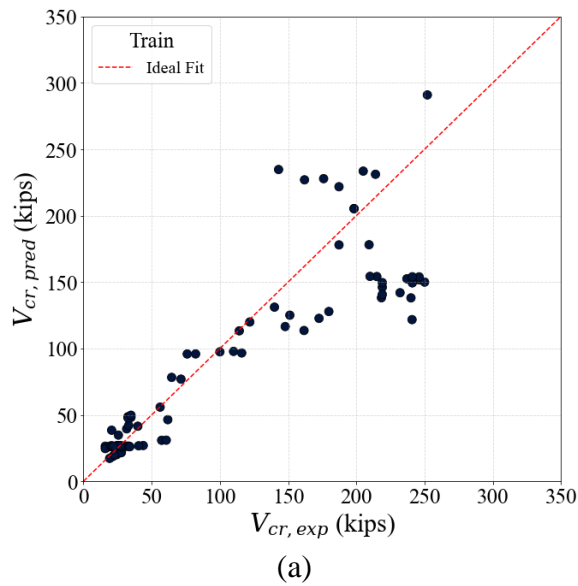
This nonlinearity complicates manual calculations for  $A_v/s$ . To simplify the comprehensive model, these two terms were dropped. Thus, in the simplified model, the shear force at the onset of diagonal cracking is assumed to remain unaffected by shear reinforcement. Similarly, the contribution of concrete to the shear force at shear failure is assumed to remain unaffected by shear reinforcement. By eliminating these two terms, the equations were transformed into a form where shear reinforcement,  $A_v/s$ , can be directly through  $V_v$ , making the model more practical for hand calculations.

Equations (10.9) and (10.10) each show the optimized results. In the current optimization results for  $V_{cr}$ , the coefficients related to  $d/10$ , representing the size effect, and the ratio of mild tensile reinforcement were both received to zero exponents from the optimization algorithm. However, for the shear force at shear failure, all factors were found to have an impact.

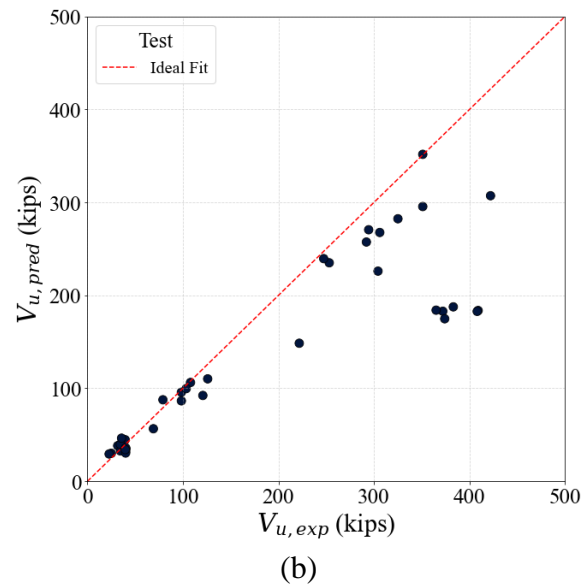
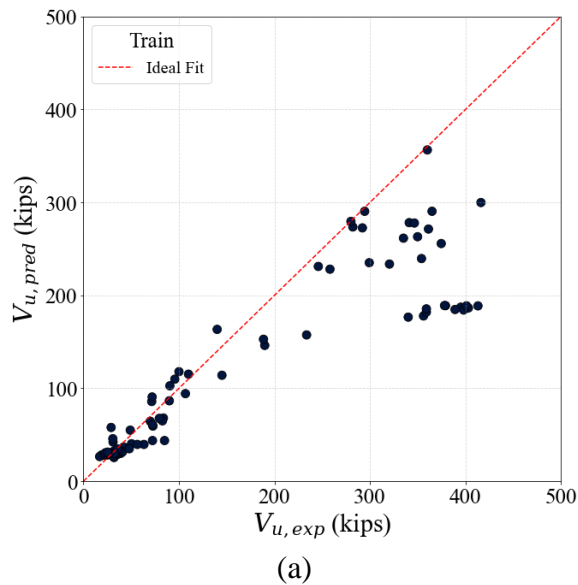
$$V_{cr} = \left[ 98.5 \left( \frac{1}{1 + \frac{a}{d}} \right)^{10.25} \left( \frac{f'_c}{5,000 \text{psi}} \right)^{6.39} + 11.71 \left( \frac{f_{pc}}{f'_c} \right)^{0.26} \right] \frac{\sqrt{f'_c} b_w d}{1,000 \text{psi}} \quad (10.9)$$

$$V_{fail} = V_s + \left[ 1.93 \left( \frac{1}{1 + \frac{d}{10 \text{ in.}}} \right)^{9.99} \left( \frac{1}{1 + \frac{a}{d}} \right)^{4.9} \left( \frac{f'_c}{5,000 \text{psi}} \right)^{2.61} (1 + \rho_w^{1.81}) + 11.7 \left( \frac{f_{pc}}{f'_c} \right)^{0.26} \right] \frac{\sqrt{f'_c} b_w d}{1,000 \text{psi}} \quad (10.10)$$

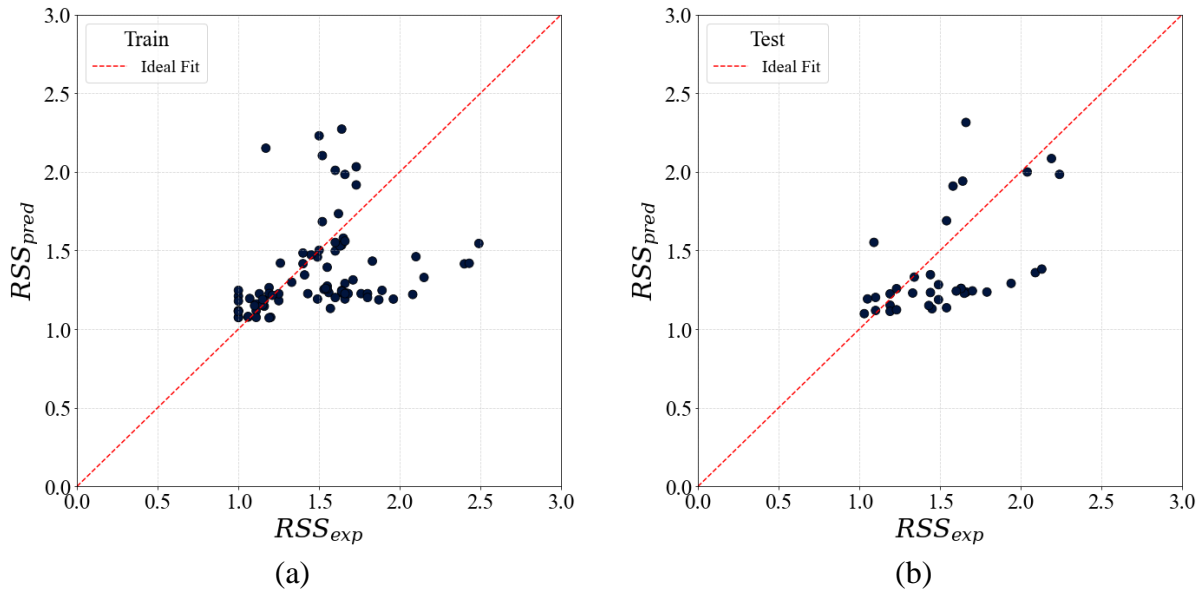
Figure 10.8 through Figure 10.10 show the results of  $V_{cr}$ ,  $V_{fail}$ , and the RSS index for both the training and test data. Both  $V_{cr}$  and  $V_{fail}$  generally display results that are somewhat close to the ideal fit. However, the RSS plot reveals that the predicted values are overall lower than the actual values.



**Figure 10.8. Predicted versus actual shear force at the onset of diagonal cracking: (a) train dataset, and (b) test dataset.**



**Figure 10.9. Predicted versus actual shear force at the shear failure: (a) train dataset, and (b) test dataset.**



**Figure 10.10. Predicted versus actual RSS index: (a) train dataset and (b) test dataset.**

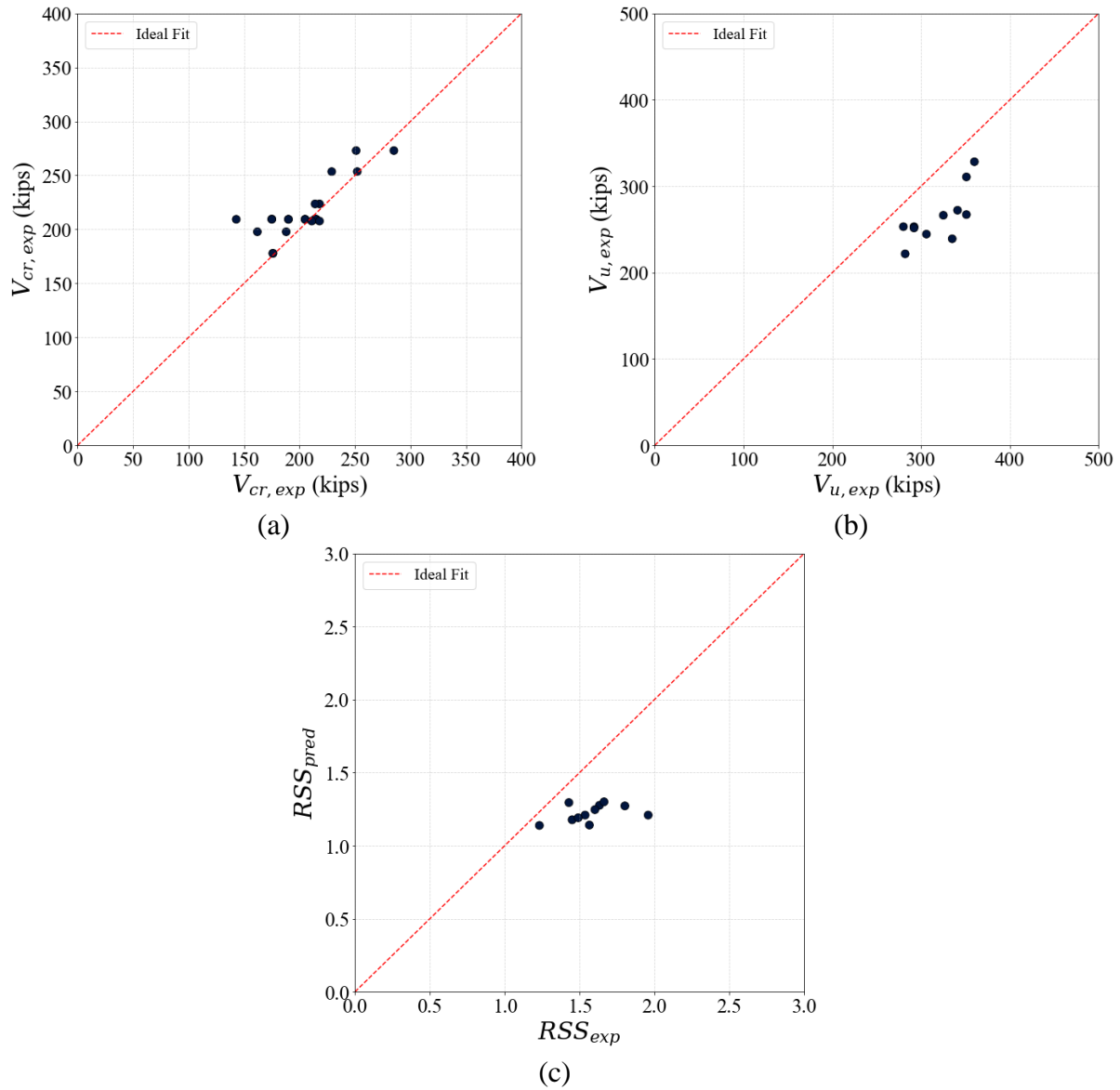
Due to the simplified model, it was observed that the RMSPE values were generally higher compared to the comprehensive complex model. However, the accuracy of the RSS was found to be relatively consistent, with the existing model showing an error of about 25 percent for  $V_{cr}$  and  $V_{fail}$  and a little over 20 percent for the RSS.

**Table 10.2. Performance evaluation for simplified explicit model.**

Performance Metric	$V_{cr}$		$V_{fail}$		RSS	
	Train	Test	Train	Test	Train	Test
RMSPE	0.3	0.25	0.31	0.26	0.23	0.21

Figure 10.11 visually represents the model's performance in predicting experimental values. In Figure 10.11(a), the predicted shear force at the onset of diagonal cracking is compared to actual values. The data points closely align with the ideal fit line, demonstrating the model's precision in predicting  $V_{cr}$ . This high degree of accuracy underscores the model's reliability in estimating the shear force at the initial cracking stage, critical for assessing the structural integrity of prestressed concrete beams. Figure 10.11(b) depicts the predicted shear force at shear failure. The data points are slightly below the ideal fit line, indicating a conservative bias in the model's predictions. This conservative tendency is advantageous in structural engineering, providing an

additional safety margin that reduces the risk of unexpected shear failures. Although the predictions are slightly lower than the actual values, they remain within an acceptable range, validating the model's effectiveness in estimating the ultimate shear capacity. Figure 10.11(c) illustrates the predicted RSS index. The RSS index predictions are less aligned with the ideal fit line than  $V_{cr}$  and  $V_{fail}$ , indicating comparatively lower accuracy. The RSS index, being derived from both  $V_{cr}$  and  $V_{fail}$ , may accumulate prediction errors from both parameters, resulting in greater variability. Despite this finding, the model provides a reasonable approximation, although further refinement may be needed to enhance predictive accuracy for the RSS index.



**Figure 10.11. Predicted versus actual experimental value: (a) shear force at the onset of diagonal cracking, (b) shear force at shear, and (c) RSS index.**

## 10.2 ESTIMATION OF RESERVE SHEAR STRENGTH INDEX

A fundamental question about using the RSS index to determine minimum shear reinforcement requirements is how to select a suitable RSS value. Although various strategies have been proposed, selection of appropriate RSS values remains an open topic. This study proposes determining appropriate RSS values by accounting for uncertainties in the models used to predicting RSS.

### 10.2.1 Reliability Analysis

In structural reliability analysis, the purpose of the reliability analysis is to account for the uncertainties associated with applied loads and structural resistances during the design process to establish a probabilistic safety margin. Numerous sources of uncertainty are inherent in the design of concrete structures, making the presence of random variables unavoidable (Aguilar et al. 2022). The structural reliability approach, which is probabilistic, has been widely employed to calibrate design procedures in contemporary structural design codes to achieve a predetermined safety margin (Nowak and Lind 1979; Nowak 1999; Szerszen and Nowak 2003; Aguilar et al. 2022).

#### 10.2.1.1 *Limit State Function*

In reliability analysis, the limit state function is a mathematical expression that delineates the boundary between safe and failure states of a system or component. It is utilized to evaluate whether a system will perform its intended function without failure under specified conditions. The limit state function,  $g(x)$ , typically depends on various random variables (such as loads, material properties, geometric dimensions, etc.) and can be expressed as:

$$g(x) = R - Q \quad (10.11)$$

where  $g(x)$  = safety margin where  $x$  is an input random variable;  $R$  = resistance; and  $Q$  = load effect. When  $g(x) > 0$ , the structure is in a safe state; when  $g(x) < 0$ , the structure is in a failure state; when  $g(x) = 0$ , the structure is at the limit state.

#### 10.2.1.2 *Statistical Parameters of Random Variables*

In reliability analysis, understanding the characteristics of random variables is essential for accurately assessing the performance and safety of engineering systems. Key information required includes the probability distribution, bias factor, and COV of these random variables. Each of these elements plays a specific role in the analysis.

The probability distribution of a random variable describes the likelihood of various outcomes and provides a comprehensive picture of its behavior. Common distributions in reliability

analysis include normal, lognormal, and Weibull distributions. The choice of distribution significantly affects the analysis results by influencing the estimation of failure probabilities and overall system reliability (Alfredo and Wilson 1975). For example, a lognormal distribution may be selected for variables that are strictly positive and exhibit right-skewness, while a normal distribution might be used for variables with symmetric properties around the mean. The bias factor, or mean-to-nominal ratio, measures the systematic deviation between the mean value of the random variable and a nominal or specified value. This factor is crucial for adjusting the analysis to account for consistent overestimation or underestimation in the data. It refines reliability predictions by correcting inherent biases, providing a more accurate assessment of system performance (Ditlevsen and Madsen 1996). The COV, or coefficient of variation, is the ratio of the standard deviation to the mean of a random variable, providing a normalized measure of dispersion. A high COV indicates greater variability relative to the mean, signaling increased uncertainty in performance predictions (Melchers and Beck 2018). Understanding the COV is vital for identifying the stability and reliability of the system under various conditions. It quantifies relative variability, enabling more informed decisions regarding safety factors and design adjustments.

Incorporating these statistical properties into reliability analysis allows engineers to develop a robust understanding of potential risks and uncertainties, which ensures the analysis is comprehensive and accounts for both central tendencies and variations in the data. Consequently, it leads to more reliable and accurate predictions of system behavior, thus enhancing safety and performance (Alfredo and Wilson 1975; Ditlevsen and Madsen 1996; Melchers and Beck 2018).

## **10.2.2 Proposed Reliability Analysis**

### *10.2.2.1 Proposed Limit State Function*

Conventional reliability analysis, as previously explained, assesses the probability of structural failure under a given load by considering the uncertainties of various variables relating to the applied loads and structural strengths. The purpose of implementing reliability analysis is to identify an appropriate RSS index value that will ensure that after the onset of diagonal cracking the strength produced by the cracked girder segment is sufficient to support the load that led to the onset of cracking. In other words, the post-cracking shear strength should be larger than the

pre-cracking shear strength. The pre-cracking shear strength is  $V_{cr}$ , because it refers to the uncracked section, whereas the post-cracking strength is the ultimate strength,  $V_u$ , because it refers to the strength of the cracked segment. The above concept is similar to the concept behind the derivation of the minimum flexural reinforcement, where ultimate moment strength of the reinforced section should not be less than the pre-cracking strength of the unreinforced section. On the basis of this strategy, the proposed limit state function is selected:

$$g = \text{RSS}_{\text{true}} - 1 \quad (10.12)$$

where  $\text{RSS}_{\text{true}}$  represents the *true* RSS. To account for uncertainties, the RSS is expressed as follows:  $\text{RSS}_{\text{true}} = C \times \text{RSS}_{\text{model}}$ , where  $\text{RSS}_{\text{model}}$  represents the values predicted by the model equations and is defined as follows:  $\text{RSS}_{\text{model}} = V_{\text{fail,model}}/V_{\text{cr,model}}$ . The model equations can be those generated earlier or any other set of predictive equation for  $V_{\text{fail,model}}$  and  $V_{\text{cr,model}}$  (or directly for  $\text{RSS}_{\text{model}}$ ). Factor  $C$  is the uncertainty factor for the  $\text{RSS}_{\text{model}}$  and constitutes a random variable that reflects the capability of the model equations to predict RSS. Using an uncertainty factor for RSS, as opposed to two individual uncertainty factors for  $V_{u,\text{model}}$  and  $V_{\text{cr,model}}$  is attractive because it avoids the need for quantifying cross-correlations between the two individual uncertainty factors for  $V_{\text{fail,model}}$  and  $V_{\text{cr,model}}$ . Based on the above, the resulting limit state function becomes:

$$g = C \frac{V_{\text{fail,model}}}{V_{\text{cr,model}}} - 1 \quad (10.13)$$

In addition to  $C$ , the proposed limit state function incorporates various input variables used in the calculation of  $V_{\text{fail,model}}$  and  $V_{\text{cr,model}}$  that can be treated as random variables, such as material strengths' member and rebar dimensions. Bias factors and COVs of these properties have been adopted from the literature and are presented in Table 10.3, while the procedure for estimating the statistics of  $C$  is explained later. There is no statistical data available for effective prestressing stress. To address this issue, Siriaksorn (1980) proposed characterizing the uncertainty of effective prestressing stress using the statistical information of the ultimate strength of prestressing reinforcement. Consequently, this value has been used in reliability analyses for effective prestressing stress to date.

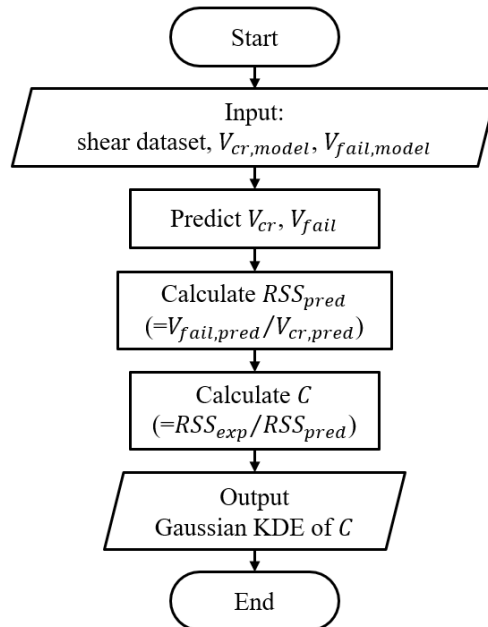


**Table 10.3. Statistical parameters of random variables.**

Random Variables	Distribution Type	Bias Factor	COV
$f'_c$	Normal	1.13	0.115
$f_{yt}$	Lognormal	1.13	0.03
$f_{pu}$ ( $f_{pc}$ )	Lognormal	1.04	0.017
$b_w$	Normal	1.01	0.04
$d$	Normal	1.00	0.025
$a$	Deterministic Value		
$A_v$	Normal	1.00	0.015
$s$	Normal	1.00	0.07
$C$	Gaussian Kernel Density Estimation		

#### 10.2.2.2 Evaluation of Model Uncertainty, $C$

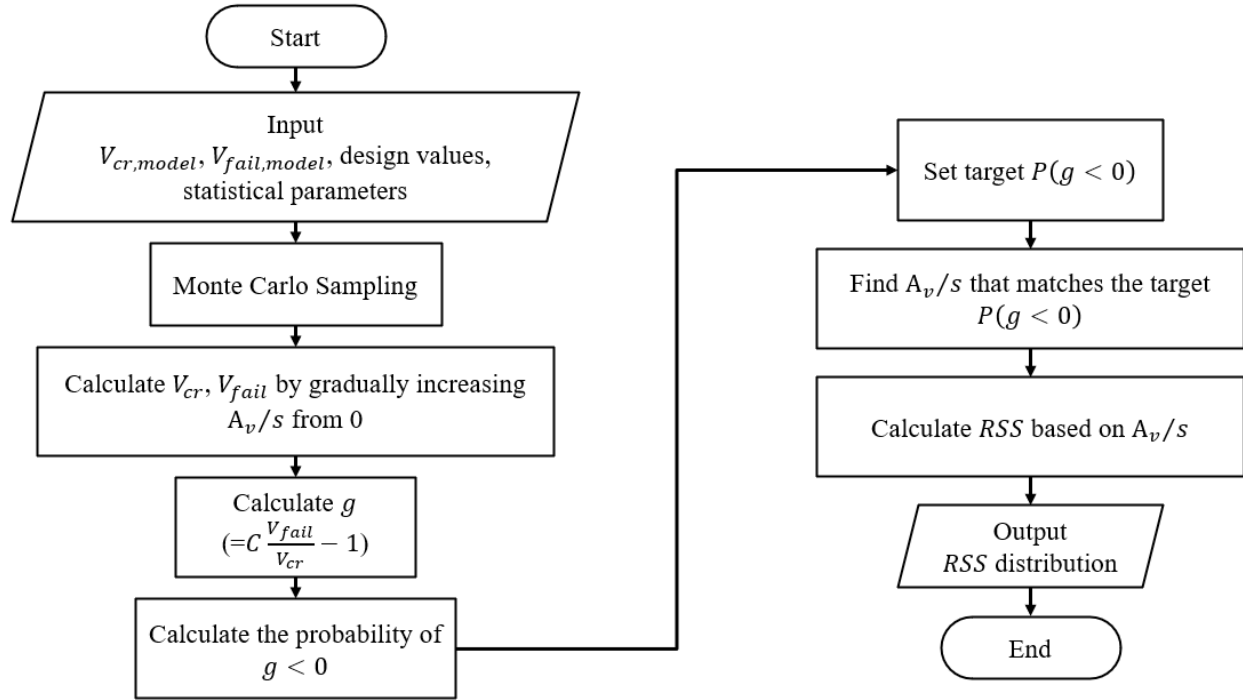
By definition, the uncertainty factor  $C$  is given as  $C = RSS_{true}/RSS_{model}$ . The  $RSS_{true}$  is herein taken as equal to that quantified by the experimental data ( $RSS_{true} = RSS_{exp}$ ). Thus, using the experimental dataset,  $C$  can be calculated as  $C = RSS_{exp}/RSS_{model}$ , for each of the test specimens of the database. Subsequently, either a predefined distribution (e.g., normal, lognormal, or Weibull) can be fitted or a kernel density estimation (KDE) can be used, which is more flexible for data following distributions that may deviate from commonly used probability density functions. This process is shown in the flowchart of Figure 10.12.

**Figure 10.12. Model uncertainty evaluation flowchart.**

### 10.2.2.3 *Proposed Reliability Methodology for RSS*

The proposed reliability analysis method begins with (Step 1) adopting a model for  $RSS_{\text{model}}$  (i.e., models for  $V_{\text{cr}}$  and  $V_{\text{fail}}$ ) and estimating the statistics of all random variables in these models, including estimating the statistics of  $C$ . Subsequently, a ***design space*** is defined (Step 2), which is a set of girder designs that are representative of the applications of interest. Because the focus of this work is on bridges in Texas, girder designs referring to TxDOT sections are primarily used herein. In Step 3, for each girder design, Monte Carlo sampling is employed to sample all random variables, and values of  $g$  are subsequently produced for incrementally increasing shear reinforcement ratios,  $A_v/s$ , starting at zero. The realizations for each  $A_v/s$  are used to produce probabilities of  $g < 0$  for each  $A_v/s$ , thus producing a curve of  $P(g < 0)$  versus  $A_v/s$  for each girder design. In Step 4, an acceptable value for  $P(g < 0)$  is selected, and for this value, a corresponding  $A_v/s$  is obtained for each girder. This  $A_v/s$  is then used to calculate an RSS value ( $= RSS_{\text{model}}$ ) for each girder design using the model equations for  $V_{\text{cr}}$  and  $V_{\text{fail}}$ . Following calculation of the RSS values for all girder designs, a distribution is produced, and a decision is made on the adopted RSS value. The adopted RSS value may be the maximum value of all produced values or a selected percentile of the distribution. The adopted RSS value is then used to obtain an equation for the minimum shear reinforcement ratio by solving the equation  $RSS = V_{\text{fail}}/V_{\text{cr}}$  with respect to  $A_v/s$ , which now represents the minimum shear reinforcement ratio.

The proposed reliability analysis is depicted in a flowchart in Figure 10.13.



**Figure 10.13. Reliability analysis flowchart.**

### 10.2.3 Implementation of Proposed Reliability Analysis Method

A reliability analysis was conducted to compare the simplified regression model of Equations (10.9) and (10.10) to a simplified version of the model of the AASHTO LRFD standard that has most likely resulted in the current minimum shear reinforcement ratio. The equations for the analysis are:

$$V_{cr,model} = V_c = 0.0316\beta\sqrt{f'_c}b_vd_v \quad (10.14)$$

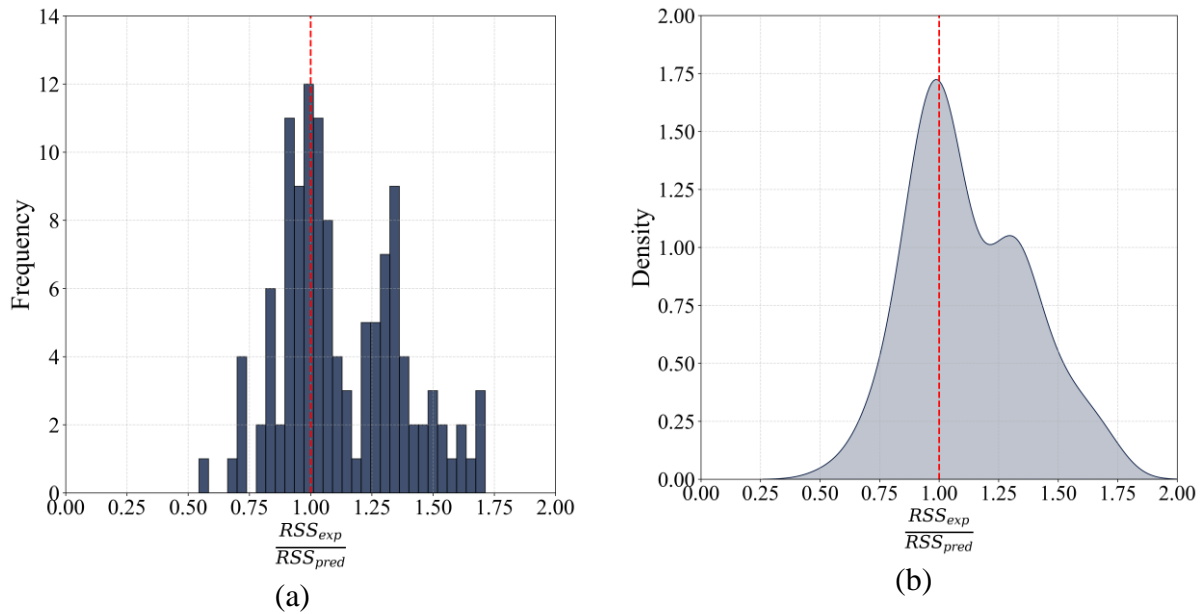
$$V_{fail,model} = V_n = V_c + V_s = 0.0316\beta\sqrt{f'_c}b_vd_v + \frac{A_vf_yd_v}{s}\cot\theta \quad (10.15)$$

where  $\beta$  and  $\theta$  are given as 5.8 and 28.5, respectively.

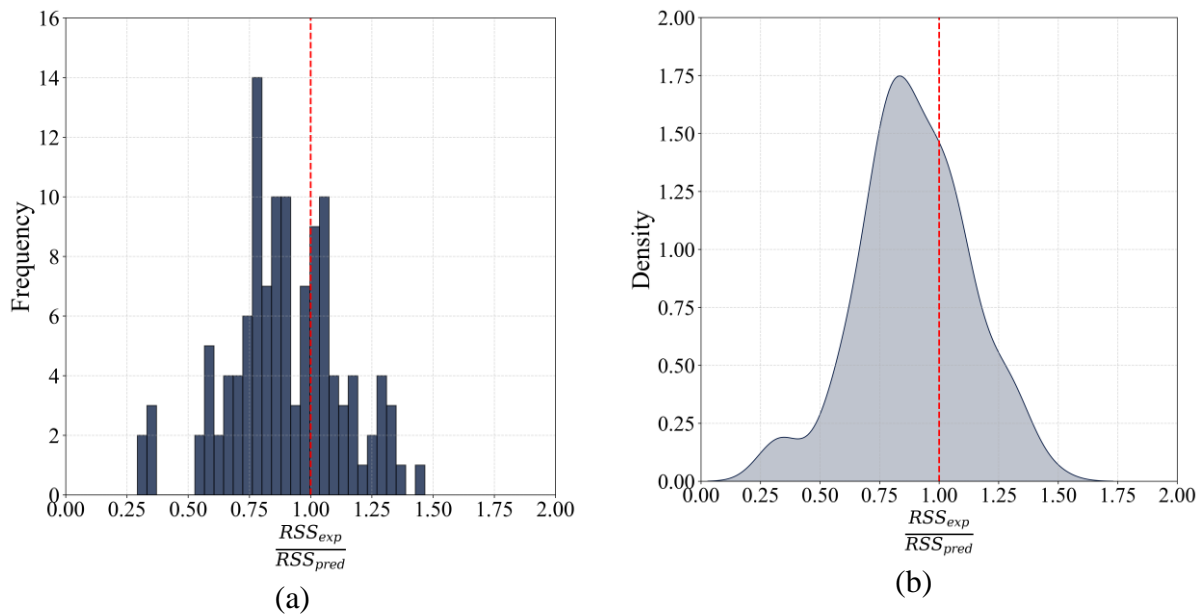
For Step 1, the distribution of the uncertainty factor  $C$  in the simplified regression model of Equations (10.9) and (10.10) and in the model of the AASHTO LRFD standard is shown in Figure 10.14 and Figure 10.15, respectively. As shown,  $C$  for the simplified regression model clusters around 1, with a significant number of values also between 1.25 and 1.5 (see Figure 10.14[a]), which results in a somewhat bimodal distribution (see Figure 10.14[b]).

Conversely,  $C$  for the simplified AASHTO LRFD model is centered around 0.8 and is skewed to the left (Figure 10.15).

For Step 2, a design space was produced consisting of a set of 50 girder designs referring to TxDOT sections (see Table 10.4).



**Figure 10.14. Simplified explicit model: (a) histogram of  $C$ , (b) Gaussian KDE of  $C$ .**



**Figure 10.15. AASHTO LRFD model: (a) histogram of  $C$ , (b) Gaussian KDE of  $C$ .**

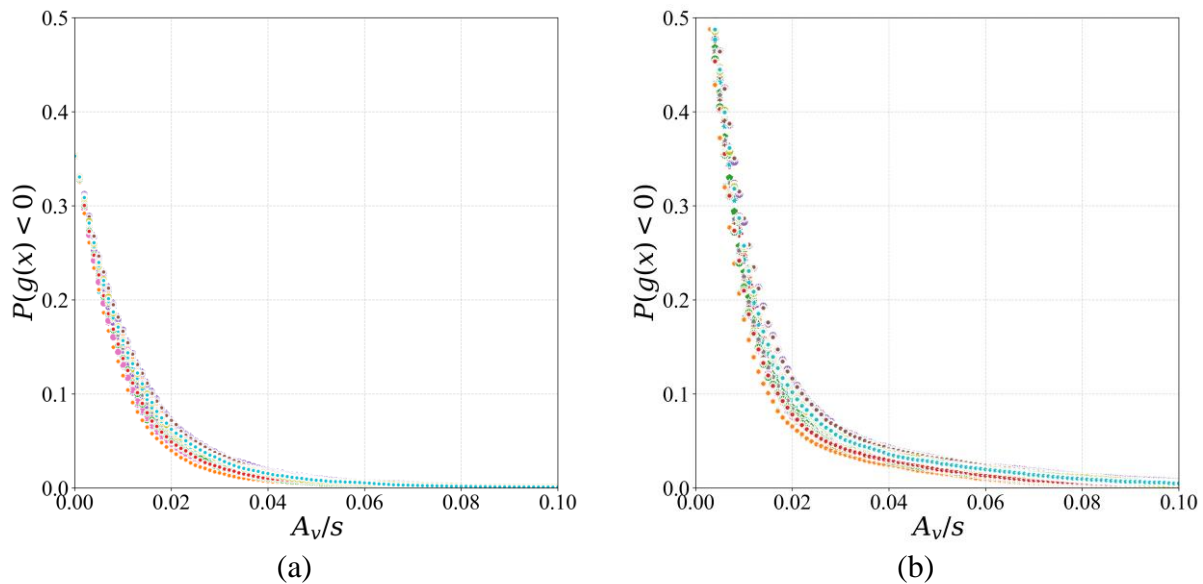
**Table 10.4. Design values based on TxDOT girders.**

No.	Girder Type	$f'_c$ (psi)	$f_{yt}$ (ksi)	$f_{pc}$ (ksi)	$b_w$ (in.)	$d$ (in.)	$d_v$ (in.)	$a$ (in.)
1	Tx 28	7000	60	1457	7	34.5	32.04	420
2	Tx 28	5000	60	826	7	34.00	32.74	300
3	Tx 28	5000	60	826	7	34.00	32.74	300
4	Tx 28	6300	60	1117	7	33.40	31.62	360
5	Tx 34	6600	60	1482	7	40.3	37.66	480
6	Tx 34	5000	60	880	7	39.75	38.31	360
7	Tx 34	5000	60	880	7	39.75	38.31	360
8	Tx 34	5700	60	1147	7	39.27	37.31	420
9	Tx 40	6800	60	1569	7	45.9	42.98	570
10	Tx 40	5000	60	834	7	45.75	44.31	390
11	Tx 40	5000	60	834	7	45.75	44.31	390
12	Tx 40	5400	60	1173	7	45.17	43.03	480
13	Tx 46	6300	60	1565	7	51.7	48.36	630
14	Tx 46	5000	60	753	7	51.75	50.30	420
15	Tx 46	5000	60	753	7	51.75	50.30	420
16	Tx 46	5100	60	1209	7	51.00	48.51	540
17	Tx 54	7100	60	1726	7	59.1	55.11	750
18	Tx 54	5000	60	780	7	59.56	57.93	450
19	Tx 54	5000	60	780	7	59.56	57.93	450
20	Tx 54	5000	60	1150	7	59.00	56.49	600
21*	Tx 54	7000	60	1289	7	57.38	51.58	155
22*	Tx 54	7000	80	1289	7	57.38	51.58	155
23*	Tx 54	7000	60	1289	7	47.38	42.64	128
24*	Tx 54	7000	80	1289	7	47.38	42.64	128
25*	Tx 54	7000	60	1289	7	47.38	42.64	128
26*	Tx 54	7000	60	1289	7	47.38	42.64	128
27*	Tx 54	7000	60	1289	7	47.38	42.64	128
28*	Tx 54	7000	60	1289	7	47.38	42.64	128
29*	Tx 54	7000	60	1289	7	47.38	42.64	107
30*	Tx 54	7000	60	1289	7	47.38	42.64	107
31*	Tx 54	7000	60	1066	7	47.04	42.33	127
32*	Tx 54	7000	60	1066	7	47.04	42.33	127
33*	Tx 54	7000	60	1487	7	45.3	40.77	122
34*	Tx 54	7000	60	1487	7	45.3	40.77	122
35*	Tx 54	5000	60	983	7	46.83	42.15	126
36*	Tx 54	5000	60	983	7	46.83	42.15	126
37*	Tx 54	8500	60	1386	7	47.39	42.66	128
38*	Tx 54	8500	60	1386	7	47.39	42.66	128
39*	Tx 54	7000	60	1289	7	47.38	42.64	171
40*	Tx 54	7000	60	1289	7	47.38	42.64	171
41	Tx 62	6400	60	1587	7	67.1	63.09	810
42	Tx 62	5000	60	792	7	67.40	65.59	570

No.	Girder Type	$f'_c$ (psi)	$f_{yt}$ (ksi)	$f_{pc}$ (ksi)	$b_w$ (in.)	$d$ (in.)	$d_v$ (in.)	$a$ (in.)
43	Tx 62	5000	60	792	7	67.40	65.59	570
44	Tx 62	5000	60	1228	7	66.47	63.43	690
45	Tx 70	7100	60	1492	7	75.2	71.07	870
46	Tx 70	5000	60	796	7	75.27	73.28	630
47	Tx 70	5000	60	796	7	75.27	73.28	630
48	Tx 70	5500	60	1207	7	73.25	70.03	750
49*	Tx 70	7000	60	1226	7	62.6	56.34	169
50*	Tx 70	7000	60	1226	7	62.6	56.34	169

\*Experimental girder specimens.

In Step 3, using Monte Carlo simulations, curves of  $P(g < 0)$  versus  $A_v/s$  were produced (one curve per girder design per model). As expected,  $P(g < 0)$  decreases as  $A_v/s$  increases. Also, for the same  $A_v/s$ , the simplified regression model produces lower  $P(g < 0)$  than the simplified AASHTO LRFD model.



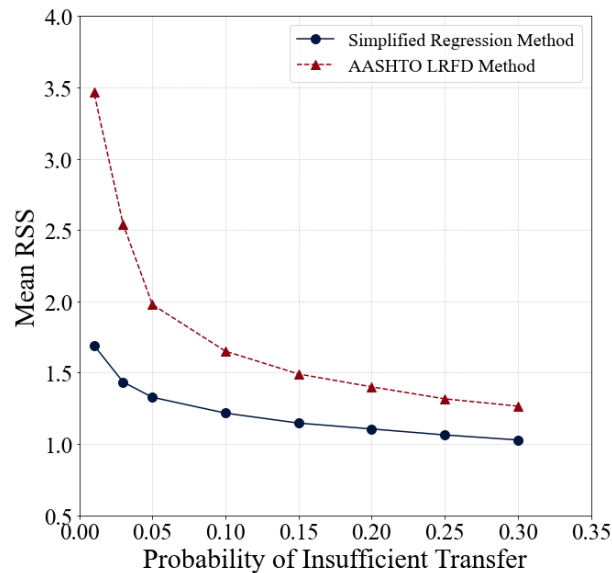
**Figure 10.16. Curves of  $P(g < 0)$  versus  $A_v/s$  for all girder designs, using the (a) simplified regression model, and (b) simplified AASHTO LRFD model.**

In step 4, specific probabilities were selected to calculate the corresponding RSS index values. To observe the trend of RSS index variation with changes in probability, probabilities of 30%, 25%, 20%, 15%, 10%, 5%, 3%, and 1% were chosen, and the RSS index values were calculated accordingly. The Table 10.5 presents the mean, standard deviation, coefficient of variation

(COV), as well as the minimum and maximum values of RSS for both the Simplified Regression Method and the AASHTO LRFD Method. For both Simplified Regression Method and the AASHTO LRFD Method, as the probability of insufficient transfer (probability of the limit state function being lower than 0), the mean RSS increased. The  $\beta$ , reliability index are also described for each  $P(g < 0)$ . Figure 10.17 describes the trend of RSS index change based on the probability of insufficient transfer.

**Table 10.5. Statistical parameter for RSS based on target  $P(g < 0)$**

$P(g < 0)$	$\beta$	Simplified Regression Method					AASHTO LRFD Method				
		Mean	Std.	COV	Min.	Max	Mean	Std.	COV	Min.	Max
30%	0.52	1.029	0.003	0.0029	1.024	1.035	1.266	0.006	0.0047	1.257	1.289
25%	0.67	1.064	0.004	0.0038	1.053	1.068	1.317	0.010	0.0076	1.304	1.335
20%	0.84	1.106	0.005	0.0045	1.098	1.115	1.401	0.015	0.0107	1.385	1.424
15%	1.04	1.147	0.003	0.0026	1.141	1.152	1.491	0.009	0.0060	1.469	1.505
10%	1.28	1.217	0.003	0.0025	1.211	1.224	1.651	0.006	0.0036	1.624	1.661
5%	1.64	1.328	0.004	0.0030	1.321	1.338	1.978	0.014	0.0071	1.961	12.002
3%	1.88	1.435	0.004	0.0028	1.426	1.446	2.542	0.021	0.0083	2.502	2.595
1%	2.33	1.693	0.007	0.0041	1.678	1.710	3.468	0.034	0.0098	3.403	3.542



**Figure 10.17.  $P(g < 0)$  vs Mean RSS index**

Two probabilities are selected:  $P(g < 0) = 25$  percent and  $P(g < 0) = 5$  percent. The resulting statistics of the calculated RSS values are shown in Table 10.6 and Table 10.7 for the 25 percent and 5 percent probabilities, respectively. It is observed that the COV in RSS is less than 1 percent (or even less than 0.5 percent), and the difference between maximum and minimum RSS values vary only in the second decimal.

For  $P(g < 0) = 25$  percent, the RSS for the simplified AASHTO LRFD model is about 1.34, and thus very close to the implicitly assumed RSS ( $\sim 1.3$  to  $1.33$ ) within the minimum shear reinforcement ratio of AASHTO LRFD. This design resulted in  $s/d$  in the order of 40 in. (see Figure 10.18), which implies that once the maximum spacing requirements of AASHTO LRFD are implemented, the resulting  $P(g < 0)$  will reduce to 10 percent or lower. For  $P(g < 0) = 25$  percent, the RSS for the simplified regression model is about 1.06, which results in very large  $s/d$ s (see Figure 10.18). The much lower RSS value for the simplified regression model is because of its much higher accuracy in comparison to the simplified AASHTO LRFD model, which significantly underestimates RSS (with mean  $C$  of about 0.8, i.e., far from unity).

For  $P(g < 0) = 5$  percent, the RSS for the simplified regression model is about 1.33, whereas the RSS of the simplified AASHTO LRFD model is about 2, that is, much larger due to the much lower accuracy of the simplified AASHTO LRFD model. The resulting  $s/d$  (Figure 10.19) is between 15 and 20 in. for the simplified regression model and between 10 and 15 in. for the simplified AASHTO LRFD model, implying that a tighter spacing is needed for the same level  $P(g < 0)$  when the simplified AASHTO LRFD model is used due to its much lower accuracy.

It may seem that the values of  $P(g < 0)$  of 5 percent (and 25 percent) are large compared to the much lower acceptable probability limits of 0.01 percent typically used in structural reliability studies. However, it should be clarified that  $P(g < 0)$  does not strictly represent a probability of failure of the girder because it does not include exposure effects, that is, the probability of the applied load reaching certain magnitudes. In fact, minimum shear reinforcement is used in regions of low loading demands.

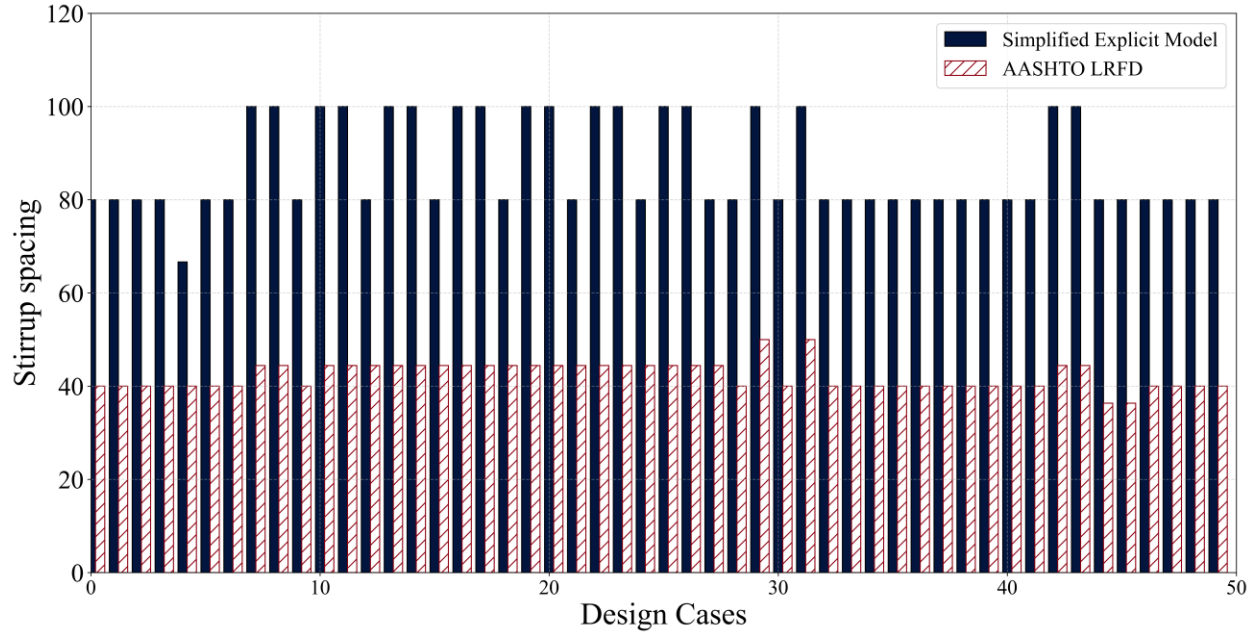
**Table 10.6. Statistical parameter for RSS when  $P(g < 0) = 0.25$ .**

Model Type	Mean	Std.	COV	Min.	Max.
<b>Simplified Regression</b>	1.064	0.004	0.0038	1.053	1.068
<b>AASHTO LRFD</b>	1.317	0.01	0.0076	1.304	1.335

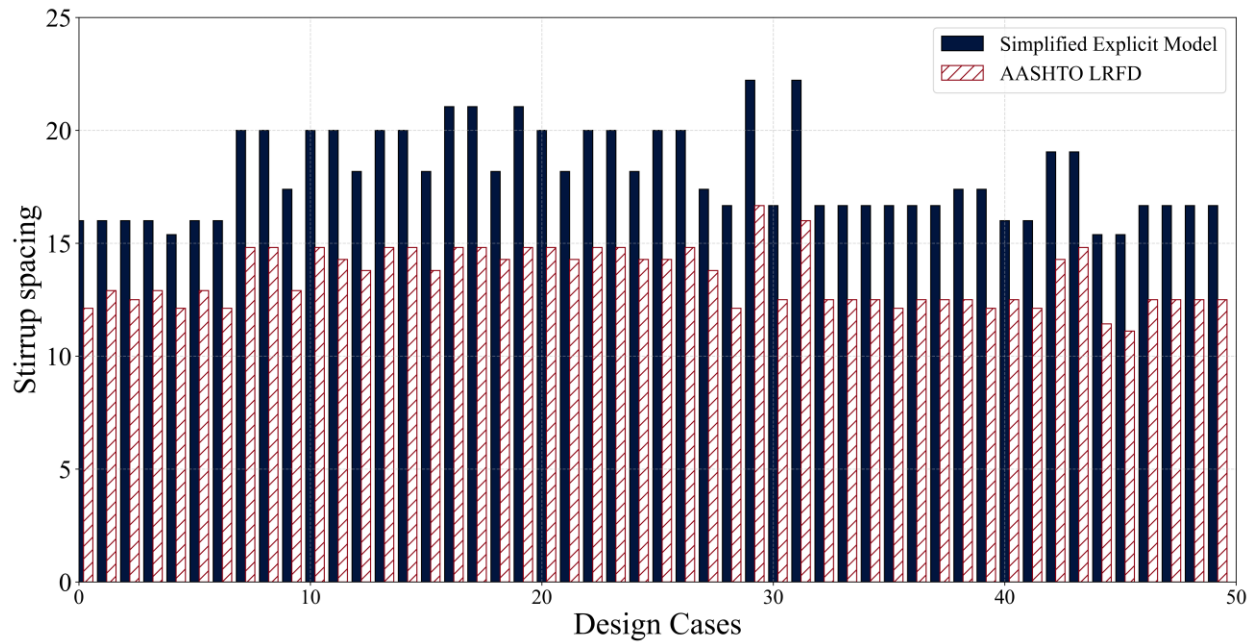
**Table 10.7. Statistical parameter for RSS when  $P(g < 0) = 0.05$ .**

Model Type	Mean	Std.	COV	Min.	Max.
<b>Simplified Regression</b>	1.328	0.004	0.003	1.321	1.338
<b>AASHTO LRFD</b>	1.978	0.014	0.007	1.961	2.002





**Figure 10.18. Stirrup spacing ( $A_v = 0.4 \text{ in}^2$ ) when  $P(g < 0) = 0.25$ .**



**Figure 10.19. Stirrup spacing ( $A_v = 0.4 \text{ in}^2$ ) when  $P(g < 0) = 0.05$ .**

### 10.3 SUMMARY

This chapter focused on developing and refining dataset-based models to predict shear capacity and assess the reliability of proposed design guidelines. Initially, earlier models developed through nonlinear regression and GP that predicted shear force at the onset of diagonal cracking

and shear failure were revisited. Despite their high accuracy, discrepancies were noted in the RSS index calculated from these predictions. To address these discrepancies, refinements to the nonlinear optimization techniques were implemented. The nonlinear optimization process was enhanced by minimizing a loss function that accounted for shear strength at the onset of diagonal cracking, shear strength at shear failure, and the RSS index. This process included filtering data to better align with the actual types of girders used by TxDOT and excluding data with section heights less than 15 in., significantly improving the model's predictive performance for real-world applications. Also, error weighting and inequality constraints were introduced to improve solution accuracy. A comprehensive regression model and a simplified regression model was developed, with both exhibiting reasonable accuracy

Furthermore, a reliability analysis method was developed to determine RSS values that achieve prescribed probabilities of insufficient transfer of a proposed limit state. The reliability analysis accounted for uncertainties in all design parameters and in the model accuracy and precision. The results indicated that the simplified regression model and the equations of AASHTO represent very different probabilities if they use the same RSS. In fact, the AASHTO minimum shear reinforcement ratio equation required an RSS of about 2 to achieve the same probability as that of the simplified regression model for an RSS of about 1.33. Application of both models showed that the simplified regression model can provide larger stirrups spacings, thus leading to more economical designs. However, the spacings still need to ensure that the shear cracks are intercepted by at least two stirrups for safe transfer.

## **CHAPTER 11:**

### **DESIGN GUIDELINES FOR MINIMUM SHEAR REINFORCEMENT**

The key objective of this research is to evaluate existing provisions for minimum shear reinforcement and further provide design guidelines and recommendations. This chapter details the evaluation of minimum shear reinforcement from different codes of practice and compares them in terms of spacing for potential TxDOT I-girders. Based on these selected design prototypes, the spacing provisions are compared along with the proposed design guidelines. The proposed design guidelines involve two aspects: minimum shear reinforcement ratio and maximum spacing. The chapter summarizes the prototype girders selected, evaluation of provisions, and development of the proposed guidelines.

#### **11.1 PROTOTYPE GIRDERS**

For the evaluation of the code provisions and proposed guidelines, the prototype girders need to be selected that are designed based on *TxDOT Bridge Design Manual LRFD* and *AASHTO LRFD Bridge Design Specifications*. The selected girders should satisfy all steps and stress checks that are involved in the design of bridge girders. The key variation is at the transverse shear design where the shear reinforcement spacing is enforced with the reinforcement limits.

The bridge selected for this prototype is a 44 ft roadway span with varying span length based on the size of the girder. As a part of the evaluation, the different girder sizes in TxDOT I-girders ranging from Tx28 to Tx70 are designed to have a comprehensive overview of the spacing limits. The span length of I-girders for TxDOT LRFD are selected based on the recommended economic span limit for each girder size (TxDOT 2023). The economic span lengths are shown in Table 11.1.

**Table 11.1. Economic span lengths of TxDOT I-girders.**

Beam Type	Beam Depth (in.)	Economic Span (ft)
Tx28	28	70
Tx34	34	80
Tx40	40	95
Tx46	46	105
Tx54	54	125
Tx62	62	135
Tx70	70	145

These girders are designed based on the *TxDOT Bridge Design Manual* (TxDOT 2023) and AASHTO (2020). The design steps are also detailed in the design guidelines document of this research (FHWA/Tx-24/0-7114-P1). Table 11.2 summarizes some of the key design values for these girders.

**Table 11.2. Design parameters of economical span TxDOT I-girders.**

Girder	Length (ft)	$f'_{ci}$ (ksi)	$f'_c$ (ksi)	$f'_{yt}$ (ksi)	# of strands	Harped tendons	$h_{Harp}$ (in.)	$a/d_v$	$d_v$ (in.)	$f_{pc}/f'_c$ (%)
Tx28	70	5.6	7	60	28	Yes (4)	24.5	13.1	32.0	20.82
Tx34	80	5.9	6.6	60	30	Yes (6)	28.5	12.7	37.6	22.46
Tx40	95	5.8	6.8	60	34	Yes (6)	28.5	13.2	42.9	23.07
Tx46	105	5.5	6.3	60	38	Yes (6)	38.5	13.0	48.3	24.84
Tx54	125	5.8	7.1	60	46	Yes (8)	50.5	13.6	55.1	24.31
Tx62	135	5.5	6.4	60	46	Yes (8)	58.5	12.8	63.0	24.79
Tx70	145	5.8	7.1	60	46	Yes (8)	66.5	12.2	71.0	21.01

For these girders, the minimum shear reinforcement from different provisions is computed and compared to give a comparative understanding.

## 11.2 EVALUATION OF EXISTING PROVISIONS

The design of these girders includes the step for minimum shear reinforcement ratio and maximum spacing from AASHTO Bridge Design LRFD specifications. In addition, the minimum shear reinforcement and maximum spacing provisions from ACI 318-19 (2019) are also calculated. Furthermore, the spacing provided by TxDOT standard drawings is also compared over the span of the girder for a comprehensive understanding. The abovementioned provisions are detailed in Section 2.6 of this report.

Table 11.3 shows a comparison of spacing from these different provisions for the economical span lengths of the girders at an  $x/L$  of 0.35, which typically has very low shear demand from the stirrups. This  $x/L$  is typically governed by the minimum shear reinforcement provisions. The spacings are computed by selecting the R-bars for stirrups, which are #4 Grade 60 steel bars typically used in TxDOT girders.

**Table 11.3. Comparison of minimum shear spacing from different provisions.**

Girder	Length (ft)	$f'_c$ (ksi)	# of strands	TxDOT drawings	AASHTO		ACI	
					Spacing from $\frac{A_v}{s} \Big _{\min}$	Max. spacing	Spacing from $\frac{A_v}{s} \Big _{\min}$	Max. spacing
Tx28	70	7	28 (4)	12	41.01	24	16.0	30.8
Tx34	80	6.6	30 (6)	12	42.23	24	16.7	26.7
Tx40	95	6.8	34 (6)	18	41.61	24	16.0	24
Tx46	105	6.3	38 (6)	18	43.23	24	14.8	24
Tx54	125	7.1	46 (8)	18	40.72	24	13.8	24
Tx62	135	6.4	46 (8)	18	42.88	24	14.3	24
Tx70	145	7.1	46 (8)	18	40.72	24	15.4	24

Based on earlier calculations, the significant difference between AASHTO and ACI minimum shear equations is the absence of contribution of prestressing in the AASHTO minimum shear provision. However, the ACI equations tend to recommend closer spacing values for deeper

girders, which can be seen to have higher RSS for wider spacings because of the size effects. The maximum spacing provision from AASHTO does not vary as the girder depth varies, and a similar trend is observed in ACI maximum spacing calculations as well. Thus, the maximum spacing provision can also be redefined based on higher RSS observed during the experimental study due to spacing from geometric constraints. Therefore, new design guidelines are proposed in terms of both minimum shear reinforcement ratio and maximum spacing to incorporate the effects of various factors along with uncertainties associated with them by reliability analysis, as described in Chapter 10.

### **11.3 PROPOSED DESIGN GUIDELINES**

In addition to the minimum shear reinforcement limits in the previous step for transverse shear design of the girder, the proposed guidelines will be appended to this step. The proposed guidelines for minimum shear reinforcement include two aspects: minimum shear reinforcement ratio and maximum spacing limits. Based on a selected bar for stirrups resulting in the area of shear reinforcement, the spacing from the minimum shear reinforcement ratio can be calculated and finally compared to the maximum spacing limits. The proposed guidelines are summarized below.

#### **11.3.1 Recommendation on Minimum Shear Reinforcement Ratio**

The proposed guidelines involve two strategies for the minimum shear reinforcement ratio based on reliability analysis with RSS, as discussed in Chapter 9 of this report. The strategies are summarized below.

##### ***11.3.1.1 Strategy 1: Minimum Shear Reinforcement Ratio Derived from Mechanics-Informed Data-Driven Model***

Based on the data analysis, the explicit form is developed for nominal shear strength and cracking shear strength of the beams. Using the explicit equations, the RSS-based minimum shear reinforcement ratio is computed as shown below:

$$\frac{A_v}{s} \Big|_{\min} = (C_{cr} \cdot \text{RSS} - C_u) \frac{\sqrt{f'_c} b_w}{1000 f_{yt}} \quad (11.1)$$

where:

$C_{cr}$  = Shear coefficient at onset of diagonal cracking =  $C_{cr,1} + C_{cr,2}$

RSS = Reserve shear strength index

$C_u$  = Shear coefficient at shear failure =  $C_{u,1} + C_{u,2}$

The shear coefficients include the effect of geometric, material, and prestressing components and are calculated as follows.

Contribution of geometric and material properties at diagonal cracking:

$$C_{cr,1} = 98.5 \left( \frac{1}{1 + \frac{a}{d}} \right)^{10.25} \left( \frac{f'_c(\text{psi})}{5000\text{psi}} \right)^{6.39} \quad (11.2)$$

Contribution of prestressing at diagonal cracking:

$$C_{cr,2} = 11.71 \left( \frac{f_{pc}}{f'_c} \right)^{0.26} \quad (11.3)$$

Contribution of geometric and material properties at ultimate shear failure:

$$C_{u,1} = 1.93 \left( \frac{1}{1 + \frac{d}{10}} \right)^{9.99} \left( \frac{1}{1 + \frac{a}{d}} \right)^{4.9} \left( \frac{f'_c(\text{psi})}{5000\text{psi}} \right)^{2.61} (1 + \rho_w^{1.81}) \quad (11.4)$$

Contribution of prestressing at ultimate shear failure:

$$C_{u,2} = 11.71 \left( \frac{f_{pc}}{f'_c} \right)^{0.26} \quad (11.5)$$

The RSS is selected as 1.33 for this model, giving a probability of insufficient transfer of 5.1 percent, as opposed to the AASHTO minimum shear equation, which, when yielding a

similar RSS, has a probability of 25 percent. However, the RSS can be varied for this model upon selection of an acceptable probability of insufficient transfer.

#### 11.3.1.2 Strategy 2: Minimum Shear Reinforcement Ratio Derived from Reliability Analysis of AASHTO Equations

This strategy is developed similarly to the previous strategy, with shear strength capacities taken from AASHTO LRFD equations. The RSS is selected to be 1.998~2 for the same probability of insufficient transfer of 5.1 percent for the explicit form via data analysis. The shear strength capacities are taken from AASHTO, where  $V_{cr}$  is taken as contribution of concrete  $V_c$ , and  $V_{fail}$  is taken as the nominal shear strength  $V_n$ . Now, the RSS equation becomes:

$$RSS = \frac{V_{fail}}{V_{cr}} = \frac{V_n}{V_c} = \frac{V_c + V_s}{V_c} \quad (11.6)$$

Using the contribution of stirrups  $V_s$  from AASHTO, the minimum shear reinforcement ratio can be calculated as follows:

$$\left. \frac{A_v}{s} \right|_{min} = (RSS - 1) \frac{\beta}{(\cot\theta)} 0.0316\lambda \frac{\sqrt{f'_c} b_v}{f_y} \quad (11.7)$$

where:

- $\lambda$  = Concrete density modification factor
- = 1 for normal weight concrete

The minimum shear reinforcement ratio is calculated by selecting the RSS based on the reliability analysis of the equation, which is 2.

### 11.3.2 Recommendation on Maximum Stirrup Spacing

In addition to the computation of the minimum shear reinforcement ratio, the code provisions also include maximum spacing limits to ensure an appropriate number of stirrups intercepting the cracks. For TxDOT girders, the  $A_v$  is 0.4 in<sup>2</sup> for R-bars, and the spacing from the proposed minimum shear reinforcement ratio guidelines is calculated. The next step is to compare this spacing with the maximum spacing limits. The maximum spacing is determined using geometric



properties such that each diagonal crack is intercepted by a minimum of two stirrups. This research study investigated with a geometric based spacing of  $h_w/2 \tan \theta$ , which showed adequate RSS (more than 1.3) from the experiments. However, for more reliable design, the geometric constraint is updated based on two stirrups crossing the diagonal crack over the span of effective shear depth. In addition, the geometric constraint is appended with an upperbound of maximum spacing from AASHTO LRFD provision to avoid recommending tighter spacings for smaller depth girders. The resulting maximum spacing provision becomes:

$$s_{\max} = \max\left(\frac{d_v}{4 \tan \theta}, s_{\max, \text{AASHTO}}\right) \quad (11.8)$$

The angle of compression diagonal stresses,  $\theta$ , is computed using an iterative method based on AASHTO LRFD provisions.

### 11.3.3 Comparison of Proposed Guidelines with Existing Provisions

For the selected prototype girders, the minimum shear reinforcement provisions were evaluated in earlier Section 11.2. Now, these provisions are herein compared with the proposed guidelines to have a detailed understanding in terms of spacing. The AASHTO minimum shear equation, when compared to an RSS-based approach, results in the following equation:

$$\begin{aligned} \text{RSS} = \frac{V_{\text{fail}}}{V_{\text{cr}}} = \frac{V_n}{V_c} \Rightarrow V_s &= (\text{RSS} - 1)V_c \Rightarrow \frac{A_v f_y d_v (\cot \theta)}{s} \\ &= (\text{RSS} - 1) 0.0316 \beta \sqrt{f'_c} b_v d_v \end{aligned} \quad (11.9)$$

The resulting shear reinforcement ratio will be:

$$\frac{A_v}{s} = (\text{RSS} - 1) \frac{\beta}{(\cot \theta)} 0.0316 \frac{\sqrt{f'_c} b_v}{f_y} \quad (11.10)$$

When this equation is compared to the AASHTO minimum shear reinforcement equation, we obtain the RSS in terms of  $\beta$  and  $\theta$ :

$$\frac{A_v}{s} \geq 0.0316\sqrt{f'_c} \frac{b_v}{f_y} \Rightarrow \text{RSS} = 1 + \frac{(\cot\theta)}{\beta} \quad (11.11)$$

The typical range of  $(\cot\theta)/\beta$  for the prototype girders is 0.3–0.33 in the minimum shear reinforcement zone, putting the RSS in the range of 1.3–1.33. When considering this as the target RSS for the AASHTO minimum shear reinforcement equation, the reliability analysis resulted in a probability of insufficient transfer of 24.89 percent. However, using the simplified regression model proposed with a similar target RSS of 1.33, the probability of insufficient transfer is 5.1 percent. Based on this strategy, RSS for AASHTO capacity-based methods is computed for the same probability, resulting in an RSS of 2 for AASHTO capacity-based strategy. The comparison of proposed guidelines can be seen in Table 11.4.

**Table 11.4. Comparison of minimum shear spacing from proposed guidelines.**

<b>Girder</b>	<b>Current AASHTO</b>		<b>ACI</b>		<b>Simplified Regression Model</b>	<b>Modified AASHTO Model</b>	$\frac{d_v}{4 \tan \theta}$
	<b>Spacing from <math>\frac{A_v}{s} \Big _{\min}</math></b>	<b>Max. spacing</b>	<b>Spacing from <math>\frac{A_v}{s} \Big _{\min}</math></b>	<b>Max. spacing</b>	<b>Spacing from <math>\frac{A_v}{s} \Big _{\min}</math> with RSS = 1.33 (PoF = 5.1%)</b>	<b>Spacing from <math>\frac{A_v}{s} \Big _{\min}</math> with RSS = 2 (PoF = 5.1%)</b>	<b>Max. spacing</b>
Tx28	41.01	24	16.00	21	15.89	15.70	13.82
Tx34	42.23	24	16.67	24	16.09	16.17	16.36
Tx40	41.61	24	16.00	24	15.84	16.98	18.54
Tx46	43.23	24	14.81	24	16.04	16.48	21.21
Tx54	40.72	24	13.79	24	15.20	15.29	24.33
Tx62	42.88	24	14.29	24	15.93	16.32	27.87
Tx70	40.72	24	15.38	24	15.79	15.94	31.17

## 11.4 SUMMARY

This chapter summarizes the evaluation's existing provisions for minimum shear reinforcement and develops enhanced design guidelines and recommendations. The study compares spacing requirements from various codes of practice for potential TxDOT I-girders, selecting prototype girders based on the *TxDOT Bridge Design Manual LRFD* and AASHTO LRFD specifications.

Different TxDOT I-girder sizes (Tx28 to Tx70) with economic span lengths ranging from 70 to 145 ft are evaluated to provide a comprehensive overview of shear reinforcement spacing limits. The analysis reveals notable differences in minimum shear reinforcement and maximum spacing among TxDOT design manual, AASHTO LRFD specification, and ACI design code, with ACI requiring closer spacing for deeper girders due to size effects and AASHTO not accounting for prestressing effects.

The proposed design guidelines focus on two main aspects: the minimum shear reinforcement ratio and the maximum spacing limits. The evaluation highlights that ACI equations recommend closer spacing values for deeper girders, while AASHTO's provisions remain constant regardless of girder depth. To address the various influencing factors and uncertainties identified through reliability analysis, new design guidelines incorporating minimum shear reinforcement ratios and maximum spacing are proposed. The guidelines employ two strategies: one using an equation developed from data analysis and the other using AASHTO LRFD equations; both consider geometric, material, and prestressing components to ensure reliable and safe girder designs.

After calculating the minimum shear reinforcement ratio, maximum spacing limits are applied to ensure sufficient stirrups intercept cracks. For TxDOT girders, the proposed guidelines calculate spacing for R-bars and compare it with geometrically determined maximum spacing to ensure each diagonal crack is intercepted by at least two stirrups. The updated maximum spacing provision involves computing the angle iteratively based on AASHTO LRFD provisions, ensuring a robust and comprehensive approach to shear reinforcement design in prestressed concrete girders.



## **CHAPTER 12:**

### **SUMMARY AND CONCLUSIONS**

This research report discusses the entire research project and all significant outcomes. The report details the comprehensive literature review that covers the theoretical foundations of shear failure in beams and emphasizes the necessity of minimum shear reinforcement. It examines failure modes, shear transfer mechanisms, shear strength models, factors influencing shear capacity, and current practices while summarizing experimental shear test data. Chapter 3 focuses on the development and analysis of an experimental test database on prestressed concrete beams, identifies gaps in the literature, and quantifies significant parameters. The full-scale experimental program detailed in Chapter 4 summarizes the setup, prototype design, and test matrix development. Chapter 5 covers the construction of test specimens. Chapters 6 and 7 present the experimental testing procedures and observations and highlight key comparisons of significant parameters influencing shear strength and minimum shear reinforcement.

Subsequent chapters further explore these experimental insights via advanced computational modeling. Chapter 8 describes an FE model development strategy and its validation against experimental data, as well as a parametric study that provides additional insights for girder designs beyond those used in the experimental program. Chapter 9 summarizes the key findings from both the experimental and computational studies. Chapter 10 develops a minimum shear reinforcement ratio equation by combining mechanics-based data-driven models and reliability analysis, while reliability analysis is further used to refine the minimum shear reinforcement ratio equation of AASHTO LRFD provisions. Chapter 11 focuses on the main objective of this study, providing design guidelines for minimum shear reinforcement by comparing various spacing provisions as applied to TxDOT girders. The final chapter, Chapter 12, synthesizes the major findings from each phase of the research, offering clear conclusions and practical recommendations for future applications in structural engineering. The appendix supports these conclusions with detailed drawings and instrumentation plans, ensuring the reproducibility and practical implementation of the experimental work conducted.

## **12.1 EVALUATION OF MINIMUM SHEAR REINFORCEMENT VIA LITERATURE REVIEW**

The literature review encompassed theoretical understanding of the shear failure modes and mechanisms of shear transfer, highlighting the key factors that affect shear capacity of girders and the importance of minimum shear reinforcement. This discussion is followed by evaluation of the minimum shear reinforcement provisions in various codes of practice and identification of key research studies that looked into development of these provisions. After identifying the key parameters affecting minimum shear reinforcement and an overview of the existing provisions, the research aimed to study the following research questions:

- What is the significance of different design parameters, such as geometric and material properties and reinforcing details, on minimum shear reinforcement requirements?
- Can existing experimental data be utilized to determine the minimum shear reinforcement requirements for TxDOT girders through data-driven methods?
- How are shear minimum reinforcement equations determined?
- How do code provisions account for uncertainty in minimum shear reinforcement requirements?
- How can minimum shear reinforcement provisions in current codes be revised based on girder performance?

Major findings of the literature review included:

1. The minimum shear reinforcement has been studied in previous research studies using experimental tests on reinforced and prestressed concrete beams. Based on various findings, the factors affecting minimum shear reinforcement are summarized into material, geometric, and prestressing design properties.
2. A key parameter that has been used in most code equations relating to minimum shear reinforcement ratios is the RSS, which quantifies the reserve strength in beams after the onset of diagonal shear cracking. The minimum shear reinforcement provisions in existing codes of practice, such as ACI318-19 (2019) and AASHTO (2020), have evolved over the years.

3. Surprisingly, the minimum shear reinforcement ratio equation in AASHTO (2020) does not account for prestressing effects, unlike ACI318-19 (2019), which does. In addition, in most practical designs, the maximum spacing provision always governs due to a very underestimated minimum shear reinforcement ratio in AASHTO.
4. The maximum  $s/d$  in TxDOT standard practice is 12 in. for Tx28 and Tx 34 and 18 in. for all the other (larger) I-girders in the minimum shear reinforcement zone. DOTs in several states follow the AASHTO provisions for minimum shear reinforcement. Consequently, potential improvements in these minimum shear reinforcement provisions, such as accounting for all major factors affecting shear behavior, can be beneficial to TxDOT and other state DOTs.

## 12.2 DATABASE DEVELOPMENT

In this study, a comprehensive database of shear tests for prestressed concrete beams was meticulously developed to support the research objectives. The development process involved several critical steps to ensure the database was both extensive and reliable. Experimental data were collected from a wide range of published studies that focused on shear tests of prestressed concrete beams. The database includes detailed information on beam dimensions, material properties (e.g., concrete compressive strength, reinforcement types, and properties), and loading conditions. Each entry was carefully validated to ensure accuracy and consistency across different studies, which involved cross-referencing reported values and re-calculating where necessary to correct any discrepancies. Key parameters influencing shear behavior, such as  $a/d$ , reinforcement ratio, and effective depth, were included. Statistical distributions of these parameters were analyzed to identify common trends and outliers within the dataset. The database was subjected to a thorough validation process that compared database entries against original experimental reports to verify accuracy. When necessary, data entries were refined and updated to ensure the highest level of data integrity. Furthermore, the database was used to develop and validate preliminary, and later more advanced, predictive models of shear strength through nonlinear regression analysis and GP. Nonlinear regression techniques were applied to model the relationships between key variables and shear strength, thereby capturing the complex interactions within the data. GP was employed to further enhance these models, optimizing the

functional forms and coefficients to improve predictive accuracy. Key findings from the database development include the following:

1. It was found that the effective depth of beams showed no clear trend with normalized shear stress at both the diagonal crack and shear failure for beams with stirrups. However, a mild correlation was observed for beams without stirrups, indicating that the shear-span-to-effective-depth ratio significantly impacts shear stress at diagonal cracking and failure. Additionally, the effective prestress in concrete displayed a positive correlation with normalized shear stress at both the diagonal crack and shear failure, with similar trends observed irrespective of the presence of stirrups. Furthermore, the  $s/d$  exhibited a clear trend with normalized shear stress; as  $s/d$  decreased, shear stress increased, especially at shear failure. This result highlights the importance of  $s/d$  in enhancing shear capacity. These scatterplot analyses provided crucial insights into the interplay between these variables, contributing to a more nuanced understanding of shear behavior in prestressed concrete beams.
2. The dataset analysis highlighted gaps in existing research, particularly in terms of underrepresented beam types and loading scenarios, which suggested areas for future study. Identifying these gaps informed the design of the experimental program. Specifically, it was observed that a larger cross section is much fewer in the database, which led to the experimental program focusing on larger girders (Tx54 and Tx70).
3. Nonlinear regression analysis was used to develop predictive equations for shear force at the onset of diagonal cracking and at shear failure. As an optimization problem based on the dataset, RMSE was used as the loss function to optimize the prediction accuracy for the given mathematical model coefficients. The analysis results showed that the predictive model for shear force at the onset of diagonal cracking had an RMSE of 18.76 on the training dataset and 13.48 on the test dataset, with  $R^2$  values of 0.91 and 0.94, respectively. This result indicates that the model demonstrated high prediction accuracy for both training and test data without overfitting. Furthermore, the predictive model for shear force at shear failure had an RMSE of 22.92 on the training dataset and 25.32 on the test dataset, with  $R^2$  values of 0.95 and 0.94, thus showing high predictive performance. These results confirm that the nonlinear regression model is effective in predicting shear force at the onset of diagonal cracking and at shear failure.



4. GP was used to develop a model for predicting the shear force at shear failure. GP successfully identified the optimal functional form, resulting in more accurate predictions than the traditional nonlinear regression model. Specifically, the GP model achieved an RMSE of 10.98 and an  $R^2$  of 0.97 on the training dataset and demonstrated similar performance on the test dataset. Additionally, predictions made using the GP model exhibited fewer residuals than the nonlinear regression model, indicating a smaller discrepancy between actual and predicted values. These results suggest that GP can provide more conservative and accurate predictions.

### 12.3 FULL-SCALE TESTING

The full-scale testing program produced a unique dataset and enabled studying the effect of various design parameters on minimum shear reinforcement requirements. Girder performance was mainly characterized via the RSS and serviceability criteria (such as crack measurements).

In addition, the experimental part of this task focused on a parametric design study that enabled identification of key design parameters that can be varied in the tests. Ultimately, various factors such as the presence/absence of deck, concrete strength, yield strength of stirrups,  $s/d$ , shear-span-to-depth ratio, prestressing strands, harped strands, and girder depth were varied as a part of this parametric design study. The combination of the parametric design study, along with the experimental study, gave a more comprehensive understanding of the influence of different provisions on shear behavior. The experimental tests permitted acquisition of unique data that played a vital role in effective comparisons. Key findings from the full-scale testing include the following:

1. Based on the parametric study on prototype girders, the minimum shear reinforcement ratio equation from AASHTO LRFD always provided a large  $s/d$  for most girders because it did not account for a number of design parameters, such as the prestressing ratio, which was found to contribute significantly to the minimum shear reinforcement ratio.
2. The presence of the deck slab did not provide larger shear strength despite the larger effective depth, partially because at ultimate conditions interface slippage reduced the composite action, although the girder was designed with sufficient interface shear

reinforcement per AASHTO LRFD. The girder with the deck exhibited larger crack widths.

3. Lower  $s/d$  (18 in.) was found to significantly enhance girder shear strength, particularly in designs without harped tendons, whereas girders with harped tendons showed less sensitivity to  $s/d$  variations.
4. Higher-grade shear reinforcement (80 ksi versus 60 ksi stirrups) significantly impacted girder behavior, with experiments showing that while girders using 60 ksi bars with closer spacing exhibited slightly higher maximum strength, girders with 80 ksi bars had better RSS with lower cracking strength and greater shear deformability.
5. The effectiveness of harped strands in enhancing shear capacity and crack propagation was found to vary with reinforcement spacing. Although harped strands were found to slightly reduce the shear strength at low  $s/d$  (18 in.), they improved the shear strength at larger  $s/d$  (26 in.), implying that the benefits of harped strands to the shear strength might be more pronounced in larger  $s/d$ s.
6. Higher prestressing ratios significantly enhance structural performance under shear loading by increasing the shear strength at first cracking and at shear failure. Higher prestressing ratios also resulted in more closely spaced cracks and lower RSS values, as opposed to wider crack distribution in girders with lower prestressing ratios.
7. Larger concrete strengths significantly enhanced both cracking and ultimate shear strengths, leading to better performance across different shear reinforcement ratios and  $s/d$ s. However, the RSS did not show consistent patterns.
8. Lower values of the  $a/d_v$  resulted in higher shear strengths. Comparative studies showed that higher  $a/d_v$  leads to reduced cracking and ultimate shear strengths and higher RSS values. Also, girders with higher  $a/d_v$  exhibited more cracks and broader crack distributions.
9. Regarding the effect of the cross-section depth, larger (Tx70) girders exhibited lower RSS for larger  $s/d$  and similar RSS for TxDOT-provided spacing despite higher cracking and larger ultimate shear strength than smaller (Tx54) girders. Tx70 girders had widely spaced cracks with failure in the web-bottom flange connection, while Tx54 girders showed brittle failure under larger  $s/d$ .

## 12.4 PARAMETRIC FINITE ELEMENT ANALYSIS STUDY

The FE modeling was also a vital part in this task because it was used in the structural analysis of the TxDOT girders and to replicate the failure mechanisms from the experiment tests. The modeling phase of this task began with appropriate FE model development in terms of geometry, material parameters, and FE parameters. Further, the FE models were validated using existing literature by modeling the test specimens and comparing their response to the numerical analysis. This process further strengthened the FE models moving forward in the study of crucial factors such as shear reinforcement spacing, deck slab presence, concrete strength variations, different prestressing force levels, distinct tendon path types (harped strands and straight strands), and various  $a/d$  ratios.

Those parameters were selected due to their potential impact on both shear capacity and overall bridge girder performance. Comprehensive numerical simulations were conducted to uncover the specific influences of each factor on shear behavior. The outcomes from the FE analysis encompass a range of parameters, comprising the cracking load, ultimate load, RSS index, percentage of damage on the concrete specimen's surface, and stress distribution within the shear reinforcement. Key findings from the parametric FE analysis studies include:

1. Girders with deck slabs exhibited higher shear strength at the onset of cracking and at shear failure, and larger RSS values. This observation is contradictory to the experimental observation that identified reduced composite action due to slippage at the deck-to-girder interface. However, the FE model did not account for interfacial sliding. Girders with deck slabs also exhibited steeper crack angles, lower concrete strains, and axial stress in the stirrups at ultimate conditions. The FE analyses indicated higher shear capacity values than those predicted by AASHTO and ACI, suggesting a conservative approach in current design guidelines.
2. The FE analysis results showed that deck slabs with widths of 3 ft and 8 ft produced similar responses, validating the use of smaller width slabs.
3. The study on shear reinforcement grade revealed that while the grade did not affect shear cracking load initiation, higher-grade reinforcement (Grade 100) significantly increased ultimate shear strength, RSS values, and crack angles. In addition, Tx54 with Grade 100

exhibited higher concrete surface strain, and Tx70 girders showing higher strains with Grade 60 depicted a difference in strain behavior based on girder size. FE analysis predictions of shear capacity were generally higher than those from ACI and AASHTO guidelines, with AASHTO often underestimating shear loads, except for Tx70 girders with Grade 100 reinforcement.

4. The study on the size of shear reinforcement found that increasing the size/diameter of shear reinforcement significantly enhances both cracking force and shear capacity in Tx54 and Tx70 girders. Larger shear reinforcement sizes/diameters also resulted in higher RSS values, steeper crack angles, increased crack intensity, and reduced plastic strain in concrete. Additionally, the axial stress in stirrups decreased with larger reinforcement sizes/diameters. FE analysis predictions consistently showed higher shear loads than AASHTO and ACI standards, indicating the conservative nature of the code standards.
5. Lower  $a/d$  ratios were found to significantly increase shear strength at the onset of cracking and at failure in Tx54 and Tx70 girders, producing higher strains and steeper crack angles. Lower  $a/d$  ratios improved shear capacities by up to 58.3 percent for Tx54 and 22.6 percent for Tx70, while RSS values increased with decreasing  $a/d_v$ . FEM predictions consistently exceeded AASHTO and ACI standards, indicating conservative estimates by the codes.
6. Increasing concrete compressive strength significantly boosted cracking and ultimate shear capacities in Tx54 and Tx70 girders, with up to 81 percent and 58 percent gains, respectively, from 5 ksi to 14 ksi concrete. Higher strength also resulted in lower RSS values and higher axial stress in R-bars.
7. Increasing the prestressing ratio in Tx54 and Tx70 girders enhances cracking and ultimate shear capacities, reduces RSS values, and increases crack inclination angles. FE analysis predictions of shear forces consistently exceeded AASHTO and ACI estimates.
8. Specimens with harped strands showed up to 9 percent higher cracking forces and 7 percent higher shear capacities than straight strands. Harped strands also resulted in greater crack angles, lower concrete strain, reduced axial stress in reinforcement bars, and varied RSS values. FE analysis predictions of shear strengths exceeded AASHTO and ACI standard.

## 12.5 MECHANICS-INFORMED DATA-DRIVEN MODEL DEVELOPMENT

The data-driven model development was a pivotal part of this research and aimed at creating accurate predictive models for shear strength in prestressed concrete beams. This process involved leveraging the extensive database and applying advanced statistical and machine learning techniques. Initial models were developed using direct nonlinear regression and GP to capture the complex relationships between variables affecting shear strength. However, while these techniques predicted the shear force at the onset of diagonal cracking and the shear force at shear failure accurately, they failed to accurately predict the RSS index. Additionally, GP models, although accurate, often produced results that lacked clear physical interpretability, making it challenging to derive meaningful insights from the model equations. To overcome these limitations, nonlinear optimization techniques were applied to enhance the predictive accuracy of the models. The optimization models focused on predicting shear force at diagonal cracking and ultimate shear failure by incorporating key parameters identified from the database. The models were validated against experimental results and demonstrated their effectiveness in predicting shear strength with a high degree of confidence. The developed models were rigorously tested against experimental data to validate their accuracy and reliability. Comparisons with existing design codes and empirical models highlighted the improved performance of the data-driven models. Additionally, appropriate RSS indices were developed through reliability analysis, thus accounting for uncertainties in the predictive equations and in girder properties. Key findings from data-driven model development included:

1. Through improvements in the loss function and the inclusion of cross-section height-based weighting, the optimized models were able to accurately predict experimental values, thereby demonstrating the effectiveness of these enhancements. Even simplified models showed a similar level of predictive accuracy, indicating the robustness of the model approach and its potential for practical applications.
2. The reliability analysis method provided a strategy to determine model-specific RSS values that achieve target probabilities of insufficient transfer. This approach is applicable for any model. For the developed data-driven model, an RSS of 1.33 provided a 5 percent probability of insufficient transfer, whereas the AASHTO equations achieved

the same probability for an RSS of about 2. Application of the data-driven model resulted in lower minimum shear reinforcement in most girder designs considered.

## **12.6 DESIGN GUIDELINES FOR MINIMUM SHEAR REINFORCEMENT**

The key objective of this research is to evaluate existing provisions for minimum shear reinforcement and to provide enhanced design guidelines and recommendations. The research study details the evaluation process of minimum shear reinforcement from various codes of practice and compares their spacing requirements for potential TxDOT I-girders. The evaluation involves selecting prototype girders based on the *TxDOT Bridge Design Manual LRFD* and *AASHTO Bridge Design Specifications* and ensuring they meet all design steps and stress checks. The proposed design guidelines focus on two main aspects: the minimum shear reinforcement ratio and the maximum spacing. Key findings include:

1. The evaluation of existing shear reinforcement provisions for girders designed according to TxDOT, AASHTO, and ACI specifications revealed differences in minimum shear reinforcement and maximum spacing. The analysis, detailed in Section 2.6, compares these provisions over the girder span, highlighting that ACI tends to recommend closer spacing for deeper girders, while AASHTO does not account for prestressing in its minimum shear provisions.
2. The ACI equations recommend closer spacing values for deeper girders and higher RSS for wider spacings, while AASHTO's minimum shear spacing provisions remain constant regardless of girder depth with very large spacing.
3. The maximum spacing provision for the designed TxDOT girders is typically the controlling provision for AASHTO, while for ACI minimum shear reinforcement always governs. In addition, the region which minimum shear reinforcement provisions control in the transverse shear design of the girder, the maximum spacing provision gives 24 in. for all the TxDOT I-girders according to AASHTO. However, ACI recommends closer spacing for smaller depth girders.
4. For Strategy 1, based on the explicit form with the selected RSS of 1.33 associated with the probability of insufficient transfer of 5.1 percent, the spacing resulting from minimum shear reinforcement ratio is similar to the ACI provision, which also accounts for

prestressing effects. For the similar probability-based RSS for AASHTO equations, the minimum shear reinforcement ratio resulted in slightly closer spacing than the explicit form. However, both the strategies yield almost similar spacing to the ACI minimum shear reinforcement ratio.

5. In the proposed maximum spacing based on the geometric constraint, the spacing is observed to change in accordance with the girder depth. When this proposed maximum spacing is combined with the explicit form of the proposed minimum shear reinforcement ratio, the resulting spacing for the TxDOT girders with R-bars is similar to the provided spacing in TxDOT standard drawings.
6. The explicit minimum shear reinforcement ratio combined with the geometry-based maximum spacing account for the different design parameters and prestressing effects in girder design. This approach can be used in the design standards, which can benefit TxDOT and other state DOTs by creating a standardized approach in calculating the minimum shear reinforcement.





## REFERENCES

- AASHTO (2020). *AASHTO LRFD Bridge Design Specification*, 9th Edition Edition, American Association of State Highway and Transportation Officials, Washington, D. C.
- Abaqus (2012). "Abaqus 6.11." <http://130.149>, 89(2080): v6.
- ACI318-19 (2019). *Building Code Requirements for Structural Concrete (ACI 318-19): An ACI Standard ; Commentary on Building Code Requirements for Structural Concrete (ACI 318R-19)*, American Concrete Institute. ISBN 9781641950565.
- ACI (2019). *Building Code Requirements for Structural Concrete (ACI 318-19): An ACI Standard ; Commentary on Building Code Requirements for Structural Concrete (ACI 318R-19)*, American Concrete Institute. ISBN 9781641950565.
- Aguilar, V., Barnes, R. W., Nowak, A. (2022). "Strength Reduction Factors for ACI 318 Strut-and-Tie Method for Deep Beams." *ACI Structural Journal*, 119(2): 103-112.
- Al-Nasra, M. M., Asha, N. M. (2013). "Shear reinforcements in the reinforced concrete beams." *American Journal of Engineering Research (AJER)*, 2(10): 191-199.
- Alfredo, H.-S. A., Wilson, H. (1975). "Probability concepts in engineering planning and design." *John Wiley and Sons*, 268.
- Angelakos, D., Bentz, E. C., Collins, M. P. (2001). "Effect of concrete strength and minimum stirrups on shear strength of large members." *Structural Journal*, 98(3): 291-300.
- ASTM C1611-21 (2021). "Standard Test Method for Slump Flow of Self-Consolidating Concrete." American Society for Testing and Materials.
- Athanasopoulou, A., Formichi, P., Spehl, P., Dabizheva, I., Gacesa-Moric, V., Markova, J., Calgaro, J., Malakatas, N., Lurvink, M., Croce, P. (2019). "The implementation of the Eurocodes in the National Regulatory Framework." Luxembourg: Publications Office of the European Union.
- Avendaño, A., Bayrak, O. (2008). "Shear strength and behavior of prestressed concrete beams." *Texas Department of Transportation, Technical Report IAC-88-5DD1A003-3*, University of Texas at Austin, Austin, Texas.
- Avendaño, A. R., Bayrak, O. (2011). "Efficient Shear Reinforcement Design Limits for Prestressed Concrete Beams." *ACI Structural Journal*, 108(6).
- Azad, B. (2021). "Shear strength of prestressed concrete beams without shear reinforcement: A comparison between equations."
- Behnam, H., Kuang, J., Samali, B. (2018). "Parametric finite element analysis of RC wide beam-column connections." *Computers & Structures*, 205: 28-44.

- Bennett, E. W., Banerjee, S. (1976). "Strength of beam column connections with dowel reinforcement." *Institution of Structural Engineers*, 54(4): 133-139.
- Bentz, E. C., Vecchio, F. J., Collins, M. P. (2006). "Simplified modified compression field theory for calculating shear strength of reinforced concrete elements." *ACI structural journal*, 103(4): 614.
- Bogdándy, B. (2021). "The shear resistance of a member without shear reinforcement according to Eurocode 2; the error of the calculated value and the mechanical explanation of the problem." *International Review of Applied Sciences and Engineering*, 12(3): 222-229.
- Bruce, R. (1969). "The Action of Vertical, Inclined and Prestressed Stirrups in Prestressed Concrete Beams'." *Journal of the Prestressed Concrete Institute*, 9(Part 1): 14-25.
- Byrd, R. H., Hribar, M. E., Nocedal, J. (1999). "An interior point algorithm for large-scale nonlinear programming." *SIAM Journal on Optimization*, 9(4): 877-900.
- Carmona, J. R., Ruiz, G. (2014). "Bond and size effects on the shear capacity of RC beams without stirrups." *Engineering Structures*, 66: 45-56.
- Cavagnis, F., Fernández Ruiz, M., Muttoni, A. (2018). "An analysis of the shear-transfer actions in reinforced concrete members without transverse reinforcement based on refined experimental measurements." *Structural concrete*, 19(1): 49-64.
- CEB (1990). "Comité Euro-International du Béton (CEB), 1993." London: Thomas Telford Services.
- CEB, M. (1978). "CEB-FIP Model code for concrete structures." *Comité Euro-International du Béton, Paris, France*.
- Collins, M. P., Kuchma, D. (1999). "How safe are our large, lightly reinforced concrete beams, slabs, and footings?" *Structural Journal*, 96(4): 482-490.
- Conn, A. R., Gould, N. I., Toint, P. L. (2000). *Trust region methods*, SIAM. ISBN 0898714605.
- De Wilder, K. (2014). "Shear Capacity of Prestressed and Reinforced Concrete Members: Modeling and Experimental Validation."
- Ditlevsen, O., Madsen, H. O. (1996). *Structural reliability methods*, Wiley New York,
- Dunkelberg, D., Sneed, L. H., Zilch, K., Reineck, K. H. (2018). "The 2015 ACI-DAfStb database of shear tests on slender prestressed concrete beams without stirrups—Overview and evaluation of current design approaches." *Structural Concrete*, 19(6): 1740-1759.
- fib Model Code (2010). "Fib model code for concrete structures 2010." Ernst & Sohn, Wiley.

- Frosch, R. J., Wolf, T. S. (2003). "Simplified Shear Design of Prestressed Concrete Members."
- Gandomi, A. H., Alavi, A. H., Arjmandi, P., Aghaeifar, A., Seyednour, R. (2010). "Genetic programming and orthogonal least squares: a hybrid approach to modeling the compressive strength of CFRP-confined concrete cylinders." *Journal of Mechanics of Materials and Structures*, 5(5): 735-753.
- Gandomi, A. H., Alavi, A. H. (2012). "A new multi-gene genetic programming approach to nonlinear system modeling. Part I: materials and structural engineering problems." *Neural Computing and Applications*, 21(1): 171-187.
- Gholamy, A., Kreinovich, V., Kosheleva, O. (2018). "Why 70/30 or 80/20 relation between training and testing sets: a pedagogical explanation."
- Hawkins, N. M. (2005). *Simplified shear design of structural concrete members*, Transportation Research Board. ISBN 0309088445.
- Hawkins, N. M., Kuchma, D. A. (2007a). *Application of LRFD bridge design specifications to high-strength structural concrete: Shear provisions*, Transportation Research Board. ISBN 0309098866.
- Hawkins, N. M., Kuchma, D. A. (2007b). "Application of LRFD Bridge Design Specifications to High Strength Structural Concrete: Shear Provisions, NCHRP Report 579." *Transportation Research Board, National Research Council, Washington, DC*.
- Hewson, N. R. (2003). *Prestressed concrete bridges: design and construction*, Thomas Telford. ISBN 0727732234.
- Hicks, S. (2020). *Second Generation of the Structural Eurocodes*, The University of Warwick, Institution of Civil Engineers East & West Midlands Webinar
- Hillebrand, M., Hegger, J. (2020). "Fatigue testing of shear reinforcement in prestressed concrete t-beams of bridges." *Applied Sciences*, 10(16): 5560.
- Hofer, A. A., McCabe, S. L. (1998). "Comparison of shear capacity of T-beams using Strut and Tie analysis." University of Kansas Center for Research, Inc.,
- Hu, B., Wu, Y.-F. (2018). "Effect of shear span-to-depth ratio on shear strength components of RC beams." *Engineering Structures*, 168: 770-783, DOI: 10.1016/j.engstruct.2018.05.017.
- Huber, T., Huber, P., Kollegger, J. (2019). "Influence of aggregate interlock on the shear resistance of reinforced concrete beams without stirrups." *Engineering Structures*, 186: 26-42.
- Ismail, K. S. (2016). "Shear behaviour of reinforced concrete deep beams." University of Sheffield.

- Jensen, B. C., Lapko, A. (2009). "On shear reinforcement design of structural concrete beams on the basis of theory of plasticity." *Journal of Civil Engineering and Management*, 15(4): 395-403.
- Jeon, J. S., Shafieezadeh, A., DesRoches, R. (2014). "Statistical models for shear strength of RC beam-column joints using machine-learning techniques." *Earthquake engineering & structural dynamics*, 43(14): 2075-2095.
- Kani, G. N. J. "How safe are our large reinforced concrete beams?" *Proc., Journal Proceedings*, 128-141.
- Katz, A. T. (2016). "Performance of precast, prestressed concrete I-girders employing 0.7-in. diameter prestressing strands under shear-critical loading conditions."
- Kim, C.-G., Park, H.-G., Hong, G.-H., Lee, H., Suh, J.-I. (2018). "Shear Strength of Reinforced Concrete-Composite Beams with Prestressed Concrete and Non-Prestressed Concrete." *ACI Structural Journal*, 115(4).
- Kotsovos, M. (1987). "Shear failure of reinforced concrete beams." *Engineering Structures*, 9(1): 32-38.
- Kotsovos, M. D., Pavlović, M. N. (2004). "Size effects in beams with small shear span-to-depth ratios." *Computers & structures*, 82(2-3): 143-156.
- Koza, J. R. (1994). "Genetic programming as a means for programming computers by natural selection." *Statistics and computing*, 4(2): 87-112.
- Kuchma, D., Kim, K. S., Nagle, T. J., Sun, S., Hawkins, N. M. (2008). "Shear tests on high-strength prestressed bulb-tee girders: Strengths and key observations." *ACI structural Journal*, 105(3): 358.
- Labonte, T., Hamilton III, H. (2005). "Self-consolidating concrete (SCC) structural investigation."
- Lee, J.-Y., Kim, U.-Y. (2008). "Effect of longitudinal tensile reinforcement ratio and shear span-depth ratio on minimum shear reinforcement in beams." *ACI Structural Journal*, 105(2): 134.
- Magnusson, J., Hallgren, M., Ansell, A. (2014). "Shear in concrete structures subjected to dynamic loads." *Structural Concrete*, 15(1): 55-65.
- Malm, R. (2006). "Shear cracks in concrete structures subjected to in-plane stresses." KTH.
- Martin-Pérez, B., Pantazopoulou, S. J. (2001). "Effect of bond, aggregate interlock and dowel action on the shear strength degradation of reinforced concrete." *Engineering Structures*, 23(2): 214-227.
- Melchers, R. E., Beck, A. T. (2018). *Structural reliability analysis and prediction*, John Wiley & sons. ISBN 1119265991.
- Mirgal, P., Singh, R. K., Banerjee, S. (2023). "Acoustic and fracture energy correlation in mode I fracture with concrete damage plasticity model and

- three-point bend experiment." *Journal of Materials in Civil Engineering*, 35(4): 04023002.
- Mitchell, D., Collins, M. P. (1974). "The behaviour of structural concrete beams in pure torsion." University of Toronto Toronto, ON, Canada.
- Munikrishna, A., Hosny, A., Rizkalla, S., Zia, P. (2011). "Behavior of concrete beams reinforced with ASTM A 1035 grade 100 stirrups under shear." *ACI Structural Journal*, 108(1): 34-41.
- Nakamura, E. (2011). "Shear Database for Prestressed Concrete Members." master's thesis, University of Texas at Austin, Austin, TX.
- Nawy, E. G. (1996). *Prestressed concrete. A fundamental approach*. ISBN 0131234803.
- Nguyen, T. H., Tan, K.-H., Kanda, T. (2019). "Investigations on web-shear behavior of deep precast, prestressed concrete hollow core slabs." *Engineering Structures*, 183: 579-593.
- Nocedal, J., Wright, S. J. (2006). "Numerical optimization."
- Nowak, A. S., Lind, N. C. (1979). "Practical code calibration procedures." *Canadian Journal of Civil Engineering*, 6(1): 112-119.
- Nowak, A. S. (1999). "Calibration of LRFD bridge design code." 0077-5614
- Ozcebe, G., Ersoy, U., Tankut, T. (1999). "Evaluation of minimum shear reinforcement requirements for higher strength concrete." *Structural Journal*, 96(3): 361-368.
- Rahal, K. N., Al-Shaleh, K. S. (2004). "Minimum transverse reinforcement in 65 MPa concrete beams." *Structural Journal*, 101(6): 872-878.
- Robertson, I. N. (1985). "Shear Strength of Prestressed Concrete T-Beams With Welded Wire Fabric as Shear Reinforcement." Rice University.
- Saykin, V. V., Nguyen, T. H., Hajjar, J. F., Deniz, D., Song, J. (2017). "Material characterization using finite element deletion strategies for collapse modeling of steel structures." *Engineering Structures*, 147: 125-133.
- Shioya, T. (1989). "Shear properties of large reinforced concrete member." *Special Report of Institute of Technology, Shimizu Corporation*, (25): 198.
- Sigrist, V., Bentz, E., Ruiz, M. F., Foster, S., Muttoni, A. (2013). "Background to the fib Model Code 2010 shear provisions—part I: beams and slabs." *Structural Concrete*, 14(3): 195-203.
- Słowik, M. (2013). "The Influence of Concrete Strength on Shear Capacity of Reinforced Concrete Members without Shear Reinforcement." *Budownictwo i Architektura*, 12(1): 151-158.
- Stephens, T. (2015). "GPLEarn (Version 0.4.2)." URL <https://gplearn.readthedocs.io/en/stable/index.html>. (Accessed in 2022).

- Szerszen, M. M., Nowak, A. S. (2003). "Calibration of design code for buildings (ACI 318): Part 2—Reliability analysis and resistance factors." *Structural journal*, 100(3): 383-391.
- Taylor, H. P. J. (1970). "Investigation of the forces carried across cracks in reinforced concrete beams in shear by interlock of aggregate."
- Teoh, B., Mansur, M., Wee, T. (2002). "Behavior of high-strength concrete I-beams with low shear reinforcement." *Structural Journal*, 99(3): 299-307.
- TxDOT, T. D. o. T. (2020). "Report on Texas Bridges Fiscal Year 2020." TxDOT Bridge Division,
- TxDOT, T. D. o. T. (2022). "Bridge Standard Drawings." <https://www.dot.state.tx.us/insdtdot/orgchart/cmd/cserve/standard/bridge-e.htm>. (Accessed in).
- TxDOT, T. D. o. T. (2023). "TxDOT Bridge Design Manual-LRFD." Texas Department of Transportation.
- Vecchio, F., Collins, M. (1982). "Response of Reinforced Concrete to In Plane Shear and Normal Stresses. 1982." *University of Toronto, Toronto, Canada*.
- Vecchio, F. J., Collins, M. P. (1986). "The modified compression-field theory for reinforced concrete elements subjected to shear." *ACI J.*, 83(2): 219-231.
- Vecchio, F. J., Collins, M. P. (1988). "Predicting the response of reinforced concrete beams subjected to shear using modified compression field theory." *ACI Structural Journal*, 85(3): 258-268.
- Virtanen, P., Gommers, R., Oliphant, T. E., Haberland, M., Reddy, T., Cournapeau, D., Burovski, E., Peterson, P., Weckesser, W., Bright, J. (2020). "SciPy 1.0: fundamental algorithms for scientific computing in Python." *Nature methods*, 17(3): 261-272.
- Walraven, J., Reinhardt, H. (1981). "Concrete mechanics. Part A: Theory and experiments on the mechanical behavior of cracks in plain and reinforced concrete subjected to shear loading." *Nasa Sti/recon Technical Report N*, 82: 25417.
- Wendorff, A., Botero, E., Alonso, J. J. "Comparing Different Off-the-Shelf Optimizers' Performance in Conceptual Aircraft Design." *Proc., 17th AIAA/ISSMO Multidisciplinary Analysis and Optimization Conference*, 3362.
- Wight, J. K. (2015). *Reinforced concrete: mechanics and design*, Prentice Hall. ISBN 013348596X.
- Yang, Y. (2014). "Shear behaviour of reinforced concrete members without shear reinforcement: a new look at an old problem."
- Zwoyer, E. M. (1953). "Shear strength of simply-supported prestressed concrete beams." University of Illinois Engineering Experiment Station. College of ...,





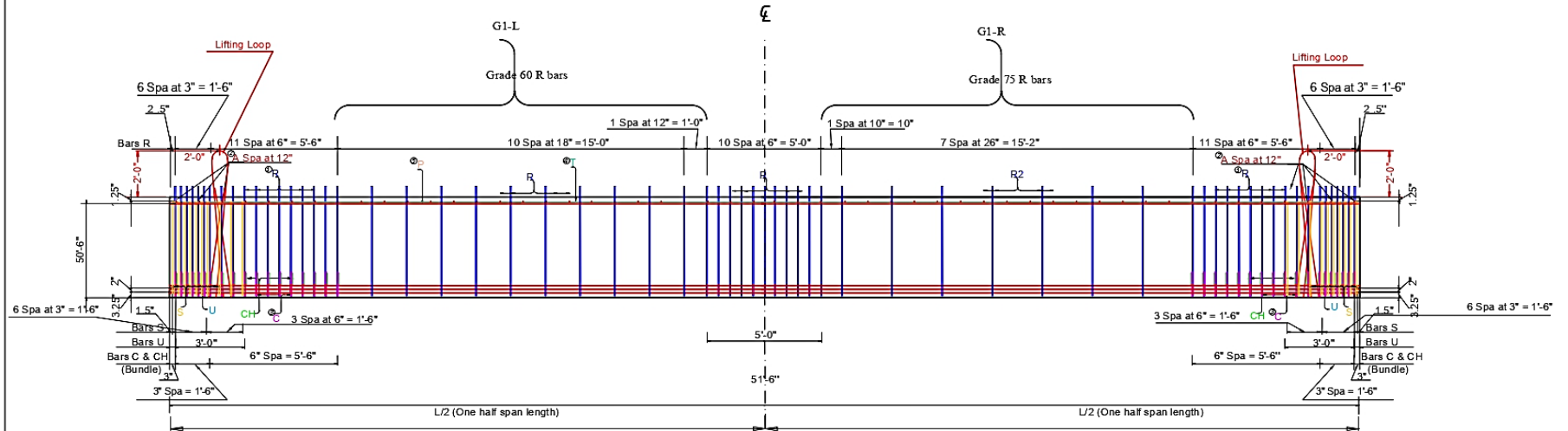


## **APPENDIX A: DETAILED DRAWINGS FOR THE PRESTRESSED CONCRETE GIRDER SPECIMENS**

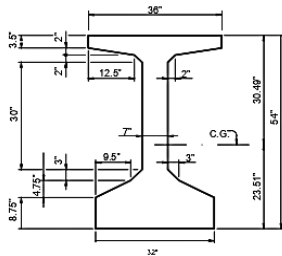
# Tx-54 Girder 1

## Two Identical Girders

GIRDER DIMENSIONS AND SECTION PROPERTIES							
Girder Type	"D"	"B"	"T"	"Y"	Area	"X"	"Y"
	(in.)	(in.)	(in.)	(in.)	(in. <sup>2</sup> )	(in.)	(in.)
Tx54	54	30	30.49	23.51	817	299,740	46,707
							880



Low Relaxation (270 ksi) Strand Pattern	
Number of strands:	34 ~ 0.6" @ 43.94 k per strand
Number of straight strands:	34 (32 Bot & 2 Top)
Number of deflected strands:	0
Concrete release strength:	6 ksi
Concrete design strength:	7 ksi
Eccentricity @ :	16.89" and @ end: 16.89"



Cross-section Geometry  
(Scale 1:30)

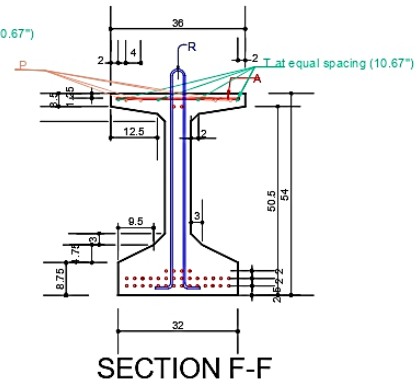
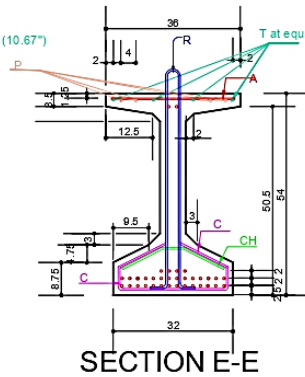
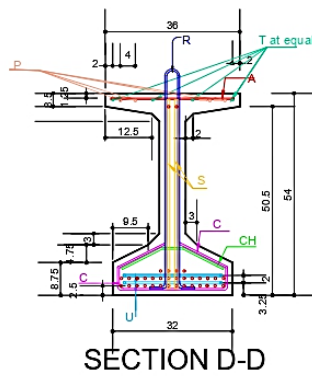
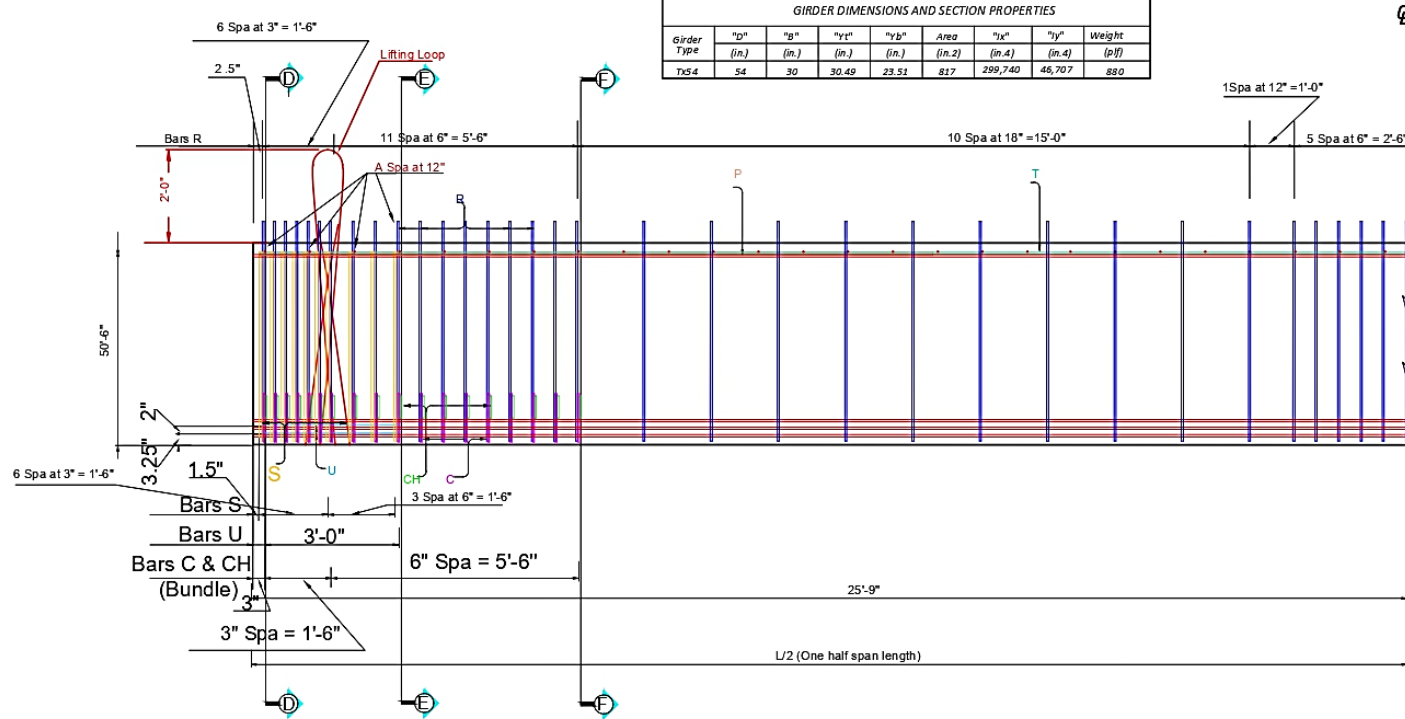
- ① The average of the spacing of Bars R cannot exceed the required spacing.
- ② Bars A at 12" c/c and tied to Bars T.
- ③ Bundled with Bars R from ends to 7'.
- ④ 4 Bars T #4.51" long at 2" side cover (effective) at both sides of top flange.
- ⑤ 4 Bars P #6 15" long at both ends of girder.
- ⑥ Based on 155 pcf total weight of concrete and reinforcing steel.

### General Notes:

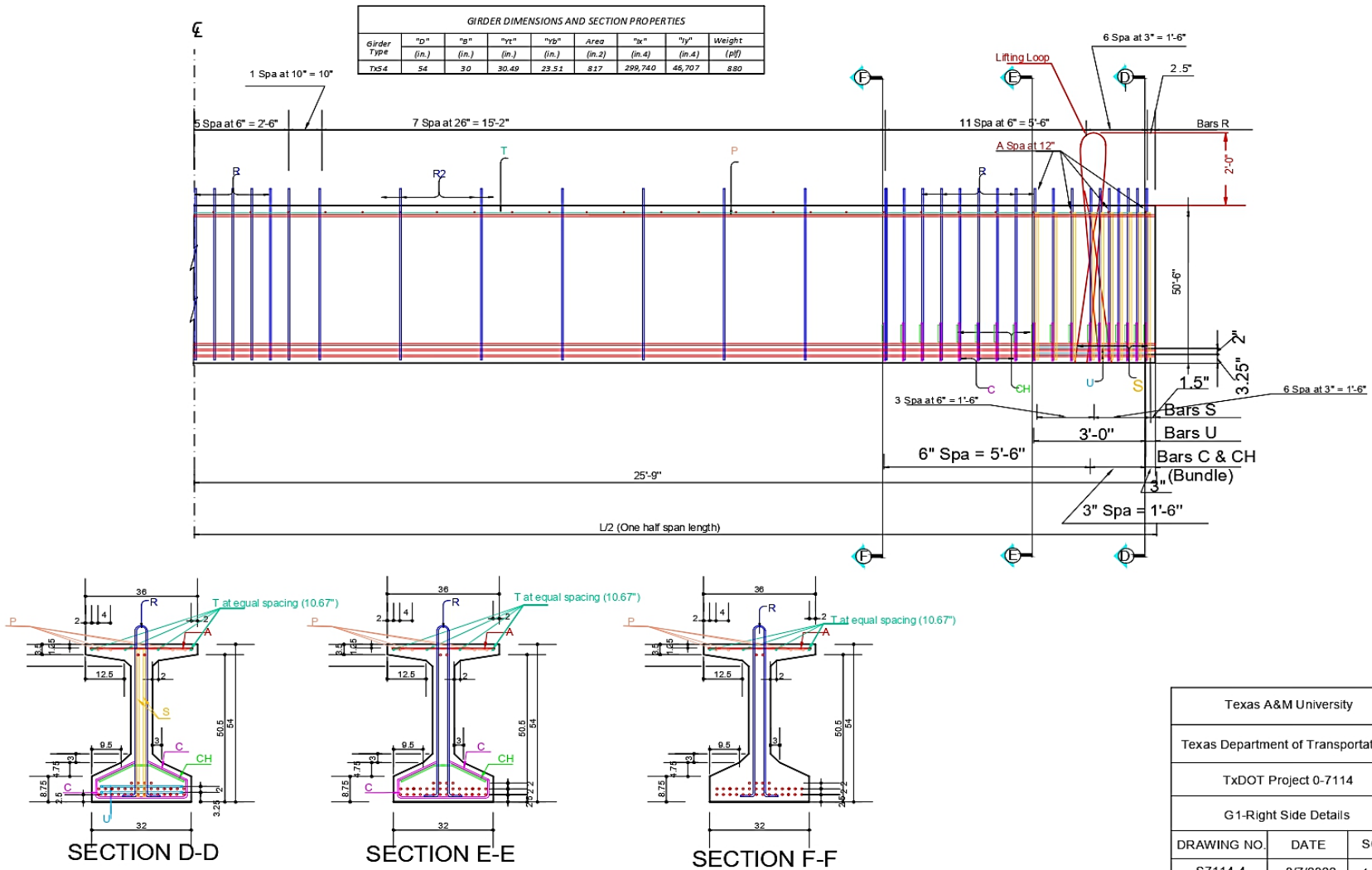
1. Half span with 18" spacing transverse reinforcement in the web with yield strength of 60 ksi, the other half with 26" spacing of transverse reinforcement in the web with yield strength of 75 ksi.
2. 1.5" clear cover unless noted otherwise.
3. For bar bending details, see drawing S7114-5.
4. Cover dimensions are clear dimensions, unless noted otherwise.
5. Reinforcing bar dimensions shown are center-to-center of bar.
6. Research team needs to be present for the installation of R bars to ensure the correct location of the gaged bars.
7. 0.6 in. diameter, seven wire low relaxation prestressing strands, 32 at bottom.
8. Total girder length of this sheet is 51'-6".
9. When cutting the strands, maintain 18" of strand projecting from each girder end. (Final dimension can be coordinated with the research team.)
10. Prior to delivery, cut the strands such that 2" of strand projects from each girder end.
11. Provide Grade 60 reinforcing steel, unless noted otherwise.

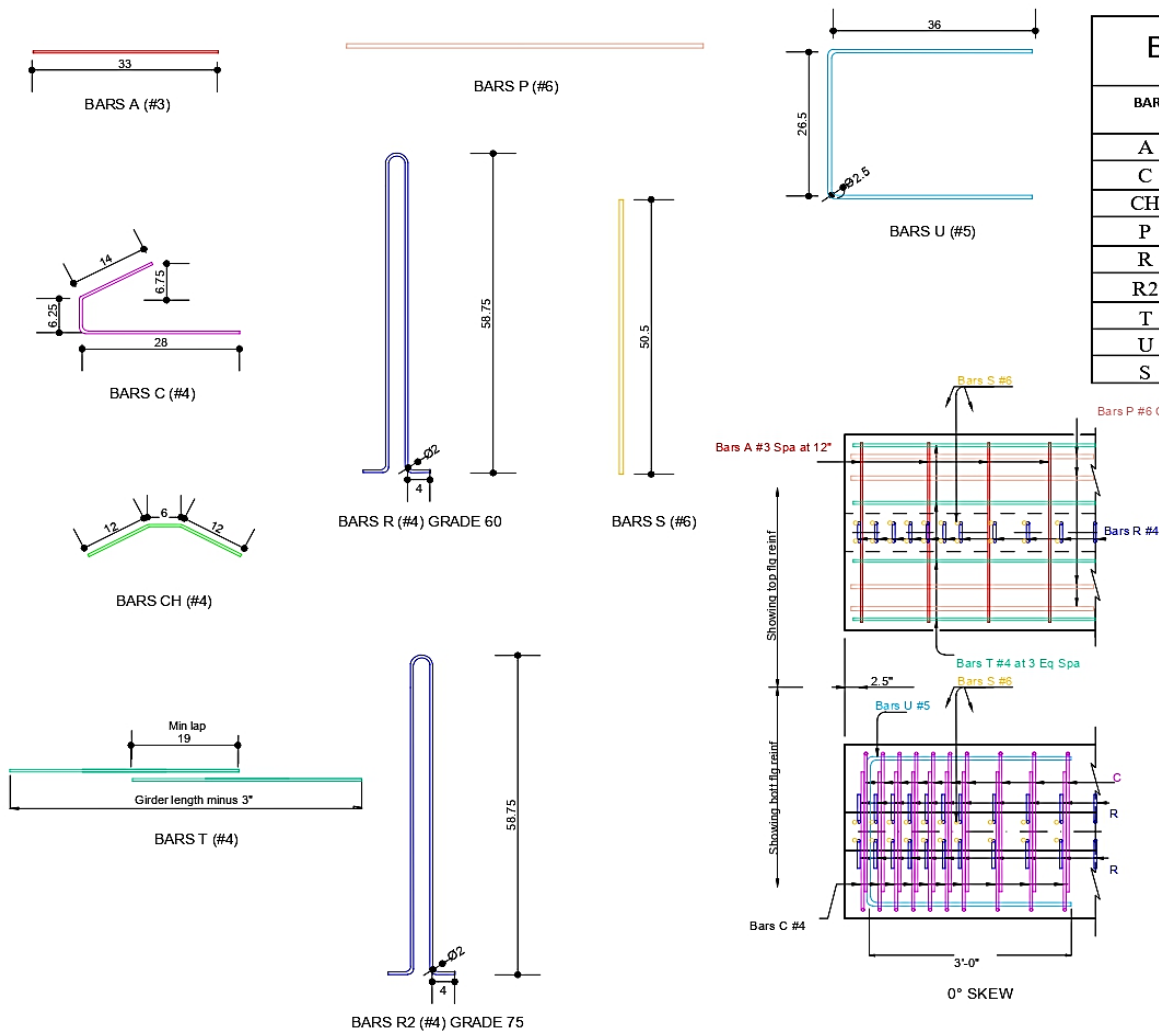
Texas A&M University		
Texas Department of Transportation		
TxDOT Project 0-7114		
Girder 1 Details		
DRAWING NO.	DATE	SCALE
S7114-2	8/7/2022	1:50

GIRDER DIMENSIONS AND SECTION PROPERTIES							
Girder Type	"D" (in.)	"B" (in.)	"Yt" (in.)	"Yb" (in.)	Area (in.²)	"Ix" (in.⁴)	"Iy" (in.⁴)
TX54	54	30	30.49	23.51	817	299,740	46,707
							Weight (plf)
							880



Texas A&M University		
Texas Department of Transportation		
TxDOT Project 0-7114		
G1-Left Side Details		
DRAWING NO.	DATE	SCALE
S7114-3	8/7/2022	1:30



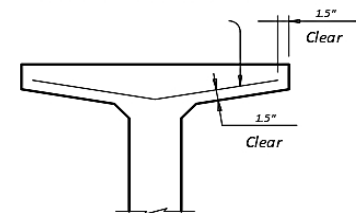


## BILL OF REINFORCEMENT STEEL

BAR	SIZE	TOTAL NO. OF BARS	LENGTH	WEIGHT (lb)
A	# 3	52	2'-9"	54
C	# 4	72	4'-0.25"	193
CH	# 4	36	2'-6"	60
P	# 6	4	15'-0"	91
R	# 4	56	10'-8"	399
R2	# 4	8	10'-8"	57
T	# 4	4	52'-3"	140
U	# 5	4	8'-2.5"	34
S	# 6	40	4'-2.5"	253

\* Standard length for T<sub>x</sub>54 girder reinforcement

To control top flange cracking that may occur during form removal, additional top flange reinforcing may be placed as shown in girder ends at the Fabricator's option.

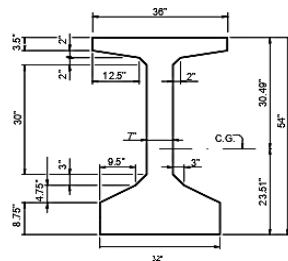
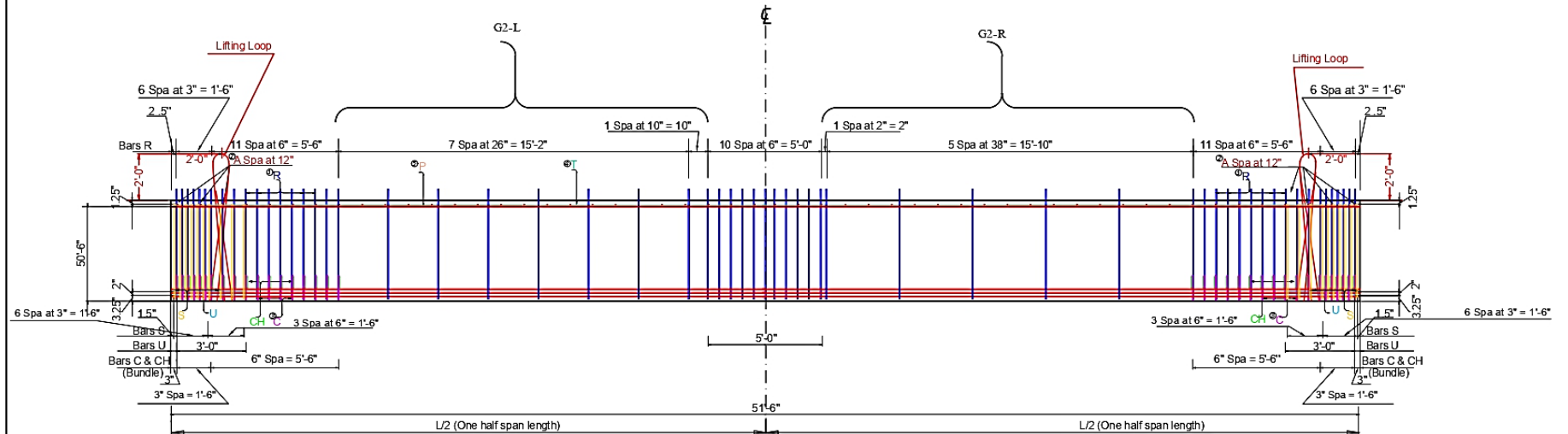


OPTIONAL TOP FLANGE  
REINFORCING DETAIL

Texas A&M University		
Texas Department of Transportation		
TxDOT Project 0-7114		
Bar Bending Details		
DRAWING NO.	DATE	SCALE
S7114-5	8/7/2022	1:20

# Tx-54 Girder 2

GIRDER DIMENSIONS AND SECTION PROPERTIES							
Girder Type	"d"	"g"	"y <sub>t</sub> "	"y <sub>b</sub> "	Area	"I <sub>x</sub> "	"I <sub>y</sub> "
	(in.)	(in.)	(in.)	(in.)	(in. <sup>2</sup> )	(in. <sup>4</sup> )	(in. <sup>4</sup> )
Tx54	54	30	30.49	23.51	817	299,740	46,707
							880



Cross-section Geometry  
(Scale 1:30)

- ① The average of the spacing of Bars R cannot exceed the required spacing.
- ② Bars A at 12" c/c and tied to Bars T.
- ③ Bundled with Bars R from ends to 7'.
- ④ 4 Bars T #4 S1'3" long at 2" side cover (effective) at both sides of top flange.
- ⑤ 4 Bars P #6 15' long at both ends of girder.
- ⑥ Based on 155 pcf total weight of concrete and reinforcing steel.

## General Notes:

1. Half span with 26" spacing transverse reinforcement in the web, the other half with 38" spacing of transverse reinforcement in the web.
2. 1.5" clear cover unless noted otherwise.
3. For bar bending details, see drawing S7114 - 9.
4. Cover dimensions are clear dimensions, unless noted otherwise.
5. Reinforcing bar dimensions shown are center-to-center of bar.
6. Research team needs to be present for the installation of R bars to ensure the correct location of the gaged bars.
7. 0.6 in. diameter, seven wire low relaxation prestressing strands, 32 at bottom.
8. Total girder length of this sheet is 51'-6".
9. When cutting the strands, maintain 18" of strand projecting from each girder end. (Final dimension can be coordinated with the research team.)
10. Prior to delivery, cut the strands such that 2" of strand projects from each girder end.
11. Provide Grade 60 reinforcing steel, unless noted otherwise.

## Low Relaxation (270 ksi) Strand Pattern

Number of strands: 34 ~ 0.6" @ 43.94 k per strand
Number of straight strands: 34 (32 Bot & 2 Top)
Number of deflected strands: 0
Concrete release strength: 6 ksi
Concrete design strength: 7 ksi
Eccentricity @ $\epsilon$ : 16.89" and @ end: 16.89"

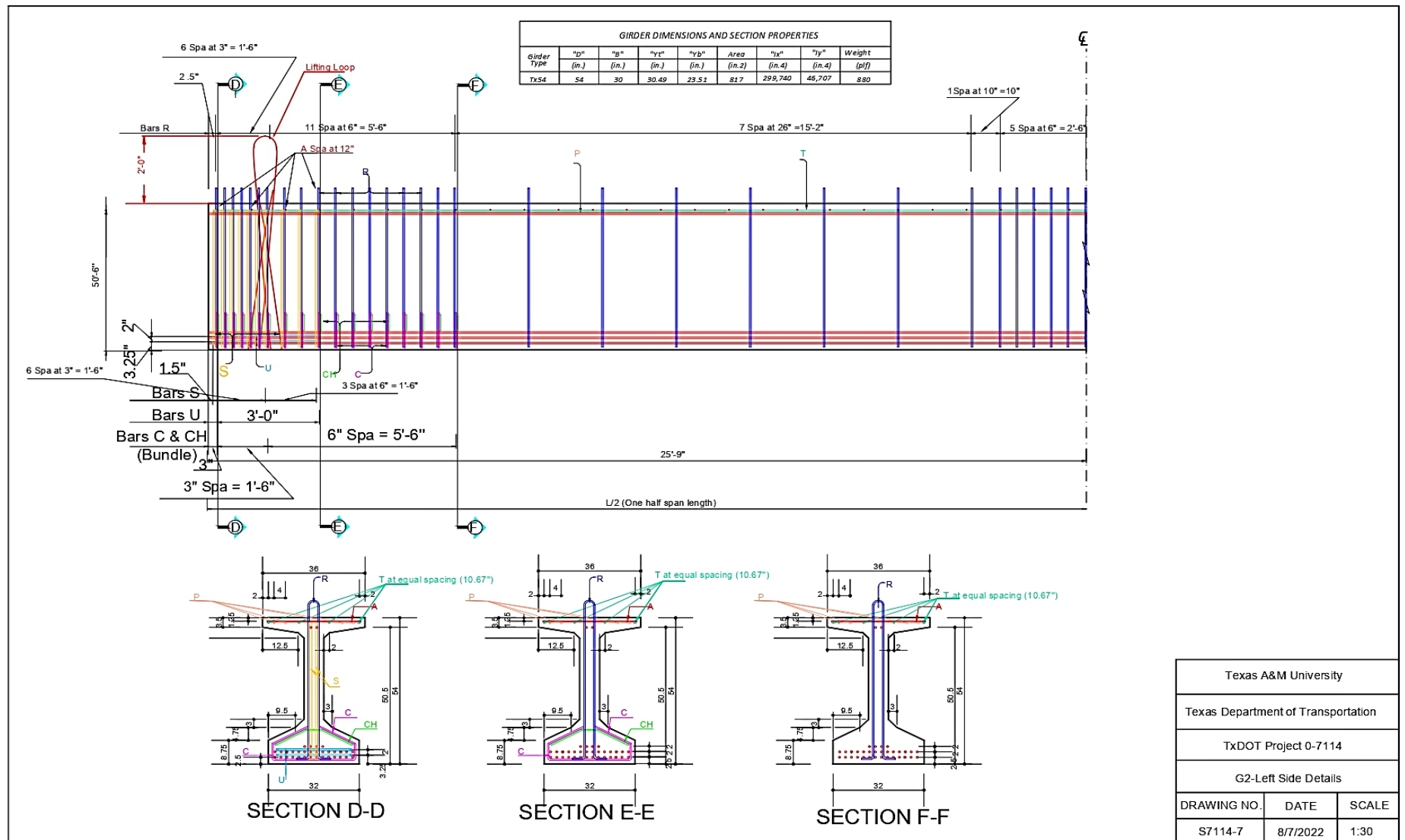
Texas A&M University

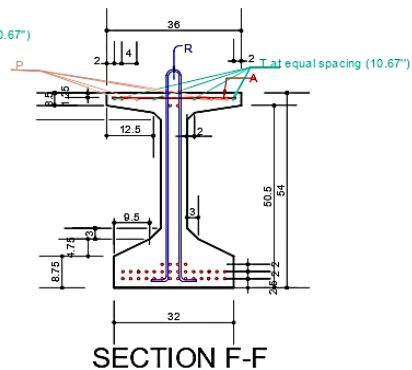
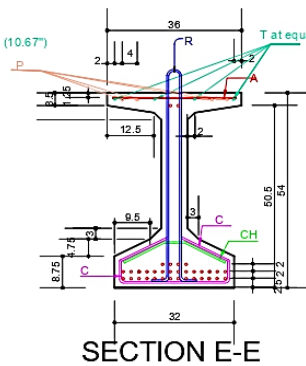
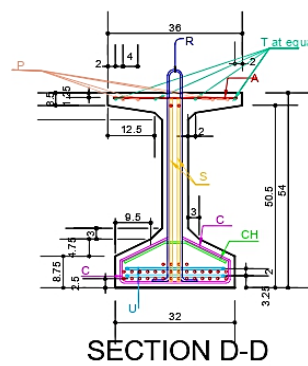
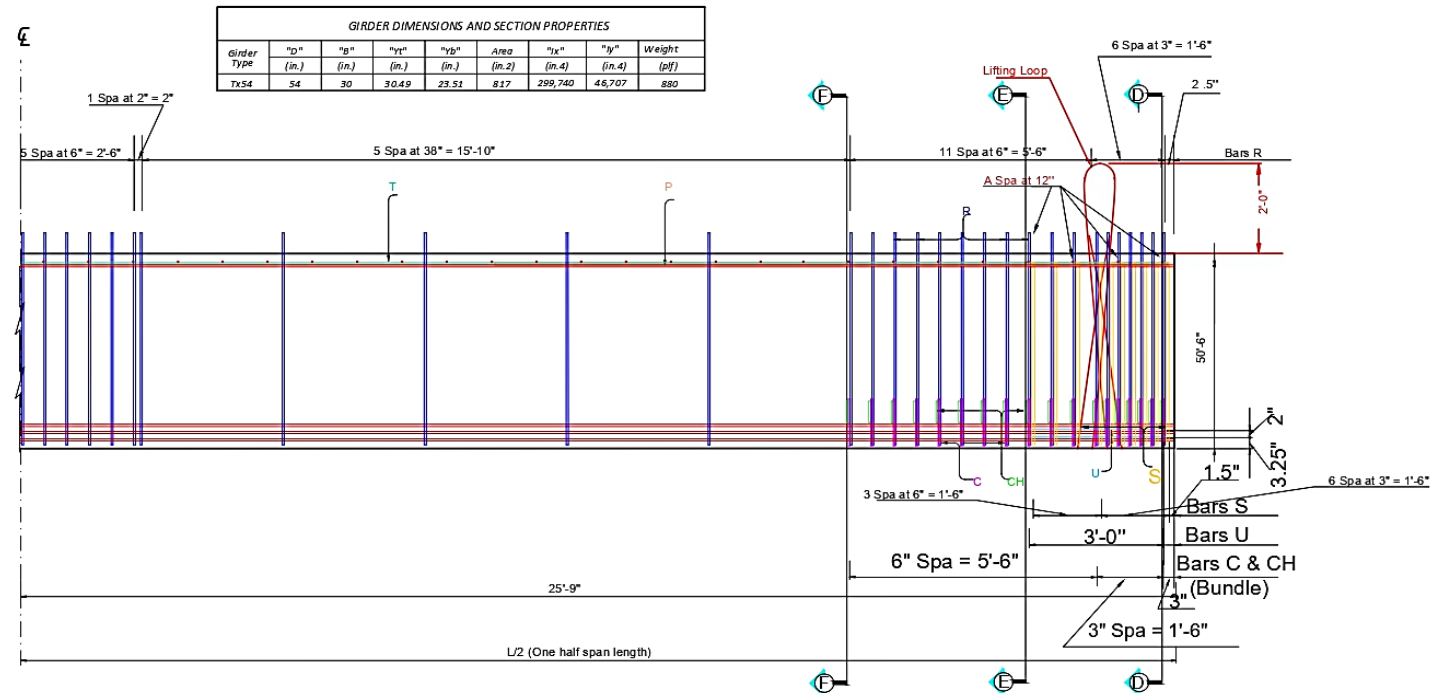
Texas Department of Transportation

TxDOT Project 0-7114

Girder 2 Details

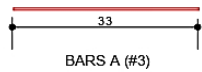
DRAWING NO.	DATE	SCALE
S7114-6	8/7/2022	1:50



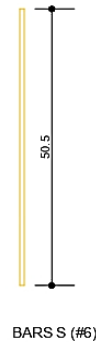
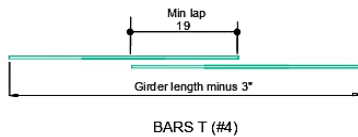
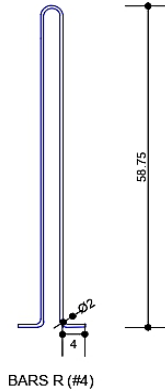
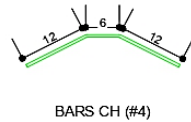
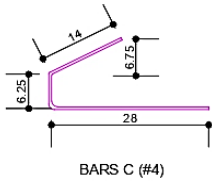
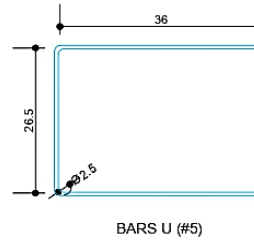


Texas A&M University		
Texas Department of Transportation		
TxDOT Project 0-7114		
G2-Right Side Details		
DRAWING NO.	DATE	SCALE
S7114-8	8/7/2022	1:30





BARS P (#6)

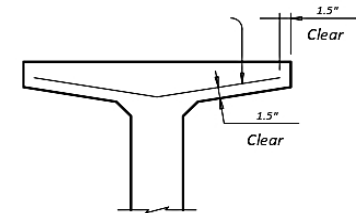


## BILL OF REINFORCEMENT STEEL

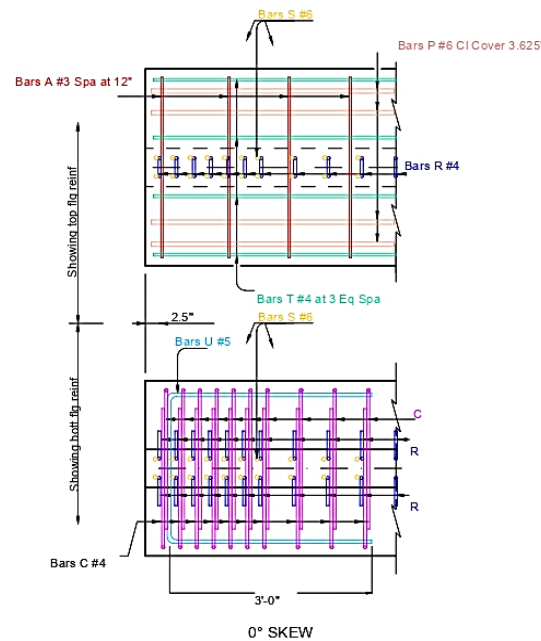
BAR	SIZE	TOTAL NO. OF BARS	LENGTH	WEIGHT (lb)
A	# 3	52	2'-9"	54
C	# 4	72	4'-0.25"	193
CH	# 4	36	2'-6"	60
P	# 6	4	15'-0"	91
R	# 4	57	10'-8"	407
T	# 4	4	52'-3"	140
U	# 5	4	8'-2.5"	34
S	# 6	40	4'-2.5"	253

\* Standard length for Tx54 girder reinforcement

To control top flange cracking that may occur during form removal, additional top flange reinforcing may be placed as shown in girder ends at the Fabricator's option.



OPTIONAL TOP FLANGE REINFORCING DETAIL



Texas A&M University

Texas Department of Transportation

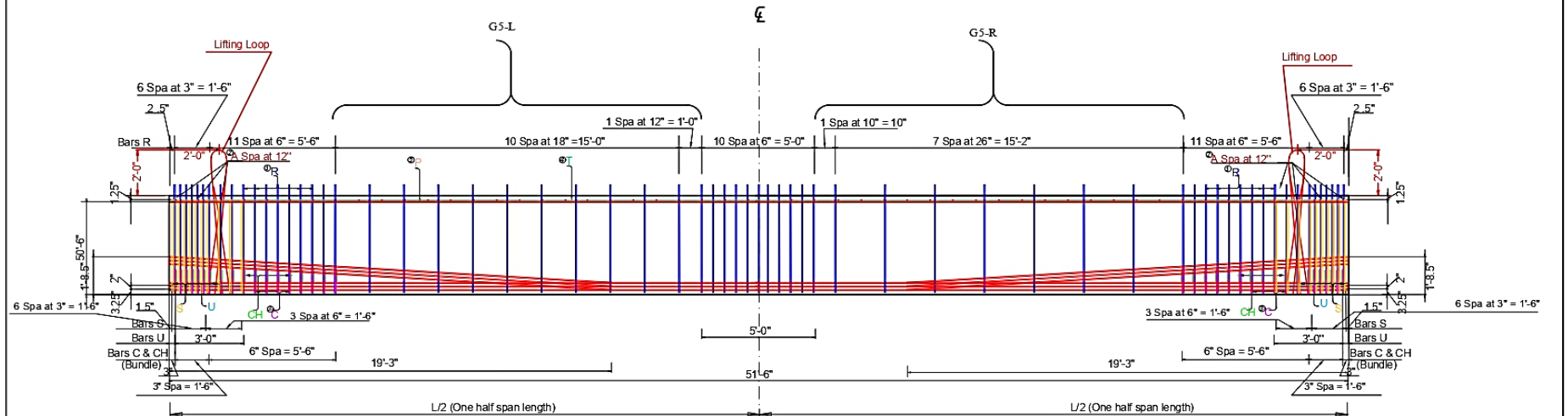
TxDOT Project 0-7114

Bar Bending Details

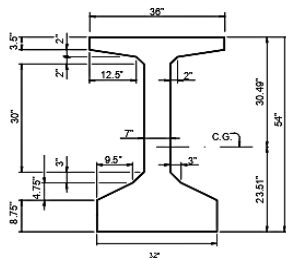
DRAWING NO.	DATE	SCALE
S7114-9	8/7/2022	1:20

# Tx-54 Girder 3

GIRDER DIMENSIONS AND SECTION PROPERTIES							
Girder Type	"b" (in.)	"t" (in.)	"w" (in.)	"d" (in.)	Area (in.²)	"I" (in.⁴)	Weight (plf)
Tx54	54	30	30.49	23.51	817	299,740	46,707



Low Relaxation (270 ksi) Strand Pattern	
Number of strands:	34 ~ 0.6" @ 43.94 k per strand
Number of straight strands:	34 (32 Bot & 2 Top)
Number of deflected strands:	6 @ 20.5
Concrete release strength:	6 ksi
Concrete design strength:	7 ksi
Eccentricity @ $\epsilon$ :	16.98" and @ end: 14.42"



Cross-section Geometry  
(Scale 1:30)

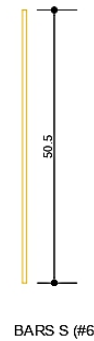
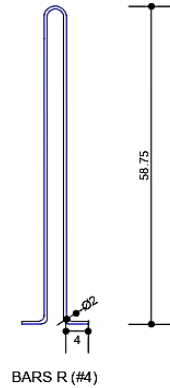
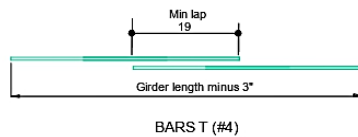
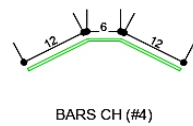
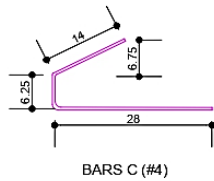
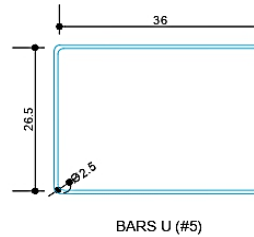
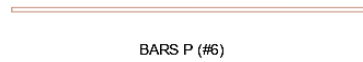
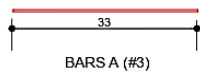
- ① The average of the spacing of Bars R cannot exceed the required spacing.
- ② Bars A at 12" c/c and tied to Bars T.
- ③ Bundled with Bars R from ends to 7'.
- ④ 4 Bars T #4 51'-3" long at 2" side cover (effective) at both sides of top flange.
- ⑤ 4 Bars P #6 15' long at both ends of girder.
- ⑥ Based on 155 pcf total weight of concrete and reinforcing steel.

- General Notes:
1. Half span with 18" spacing transverse reinforcement in the web, the other half with 26" spacing of transverse reinforcement in the web.
  2. 1.5" clear cover unless noted otherwise.
  3. For bar bending details, see drawing 57114-13.
  4. Cover dimensions are clear dimensions, unless noted otherwise.
  5. Reinforcing bar dimensions shown are center-to-center of bar.
  6. Research team needs to be present for the installation of R bars to ensure the correct location of the gaged bars.
  7. 0.6 in. diameter, seven wire low relaxation prestressing strands, 32 at bottom.
  8. Total girder length of this sheet is 51'-6".
  9. When cutting the strands, maintain 18" of strand projecting from each girder end. (Final dimension can be coordinated with the research team.)
  10. Prior to delivery, cut the strands such that 2" of strand projects from each girder end.
  11. Provide Grade 60 reinforcing steel, unless noted otherwise.

Texas A&M University		
Texas Department of Transportation		
TxDOT Project 0-7114		
Girder 3 Details		
DRAWING NO.	DATE	SCALE
S7114-10	8/7/2022	1:50

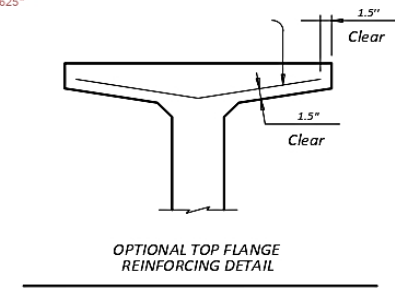
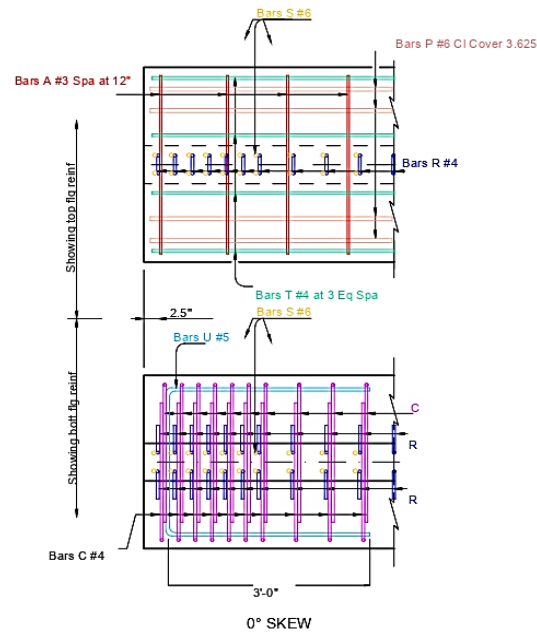






BILL OF REINFORCEMENT STEEL				
BAR	SIZE	TOTAL NO. OF BARS	LENGTH	WEIGHT (lb)
A	# 3	52	2'-9"	54
C	# 4	72	4'-0.25"	193
CH	# 4	36	2'-6"	60
P	# 6	4	15'-0"	91
R	# 4	64	10'-8"	456
T	# 4	4	52'-3"	140
U	# 5	4	8'-2.5"	34
S	# 6	40	4'-2.5"	253

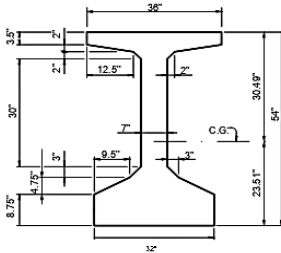
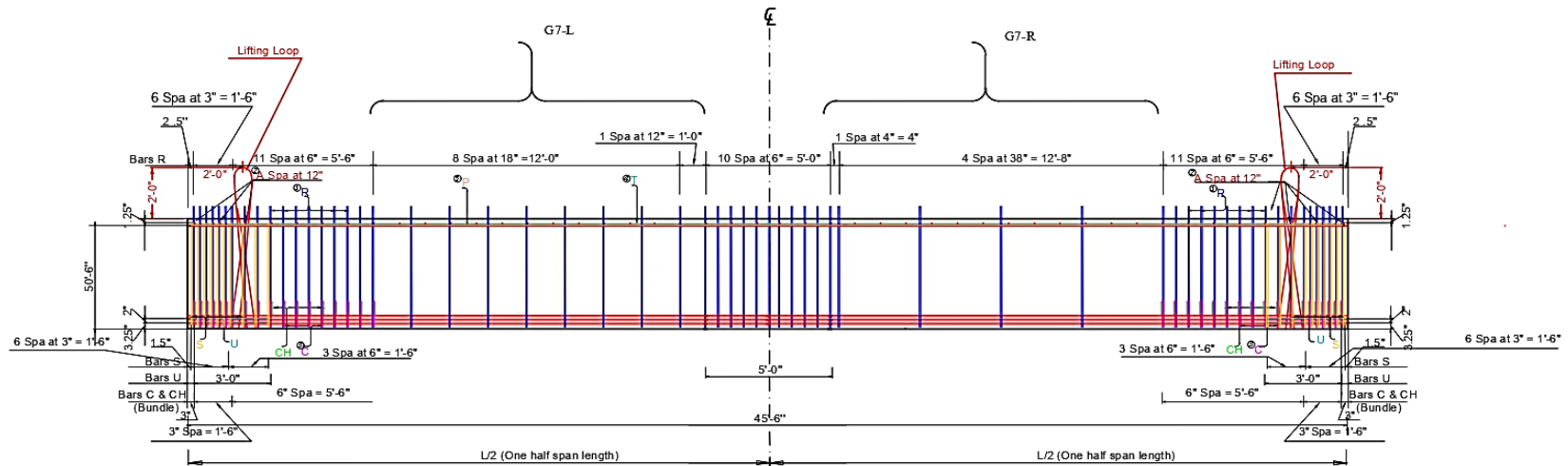
- Standard length for Tx54 girder reinforcement
- To control top flange cracking that may occur during form removal, additional top flange reinforcing may be placed as shown in girder ends at the Fabricator's option.



Texas A&M University		
Texas Department of Transportation		
TxDOT Project 0-7114		
Bar Bending Details		
DRAWING NO.	DATE	SCALE
S7114-13	8/7/2022	1:20

# Tx-54 Girder 4

GIRDER DIMENSIONS AND SECTION PROPERTIES							
Girder Type	"D" (in.)	"B" (in.)	"T" (in.)	"Yb" (in.)	Area (in.2)	"I" (in.4)	Weight (plf)
Tx54	54	30	30.49	23.51	817	299,740	46,707



Cross-section Geometry  
(Scale 1:30)

- ① The average of the spacing of Bars R cannot exceed the required spacing.
- ② Bars A at 12" c/c and tied to Bars T.
- ③ Bundled with Bars R from ends to 7'.
- ④ 4 Bars T #4 45°-3" long at 2" side cover (effective) at both sides of top flange.
- ⑤ 4 Bars P #6 45°-3" long at both ends of girder.
- ⑥ Based on 155 pcf total weight of concrete and reinforcing steel.

## General Notes:

1. Half span with 18" spacing transverse reinforcement in the web, the other half with 26" spacing of transverse reinforcement in the web.
2. 1.5" clear cover unless noted otherwise.
3. For bar bending details, see drawing S7114-17.
4. Cover dimensions are clear dimensions, unless noted otherwise.
5. Reinforcing bar dimensions shown are center-to-center of bar.
6. Research team needs to be present for the installation of R bars to ensure the correct location of the gaged bars.
7. 0.6 in. diameter, seven wire low relaxation prestressing strands, 32 at bottom.
8. Total girder length of this sheet is 45'-6".
9. When cutting the strands, maintain 18" of strand projecting from each girder end. (Final dimension can be coordinated with the research team.)
10. Prior to delivery, cut the strands such that 12" of strand projects from each girder end.
11. Provide Grade 60 reinforcing steel, unless noted otherwise.

## Low Relaxation (270 ksi) Strand Pattern

Number of strands: 34 ~ 0.6" @ 43.94 k per strand
Number of straight strands: 34 (32 Bot & 2 Top)
Number of deflected strands: 0
Concrete release strength: 6 ksi
Concrete design strength: 7 ksi
Eccentricity @ $\frac{L}{2}$ : 16.89" and @ end: 16.89"

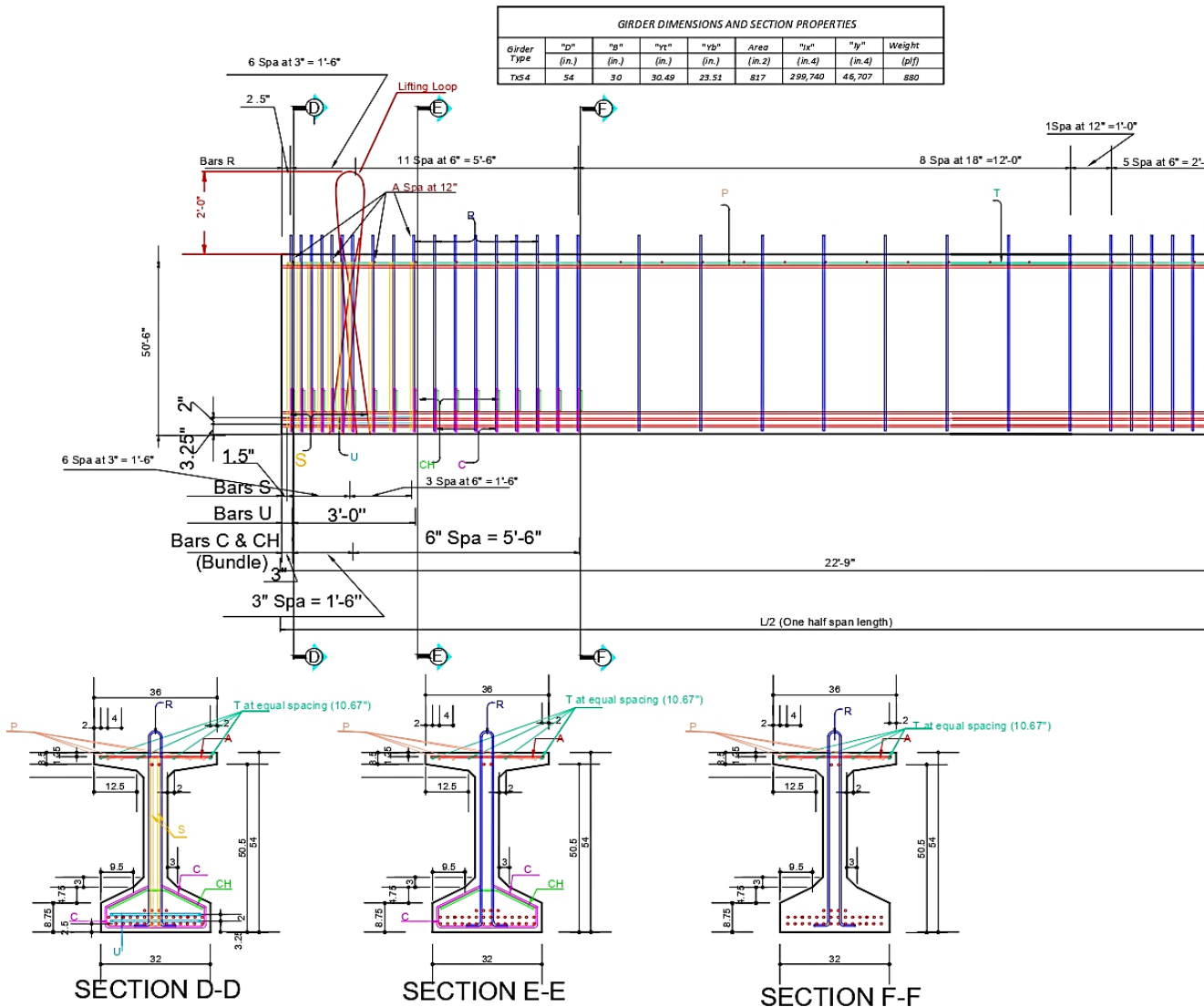
Texas A&M University

Texas Department of Transportation

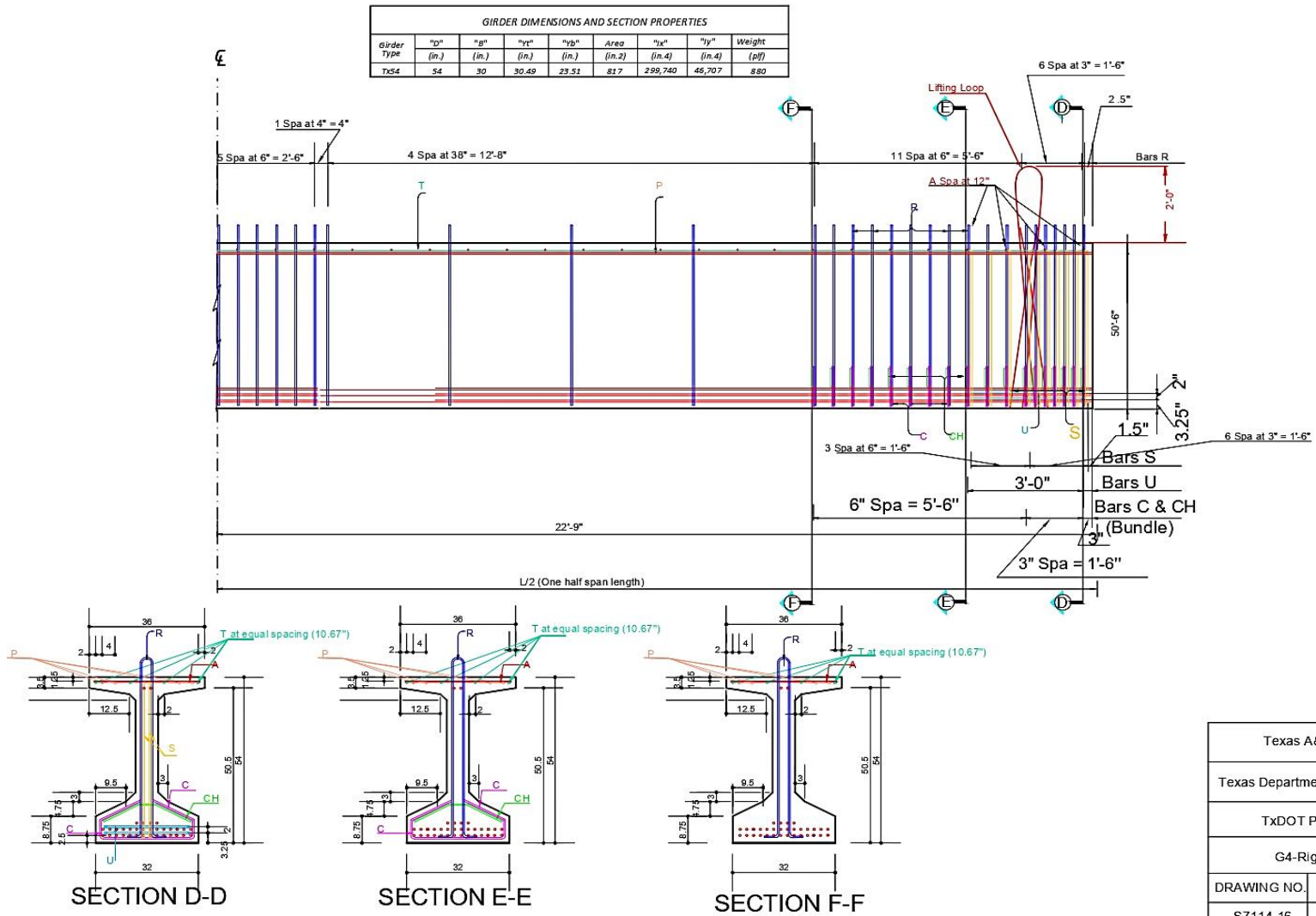
TxDOT Project 0-7114

Girder 4 Details

DRAWING NO.	DATE	SCALE
S7114-14	8/7/2022	1:50

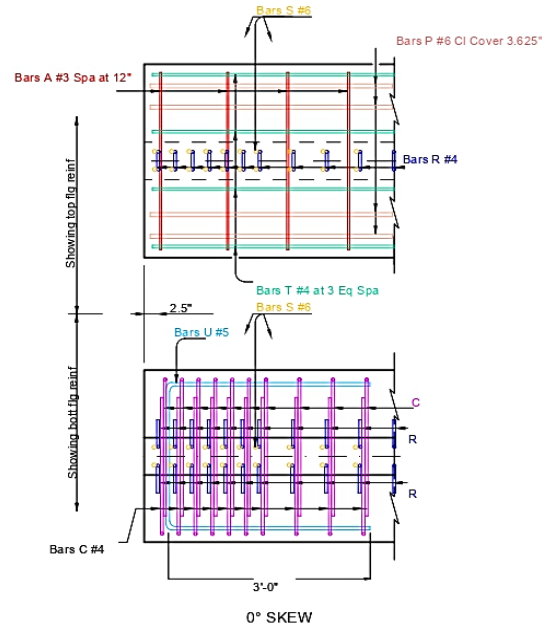
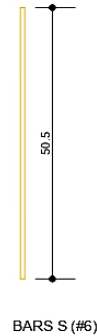
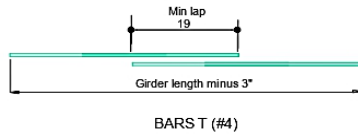
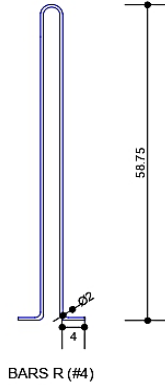
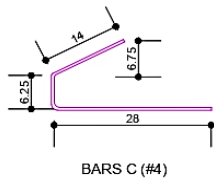
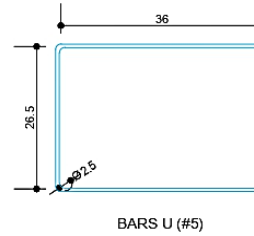
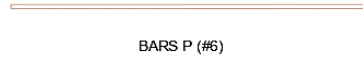
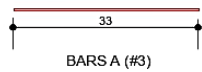


Texas A&M University		
Texas Department of Transportation		
TxDOT Project 0-7114		
G4-Left Side Details		
DRAWING NO.	DATE	SCALE
S7114-15	8/7/2022	1:30



Texas A&M University		
Texas Department of Transportation		
TxDOT Project 0-7114		
G4-Right Side Details		
DRAWING NO.	DATE	SCALE
S7114-16	8/7/2022	1:30



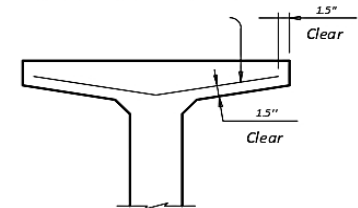


## BILL OF REINFORCEMENT STEEL

BAR	SIZE	TOTAL NO. OF BARS	LENGTH	WEIGHT (lb)
A	# 3	46	2'-9"	48
C	# 4	72	4'-0.25"	193
CH	# 4	36	2'-6"	60
P	# 6	4	45'-3"	270
R	# 4	59	10'-8"	420
T	# 4	4	45'-3"	121
U	# 5	4	8'-2.5"	34
S	# 6	40	4'-2.5"	253

\* Standard length for Tx54 girder reinforcement

To control top flange cracking that may occur during form removal, additional top flange reinforcing may be placed as shown in girder ends at the Fabricator's option.



OPTIONAL TOP FLANGE REINFORCING DETAIL

Texas A&M University

Texas Department of Transportation

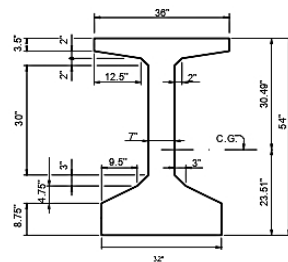
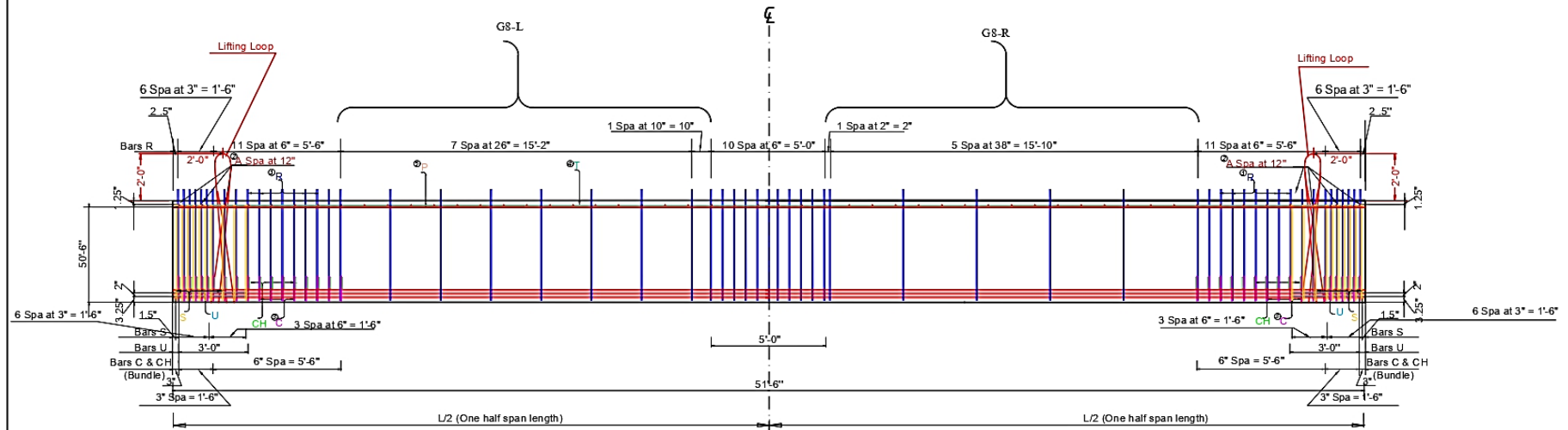
TxDOT Project 0-7114

Bar Bending Details

DRAWING NO.	DATE	SCALE
S7114-17	8/7/2022	1:20

# Tx-54 Girder 5

GIRDER DIMENSIONS AND SECTION PROPERTIES							
Girder Type	"d"	"g"	"yt"	"yb"	Area	"yx"	"yy"
	(in.)	(in.)	(in.)	(in.)	(in. 2)	(in. 4)	(in. 4)
Tx54	54	30	30.49	23.51	817	299,740	46,707
							880



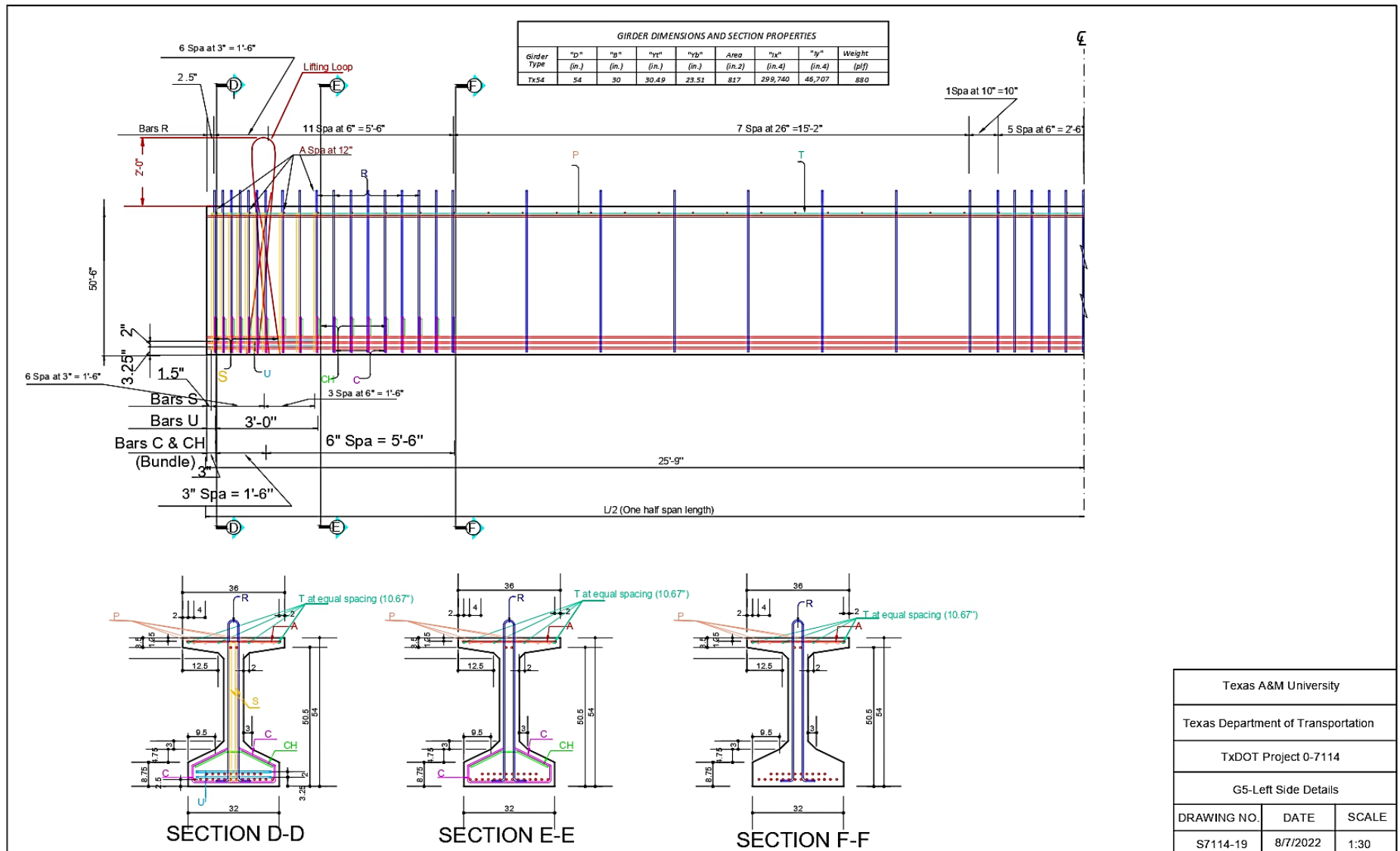
Cross-section Geometry  
(Scale 1:30)

- ① The average of the spacing of Bars R cannot exceed the required spacing.
- ② Bars A at 12" c/c and tied to Bars T.
- ③ Bundled with Bars R from ends to 7'.
- ④ 4 Bars T #4 S1'3" long at 3" side cover (effective) at both sides of top flange.
- ⑤ 4 Bars P #6 15' long at both ends of girder.
- ⑥ Based on 155 pcf total weight of concrete and reinforcing steel.

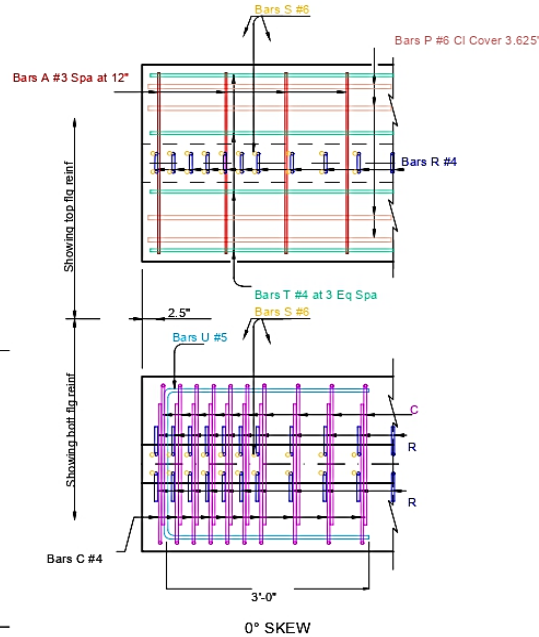
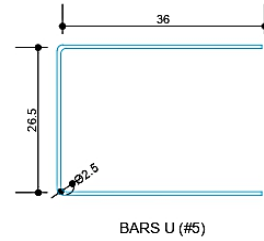
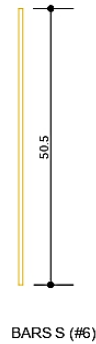
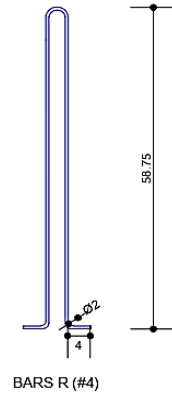
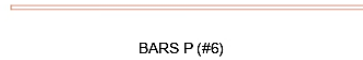
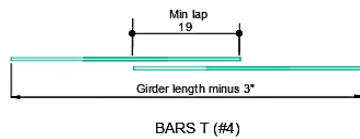
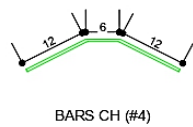
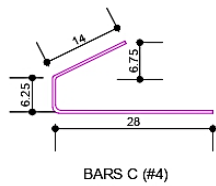
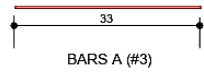
- General Notes:
1. Half span with 26" spacing transverse reinforcement in the web, the other half with 38" spacing of transverse reinforcement in the web.
  2. 1.5" clear cover unless noted otherwise.
  3. For bar bending details, see drawing S7114-21.
  4. Cover dimensions are clear dimensions, unless noted otherwise.
  5. Reinforcing bar dimensions shown are center-to-center of bar.
  6. Research team needs to be present for the installation of R bars to ensure the correct location of the gaged bars.
  7. 0.6 in. diameter, seven wire low relaxation prestressing strands, 26 at bottom.
  8. Total girder length of this sheet is 51'-4".
  9. When cutting the strands, maintain 1.8" of strand projecting from each girder end. (Final dimension can be coordinated with the research team.)
  10. Prior to delivery, cut the strands such that 2" of strand projects from each girder end.
  11. Provide Grade 60 reinforcing steel, unless noted otherwise.

Low Relaxation (270 ksi) Strand Pattern	
Number of strands:	26 ~ 0.6" @ 43.94 k per strand
Number of straight strands:	26 (24 Bot & 2 Top)
Number of deflected strands:	0
Concrete release strength:	6 ksi
Concrete design strength:	7 ksi
Eccentricity @ $\frac{L}{4}$ :	16.55"
Eccentricity @ end:	16.55"

Texas A&M University		
Texas Department of Transportation		
TxDOT Project 0-7114		
Girder 5 Details		
DRAWING NO.	DATE	SCALE
S7114-18	8/7/2022	1:50

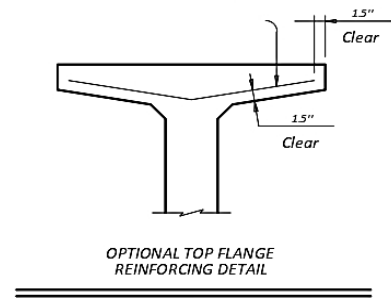






BILL OF REINFORCEMENT STEEL				
BAR	SIZE	TOTAL NO. OF BARS	LENGTH	WEIGHT (lb)
A	# 3	52	2'-9"	54
C	# 4	72	4'-0.25"	193
CH	# 4	36	2'-6"	60
P	# 6	4	15'-0"	91
R	# 4	59	10'-8"	421
T	# 4	4	52'-3"	140
U	# 5	4	8'-2.5"	34
S	# 6	40	4'-2.5"	253

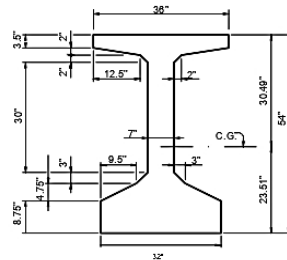
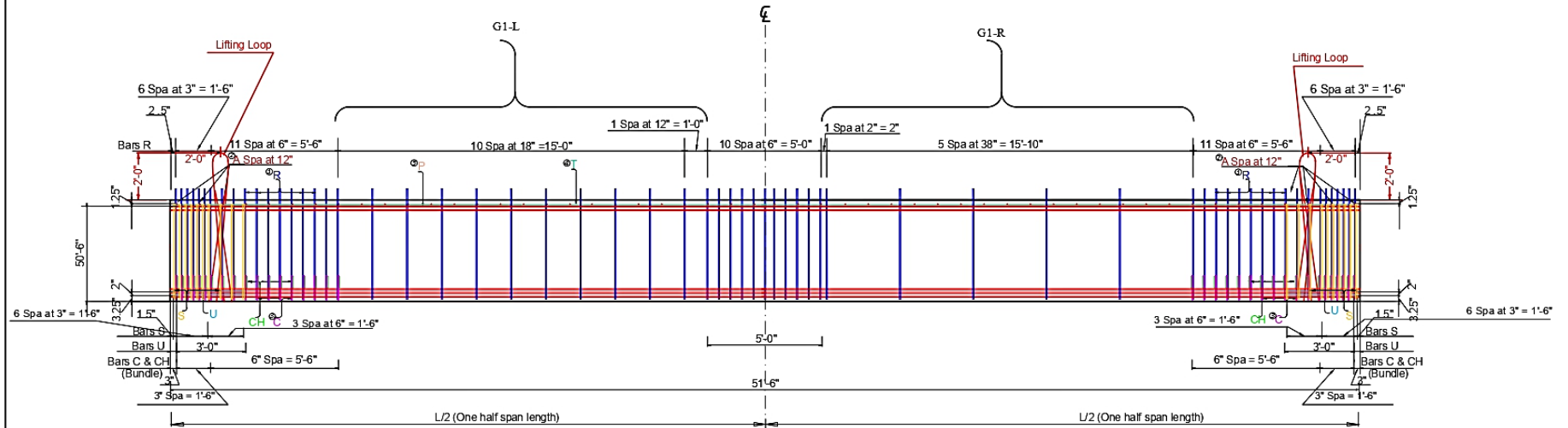
\* Standard length for Tx54 girder reinforcement  
To control top flange cracking that may occur during form removal, additional top flange reinforcing may be placed as shown in girder ends at the Fabricator's option.



Texas A&M University		
Texas Department of Transportation		
TxDOT Project 0-7114		
Bar Bending Details		
DRAWING NO.	DATE	SCALE
S7114-21	8/7/2022	1:20

# Tx-54 Girder 6

GIRDER DIMENSIONS AND SECTION PROPERTIES							
Girder Type	"d"	"g"	"yt"	"yb"	Area	"x"	"y"
(in.)	(in.)	(in.)	(in.)	(in.2)	(in.2)	(in.4)	(plf)
Tx54	54	30	30.49	23.51	81.7	299,740	46,707
							880



Cross-section Geometry  
(Scale 1:30)

- ① The average of the spacing of Bars R cannot exceed the required spacing.
- ② Bars A at 12" c/c and tied to Bars T.
- ③ Bundled with Bars R from ends to 7'.
- ④ 4 Bars T #4 51'-3" long at 2" side cover (effective) at both sides of top flange.
- ⑤ 4 Bars P #6 15' long at both ends of girder.
- ⑥ Based on 155 pcf total weight of concrete and reinforcing steel.

- General Notes:
1. Half span with 18" spacing transverse reinforcement in the web, the other half with 38" spacing of transverse reinforcement in the web.
  2. 1.5" clear cover unless noted otherwise.
  3. For bar bending details, see drawing S7114-25
  4. Cover dimensions are clear dimensions, unless noted otherwise.
  5. Reinforcing bar dimensions shown are center-to-center of bar.
  6. Research team needs to be present for the installation of R bars to ensure the correct location of the gaged bars.
  7. 0.6 in. diameter, seven wire low relaxation prestressing strands, 42 at bottom.
  8. Total girder length of this sheet is 51'-6".
  9. When cutting the strands, maintain 18" of strand projecting from each girder end. (final dimension can be coordinated with the research team)
  10. Prior to delivery, cut the strands such that 2" of strand projects from each girder end.
  11. Provide Grade 60 reinforcing steel, unless noted otherwise.

## Low Relaxation (270 ksi) Strand Pattern

Number of strands: 40 ~ 0.6" @ 43.94 k per strand
Number of straight strands: 40 (36 Bot & 4 Top )
Number of deflected strands: 0
Concrete release strength: 6.3 ksi
Concrete design strength: 7 ksi
Eccentricity @ $\ell$ : 14.71" and @ end: 14.71"

Texas A&M University

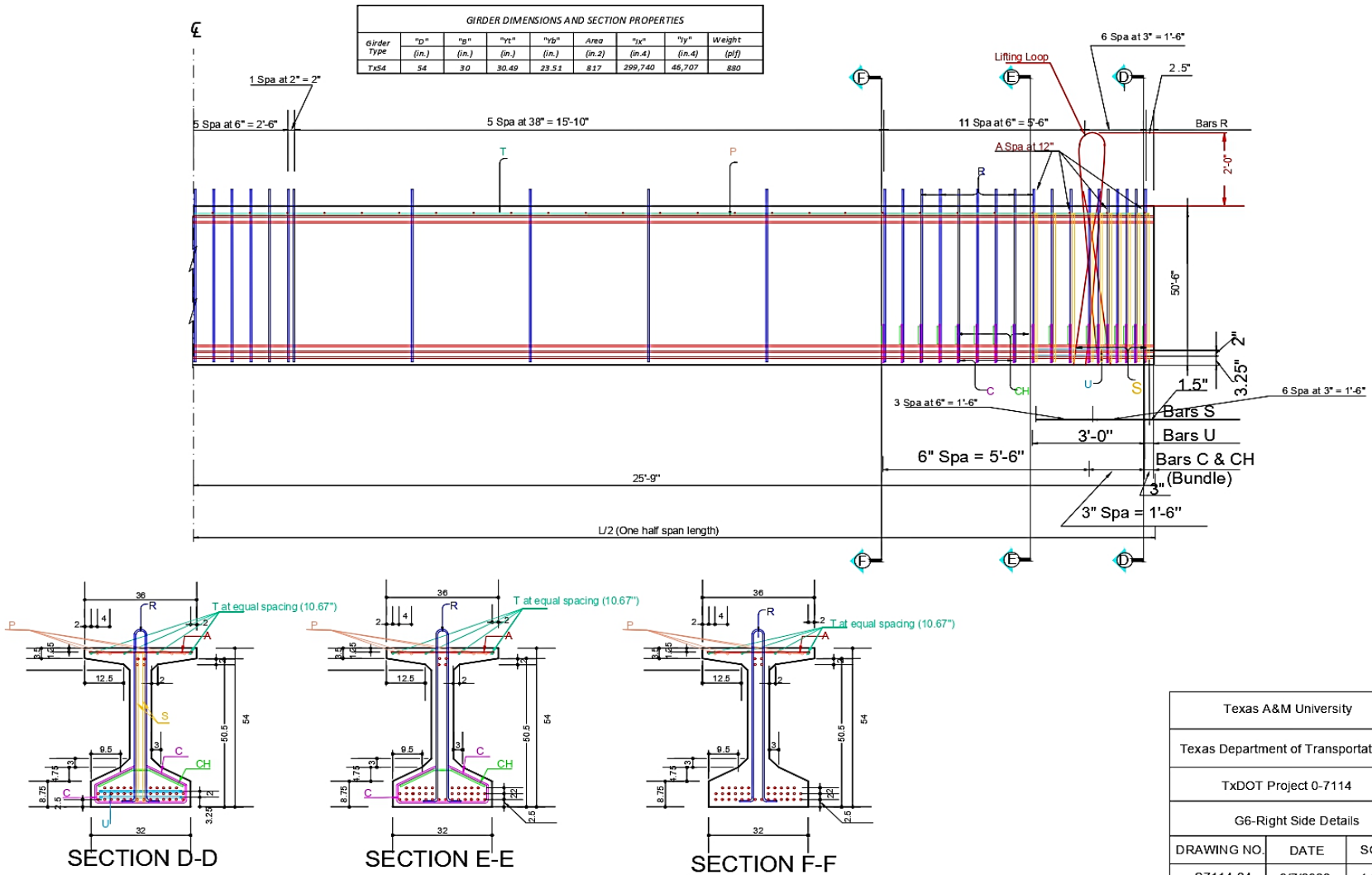
Texas Department of Transportation

TxDOT Project 0-7114

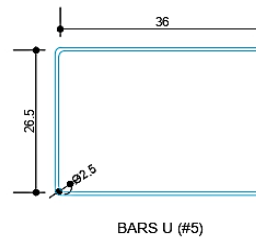
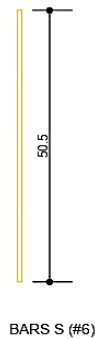
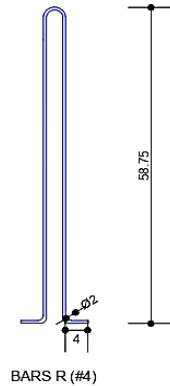
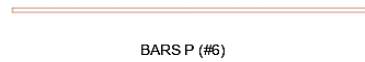
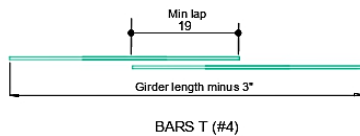
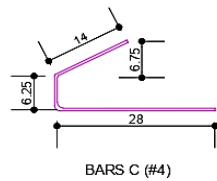
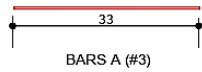
Girder 6 Details

DRAWING NO.	DATE	SCALE
S7114-22	8/7/2022	1:50



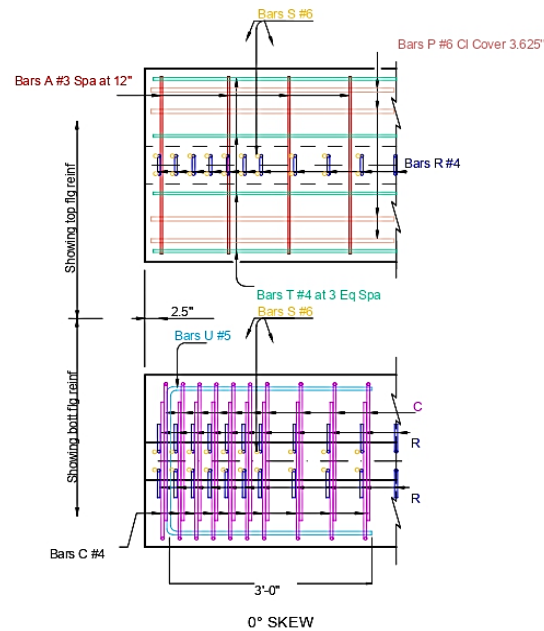




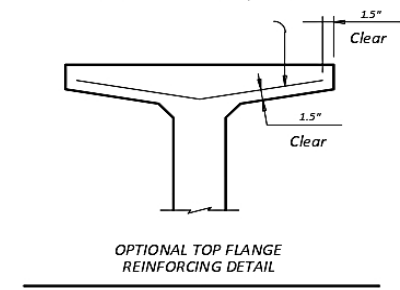


## BILL OF REINFORCEMENT STEEL

BAR	SIZE	TOTAL NO. OF BARS	LENGTH	WEIGHT (lb)
A	# 3	52	2'-9"	54
C	# 4	72	4'-0.25"	193
CH	# 4	36	2'-6"	60
P	# 6	4	15'-0"	91
R	# 4	62	10'-8"	442
T	# 4	4	52'-3"	140
U	# 5	4	8'-2.5"	34
S	# 6	40	4'-2.5"	253



- \* Standard length for Tx54 girder reinforcement  
To control top flange cracking that may occur during form removal, additional top flange reinforcing may be placed as shown in girder ends at the Fabricator's option.

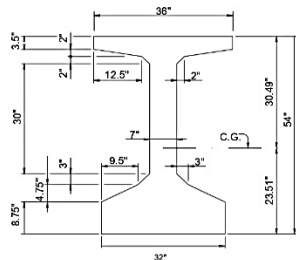
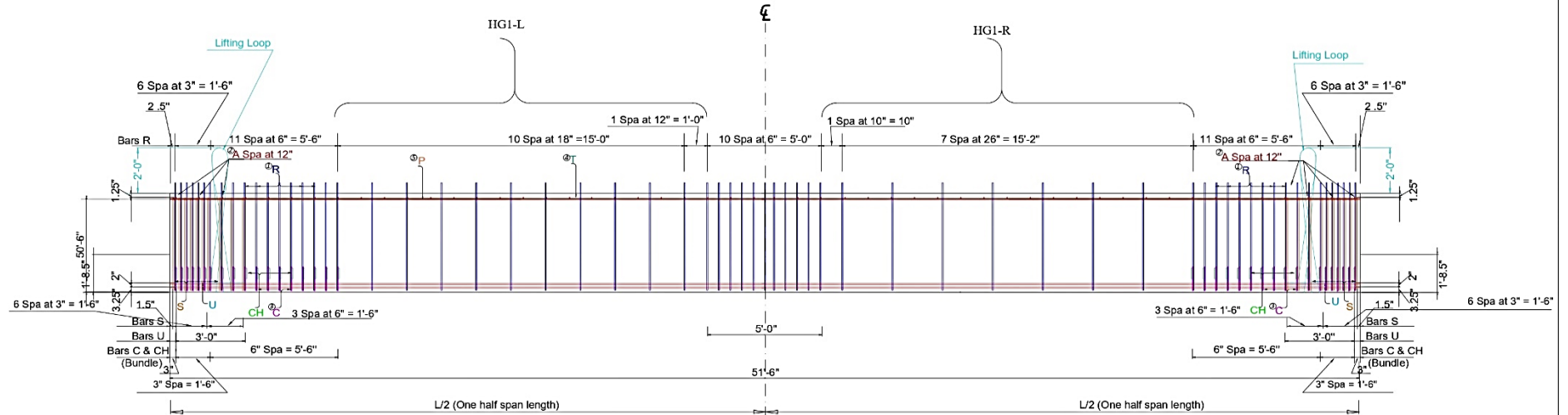


Texas A&M University		
Texas Department of Transportation		
TxDOT Project 0-7114		
Bar Bending Details		
DRAWING NO.	DATE	SCALE
S7114-25	8/7/2022	1:20



# Tx-54 Girder HG1

GIRDER DIMENSIONS AND SECTION PROPERTIES							
Girder Type	"D"	"B"	"yt"	"Yb"	Area	"Ix"	"Iy"
	(in.)	(in.)	(in.)	(in.)	(in. <sup>2</sup> )	(in. <sup>4</sup> )	(in. <sup>4</sup> )
Tx54	54	30	30.49	23.51	817	299,740	46,707
							880



Cross-section Geometry  
(Scale 1:30)

- ① The average of the spacing of Bars R cannot exceed the required spacing.
- ② Bars A at 12" c/c and tied to Bars T.
- ③ Bundled with Bars R from ends to 7'.
- ④ 4 Bars T #4 51'-3" long at 2" side cover (effective) at both sides of top flange.
- ⑤ 4 Bars P #6 15' long at both ends of girder.
- ⑥ Based on 155 pcf total weight of concrete and reinforcing steel.

## General Notes:

1. Half span with 26" spacing transverse reinforcement in the web, the other half with 18" spacing of transverse reinforcement in the web.
2. 1.5" clear cover unless noted otherwise.
3. For bar bending details, see drawing S7114-04.
4. Cover dimensions are clear dimensions, unless noted otherwise.
5. Reinforcing bar dimensions shown are center-to-center of bar.
6. Research team needs to be present for the installation of R bars to ensure the correct location of the gaged bars.
7. 0.6 in. diameter, seven wire low relaxation prestressing strands, 22 at bottom and 2 at top.
8. Total girder length of this sheet is 51'-6".
9. When cutting the strands, maintain 18" of strand projecting from each girder end. (Final dimension can be coordinated with the research team.)
10. Prior to delivery, cut the strands such that 2" of strand projects from each girder end.
11. Provide Grade 60 reinforcing steel, unless noted otherwise.

## Low Relaxation (270 ksi) Strand Pattern

Number of strands: 24 ~ 0.6" @ 34.1 k per strand
Number of straight strands: 24 (22 Bot & 2 Top)
Number of deflected strands: 0
Concrete release strength: 4 ksi
Concrete design strength: 5 ksi
Eccentricity @ $\epsilon$ : 16.34" and @ end: 16.34"

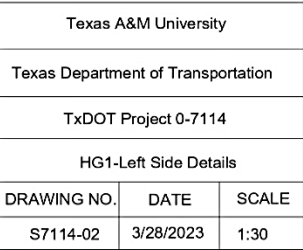
Texas A&M University

Texas Department of Transportation

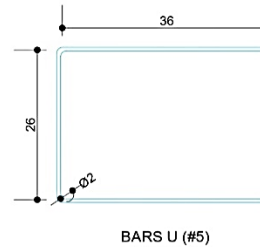
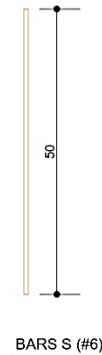
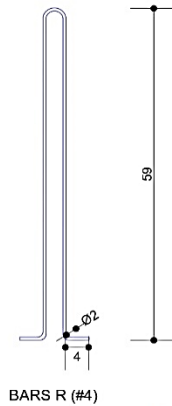
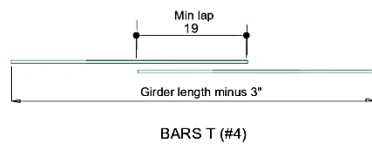
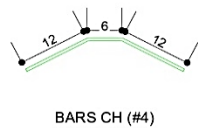
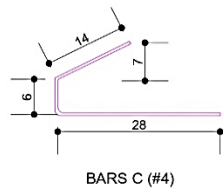
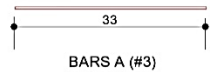
TxDOT Project 0-7114

Girder HG1 Details

DRAWING NO.	DATE	SCALE
S7114-01	3/28/2023	1:50

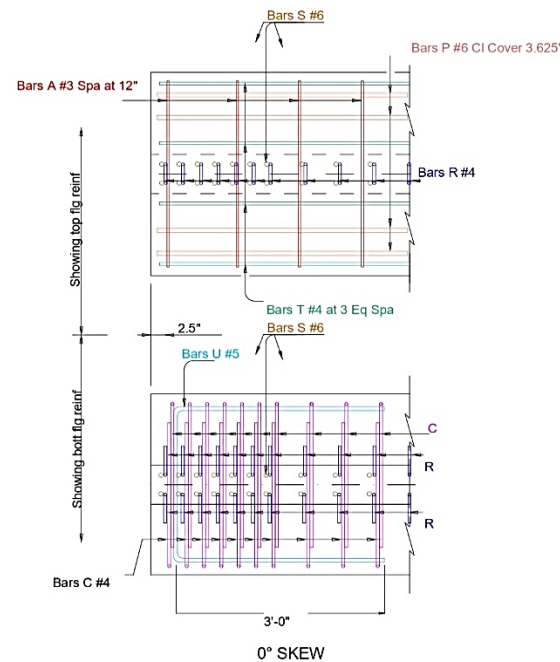






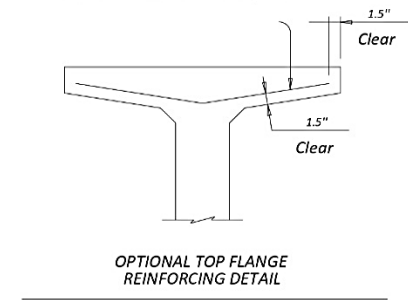
## BILL OF REINFORCEMENT STEEL

BAR	SIZE	TOTAL NO. OF BARS	LENGTH	WEIGHT (lb)
A	# 3	53	2'-9"	55
C	# 4	72	4'-0.25"	193
CH	# 4	36	2'-6"	60
P	# 6	8	15'-0"	182
R	# 4	64	10'-8"	456
T	# 4	4	52'-3"	140
U	# 5	4	8'-2.5"	34
S	# 6	40	4'-2.5"	253



\* Standard length for Tx54 girder reinforcement

To control top flange cracking that may occur during form removal, additional top flange reinforcing may be placed as shown in girder ends at the Fabricator's option.



Texas A&M University

Texas Department of Transportation

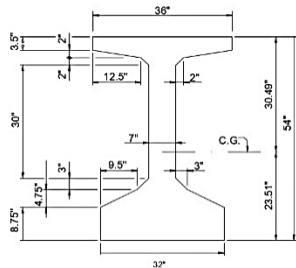
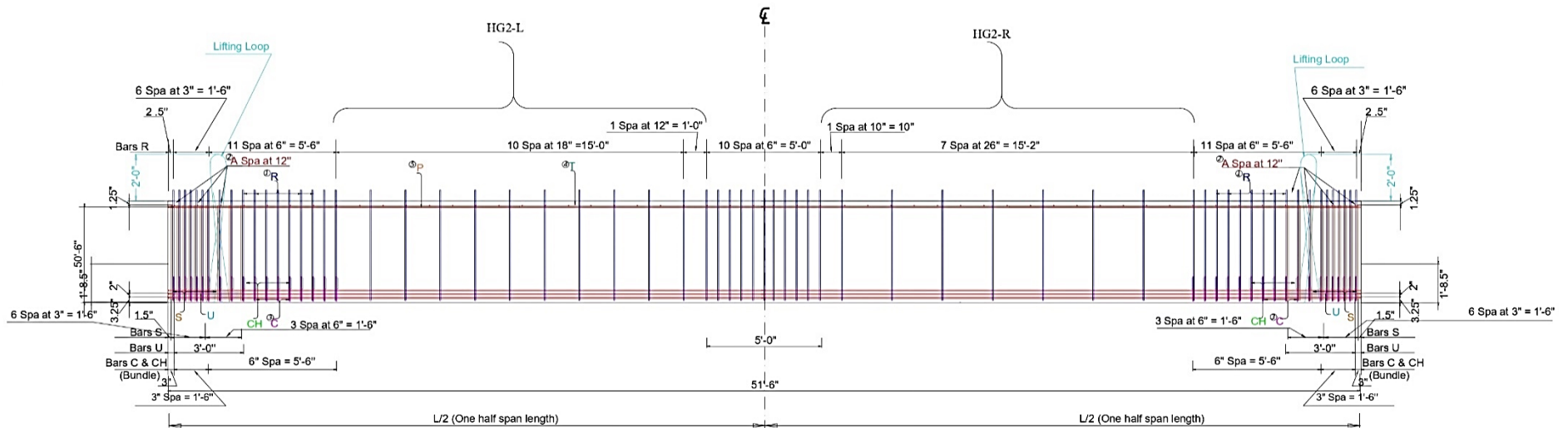
TxDOT Project 0-7114

Bar Bending Details

DRAWING NO.	DATE	SCALE
S7114-04	3/28/2023	1:20

# Tx-54 Girder HG2

GIRDER DIMENSIONS AND SECTION PROPERTIES							
Girder Type	"D"	"B"	"Yt"	"Yb"	Area	"Ix"	"Iy"
(in.)	(in.)	(in.)	(in.)	(in.2)	(in.4)	(in.4)	(in.4)
Tx54	54	30	30.49	23.51	817	299,740	46,707
							880



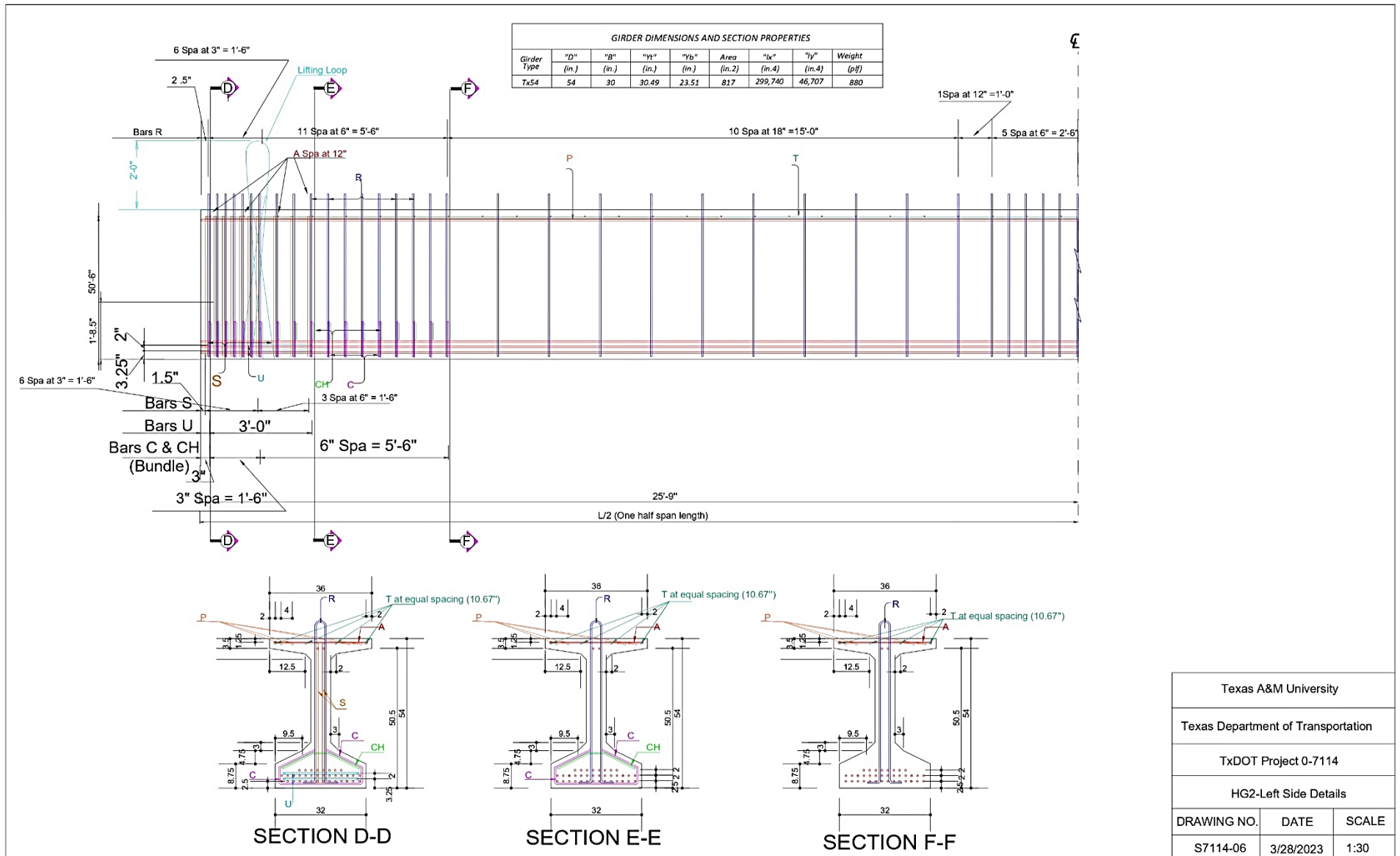
Cross-section Geometry  
(Scale 1:30)

- ① The average of the spacing of Bars R cannot exceed the required spacing.
- ② Bars A at 12\" c/c and tied to Bars T.
- ③ Bundled with Bars R from ends to 7\".
- ④ 4 Bars T #4 51\"-3\" long at 2\" side cover (effective) at both sides of top flange.
- ⑤ 4 Bars P #6 15\" long at both ends of girder.
- ⑥ Based on 155 pcf total weight of concrete and reinforcing steel.

- General Notes:
1. Half span with 26\" spacing transverse reinforcement in the web, the other half with 18\" spacing of transverse reinforcement in the web.
  2. 1.5\" clear cover unless noted otherwise.
  3. For bar bending details, see drawing S7114 - 08.
  4. Cover dimensions are clear dimensions, unless noted otherwise.
  5. Reinforcing bar dimensions shown are center-to-center of bar.
  6. Research team needs to be present for the installation of R bars to ensure the correct location of the gaged bars.
  7. 0.6 in. diameter, seven wire low relaxation prestressing strands, 36 at bottom and 2 at top.
  8. Total girder length of this sheet is 51'-6\".
  9. When cutting the strands, maintain 18\" of strand projecting from each girder end. (Final dimension can be coordinated with the research team.)
  10. Prior to delivery, cut the strands such that 2\" of strand projects from each girder end.
  11. Provide Grade 60 reinforcing steel, unless noted otherwise.

Low Relaxation (270 ksi) Strand Pattern	
Number of strands:	38 ~ 0.6\" @ 34.1 k per strand
Number of straight strands:	38 (36 Bot & 2 Top)
Number of deflected strands:	0
Concrete release strength:	6 ksi
Concrete design strength:	8.5 ksi
Eccentricity @ $\epsilon$ :	16.90\" and @ end: 16.90\"

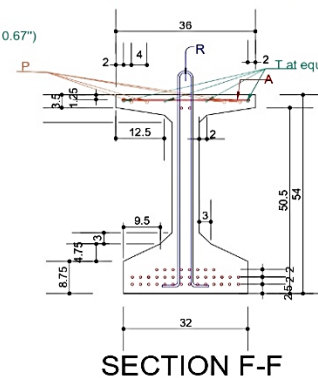
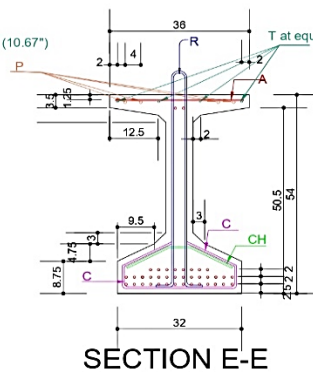
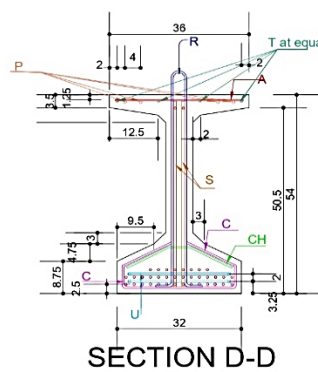
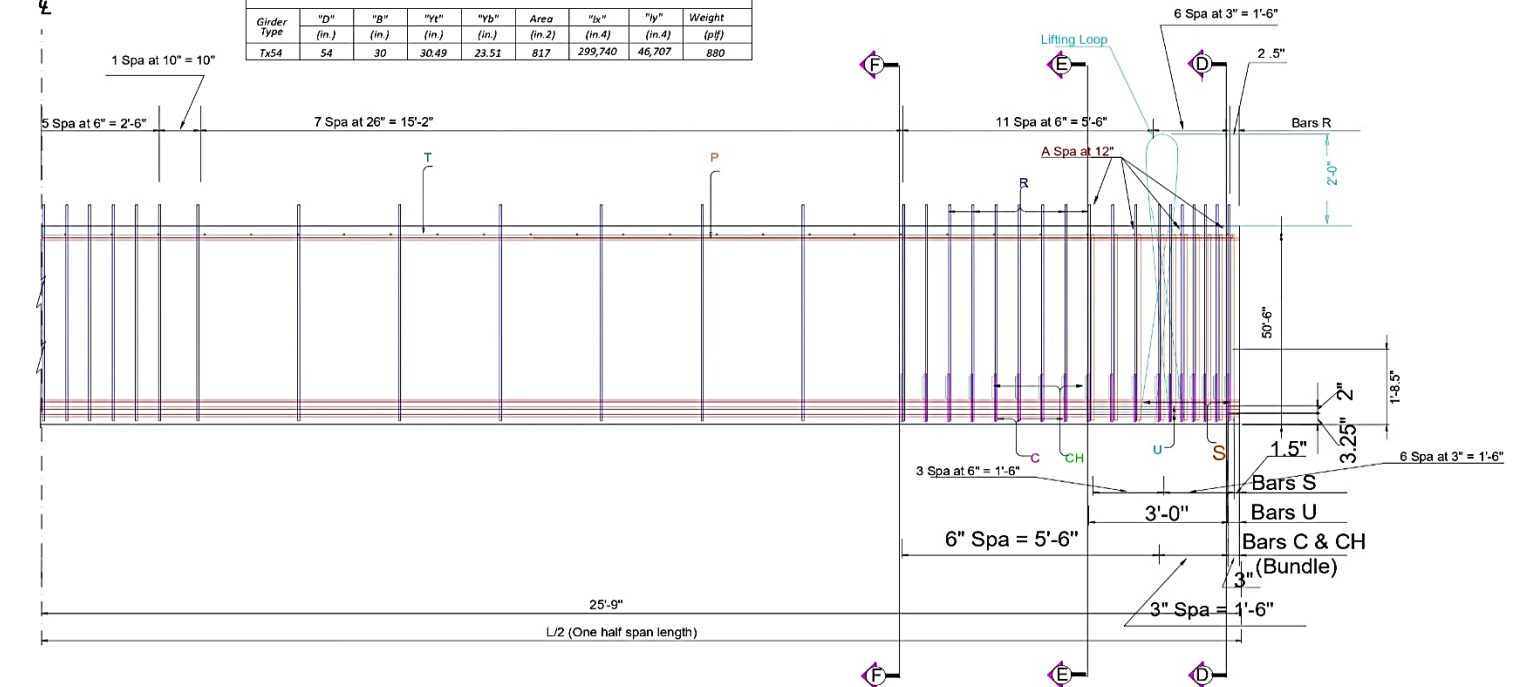
Texas A&M University		
Texas Department of Transportation		
TxDOT Project 0-7114		
Girder HG2 Details		
DRAWING NO.	DATE	SCALE
S7114-05	3/28/2023	1:50



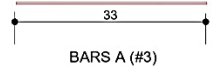


ℓ

GIRDER DIMENSIONS AND SECTION PROPERTIES							
Girder Type	"D" (in.)	"B" (in.)	"t <sub>f</sub> " (in.)	"t <sub>w</sub> " (in.)	Area (in. <sup>2</sup> )	"I <sub>x</sub> " (in. <sup>4</sup> )	Weight (p/f)
7x54	54	30	30.49	23.51	817	299,740	46,707



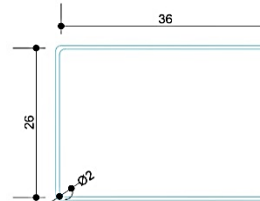
Texas A&M University		
Texas Department of Transportation		
TxDOT Project 0-7114		
HG2-Right Side Details		
DRAWING NO.	DATE	SCALE
S7114-07	3/28/2023	1:30



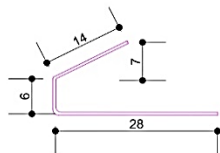
BARS A (#3)



BARS P (#6)



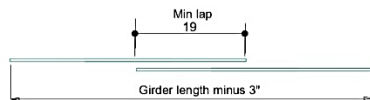
BARS U (#5)



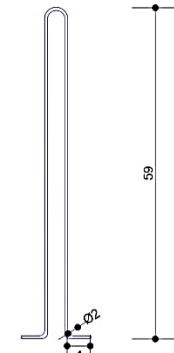
BARS C (#4)



BARS CH (#4)



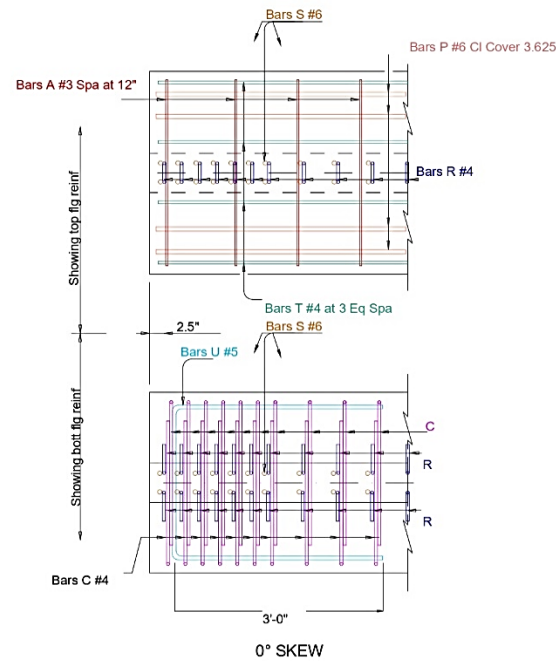
BARS T (#4)



BARS R (#4)



BARS S (#6)

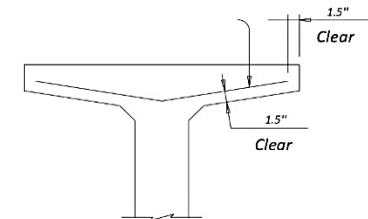


## BILL OF REINFORCEMENT STEEL

BAR	SIZE	TOTAL NO. OF BARS	LENGTH	WEIGHT (lb)
A	# 3	53	2'-9"	55
C	# 4	72	4'-0.25"	193
CH	# 4	36	2'-6"	60
P	# 6	8	15'-0"	182
R	# 4	64	10'-8"	456
T	# 4	4	52'-3"	140
U	# 5	4	8'-2.5"	34
S	# 6	40	4'-2.5"	253

\* Standard length for Tx54 girder reinforcement

To control top flange cracking that may occur during form removal, additional top flange reinforcing may be placed as shown in girder ends at the Fabricator's option.



OPTIONAL TOP FLANGE REINFORCING DETAIL

Texas A&M University

Texas Department of Transportation

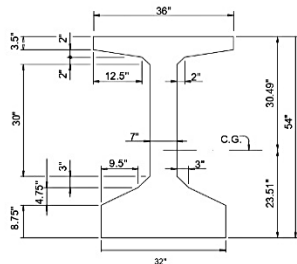
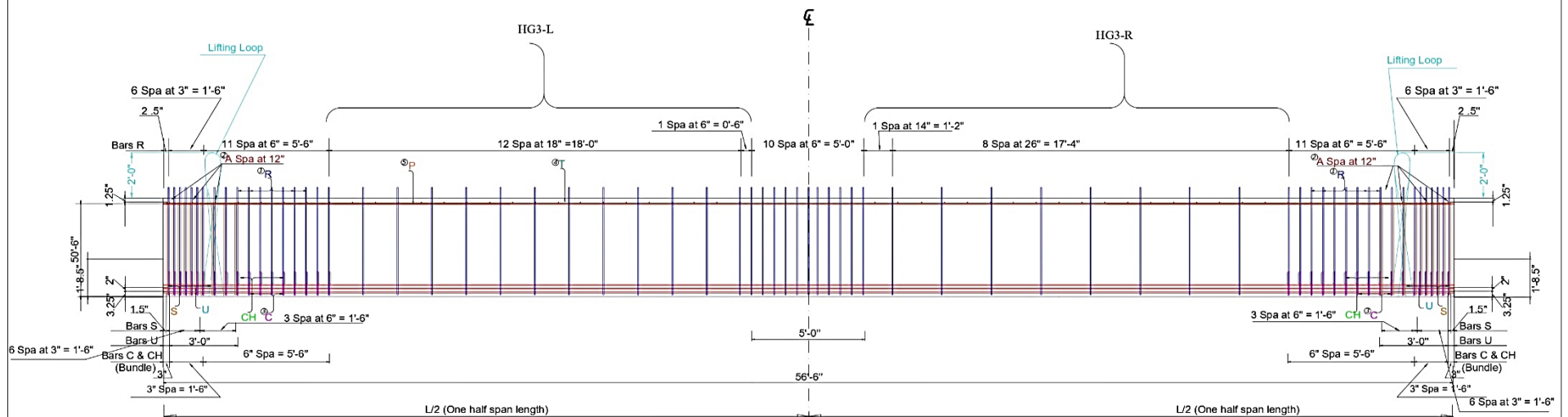
TxDOT Project 0-7114

Bar Bending Details

DRAWING NO.	DATE	SCALE
S7114-08	3/28/2023	1:20

# Tx-54 Girder HG3

GIRDER DIMENSIONS AND SECTION PROPERTIES							
Girder Type	"D" (in.)	"B" (in.)	"Yt" (in.)	"Yb" (in.)	Area (in.2)	"Ix" (in.4)	"Iy" (in.4)
Tx54	54	30	30.49	23.51	817	299,740	46,707
							Weight (plf)
							880



Cross-section Geometry  
(Scale 1:30)

- ① The average of the spacing of Bars R cannot exceed the required spacing.
- ② Bars A at 12" c/c and tied to Bars T.
- ③ Bundled with Bars R from ends to 7'.
- ④ 4 Bars T #4 56'-3" long at 2" side cover (effective) at both sides of top flange.
- ⑤ 4 Bars P #6 15' long at both ends of girder.
- ⑥ Based on 155 pcf total weight of concrete and reinforcing steel.

## General Notes:

1. Half span with 18" spacing transverse reinforcement in the web, the other half with 26" spacing of transverse reinforcement in the web.
2. 1.5" clear cover unless noted otherwise.
3. For bar bending details, see drawing S7114 - 12.
4. Cover dimensions are clear dimensions, unless noted otherwise.
5. Reinforcing bar dimensions shown are center-to-center of bar.
6. Research team needs to be present for the installation of R bars to ensure the correct location of the gaged bars.
7. 0.6 in. diameter, seven wire low relaxation prestressing strands, 32 at bottom and 2 at top.
8. Total girder length of this sheet is 56'-6".
9. When cutting the strands, maintain 18" of strand projecting from each girder end. (Final dimension can be coordinated with the research team.)
10. Prior to delivery, cut the strands such that 2" of strand projects from each girder end.
11. Provide Grade 60 reinforcing steel, unless noted otherwise.

## Low Relaxation (270 ksi) Strand Pattern

Number of strands: 34 ~ 0.6" @ 34.1 k per strand
Number of straight strands: 34 (32 Bot & 2 Top)
Number of deflected strands: 0
Concrete release strength: 6 ksi
Concrete design strength: 7 ksi
Eccentricity @ $\epsilon$ : 16.89" and @ end: 16.89"

Texas A&M University

Texas Department of Transportation

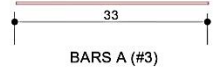
TxDOT Project 0-7114

Girder HG3 Details

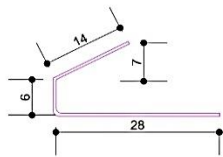
DRAWING NO.	DATE	SCALE
S7114-09	3/28/2023	1:50



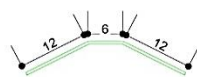




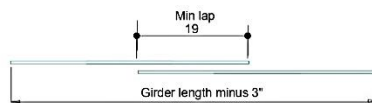
BARS A (#3)



BARS C (#4)



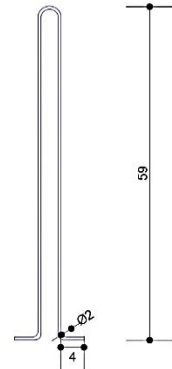
BARS CH (#4)



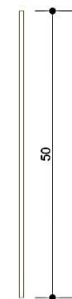
BARS T (#4)



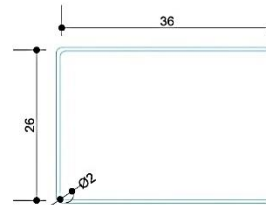
BARS P (#6)



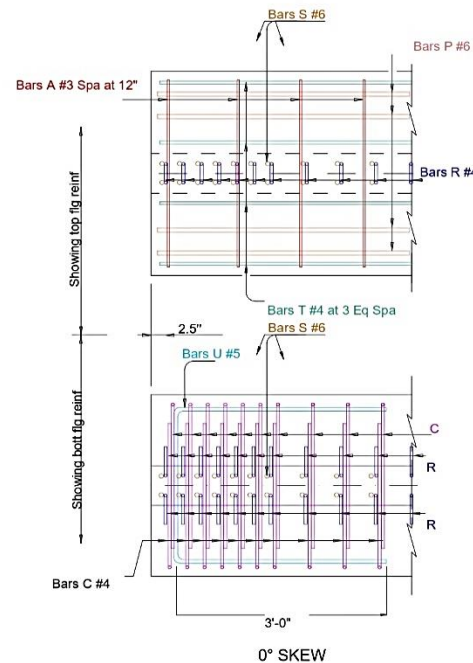
BARS R (#4)



BARS S (#6)



BARS U (#5)



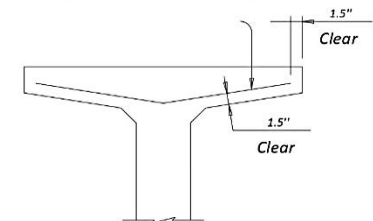
## BILL OF REINFORCEMENT STEEL

BAR	SIZE	TOTAL NO. OF BARS	LENGTH	WEIGHT (lb)
A	# 3	56	2'-9"	58
C	# 4	72	4'-0.25"	193
CH	# 4	36	2'-6"	60
P	# 6	8	15'-0"	182
R	# 4	67	10'-8"	477
T	# 4	4	56'-3"	151
U	# 5	4	8'-2.5"	34
S	# 6	40	4'-2.5"	253

Bars P #6 Cl Cover 3.625"

### \* Standard length for Tx54 girder reinforcement

To control top flange cracking that may occur during form removal, additional top flange reinforcing may be placed as shown in girder ends at the Fabricator's option.



OPTIONAL TOP FLANGE REINFORCING DETAIL

Texas A&M University

Texas Department of Transportation

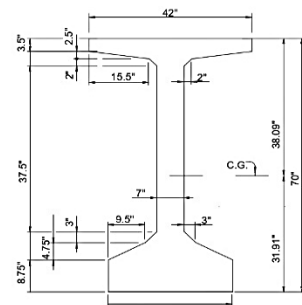
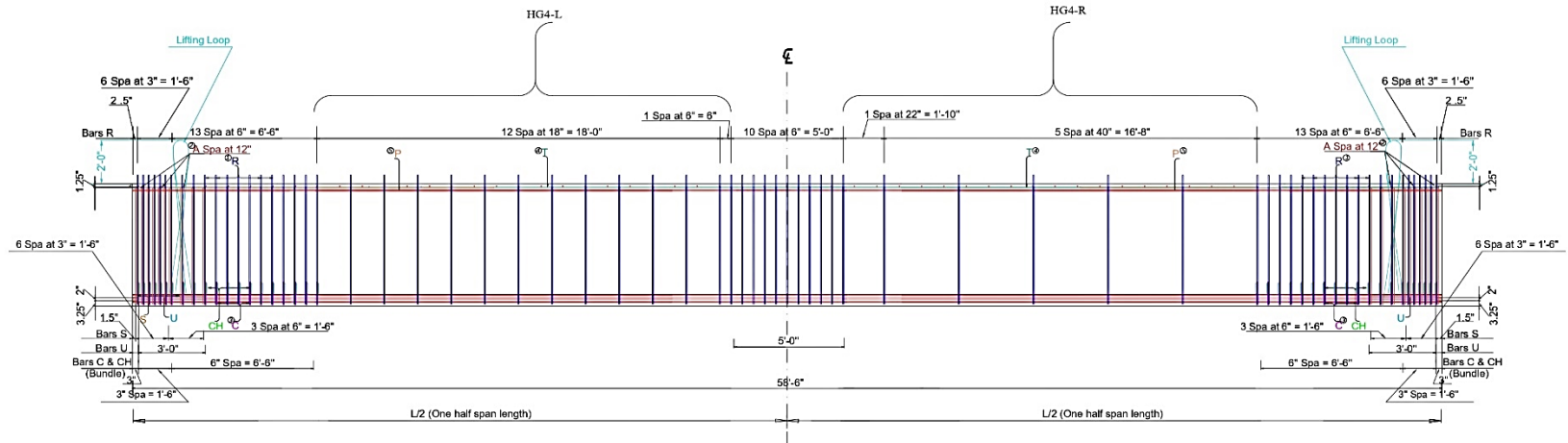
TxDOT Project 0-7114

Bar Bending Details

DRAWING NO.	DATE	SCALE
S7114-12	3/28/2023	1:20

# Tx-70 Girder HG4

GIRDER DIMENSIONS AND SECTION PROPERTIES							
Girder Type	"D"	"B"	"Yt"	"Yb"	Area	"Ix"	"Iy"
	(in.)	(in.)	(in.)	(in.)	(in. <sup>2</sup> )	(in. <sup>4</sup> )	(in. <sup>4</sup> )
Tx70	70	45.5	38.09	31.91	966	628,747	57,579
							1,040



Cross-section Geometry  
(Scale 1:30)

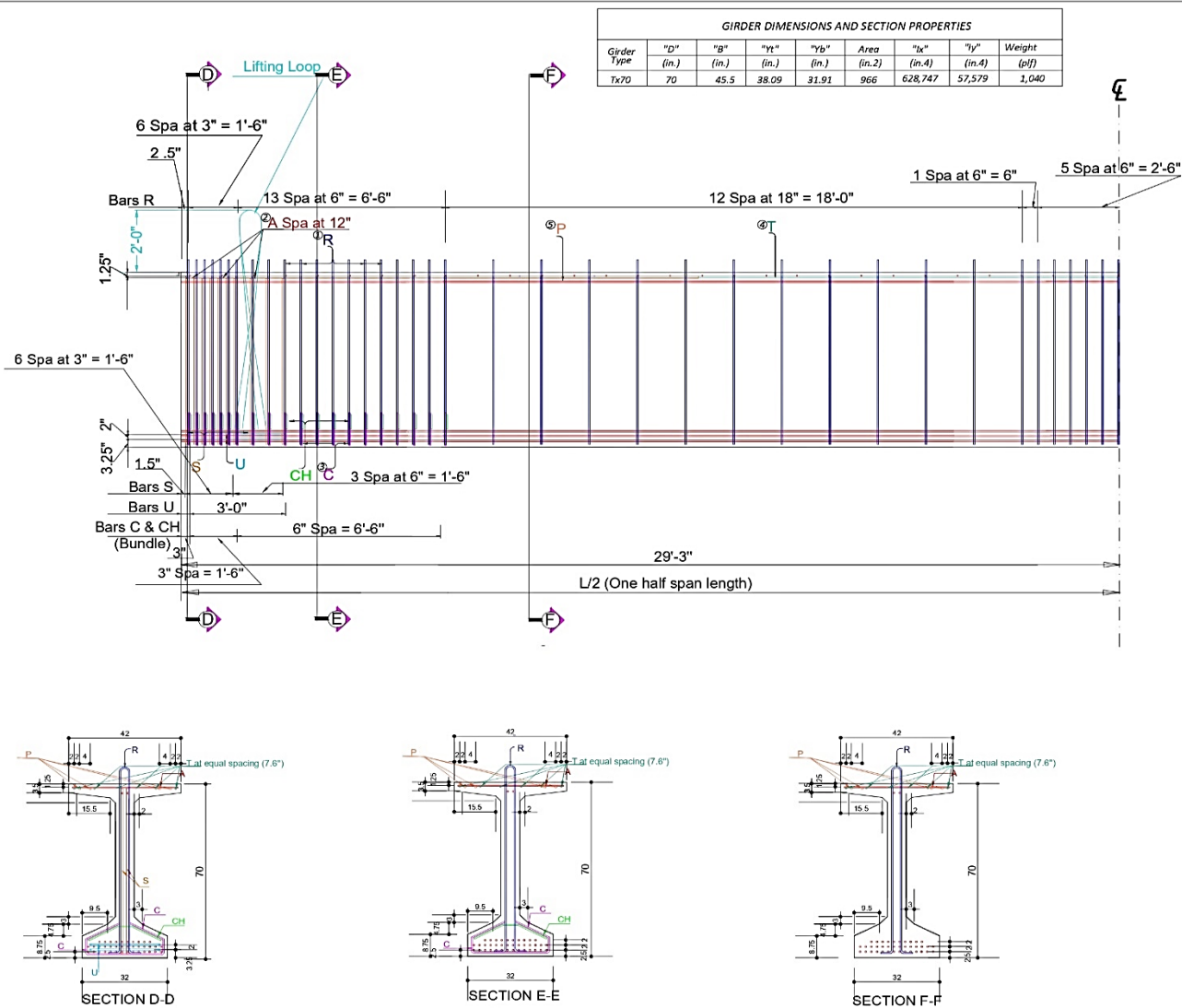
- ① The average of the spacing of Bars R cannot exceed the required spacing.
- ② Bars A at 12" c/c and tied to Bars T.
- ③ Bundled with Bars R from ends to 7'.
- ④ 4 Bars T #4 58" 3" long at 2" side cover (effective) at both sides of top flange.
- ⑤ 4 Bars P #6 15' long at both ends of girder.
- ⑥ Based on 155 pcf total weight of concrete and reinforcing steel.

- General Notes:
1. Half span with 18" spacing transverse reinforcement in the web, the other half with 40" spacing of transverse reinforcement in the web.
  2. 1.5" clear cover unless noted otherwise.
  3. For bar bending details, see drawing S7114 - 16
  4. Cover dimensions are clear dimensions, unless noted otherwise.
  5. Reinforcing bar dimensions shown are center-to-center of bar.
  6. Research team needs to be present for the installation of R bars to ensure the correct location of the gaged bars.
  7. 0.6 in. diameter, seven wire low relaxation prestressing strands, 38 at bottom and 2 at top.
  8. Total girder length of this sheet is 58'-6".
  9. When cutting the strands, maintain 18" of strand projecting from each girder end. (Final dimension can be coordinated with the research team.)
  10. Prior to delivery, cut the strands such that 2" of strand projects from each girder end.
  11. Provide Grade 60 reinforcing steel, unless noted otherwise.

Low Relaxation (270 ksi) Strand Pattern	
Number of strands:	40 ~ 0.6" @ 32 k per strand
Number of straight strands:	40 (38 Bot & 2 Top)
Number of deflected strands:	0
Concrete release strength:	6 ksi
Concrete design strength:	7 ksi
Eccentricity @ $\epsilon$ :	24.51" and @ end: 24.51"

Texas A&M University		
Texas Department of Transportation		
TxDOT Project 0-7114		
Girder HG4 Details		
DRAWING NO.	DATE	SCALE
S7114-13	3/28/2023	1:60

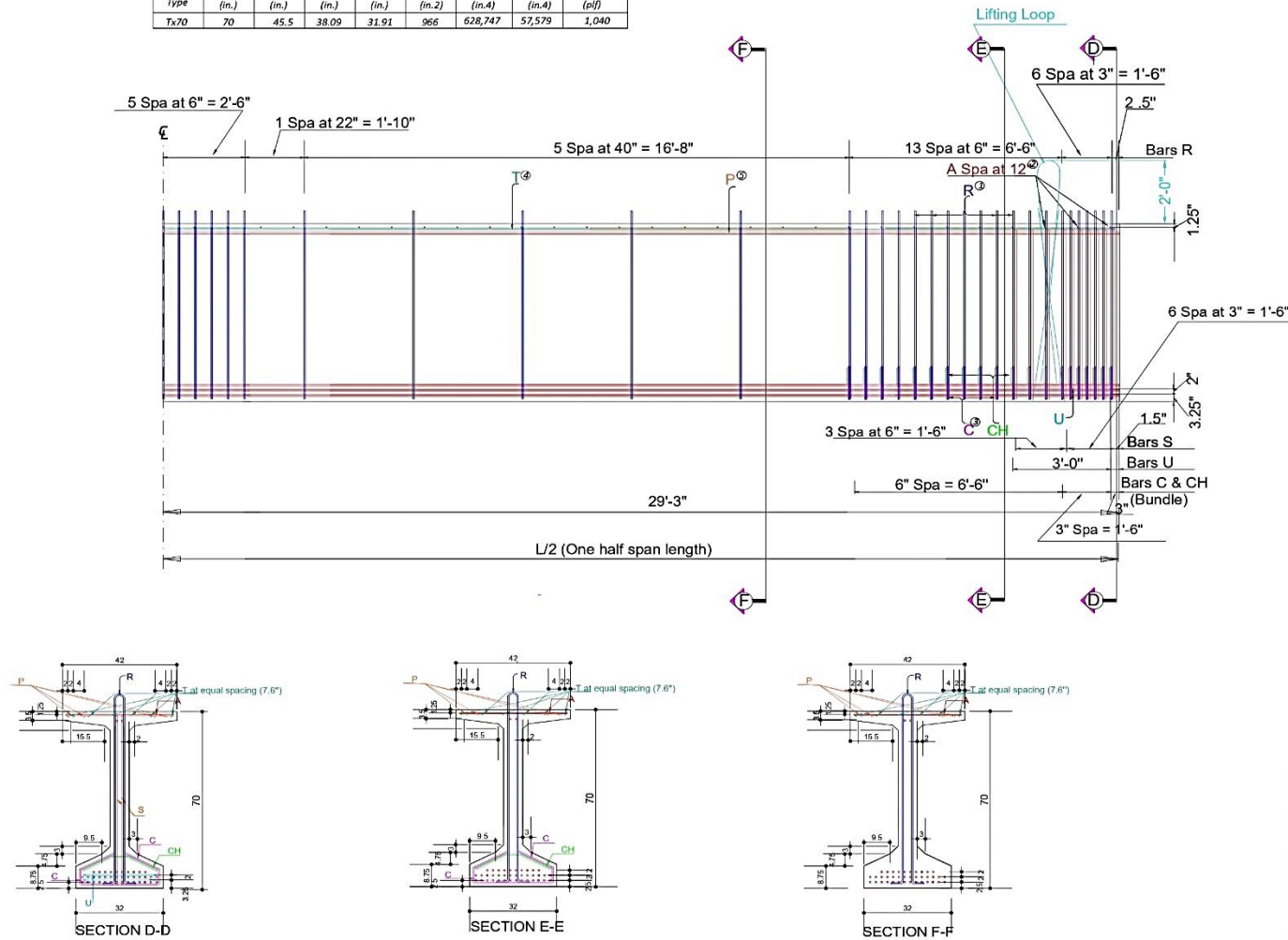




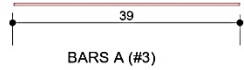
Texas A&M University		
Texas Department of Transportation		
TxDOT Project 0-7114		
HG4-Left Side Details		
DRAWING NO.	DATE	SCALE
S7114-14	3/28/2023	1:40



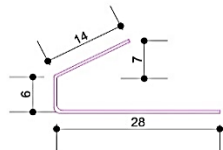
GIRDER DIMENSIONS AND SECTION PROPERTIES								
Girder Type	"D"	"B"	"Yt"	"Yb"	Area	"Ix"	"Iy"	Weight
	(in.)	(in.)	(in.)	(in.)	(in.2)	(in.4)	(in.4)	(plf)
Tx70	70	45.5	38.09	31.91	966	628,747	57,579	1,040



Texas A&M University		
Texas Department of Transportation		
TxDOT Project 0-7114		
HG4-Right Side Details		
DRAWING NO.	DATE	SCALE
S7114-15	3/28/2023	1:40



BARS A (#3)



BARS C (#4)



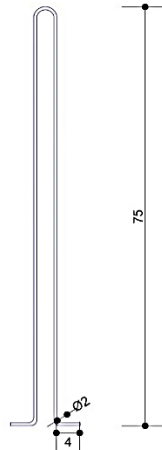
BARS CH (#4)



BARS T (#4)



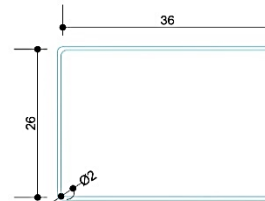
BARS P (#6)



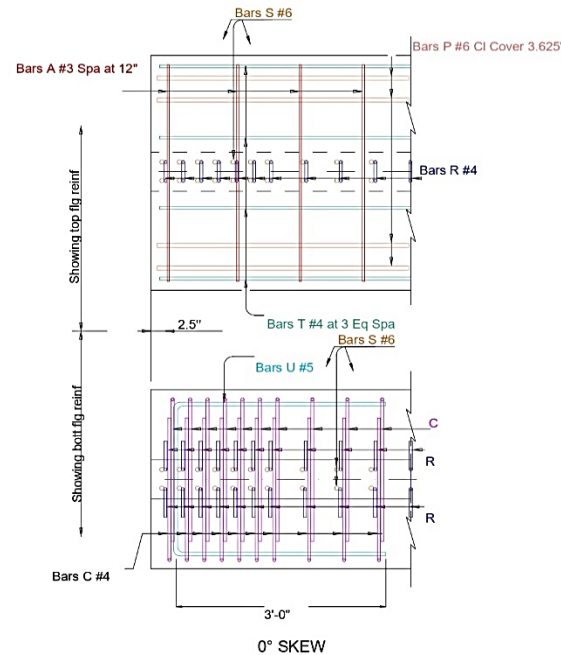
BARS R (#4)



BARS S (#6)



BARS U (#5)

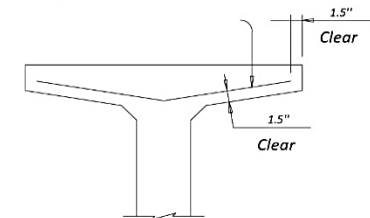


## BILL OF REINFORCEMENT STEEL

BAR	SIZE	TOTAL NO. OF BARS	LENGTH	WEIGHT (lb)
A	# 3	58	3'-3"	72
C	# 4	80	4'-0.25"	215
CH	# 4	40	2'-6"	67
P	# 6	8	15'-0"	182
R	# 4	68	13'-2"	600
T	# 4	4	58'-3"	265
U	# 5	4	8'-2.5"	34
S	# 6	40	5'-7"	337

\* Standard length for Tx70 girder reinforcement

To control top flange cracking that may occur during form removal, additional top flange reinforcing may be placed as shown in girder ends at the Fabricator's option.



OPTIONAL TOP FLANGE REINFORCING DETAIL

Texas A&M University

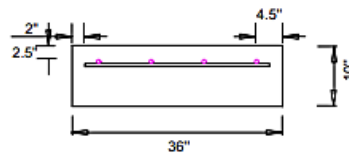
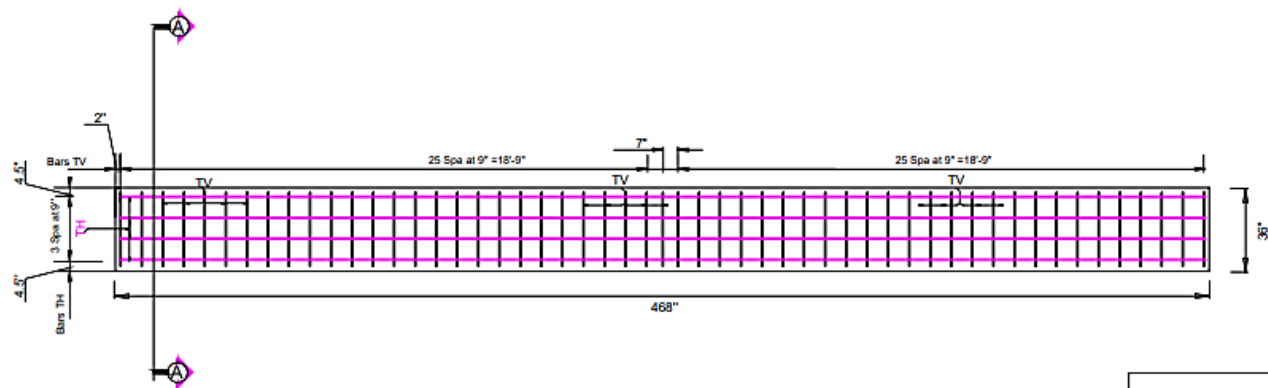
Texas Department of Transportation

TxDOT Project 0-7114

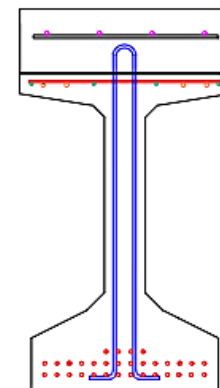
Bar Bending Details

DRAWING NO.	DATE	SCALE
S7114-16	3/28/2023	1:20

## **APPENDIX B: REINFORCEMENT DETAILING FOR THE DECK**



SECTION A-A  
(Scale 1:20)

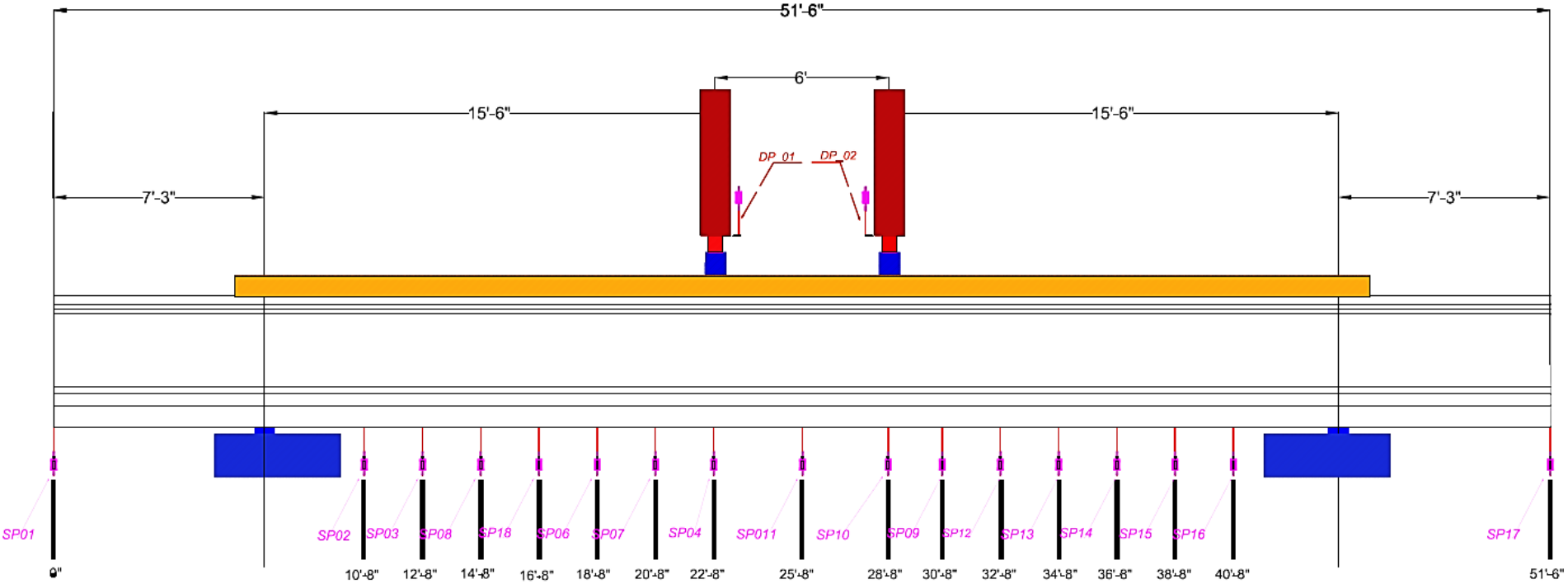


Cross-section Geometry  
(Scale 1:20)

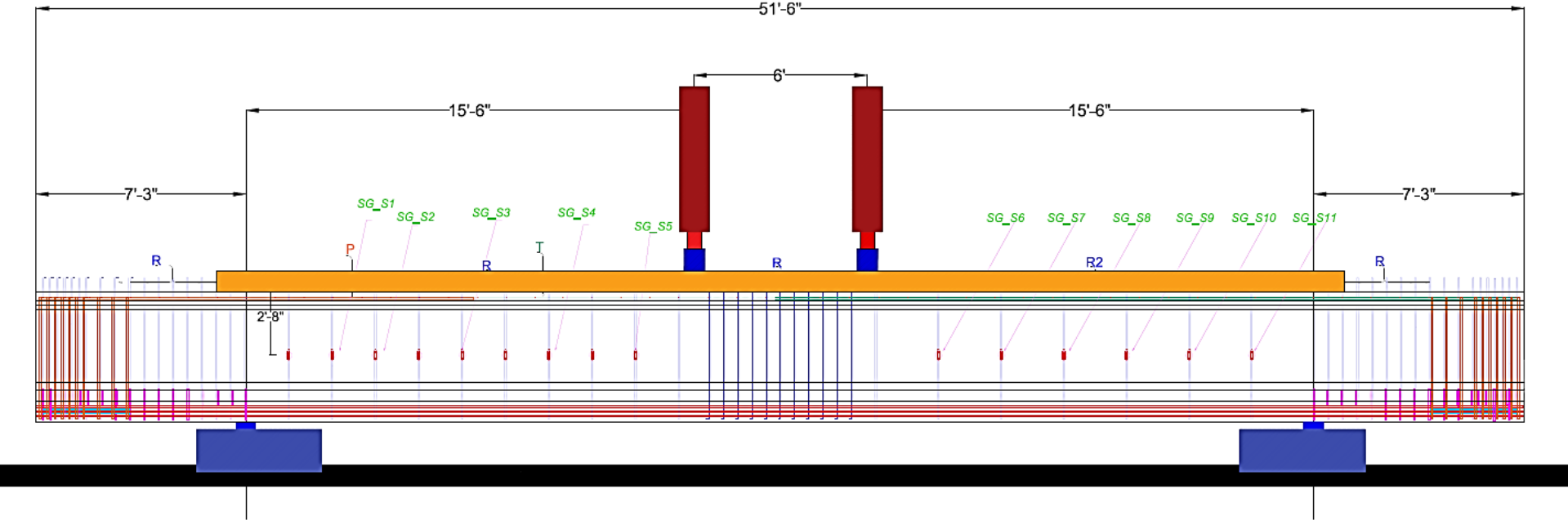
Texas A&M University		
Texas Department of Transportation		
TxDOT Project 0-7114		
Reinforcement Details for Topping Deck		
DRAWING NO.	DATE	SCALE
S7114-01	1/11/2023	1:50

## **APPENDIX C: DETAILED INSTRUMENTATION PLAN AND DRAWING**

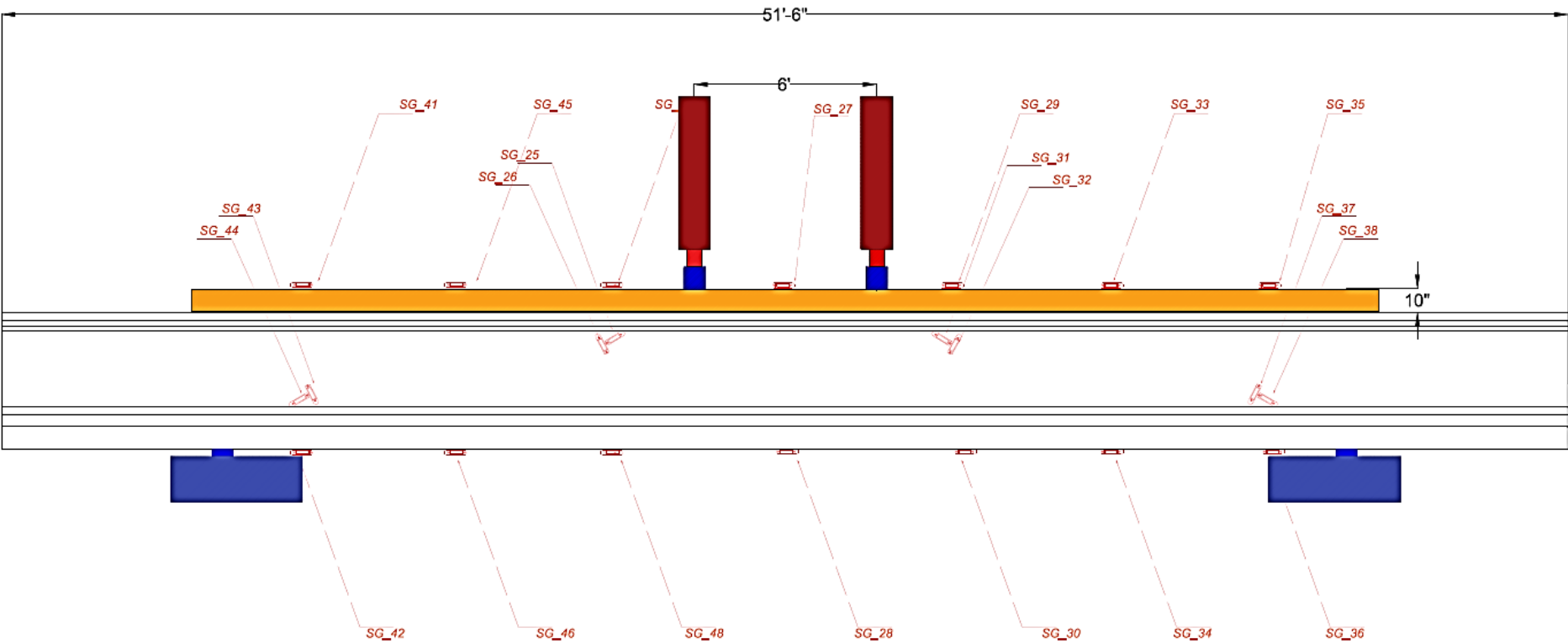
C.1 STRING POTENTIOMETERS



C.2 EMBEDDED STRAIN GAUGES ON R-BARS



C.3 CONCRETE SURFACE STRAIN GAUGES





C.4 LINEAR VARIABLE DIFFERENTIAL TRANSFORMERS

